GLIAL CELL REACTIVITY FOLLOWING BRAIN INJURY AND ITS IMPLICATION FOR CNS REGENERATION

Veronika Schwarz

Graduate School of Systemic Neurosciences

LMU Munich

Dissertation der
Graduate School of Systemic Neurosciences
der Ludwig-Maximilians-Universität München

30th November 2023

Supervisor:

Prof. Dr. Jovica Ninković

Biomedical Center (BMC)

Department of Cell Biology / Anatomy III

Ludwig-Maximilians-University Munich (LMU)

First Reviewer:	Prof. Dr. Jovica Ninković
Second Reviewer:	PD Dr. Florence Bareyre
External Reviewer	Dr. Mónica M. Sousa

Date of Submission:	30th November 2023
Date of Defense:	23rd July 2024

ABSTRACT

Traumatic brain injury (TBI) is the leading cause of morbidity in young adults and is responsible for death and disability in all age groups. TBI patients are often confronted with lifelong cognitive, physical, and emotional restrictions and are furthermore at risk for developing neurological diseases later in life. Glial cells are fundamental in maintaining central nervous system (CNS) function under physiological and pathological conditions. However, excessive, long-lasting glia-mediated neuroinflammation during the chronic injury phase is associated with continuous tissue- and functional loss. Even though prolonged glial responses are generally believed to hinder CNS repair, the implication of reactive glial cells for novel neuronal replacement strategies, such as direct neuronal reprogramming, has largely been neglected. Direct neuronal reprogramming describes the conversion of non-neuronal cells into neurons and has emerged as a novel and promising strategy to repair the damaged brain. Several hurdles that negatively impact the fate conversion process have been identified by now; however, the influence of injury-evoked environmental factors on the neuronal conversion process is largely unknown. Despite the advances over the last years in uncovering molecular mechanisms that shape TBI pathophysiology, a comprehensive understanding of injury-induced glial responses, their impact on neuronal regeneration, and their applicability for neuronal replacement strategies is still incomplete.

Utilizing the remarkable regenerative potential of adult zebrafish, we identified the innate immunity-associated pathways toll-like receptor 2 (TLR2) and chemokine receptor 3 (CXCR3) as pivotal regulators in controlling glial responses following brain injury. Pharmacological inhibition of both pathways alleviated glial reactivity and enhanced tissue restoration. Intriguingly, interference with TLR1/2 and CXCR3 pathways following cortical stab wound injury in adult mice altered the reactivity profile of injury-responsive glia, accompanied by a reduction in astrocyte proliferation and microglia morphology changes within the early post-injury phase. Moreover, we revealed the so-far unknown plastic nature of murine mature oligodendrocytes to de-differentiate into astrocytes via a transitional astroglial/oligodendroglial cell state in response to cortical stab wound injury. Although the physiological function of the oligodendrocyte-derived astrocytes and their

contribution to long-lasting glial reactivity remains unknown, this injury-evoked population may contribute to the starter cell pool targeted during *in vivo* neuronal reprogramming. Lastly, we demonstrated that the injury-induced microenvironment influences the direct neuronal conversion process. By establishing an *in vitro* culture system of postnatal astrocytes with altered growth factor combinations, we identified high mobility group box 2 (HMGB2) as a novel regulator mediating astrocyte-to-neuron conversion.

In summary, this dissertation highlights the impact of environmental factors on glial plasticity and its significance for neuronal replacement strategies. Additionally, modulation of innate immune pathways during the post-injury phase may serve as valuable targets to enhance regeneration in the injured mammalian brain.

TABLE OF CONTENTS

INTRODUCTION

The central nervous system

The nervous system comprises a highly intricate neuronal network crucial for perceiving and coordinating sensations, actions, and reflexes (Kandel et al., 1991). Environmental and body-internal stimuli are sensed by sensory neurons of the peripheral nervous system (PNS), which in turn convey the information to well-defined processing units of the central nervous system (CNS). The CNS immediately processes the information and subsequently instructs peripheral located effector units to induce adequate behavior responses such as body movements or internal organ function adjustments (Purves et al., 2018). Therefore, the CNS can be considered as the processing center of the body (Purves et al., 2018). To protect the vulnerable CNS tissue and ensure continuous function, the two main parts of the CNS, the brain and the spinal cord, are protected in several ways. Both the brain and spinal cord are enwrapped by three protective tissue layers: the dura mater, arachnoid mater, and pia mater, which are collectively known as the meninges (Zigmond et al., 1999). Additionally, to secure further protection, the brain is embedded in the hard bones of the skull and the spinal cord in the vertebral canal of the spine (Zigmond et al., 1999). Moreover, the blood-brain barrier (BBB) and the blood-spinal cord barrier (BSCB) control the exchange of substances between the blood and the CNS tissue. BBB and BSCP restrict the entrance of toxins and pathogens to the CNS and supply the brain with essential nutrients to secure proper CNS function (Bartanusz et al., 2011; Kadry et al., 2020; Knox et al., 2022).

To achieve controlled behavioral responses to internal or external stimuli, the nervous system relies on well-regulated communication processes facilitated by the roughly 86 billion neurons that constitute the CNS (Herculano-Houzel, 2009; Kandel et al., 1991; von Bartheld et al., 2016). The enormous anatomical complexity of the human CNS was first acknowledged by Ramón y Cajal in the late nineteenth century (Kandel et al., 1991). Using the silver staining impregnation method developed by Camillo Golgi some years prior, Cajal was able to label individual CNS cells and proposed that the nervous system is composed of individual signaling units (= neurons), which communicate to each other at specialized intercellular gaps: the synapse (Kandel et al., 1991; Zigmond et al.,

1999). Depending on the number of processes originating from the cell body, Cajal further classified neuronal cells into different categories. Although neuronal cells display tremendous structural heterogeneity, the core function of neurons to transduce signals is independent of the cells' anatomical appearance (Kandel et al., 1991; Zigmond et al., 1999). Next to the 86 billion neurons, the human CNS contains about 86 billion (neuro)glial cells (von Bartheld et al., 2016). At the time of discovery in the late 19th century, the term glia (Greek word for 'glue') resembled the prevailing opinion within the neuroscientific field that glial cells solely serve as an inactive connective scaffold holding neurons in the CNS together (Purves et al., 2018; Zigmond et al., 1999). However, intensive research on glial cells over the last decades has uncovered an undisputable role of these cells in promoting and maintaining proper CNS function (Park & Lee, 2020). Therefore, it is worthwhile to gain closer insights into the function of glial cells in the upcoming chapter.

Glial cells in the CNS

The population of glial cells can be segregated into two distinct classes: micro- and macroglia cells. Microglia in the mature, non-pathological brain are highly ramified cells with small somata and fine processes that are evenly distributed throughout the entire CNS. Microglia account for 5 - 15 % of all cells residing in the CNS (Kettenmann et al., 2011). Within the CNS parenchyma and under normal physiological conditions, microglia occupy their own territorial domains that do not overlap with those of neighboring cells (Sousa et al., 2017). During development, microglia are crucial for establishing functional neuronal circuitries. They eliminate neuronal cells that are not functionally integrated with established circuitries and shape neuronal synapses by selectively phagocyting dendritic spines that do not receive appropriate inputs from presynaptic cells (Colonna & Butovsky, 2017). Besides their important function during early development, microglia also fulfill essential roles in the mature brain. Although the entire functional repertoire of microglia, especially in the adult brain, is still not fully disclosed, the role of microglia in CNS immune defense is undisputable and intensively investigated (Sousa et al., 2017). By dynamically retracting and extending their fine processes, microglia actively monitor their environment to immediately sense and react to perturbations in the CNS (Davalos et al., 2005; Hanisch & Kettenmann, 2007). Despite being part of the CNS' glial cell population, microglia, in

direct contrast to macroglia, do not originate from neuroectodermal tissue but are of endodermal origin as they derive from yolk-sac myeloid progenitors (Sousa et al., 2017). In the murine CNS, these progenitor cells populate the developing CNS via the bloodstream at embryonic (E) day 8.5 – 9.5 once the embryonic circulation is established (Sousa et al., 2017; Speicher et al., 2019). The infiltrated cells locally proliferate and occupy the entire tissue compartment (Bruttger et al., 2015; Lenz & Nelson, 2018). Interestingly, microglia are a self-sustaining population, as throughout the entire mouse lifespan, these cells are efficiently self-renewing (Bruttger et al., 2015; W. Wang et al., 2023).

The CNS macroglia population is comprised of astrocytes and oligodendrocyte lineage cells. Astrocytes (αστρον κψτομς = Greek for star and kytos), the most abundant glial cell population, are star-shaped cells that tile the entire mammalian CNS (Sofroniew, 2020; Verkhratsky & Nedergaard, 2018). Based on their anatomical location and morphology, astrocytes can be classified into at least two distinct astrocytic subtypes: protoplasmic- and fibrous astrocytes (Barres, 2008; Sofroniew & Vinters, 2010). Protoplasmic astrocytes, mainly present in the grey matter, display short, thick, and extensively branched processes. On the contrary, fibrous astrocytes, primarily found in the white matter, exhibit long, thin, and less branched processes. Astrocytes in different brain areas display distinct morphological characteristics accompanied by heterogeneous gene expression profiles (Batiuk et al., 2020; Sofroniew & Vinters, 2010). Intriguingly, even astrocytes of the same anatomical region exhibit distinct transcriptional signatures (Bayraktar et al., 2020), further emphasizing the heterogeneous nature of these cells. Nevertheless, the extent to which the observed heterogeneity is reflected in region-specific functions is still not fully disclosed. Even though protoplasmic astrocytes maintain specific, non-overlapping territories under physiological conditions, their most distal tips are intertwined with those of neighboring astrocytes (Sofroniew & Vinters, 2010). The individual coupling of astrocytes is facilitated through gap junctions or hemichannels, which enables astrocytes to create a highly interconnected network, allowing fast intercellular exchange and distribution of ions and metabolites (Xing et al., 2019). Generally, astrocytes are considered key players in maintaining physiological CNS function (Chen et al., 2020; Sofroniew, 2020). Astrocytes have large cell bodies and possess numerous processes, which are in close contact with neighboring cells (Park & Lee, 2020). The proximity of protoplasmic astrocytes to neuronal synapses, for example, enables

astrocytes to regulate the extracellular concentration of ions and neurotransmitters (Kim et al., 2019). Upon neuronal activity, K^+ ions are released in the extracellular space and subsequently taken up by K^+ channels, which are highly abundant in astrocytes (Bellot-Saez et al., 2017). Similar to K^+ ions, astrocytes can efficiently uptake synaptically released neurotransmitters such as glutamate, γ-aminobutyric acid (GABA), and glycine from the extracellular space (Mahmoud et al., 2019; Sofroniew & Vinters, 2010). In the case of glutamate, for example, astrocytes convert the internalized neurotransmitter via the glutamine synthetase into its precursor glutamine, which in turn is shuttled back to neurons and can hence be resynthesized to glutamate (Mahmoud et al., 2019). Intriguingly, microglia express receptors for several neurotransmitters, including glutamate and GABA (Färber et al., 2005). For example, activating glutamate receptors on microglia instructs diverse cellular responses and alters their homeostatic function (Liu et al., 2009; Zhang et al., 2020). Hence, by clearing K^+ ions and neurotransmitters from the synaptic cleft, astrocytes control microglia activity, modulate neuronal excitability, and thus restrict network hyperexcitability. Insufficient uptake of K^+ ions or neurotransmitters from the extracellular space has been associated with several pathological conditions, including epilepsy, depression, and neurodegenerative diseases (David et al., 2009; Dong et al., 2009; Somjen, 2002). Astrocytes interact not only with neurons or neighboring astrocytes but also cover the cerebral vasculature with their endfeet (Kubotera et al., 2019; Mathiisen et al., 2010). Through this interaction, astrocytes can directly shuttle nutrients from the systemic bloodstream to neurons (Hösli et al., 2022; Sofroniew & Vinters, 2010). The circuitous transport of nutrients through astrocytes is inevitable as, under physiological conditions, the brain parenchyma is separated from the systemic bloodstream by a protective diffusion barrier: the blood-brain barrier (BBB) (Abbott et al., 2006). The BBB is formed by endothelial cells that are connected through tight junctions, in addition to pericytes and astrocyte endfeet (Abbott et al., 2006; Kubotera et al., 2019; Sweeney et al., 2018). Interestingly, astrocytic endfeet covering may not be directly responsible for adequate barrier formation. Instead, astrocytes might support the BBB integrity by maintaining tight junctions between endothelial cells (Knox et al., 2022; Kubotera et al., 2019).

Oligodendrocyte lineage cells, the second macroglial population in the CNS, comprise oligodendrocyte precursor cells (OPCs) that, via multiple differentiation states,

differentiate into mature oligodendrocytes (OLs). Due to the high abundance of the neuron-glial antigen 2 (NG2) on the OPC surface, these precursor cells are also termed NG2-glia (Ampofo et al., 2017; Dimou & Gallo, 2015). NG2-glia are equally distributed throughout the entire CNS and account for roughly 5 % of all parenchymal glial cells (J. Q. Wang et al., 2023). During development and throughout adulthood, NG2-glia differentiate into mature myelinating oligodendrocytes. However, the differentiation process of NG2-glia into mature OLs is region-dependent. For example, in the cortical white matter of the adult murine cerebral cortex, a high proportion of NG2-glia differentiated into mature, myelinating OLs, whereas in the grey matter, most NG2-glia remained in an undifferentiated state (Dimou et al., 2008). The functional implication of this heterogeneity is still not fully disclosed. Myelin-producing oligodendrocytes enwrap neuronal axons and subsequently supply neurons with vital nutrients such as the glial cell line-derived neurotrophic factor (GNDF), brain-derived neurotrophic factor (BDNF) and insulin-like growth factor 1 (IGF-1) (Bradl & Lassmann, 2010; J. Q. Wang et al., 2023). In addition to its nourishing function, myelin sheets further serve as insulators of nerve fibers, thereby modulating the conduction speed of nerve impulses within axons (Mira et al., 2021; Simons & Nave, 2015). In the mature rodent brain and under physiological conditions, NG2-glia maintain a well-controlled homeostatic network. If NG2-glia are differentiating into mature oligodendrocytes or are dying, the remaining gap is immediately sensed and filled by adjacent NG2-glia. Since oligodendrogenesis occurs throughout the entire lifespan, the NG2-glia network is a considerably dynamic system. Within the mature brain and under normal physiological conditions, NG2-glia represent the most proliferative glial population (Dimou et al., 2008; Jäkel & Dimou, 2017).

Macro- and microglia cells are essential for generating a well-balanced, neuron-supportive environment that facilitates proper CNS function. Consequently, any disturbance to this highly dynamic and interconnected system has tremendous aftereffects. Therefore, the forthcoming chapter will examine the consequences of an imbalanced CNS in more detail.

CNS disturbances and functional consequences following brain injury

Nervous system dysfunction arises not only from acute neuronal and glial cell loss caused by stroke or traumatic brain injury (TBI) (Andreone et al., 2020; Giaume et al., 2007) but also occurs in the context of neurodegenerative disorders such as Alzheimer's disease (AD), Parkinson's disease (PD) or Amyotrophic lateral sclerosis (ALS), where neuronal function deteriorates gradually over time (Andreone et al., 2020; Dugger & Dickson, 2017). Whereby aging is the primary risk factor for developing neurodegenerative diseases (Dumurgier & Tzourio, 2020; Hou et al., 2019), TBI occurs frequently among various age groups (Brazinova et al., 2021; Maas et al., 2022). Annually, in the European Union alone, approximately 57,000 deaths and 1.5 million hospitalization admissions are associated with TBIs (Brazinova et al., 2021; Majdan et al., 2017). Although TBI-related hospital admissions are age-independent, a strong correlation between increasing age and concomitant hospitalization admission frequencies and TBI-associated deaths has been reported (Maas et al., 2022) (Fig. 1). TBIs are predominantly caused by external kinetic forces to the head as a result of road traffic accidents, interpersonal violence cases, falls, and sport-related incidents (Abio et al., 2021). Despite the continuous effort to improve the clinical health care of TBI patients to yield better outcomes after injury, patients suffering from TBIs are often facing life-long consequences (Maas et al., 2022). Depending on the severity and the location of the injury, TBI patients are often confronted with impaired cognitive, physical, and emotional functions (Fan et al., 2022). De Silva and colleagues reported that within six months following injury, on average, 25 % of all TBI patients die, an additional 25 % experience moderate or severe disabilities, and only 50 % recover well within the six-month timeframe (de Silva et al., 2009). In addition to the acute risk of facing functional impairments, surviving TBI patients are at an elevated risk of developing neurodegenerative diseases (Abio et al., 2021; Cruz-Haces et al., 2017) and psychiatric disorders later in life (Ponsford et al., 2018). Hence, TBI aftereffects negatively impact the patient's quality of life (Fan et al., 2022). Additionally, considering the extensive post-injury patient care, TBIs bear an enormous economic burden for healthcare systems worldwide (Abio et al., 2021; Maas et al., 2017).

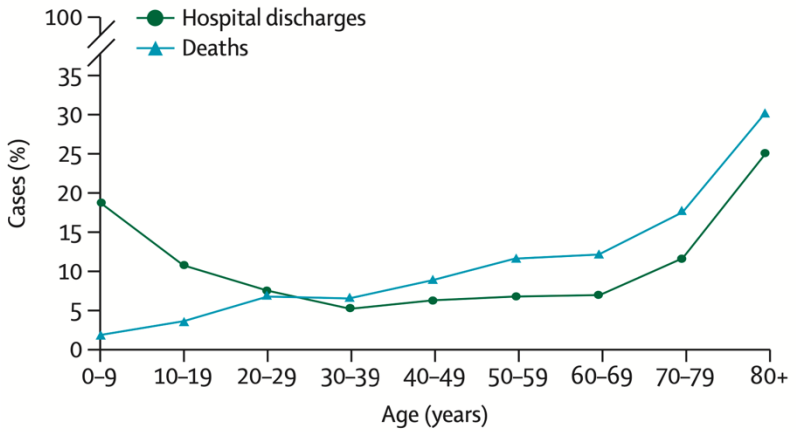

Figure 1: Hospital discharge frequencies and death cases of European TBI patients. Figure reprinted and modified from The Lancet Neurology, 21(11), Maas et al., *Traumatic brain injury: progress and challenges in prevention, clinical care, and research*, 1004-1060, DOI: 10.1016/S1474-4422(22)00309-X, © 2022 Elsevier Ltd, with permission from Elsevier (license number: 5627550017365).

TBI pathophysiology

TBI causes tissue damage of varying severity, with the extent of damage and possible functional impairment strongly dependent on the initial impact (Andriessen et al., 2010). Generally, TBI can be classified as closed head injury (CHI) or penetrating brain injury (PBI) (Ginsburg & Huff, 2023). PBI occurs whenever an object perforates the skull and concomitantly enters and injures the brain parenchyma. PBIs are typically caused by high-velocity objects, such as missiles or projectiles, which strike the brain and result in complex injuries with high mortality rates. On the contrary, PBIs induced by low-velocity objects, such as knives, hammers, or arrows, primarily damage the brain locally, often resulting in better outcomes (Kazim et al., 2011). In CHI, brain damage results from strong external collision forces applied to the head, leading to brain tissue deformation, structural abnormalities, and potential brain circuit dysfunction (Andriessen et al., 2010; Mckee & Daneshvar, 2015). CHIs are the leading cause of falls, traffic accidents, sport-related incidents, and physical abuse (Ng & Lee, 2019). Clinicians commonly assess the injury severity upon hospital admission using the Glasgow Coma Scale (GCS) scoring system. The GCS helps to evaluate the patient's responsiveness, including eye-, verbal- and motor responses, and grades the injury severity in mild (GCS 13-15), moderate (GCS 9-12), or severe (GCS ≤ 8) TBI (Andriessen et al., 2010; Mckee & Daneshvar, 2015). Mild TBIs (mTBIs) account for approximately 90 % of all evaluated TBI cases administered to the hospital (Maas et al., 2022). Although the GCS score is vital to determining adequate treatment

options and prognostications, it is important to emphasize that the GCS score does not capture the patients' pathophysiological circumstances (Ganti et al., 2019; Maas et al., 2022). Consequently, TBI patients of all GCS grades are at risk of experiencing long-term consequences (Mckee & Daneshvar, 2015).

The extent of TBI-induced tissue damage and associated changes in brain function are determined within the primary and secondary injury phases. Primary brain injury occurs due to the direct mechanical disruption of brain tissue during the initial impact, leading to contusion, laceration, and intracranial hemorrhage (Ng & Lee, 2019; Weber, 2012). Thus, primary brain injury results in the destruction of neurons, glial cells, blood vessels, and the BBB, ultimately leading to immediate impairment of brain function (Greve & Zink, 2009; Nasser et al., 2016). Depending on the mechanical impact, TBIs can result in focal or diffuse brain injuries. Focal injuries result from strong collision forces striking the head. Consequently, brain tissue directly underneath (coup) or oppositely (contre-coup) of the impact site is strongly decompressed (Andriessen et al., 2010; Ng & Lee, 2019). In contrast, diffuse injuries are caused by rapid acceleration-deceleration movements of the head upon strong external forces, for example, in high-speed traffic accidents. Fast movements of the soft brain tissue inside the bony skull often cause diffuse axonal injuries (DIA) (Andriessen et al., 2010; Weber, 2012). Axons bear extensive viscoelastic properties, enabling them to restore their normal shape and structure upon deformation, for example, in the case of ordinary head turns. However, sudden translational or rotational forces lead to extensive axonal shearing and stretching that exceeds the axonal viscoelastic capacity. Thus, acceleration-deceleration elicited brain injuries induce widespread axonal damage and brain swellings, correlating to the patient's functional impairment (Ng & Lee, 2019; Weber, 2012).

The primary damage induces many biochemical and cellular events that initiate the secondary injury phase (Karve et al., 2016). Notably, secondary injury cascades are already commenced at the time of injury but are not clinically relevant for hours or even days following the impact (Weber, 2012). The secondary injury phase comprises excitotoxicity, mitochondrial dysfunction, oxidative stress, and neuroinflammation, leading to delayed tissue loss and further neuronal dysfunction (Ng & Lee, 2019; Wofford et al., 2019). Of note, secondary injury mechanisms determine the magnitude of tissue damage and manifest symptom persistence in patients (Karve et al., 2016; Mira et al., 2021). Therefore,

therapeutic interventions typically target secondary injury mechanisms to ameliorate TBI pathophysiology (Wofford et al., 2019).

Neuronal repair strategies to enhance functional regeneration of the injured CNS

Neurodegenerative diseases, or traumatic injury to the brain or spinal cord, result in irreversible neuronal loss, often accompanied by lifelong physical and/or cognitive impairment in most mammals, including humans (Lamptey et al., 2022; Maas et al., 2017). Even though the adult mammalian brain is generally incompetent to regenerate functionally, the brain displays a high degree of plasticity (Grade & Götz, 2017; Jessberger, 2016). Patients diagnosed with PD, for example, start to exhibit clinical symptoms when almost 80 % of the nigrostriatal dopaminergic innervations are lost (Stricker et al., 1990). This observation implies that the human brain functionally compensates for disease-induced alterations, thereby restricting functional impairment and masking disease progression. However, the plastic nature of the mammalian brain is limited, particularly in cases of severe injuries, where a significant number of neurons are lost at the time of injury, and ongoing cell death is evident during the secondary injury phase (Grade & Götz, 2017; Karve et al., 2016; Wofford et al., 2019). Thus, alternative approaches are required to replace lost neurons to foster functional regeneration following TBI. Up to now, three different neuronal replacement strategies have been extensively explored: 1.) Recruitment of endogenous cells from neurogenic niches, 2.) induced conversion of local glial cells into neurons, and 3.) cell replacement therapy using exogenous cells (Barker et al., 2018; Götz & Bocchi, 2021; Grade & Götz, 2017). Transplantation of embryonic tissue, embryonic stem cells (ESCs), and induced pluripotent stem cells (iPSCs) into CNS-injured rodents has been successful in terms of integration and behavior recovery (Falkner et al., 2016; Gaillard et al., 2007; Imai et al., 2023; Michelsen et al., 2015). However, translatability and applicability to humans are (at this point) uncertain. Considering the ethical concern of using fetal or embryonic human tissue and the increased likelihood of immunological graft rejection, it is unlikely that these cells will serve as the primary source for future human transplantations. In contrast, individual patient iPSC-derived transplants will decrease the risk of graft rejection; however, culturing and differentiating patient-specific cells is rather cost-intensive and laborious (Parmar & Björklund, 2020; Stoker et al., 2017). Thus, utilizing

endogenous brain cells for neuronal replacement strategies could represent a safer and less laborious approach to replacing damaged neurons. Hence, the potential of endogenously recruited and reprogrammed cells for neuronal replacement strategies will be examined in more detail in the following chapters.

Adult mammalian neurogenesis and brain injury

If neurons in the mammalian brain die, either in the context of neurodegenerative diseases or as a direct consequence of traumatic injuries, these lost cells cannot easily be replaced. Although the adult mammalian brain can generate new functional neurons from corresponding neural stem cells (NSCs) throughout life, the neurogenic ability is insufficient for adequate tissue repair (Hayashi et al., 2018; Ming & Song, 2011). In rodents, adult neurogenesis is spatially restricted to two distinct brain regions: the subventricular zone of the lateral ventricles (SVZ) and the subgranular zone (SGZ) in the dentate gyrus (DG) of the hippocampus (Ming & Song, 2011) (Fig. 2). NSCs located in the SGZ of the hippocampal DG, give rise to excitatory dentate granule neurons. Newborn neurons in the SGZ of the DG must surpass several developmental stages before being functionally integrated into the persisting hippocampal circuitry (Gonçalves et al., 2016). Rodent studies have demonstrated that adult-born granule cells are crucial for hippocampal-dependent learning and memory formation (Gonçalves et al., 2016; Ngwenya & Danzer, 2019; Ninkovic et al., 2007). In the SVZ, the second adult mammalian stem cell containing niche, NSCs give rise to neuroblasts, which migrate along the rostral migratory stream (RMS) to the olfactory bulb (OB), where they tangentially migrate and mature to mainly GABAergic interneurons and subsequently integrate into the granular cell layer and the glomerular layer of the OB. Hence, adult-generated neurons in the OB are important for sensory processing (Ming & Song, 2011; Ninkovic et al., 2007). Under physiological conditions, neurogenesis is restricted to the hippocampus and the SVZ/OB. However, in response to several pathophysiological events, atypical migration routes of neuronal progenitors have been observed (Arvidsson et al., 2002; Saha et al., 2013; N. Wu et al., 2023). In response to various brain pathologies, SVZ-located progenitor cells significantly increase their proliferation rate and differentiate into neuroblasts (W. Di Lee et al., 2016). These neuroblasts display great migratory capacity and are capable of overcoming long distances

by traveling along blood vessel- and astrocytic networks to reach the lesioned area (Saha et al., 2013; N. Wu et al., 2023) (Fig. 2). The extensive migration of neuroblasts throughout the adult brain tissue is facilitated by individual guidance cues, such as blood-vessel derived BDNF, vascular endothelial growth factor (VEGF), Angiopoetin-1 (ANG-1) or the astrocyte-secreted stromal cell-derived factor-1 alpha (SDF-1α) (N. Wu et al., 2023). However, once the neuroblasts settle in the injured area, only a small proportion of cells differentiate into mature neurons. Most precursor cells give rise to mature astrocytes and oligodendrocytes (Saha et al., 2013). Moreover, in a rodent stroke model, the majority of newly generated neurons in the lesioned area died within six weeks after stroke. Hence, brain injury induces a distinct microenvironment that hampers the long-term survival of the newly generated neurons and is a significant barrier to successful tissue restoration (Arvidsson et al., 2002).

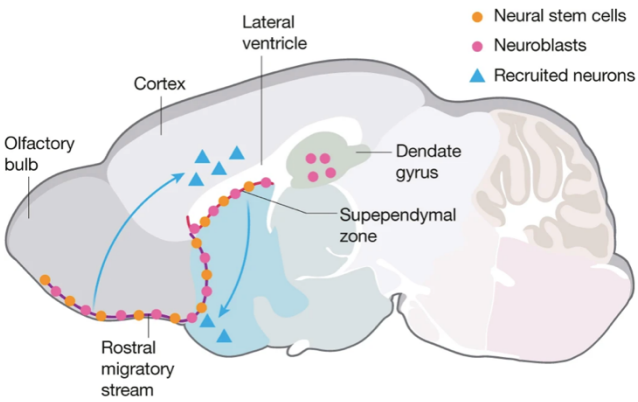

Figure 2: Neurogenic niches and migration routes of new neurons in response to brain injury in the adult rodent brain. Figure adapted and modified from Barker et al., *New approaches for brain repair – from rescue to reprogramming*, Nature, 557(7705):329-334, 2018, DOI: 10.1038/s41586-018-0087-1, © 2018, Macmillan Publishers Ltd. (part of Springer Nature), reproduced with permission from Springer Nature (license number: 5627251329708).

Direct neuronal reprogramming

The functional restoration of disrupted neural circuits has been viewed as the holy grail of regenerative medicine. One promising approach to replace lost neurons is through direct cellular reprogramming, which describes the conversion of one differentiated cell to another without passing through an intermediate pluripotent state (Bocchi et al., 2022; Vasan et al., 2021). The study of Heins et al. in the early 2000s paved the way for glial cells as a valuable source for direct neuronal reprogramming. Forced expression of the neurogenic transcription factor (TF) paired box 6 (Pax6) in postnatal astrocytes enabled glial fibrillary acidic protein^{+} (GFAP^{+}) astrocytes to transform into β-tubulin-III^{+} neurons *in*

vitro (Heins et al., 2002; Walther & Gruss, 1991). Since then, several other TFs, including achaete schute homolog 1 (Ascl1) and neurogenin-2 (Neurog2), have been identified to convert an array of cell types (e.g., astrocytes, pericytes, fibroblasts) into functional neurons *in vitro* (Berninger et al., 2007; Chanda et al., 2014; Karow et al., 2012). However, direct cellular reprogramming cannot only be realized *in vitro*; conversion of local glial cells into neurons has also been achieved *in vivo* (Buffo et al., 2005; Grande et al., 2013; Heinrich et al., 2014; Mattugini et al., 2019). Although glia-to-neuron conversion in the injured murine cerebral cortex was successfully achieved almost 20 years ago, low conversion- and long-term survival rates of the reprogrammed cells were a commonly faced problem (Buffo et al., 2005; Grande et al., 2013). Interestingly, neuronal maturation and survival efficiency were tremendously enhanced whenever TFs were co-transduced with growth factors, including the epidermal growth factor (EGF) or the basic fibroblast growth factor (bFGF) (Grande et al., 2013). Additionally, co-expression of Neurog2 with the pro-survival factor B-cell lymphoma 2 (Bcl2) in combination with an antioxidant treatment following cortical stab wound injury (SWI) was sufficient to convert about 90 % of all retrovirally transduced proliferating glia into neurons. Intriguingly, these converted cells displayed complex pyramidal neuronal morphology and expressed markers reminiscent of layer V pyramidal neurons (Gascón et al., 2016; Youle & Strasser, 2008).

Direct neuronal reprogramming offers unique benefits over other neuronal replacement strategies, such as recruiting endogenous precursors from adjacent neurogenic niches. Although neuroblasts display enormous migratory capacity in response to CNS damage, most of these cells lack the potential to differentiate into mature neurons, and even those that do differentiate exhibit limited long-term survival. In fact, poor survival rates are primarily attributed to the surrounding aversive microenvironment (Arvidsson et al., 2002). Therefore, targeting (glial) cells that contribute to the aversive injury milieu for the direct neuronal conversion process could help alleviate the detrimental and non-regenerative impact of the environment on neuronal maturation and survival. On the other hand, by simultaneously increasing the neuronal pool, lost neurons can be replaced, and ideally, functional recovery can be reestablished (Grade & Götz, 2017).

However, the exact and appropriate time point to induce glia-to-neuron fate conversion after brain injury is relatively unexplored and should be thoroughly investigated in future studies. Initially, glial cell responses to brain insults are vital as these cells restrict

neuroinflammation by separating the injured from the adjacent healthy tissue to preserve neuronal integrity and function. However, long-lasting glial reactivity has been demonstrated to adversely affect neuronal survival and CNS regeneration (Burda et al., 2016; Faden et al., 2016; Mira et al., 2021; Zambusi et al., 2022). Thus, to understand the dual role of activated glia upon brain injury, the reaction of macro- and microglia in response to TBI will be reviewed in more detail in the upcoming chapter.

Immune- and glial cell response following TBI

TBI patients often experience lifelong disabilities in response to brain insults. These detrimental aftereffects are a consequence of the immediate tissue loss caused by the initial damage, which in turn elicits distinct molecular and cellular events, further promoting cellular dysfunction and cell death during the secondary injury phase (Mira et al., 2021; Wofford et al., 2019). One of the key drivers contributing to the degree of secondary tissue damage is the TBI-induced neuroinflammatory environment. Importantly, TBI-induced neuroinflammation is a complex interplay of brain-resident glial cells and peripheral-derived immune cells (Loane & Kumar, 2016). Immune cells play a pivotal role in clearing cellular debris during the acute phase after TBI and release neurotrophic factors to initiate tissue repair and protect the CNS from further infection. However, prolonged, exacerbated neuroinflammation in the chronic phase after TBI can induce further damage and consequently prohibit a return to complete tissue homeostasis (Daglas et al., 2023; Russo & McGavern, 2016).

Microglia

Upon TBI, damaged- or necrotic cells release damage-associated molecular patterns (DAMPs) to alert glial- and peripheral immune cells (Loane & Kumar, 2016). DAMPs comprise a variety of molecules, including proteins and nucleic acids, that are generally localized within the cell and are only released in high amounts upon cellular damage (Kumar & Loane, 2012; Wofford et al., 2019). Microglia express a variety of pathogen recognition receptors (PRRs) through which they can immediately sense extracellularly secreted DAMPs, including High mobility group box 1 protein (HMGB1), S100 proteins, heat shock proteins (HSPs), uric acid, heparin sulfate, and adenosine triphosphate

(ATP) (Braun et al., 2017; Wofford et al., 2019). For example, ATP released from dying cells is sensed by microglia and facilitates the rapid migration and extension of microglial processes toward the site of injury (Davalos et al., 2005; Kettenmann et al., 2011). In response to tissue damage, microglia switch from a surveying to an alerted/activated state accompanied by morphological alterations and increased proliferation. Under physiological conditions, surveying microglia display small cell bodies and thin, highly ramified processes. However, upon activation, microglia exhibit an ameboid morphology characterized by increased cell somata size as well as shortened and thickened processes (Johnson et al., 2023; Kettenmann et al., 2011; Leyh et al., 2021; Q. Li & Barres, 2018; Zheng et al., 2022). In addition to morphological changes, activated microglia release chemokines and cytokines, which provide in part chemotactic cues to recruit peripheral immune cells to the injury site in an attempt to restore brain homeostasis (Alam et al., 2020; Loane & Kumar, 2016; Russo & McGavern, 2016). To conceptualize microglia activity, it was generally accepted that in response to CNS injury, different stimuli drive microglia into either a pro-inflammatory, cytotoxic M1 or an anti-inflammatory, protective M2 polarization state (S. W. Lee et al., 2019; Q. Li & Barres, 2018; Mira et al., 2021). However, with the technical advances over the last years, it has been demonstrated that the microglial M1/M2 polarization theory is far too simplistic. Whether pure M1 or M2 microglial phenotypes exist *in vivo* is questionable, as previous transcriptomic studies have failed to identify these unique polarization states in different pathologies (Colonna & Butovsky, 2017; Ransohoff, 2016). In line with the failure to identify pure M1/M2 polarization states, Izzy and colleagues have revealed a mixed microglial expression profile comprised of pro-inflammatory (e.g., interferon gamma (IFNγ)-related genes) and anti-inflammatory genes (e.g., genes related to interleukin-4 (IL-4) and IL-10 pathways) in a TBI model of controlled cortical impact (CCI) 14 days post-injury (dpi) (Izzy et al., 2019). Therefore, microglia polarization is not a linear development but a highly dynamic, multidimensional, and context-dependent process (Q. Li & Barres, 2018; Ransohoff, 2016).

By clearing cell debris, releasing neuroprotective factors, and promoting neurorestorative processes, activated microglia are beneficial for nervous tissue repair (Herzog et al., 2019; Loane & Kumar, 2016; Prinz et al., 2019; Roth et al., 2014). However, dysregulated or chronically activated microglia release neurotoxic factors, including reactive oxygen species (ROS) or pro-inflammatory cytokines such as interleukin-1 beta (IL-

1β), IL-18, and the tumor necrosis factor alpha (TNFα), which have been associated with prolonged tissue damage and persistent functional impairment following TBI (Kumar & Loane, 2012; Xiong et al., 2018; Xu et al., 2018). Hence, the depletion of chronically activated microglia during the chronic injury phase following TBI significantly alleviated neuronal cell death and increased long-term motor and cognitive recovery of experimental mice (Henry et al., 2020; Rice et al., 2017). Conversely, exacerbated neuronal loss was observed if microglia were absent during injury (Rice et al., 2015). Thus, microglia exert beneficial effects during the early wound-healing phase but acquire a deleterious phenotype promoting post-injury neuronal damage whenever chronically activated (Loane & Kumar, 2016; Shao et al., 2022).

Leukocytes

TBI disrupts the BBB, which promotes blood-circulating neutrophils, monocytes/macrophages, and lymphocytes to populate the brain tissue (Kumar & Loane, 2012). Importantly, peripheral immune cells display distinct temporal infiltration kinetics upon tissue damage (Gadani et al., 2015; Gyoneva & Ransohoff, 2015; Jin et al., 2012) (Fig. 3). Upon CCI, Jin and colleagues demonstrated that cluster of differentiation 45^+/protein gamma response 1^+ ($CD45^+/Gr1^+$) neutrophil numbers peak 1 dpi and decline by 7 dpi. Of note, increased expression of the vascular adhesion molecules E-selection (CD62E) and the intracellular adhesion molecule 1 (CD54) on endothelial cells greatly enhance neutrophil transmigration to the brain parenchyma (D. W. Simon et al., 2017). Interestingly, in the ischemic brain, a second wave of infiltrating neutrophils has been observed to occur from 7 to 15 dpi (Weston et al., 2007). Like neutrophils, monocytes get recruited to the impact site early in the acute phase (Alam et al., 2020; Gadani et al., 2015). Based on surface marker expression and their distinct functional profiles, two classes of blood monocytes have been identified: 1.) $Ly6C^{high}$ monocytes, which express high levels of the CC-chemokine receptor 2 (CCR2) and low levels of the C-X3-C motif chemokine receptor 1 (CX3CR1) and 2.) $Ly6C^{low}$ monocytes, which express high levels of CX3CR1. In response to injury, different chemokine attractants, including the CC-chemokine ligand 2 (CCL2), guide $Ly6C^{high}$ monocytes to the site of injury, where they differentiate into macrophages ($CD45^{high}/CD11b^+$) (Gadani et al., 2015). Following CCI, macrophage numbers peak at 1 dpi

and gradually decrease to baseline level by 7 dpi (Jin et al., 2012). Infiltration of neutrophils and macrophages in response to brain damage has beneficial and detrimental consequences for CNS repair. In the ischemic brain, neutrophil infiltration positively correlates with the injury volume (Jayaraj et al., 2019; Weston et al., 2007). Moreover, recruited neutrophils secrete a battery of effector molecules, including TNFα, different metalloproteinases, and ROS (Alam et al., 2020; Corps et al., 2015; Gadani et al., 2015). The release of the factors mentioned above causes further breakdown of the BBB and induces secondary neuronal death (Corps et al., 2015). Therefore, neutrophils have traditionally been considered detrimental to tissue repair. In contrast to the prevailing deleterious role, neutrophil depletion prior to spinal cord injury (SCI) in mice exhibited worse functional hindlimb recovery, which was accompanied by delayed astrocyte reactivity, suggesting that infiltrating neutrophils may orchestrate local glial reactivity (Corps et al., 2015; Stirling et al., 2009; J. Wang, 2018). Yet, the entire spectrum of neutrophil function is still not fully disclosed and requires further investigation (Corps et al., 2015). Like neutrophils, macrophages also have a beneficial role in brain repair. They phagocytose cell debris and release tissue-protective factors such as the glial cell line-derived neurotrophic factor (GDNF), BDNF, and IL-10 to aid tissue repair (Gadani et al., 2015). Besides their tissue-protective function, monocyte-derived macrophages also bear harmful properties, especially in the chronic phase after TBI (Corps et al., 2015). One prominent chemoattractant to direct blood-derived monocytes to the injury site is the chemokine ligand CCL2, which is abundantly present in the injured environment. Previous studies demonstrated that brain-injured mice lacking CCL2 or its receptor CCR2 display altered cytokine expression profiles and improved functional recovery in the late phases following injury (Hsieh et al., 2014; Semple et al., 2010). Upon CCI, the number of infiltrated macrophages was significantly reduced by 80 – 90 % in $CCR2^{-/-}$ mice compared to controls. In line with the reduction in macrophage cell number, $CCR2^{-/-}$ mice displayed increased neuronal density and improved functional recovery of locomotor and cognitive function 8 weeks post-injury (Hsieh et al., 2014). Moreover, stab wound-injured $CCR2^{-/-}$ mice exhibited increased astrocyte proliferation and reduced glial scar formation (Frik et al., 2018), highlighting the impact of monocytes on regulating long-term glial responses. Thus, monocyte/macrophage populations comprise somewhat opposing roles in response to injury.

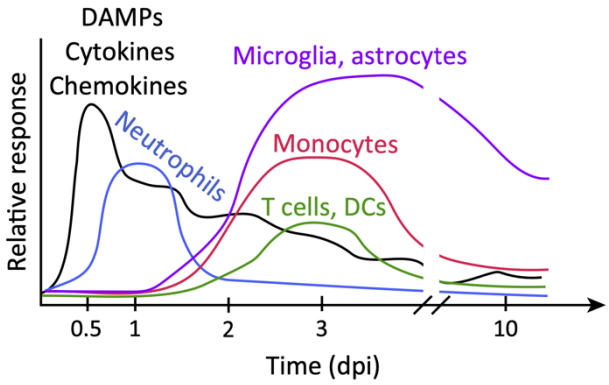

Figure 3: Temporal infiltration and reactivity profile of TBI-induced mediators. Figure reprinted and modified from Trends in Pharmacological Sciences, 36(7):471-80, 2015, Gyoneva and Ransohoff, *Inflammatory reaction after traumatic brain injury: Therapeutic potential of targeting cell-cell communication by chemokines*, DOI: 10.1016/j.tips.2015.04.003, © 2015, Elsevier Ltd, with permission from Elsevier (license number: 5627670999939).

Astrocytes

Astrocytes react to a multitude of CNS disorders, including traumatic injuries, autoimmunity, infections, cancer, and neurodegenerative diseases. Astrocyte reactivity is characterized by morphological, molecular, and functional changes that affect CNS function (Escartin et al., 2021; Sofroniew, 2020). Of note, astrocyte reactivity should not be perceived as a uniform process; instead, astrocytes can acquire different reactive states that strongly depend on the pathological context (Burda et al., 2016; Hasel et al., 2021; Sofroniew, 2020). Independent of the pathology, one hallmark of reactive astrocytes is the increased expression of intermediate filaments such as GFAP and vimentin (Michinaga & Koyama, 2021; Schiweck et al., 2018). Furthermore, astrocytes display cellular hypertrophy characterized by enlarged cell bodies and increased process number, thickness, and length (Acaz-Fonseca et al., 2019; Sofroniew & Vinters, 2010). Although all reactive astrocytes share common morphological features, the exact astrocytic reaction profile is determined by the nature, severity, and location of the tissue damage (Mattugini et al., 2018; Schiweck et al., 2018). Upon acute and diffuse trauma, astrocytes elicit transient upregulation of intermediate filaments, including GFAP, and exhibit minor and reversible hypertrophy. Although reactive astrocytes undergo profound morphological changes, in this pathology, astrocytes do not proliferate and maintain their physiological tiling properties (Sofroniew & Vinters, 2010; Wilhelmsson et al., 2004). On the contrary, upon severe TBI, hypertrophic

astrocytes become polarized and extend their long processes toward the impact site (Bardehle et al., 2013). Additionally, severe tissue damage triggers astrocytes near the impact site to proliferate (Schiweck et al., 2018). Although different experimental TBI models have observed proliferating GFAP$^+$ astrocytes in the acute phase after injury, the peak of astrocyte proliferation, however, ranges between 3 days after CCI (Susarla et al., 2014) and 5 days in response SWI (Frik et al., 2018). In the case of penetrating TBI, such as SWI, reactive astrocytes neglect their domain properties and intrude their processes through individual astrocytic territories. The substantial GFAP increase around the impact site results solely from accumulated, polarized, and intermingled astrocytic processes and not from migrating GFAP$^+$ astrocytes, as live imaging has depicted no astrocytic migration away or towards the injury site (Bardehle et al., 2013; Frik et al., 2018; Lange Canhos et al., 2021). Interestingly, astrocyte morphology strongly correlates with the distance to the injury site. GFAP$^+$ astrocytes in the immediate injury vicinity display prominent cellular hypertrophy accompanied by process polarization. Cells closer to the injury site redirect many of their processes toward the impact site, whereas astrocytes further apart only appear hypertrophic but do not reveal any preferences on process orientation (Schiweck et al., 2018) (Fig. 4).

Astrocyte reactivity is inevitable for preserving tissue integrity and for maintaining CNS function. Upon injury, reactive astrocytes control secondary tissue damage by engulfing cellular debris (Morizawa et al., 2017; G. L. Yu et al., 2021) and by forming an astrocytic border around the injury site to segregate the damaged and inflamed tissue from the nearby healthy tissue. Several loss-of-function studies have highlighted the essential role of border-forming astrocytes in BBB repair and neuronal tissue protection. Loss or attenuation of proliferating astrocytes in different rodent TBI models generally resulted in increased spread of inflammation and prominent neuronal loss, often accompanied by functional deficits (Sofroniew, 2015, 2020). Moreover, TBIs negatively impact normal, homeostatic astrocyte function, including glutamate buffering, which ultimately contributes to the extent of secondary brain injury following TBI (Mira et al., 2021). Upon brain damage, an increase in extracellular concentration of excitatory amino acids, including glutamate, has been observed (Amorini et al., 2017; Mahmoud et al., 2019). To prevent excessive glutamate concentrations under physiological conditions, astrocytes reuptake glutamate from the synaptic cleft via the excitatory amino acid transporter 1

(EAAT1 or GLAST) or EAAT2 (GLT-1) (Karve et al., 2016; Mira et al., 2021). Previous post-mortem human TBI tissue studies revealed a significant decrease in glial GLAST and GLT-1 expression (Beschorner et al., 2007; Van Landeghem et al., 2006). Thus, downregulation of the glial glutamate transporter in the injured brain enhances excessive glutamate concentration in the extracellular space, which may promote excitotoxicity-induced neurodegeneration (Karve et al., 2016). In line with this thought, blocking GLAST and GLT1 in rats using antisense oligonucleotides triggered an increase in extracellular glutamate and resulted in excitotoxicity and neurodegeneration (Rothstein et al., 1996).

Although astrocytes play an important role in maintaining BBB integrity under physiological conditions, the impact of reactive astrocytes on BBB maintenance and repair is controversial (Zhou et al., 2020). Previous studies revealed that astrocyte-derived molecules, including ANG-1, sonic hedgehog (SHH), retinoic acid (RA), insulin-like growth factor 1 (IGF1), or GDNF, can boost BBB integrity not only by limiting endothelial cell apoptosis but also by increasing tight junction reassembly (Burda et al., 2016; Y. Zhou et al., 2020). Contrary, injury-induced IL1-β secretion triggered astrocytes to release VEGF-A resulting in the downregulation of the endothelial proteins claudin-5 (CLN-5) and occludin, which subsequently disrupted the BBB (Argaw et al., 2012; Burda et al., 2016; Michinaga & Koyama, 2019). In addition, astrocyte-secreted apolipoprotein-E (APOE) has been described as a potent regulator of BBB integrity. A recent study by Main and colleagues demonstrated that the acute decrease of APOE levels in the early days following CCI correlates with BBB dysfunction (Main et al., 2018). APOE controls BBB integrity by signaling through Low-Density Lipoprotein Receptor-Related Protein 1 (LRP1), which suppresses the pro-inflammatory cyclophilin A (CypA)-nuclear factor-κB-matrix (NF-kB)-metalloproteinase-9 (MMP-9) pathway in pericytes (Bell et al., 2012). In response to injury, the reduction of APOE levels at 1 dpi increases the production and activity of MMP-9 in pericytes at the neurovascular unit (NVU), resulting in acute pericyte loss and reduced expression of the tight-junction proteins zonula occludens-1 (ZO-1) and occludin, which concomitantly resulted in increased BBB permeability. Of note, the time-dependent increase of APOE 3 - 7 days following CCI correlated with reduced MMP-9 levels and attenuation of BBB dysfunction (Main et al., 2018). Taken together, in the acute phase following TBI, reactive astrocytes play fundamental roles in restraining inflammation to prevent further tissue loss; however, by a multitude of signaling mechanisms, reactive

astrocytes can actively influence inflammation progression and even induce direct neuronal cell death.

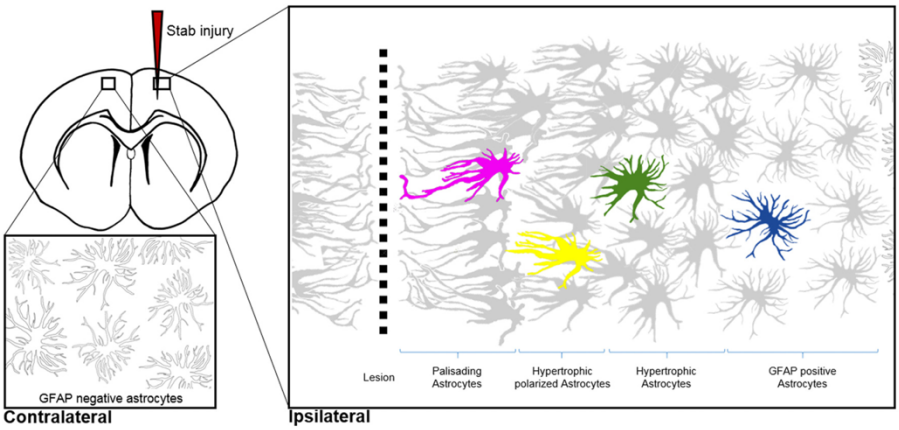

Figure 4: Reactive astrocytes display heterogeneous morphological characteristics in response to cortical stab wound injury. Figure adapted and modified from Schiweck et al., *Important shapeshifter: Mechanisms allowing astrocytes to respond to the changing nervous system during development, injury and disease*, Frontiers in Cellular Neuroscience, 12:261, 2018, DOI: 10.3389/fncel.2018.00261, © 2018 Schiweck, Eickholt and Murk. This figure belongs to an open-access article distributed under the terms of the Creative Commons Attribution-Noncommercial License (https://creativecommons.org/licenses/by-nc/4.0/), which permits the use, distribution, and reproduction in any medium or format.

NG2-glia

Like microglia, NG2-glia are motile and highly dynamic cells that continuously extend and retract their processes to surveil their local environment (Hughes et al., 2013). Under physiological conditions, NG2-glia maintain a constant cell density and preserve their territorial organization through self-repulsion. Consequently, loss of NG2-glia by differentiation, death, or ablation induces immediate migration and proliferation of neighboring cells to restore cell density (Hughes et al., 2013). In alignment with the continuous surveillance of their environment under physiological conditions, CNS injuries trigger rapid NG2-glia responses. Upon detrimental stimuli, NG2-glia exhibit increased levels of NG2 messenger ribonucleic acid (mRNA) and immunoreactivity (Levine, 1994) alongside acute hypertrophy and polarization of their processes towards the impact site (Dean et al., 2023). Furthermore, NG2-glia rapidly migrate to the injured area and strongly expand their cell numbers between 2 - 6 days following SWI, thereby neglecting their well-organized homeostatic network (Buffo et al., 2005; Simon et al., 2011; von Streitberg et al., 2021). Interestingly, live imaging *in vivo* revealed a heterogeneous response of NG2-glia upon SWI. Firstly, the NG2-glia response depended on the distance to the injury, whereby

cells in direct proximity to the injury core exhibited stronger reactions than cells further away. Of note, hypertrophy, migration, and polarization of NG2-glia correlated substantially with the distance to the injury; however, proliferation appeared to be distance-independent. Secondly, NG2-glia reactivity was more pronounced after a stab- than punctate wound injury, suggesting that the injury severity strongly impacts the NG2-glia reaction (von Streitberg et al., 2021). Intriguingly, NG2-glia reactivity is essential for early wound healing processes as the reduction of proliferating NG2-glia in stab wound-injured mice resulted in delayed wound closure at 4 and 7 dpi (von Streitberg et al., 2021). However, the long-term impact of TBI-induced NG2-glia responses on disease progression is not well understood (Dean et al., 2023; Jäkel & Dimou, 2017).

TLR2 and CXCR3 pathway signaling and their role in neuroinflammation following brain injury

Toll-like receptor 2 (TLR2)

Toll-like receptors (TLRs) are one of the earliest and most studied PRRs and play essential roles in activating the innate immune system (D. Li & Wu, 2021). TLRs are composed of a variable number of leucine-rich repeats (LRRs) at the N-terminus, a transmembrane domain, and a C-terminal Toll/interleukin-1 receptor (TIR) domain (C. Y. Chen et al., 2019). N-terminal resident LRRs form horseshoe structures, which facilitate pattern recognition, whereby the C-terminal TIR domain binds different adaptor molecules to induce downstream signaling (C. Y. Chen et al., 2019). To date, twelve different TLRs have been characterized in mice and ten in humans, which can recognize an array of pathogen-associated molecular patterns (PAMPs) or endogenous DAMPs. Based on their sequence similarities, TLRs can be subdivided into six subfamilies, whereby TLRs of the same subfamily tend to recognize similar molecular patterns. In addition, to further increase their recognition specificity, TLRs form hetero- or homodimers. Heterodimerization of TLR2 with TLR1, for example, facilitates the recognition of triacylated lipopeptides, whereas TLR2 dimerization with TLR6 enables the recognition of diacylated lipopeptides (Crack & Bray, 2007; D. Li & Wu, 2021). Furthermore, TLRs can be divided into two distinct groups based on their subcellular localization on plasma- or

endosomal membranes (C. Y. Chen et al., 2019). TLRs expressed on endosomal membranes (TLR3, 7, 8, 9) detect mainly nucleic acids of pathogenic microorganisms, whereas plasma membrane-based TLRs (TLR1, 2, 4, 5, 6, 10) profoundly recognize membrane components of invading microorganisms or endogenous ligands such as lipids, lipoproteins, and proteins (D. Li & Wu, 2021). Upon ligand binding and TLR dimerization, binding of one or more adaptor molecules to the cytoplasmatic TIR domain drives downstream signaling through myeloid differentiation primary response 88 (MYD88)- or TIR domain-containing adaptor-inducing interferon-β (TRIF)-dependent pathways (D. Li & Wu, 2021). The majority of TLRs (TLR2, 4, 5, 7, 9) signal through the adaptor protein MYD88-dependent pathway, whereas TLR3 and 4 initiate downstream signaling through the TRIF-dependent pathway (C. Y. Chen et al., 2019; Crack & Bray, 2007). MYD88- and TRIF induction activates inflammatory TFs such as NF-κB, interferon regulatory factors 3, 5, and 7 (IRF3, 5, 7), and the activator protein-1 (AP-1), resulting in an increased expression of inflammatory cytokines and type I interferons (C. Y. Chen et al., 2019; Crack & Bray, 2007; Kawai & Akira, 2007, 2010; Z. Wu et al., 2021) (Fig. 5).

Among all TLRs, TLR2 plays a key role in molecular pattern recognition. So far, TLR2 is the only receptor that forms functional heterodimers with additional TLRs (TLR1/6) and interacts with other non-TLR molecules (Oliveira-Nascimento et al., 2012). Through these interactions, TLR2 possesses a remarkable capacity to recognize a multitude of PAMPs originating from different bacteria and fungi (D. Li & Wu, 2021; Oliveira-Nascimento et al., 2012). TLR2 signaling is not only induced by PAMPs but also by endogenous ligands (DAMPs), including HMGB1 and HSPs that are released from damaged or dying cells following trauma, including TBI (Curtin et al., 2009; Oliveira-Nascimento et al., 2012; Wofford et al., 2019). Interestingly, TLR2 expression is not restricted to classical immune cells (Oliveira-Nascimento et al., 2012) but can also be found on several brain-resident cells, including microglia (Olson & Miller, 2004), astrocytes (Bowman et al., 2003), oligodendrocytes (Lehnardt et al., 2006) and even neurons (Tang et al., 2007). Notably, brain-injured TLR2-deficient mice exhibited lower expression of inflammatory cytokines and chemokines, which correlated with reduced injury size and improved behavioral performance of experimental animals (Babcock et al., 2006; Lehnardt et al., 2007; Z. Q. Yu & Zha, 2012). Thus, these studies depict a pivotal role of TLR2 signaling in regulating

inflammatory modulators that can subsequently alleviate the extent of the secondary brain damage.

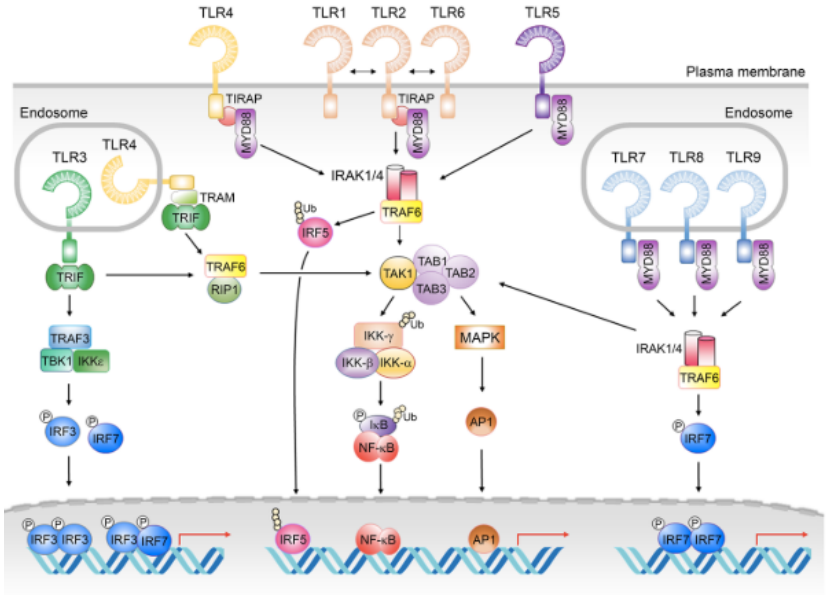

Figure 5: TLR activation and subsequent downstream signaling triggers the release of pro-inflammatory mediators. Figure adapted and modified from Chen et al., *Beyond defense: regulation of neuronal morphogenesis and brain functions via Toll-like receptors,* Journal of Biomedical Sciences, 26(1):90, 2019, DOI: 10.1186/s12929-019-0584-z.

Chemokine receptor 3 (CXCR3)

Chemoattractant cytokines (chemokines) are 8 - 15 kDa small, secreted proteins comprised of roughly 70 - 90 amino acids, which are best known to attract leukocytes and navigate their migration during inflammatory responses (Cartier et al., 2005; Koper et al., 2018). However, besides their role in chemotaxis, chemokines are implicated in a multitude of other biological processes, including cell adhesion, phagocytosis, cytokine secretion, cell activation, proliferation, apoptosis, and angiogenesis (Cartier et al., 2005; Ramesh et al., 2013). To date, around 50 chemokines have been identified, divided into four subtypes (XC, CC, CXC, and CX3C) based on the number and spacing of cysteine (C) residues in their sequence (Cartier et al., 2005; Koper et al., 2018; Rostène et al., 2007). The presence of the glutamic acid-leucine-arginine (ELR) motif near the N-terminus allows further subcategorization of CXC into ELR^+ or ELR^- chemokines (Müller et al., 2010). Chemokines mediate their biological function through seven transmembrane domain G protein-coupled receptors (GPCRs) located on the cell surface. Chemokine receptors are categorized into

four distinct subtypes, depending on the chemokine class that interacts with the respective receptor: XCR, CCR, CXCR, and CX3CR (Cartier et al., 2005; Koper et al., 2018). Most chemokine receptors interact with multiple chemokines; even individual chemokines can bind to different chemokine receptors (Nomiyama et al., 2011). Chemokine binding triggers conformational changes in the chemokine receptor and induces activity by dissociating the heterotrimeric G protein into its α- and βγ subunit (Cartier et al., 2005; Koper et al., 2018). Importantly, downstream signaling can be mediated simultaneously by the α- and βγ subunit (Cartier et al., 2005). Chemokine receptor activation often induces an array of phospholipid-modifying enzymes, mitogen-activated protein kinases (MAPK), and small G proteins, which modulate cell migration by altering actin polymerization, cell adhesion, and membrane protrusion formation (Bachelerie et al., 2014; Gyoneva & Ransohoff, 2015).

Chemokines are often exclusively seen in the context of (neuro)inflammation as inflammatory chemokines are released at high levels after injury. Secretion of inflammatory chemokines in the extracellular space attracts and recruits effector cells, such as monocytes or effector T-cells, to the injury site. In contrast to inflammatory chemokines, so-called homeostatic chemokines are ubiquitously expressed in lymphoid tissues as well as other organs, where they mediate homeostatic trafficking and homing of immune cells (Cartier et al., 2005; Gyoneva & Ransohoff, 2015; Müller et al., 2010; Zlotnik & Yoshie, 2012). In addition, a minority of chemokines are classified as dual-function chemokines, as they exhibit both inflammatory and homeostatic properties (Zlotnik & Yoshie, 2012).

The chemokine receptor 3 (CXCR3) belongs to the CXC-type receptor family and fulfills essential roles in health and disease (Koper et al. 2018). CXCR3 activity is mediated by the binding of the IFNγ-inducible, ELR^- inflammatory chemokines CXCL9, CXCL10, and CXCL11. Under physiological conditions, the expression of these three chemokines in non-lymphoid tissue is negligible. However, during infection, injury, and inflammatory responses, several cytokines, most prominently IFNγ, induce strong upregulation of CXCL9, 10, and 11 (Müller et al., 2010). Even though CXCL9, 10, and 11 bind the same receptor, they exhibit unique temporal and spatial expression patterns during inflammatory responses and display different receptor binding properties (Müller et al., 2010; Van Raemdonck et al., 2015). In contrast to rodents, humans possess three splice variants of CXCR3: CXCR3-A, CXCR3-B, and CXCR3-alt (Koper et al., 2018; Van Raemdonck et al., 2015).

The splice variant CXCR3-A is abundantly expressed by $CD4^+$ T helper type 1 (Th1) cells, naïve and memory $CD8^+$ T cells, natural killer cells, and activated B cells. CXCL11 has the highest affinity for CXCR3-A, whereas CXCL9 has the lowest (Van Raemdonck et al., 2015). Activation of CXCR3-A triggers classical inflammatory chemokine-induced cellular responses, including chemotaxis, proliferation, and cell survival. Similar to CXCR3-A, CXCL11 binding to CXCR3-alt induces cellular chemotaxis of CXCR3-alt-expressing cells. In contrast, the CXCR3-B splice variant, which is mainly present in endothelial cells, reduces DNA synthesis, induces apoptosis, and suppresses blood vessel growth (Koper et al., 2018; Lasagni et al., 2003; Nguyen et al., 2023; Van Raemdonck et al., 2015). In addition to CXCL9, 10, and 11, CXCR3-A and CXCR3-B are activated by the platelet-derived chemokines CXCL4 and CXCL4L1. Contrary to CXCL9, 10, and 11, these chemokines are not IFNγ-inducible but primarily secreted by activated platelets (Van Raemdonck et al., 2015). Notably, CXCR3 expression is not restricted to blood-circulating immune cells but can also be detected in microglia, astrocytes (Biber et al., 2002), oligodendrocytes (Omari et al., 2005), and neurons (Goldberg et al., 2001).

Extracellular matrix changes and functional recovery following CNS injury

For a long time, it was believed that CNS neurons lack regenerative potential. However, this view was partially challenged by the pioneering experiments of Aguayo and his colleagues in the early 1980s. Aguayo et al. revealed that CNS neurons that sustained an axonal injury close to the cell body partially re-grew their axons, but only if they were surrounded by a permissive environment, such as peripheral nerve grafts (Benfey & Aguayo, 1982; David, S; Aguayo, 1981; Siebert et al., 2014). Further experimental studies corroborated Aguayo's findings (Fernandes et al., 1999; Hossain-Ibrahim et al., 2006; Mason et al., 2003), which led to the assumption that CNS neurons generally possess the capacity to regenerate axons; however, the damaged CNS comprises an inhibitory environment that overall hampers axonal regeneration (Quraishe et al., 2018; Siebert et al., 2014).

The regeneration-unfavorable environment is evoked by micro- and macroglia cells that react to CNS insults. Glial cell activation is critical for initial debris clearance and the formation of a compact border to limit further inflammatory damage and preserve tissue

integrity (Adams & Gallo, 2018; Dias et al., 2021). Severe CNS damage, however, results in long-term border formation (also known as scar tissue), which acts as a permanent barrier that negatively impacts neuronal regeneration and CNS repair (Dias et al., 2021; Kjell & Götz, 2020). The scarring tissue comprises a heterogeneous mix of brain-resident and invading blood-derived cells, and its composition depends strongly on the injury type and damage severity. Scar tissue following SCI, for example, is typically characterized by a lesion core that is primarily composed of stromal-derived fibroblasts and inflammatory immune cells and an adjacent glial border composed of reactive glial cells (Bradbury & Burnside, 2019; Dias et al., 2021; Kjell & Götz, 2020). Intriguingly, small stab wound lesions restricted to the cerebral cortex trigger pronounced reactive gliosis; however, a prominent fibrotic core, as seen after SCI, is missing (Buffo et al., 2008; Dias et al., 2021; Frik et al., 2018). On the contrary, larger stab lesions, harming either cortical-striatal or only cortical areas, trigger robust glial reactions and additionally exhibit fibrotic scar tissues (Dias et al., 2021).

Chondroitin sulfate proteoglycans (CSPGs) are extensively synthesized and secreted in the extracellular space in response to CNS injury (George & Geller, 2018; Silver & Miller, 2004). CSPGs are glycoproteins characterized by a core protein to which unbranched, sulfated glycosaminoglycan (GAG) sugar chains are attached. Based on the core protein, CSPGs are additionally categorized into lecticans, phosphacan, and NG2 (George & Geller, 2018). Importantly, CSPGs are essential in CNS pathophysiology and critical for terminating brain plasticity during development (Gundelfinger et al., 2010). In the adult mammalian brain, specialized extracellular matrix (ECM) structures, termed perineuronal nets (PNNs), enwrap the soma, proximal dendrites, and the initial axonal segments of parvalbumin (PV)-expressing interneurons (Brückner et al., 1993; Song & Dityatev, 2018). PNNs are composed of hyaluronic acid (HA), which serves as backbones on which CSPGs of the lectican family can bind. Additionally, these structures are stabilized by link proteins, such as the cartilage link protein 1 (HAPLN1) and Tenescin-R (Tn-R) (Song & Dityatev, 2018). Interestingly, increased expression of PNN-related components during postnatal development correlates with the maturation of PV interneurons and consequently closes the critical period for synaptic plasticity (George & Geller, 2018; Gundelfinger et al., 2010; Reichelt et al., 2019). In response to brain injury, a variety of (reactive) cell types synthesize and deposit different CSPGs in the damaged area. Simultaneously, CSPGs, as part of PNN structures, are lost in the injury-adjacent regions (Harris et al., 2009). The selective loss of

CSPGs from PNNs *in vivo* might be an intrinsic regulatory mechanism to increase synaptic plasticity. However, the presence of the newly synthesized CSPGs in the lesioned area, used to isolate the damaged area from the adjacent healthy tissue, may repel axonal outgrowth as it has been demonstrated in several *in vitro* assays before (Dou & Levine, 1994; Harris et al., 2009; McKeon et al., 1991). Degradation of CSPG CAG chains *in vivo*, using the bacterial chondroitinase ABC, improved functional recovery after SCI (Bradbury et al., 2002), further validating the inhibitory nature of CSPGs in the chronic phase following injury. Besides the negative aspects of CSPG deposition during the chronic phase, selected CSPGs are vital for wound healing processes during the early stages following injury. For example, CCI in NG2-KO mice resulted in prolonged BBB leakage and an altered neuroinflammatory response of astrocytes and microglia. Additionally, NG2-KO mice displayed pronounced short- and long-term neurobehavioral deficits compared to brain-injured wild-type mice (Dean et al., 2023; Huang et al., 2016).

In addition to CSPGs, CNS injury induces increased deposition of the ECM molecules Tn-R and tenascin-C (Tn-C) within the damaged area (Kjell & Götz, 2020). Although it is believed that Tn-R acts as a repellant for axonal growth, the exact role of Tn-C in the context of neuronal regeneration remains controversial (George & Geller, 2018). Besides depositing inhibitory ECM molecules, CNS injury triggers (reactive) glia and neurons to release proteases, most prominently metalloproteinases (MMPs), which further degrade and modify the ECM. For example, MMP-9 induces BBB hyperpermeability and activates pro-inflammatory cytokines, such as TFNα, IL-1β, and Osteopontin (OPN), thereby exacerbating inflammation. In contrast, the release of MMP-3 in response to TBI promotes neuronal regeneration by degrading the deposited inhibitory CSPGs (George & Geller, 2018).

CNS repair in regeneration-competent species

Long-lasting gliosis and the simultaneous formation of scar tissue in mammals are widely believed to prevent neuronal regeneration. Successful CNS repair in regeneration-incompetent species would require prompt glial reactivity to initiate inflammatory cascades and to establish proper border formation, followed by distinct temporal regulation of glial reactivity to prevent the formation of the long-lasting inhibitory scar

tissue (Blackshaw, 2022; Lust & Tanaka, 2019). This concept, however, is far away from being novel. For many years, research has been conducted to identify key molecules and mechanisms that can influence and promote mammalian CNS regeneration. An elegant approach to identifying key factors necessary for appropriate CNS repair is to study regeneration-competent species, such as teleost fish and salamanders, which possess remarkable regenerative potential of several organs, including the CNS. Regeneration-competent animals, including zebrafish, retain their regeneration ability even into adulthood (Lust & Tanaka, 2019; Zambusi & Ninkovic, 2020). Studies of the injured adult zebrafish brain have affirmed neuroinflammation as a critical factor for successful tissue regeneration. Similar to mammals, SWI in the adult zebrafish telencephalon causes cell death that triggers the release of ATP in the extracellular space. Consequently, ATP is sensed by microglia via the P2Y12 receptor, resulting in morphological changes and migration of microglia and OPCs towards the injury site. However, in contrast to mammals, glial accumulation is quickly resolved, which facilitates the migration of intermediate progenitor cells to the injury site, where they further differentiate into mature neurons (Zambusi & Ninkovic, 2020) (Fig. 6). Kyritsis and colleagues demonstrated that the injured zebrafish brain relies on acute neuroinflammatory stimuli to initiate increased proliferation of zebrafish stem cells, so-called radial glial cells, thereby setting the baseline for successful tissue repair. In fact, radial glial proliferation was significantly reduced in immunosuppressed brain-injured zebrafish, resulting in fewer newborn neurons in the damaged brain parenchyma (Kyritsis et al., 2012). It is, however, necessary to timely resolve the initial neuroinflammation in order to activate neurorestorative molecular programs in radial glial cells, including the aryl hydrocarbon receptor (AhR) pathway, to achieve adequate tissue repair (Di Giaimo et al., 2018).

Zebrafish are valuable models to gain deeper insights into the core mechanisms enabling successful CNS regeneration. Ideally, zebrafish findings can be transferred to non-regenerative species, such as mice or humans, to promote endogenous CNS repair. Unfortunately, zebrafish as an animal model possesses several constraints that are of considerable importance for translational studies (Zambusi & Ninkovic, 2020). One major limitation between zebrafish and mammals is their difference in brain tissue composition. Mammalian CNS injury is directly associated with reactive astrocytes and, in severe cases, glial border formation; however, so far, *bona fide* astrocytes have not yet been identified

in the adult zebrafish brain. Whether other cell types execute astrocyte function in the zebrafish brain is still debatable (J. Chen et al., 2020; Scheib & Byrd-Jacobs, 2020; Zambusi & Ninkovic, 2020). For better translatability, cross-comparisons between non-regenerative and regenerative organisms of the same biological class, equipped with identical cellular tissue composition, would therefore be of great interest. However, as most vertebrates lack the ability to regenerate, it was commonly presumed that this capacity has been lost throughout evolution (Blackshaw, 2022). This assumption needs to be reconsidered as recent studies by Streeter, Nogueira-Rodrigues, and colleagues have revealed functional axonal regeneration of the mammalian spiny mouse (*Acomys cahirinus*) in response to SCI (Nogueira-Rodrigues et al., 2022; Streeter et al., 2020). Interestingly, spinal cord-injured *Acomys* exhibited reduced inflammation and fibrotic scarring in comparison to injured *Mus Musculus* (C57BL/J) 4 weeks post-injury (Streeter et al., 2020). Moreover, following complete spinal cord transection, *Acomys* spontaneously regenerated multiple axon tracts, thus improving motor function and bladder control (Nogueira-Rodrigues et al., 2022). In contrast, stab wound injury in the aging African turquoise killifish (*Nothobranchius furzeri*) induced exacerbated glial reaction alongside reduced regenerative capacity reminiscent of regenerative-incompetent mammals (Van Houcke et al., 2021). Thus, glial scarring and tissue regeneration are rather regulated processes than simple evolutionary traits.

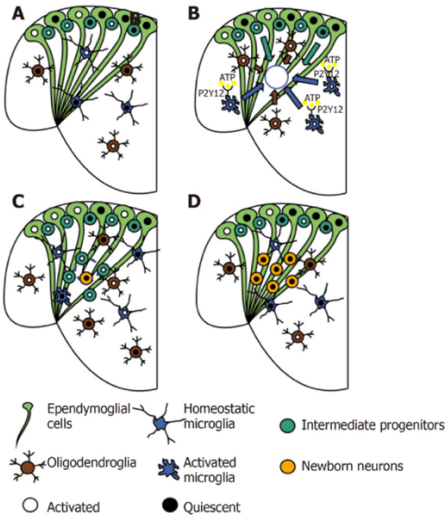

Figure 6: TBI-induced cellular reaction and tissue regeneration in the adult zebrafish telencephalon. Figure adapted and modified from Zambusi and Ninkovic, *Regeneration of the central nervous system-principles from brain regeneration in adult zebrafish,* World Journal of Stem Cells, 12(1):8-24, 2020, DOI: 10.4252/wjsc.v12.i1.8. © The author(s) 2020. This figure belongs to an open-access article distributed under the terms of the Creative Commons Attribution-Noncommercial License (https://creativecommons.org/licenses/by-nc/4.0/), which permits use, distribution, and reproduction in any medium or format.

AIM OF THE THESIS

Glial cells are crucial for maintaining CNS function under physiological conditions and are critical players during pathology. CNS injury triggers prompt neuroinflammatory responses initiated by peripheral-derived cells and brain-resident glia and induces the formation of a compact glial border to segregate the damaged, inflamed tissue from the nearby healthy regions to prevent the spread of inflammation. Initial glial responses are essential for preserving tissue integrity and promoting tissue repair. However, long-term excessive glia-mediated neuroinflammation hampers tissue restoration and promotes neurodegeneration (Adams & Gallo, 2018; Karve et al., 2016; Mira et al., 2021; Puntambekar et al., 2018; Russo & McGavern, 2016). The dual role of glial cells, being beneficial during the acute injury phase and detrimental during later stages, opens a critical time window for targeted therapeutic intervention to mitigate the adverse properties of reactive glia and ultimately enhance CNS repair. While prolonged glial reactivity is often solely associated with impaired CNS regeneration upon injury, the potential of reactive glial cells for novel neuronal replacement strategies is generally disregarded. Glial cells represent a promising cell source for direct neuronal reprogramming: By decreasing the number of reactive glia, thereby modulating the aversive injury environment, and simultaneously increasing the neuronal pool, injury-induced neuronal loss and function might ideally be reestablished (Bocchi et al., 2022; Grade & Götz, 2017). Despite tremendous efforts in recent years to disentangle the complex cellular reactions that drive TBI pathophysiology, a comprehensive understanding of injury-induced glial responses, their impact on neuronal regeneration, and their suitability for neuronal replacement strategies remains incomplete.

During my Ph.D., I aimed to characterize glial cell responses upon brain injury in regeneration-competent and incompetent species to uncover mechanisms regulating prolonged glial reactivity limiting CNS repair and to explore the influence of environmental factors on direct neuronal reprogramming.

RESULTS

Aim of study I

This study aimed to characterize the effect of long-term OPC activation on tissue regeneration in the injured adult zebrafish brain. Furthermore, this study identified the innate immunity-associated pathways TLR1/2 and CXCR3 as pivotal regulators in mediating long-term, exacerbated glial reactivity in the zebrafish brain.

Innate Immune Pathways Promote Oligodendrocyte Progenitor Cell Recruitment to the Injury Site in Adult Zebrafish Brain

Rosario Sanchez-Gonzalez, Christina Koupourtidou, Tjasa Lepko, Alessandro Zambusi, Klara Tereza Novoselc, Tamara Durovic, Sven Aschenbroich, Veronika Schwarz, Christopher T. Breunig, Hans Straka, Hagen B. Huttner, Martin Irmler, Johannes Beckers, Wolfgang Wurst, Andreas Zwergal, Tamas Schauer, Tobias Straub, Tim Czopka, Dietrich Trümbach, Magdalena Götz, Stefan H. Stricker and Jovica Ninkovic

For this study, I was involved in FACS sorting and the RNA-seq library preparation from FACS-sorted cells. Furthermore, I participated in paper editing and reviewing.

This study has been published in Cells (2022), 11(3):520.

DOI: https://doi.org/10.3390/cells11030520

cells

MDPI

Article

Innate Immune Pathways Promote Oligodendrocyte Progenitor Cell Recruitment to the Injury Site in Adult Zebrafish Brain

Rosario Sanchez-Gonzalez [1,2], Christina Koupourtidou [1,3,4], Tjasa Lepko [1,3,4], Alessandro Zambusi [1,3,4], Klara Tereza Novoselc [1,3,4], Tamara Durovic [1,3,4], Sven Aschenbroich [1,3,4], Veronika Schwarz [1,3,4], Christopher T. Breunig [5,6], Hans Straka [2], Hagen B. Huttner [7], Martin Irmler [8], Johannes Beckers [8,9,10], Wolfgang Wurst [11,12,13,14], Andreas Zwergal [15], Tamas Schauer [16], Tobias Straub [16], Tim Czopka [17], Dietrich Trümbach [11,†], Magdalena Götz [1,12,18], Stefan H. Stricker [5,6] and Jovica Ninkovic [1,3,12,*]

1 Institute of Stem Cell Research, Helmholtz Center Munich, 85764 Oberschleißheim, Germany; rosario.sanchez@biologie.uni-muenchen.de (R.S.-G.); koupourtidou@helmholtz-muenchen.de (C.K.); lepko.tjasa@gmail.com (T.L.); alessandro.zambusi@helmholtz-muenchen.de (A.Z.); klara.novoselc@helmholtz-muenchen.de (K.T.N.); durovictamara90@gmail.com (T.D.); sven.aschenbroich@helmholtz-muenchen.de (S.A.); schwarz.veronika@campus.lmu.de (V.S.); magdalena.goetz@helmholtz-muenchen.de (M.G.)
2 Department Biology II, University of Munich, 80539 München, Germany; straka@biologie.uni-muenchen.de
3 Biomedical Center (BMC), Division of Cell Biology and Anatomy, Faculty of Medicine, LMU Munich, 80539 München, Germany
4 Graduate School Systemic Neurosciences, LMU, 80539 Munich, Germany
5 Reprogramming and Regeneration, Biomedical Center (BMC), Physiological Genomics, Faculty of Medicine, LMU Munich, 80539 München, Germany; christopher.breunig@helmholtz-muenchen.de (C.T.B.); stefan.stricker@helmholtz-muenchen.de (S.H.S.)
6 Epigenetic Engineering, Institute of Stem Cell Research, Helmholtz Center Munich, 85764 Oberschleißheim, Germany
7 Department of Neurology, Justus-Liebig-University Giessen, Klinikstrasse 33, 35392 Giessen, Germany; hagen.huttner@neuro.med.uni-giessen.de
8 Institute of Experimental Genetics, Helmholtz Center Munich, 85764 Oberschleißheim, Germany; martin.irmler@helmholtz-muenchen.de (M.I.); beckers@helmholtz-muenchen.de (J.B.)
9 German Center for Diabetes Research (DZD e.V.), 85764 Neuherberg, Germany
10 Chair of Experimental Genetics, School of Life Sciences Weihenstephan, Technical University Munich, 80333 München, Germany
11 Institute of Developmental Genetics, Helmholtz Center Munich, 85764 Oberschleißheim, Germany; wurst@helmholtz-muenchen.de (W.W.); dietrich.truembach@helmholtz-muenchen.de (D.T.)
12 Munich Cluster for Systems Neurology SYNERGY, LMU, 80539 Munich, Germany
13 Chair of Developmental Genetics c/o Helmholtz Zentrum München, School of Life Sciences Weihenstephan, Technical University Munich, 80333 München, Germany
14 German Center for Neurodegenerative Diseases (DZNE), Site Munich, 80539 Munich, Germany
15 Department of Neurology, Ludwig-Maximilians University, Campus Grosshadern, 81377 Munich, Germany; andreas.zwergal@med.uni-muenchen.de
16 Biomedical Center (BMC), Bioinformatic Core Facility, Faculty of Medicine, LMU Munich, 80539 München, Germany; tamas.schauer@med.uni-muenchen.de (T.S.); tstraub@bmc.med.lmu.de (T.S.)
17 Centre for Clinical Brain Sciences, University of Edinburgh, Edinburgh EH8 9YL, UK; tim.czopka@tum.de
18 Biomedical Center (BMC), Division of Physiological Genomics, Faculty of Medicine, LMU Munich, 80539 München, Germany
* Correspondence: ninkovic@helmholtz-muenchen.de
† Present address: Institute of Metabolism and Cell Death, Helmholtz Center, Munich, 85764 Neuherberg, Germany.

check for updates

Citation: Sanchez-Gonzalez, R.; Koupourtidou, C.; Lepko, T.; Zambusi, A.; Novoselc, K.T.; Durovic, T.; Aschenbroich, S.; Schwarz, V.; Breunig, C.T.; Straka, H.; et al. Innate Immune Pathways Promote Oligodendrocyte Progenitor Cell Recruitment to the Injury Site in Adult Zebrafish Brain. *Cells* **2022**, *11*, 520. https://doi.org/10.3390/cells11030520

Academic Editors: Sepand Rastegar and Luisa Lübke

Received: 26 December 2021
Accepted: 18 January 2022
Published: 2 February 2022

Abstract: The oligodendrocyte progenitors (OPCs) are at the front of the glial reaction to the traumatic brain injury. However, regulatory pathways steering the OPC reaction as well as the role of reactive OPCs remain largely unknown. Here, we compared a long-lasting, exacerbated reaction of OPCs to the adult zebrafish brain injury with a timely restricted OPC activation to identify the specific molecular mechanisms regulating OPC reactivity and their contribution to regeneration. We demonstrated that the influx of the cerebrospinal fluid into the brain parenchyma after injury simultaneously activates the toll-like receptor 2 (Tlr2) and the chemokine receptor 3 (Cxcr3) innate immunity pathways, leading to increased OPC proliferation and thereby exacerbated glial reactivity.

These pathways were critical for long-lasting OPC accumulation even after the ablation of microglia and infiltrating monocytes. Importantly, interference with the Tlr1/2 and Cxcr3 pathways after injury alleviated reactive gliosis, increased new neuron recruitment, and improved tissue restoration.

Keywords: brain regeneration; oligodendrocyte progenitors; reactive gliosis; innate immunity pathways; zebrafish; neurogenesis; brain injury

1. Introduction

Wound healing in the brain is triggered by a temporarily regulated neuroinflammatory response that activates glial cells (reactive gliosis) and induces their recruitment to the injury [1,2]. Despite the many different approaches to model brain injury, there is an emergence of a common pattern in the cellular dynamics of brain resident cells following an insult [3]. Microglia respond to injury within 24 h by changing their morphology, increasing their proliferation rate, and migrating towards the injury site [4]. The activated microglia together with infiltrating monocytes not only phagocyte the cellular debris, but also release several damage-associated molecules (DAMs) to coordinate the subsequential glial reactivity [3,5–8]. In line with the inductive role of microglia released DAMs, the astrocyte reactivity (also termed astrogliosis) typically starts later on (2–3 days after injury) and varies depending on the extent of the damage [9]. Astrogliosis forms the border of GFAP$^+$ reactive astrocytes surrounding the injury site by the hypertrophy of astrocytic processes, the upregulation of GFAP, and the increased proliferation of juxtavascular astrocytes [5,10,11]. Ablation experiments have demonstrated that the initial reaction of astrocytes is essential for wound closure and the restoration of the normal brain milieu [12,13]. Moreover, border-forming reactive astrocytes have been described to be necessary for axonal regeneration after spinal cord injury [5,14]. On the other hand, multiple studies have shown that prolonged astroglial reactivity induced aversive extracellular matrix modifications and exacerbated inflammation [15–17] that negatively impact on functional recovery. Recent reports have demonstrated a reciprocal regulatory loop between astrocytes and immune cells. While DAMs released by microglia induce a neurotoxic phenotype in astrocytes [18], astrocytes regulate the extravasation of monocytes and in turn, the long lasting neuroinflammatory response [12,19].

Strikingly, oligodendrocyte progenitor cells (OPCs) react to insults such as demyelination [20,21], traumatic brain injury (TBI) [22], or neurodegenerative disorders [23] as fast as the residential microglial cells. In physiological conditions these slow proliferating progenitors display very limited and short-range migration [24,25] and maintain their non-overlapping cellular domains by balancing cellular proliferation and cell death [22,24–27]. However, a rapid and heterogeneous reaction of OPCs has been documented in response to brain injury [22,24,25,28]. The OPCs polarize shortly after an insult [29] and become fully hypertrophic [24,25] within 48 h after injury. This reaction is followed by migration towards the injury site [24,25] and an increased proliferation rate in the case of a bigger injury [25]. Importantly, during the wound healing process the OPCs do not maintain the non-overlapping domains anymore and they accumulate at the injury site [25]. This accumulation is resolved 4 weeks after the injury and the cellular repulsion mechanisms maintaining the non-overlapping domains are established again. Despite the precise description of the cellular dynamics, our understanding of the OPC reaction to brain injuries and its relevance is still far from being understood. Several reports have suggested that the OPC accumulation at the injury site could promote wound healing [25] and the co-depletion of proliferating microglia and OPCs shown enhanced axonal regeneration [30,31]. In contrast, the accumulation of OPC-derived proteoglycan NG-2 has been associated with the inhibition of axonal growth [32]. These rather opposing observations support the need to identify the pathways regulating the reaction of OPCs to brain injury and to associate them with the observed regenerative outcomes after injury.

The temporal sequence of the glial reaction to injury in the adult zebrafish brain shares some interesting similarities with the injured mammalian brain [1,33,34]. However, in contrast to the exacerbated gliotic wound closure described above for the mammalian brain, the glial response leads to full tissue restoration in zebrafish [1,34–37]. Complete recovery in the zebrafish brain correlates with the capacity to regulate the neuroinflammatory landscape and induce the restorative neurogenesis (neuronal replacement) from endogenous sources [37]. The basis for neuronal replacement resides in the injury-induced activation of neural stem cell-like ependymoglial cells [1]. The initial microglial reaction to injury activates developmental and/or injury-specific regulatory pathways in ependymoglial cells [1], regulating the timely production of new neurons necessary for tissue recovery. Although several regulatory mechanisms mediating the crosstalk between immune and ependymoglial cells have been identified [1], little is known about how OPCs contribute, if at all, to the permissive time window for the integration of new neurons. Zebrafish OPCs exhibit a different reaction to the stab wound injury depending on the injury paradigm [37–39]. While injuries performed rostro-caudally through the nostrils (nostril injury) induced no increased proliferation and no recruitment of OPCs to the damaged area [37], injuries along the dorso–ventral axis (skull injury) induced a long lasting accumulation of OPCs at the injury site [39]. The reaction of the OPCs to the skull injury is indeed very similar to the OPC reaction in the injured mammalian cortex, including the temporal resolution only after 4 weeks [22,34,39]. Nostril and skull injury paradigms offer an ideal comparative model by which to identify specific molecular pathways regulating OPC reactivity and its potential impact on tissue restoration and neuronal replacement as a means for functional recovery. We applied a comparative analysis of "nostril versus skull" zebrafish forebrain tissue to identify novel molecular mechanisms regulating exacerbated and prolonged OPC activation. We identified the toll-like receptor 2 (Tlr2) and the chemokine receptor 3 (Cxcr3) innate immune pathways as key regulators of OPC proliferation. Interference with these signaling pathways after injury not only alleviated the OPC accumulation at the injury site, but it also improved wound healing and restorative neurogenesis. We also showed that prolonged exposure of murine OPCs to human cerebrospinal fluid content activated Tlr2/Cxcr3 signaling and in turn increased OPC proliferation. Taken together, we identified signaling pathways and the source of their ligands regulating exacerbated and prolonged OPC reactivity, opening a new avenue for targeting therapies.

2. Materials and Methods

2.1. Animals

Adult 4–6 month old wild-type zebrafish (Danio rerio) of the AB/EK strain, or of the transgenic lines, Tg(olig2:gfp) [40], Tg(olig2:DsRed) [40], Tg(fli1:egfp) [41], Tg(gfap:GFP) [42], Tg(mbp:nslGFP) [43] and Tg(mpeg1:mCherry) [44] were used for all the experiments. Fish were kept under standard husbandry conditions [45] and experiments were performed according to the handling guidelines and regulation of the EU and the Government of Upper Bavaria (AZ 55.2-1-54-2532-09-16).

2.2. Stab Wound Injuries

We carried out three different stab wound injury paradigms: nostril, skull, and small skull injuries (Figures 1 and 6). Fish were anesthetized with buffered 0.02% MS-222 for 45 s to a minute and then placed in a Tricaine-soaked sponge. With the visual aid of a dissecting microscope, injuries were performed in both telencephalic hemispheres. The nostril injury [37] was performed using a 100 × 0.9 mm glass capillary needle (KG01, A. Hartenstein). Capillaries were pulled on a Narishige Puller (model PC-10) using a "One-stage" pull setting at a heater level of 63.5 °C. The final dimensions of the capillaries were 5 mm in length and 0.1 mm in diameter. For the skull injury, a micro-knife (Fine Science Tools) was inserted vertically through the skull into the medial region of the telencephalon. To perform the small skull injury, the skull was thinned above the telencephalon area using a micro-driller (Foredom) and the glass capillary (identical to that used for the nostril injury)

was inserted vertically through the skull and brain parenchyma. After the injury, fish were placed in fish water with oxygenation to assure complete recovery from the anesthesia.

2.3. Tlr2 Agonist (Zymosan A Bioparticles, Invitrogen) Administration

Fish were anaesthetized in 0.02% MS-222 and a small hole, using a micro-knife (Fine Science Tools), was made into the skull (above the telencephalic ventricle). A glass capillary loaded with 10 mg/mL Zymosan or artificial cerebrospinal fluid with Fast Green dye to visualize the injection site (0.3 mg/mL; Sigma) was inserted into the hole and ~1 μL of solution was injected at a pressure of 150 hPa using a microinjector (Eppendorf, Hamburg, Germany). Artificial cerebrospinal fluid was used as a control for the ventricular injections since its composition closely matches the electrolyte concentrations of cerebrospinal fluid (Figure 2).

2.4. Cxcr3 Agonist (VUF 11222, R & D Systems) Administration

Fish were anaesthetized as previously described and the solution was injected intraperitoneally using a 30 G needle (Braun). A total of 4 μL of VUF 11222 (300 mg/kg) or DMSO vehicle with the Fast Green dye (0.3 mg/mL; Sigma) was intraperitoneally injected (Figure 2). We did not observe any aversive effects by IP injecting up to 4 μL of the 80% DMSO solution.

2.5. Inhibitor Administration

Intraperitoneal injections were performed as described above. All inhibitors were dissolved in DMSO with Fast Green dye (0.3 mg/mL; Sigma) for visualization. Cxcr3 inhibitors (NBI 74330 (300 mg/kg, R & D Systems, Minneapolis, MN, USA) and AMG 487 (112 mg/kg, R & D Systems)), and Tlr1/2 inhibitor (CU CPT 22 (150 mg/kg, R & D Systems)) were injected independently (NBI 74330 or CU CPT 22) or in combination (NBI 74330 + CU CPT 22 or AMG 487 + CU CPT 22) (Figure 3 and Figure S5). NBI 74330 and CU CPT 22 were injected daily, while AMG 487 was injected twice per day. The vehicle solution consisted of DMSO and Fast Green dye. A total of 4 μL was administrated per injection and the maximum number of intraperitoneal injections was 2 injections per day at an interval of 72 h. The mortality rate was less than 5% after any of the treatments.

2.6. BrdU Labelling Experiments

To label proliferating cells and their progeny, we carried out long term bromo-deoxyuridine (BrdU; Sigma Aldrich, St. Louis, MO, USA) incorporation. Fish were kept in BrdU-containing aerated water (10 mM) for 21 h/day or 14 h/day as stated in specific experiments (Figures 4–6).

2.7. Immune Cell Depletion Assay

A two-step approach was used to deplete the immune cells: 2 μL of Clodrosome (Encapsula NanoSciences, Brentwood, TN, USA) was injected into the telencephalic ventricle every second day for one week prior to the injury (4 injections in total prior to the injury). Ccr2 inhibitor (MK-0812, 82.5 mg/kg, Cayman Chemical, Ann Arbor, MI, USA) was administered by intraperitoneal injection daily, starting 2 days before the injury (Figures 5 and S6). As a control for the ventricular injection, we used empty liposomes (Encapsome) and DMSO for the intraperitoneal administration.

2.8. Human CSF Sample Collection

Human CSF samples were obtained from two different sources. The first one was Erlangen University Hospital. The patients underwent a lumbar puncture to exclude intracranial hemorrhage or inflammatory diseases of the CNS and they were considered healthy based on normal values for CSF (color, cell count, and total protein). CSF analysis was approved by the institutional review board of Erlangen University Hospital (ethics committee number 3950) and patients gave informed consent. After lumbar puncture, a

protease inhibitor was added to CSF according to the manufactureR′s instructions (Roche) and CSF was directly frozen at −80 °C. The second source was the University Hospital at LMU Munich (project number 159/03). Human CSF samples were obtained from patients who underwent a lumbar puncture to exclude intracranial hypertension or inflammatory CNS diseases. Routine analysis of CSF (cell count, total protein, glucose) revealed no abnormal values in all samples. All patients gave their informed written consent.

2.9. Human Plasma, Cerebrospinal Fluid, and Heat-Inactivated Cerebrospinal Fluid Administration

A 100 × 0.9 mm glass capillary needle (KG01, A. Hartenstein, Würzburg, Germany) was loaded with human plasma (Sigma Aldrich), human cerebrospinal fluid, or heat-inactivated human cerebrospinal fluid (single healthy donor). Human cerebrospinal fluid was incubated for 15 min at 90° to generate heat-inactivated human cerebrospinal fluid. Fish were anesthetized with 0.02% MS-222 (Sigma-Aldrich). The glass capillary was introduced through the nostril and ~1 μL of the solution was injected at a pressure of 150 hPa into the injury track in the telencephalic parenchyma (Figure 6).

2.10. Plasmid Electroporation

The plasmid pCS2-tdTomatomem was diluted in sterile water and Fast green (1 mg/mL), reaching a final concentration of 1 μg/μL. ~0.5 μL of the solution was injected in the telencephalic ventricle as described previously [46]. Next, the electroporation was carried out by placing the positive electrode at the ventral side of the fisH′s head and the negative electrode on the dorsal side and giving five pulses at 40 V for 50 ms each at 1-s intervals [47].

2.11. Tissue Preparation and Immunohistochemistry

Animals were sacrificed by an MS-222 overdose. Brains were dissected and fixed for 3 h at 4 °C in 4% paraformaldehyde (PFA) in phosphate-buffered saline (PBS), washed three times with PBS, and sectioned. For sectioning, whole brains were embedded in 3% agarose in PBS and cut serially at a 100 μm thickness with a microtome (HM 650 V, Microm). Primary antibodies (Table S1) were dissolved in 0.5% Triton X and 10% normal goat serum. Subclass-specific secondary antibodies (1:1000, Thermofisher, Waltham, MA, USA) were used to detect the primary antibodies. Nuclear staining was performed with 40,6-diamidino-2-phenylindole dihydrochloride (DAPI) (Sigma). All sections were mounted using Aqua Polymount (Polyscience, Niles, IL, USA). BrdU immunodetection required 2N HCl pre-treatment for 20 min at room temperature. Pre-treatment of the sections with Dako target retrieval solution (Agilent, Santa Clara, CA, USA) was necessary for the detection of the L-plastin. For whole-mount infarct tissue imaging, 500 μm thick telencephalic sections were cleared using BABB (1 part benzyl alcohol, 2 parts benzyl benzoate method) and stained as previously described [48].

Cryo-sectioning was used for RNAscope (see below). After fixation, whole brains were cryoprotected in a 30% sucrose solution overnight at 4 °C. The tissue was embedded in a tissue freezing medium (Leica) and frozen using dry ice. Serial sectioning at 20 μm thickness with a cryostat (Leica) was performed. Sections were stored at −20 °C until further processing.

2.12. RNAscope

We used an RNAscope Multiplex Fluorescent Reagent Kit v2 (ACD) to identify and label specific zebrafish RNAs. For tissue processing, pre-treatment, and RNAscope assay we followed the manufactureR′s instructions. The RNAscope probes were designed by ACD using the following target sequences: Cxcr3.2 (NM_001007314.1), MYD88 (NM_212814.2), Mxc (NM_001007284.2), Tlr8b (NM_001386709.1), and GFP (Synthetic construct Cox8ND6gfp). For visualization, the TSA Plus Cyanine 3/5 (Perkin Elmer) kit was utilized.

2.13. Image Acquisition and Processing

All immunofluorescence microscopy on sections was performed and analyzed with an Olympus FV1000 cLSM system (Olympus, Tokyo, Japan), using the FW10-ASW 4.0 software (Olympus). Bright field images were taken with a Leica DM2500 microscope at the Core Facility Bioimaging at the Biomedical Center (BMC). For whole-mount infarct tissue analysis, images were acquired with a Leica SP8X microscope, using LASX software (Leica) and deconvolved using Huygens Professional deconvolution software (SVI). The injury site was analyzed using Imaris software version 8.4 (Bitplane, Concord, USA). The 3D surface object was generated from manually created contours on 2D slices using the Surface tool to calculate the volume of the Surface object. Animations were made using the Key Frame Animation function (Imaris).

2.14. Quantitative Analysis

For each experiment, animals were randomly distributed into groups and all manual counts were performed blind. For all quantifications 4 to 6 brains were analyzed, coming from at least 2 independent experiments. All the sections belonging to the telencephalon were quantified (sections with the olfactory bulb or optic tectum were excluded), from which we analyzed the entire rostro-caudal extent of the injured tissue. The injured volume was calculated by multiplying the area and the depth of the DAPI dense accumulation for each section. The total injured volume was the sum of all the injured sections. The density of the positive cells in the injured volume was defined by the total number of cells located in the volume occupied by DAPI dense accumulation. Controls for the "injured volume" were measured in uninjured, age matched fish using equivalent volumes for each of the injury paradigms. For 4C4 quantifications. single-channel immunofluorescent images were converted to black and white, thresholded, and the extent of the stained area was measured using NIH ImageJ software. For the analysis of OliNeu proliferation, 25 randomly selected images per coverslip were used for the analysis. The analysis was performed using the automated ImageJ pipeline that is available upon request.

2.15. Statistical Analysis

Data are presented as the mean +/− standard error of the mean (SEM) and each dot represents one animal. Statistical analysis was performed using R (version 3.6.1). Data were investigated to test whether assumptions of parametric tests were satisfied (e.g., *t*-test or Anova). Residuals (fitted by lm function, stats package, version 3.6.1) were tested for normality by the Shapiro–Wilk normality test (shapiro_test function, rstatix package, version 0.6.0). Further diagnostics of residuals were carried out using the DHaRMa package (version 0.3.3.0). The homogeneity of variance assumption was tested using Levene's test (leveneTest function, car package, version 3.0–10). If both normality and equal group variances assumption were met, Student's *t*-test (*t*.test function with var.equal = TRUE, stats package, version 3.6.1) for single comparisons and one-way anova (aov function, stats package, version 3.6.1) for multiple group design was used. Anova post-hoc tests, i.e., Tukey or Dunett tests, were applied either for all pair-wise comparisons (tukeyTest function, PMCMRplus package, version 1.9.0) or Many-to-One comparisons (dunnettTest function, PMCMRplus package, version 1.9.0), respectively. If the normality assumption was satisfied but groups had unequal variances, WelcH's *t*-test (*t*.test function with var.equal = FALSE, stats package, version 3.6.1) for single comparisons and WelcH's one-way Anova (oneway.test function, stats package, version 3.6.1) for multiple group design was used. As a post-hoc test, Dunnett's T3 test for data with unequal variances was applied (dunnettT3Test function, PMCMRplus package, version 1.9.0). For Figure S2E only selected contrasts were tested (i.e., coronal vs. sagittal in each group) using the multcomp package (glht function, version 1.4–15). If the normality assumption was not met, the data were log-transformed to achieve normality of the residuals. In such a case, parametric tests were carried out as described above. If log-transformation did not satisfy the assumption, non-parametric tests were used i.e., Wilcoxon rank sum test (wilcox.testfunction, stats package,

version 3.6.1) for single comparisons and Kruskal–Wallis test (kruskal_test function, rstatix package, version 0.6.0) for multiple group design. In the latter case, the post-hoc Dunn test (kwManyOneDunnTest function, PMCMRplus package, version 1.9.0) was performed for Many-to-One comparisons. Dose-response in Figure 7D was analyzed by linear regression on square-root transformed outcome values. *p*-values were obtained for the regression coefficients: the slope for OliNeu and the difference in slopes (interaction term) for clone1 or clone2 relative to OliNeu. The detailed statistical analysis for all data sets is presented in the Supplementary Materials.

2.16. Analysis of Restorative Neurogenesis

Restorative neurogenesis was defined as the proportion of new neurons that migrated into the parenchyma. Zebrafish were kept in BrdU-containing aerated water (10 mM) overnight during the first 3 days. Simultaneously, vehicle and double inhibitors were injected daily under normal conditions (Figure 4C–H) or after immune cell depletion (Figure 4M–R). Animals were sacrificed at 7 dpi and the expression pattern of HuC/D and BrdU was analyzed. We assessed restorative neurogenesis as completed previously [49] by calculating the proportion of new neurons ($HuC/D^{+}BrdU^{+}$) that had migrated from the ventricular zone into the parenchyma as a result of the injury.

2.17. RNA Extraction, cDNA Synthesis, and RT-qPCR

Total RNA was isolated using the Qiagen RNeasy kit for microarray analysis and qPCR experiments. RNA isolation from FACS purified was performed with a PicoPure RNA isolation kit (Thermo Scientific). cDNA synthesis was performed using random primers with the Maxima first strand synthesis kit (Thermo Scientific). The manufactureR's instructions were followed for all the mentioned kits. The real-time qPCR was conducted using SYBR green and Thermo Fisher Quant Studio 6 machine (Table S2).

2.18. Microarray Analysis

Total RNA (20 ng) was amplified using the Ovation Pico WTA System V2 in combination with the Encore Biotin Module (Nugen). Amplified cDNA was hybridized on Affymetrix Zebrafish 1.0 ST arrays. Staining and scanning were performed according to the Affymetrix expression protocol including minor modifications as suggested in the Encore Biotion protocol. An expression console (v.1.3.1.187, Affymetrix) was used for quality control and to obtain annotated normalized RMA gene-level data (standard settings including median polish and sketch-quantile normalization). Statistical analyses were performed by utilizing the statistical programming environment R (R Development Core Team implemented in CARMAweb [50]). Genewise testing for differential expression was performed by employing the limma *t*-test. Regulated gene sets were defined by $p < 0.05$, fold-change > 1.6x and linear average expression in at least one group >20. The array data have been submitted to the GEO database at NCBI (GSE98217).

2.19. Assignment of Zebrafish Array Probes to Homologous Mouse Genes

The genomic positions of all probe sets in the presented zebrafish microarray study were extracted from Affymetrix (http://www.affymetrix.com/analysis/index.affx; accessed on 24 November 2016) by applying a Batch Query on the GeneChip Array "Zebrafish Gene 1.x ST" (genome version Zv9 from 2011). With the help of a custom-written Perl script and the extracted genomic positions of the probe sets, zebrafish gene identifiers were derived from the Ensembl database via the Application Programming Interface (API), version 64, and subsequently passed to the Ensembl Compara database in order to retrieve homologous mouse genes. The Compara database stores pre-calculated comparative genomics data of different species including information on homologous genes, protein family clustering, and whole genome alignments [51]. For the assignment of zebrafish to mouse genes, all kinds of homology (i.e., one-to-one, one-to-many and many-to-many orthologous genes) were taken into account. Gene Ontology enrichment analyses were

performed using the equivalent mouse symbols and DAVID Bioinformatics Resources 6.7 (p-value 0.05, fold change > 2) [52,53].

2.20. FACS Analysis

Animals from the Tg(olig2:DsRed) transgenic lines were sacrificed by an MS-222 overdose and the telencephalon was dissected from each animal. A single cell suspension was prepared according to previously published protocols [54,55] and cells were analyzed using a FACS Aria III (BD) in BD FACS Flow TM medium. Debris and aggregated cells were gated out by forward scatter–sideward scatter; single cells were gated in by FSC-W/FSC-A. Gating for fluorophores was performed using AB/EK animals. Cells were directly sorted into an extraction buffer from PicoPure RNA isolation kit (Thermofisher) and stored at −80 °C until RNA preparation was performed.

2.21. Preparation of Libraries for Deep Sequencing

cDNA was synthesized from 1 ng of total RNA using SMART-Seq v4 Ultra Low Input RNA kit for Sequencing (Clontech), according to the manufactureR's instructions. The quality and concentration of cDNA was assessed on an Agilent 2100 Bioanalyzer before proceeding to the library preparation using a MicroPlex Library Preparation kit v2 (Diagenode). All libraries (minimum of 3 biological replicates per condition) were processed together to minimize batch effects. Final libraries were evaluated and quantified using an Agilent 2100 Bioanalyzer and the concentration was measured additionally with a Quant-iT PicoGreen dsDNA Assay Kit (Thermo Fisher) before sequencing. The uniquely barcoded libraries were multiplexed onto one lane, and 150-bp paired-end deep sequencing was carried out on HiSeq 4000 (Illumina) that generated approximately 20 million reads per sample.

2.22. RNAseq Analysis

The RNA-seq analysis was completed using the kallisto pipeline for the reads mapping and quantification followed with the Sleuth pipeline for the statistical analysis. The cut-off for the differentially regulated genes was based on the expression fold change (>2 fold) and p-value adjusted for the 10% false discovery rate (q-value < 0.05). FastQ files are deposited at (accession number pending). Gene Ontology enrichment analyses was performed using DAVID Bioinformatics Resources 6.8 (p-value 0.05, fold change > 2) [52,53].

2.23. Primary OPC Culture and Clonal Analysis

Primary cultures of the OPCs were performed as previously published [56]. Cortices of P0 mice were dissected avoiding the inclusion of white matter and grown for 10 days. After the initial culturing, cells were plated in 24-well plates at 727 cells/mm^2 density. OPC primary cultures were transduced with a GFP encoding MLV-based virus for clonal analysis as previously described [57]. A total of 12 hrs after the transduction, the cells were treated with 1 μM NBI 74330 and 8 μM CU CPT 22 and analyzed 5 days later and the clonal analysis was performed as described previously [57].

2.24. Generation of gRNAs for CRISPR/Cas9-Mediated Deletion

Target sequences were chosen within 600 bp after the first ATG of the ORF of Cxcr3 (ENSMUSG00000050232) and Tlr2 (ENSMUSG00000027995). gRNAs were generated using Benchling (www.benchling.com, accessed on 24 September 2019) and chosen according to a high (>30) specificity score. Multiplexed gRNA vectors were generated using the STAgR protocol [58]. Single gRNA expression units were amplified using overhang primers, employing the N20 targeting sequence as homology for Gibson assembly. gRNAs were assembled into a gRNA expression vector containing a TdTomato reporter, modified after pgRNA1 [59].

2.25. DNA Extraction and PCR

For the DNA extraction from the cells, the DNeasy blood and tissue kit was used (Qiagen, 69504). The region containing the prospective mutation was amplified using the standard PCR condition (denaturation: 20″; annealing 20″; extension 60″; 30 PCR cycles) and locus-specific primer pairs from the positive and negative clones. Tlr2: 5′-ggacaaattcaggaagcgca and 5′-tgagagatcacggaccaagg; Cxcr3: 5′-cctcatagctcgaaaaacgcc and 5′-ccccggagagaaagagtcag. PCR products were cloned using a PCR cloning kit according to the manufactureR′s instructions (Stratagene) and were analyzed for the mutation using SANGER sequencing.

2.26. Generation of the Oli-Neu Cell Line Deficient for Cxcr3 and Tlr2

Oli-Neu cells were cultured in a SATO medium containing 1% horse serum. For each transfection, 200,000 cells/well were seeded into 6-well plates and coated with poly-L-lysin (Sigma). A total of 1 µg of each STAgR (encoding for gRNAs and TdTomato reporter) or control plasmid (encoding for dsRed) in addition to 1 µg of Cas9 plasmid (with a puromycin resistance cassette) was transfected per sample using Lipofecatmin 2000 (Invitrogen, Waltham, MA, USA) according to the manufactureR′s instructions. Cells were plated in low density and selected with 0.8 µg/mL puromycin for Cas9 expression. Five days later, clones transfected with STAgR (TdTomato reporter^{+}, positive clones) or only Cas9 (TdTomato reporter^{-}, negative clones) were selected and expanded. The proliferation analysis was performed using two independent clones with different deletions in both Tlr2 and Cxcr3 genes. To analyze the clones, 25,000 cells/well were plated in 24-well plates on poly-L-lysine-coated coverslips and analyzed after 48 h. Cell were fixed in 4% paraformaldehyde (PFA) in phosphate-buffered saline (PBS) for 15 min at room temperature and processed for the antibody staining.

2.27. Screen for Cxcr3 Ligands from the CSF

As the screen requires many cells, we decided to conduct it in the oligodendrocyte progenitor line (OliNeu) that also allows for the genetic inactivation of Cxcr3 and Tlr2 as described in Section 2.26. Both WT Oli-Neu and Cxcr3 and Tlr2 deficient clones were expanded onto a SATO medium containing 1% horse serum. After expansion, cells were re-plated on PLL-coated coverslips at an equal density (272 cells/mm^2) and cultured for 2 h. After this pre-incubation, cells were treated with different CSF concentrations and vehicles. All cytokine treatments were performed using the WT Oli-Neu cells in quadruplets and at 3 different concentrations (Table S3) that were used as independent replicates for the analysis. Cells were fixed with 4% PFA 24 h after the treatment and assessed for proliferation using the anti-PH3 immunostaining.

2.28. Human Cytokine Antibody Array

Four cerebrospinal fluid samples, derived from healthy patients, were analyzed using a Human Cytokine Antibody Array (abcam, ab133997). All samples induced a scarring reaction upon injection into the nostril injury track. The positive controls were used to normalize signal responses across multiple arrays.

3. Results

3.1. Skull and Nostril Models of Zebrafish Telencephalon Injury Differ in the Kinetics of the Glial Reaction

To identify the molecular and cellular basis for OPC activation during wound healing, we set out to follow the reaction of different cell types to an injury in the zebrafish telencephalon using two paradigms in parallel, one with long-term, exacerbated OPC reactivity (referred to as skull injury, Figure 1A) and the other resulting in time-restricted gliosis and full tissue recovery (referred to as nostril injury, Figure 1B). Injuries were performed in both telencephalic hemispheres and the injury site was defined based on the DAPI accumulation throughout the manuscript (e.g., Figure S1I,K). Damage-associated molecules trigger the

early inflammatory response that induces the recruitment of peripheral neutrophils into the injury site in the mammalian brain [60]. In zebrafish, we observed Lys$^+$ neutrophils 12 h after both injuries in the brain parenchyma (Figure S1A,D). Interestingly, Lys$^+$ cells accumulated at the injury site after the nostril injury (Figure S1B), while they were dispersed throughout the injured parenchyma after the skull injury (Figure S1D). Moreover, Lys$^+$ neutrophil accumulation resolved 24 h after nostril injury and we could not detect any difference 48 h after injury (Figure S1C) compared to the intact brain. In contrast, we did not observe the fast clearance of Lys$^+$ cells after skull injury (Figure S1E).

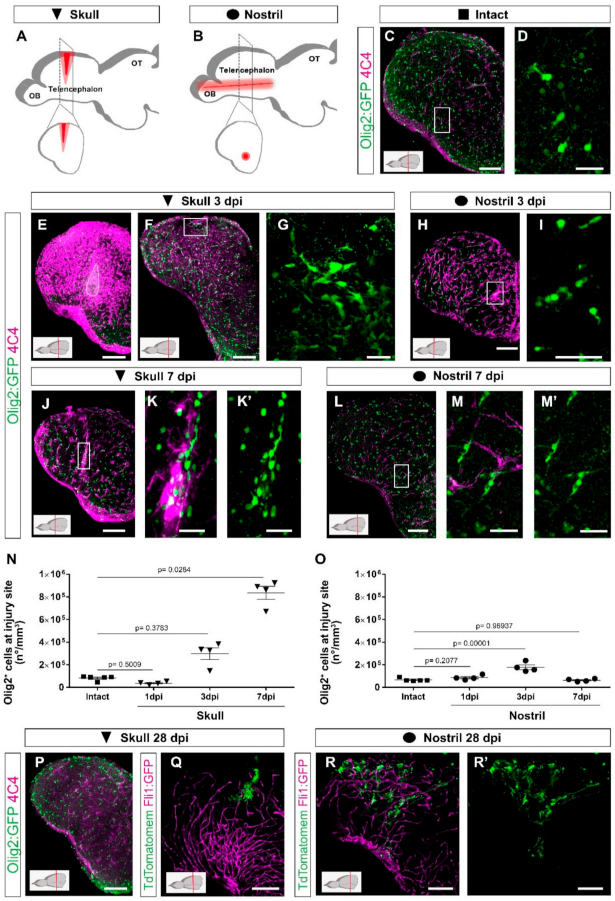

Figure 1. Distinct injury paradigms in the zebrafish telencephalon led to either scarless regeneration or prolonged glial reactivity. (**A**,**B**) Schemes depicting skull (**A**) and nostril (**B**) injury paradigms. Red triangle (**A**) and red line (**B**) illustrate the injury track. (**C**,**D**) Micrographs of a telencephalic section showing the distribution of Olig2:GFP$^+$ oligodendroglia and 4C4$^+$ microglia/monocytes in the intact brain. (**E**,**F**) Images of 3 dpi skull-injured sections (4C4$^+$ and Olig2:GFP$^+$ cells) at the level of the injury core delineated by a white line (**E**) and lateral to the injury core depicting the first signs of Olig2:GFP$^+$ cells to accumulation indicated by the boxed area (**F**). (**H**) Image showing the distribution of Olig2:GFP$^+$ and 4C4$^+$ cells at 3 dpi after a nostril injury. (**G**,**I**) are magnifications of the boxed areas in (**F**) and (**H**), depicting Olig2:GFP$^+$ cell distribution. (**J**–**M′**) Images showing the reactivity of 4C4$^+$

and Olig2:GFP$^+$ cells at 7 days after skull (**J**) and nostril (**L**) injury. (**K**,**K′**,**M**,**M′**) are magnifications of the boxed area in the respective images. (**N**,**O**) Graphs depicting the density of Olig2:GFP$^+$ cells at the injury site after skull (**N**) and nostril (**O**) injury. Data are shown as mean ± SEM; each data point represents one animal. Statistical analysis is based on a non-parametric Kruskal–Wallis Test (p-value = 0.0021) with a post-hoc Dunn test (Many-to-One) in (**N**) and a one-way ANOVA (p-value = 2.483×10^{-5}) with a post-hoc Dunnett test (many-to-one) in (**O**). (**P**) The accumulation of 4C4$^+$ and Olig2:GFP$^+$ cells resolved at 28 days after skull injury. (**Q**–**R′**) Images showing the morphology of ependymoglial cells (labelled by electroporation of TdTomatomem) 28 days after skull (**Q**) and nostril injury (**R**,**R′**). While we observed the restoration of the radial morphology of the labelled ependymoglia that contacts the basement membrane after nostril injury (similar to the intact brain), the ependymoglia after skull injury failed to restore radial morphology and built extensive contacts with Fli1-positive blood vessels. All images are full z-projections of a confocal stack; insets indicate the rostro-caudal levels of the sections. Scale bars in (**C**,**E**,**F**,**H**,**J**,**L**,**P**,**Q**,**R**,**R′**) = 100 µm; Scale bars in (**D**,**G**,**I**,**K**,**K′**,**M**,**M′**) = 20 µm. Abbreviations: OB: olfactory bulb, OT: optic tectum, dpi: days post-injury; AFOG: acid fuchsin orange G. Symbol description: black triangle: skull injury; black circle: nostril injury.

As neutrophils regulate the activity state of microglia and extravasating monocytes and consequently the regenerative response [60], we analyzed both populations based on the expression of two different immunohistochemical markers (4C4 and L-plastin) as well as the transgenic line Tg(mpeg1:mCherry) [44] labelling both cell types (Figure S1F–H‴). In the intact condition, the majority of microglia co-expressed all three markers although at the different levels (Figure S1F–F‴). However, after both nostril and skull injury, we observed an increase in 4C4$^+$ cells and only a proportion of them were colocalized with L-plastin and/or with mpeg1:mCherry$^+$ cells (Figure S1G–H‴). Taken together, these data suggest that 4C4 was the broadest marker to identify microglia/monocyte population and, therefore, we used it further in our study. While the initial activation pattern of 4C4$^+$ cells was similar in both injury paradigms with the first signs of reactivity detectable already at 24 h after injury (Figure S1J,L), the skull injury induced a stronger reactivity and a long-lasting accumulation of 4C4$^+$ cells at the injury site (Figure 1E–M′).

The accumulation of cells belonging to the oligodendrocyte lineage (OPCs and mature oligodendrocytes were labeled using the transgenic line [Tg(Olig2:GFP)] [40]) at the injury site was slightly delayed in comparison with the microglia/monocytes (Figure S1I,K). The density of Olig2:GFP$^+$ cells was increased at the injury site 3 days after both skull (Figure 1F,G,N) and nostril injury (Figure 1H,I,O), although to different extents. The accumulation of Olig2:GFP$^+$ cells was rapidly resolved and returned to pre-injury conditions within 7 days after the nostril injury (Figure 1L–M′,O), in agreement with previously published studies [33,37,38]. In contrast, the density of Olig2:GFP$^+$ cells further increased and still persisted at 7 days post-injury (dpi) in the skull injury paradigm (Figure 1J–K′,N). We analyzed coronal brain sections depicting the skull injury in its full extent, but only part of the nostril injury. Therefore, the accumulation of both 4C4$^+$ and Olig2:GFP$^+$ cells observed exclusively after skull injury could be a consequence of a bias in the analysis. To exclude any technical bias, the number of Olig2:GFP$^+$ cells accumulating at the nostril injury site was also analyzed in sagittal sections depicting the full extent of the nostril injury (Figure S2A–D). No differences were observed at any of the analyzed time points (Figure S2E). Moreover, injury sites were analyzed in BABB-cleared brains. While we could observe a clear accumulation of Sox10$^+$ (classical marker for the oligodendrocyte lineage) and 4C4$^+$ cells 3 days after nostril injury, 7 days after injury Sox10$^+$ and 4C4$^+$ cells showed distributions that were indistinguishable from samples of intact brains (Videos S1–S3).

In the zebrafish telencephalon the resident neural stem cell [48,61], the ependymoglial cells, express GFAP. So next, we used the Tg(gfap:GFP) transgenic line [42] to label and characterize the reactivity of ependymoglial cells after both types of injury. Gfap:GFP$^+$ cell bodies line up at the ventricular wall of the brain surface with processes reaching

basement membrane (Figure S3A); therefore, after a nostril injury, only some processes of ependymoglia, located in the deep parenchyma, were wounded (Figure S3B,C). Importantly, no sign of damage was observed at 7 days after nostril injury (Figure S3F). On the other hand, upon skull injury, the ependymoglial cell layer was disrupted (Figure S3D,E), but was already restored 7 days after skull injury (Figure S3G). Despite this recovery, we still observed hypertrophic processes and a few misplaced Gfap:GFP$^+$ cells at the injury site (Figure S3H).

The accumulation of Olig2:GFP$^+$ and immune 4C4$^+$ cells was resolved 28 days after the skull injury (Figure 1P), resembling the behavior of OPCs and microglia in the injured mammalian cerebral cortex [19,22]. However, even after the accumulation of Olig2:GFP$^+$ and immune 4C4$^+$ cells was resolved, the tissue architecture was not fully restored, based on the Gfap:GFP$^+$ ependymoglial cell morphology (Figure 1Q–R′). To assess the ependymoglial morphology, we labelled them using the electroporation of the TdTomatomem plasmid both after nostril and skull injury and analyzed their morphology and localization 28 dpi. In line with previous reports [37,47], the nostril injury did not change the morphology or the localization of ependymoglial cells compared to the intact brain. We found ependymoglial cell bodies lining up at the telencephalic ventricular wall with processes mostly spanning the brain parenchyma and anchoring at the basement membrane 28 dpi (Figure 1R,R′). However, after skull injury, several of the labelled ependymoglial cells had a bushy morphology and did not reach the basement membrane (Figure 1Q; Video S4).

These data demonstrate the differential reactions of neutrophils, microglia/monocytes, and oligodendrocyte lineage cells in two injury paradigms. The prolonged reaction of these cells correlates with the deley in the tissue restoration.

3.2. Activation of Innate Immunity Pathways Induces Prolonged Glia Reactivity after Injury in the Zebrafish Telencephalon

In view of the above findings, comparing the transcriptome induced by nostril and skull injury offers a unique opportunity to disentangle the specific molecular programs inducing exacerbated gliosis from the beneficial pathways promoting wound healing. We reasoned that some signaling pathways that were activated after a skull injury, but not after a nostril injury, could account for the long-lasting glial accumulation at the injury site and the absence of full tissue restoration. Therefore, we analyzed the gene expression during regeneration (1, 2, 3, and 7 dpi) after a nostril or skull brain injury in the whole telencephalon, using the Affymetrix Zebrafish Gene ST 1.0 array (Figure 2A). Both types of injuries initially induced comparable transcriptome changes, as reflected by a similar number of significantly regulated genes (fold change > 1.6, $p < 0.05$) and a large overlap in significantly overrepresented Gene Ontology (GO) terms (based on DAVID analysis, fold enrichment ≥ 2; $p < 0.01$) at 1 and 2 dpi (Figure 2B, Table S4). However, we observed a striking difference in the number of regulated GO terms after nostril and skull injury at 3 dpi (Figure 2B), with 1012 transcripts regulated after a skull but not nostril injury (Figure 2C). Interestingly, this large number of uniquely regulated genes at 3 dpi correlates with differences in the reaction of Olig2:GFP$^+$ cells and microglia/monocytes between the two injury paradigms (Figure 1N,O), supporting the idea that understanding these transcriptional differences could identify specific programs inducing long-lasting OPC accumulation and neuroinflammation. To further validate the applicability of this approach, we analyzed the differential expression of genes possibly involved in the ECM modifications, as the specific ECM changes could be associated with exacerbated glial activation [16]. Towards this end, we selected genes related to the GO terms "Extracellular matrix" (GO_0031012) and "Extracellular region" (GO_0005576) and analyzed their expression at 3 days post skull and nostril injury. Among all the regulated ECM-related transcripts (131), 69 of them were exclusively regulated after the skull injury (Figure 2D). These transcripts were overrepresented in GO terms related to the immune response, regulation of immune system process, and proteolysis (Figure 2E, Table S5), processes implicated in the exacerbated glial reaction after wound closure. Moreover, some of these genes encoded for factors reported to regulate

either glial reactivity (Ptpn6, Cst B, C1qa, C1qb, Mmp9, Fga) [62–66] or fibrosis [67–71] (Figure 2F). Because the two types of injuries show different kinetics in cellular response, some genes could still be differentially regulated at different time points after nostril injury. Therefore, we filtered out from the 1012 transcript set (Figure 2C) all transcripts regulated after nostril injury at any analyzed time point. We identified 812 transcripts regulated 3 days after skull injury but not at any time point after nostril injury (Figure 2G). Most of the GO terms significantly enriched in this gene set (2-fold enrichment and $p < 0.01$) were related to metabolism, immune, and innate immune response (Figure 2H, Table S6).

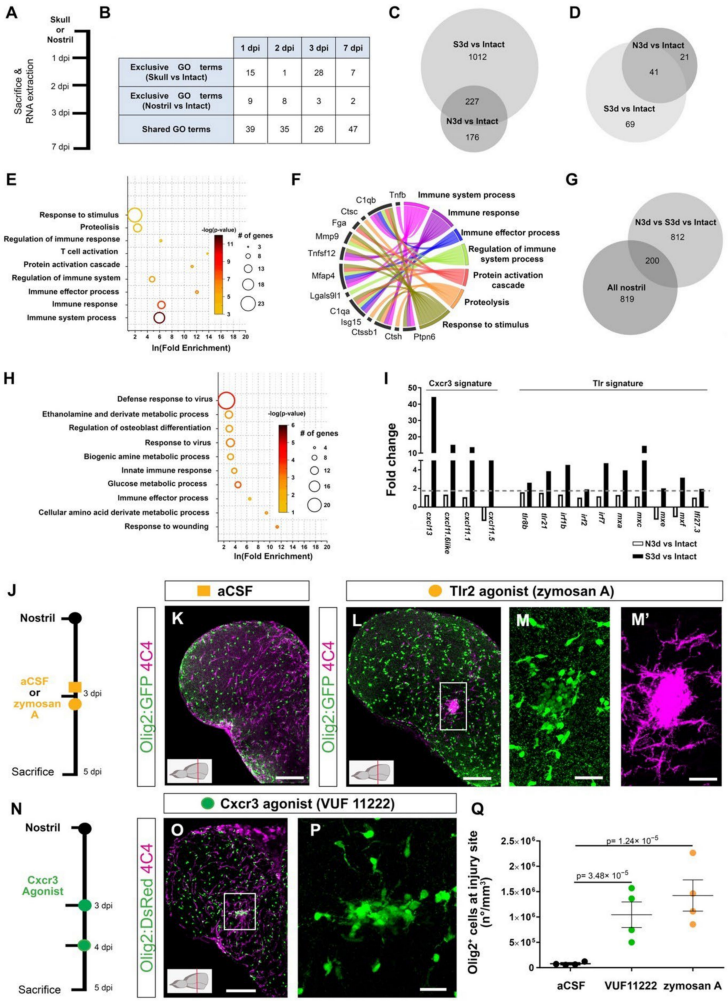

Figure 2. Activation of innate immunity pathways after injury induced a prolonged glial reaction in the zebrafish telencephalon. (**A**) Experimental design to analyze transcriptome changes occurring upon nostril and skull injury. (**B**) Table depicting the number of significantly regulated Gene Ontology terms (Injury vs. Intact) at different time points after nostril and skull injury. (**C**) Comparative analysis

using a Venn diagram illustrating the number of genes exclusively regulated 3 days after skull injury (Skull vs. Intact) and not after nostril 3 dpi (Nostril vs. Intact). (**D**) Venn diagram depicting the overlap between ECM-related genes regulated at 3 days after skull and nostril injury. Regulated genes were defined by a *p*-value < 0.05, fold-change > 1.6, and a linear average expression > 20. (**E**) Significantly enriched Gene Ontology (GO) terms of biological processes (color indicates *p*-values and symbol size number of identified genes within the term) in an ECM-related gene set regulated exclusively 3 days after skull injury (69 genes in panel (**D**)). (**F**) Chord diagram depicting selection of regulated ECM-related genes and associated GO terms biological processes. (**G**) Venn diagram depicting the overlap between genes exclusively regulated at 3 days after skull injury and genes regulated after the nostril injury at any time point. Note that 80% of the genes were exclusively regulated after skull injury at 3 dpi but were never regulated after nostril injury. (**H**) Plot showing significantly enriched (*p*-values indicated on bars) GO terms related to biological processes in a gene set regulated exclusively 3 days after skull injury (Skull 3 dpi vs. Nostril at any time point), correlating with glial accumulation. (**I**) Histogram depicting the regulation of genes related to Cxcr3 and Tlr signatures after nostril and skull injury. The dotted, gray line shows the 1.6-fold change cut off. (**J**) Scheme of the experimental design analyzing the ability of the Tlr2 agonist to induce glia accumulation after nostril injury. (**K**,**L**) Images of 5-day-injured telencephalic sections in the *Tg(Olig2:GFP)* line after nostril injury and aCSF (**K**) or zymosan A injections (**L**). (**M**,**M′**) Magnifications of the boxed area in L depict the exacerbated accumulation of Olig2:GFP$^+$ (**M**) and 4C4$^+$ (**M′**) cells at the injury site. (**N**) Scheme representing the experimental design to analyze the capacity of the Cxcr3 agonist (VUF 11222) to induce a reactive gliosis. (**O**) Micrograph illustrating the reactivity of Olig2:DsRed$^+$ and 4C4$^+$ cells after Cxcr3 activation. (**P**) Magnification of the injured area in (**O**). (**Q**) Graph showing the density of Olig2:GFP$^+$ cells in the injured area 5 days after nostril injury with aCSF, Cxcr3 or Tlr2 agonist treatments. Data are shown as mean ± SEM; each data point represents one animal. *p*-values are based on a one-way ANOVA (*p*-value = 1.183×10^{-5}) with a post-hoc Dunnett test (Many-to-One). All images are full z-projections of a confocal stack. Insets indicate the rostro-caudal levels of the sections. Scale bars in (**K**,**L**,**O**) = 100 μm; scale bars in (**M**,**M′**,**P**) = 20 μm; Abbreviations: dpi: days post-injury, N3d: nostril 3 dpi, S3d: skull 3 dpi; Ctrl: control; aCSF: artificial cerebrospinal fluid. Symbol description: orange square: ventricular injection of aCSF; orange circle: ventricular injection of zymosan A, Tlr2 agonist; green circle: VUF 11222, Cxcr3 agonist; black circle: nostril injury.

In particular, we observed the upregulation of genes indicative of the activation of the Toll-like receptor, Tlr, (*mxc*, *mxe*, *irf7*, *irf2*) [72–74] and chemokine family 11 (*cxcl11.1*, *cxcl11.5*, *cxcl11.6like*, and *cxcl13*) [75] mediated innate immune response, at 3 days after skull injury (Figure 2I). Innate immunity orchestrates the initial events of wound healing after skin [76], heart [77], and CNS [9] injury, and its regulation determines the extent of tissue restoration [78]. Therefore, we set out to address whether the activation of either Tlr- or Cxcl11 family-mediated innate immunity leads to the induction of exacerbated glial reactivity in the zebrafish telencephalon. We first activated the Tlr-mediated innate immune response by injecting zymosan A microparticles [2] 3 days after nostril injury (Figure 2J) to mimic the temporal activation of this pathway observed after skull injury. Zymosan A was injected in the telencephalic ventricle and the glial reactivity was analyzed at 5 dpi, when the Olig2:GFP$^+$ cell accumulation was already resolved after nostril and detected only after skull injury (Figure 2J,K,Q). Indeed, the vehicle (artificial cerebrospinal fluid, aCSF) treatment did not alter the reaction of Olig2:GFP$^+$ cells and no accumulation was detected at 5 dpi (compare nostril 3 dpi Figure 1O with Figure 2Q for vehicle). In contrast, zymosan A treatment not only prolonged the accumulation of both 4C4$^+$ and Olig2:GFP$^+$ cells at the injury site (Figure 2K–M′,Q), but it also increased 7-fold the number of Olig2:GFP$^+$ cells accumulating at the injury site 5 dpi compared with the vehicle treatment (Figure 2Q). Thus, zymosan A treatment turned the initial short-term glial activation into a prolonged and exacerbated accumulation of glial cells at the injury site after nostril injury. The toll-like receptor 2 (Tlr2) mediates the sterile inflammation induced by zymosan A in other systems [72,79], and Tlr2 was expressed in the intact as well as the injured zebrafish telencephalon (Figure S4A). Therefore, we tested whether interfering

with Tlr1/2 pathway activation using a Tlr1/2-specific competitive inhibitor (CU CPT22) would abolish the capacity of zymosan A to induce an exacerbated glial reaction after nostril injury (Figure S4B). Indeed, interference with the activation of the Tlr1/2 pathways prevented the accumulation of Olig2:GFP$^+$ cells at the injury site after zymosan A injection (Figure S4C–G), suggesting that activation of Tlr1/2 is sufficient to induce a prolonged accumulation of Olig2:GFP$^+$ cells and 4C4$^+$ cells at the injury site.

Similar to Tlr2-induced innate immunity, we set out to test whether the Cxcl11 family has a role in prolonged glial activation, in line with the induction of these ligands exclusively after skull injury. As up-regulated Cxcl11-family ligands (Figure 2I) signal through the same chemokine receptor, Cxcr3 [80], we analyzed the ability of a specific Cxcr3 agonist (VUF 11222 [81]) to induce glial accumulation in the nostril injury paradigm (Figure 2N). Similar to the reactivity observed upon Tlr2 pathway activation (Figure 2K–M′,Q), treatment with the Cxcr3 agonist was sufficient to trigger exacerbated 4C4$^+$ and Olig2:GFP$^+$ cell accumulation at the injury site at 5 dpi (Figure 2O–Q).

Taken together, our data suggest that the activation of either Tlr2 or Cxcr3 is sufficient to induce an exacerbated glial reaction after nostril injury.

3.3. Tlr1/2 and Cxcr3 Pathways Cooperatively Control Reactive Gliosis after Injury in the Zebrafish Telencephalon

Because the activation of either Tlr2 or Cxcr3 signaling induced exacerbated glial reactivity in the nostril injury and the transcriptome analysis demonstrated the activation of both pathways exclusively after skull injury, we asked whether interference with these pathways would block the exacerbated gliosis after skull injury. We inhibited the activation of the two signaling pathways by using specific inhibitors: CU CPT22 for the Tlr1/2 [67] pathway and NBI-74330 for the Cxcr3 [68] pathway (Figure 3A). Strikingly, interference with the Tlr1/2 pathway did not change the accumulation of Olig2:GFP+ cells after skull injury (Figure 3A–C,F), despite a significant reduction in the area covered by 4C4+ immune cells (Figure S5A–C,F). Likewise, the inhibition of the Cxcr3 pathway did not affect the accumulation of either 4C4+ or Olig2:GFP+ cells (Figure 3D,F and S5D,F). These data suggest that the two signaling pathways might be functionally redundant in controlling the accumulation of Olig2:GFP+ cells. To assess their redundancy, we simultaneously inhibited the Tlr1/2 and Cxcr3 pathways with respective inhibitors after skull injury (Figure 3A). Indeed, we observed a significant decrease in the number of Olig2:GFP+ cells accumulating at the injury site by 4 dpi in inhibitor-treated animals compared to vehicle (Figure 3E,F). Moreover, Sox10+ cells, representing oligodendrocyte lineage cells [69], showed a similar reduction, supporting the idea that the effect of inhibitors on the oligodendrocyte lineage was mainly in regulating their accumulation at the injury site, rather than affecting Olig2-driven expression of GFP (Figure 3B–E). In addition, the area covered by 4C4+ microglia/monocytes was also significantly reduced after double-inhibitor treatment (Figure S5E,F). A reduction in the accumulation of Olig2:GFP+ cells at the injury site was also observed after Tlr1/2 inhibitor treatment (CU CPT22) combined with a different Cxcr3 inhibitor (AMG-48744) (Figure S5G–J). Thus, the possibility of this phenotype being induced by the off-target effects of our pharmacological treatment is rather low. These effects of the inhibitor cocktail on alleviating Olig2:GFP+ glia and microglia/monocytes accumulation persisted also at later time points as no sign of Olig2:GFP+ cell accumulation was detectable following the double-inhibitor treatment 7 dpi in the skull injury paradigm (Figure 3G–J).

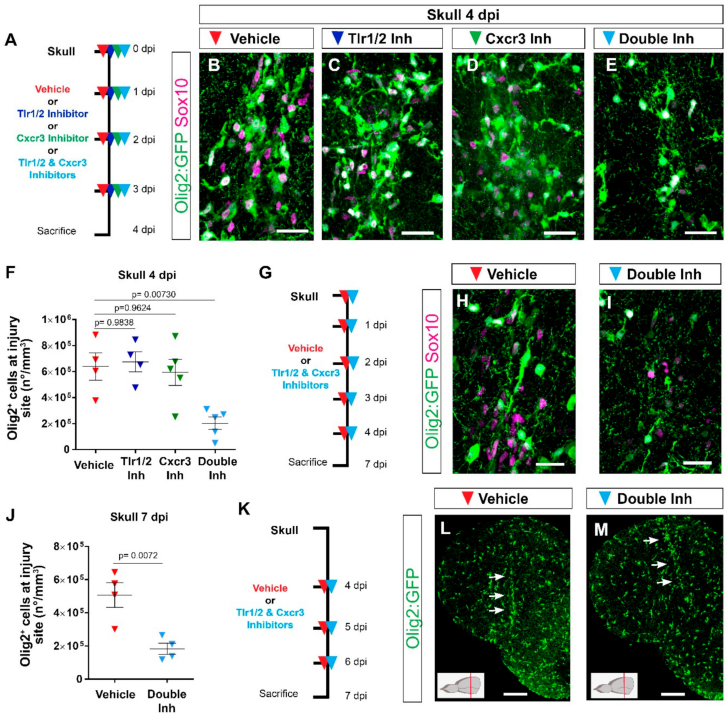

Figure 3. Tlr1/2 and Cxcr3 pathways redundantly control the accumulation of Olig2:GFP$^+$ cells but not their maintenance at the injury site in the zebrafish telencephalon. (**A**) Scheme of the experimental setup to address the role of Cxcr3 and Tlr1/2 in the reactive gliosis 4 days after injury. (**B**–**E**) Micrographs of telencephalic sections obtained after 4 dpi depicting Olig2:GFP$^+$ and Sox10$^+$ oligodendroglia reactivity with vehicle (**B**), Tlr1/2 inhibitor (**C**), Cxcr3 inhibitor (**D**), and double-inhibitor (**E**) treatments. (**F**) Graph showing the density of Olig2:GFP$^+$ cells located at the injury site after vehicle, Tlr1/2 inhibitor (CU CPT22), Cxcr3 inhibitor (NBI 74330) and double-inhibitor combination (NBI 74330 + CU CPT22) treatment. Note that only the double-inhibitor cocktail reduces the number of Olig2:GFP$^+$ cells accumulating at the injury site. Data shown as mean ± SEM; each data point represents one animal. *p*-values are based on a one-way ANOVA (*p*-value = 4.074×10^{-3}) with a post-hoc Dunnett test (Many-to-One). (**G**) Experimental outline to assess the effect of vehicle and double-inhibitor treatment 7 dpi. (**H**,**I**) Micrographs of telencephalic sections 7 days after skull injury depicting Olig2:GFP$^+$ and Sox10$^+$ oligodendroglia after vehicle (**H**) and inhibitor cocktail (NBI 74330 and CU CPT22) (**I**) treatment. (**J**) Graph illustrating the density of Olig2:GFP$^+$ cells located within the injured volume after vehicle and double-inhibitor treatment. An equal volume was quantified in both conditions (*p*-values is based on Student's *t*-test with equal variances). (**K**) Scheme depicting the experimental design to assess the capacity of the vehicle and double inhibitors treatment to resolve glial accumulation. (**L**,**M**) Micrographs showing telencephalic sections 7 days after skull injury and vehicle (**L**) or double-inhibitor (**M**) treatment. White arrows indicate the injury site. Note that both vehicle and inhibitor treatments failed to resolve Olig2:GFP$^+$ accumulation. All images are full *z*-projections of confocal stack. The level of the cross-section is indicated in the inset. Scale bars in (**L**,**M**) = 100 µm; scale bars in (**B**–**E**,**H**,**I**) = 20 µm. Abbreviations: dpi: days post-injury, Inh: inhibitor. Symbol description: red triangle: vehicle; dark blue triangle: Tlr1/2 inhibitor, CU CPT22; green triangle: Cxcr3 inhibitor, NBI 74330; light blue triangle: double inhibitors, NBI 74330 and CU CPT22.

The reduction in the number of reactive glial cells accumulating at the injury site after double-inhibitor treatment suggests a role of these pathways in the initial induction of the glial cell reaction, their maintenance at the injury site, or both. To further disentangle the role of Tlr1/2 and Cxcr3 signaling in the maintenance of Olig2:GFP+ cells at the injury site, we pharmacologically blocked both pathways after the initial accumulation of Olig2:GFP+ cells at 4 dpi (Figure 3K). Once the glial cells had accumulated at the injury site (4 dpi), interference with the activation of both pathways failed to resolve the accumulation of Olig2:GFP+ cells 7 dpi (Figure 3L,M), in strong contrast to the improvement observed in the early inhibition protocol (Figure 3G,J). Taken together, these data support the role of Tlr1/2 and Cxcr3 signaling during the initial phase of glial accumulation.

Because immunohistochemical analysis showed a similar initial accumulation of glial cells at the injury site at 3 days following nostril and skull injury (Figure 1N,O), we asked whether interference with Tlr1/2 and Cxcr3 signaling could alter the accumulation of Olig2:GFP+ cells in the nostril injury paradigm. To address this question, we treated nostril-injured animals with Tlr1/2 and Cxcr3 inhibitors and assessed the accumulation of Olig2:GFP+ cells at the injury site (Figure S5K). We observed a similar initial recruitment of Olig2:GFP+ at the injury site in untreated and vehicle-treated animals (Figure S5N). Importantly, double-inhibitor treatment did not interfere with this initial accumulation of Olig2:GFP+ cells (Figure S5L–N), in agreement with the absence of the transcriptional signature indicative of innate immunity activation after the nostril injury.

In conclusion, our data support the hypothesis that the restricted glial response correlating with complete tissue restoration and the long-lasting, reactive gliosis rely largely on different molecular mechanisms. The simultaneous activation of Tlr1/2 and Cxcr3 during the wound healing period is sufficient and necessary to induce a prolonged accumulation of both microglia/monocytes and Olig2:GFP+ cells at the injury site, leading to a long-lasting, exacerbated glial reaction.

3.4. Reduction in Glial Accumulation Correlates with Better Tissue Recovery

The reduction in the exacerbated accumulation of Olig2:GFP$^+$ and microglia/monocytes after double-inhibitor treatment following skull injury prompted us to investigate the effect of prolonged injury-induced gliosis on brain regeneration by measuring the volume of the injured tissue (Figure 4A,B). We observed a significant reduction in the size of the injured tissue 7 dpi after double-inhibitor treatment compared with vehicle treatment (Figure 4B and Video S5). This reduction in the injured volume was not observed in animals treated only with the Tlr1/2 pathway inhibitor (CU CPT22, Figure 4B) that maintains the Olig2:GFP$^+$ cell accumulation but reduces microglial reactivity at 4 dpi (Figure S5C,F). This finding supports the hypothesis that the decrease in the number of reactive Olig2:GFP$^+$ cells at the injury site leads to improved tissue restoration.

We next tested whether the improved tissue recovery induced by the double-inhibitor treatment was accompanied by an addition of new, adult-generated HuC/D$^+$ neurons to the injured brain parenchyma (restorative neurogenesis). As ependymoglial cells lining the ventricle surface increase their proliferation and generate new neurons in response to an injury [2,33,37], we used BrdU-based birth dating to determine whether the decreased glial reactivity after double-inhibitor treatment also correlated with improved restorative neurogenesis. To assess injury-induced neurogenesis, BrdU was added to the fish water during the first 3 days after injury to label all cells synthesizing DNA; that is, mostly dividing progenitors. The BrdU-incorporation phase was followed by a 4-day chase period, allowing progenitor differentiation, and correlating with the resolution of the glial accumulation upon inhibitor treatment (Figure 4C). We previously showed that the majority of newly generated neurons in the intact brain (BrdU$^+$ and HuC/D$^+$) reside in the ventricular zone (hemisphere periphery, Figure 4G) and display very low migratory potential [47]. Therefore, we analyzed the proportion of HuC/D$^+$ and BrdU$^+$ cells residing outside this neurogenic zone, as we observed the migration of new neurons towards this area only after injury [47]. Both control and inhibitor-treated animals generated

similar total numbers of new neurons (HuC/D$^+$ and BrdU$^+$) after injury (Figure 4D–F). However, we observed a significantly increased proportion of new neurons located in the brain parenchyma after double-inhibitor treatment (HuC/D$^+$ and BrdU$^+$ located in the parenchyma in respect to all HuC/D$^+$ and BrdU$^+$ cells) (Figure 4G,H). As we did not observe any difference in the total number of generated neurons between control and double-inhibitor treated animals, our data exclude an effect of inhibitor treatment on injury-mediated stem cell activation, but rather support the interpretation that the resolution of a long-lasting, exacerbated glial reaction contributed to the better recruitment, survival, or integration of newly generated neurons into the injured brain parenchyma.

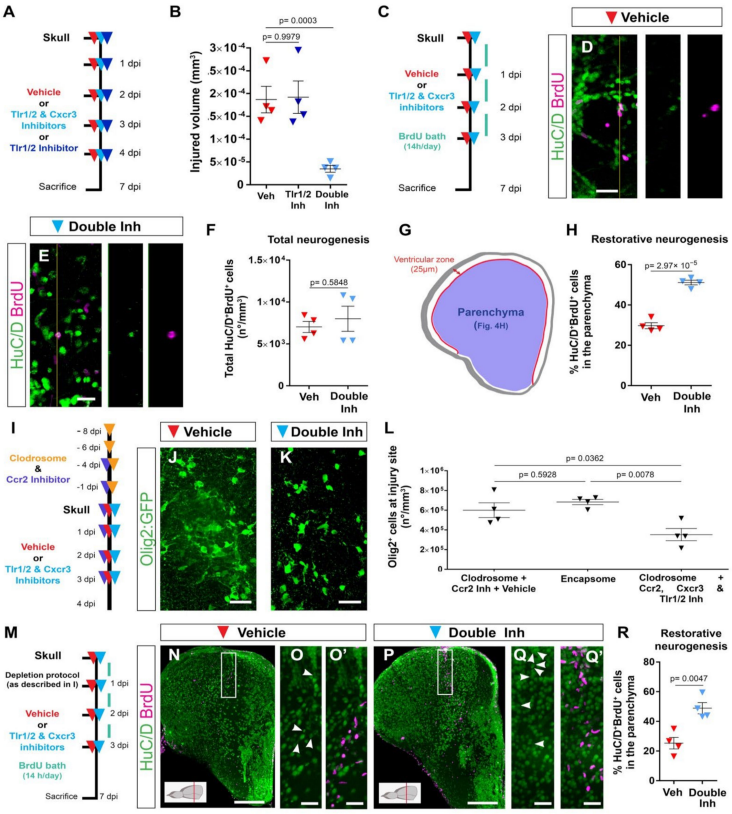

Figure 4. Activation of Tlr1/2 and Cxcr3 creates a detrimental environment by inducing oligodendroglia accumulation in a microglia/monocyte-independent manner. (**A**) Scheme of the experimental design to analyze the consequences of double-inhibitor treatment (NBI 74330 and CU CPT22). (**B**) Graph illustrating the size of the injured volume 7 days after skull injury and vehicle, Tlr1/2 inhibitor (CU CPT22), or double Tlr1/2 and Cxcr3 inhibitor (NBI 74330 and CU CPT22) treatment. *p*-values are based on a one-way ANOVA (*p*-value = 1.971×10^{-4}) with a post-hoc Dunnett test (Many-to-One). (**C**) Experimental scheme designed to study restorative neurogenesis upon different treatments. (**D**,**E**) Images depicting HuC/D$^+$ and BrdU$^+$ cells located in the parenchyma following vehicle (**D**) and double-inhibitor (**E**) treatment. (**F**) Dot-plot showing the total density (whole telencephalon) of HuC/D$^+$ and BrdU$^+$ after vehicle and Tlr1/2 and Cxcr3 inhibitor treatment. *p*-value is based on WelcH's *t*-test with unequal variances. (**G**) Diagram illustrating the ventricular zone

(25 μm from the ventricle surface) and the parenchyma (blue area) in the telencephalic region. Restorative neurogenesis was measured by the proportion of newly generated neurons (HuC/D$^+$ and BrdU$^+$) that migrated towards the parenchyma with respect to the total number (ventricular zone and parenchyma) of new neurons. (**H**) Graph depicting the proportion of HuC/D$^+$ and BrdU$^+$ cells located in the telencephalic parenchyma after vehicle and Tlr1/2 and Cxcr3 inhibitor treatment. *p*-value is based on Student's *t*-test with equal variances. (**I**) Design of the experimental workflow to analyze the effect of Tlr1/2 and Cxcr3 inhibitors on accumulation of Olig2:GFP$^+$ cells after microglia/monocytes depletion. (**J**,**K**) Micrographs depicting the reactivity of Olig2:GFP$^+$ cells after skull injury at 4 dpi with microglia/monocyte depletion and vehicle (**J**) or Tlr1/2 and Cxcr3 inhibitor treatments (**K**). (**L**) Graph illustrating the density of Olig2:GFP$^+$ cells at the injury site at 4 dpi following Clodrosome + Ccr2 (MK-0812) inhibitor treatment (microglia/monocyte depletion protocol), Encapsome (empty liposomes, control for Clodrosome; ventricular injection) and Clodrosome + Ccr2 + Tlr1/2 (CU CPT22) + Cxcr3 (NBI 74330) inhibitor treatments. The decrease in Olig2:GFP$^+$ cell accumulation after Tlr1/2 and Cxcr3 inhibitor treatment was maintained in microglia/monocyte-depleted brain. *p*-values are based on a one-way ANOVA (*p*-value = 7.957×10^{-3}) with a post-hoc Tukey Test (All Pairs). (**M**) Design of the experimental protocol used to analyze injury-induced neurogenesis (BrdU-based birth dating) in microglia/monocyte-depleted brains treated with vehicle or Tlr1/2 and Cxcr3 inhibitor cocktail. (**N**,**P**) Micrographs of injured telencephala at 7 dpi showing the generation of new neurons (HuC/D$^+$/BrdU$^+$) after vehicle (**N**) and Tlr1/2 and Cxcr3 inhibitor (**P**) treatment in microglia/monocyte-depleted brains. (**O**,**O′**,**Q**,**Q′**) are magnifications of the areas boxed in (**N**,**P**), respectively. White arrowheads depict double HuC/D$^+$ and BrdU$^+$ cells. The level of the cross-section is indicated in the inset. (**R**) Graph depicting the proportion of HuC/D$^+$ and BrdU$^+$ cells located in the telencephalic parenchyma after vehicle and Tlr1/2 and Cxcr3 inhibitor treatment. *p*-value is based on Student's *t*-test with equal variances. All images are full z-projections of a confocal stack. Data are shown as mean ± SEM; each data point represents one animal. Scale bars in (**N**,**P**) = 100 μm; scale bars in (**D**,**E**,**J**,**K**,**O**,**O′**,**Q**,**Q′**) = 20 μm. Abbreviations: dpi: days post-injury; Veh: vehicle; Inh: inhibitors. Symbol description: red triangle: vehicle; dark blue triangle: Tlr1/2 inhibitor, CU CPT22; light blue triangle: double inhibitors, NBI 74330 and CU CPT22; orange triangle: ventricular Clodrosome injection; purple triangle: intraperitoneal Ccr2 inhibitor injection, MK-0812.

3.5. Microglia/Monocytes Depletion Does Not Alter the Innate Immunity-Regulated Accumulation of Olig2:GFP$^+$ Cells at the Injury Site

The simultaneous inhibition of Tlr1/2 and Cxcr3 improved tissue regeneration. However, decreasing only 4C4$^+$ cell reactivity with the Tlr1/2 inhibitor without changing Olig2:GFP$^+$ cell accumulation showed no beneficial effect on infarct tissue volume (Figure 4B). These data suggest that microglia/monocytes might be unnecessary for the glial response regulated by the Tlr1/2 and Cxcr3 signaling pathways. To directly assess this hypothesis, we analyzed the accumulation of Olig2:GFP$^+$ cells at the injury site in brains depleted of microglia/monocytes. A combination of Clodrosome and a Ccr2 inhibitor prior to skull injury depleted 95% of 4C4$^+$ cells (microglia and infiltrating monocytes, Figure S6C–F). The 4C4-free condition was then maintained by continuously blocking monocyte extravasation through Ccr2 inhibitor (Figure S6G–I) during the restricted time window when the Tlr1/2 and Cxcr3 pathways induced the long lasting reaction of Olig2:GFP$^+$ cells (Figures 2I and 3A–F,K–M). Initial microglia/monocyte depletion did not alter Olig2:GFP$^+$ cell accumulation at 4 days after skull injury compared with the control Encapsome treatment (Figures 4I,J,L and S6J,K). Importantly, the inhibition of Tlr1/2 and Cxcr3 successfully blocked the prolonged, exacerbated accumulation of Olig2:GFP$^+$ cells in microglia/monocyte-depleted brains (Figure 4K,L) to the same extent these inhibitors prevent the accumulation of Olig2:GFP$^+$ cells in brains populated with microglia/monocytes (compare double inhibitor in Figures 3F and 4L. Consistent with this, our expression analysis of FACS-purified Olig2:DsRed$^+$ cells (labeling the same oligodendroglia population as Olig2:GFP$^+$) showed that they express Cxcr3 (Cxcr3.2 and Cxcr3.3) and Tlr2 (Tlr18) isoforms in both intact and injured brains (Figure S6L). Moreover, the RNAscope analysis

revealed the expression of genes involved in both innate immune pathways (*Cxcr3.2*, *Tlr8b*, *MYD88* and *Mxc*) in the Olig2:GFP$^+$ population after skull injury (Figure S6M–R). These data support the concept that the activation of microglia and/or invading monocytes is not necessary for Tlr1/2 and Cxcr3 injury-induced oligodendroglial reactivity and their initial accumulation at the injury site in zebrafish.

We next tested the effect of microglia/monocytes depletion on the restorative neurogenesis. To this end, we combined the depletion protocol with the BrdU-based neuronal birth dating used previously (Figure 4M). The initial depletion of injury-activated microglia/monocytes did not alter incorporation of new neurons (Figure 4N–O′) compared with untreated control animals (compare Veh in Figure 4H,R), supporting the hypothesis that the activated microglia/monocytes are not the only populations contributing to the adverse environment, restricting new neuron recruitment. Importantly, the inhibition of the Tlr1/2 and Cxcr3 pathways in microglia/monocyte-depleted brains still improved the addition of new neurons (Figure 4M–R), similar to the beneficial effects observed in animals with an intact immune system and further associating the beneficial effects of the double-inhibitor treatment with the resolution of prolonged Olig2:GFP$^+$ cell accumulation.

Taken together, our results support the hypothesis that the Tlr1/2 and Cxcr3 pathways promote the accumulation of Olig2:GFP$^+$ cells at the injury site and the injury-induced impairment of neuronal recruitment to the injury.

3.6. Olig2:dsRed$^+$ Cells Activate Both Innate Immunity Pathways and Transcription Programs Involved in Cell Proliferation in Response to an Injury

In order to understand the regulatory mechanisms of accumulation of Olig2:GFP$^+$ cells downstream of innate immunity pathways after skull injury, we analyzed the injury-induced transcriptomic changes in Olig2:dsRed$^+$ cells (enriched for OPCs [82]) acutely isolated from the injured zebrafish telencephalon 3 days after either vehicle or inhibitor treatment. We observed 1649 significantly regulated transcripts in dsRed$^+$ cells after injury in vehicle-treated brains compared with intact brains (Figure S7A). Interestingly, a minority of transcripts were downregulated (114), suggesting that upon injury OPCs still maintain their oligodendrocyte lineage identity and gain additional features, leading to their reactivity. The distribution of upregulated genes in the biological pathways (Panther-based analysis) revealed the activation of FGF-, EGF-, PDGF-signaling pathways (Figure S6B), which have previously been implicated in the proliferation of OPCs [83–86]. In line with those activated pathways, GO term analysis revealed an enrichment of the processes involved in reactive gliosis, such as cell migration and response to cytokines and chemokines (Figure S7C). Surprisingly, most of the enriched GO terms were related to inflammation (63% of all enriched terms, Figure S7C), including the activation of innate immunity. Importantly, the genes belonging to both cytokine and toll-like receptor signaling were upregulated in response to injury (Figure S7B,C; Table S7). Moreover, 45% of ECM- related genes specifically regulated at 3 days after skull injury in the entire telencephalon were also regulated in the Olig2:dsRed$^+$ cell population (Figure S7D). This unbiased transcriptome analysis further corroborated our hypothesis that cells of the oligodendrocyte lineage activate molecular pathways of the innate immune response, including Tlr2 and Cxcr3, which allows their microglia/monocyte-independent reaction and accumulation at the injury site.

The transcriptomic changes after skull injury, supporting the activation of innate immunity pathways directly in Olig2$^+$ cells, prompted us to further analyze the effect of the inhibitor cocktail on gene expression in Olig2$^+$ cells isolated from injured brains. Interestingly, the inhibitor treatment did not change the overall transcriptome of Olig2$^+$ cells. Approximately 80% of regulated transcripts after inhibitor treatment were also regulated in vehicle-treated brains (Figures 5A and S7A,E). This suggests that the inhibitor cocktail treatment did not change the overall transcriptome of Olig2:dsRed$^+$ cells, but rather restricted regulatory pathways involved in their long-term reactivity. Importantly, both cytokine receptor signaling and toll-like receptor signaling were no longer regulated in Olig2:dsRed$^+$ cells after inhibitor treatment (Figure 5A,B; Table S8). However, the

regulation of number of biological processes linked to the immune response was still present (Table S9). A comparison of injury-regulated genes in Olig2$^+$ cells isolated from vehicle- and inhibitor cocktail-treated brains identified a set of 510 genes (597 transcripts) exclusively regulated after brain injury and vehicle treatment (Figure 5A) and, therefore, were likely involved in reactive gliosis downstream of the Tlr1/2 and Cxcr3 pathways. These genes were overrepresented in GO terms related to proliferation and cell migration (Figure 5B, Table S9), both being biological processes at the core of the oligodendroglial reaction to injury and prolonged gliosis in mammals [87,88].

3.7. Regulation of Oligodendrocyte Progenitor Cell Proliferation by Tlr1/2 and Cxcr3 Signaling

Transcriptome data support the role of Tlr1/2 and Cxcr3 signaling pathways in the direct regulation of OPC proliferation leading to persistent accumulation at the injury site. Therefore, we first assessed the proliferation of Olig2:GFP+ cells after skull injury in the zebrafish telencephalon. Accordingly, we labeled all cells undergoing S-phase by BrdU within 5 days after the injury to find out if the proliferation contributes to the observed accumulation of oligodendroglia at the injury site (Figure 5C). As expected, we observed an accumulation of Olig2:GFP+ cells at the injury site, indicating that the BrdU treatment did not alter the behavior of Olig2:GFP+ cells. Importantly, we observed that 45% of all Olig2:GFP+ cells at the injury site were BrdU+ and hence went through at least one cell cycle during 5 days of labelling (Figure 5D–F), supporting the concept that the Olig2:GFP+ accumulation at the skull injury site was, at least in part, achieved by the increased proliferation of progenitor cells labelled by Olig2:GFP transgenic line (OPCs). We next analyzed if these accumulated OPCs further differentiated into mature oligodendrocytes. We made use of the transgenic line Tg(Mbp:nls-GFP) [77] and a BrdU-based birth dating protocol to identify the proportion of the injury-activated OPCs that matured into oligodendrocytes 7 days after the skull injury (Figure S7F). We observed neither a significant increase in the total number of oligodendrocytes nor an increase in the proportion of newly matured, BrdU+ oligodendrocytes upon skull injury (Figure S7G–K), supporting the concept that OPCs and not mature oligodendrocytes accumulate at the injury site [25].

Next, we analyzed whether the inhibitor cocktail treatment may alter the proliferation of Olig2:GFP+ cells as the cellular basis for reduction in their accumulation at the injury site. As Olig2:GFP+ cells display the first signs of exacerbated reactivity 3 days after skull injury, yet without the significant change in total number of Olig2:GFP+ cells, we analyzed the proliferation of Olig2:GFP+ cells 3 dpi after vehicle and inhibitor treatment (Figure 5G). This experiment revealed a significant reduction in the total number of BrdU+ Olig2:GFP+ cells after inhibitor cocktail treatment compared with the vehicle treatment (Figure 5H–L). To confirm the activation of Tlr1/2 and Cxcr3 pathways directly in OPCs, we made use of a murine OPC culture system. Moloney murine leukemia virus (MLV)-based clonal analysis was performed in pure primary OPC cultures isolated from P0 mouse cerebral cortex after vehicle or double-inhibitor treatment (Figure 5M). OPCs were permanently labeled with GFP expressing retrovirus and the size of clones produced by transduced progenitors within 5 days was measured (Figure 5N–P). Double-inhibitor treatment reduced the GFP+ clone size produced by OPCs, supporting a direct role of Tlr1/2 and Cxcr3 pathways in OPC proliferation (Figure 5P).

Taken together, our data indicate a direct role of Tlr1/2 and Cxcr3 pathways in regulating Olig2+ OPC proliferation to achieve long-lasting accumulation at the injury site in the zebrafish telencephalon.

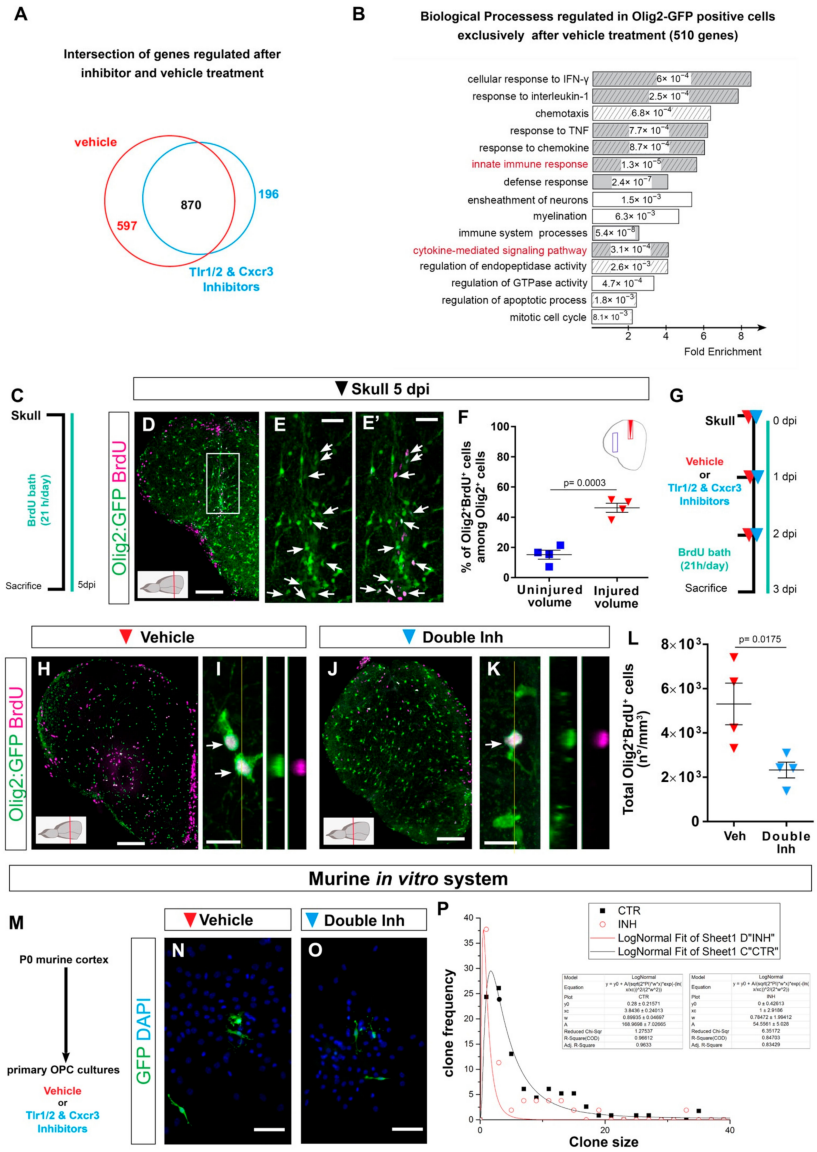

Figure 5. Transcriptome analysis of zebrafish oligodendrocyte lineage reveals the activation of innate immunity and cell cycle pathways after skull injury. (**A**) Venn diagram of genes regulated at 3 dpi in Olig2-GFP^{+} cells after vehicle (red) and Tlr1/2 and Cxcr3 inhibitor (cyan) treatment. (**B**) Histogram depicting GO biological process terms significantly enriched (*p*-values indicated on bars) in a gene set (597 genes in (**A**)) normalized after inhibitor treatment and therefore regulated exclusively after vehicle treatment. GO terms related to inflammatory response are shown by gray bars; patterned bars indicate processes previously reported to be activated in response to injury. Note that both innate

immunity and cytokine-mediated signaling pathways are normalized upon inhibitor treatment. (**C**) Scheme depicting the experimental design to analyze the proliferative capacity of Olig2:GFP$^+$ cells during the first 5 days after skull injury. (**D**) Micrograph of injured section 5 days after skull injury stained for GFP and BrdU. (**E**,**E′**) Magnification of the oligodendroglial accumulation boxed in (**D**). Double Olig2:GFP$^+$ and BrdU$^+$ cells are marked with white arrows. (**F**) Graph illustrating the proportion of Olig2:GFP$^+$ and BrdU$^+$ cells located at the injury site and in an equivalent uninjured volume in the same section. Note that 45% of the Olig2:GFP$^+$ cells at the injury site proliferated after skull injury. (**G**) Scheme of the experimental design to assess the proliferation of Olig2-GFP$^+$ cells after vehicle and inhibitors treatment. (**H**,**J**) Images of telencephalic sections 3 days after skull injury and BrdU bath with vehicle (**H**) and double inhibitors (**J**) treatments. (**I**,**K**) Micrographs with orthogonal projections of proliferating (BrdU$^+$) Olig2:GFP$^+$ cells after vehicle (**I**) and Tlr1/2 and Cxcr3 inhibitor (**K**) treatment. (**L**) Graph depicting the density of Olig2:GFP$^+$ and BrdU$^+$ cells 3 dpi in vehicle and Tlr1/2 and Cxcr3 inhibitor treated animals. (**M**) Experimental design to measure the clonal growth of murine OPCs primary cultures after vehicle and Tlr1/2 and Cxcr3 inhibitor cocktail treatment. OPCs were permanently labeled with GFP expressing retrovirus. (**N**,**O**) Micrographs depicting OPC derived clones 5 days after retroviral infection in vehicle (**N**) and Tlr1/2 and Cxcr3 inhibitor (NBI 74330 and CU CPT22) cocktail (**O**) treated primary OPCs culture. (**P**) Graph depicting the frequency of different clone sizes in the vehicle (CTR) and Tlr1/2 and Cxcr3 inhibitor cocktail (INH) treated primary OPCs culture. Data are shown as mean ± SEM; each data point represents one animal. *p*-values are based on Student's *t*-test with equal variances. All images are full z-projections of a confocal stack. The level of the cross-section is indicated in the inset. Scale bars in (**D**,**H**,**J**) = 100 μm; scale bars in (**N**,**O**) = 50μm, scale bars in (**E**,**E′**) = 20 μm; scale bars in (**I**,**K**) = 10 μm. Abbreviations: dpi: days post-injury; Veh: vehicle; Inh: inhibitors; OPC: oligodendrocyte progenitor cell. Symbol description: Triangle: skull injury; blue square: uninjured volume; red triangle: vehicle; light blue triangle: double inhibitors, NBI 74330 and CU CPT22; black square: control primary OPCs; red circle: double inhibitor (NBI 74330 and CU CPT22) treated primary OPCs.

3.8. Cerebrospinal Fluid Induces Exacerbated Glial Reactivity by Increasing OPC Proliferation

To identify the source and nature of the ligands activating the prolonged accumulation of OPCs after brain injury, we first examined the size of the skull versus nostril injury. As the volume of the skull injury was larger than the nostril injury (Figure 6A), we first set out to determine whether this was the cause of the reactive gliosis. We reduced the volume of the skull injury to one-third (small skull injury) using the same glass capillary as for the nostril injury (Figure 6B). The small skull injury still induced a strong reactivity of both 4C4+ and Olig2:GFP+ cells 7 days after the injury (Figure 6C,D). This reaction was comparable to the outcome of the initial skull injury, allowing us to exclude the size of the injury as a major determinant of differential glial reactivity.

We next hypothesized that an injury-induced ligand that activates the exacerbated reaction must be present only after skull injury. The telencephalic ventricle is located dorsally in the zebrafish brain [78,79] and, therefore, is exclusively damaged during the dorso-ventrally performed skull injury. Cerebrospinal fluid (CSF), which is confined to the ventricles, is rich in cytokines and growth factors that maintain normal homeostasis and nurture the brain; however, direct interaction with the brain parenchyma is restricted and regulated by the CSF–brain barrier [80]. Rupture of the ventricular barrier might allow an influx of CSF-derived molecules into the brain parenchyma, potentially explaining the activation of the Tlr1/2 and Cxcr3 pathways only after skull injury. To validate the potential of CSF to induced OPC reaction, we injected human CSF in the nostril injury site and analyzed glial reactivity (Figure 6E). Notably, we observed an 8-fold increase in the number of Olig2:GFP+ cells accumulating at the injury site (Figure 6F,M). As we inject the human CSF, the observed reaction could be a result of xenobiotic response. Therefore, we heat-inactivated the human CSF and probed its capacity to induce the reaction of OPCs in the nostril injury. Importantly, the dramatic CSF effect was not observed upon the administration heat-inactivated human CSF (Figure S8) Moreover, the administration of the human

plasma containing many of the CSF components failed to induce the response (Figure S8), indicating that the prolonged OPC reactivity was not due to xenobiotic inflammation or misfolded proteins present in the CSF. The extraordinary potential of the CSF to induce exacerbated gliosis prompted us to investigate the cellular basis for the Olig2:GFP+ cell accumulation in response to the CSF. As the accumulation of OPCs after a skull injury was achieved, at least in part, by an increased proliferation of OPCs (Figure 6C–F), we assessed whether the proliferation of Sox10+ cells was also induced by the CSF injection into the nostril injury site (Figure 6G). Indeed, we observed that the majority of Sox10+ cells accumulating around the injury site incorporated BrdU during the initial 3 days after the injury and CSF administration (Sox10+ and BrdU+ cells in respect to all Sox10 + cells) (Figure 6H,H′,J). The induced proliferation was not, however, observed after the injection of heat-inactivated CSF (Figure 6I,J), in line with the significantly smaller accumulation of Olig2:GFP+ cells at the injury site observed after heat-inactivated CSF treatment (Figure S8C,D). The similarity in OPC reaction induced by CSF injection into the nostril injury and the skull injury motivated us to assess whether CSF-induced accumulation of OPCs involved the activation of the Tlr1/2 and Cxcr3 pathways. Therefore, we inhibited the Tlr1/2 and Cxcr3 pathways together with the administration of human CSF after nostril injury (Figure 6K). Importantly, the accumulation of Olig2:GFP+ cells was prevented upon Cxcr3 and Tlr1/2 inhibition, despite the accessibility of the CSF at the injury site (Figure 6L,M). Taken together, these data suggest that the OPC accumulation observed upon skull injury is likely triggered by leakage of CSF into the brain parenchyma and the subsequent activation of the Tlr1/2 and Cxcr3 pathways.

To identify potential ligands activating innate immunity pathways in the CSF, we set up an in vitro system that relays on the proliferation of a murine OPC cell line (OliNeu). Importantly, the addition of CSF to the OliNeu culture medium induced a dose-dependent increase in the proportion of proliferating, phospho-histone H3 (pH3) positive cells (Figure 7A–D), in line with our data that human CSF can directly regulate OPC proliferation in vivo (Figure 6J). Moreover, this dose-dependent response was completely abolished in the double Tlr2 and Cxcr3 knockout clones generated using CRISPR-Cas9 technology (Figures 7D,Q and S9). These results not only confirmed the pivotal role of Tlr2 and Cxcr3 signaling in the CSF induced proliferation of OPCs, but also additionally validated the specificity of our pharmacological inhibitor treatment in vivo.

As cytokines have been reported to activate both Cxcr3 and Tlr2 signaling [61,65,81], we first studied the composition of four healthy donor-derived CSFs using a cytokine antibody array (Figure 7E,F). It is important to mention that all four samples increased proliferation in vivo. Strikingly, 90% of the analyzed cytokines were present in at least one of the samples and 57% in all four samples (Figure 7E,F).

Out of these cytokines, we pre-selected 30 potential candidates (Figure 7E; Table S3) that were present in at least one CSF sample and available as recombinant protein for further functional screening using OliNeu proliferation as a read-out (Figure 7G). We used three different concentrations of the selected candidates and six of them (Ccl5, EGF, Ccl7, IL-10, Cxcl9 and IL-3) significantly increased the proportion of mitotic pH3+ cells (Figure 7G), including a known Cxcr3 ligand (Cxcl9). Interestingly, some candidates such as Cxcl9 were not detected in all CSF samples despite the ability of all four CSF samples to induce the accumulation of Olig2:GFP+ cells, suggesting redundancy of ligands in their capacity to activate OPC proliferation. Taken together, our data suggest that the CSF cytokines activate the innate immunity to regulate OPC proliferation in a redundant manner and therefore regulate the reactive gliosis.

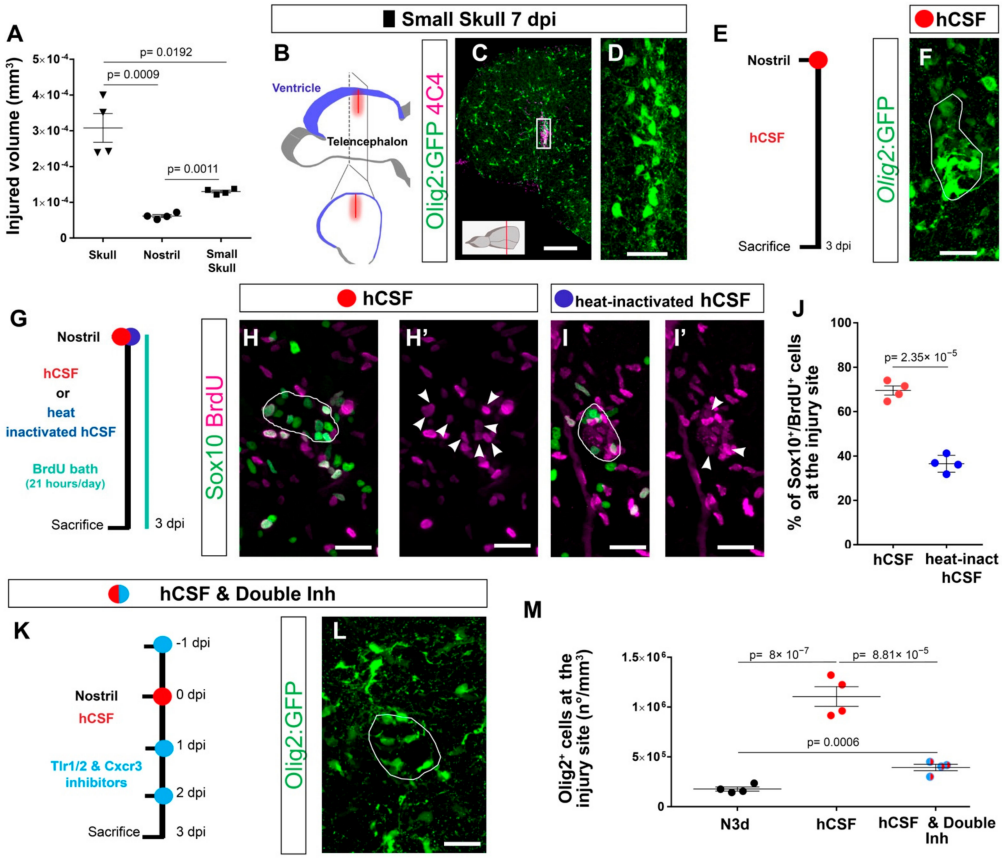

Figure 6. Cerebrospinal fluid-derived molecules induce the proliferation of OPCs and a reactive gliosis-like phenotype. (**A**) Graph depicting the size of the injured volume after skull, nostril, and small skull injury at 1 dpi. *p*-values are based on a Welch one-way ANOVA (unequal variances; *p*-value = 3.034×10^{-4}) with a post-hoc Dunnett T3 test with unequal variances (all pairs). (**B**) Scheme depicting the small skull injury model. Nostril and small skull injuries were performed with a glass capillary. The red line indicates the dorso-ventral injury through the skull and blue indicates the location of the telencephalic ventricle. (**C**) Image illustrating the reactivity of Olig2:GFP$^+$ and 4C4$^+$ cells 7 days after small skull injury. (**D**) Magnification of the oligodendroglial accumulation boxed in (**C**). (**E**) Design of the experimental workflow to analyze the effect of human CSF administration. (**F**) Image illustrating the reactivity of Olig2:GFP$^+$ cells 3 days after nostril injury and hCSF treatment. White line depicts the injury site. (**G**) Experimental design to analyze the proliferative capacity (BrdU incorporation) of Sox10$^+$ cells after nostril injury at 3 dpi and hCSF or heat-inactivated hCSF administration. (**H**–**I′**) Images showing the accumulation of Sox10$^+$ and BrdU$^+$ cells at the nostril injury site after hCSF (**H**,**H′**) or heat-inactivated human CSF (**I**,**I′**) administration. White lines depict the injury site and white arrowheads the colocalization of BrdU and Sox10. (**J**) Dot-plot depicting the proportion of Sox10$^+$ and BrdU$^+$ cells accumulating at the nostril injury site after hCSF or heat-inactivated hCSF administration. *p*-value is based on Student's *t*-test with equal variances. (**K**) Workflow to study the effect of the Tlr1/2 and Cxcr3 inhibitor treatment after human CSF

injection. (**L**) Micrograph of a nostril-injured telencephalon at 3 dpi depicting Olig2:GFP^{+} cell reactivity following human CSF and inhibitor treatment. The white line depicts the injury site. (**M**) Graph showing the density of Olig2:GFP^{+} cells at the injury site at 3 dpi after nostril injury, treatment hCSF, and treatment with hCSF and double-inhibitor. *p*-values are based on one-way ANOVA (p-value = 1.042×10^{-6}) with post-hoc Tukey Test (all pairs). Data are shown as mean ± SEM; each data point represents one animal. All images are full z-projections of confocal stack. Scale bars in (**C**) = 100 µm; scale bars in (**D**,**F**,**H**,**H′**,**I**, **I′**,**L**) = 20 µm. Abbreviations: dpi: days post-injury; hCSF: human cerebrospinal fluid; Inh: inhibitors; N3d; nostril 3 dpi. Symbol description: black triangle: skull injury; black circle: nostril injury; black rectangle: small skull injury; red circle: human CSF administration; blue circle: heat-inactivated hCSF treatment; light blue circle: double inhibitors, NBI 74330 and CU CPT22.

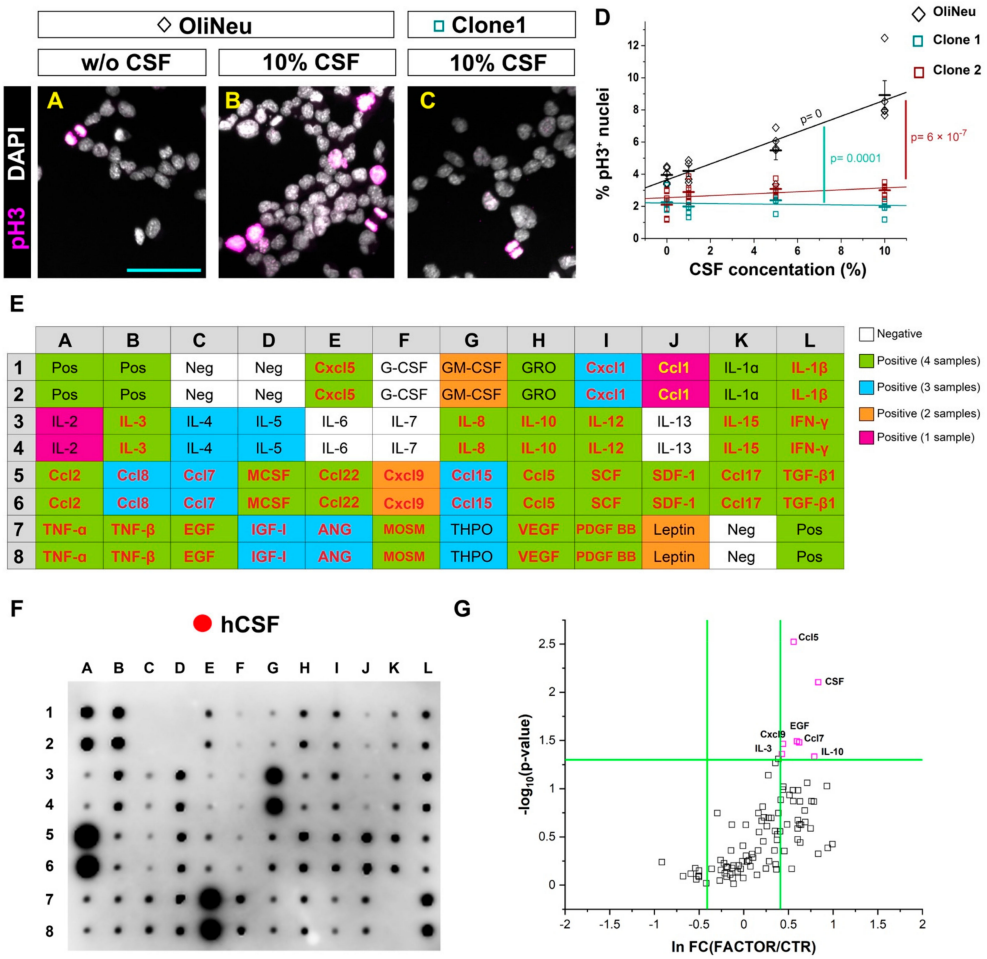

	A	B	C	D	E	F	G	H	I	J	K	L
1	Pos	Pos	Neg	Neg	Cxcl5	G-CSF	GM-CSF	GRO	Cxcl1	Ccl1	IL-1α	IL-1β
2	Pos	Pos	Neg	Neg	Cxcl5	G-CSF	GM-CSF	GRO	Cxcl1	Ccl1	IL-1α	IL-1β
3	IL-2	IL-3	IL-4	IL-5	IL-6	IL-7	IL-8	IL-10	IL-12	IL-13	IL-15	IFN-γ
4	IL-2	IL-3	IL-4	IL-5	IL-6	IL-7	IL-8	IL-10	IL-12	IL-13	IL-15	IFN-γ
5	Ccl2	Ccl8	Ccl7	MCSF	Ccl22	Cxcl9	Ccl15	Ccl5	SCF	SDF-1	Ccl17	TGF-β1
6	Ccl2	Ccl8	Ccl7	MCSF	Ccl22	Cxcl9	Ccl15	Ccl5	SCF	SDF-1	Ccl17	TGF-β1
7	TNF-α	TNF-β	EGF	IGF-I	ANG	MOSM	THPO	VEGF	PDGF BB	Leptin	Neg	Pos
8	TNF-α	TNF-β	EGF	IGF-I	ANG	MOSM	THPO	VEGF	PDGF BB	Leptin	Neg	Pos

Figure 7. In vitro screening to identify potential candidates from the human cerebrospinal fluid inducing OPC proliferation. (**A**–**C**) Micrographs illustrating the proportion of proliferating (pH3 positive) cells in a control wildtype (WT) (**A**,**B**) and Tlr2 and Cxcr3-deficient (**C**) OliNeu oligodendrocyte progenitor cell line in basal conditions (**A**) and in response to the CSF treatment (**B**,**C**). (**D**) Dot-plot

depicting the proportion of proliferating WT and Tlr2 and Cxcr3-deficient Oli-Neu cells after CSF treatment. The line indicates the corresponding linear data-fit. Data are shown as mean ± SEM; each data point represents one independent experiment. Adjusted *p*-values assess the quality of the linear fit for the WT clone (black) and difference in the slopes of the linear fits (color-coded) using the linear regression model. (**E**) Table showing the map of the array in (**F**). Color-code illustrates the presence of each cytokine in CSF samples (White: negative in all samples; Green: positive in all samples; Blue: positive in 3 out 4 samples; Orange: positive in 2 out of 4 samples; Magenta: Positive in 1 out 4 samples). Cytokines names colored in red or yellow were selected for the screening in (**G**). (**F**) Representative image of a cytokine antibody array depicting the cytokine composition of a healthy donor-derived CSF. (**G**) Dot plot depicting proliferation of Oli-Neu cells after treatment with different cytokines and CSF. Scale bars in (**A**–**C**) = 50µm Abbreviations: hCSF: human cerebrospinal fluid. Symbol description: Black diamond: control OliNeu cells; green square: Tlr2 and Cxcr3-deficient clone 1; red square Tlr2 and Cxcr3-deficient clone 2; red circle: human CSF administration.

4. Discussion

Despite the general agreement that mammals exhibit a limited regenerative capacity after CNS trauma, it remains controversial which specific cellular and molecular mechanisms trigger the long-lasting glial reaction that in turn, negatively impact the endogenous regeneration. Comparative studies analyzing the regeneration of competent and incompetent species have failed to identify the specific mechanisms involved in the pathogenesis of traumatic injuries [89–94], even after comparing evolutionarily close species [95–97]. This is due to the complexity of the wound healing response that involves a number of molecular pathways and different cell types [9,34]. There has been a long-held belief that microglia and astrocytes are at the core of the poor regenerative outcome [98,99]. However, recent studies have challenged this concept [5,14]. Ablation of microglia upon CNS injury failed to improve neuronal survival and functional recovery and in some cases, even worsened the regenerative outcome [100,101]. Astrocytic activation after trauma appeared to be more complex than originally expected. Microglia-induced inflammation regulates the activation of different types of reactive astrocytes named "A1" and "A2" [18]. While A1 displayed a neurotoxic phenotype, A2 astrocytes appeared to exert neuroprotective functions [64]. The differential activation of A1 and/or A2 astrocytes might explain the controversy about the functional consequences of astrogliosis and whether reactive astrocytes promote endogenous regeneration or contribute to the detrimental reactive gliosis. Surprisingly, and despite their rapid and robust reaction to injury, it is largely unknown how the oligodendrocyte progenitors (OPCs) fit in this inflammatory cascade. To study the role of OPCs during the wound healing process, we performed a comparative analysis of two injury paradigms displaying differential OPC reactivity in the same organ and model organism. In contrast to the previously described nostril injury of brain parenchyma [33,37,38], skull injury showed more similarities to the glial response reported in mammals, such as prolonged OPC accumulation, lack of tissue restoration, extracellular matrix modifications, and exacerbated inflammatory response [34,102].

Comparative analysis (nostril vs. skull) revealed a shared cellular reaction and large overlap in gene regulation shortly after injury, highlighting the common features of the initial wound healing processes regardless if it is associated with prolonged, exacerbated, or restricted glial reactivity [9]. Importantly, a unique molecular signature, including specific innate immunity pathways, was expressed 3 days after the skull injury, correlating with the first signs of the exacerbated glial reaction. These pathways were never regulated during the nostril wound healing, validating the theory that the prolonged, reactive gliosis is induced by a specific molecular program independent of the initial wound healing response [19]. Our study does not support the concept that the regenerative capacity of the CNS is an evolutionarily fixed feature of a given species [103,104]; rather, it is a highly regulated, adaptive response to a specific type of injury. This concept is shared with skin regeneration, in which the depth of the injury determines the scar response [105].

We identified two receptors, Tlr1/2 and Cxcr3, as main regulators of the exacerbated glial reactivity. Interestingly, the inhibition of either of the two pathways separately showed no beneficial effect, whereas the activation of either Tlr2 or Cxcr3 in the nostril paradigm was sufficient to induce gliosis. Hence, both signaling pathways control reactive gliosis in a redundant and synergistic manner. As previously discussed, the complex cross-regulation of immune cells (monocytes and microglia) and astrocytes after brain injury is crucial for the regenerative outcome [19,106–108]. The classical inflammatory cascade is initiated by activation and polarization of microglia and invading monocytes. Consequently, these cells regulate the reactivity of astrocytes that, in turn, limits the inflammatory response [17,19,109,110]. However, our data demonstrate, for the first time, that microglia/monocytes are not essential for the initial activation of OPCs and that the Tlr1/2 and Cxcr3 pathways can be directly regulated in this population. Our study, therefore, brings forth a new concept that OPCs can sense and react to injury-induced signals independent of microglia and invading monocytes. However, we cannot exclude any involvement of microglia/monocytes in other aspects of the wound healing. As we did not perform cell-specific interference and because both receptors are expressed in several cell types (microglia/monocytes [111,112]; astrocytes [113,114]; oligodendroglia [114]; neurons [113,115]), we cannot exclude the possibility that other cell types contribute to the induction of the wound closure via the Tlr1/2 and Cxcr3 signaling pathways. However, our knockout in vitro model validated the role of the Tlr2 and Cxcr3 pathways in directly activating OPC proliferation and hence, demonstrated that they are clearly involved in a crucial manner in the reactive gliosis. Moreover, the improvement in tissue recovery (reduced injured volume and enhanced restorative neurogenesis) observed after double-inhibitor treatment correlates nicely with a reduction in the number of accumulating Olig2$^+$ cells. Our data support the hypothesis that the detrimental environment classically associated with the reactive gliosis might be driven specifically by reactive OPCs.

The central role of the Tlr1/2 and Cxcr3 pathways in regulating gliosis and tissue restoration motivated us to investigate injury-induced mechanisms. Our study suggests that the ligand(s) activating the Tlr1/2 and Cxcr3 pathways are part of the CSF that leaks into the CNS parenchyma upon traumatic injury [116]. The capability of the CSF to directly induce OPC proliferation in a Tlr2 and Cxcr3-dependent manner, further corroborates the pivotal role of OPCs in initiating the long-lasting glial response and generating a harmful environment. Although the specific CSF-derived molecule/s driving the reactive gliosis in vivo remain unidentified, our in vitro screening suggests that some of the cytokines present in the CSF could be responsible for the OPC activation induced by the traumatic brain injury. These data support a central regulatory role of CSF in controlling not only the activation of neural stem cells in the intact brain, but also the activation state of CNS glia after injury [117,118]. Overall, our work highlights novel pathways in exacerbated OPC activation as potential targets for developing efficient therapies improving regeneration in the mammalian brain.

Supplementary Materials: The following supporting information can be downloaded at: https://www.mdpi.com/article/10.3390/cells11030520/s1, Figure S1. Immune cell reactivity after nostril and skull injury. (A,C) Images of Lys$^+$ neutrophils and 4C4$^+$ cells accumulating at the injury site 12 h (A) and 2 days (C) after the nostril injury. (B) Magnification of the boxed area in A. The number of neutrophils located in the telencephalic parenchyma already decreased at 2 dpi. (D,E) Images of Lys$^+$ neutrophils and 4C4$^+$ cells 12 h (D) and 2 days (E) after the skull injury. Note that already 12 h after the skull injury neutrophils were distributed throughout the whole parenchyma and they maintained such distribution even after 2 days. (F–H‴) Micrographs illustrating the distribution and morphology of 4C4$^+$, L-plastin$^+$ and Mpeg1:mCherry$^+$ cells in intact condition (F–F‴), 3 days after nostril (G–G‴) and 3 days after skull (H–H‴) injury. Note that most of the microglia in the intact brain co-expressed all three markers, although 4C4$^+$ single-expressing cells can be often observed (yellow arrows). Both nostril (G–G‴) and skull injury (H–H‴) changed the morphology and expression pattern of microglia/monocytes. (I–L) Micrographs illustrating the Olig2:GFP (I,K) and 4C4 (J,L) reactivity 1 day after skull (I,J) and nostril (K,L) injury. White lines outline the injured area. All images are full

z-projections of a confocal stack. Scale bars in A, C, D, E, I, J, K and L = 100 μm; Scale bars in B, F, F′, F″, F‴, G, G′, G″, G‴, H, H′, H″, H‴= 20 μm. Abbreviations: dpi: days post-injury; hpi: hours post-injury. Symbol description: black rectangle: intact; black triangle: skull injury; black -circle: nostril injury. Figure S2. Nostril injury does not induce long-lasting accumulation of Olig2:GFP$^+$ cells in the zebrafish telencephalon. (A) Experimental design to analyze the kinetics and reactivity of the Olig2:GFP$^+$ cell population after sagittal sectioning. (B–D) Micrographs of sagittal telencephalic sections at 1 day (B), 3 days (C) and 7 days (D) after nostril injury illustrating the 4C4 and Olig2:GFP reactivity. (E) Dot plot comparing the density of Olig2:GFP$^+$ cells located at the injury site after coronal (data presented in Figure 1N) and sagittal sectioning. Data are shown as mean ± SEM; each data point represents one animal. *p*-values are based on one-way ANOVA (*p*-value = 2.419×10^{-6} and Multiple Comparisons of Means (adjusted *p*-values reported, single-step method) was performed. All images are full z-projections of confocal stack. Scale bars in B, C, D, = 100 μm. Abbreviation: dpi: days post-injury. Figure S3. Reactivity of Gfap$^+$ ependymoglia after nostril and skull injury in the zebrafish telencephalon. (A) Image of an uninjured telencephalic section from the *Tg*(*gfap:GFP*) line. White arrow indicates the basment membrane. (B,D) Micrographs of nostril (B) and skull (D) injured sections at 3 dpi illustrating the reactivity of 4C4$^+$ and Gfap:GFP$^+$ cells. C and E are magnifications from the boxed areas in (B,D). (F,G) Images depicting the reactivity of Gfap:GFP$^+$ cells at 7 days after nostril (F) and skull (G) injury. Note that 7 days after skull injury, the ependymoglial cell layer is restored. (H) Magnification of the injured area boxed in (G); white arrows illustrate misplaced Gfap:GFP$^+$ cells and arrowheads depict hyperreactive Gfap:GFP$^+$ processes. All images are full z-projections of confocal stack. Insets indicate the rostro-caudal levels of the sections. Scale bars in A, B, D, F and G = 100 μm; scale bars in C, E and H = 20 μm. Abbreviation: dpi: days post-injury. Symbol description: black rectangle: intact; black triangle: skull injury; black circle: nostril injury. Figure S4. Activation of Tlr1/2 innate immunity pathways induces prolonged accumulation of Olig2:GFP$^+$ cells after nostril injury. (A) Histogram illustrating the expression level of *Tlr2* in the intact and injured adult zebrafish telencephalon measured by qPCR. Data are shown as mean ± SEM (n = 3 animals). (B) Scheme of the experimental design to identify receptor mediating zymosan A effect. (C,E) Micrographs of zymosan A-treated telencephalic sections of the *Tg*(*Olig2:GFP*) line 5 days after nostril injury and vehicle (C) or Tlr1/2 inhibitor (E) treatment. (D,F) are magnifications of the boxed areas in (C,E), respectively. (G) Graph depicting the density of Olig2:GFP$^+$ cells located at the injured area after aCSF, zymosan A, and zymosan A and Tlr1/2 inhibitor treatment. Data are shown as mean ± SEM, each data point represents one animal. *p*-values are based on a one-way ANOVA (*p*-value = 1.312×10^{-5}) with a post-hoc Tukey Test. All images are full z-projections of confocal stack. Inlets indicate the rostro-caudal levels of the sections. Scale bars in C and D = 100 μm; scale bars in D and F = 20 μm. Abbreviations: N3d: nostril 3 days post-injury; S3d: skull 3 days post-injury; aCSF: artificial cerebrospinal fluid; Inh: inhibitor. Symbol description: black circle: nostril injury; red circle: intraperitoneal injection of vehicle; dark blue circle: intraperitoneal injection of Tlr1/2 inhibitor, CU CPT22; orange circle: ventricular zymosan A injection; orange rectangle: aCSF. Figure S5. Innate immunity pathways and glial reactivity 4 days after skull and nostril injury. (A) Experimental outline to assess the reaction of 4C4$^+$ cells after skull injury with vehicle, Tlr1/2 inhibitor (CU CPT22), Cxcr3 inhibitor (NBI 74330) and Cxcr3 and Tlr1/2 inhibitor (NBI 74330 and CU CPT22) treatment. (B–E) Micrographs depicting telencephalic sections 4 days after skull injury stained for 4C4 after vehicle (B), Tlr1/2 inhibitor (C), Cxcr3 inhibitor (D) and double Tlr1/2 and Cxcr3 inhibitor treatment. Cyan line delineates telencephalic hemisphere. (F) Graph illustrating the proportion of area covered by 4C4 signal after different treatments. *p*-values are based on One-way ANOVA (*p*-value = 7.021×10^{-5}) with post-hoc Dunnett Test (Many-to-One). (G) Scheme of the experimental workflow to analyze the effect of the second inhibitor combination (CU CPT22 + AMG-487) on reactive gliosis. (H,I) Images of injured Tg(Olig2:GFP) section at 4 dpi stained for GFP and Sox10 after vehicle (H) and CU CPT22 + AMG-487 inhibitor (I) treatment. (J) Dot-plot showing the accumulation of Olig2:GFP$^+$ cells at the injury site after vehicle, first combination of double inhibitors, and second combination of double inhibitors treatment. Note that both double-inhibitor combinations reduced oligodendroglia accumulation to the same extent. *p*-values are based on a one-way ANOVA (*p*-value = 1.221×10^{-3}) with a post-hoc Dunnett Test (Many-to-One). (K) Scheme depicting the experimental design to analyze oligodendroglial reaction after nostril injury and vehicle or double Tlr1/2 and Cxcr3 inhibitor (NBI 74330 and CU CPT22) treatment. (L–M′) Micrographs illustrating accumulation of oligodendroglia (Olig2:GFP$^+$ cells) at the injury site 3 days after nostril injury and vehicle (L,L′) or double inhibitor treatment (M,M′). White lines delineate the injury site. (N) Graph depicting the density of

Olig2:GFP$^+$ cells located at the injury area as a function of Tlr1/2 and Cxcr3 pathways. *p*-values are based on a one-way ANOVA (*p*-value = 3.674×10^{-1}) with a post-hoc Dunnett Test (Many-to-One). All images are full z-projections of a confocal stack. Insets indicate the rostro-caudal levels of the sections. Data are shown as mean ± SEM; each data point represents one animal. Scale bars in B, C, D, and E = 100 μm; scale bars in H, I, L, L′, M and M′ = 20 μm. Abbreviations: dpi: days post-injury; N3d: nostril 3 days post-injury; Inh: inhibitor. Symbol description: red triangle: vehicle; dark blue triangle: Tlr1/2 inhibitor, CU CPT22; green triangle: Cxcr3 inhibitor, NBI 74330; light blue triangle: double inhibitors, NBI 74330 and CU CPT22; orange triangle: CU CPT22 + AMG-487 injection; black circle: nostril injury; red circle: vehicle; light blue circle: double inhibitors, NBI 74330 and CU CPT22. Figure S6. Tlr1/2 and Cxcr3 pathways regulate exacerbated oligodendroglia activation independently from microglial and monocyte activation. (A) Scheme of the experimental setting to address the role of Cxcr3 and Tlr1/2 in tissue restoration. (B) Graph showing the volume of the injured tissue after different treatments. *p*-value is based on one-way ANOVA (*p*-value = 1.801×10^{-1}) with post-hoc Dunnett test. (C) Image of an uninjured section stained for two microglia/monocyte markers (L-plastin and 4C4). (D) Scheme of the experimental setting to eliminate microglia and infiltrating monocytes using Clodrosome to deplete resident microglia and Ccr2 inhibitor to block the extravasation of monocytes. (E) Micrograph illustrating the depletion of L-plastin$^+$ and 4C4$^+$ cells in intact brain. (F) Graph depicting the proportion of the section covered with a 4C4 signal in untreated and treated brains; 95% of the 4C4$^+$ signal was depleted after combined Clodrosome and Ccr2 inhibitor treatment. *p*-value is based on WelcH′s *t*-test with unequal variances. (G) Scheme of the experimental setting to analyze 4C4 reactivity upon skull injury and microglia/monocyte depletion. (H,I) Micrographs illustrating 4C4 depletion 1 (H) and 2 (I) days after skull injury. White lines depict the injury site and section profiles are delimited by yellow and blue lines. (J) Scheme of the experimental design to analyze reactive gliosis after injecting empty control liposomes used as vehicle for Clodrosome (Encapsome). (K) Image depicting the Olig2:GFP$^+$ cell accumulation at the injury site in Encapsome-treated brains. Note that repetitive ventricular injections did not alter oligodendroglial accumulation. (L) Graph illustrating the expression levels of Cxcr3 (Cxcr3.1, Cxcr3.2, Cxcr3.3) and Tlr2 (Tlr2, Tlr18) zebrafish orthologs in Olig2:dsRed$^+$ cells analyzed by RNA sequencing. (M–P) Micrographs with orthogonal projections illustrating the expression of Cxcr3.2 (M), Tlr8b (N), MYD88 (O) and Mxc (P) genes in the Olig2:GFP+ cells 3 days after skull injury. (Q,R) Images showing the RNAscope negative controls for the Cy3 (Q) and Cy5 (R) channels. All images are full z-projections of confocal stack. The level of the cross-section is indicated in the inset. Data are shown as mean ± SEM and each data point represents one animal. Scale bars in C, E, H, and I = 100 μm; scale bar in K = 20 μm; scale bar in M, N, O, P, Q, R = 10 μm. Abbreviations: TPM: transcripts per million reads; dpi: days post-injury; Inh: inhibitor. Symbol description: red triangle: vehicle; dark blue triangle: Tlr1/2 inhibitor, CU CPT22; green triangle: Cxcr3 inhibitor, NBI 74330; light blue triangle: double inhibitors, NBI 74330 and CU CPT22; black rectangle: intact; orange square: ventricular injection of clodrosome; purple square: intraperitoneal injection of Ccr2 inhibitor; black triangle: skull injury; gray triangle: encapsome; Orange triangle: ventricular injection of clodrosome; purple triangle: intraperitoneal injection of Ccr2 inhibitor. Figure S7. Oligodendrocyte lineage cells respond to injury by activation of innate immunity, cell proliferation and cell migration pathways. (A) Dot plot depicting up- and down-regulated genes in FACS-purified Olig2:dsRed$^+$ cells isolated from the injured zebrafish telencephalon after vehicle treatment. Lines indicate cut-off borders (*p*-value < 0.05 and FC ≥ 2). (B) Pie chart showing the proportion of injury-regulated genes in zebrafish Olig2$^+$ cells belonging to different pathways based on a Panther analysis. (C) Histogram depicting GO terms related to biological process significantly enriched (*p*-values indicated on bars) in a gene set upregulated after brain injury in zebrafish Olig2$^+$ cells. GO terms related to inflammatory response are shown by gray bars; patterned bars indicate processes previously reported to be activated in response to injury. Note that both toll-like receptor signaling and the response to the cytokine are induced by the injury. (D) Dot plot depicting the coregulation of ECM-related genes in the entire telencephalon and Olig2$^+$ cells after 3 days after skull injury. Lines indicate cut-off borders (*p*-value < 0.05 and FC ≥ 2). (E) Dot plot depicting up- and down-regulated genes in FACS-purified Olig2:dsRed-positive cells isolated from the injured zebrafish telencephalon after Tlr1/2 and Cxcr3 inhibitor treatment. (F) Experimental design to analyze the density and maturation rate of oligodendrocytes after skull injury. (G–I′) Images depicting the distribution of Mbp:nls-GFP$^+$ cells and BrdU$^+$ cells in intact condition (G–H′) and 7 days after skull injury (I,I′). Double positive Mbp:nls-GFP and BrdU cells (White arrow) represent oligodendrocyte progenitor cells that differentiated into mature oligodendrocyte

after the injury. (J,K) Dot plots showing the total density of Mbp:nls-GFP$^+$ cells (J) and the proportion of newly matured oligodendrocytes (K) in intact brains and 7 days after skull injury. Data are shown as mean ± SEM; each data point represents one animal. *p*-values are based on Student's *t*-test with equal variances. All images are full z-projections of a confocal stack. Scale bars in G, I, I′ = 100 µm; scale bars in H, H′ = 20 µm. Abbreviations: dpi: days post-injury; VEH: vehicle; INT: intact; INH: inhibitor. Symbol description: black rectangle: intact; black triangle: skull injury. Figure S8. Human plasma and heat-inactivated human CSF do not induce accumulation of Olig2:GFP$^+$ cells. (A–C′) Micrographs showing the Olig2:GFP and 4C4 reactivity after nostril injury and the administration of either human plasma (A–B′) or heat-inactivated hCSF (C–C′). White lines delineate the injury site. (D) Dot plot illustrating the density of Olig2:GFP$^+$ cells at the injury site after different treatments. Data are shown as mean ± SEM; each data point represents one animal. *p*-values are based on a one-way ANOVA (*p*-value = 2.091×10^{-4} with a post-hoc Dunnett test (Many-to-One). All images are full z-projections of a confocal Z-stack. Scale bars: 20 µm. Abbreviations: dpi: days post-injury; hPlasma: human plasma; hCSF: human cerebrospinal fluid. Symbol description: red circle: hCSF; green circle: human plasma; blue circle: heat-inactivated hCSF. Figure S9. Generation of the Tlr2 and Cxcr3 OliNeu knockout line. (A,B) Sequence alignment of the Cxcr3 (A) and Tlr2 (B) locus depicting the Cas9-mediated bi-allelic deletions (green blocks) leading to the premature STOP codon generation (red asterisk) in oligodendrocyte progenitor OliNeu cell line. The position of gRNAs is indicated with grey boxes. (C,D) Micrographs depicting Ki67-positive cells in WT OliNeu cell clone (only transfected with Cas9) (C) and Cxcr3/Tlr2 mutant clone 1 (D). (E) Dot plot depicting the proportion of pH3 positive cells in WT OliNeu cells and two mutant cell clones (Clone 1, Clone 2). Data are shown as mean ± SEM; each data point represent single coverslip. *p*-value is based on one-way ANOVA (*p*-value = 2.473×10^{-3}) and Dunnett Test (Many-to-One). Scale bars in C, D = 50µm. Symbol description: Black diamond: control OliNeu cells; green square: Tlr2 and Cxcr3-deficient clone 1; red square Tlr2 and Cxcr3-deficient clone 2. Table S1. List of all the primary antibodies used in this study, and the correspondent information about each antibody. Table S2. List of primers used in this study for RT-qPCR. Table S3. List of recombinant proteins used for the screening in Figure 7G (www.rndsystems.com accessed on 24 September 2019). Table S4. Microarray data illustrating the GO Terms Biological Processes enriched in genes commonly or exclusively regulated in skull and nostril injury at different time points (related to Figure 2B). Table S5. RNAseq data depicting the gene ontology terms related to the biological processes significantly enriched in an ECM-related gene set (69 genes) regulated exclusively 3 days after skull injury (Related to Figure 2E). Table S6. Microarray data illustrating the GO terms related to the biological processes enriched in genes exclusively regulated 3 days after skull injury (related to Figure 2H). Table S7. RNAseq data showing the GO Terms related to the biological processes (PANTHER) upregulated after brain injury in zebrafish Olig2$^+$ cells (Related to Figure S7C, GO Terms marked in red are shown in the graph S7C). Table S8. RNAseq data depicting the Gene Ontology terms related to biological processes (PANTHER) significantly enriched in a gene set (597 genes) with normalized expression after Tlr1/2 and Cxcr3 inhibitor treatment in zebrafish. (Related to Figure 5B). Table S9. RNAseq data depicting the gene ontology terms related to biological processes (PANTHER) significantly enriched in a gene set still regulated after inhibitor treatment. (Related to Figure 5). Video S1. Three-dimensional reconstruction of cleared intact telencephalic tissue stained for Sox10 (magenta), 4C4 (cyan) and DAPI (blue). Video S2. Three-dimensional reconstruction of cleared telencephalic tissue stained for Sox10 (magenta), 4C4 (cyan) and DAPI (blue) 3 days after nostril injury. Video S3. Three-dimensional reconstruction of cleared telencephalic tissue stained for Sox10 (magenta), 4C4 (cyan) and DAPI (blue) 7 days after nostril injury. Video S4. Three-dimensional reconstruction of Tg(fli1:eGFP) transgenic line 28 days after nostril and skull injury. Ependymoglial cells were labeled by electroporation of a plasmid encoding for membrane localized tdTomato 21 days after injury. Video S5. Three-dimensional reconstruction of cleared infarct tissue stained for Sox10 and DAPI 7 days after skull injury and vehicle or double inhibitor treatment.

Author Contributions: Conceptualization, R.S.-G., J.N. and M.G.; methodology, R.S.-G., J.N., C.K., T.L., A.Z. (Alessandro Zambusi), K.T.N., T.D., M.I., S.A., V.S., C.T.B. and S.H.S.; software, D.T. and W.W.; formal analysis, T.S. (Tamas Schauer), R.S.-G., T.S. (Tobias Straub), M.I., J.B. and J.N.; resources, H.S., H.B.H., A.Z. (Andreas Zwergal) and T.C.; writing—original draft preparation, R.S.-G. and J.N.; writing—review and editing, all authors. All authors have read and agreed to the published version of the manuscript.

Funding: We gratefully acknowledge funding to JN from the German Research foundation (DFG) by the SFB 870, SPP1757, TRR274; to MG the German Research foundation (DFG) by the SFB 870, and the ERC grant ChroNeuroRepair: GA No. 340793; Work in W. W. lab is by the German Science Foundation Collaborative Research Centre (CRC) 870; funds from the Bayerisches Staatsministerium für Bildung und Kultus, Wissenschaft und Kunst within Bavarian Research Network "Human Induced Pluripotent Stem Cells" (ForIPS) and (in part) by the Helmholtz Portfolio Theme 'Supercomputing and Modelling for the Human Brain' (SMHB). H.S. is supported by the DFG (CRC 870). Dr. Huttner was supported by a research grant from the German Research Foundation (DFG-HU1961/2-1).

Institutional Review Board Statement: The animal study protocol was approved by the Government of Upper Bavaria (AZ 55.2-1-54-2532-09-16).

Informed Consent Statement: Patient consent was waived as CSF from different patients was pooled and individual patients can not be identified.

Data Availability Statement: All data are available upon request.

Acknowledgments: We want to thank Pamela Raymonds for sharing the Tg(gfap:GFP)mi2001 fish line and Bruce Apple for sharing Tg(Olig2:GFP) and Tg(Olig2:DsRed) fish lines. We are thankful to Andrea Steiner-Mazzardi, Sarah Hübinger and Beate Stiening for excellent technical help, and to Sofia Grade and Clayton Gordy for critical reading of the manuscript.

Conflicts of Interest: The authors declare no conflict of interest. The funders had no role in the design of the study; in the collection, analyses, or interpretation of data; in the writing of the manuscript, or in the decision to publish the results.

References

1. Zambusi, A.; Ninkovic, J. Regeneration of the central nervous system-principles from brain regeneration in adult zebrafish. *World J. Stem Cells* **2020**, *12*, 8–24. [CrossRef] [PubMed]
2. Kyritsis, N.; Kizil, C.; Zocher, S.; Kroehne, V.; Kaslin, J.; Freudenreich, D.; Iltzsche, A.; Brand, M. Acute inflammation initiates the regenerative response in the adult zebrafish brain. *Science* **2012**, *338*, 1353–1356. [CrossRef] [PubMed]
3. Sofroniew, M.V. Astrocyte Reactivity: Subtypes, States, and Functions in CNS Innate Immunity. *Trends Immunol.* **2020**, *41*. [CrossRef] [PubMed]
4. Donat, C.K.; Scott, G.; Gentleman, S.M.; Sastre, M. Microglial activation in traumatic brain injury. *Front. Aging Neurosci.* **2017**, *9*, 208. [CrossRef]
5. Anderson, M.A.; Burda, J.E.; Ren, Y.; Ao, Y.; O'Shea, T.M.; Kawaguchi, R.; Coppola, G.; Khakh, B.S.; Deming, T.J.; Sofroniew, M.V. Astrocyte scar formation AIDS central nervous system axon regeneration. *Nature* **2016**, *532*, 195–200. [CrossRef]
6. Dias, D.O.; Kim, H.; Holl, D.; Solnestam, B.W.; Lundeberg, J.; Carlen, M.; Goritz, C.; Frisen, J. Reducing Pericyte-Derived Scarring Promotes Recovery after Spinal Cord Injury. *Cell* **2018**, *173*, 153–165.e22. [CrossRef]
7. Goritz, C.; Dias, D.O.; Tomilin, N.; Barbacid, M.; Shupliakov, O.; Frisen, J. A pericyte origin of spinal cord scar tissue. *Science* **2011**, *333*, 238–242. [CrossRef]
8. O'Shea, T.M.; Burda, J.E.; Sofroniew, M.V. Cell biology of spinal cord injury and repair. *J. Clin. Investig.* **2017**, *127*, 3259–3270. [CrossRef] [PubMed]
9. Burda, J.E.; Sofroniew, M.V. Reactive gliosis and the multicellular response to CNS damage and disease. *Neuron* **2014**, *81*, 229–248. [CrossRef]
10. Bardehle, S.; Kruger, M.; Buggenthin, F.; Schwausch, J.; Ninkovic, J.; Clevers, H.; Snippert, H.J.J.; Theis, F.J.J.; Meyer-Luehmann, M.; Bechmann, I.; et al. Live imaging of astrocyte responses to acute injury reveals selective juxtavascular proliferation. *Nat. Neurosci.* **2013**, *16*, 580–586. [CrossRef]
11. Shandra, O.; Winemiller, A.R.; Heithoff, B.P.; Munoz-Ballester, C.; George, K.K.; Benko, M.J.; Zuidhoek, I.A.; Besser, M.N.; Curley, D.E.; Edwards, G.F.; et al. Repetitive diffuse mild traumatic brain injury causes an atypical astrocyte response and spontaneous recurrent seizures. *J. Neurosci.* **2019**, *39*, 1944–1963. [CrossRef] [PubMed]
12. Bush, T.G.; Puvanachandra, N.; Horner, C.H.; Polito, A.; Ostenfeld, T.; Svendsen, C.N.; Mucke, L.; Johnson, M.H.; Sofroniew, M.V. Leukocyte infiltration, neuronal degeneration, and neurite outgrowth after ablation of scar-forming, reactive astrocytes in adult transgenic mice. *Neuron* **1999**, *23*, 297–308. [CrossRef]
13. Hol, E.M.; Pekny, M. Glial fibrillary acidic protein (GFAP) and the astrocyte intermediate filament system in diseases of the central nervous system. *Curr. Opin. Cell Biol.* **2015**, *32*, 121–130. [CrossRef] [PubMed]
14. Willis, E.F.; MacDonald, K.P.A.; Nguyen, Q.H.; Garrido, A.L.; Gillespie, E.R.; Harley, S.B.R.; Bartlett, P.F.; Schroder, W.A.; Yates, A.G.; Anthony, D.C.; et al. Repopulating Microglia Promote Brain Repair in an IL-6-Dependent Manner. *Cell* **2020**, *180*, 833–846. [CrossRef]
15. Silver, J.; Miller, J.H. Regeneration beyond the glial scar. *Nat. Rev. Neurosci.* **2004**, *5*, 146–156. [CrossRef] [PubMed]

16. Busch, S.A.; Silver, J. The role of extracellular matrix in CNS regeneration. *Curr. Opin. Neurobiol.* **2007**, *17*, 120–127. [CrossRef] [PubMed]
17. Fitch, M.T.; Silver, J. CNS injury, glial scars, and inflammation: Inhibitory extracellular matrices and regeneration failure. *Exp. Neurol.* **2008**, *209*, 294–301. [CrossRef]
18. Liddelow, S.A.; Guttenplan, K.A.; Clarke, L.E.; Bennett, F.C.; Bohlen, C.J.; Schirmer, L.; Bennett, M.L.; Münch, A.E.; Chung, W.S.; Peterson, T.C.; et al. Neurotoxic reactive astrocytes are induced by activated microglia. *Nature* **2017**, *541*, 481–487. [CrossRef]
19. Frik, J.; Merl-Pham, J.; Plesnila, N.; Mattugini, N.; Kjell, J.; Kraska, J.; Gomez, R.M.; Hauck, S.M.; Sirko, S.; Gotz, M. Cross-talk between monocyte invasion and astrocyte proliferation regulates scarring in brain injury. *EMBO Rep.* **2018**, *19*, e45294. [CrossRef]
20. Di Bello, I.C.; Dawson, M.R.L.; Levine, J.M.; Reynolds, R. Generation of oligodendroglial progenitors in acute inflammatory demyelinating lesions of the rat brain stem is associated with demyelination rather than inflammation. *J. Neurocytol.* **1999**, *28*, 365–381. [CrossRef]
21. Domingues, H.S.; Portugal, C.C.; Socodato, R.; Relvas, J.B. Oligodendrocyte, astrocyte, and microglia crosstalk in myelin development, damage, and repair. *Front. Cell Dev. Biol.* **2016**, *4*, 71. [PubMed]
22. Simon, C.; Dimou, L.; Gotz, M. Progenitors in the adult cerebral cortex—Cell cycle properties and regulation by physiological stimuli and injury. *Glia* **2011**, *59*, 869–881. [CrossRef] [PubMed]
23. Kang, S.H.; Li, Y.; Fukaya, M.; Lorenzini, I.; Cleveland, D.W.; Ostrow, L.W.; Rothstein, J.D.; Bergles, D.E. Degeneration and impaired regeneration of gray matter oligodendrocytes in amyotrophic lateral sclerosis. *Nat. Neurosci.* **2013**, *16*, 571–579. [CrossRef] [PubMed]
24. Hughes, E.G.; Kang, S.H.; Fukaya, M.; Bergles, D.E. Oligodendrocyte progenitors balance growth with self-repulsion to achieve homeostasis in the adult brain. *Nat. Neurosci.* **2013**, *16*, 668–676. [CrossRef]
25. Von Streitberg, A.; Jäkel, S.; Eugenin von Bernhardi, J.; Straube, C.; Buggenthin, F.; Marr, C.; Dimou, L. NG2-Glia Transiently Overcome Their Homeostatic Network and Contribute to Wound Closure After Brain Injury. *Front. Cell Dev. Biol.* **2021**, *9*, 762. [CrossRef]
26. Komitova, M.; Zhu, X.; Serwanski, D.R.; Nishiyama, A. NG2 cells are distinct from neurogenic cells in the postnatal mouse subventricular zone. *J. Comp. Neurol.* **2009**, *512*, 702–716. [CrossRef]
27. Nishiyama, A.; Komitova, M.; Suzuki, R.; Zhu, X. Polydendrocytes (NG2 cells): Multifunctional cells with lineage plasticity. *Nat. Rev. Neurosci.* **2009**, *10*, 9–22. [CrossRef]
28. Buffo, A.; Vosko, M.R.; Erturk, D.; Hamann, G.F.; Jucker, M.; Rowitch, D.; Gotz, M. Expression pattern of the transcription factor Olig2 in response to brain injuries: Implications for neuronal repair. *Proc. Natl. Acad. Sci. USA* **2005**, *102*, 18183–18188. [CrossRef]
29. Wellman, S.M.; Kozai, T.D.Y. In vivo spatiotemporal dynamics of NG2 glia activity caused by neural electrode implantation. *Biomaterials* **2018**, *164*, 121–133. [CrossRef]
30. Rhodes, K.E.; Moon, L.D.F.; Fawcett, J.W. Inhibiting cell proliferation during formation of the glial scar: Effects on axon regeneration in the CNS. *Neuroscience* **2003**, *120*, 41–56. [CrossRef]
31. Busch, S.A.; Horn, K.P.; Cuascut, F.X.; Hawthorne, A.L.; Bai, L.; Miller, R.H.; Silver, J. Adult NG2+cells are permissive to neurite outgrowth and stabilize sensory axons during macrophage-induced axonal dieback after spinal cord injury. *J. Neurosci.* **2010**, *30*, 255–265. [CrossRef]
32. Chen, Z.J.; Ughrin, Y.; Levine, J.M. Inhibition of axon growth by oligodendrocyte precursor cells. *Mol. Cell. Neurosci.* **2002**, *20*, 125–139. [CrossRef]
33. Kroehne, V.; Freudenreich, D.; Hans, S.; Kaslin, J.; Brand, M. Regeneration of the adult zebrafish brain from neurogenic radial glia-type progenitors. *Development* **2011**, *138*, 4831–4841. [CrossRef]
34. Dimou, L.; Gotz, M. Glial cells as progenitors and stem cells: New roles in the healthy and diseased brain. *Physiol. Rev.* **2014**, *94*, 709–737. [CrossRef]
35. Reimer, M.M.; Kuscha, V.; Wyatt, C.; Sorensen, I.; Frank, R.E.; Knuwer, M.; Becker, T.; Becker, C.G. Sonic hedgehog is a polarized signal for motor neuron regeneration in adult zebrafish. *J. Neurosci.* **2009**, *29*, 15073–15082. [CrossRef]
36. Reimer, M.M.; Sorensen, I.; Kuscha, V.; Frank, R.E.; Liu, C.; Becker, C.G.; Becker, T. Motor neuron regeneration in adult zebrafish. *J. Neurosci.* **2008**, *28*, 8510–8516. [CrossRef]
37. Baumgart, E.V.V.; Barbosa, J.S.S.; Bally-Cuif, L.; Gotz, M.; Ninkovic, J.; Götz, M.; Ninkovic, J. Stab wound injury of the zebrafish telencephalon: A model for comparative analysis of reactive gliosis. *Glia* **2012**, *60*, 343–357. [CrossRef]
38. Ayari, B.; Elhachimi, K.H.; Yanicostas, C.; Landoulsi, A.; Soussi-Yanicostas, N. Prokineticin 2 expression is associated with neural repair of injured adult zebrafish telencephalon. *J. Neurotrauma* **2010**, *27*, 959–972. [CrossRef] [PubMed]
39. Marz, M.; Schmidt, R.; Rastegar, S.; Strahle, U. Regenerative response following stab injury in the adult zebrafish telencephalon. *Dev. Dyn.* **2011**, *240*, 2221–2231. [CrossRef] [PubMed]
40. Shin, J.; Park, H.C.; Topczewska, J.M.; Mawdsley, D.J.; Appel, B. Neural cell fate analysis in zebrafish using olig2 BAC transgenics. *Methods Cell Sci* **2003**, *25*, 7–14. [CrossRef] [PubMed]
41. Lawson, N.D.; Weinstein, B.M. In vivo imaging of embryonic vascular development using transgenic zebrafish. *Dev Biol.* **2002**, *248*, 307–318. [CrossRef] [PubMed]
42. Bernardos, R.L.; Raymond, P.A. GFAP transgenic zebrafish. *Gene Expr. Patterns* **2006**, *6*, 1007–1013. [CrossRef] [PubMed]
43. Jung, S.H.; Kim, S.; Chung, A.Y.; Kim, H.T.; So, J.H.; Ryu, J.; Park, H.C.; Kim, C.H. Visualization of myelination in GFP-transgenic zebrafish. *Dev. Dyn.* **2010**, *239*, 592–597. [CrossRef]

44. Bernut, A.; Herrmann, J.L.; Kissa, K.; Dubremetz, J.F.; Gaillard, J.L.; Lutfalla, G.; Kremer, L. Mycobacterium abscessus cording prevents phagocytosis and promotes abscess formation. *Proc. Natl. Acad. Sci. USA* **2014**, *111*, E943–E952. [CrossRef] [PubMed]
45. Westerfield, M. *The Zebrafish Book. A Guide for the Laboratory Use of Zebrafish (Danio Rerio)*, 4th ed.; Univ. of Oregon Press: Eugene, OR, USA, 2000.
46. Durovic, T.; Ninkovic, J. Electroporation method for in vivo delivery of plasmid dna in the adult zebrafish telencephalon. *J. Vis. Exp.* **2019**, *13*, e60066. [CrossRef]
47. Barbosa, J.S.S.; Sanchez-Gonzalez, R.; Di Giaimo, R.; Baumgart, E.V.V.; Theis, F.J.J.; Götz, M.; Ninkovic, J.; Gotz, M.; Ninkovic, J.; Gonzalez-Sanchez, R.; et al. Live imaging of adult neural stem cell behavior in the intact and injured zebrafish brain. *Science* **2015**, *348*, 789–793. [CrossRef]
48. Barbosa, J.S.S.; Di Giaimo, R.; Götz, M.; Ninkovic, J.; Gotz, M.; Ninkovic, J. Single-cell in vivo imaging of adult neural stem cells in the zebrafish telencephalon. *Nat. Protoc.* **2016**, *11*, 1360–1370. [CrossRef]
49. Di Giaimo, R.; Durovic, T.; Barquin, P.; Kociaj, A.; Lepko, T.; Aschenbroich, S.; Breunig, C.T.T.; Irmler, M.; Cernilogar, F.M.M.; Schotta, G.; et al. The Aryl Hydrocarbon Receptor Pathway Defines the Time Frame for Restorative Neurogenesis. *Cell Rep.* **2018**, *25*, 3241–3251. [CrossRef]
50. Rainer, J.; Sanchez-Cabo, F.; Stocker, G.; Sturn, A.; Trajanoski, Z. CARMAweb: Comprehensive R- and bioconductor-based web service for microarray data analysis. *Nucleic Acids Res.* **2006**, *34*, W498–W503. [CrossRef]
51. Herrero, J.; Muffato, M.; Beal, K.; Fitzgerald, S.; Gordon, L.; Pignatelli, M.; Vilella, A.J.; Searle, S.M.J.; Amode, R.; Brent, S.; et al. Ensembl comparative genomics resources. *Database* **2016**, *2016*, baw053. [CrossRef]
52. Huang, D.W.; Sherman, B.T.; Lempicki, R.A. Systematic and integrative analysis of large gene lists using DAVID bioinformatics resources. *Nat. Protoc.* **2009**, *4*, 44–57. [CrossRef] [PubMed]
53. Huang, D.W.; Sherman, B.T.; Lempicki, R.A. Bioinformatics enrichment tools: Paths toward the comprehensive functional analysis of large gene lists. *Nucleic Acids Res.* **2009**, *37*, 1–13. [CrossRef] [PubMed]
54. Fischer, J.; Beckervordersandforth, R.; Tripathi, P.; Steiner-Mezzadri, A.; Ninkovic, J.; Gotz, M.; Götz, M. Prospective isolation of adult neural stem cells from the mouse subependymal zone. *Nat. Protoc* **2011**, *6*, 1981–1989. [CrossRef] [PubMed]
55. Di Giaimo, R.; Aschenbroich, S.; Ninkovic, J. Fluorescence-Activated Cell Sorting-Based Isolation and Characterization of Neural Stem Cells from the Adult Zebrafish Telencephalon. *Adv. Struct. Saf. Stud.* **2019**, *1938*, 49–66.
56. He, D.; Meyer, B.; Lu, R. Isolation and Culture of Oligodendrocyte Precursor Cells from Prenatal and Postnatal Rodent Brain. In *Stem Cell Technologies in Neuroscience*; Humana Press: New York, NY, USA, 2017.
57. Walcher, T.; Xie, Q.; Sun, J.; Irmler, M.; Beckers, J.; Öztürk, T.; Niessing, D.; Stoykova, A.; Cvekl, A.; Ninkovic, J.; et al. Functional dissection of the paired domain of Pax6 reveals molecular mechanisms of coordinating neurogenesis and proliferation. *Development* **2013**, *140*, 1123–1136. [CrossRef] [PubMed]
58. Breunig, C.T.; Durovic, T.; Neuner, A.M.; Baumann, V.; Wiesbeck, M.F.; Köferle, A.; Götz, M.; Ninkovic, J.; Stricker, S.H. One step generation of customizable gRNA vectors for multiplex CRISPR approaches through string assembly gRNA cloning (STAgR). *PLoS ONE* **2018**, *13*, e0196015. [CrossRef]
59. Koferle, A.; Worf, K.; Breunig, C.; Baumann, V.; Herrero, J.; Wiesbeck, M.; Hutter, L.H.; Gotz, M.; Fuchs, C.; Beck, S.; et al. CORALINA: A universal method for the generation of gRNA libraries for CRISPR-based screening. *BMC Genomics* **2016**, *17*, 917. [CrossRef] [PubMed]
60. Soehnlein, O.; Lindbom, L. Phagocyte partnership during the onset and resolution of inflammation. *Nat. Rev. Immunol.* **2010**, *10*, 427–439. [CrossRef]
61. Adolf, B.; Chapouton, P.; Lam, C.S.; Topp, S.; Tannhauser, B.; Strahle, U.; Gotz, M.; Bally-Cuif, L. Conserved and acquired features of adult neurogenesis in the zebrafish telencephalon. *Dev. Biol.* **2006**, *295*, 278–293. [CrossRef]
62. Horvat, A.; Schwaiger, F.W.; Hager, G.; Bröcker, F.; Streif, R.; Knyazev, P.G.; Ullrich, A.; Kreutzberg, G.W. A novel role for protein tyrosine phosphatase SHP1 in controlling glial activation in the normal and injured nervous system. *J. Neurosci.* **2001**, *21*, 865–874. [CrossRef]
63. Zhu, Y.M.; Gao, X.; Ni, Y.; Li, W.; Kent, T.A.; Qiao, S.G.; Wang, C.; Xu, X.X.; Zhang, H.L. Sevoflurane postconditioning attenuates reactive astrogliosis and glial scar formation after ischemia–reperfusion brain injury. *Neuroscience* **2017**, *356*, 125–141. [CrossRef] [PubMed]
64. Liddelow, S.A.; Barres, B.A. Reactive Astrocytes: Production, Function, and Therapeutic Potential. *Immunity* **2017**, *46*, 957–967. [CrossRef]
65. Hsu, J.Y.C.; Bourguignon, L.Y.W.; Adams, C.M.; Peyrollier, K.; Zhang, H.; Fandel, T.; Cun, C.L.; Werb, Z.; Noble-Haeusslein, L.J. Matrix metalloproteinase-9 facilitates glial scar formation in the injured spinal cord. *J. Neurosci.* **2008**, *28*, 13467–13477. [CrossRef] [PubMed]
66. Schachtrup, C.; Ryu, J.K.; Helmrick, M.J.; Vagena, E.; Galanakis, D.K.; Degen, J.L.; Margolis, R.U.; Akassoglou, K. Fibrinogen triggers astrocyte scar formation by promoting the availability of active TGF-β after vascular damage. *J. Neurosci.* **2010**, *30*, 5843–5854. [CrossRef] [PubMed]
67. Rünger, T.M.; Quintanilla-Dieck, M.J.; Bhawan, J. Role of cathepsin K in the turnover of the dermal extracellular matrix during scar formation. *J. Investig. Dermatol.* **2007**, *127*, 293–297. [CrossRef]
68. Li, X.; Wu, Z.; Ni, J.; Liu, Y.; Meng, J.; Yu, W.; Nakanishi, H.; Zhou, Y. Cathepsin B Regulates Collagen Expression by Fibroblasts via Prolonging TLR2/NF-κB Activation. *Oxid. Med. Cell. Longev.* **2016**, *2016*, 7894247. [CrossRef] [PubMed]

69. Lalmanach, G.; Saidi, A.; Marchand-Adam, S.; Lecaille, F.; Kasabova, M. Cysteine cathepsins and cystatins: From ancillary tasks to prominent status in lung diseases. *Biol. Chem.* **2015**, *396*, 111–130. [CrossRef]
70. Pan, Z.; Yang, K.; Wang, H.; Xiao, Y.; Zhang, M.; Yu, X.; Xu, T.; Bai, T.; Zhu, H. MFAP4 deficiency alleviates renal fibrosis through inhibition of NF-κB and TGF-β/Smad signaling pathways. *FASEB J.* **2020**, *34*, 14250–14263. [CrossRef]
71. Sulimai, N.; Lominadze, D. Fibrinogen and Neuroinflammation During Traumatic Brain Injury. *Mol. Neurobiol.* **2020**, *57*, 4692–4703. [CrossRef]
72. Dietrich, N.; Lienenklaus, S.; Weiss, S.; Gekara, N.O. Murine Toll-Like Receptor 2 Activation Induces Type I Interferon Responses from Endolysosomal Compartments. *PLoS ONE* **2010**, *5*, e10250. [CrossRef]
73. Owens, B.M.J.; Moore, J.W.J.; Kaye, P.M. IRF7 regulates TLR2-mediated activation of splenic CD11chi dendritic cells. *PLoS ONE* **2012**, *7*, e41050. [CrossRef]
74. Liljeroos, M.; Vuolteenaho, R.; Rounioja, S.; Henriques-Normark, B.; Hallman, M.; Ojaniemi, M. Bacterial ligand of TLR2 signals Stat activation via induction of IRF1/2 and interferon-α production. *Cell. Signal.* **2008**, *20*, 1873–1881. [CrossRef]
75. Nomiyama, H.; Osada, N.; Yoshie, O. The evolution of mammalian chemokine genes. *Cytokine Growth Factor Rev.* **2010**, *21*, 253–262. [CrossRef]
76. Portou, M.J.; Baker, D.; Abraham, D.; Tsui, J. The innate immune system, toll-like receptors and dermal wound healing: A review. *Vasc. Pharmacol.* **2015**, *71*, 31–36. [CrossRef]
77. Mann, D.L.; Topkara, V.K.; Evans, S.; Barger, P.M. Innate immunity in the adult mammalian heart: For whom the cell tolls. *Trans. Am. Clin. Clim. Assoc.* **2010**, *121*, 31–34.
78. Griffiths, M.R.; Gasque, P.; Neal, J.W. The regulation of the CNS innate immune response is vital for the restoration of tissue homeostasis (repair) after acute brain injury: A brief review. *Int. J. Inflam* **2010**, *2010*, 151097. [CrossRef] [PubMed]
79. Sato, M.; Sano, H.; Iwaki, D.; Kudo, K.; Konishi, M.; Takahashi, H.; Takahashi, T.; Imaizumi, H.; Asai, Y.; Kuroki, Y. Direct Binding of Toll-Like Receptor 2 to Zymosan, and Zymosan-Induced NF-κB Activation and TNF-α Secretion Are Down-Regulated by Lung Collectin Surfactant Protein A. *J. Immunol.* **2003**, *171*, 417–425. [CrossRef] [PubMed]
80. Marcel, L.; Pius, L.; Nicole, B.; Eckart, M.; Bernhard, M. Lymphocyte-specific chemokine receptor CXCR3: Regulation, chemokine binding and gene localization. *Eur. J. Immunol.* **1998**, *28*, 3696–3705.
81. Wijtmans, M.; Scholten, D.J.; Roumen, L.; Canals, M.; Custers, H.; Glas, M.; Vreeker, M.C.A.; de Kanter, F.J.J.; de Graaf, C.; Smit, M.J.; et al. Chemical subtleties in small-molecule modulation of peptide receptor function: The case of CXCR3 biaryl-type ligands. *J. Med. Chem.* **2012**, *55*, 10572–10583. [CrossRef]
82. Zambusi, A.; Pelin Burhan, Ö.; Di Giaimo, R.; Schmid, B.; Ninkovic, J. Granulins Regulate Aging Kinetics in the Adult Zebrafish Telencephalon. *Cells* **2020**, *9*, 350. [CrossRef] [PubMed]
83. Kuroda, M.; Muramatsu, R.; Maedera, N.; Koyama, Y.; Hamaguchi, M.; Fujimura, H.; Yoshida, M.; Konishi, M.; Itoh, N.; Mochizuki, H.; et al. Peripherally derived FGF21 promotes remyelination in the central nervous system. *J. Clin. Investig.* **2017**, *127*, 3496–3509. [CrossRef]
84. Yang, J.; Cheng, X.; Qi, J.; Xie, B.; Zhao, X.; Zheng, K.; Zhang, Z.; Qiu, M. EGF enhances oligodendrogenesis from glial progenitor cells. *Front. Mol. Neurosci.* **2017**, *10*, 106. [CrossRef] [PubMed]
85. Vinukonda, G.; Hu, F.; Mehdizadeh, R.; Dohare, P.; Kidwai, A.; Juneja, A.; Naran, V.; Kierstead, M.; Chawla, R.; Kayton, R.; et al. Epidermal growth factor preserves myelin and promotes astrogliosis after intraventricular hemorrhage. *Glia* **2016**, *64*, 1987–2004. [CrossRef] [PubMed]
86. Pei, D.; Liu, N.; Li, D.; Yan, H.; Wang, Q.B.; Fang, Y.; Xie, L.; Li, H.P. Inhibition of platelet-derived growth factor receptor β reduces reactive glia and scar formation after traumatic brain injury in mice. *Brain Res. Bull.* **2017**, *134*, 121–127. [CrossRef] [PubMed]
87. Robel, S.; Berninger, B.; Götz, M.; Gotz, M. The stem cell potential of glia: Lessons from reactive gliosis. *Nat. Rev. Neurosci.* **2011**, *12*, 88–104. [CrossRef]
88. Eugenín-von Bernhardi, J.; Dimou, L. NG2-glia, more than progenitor cells. In *Glial Cells in Health and Disease of the CNS*; Advances in Experimental Medicine and Biology; Springer: Cham, Switzerland, 2016; pp. 27–45. [CrossRef]
89. Zupanc, G.K. Adult neurogenesis and neuronal regeneration in the brain of teleost fish. *J. Physiol.* **2008**, *102*, 357–373. [CrossRef]
90. Zupanc, G.K. Towards brain repair: Insights from teleost fish. *Semin Cell Dev. Biol.* **2009**, *20*, 683–690. [CrossRef]
91. Zupanc, G.K. Neurogenesis and neuronal regeneration in the adult fish brain. *J. Comp. Physiol. A Neuroethol. Sens Neural Behav. Physiol.* **2006**, *192*, 649–670. [CrossRef] [PubMed]
92. Alunni, A.; Bally-Cuif, L. A comparative view of regenerative neurogenesis in vertebrates. *Development* **2016**, *143*, 741–753. [CrossRef]
93. Kizil, C.; Dudczig, S.; Kyritsis, N.; Machate, A.; Blaesche, J.; Kroehne, V.; Brand, M. The chemokine receptor cxcr5 regulates the regenerative neurogenesis response in the adult zebrafish brain. *Neural Dev.* **2012**, *7*, 27. [CrossRef] [PubMed]
94. Labbe, R.M.; Irimia, M.; Currie, K.W.; Lin, A.; Zhu, S.J.; Brown, D.D.; Ross, E.J.; Voisin, V.; Bader, G.D.; Blencowe, B.J.; et al. A comparative transcriptomic analysis reveals conserved features of stem cell pluripotency in planarians and mammals. *Stem Cells* **2012**, *30*, 1734–1745. [CrossRef]
95. Simkin, J.; Gawriluk, T.R.; Gensel, J.C.; Seifert, A.W. Macrophages are necessary for epimorphic regeneration in African spiny mice. *eLife* **2017**, *6*, e24623. [CrossRef] [PubMed]
96. Seifert, A.W.; Kiama, S.G.; Seifert, M.G.; Goheen, J.R.; Palmer, T.M.; Maden, M. Skin shedding and tissue regeneration in African spiny mice (Acomys). *Nature* **2012**, *489*, 561–565. [CrossRef] [PubMed]

97. Brant, J.O.; Yoon, J.H.; Polvadore, T.; Barbazuk, W.B.; Maden, M. Cellular events during scar-free skin regeneration in the spiny mouse, Acomys. *Wound Repair Regen.* **2016**, *24*, 75–88. [CrossRef]
98. Sofroniew, M.V. Molecular dissection of reactive astrogliosis and glial scar formation. *Trends Neurosci.* **2009**, *32*, 638–647. [CrossRef] [PubMed]
99. Pekny, M.; Nilsson, M. Astrocyte activation and reactive gliosis. *Glia* **2005**, *50*, 427–434. [CrossRef] [PubMed]
100. Jin, W.N.; Shi, S.X.Y.; Li, Z.; Li, M.; Wood, K.; Gonzales, R.J.; Liu, Q. Depletion of microglia exacerbates postischemic inflammation and brain injury. *J. Cereb. Blood Flow Metab.* **2017**, *37*, 2224–2236. [CrossRef] [PubMed]
101. Fu, H.; Zhao, Y.; Hu, D.; Wang, S.; Yu, T.; Zhang, L. Depletion of microglia exacerbates injury and impairs function recovery after spinal cord injury in mice. *Cell Death Dis.* **2020**, *11*, 528. [CrossRef]
102. Grade, S.; Götz, M. Neuronal replacement therapy: Previous achievements and challenges ahead. *npj Regen. Med.* **2017**, *2*, 29. [CrossRef]
103. Grandel, H.; Brand, M. Comparative aspects of adult neural stem cell activity in vertebrates. *Dev. Genes Evol.* **2013**, *223*, 131–147. [CrossRef]
104. Kizil, C.; Kaslin, J.; Kroehne, V.; Brand, M. Adult neurogenesis and brain regeneration in zebrafish. *Dev. Neurobiol.* **2012**, *72*, 429–461. [CrossRef] [PubMed]
105. Dunkin, C.S.; Pleat, J.M.; Gillespie, P.H.; Tyler, M.P.; Roberts, A.H.; McGrouther, D.A. Scarring occurs at a critical depth of skin injury: Precise measurement in a graduated dermal scratch in human volunteers. *Plast. Reconstr. Surg.* **2007**, *119*, 1722–1724. [CrossRef] [PubMed]
106. Bouabe, H.; Liu, Y.; Moser, M.; Bosl, M.R.; Heesemann, J. Novel highly sensitive IL-10-beta-lactamase reporter mouse reveals cells of the innate immune system as a substantial source of IL-10 in vivo. *J. Immunol.* **2011**, *187*, 3165–3176. [CrossRef] [PubMed]
107. Hsieh, C.L.; Niemi, E.C.; Wang, S.H.; Lee, C.C.; Bingham, D.; Zhang, J.; Cozen, M.L.; Charo, I.; Huang, E.J.; Liu, J.; et al. CCR2 deficiency impairs macrophage infiltration and improves cognitive function after traumatic brain injury. *J. Neurotrauma* **2014**, *31*, 1677–1688. [CrossRef] [PubMed]
108. Wattananit, S.; Tornero, D.; Graubardt, N.; Memanishvili, T.; Monni, E.; Tatarishvili, J.; Miskinyte, G.; Ge, R.; Ahlenius, H.; Lindvall, O.; et al. Monocyte-Derived Macrophages Contribute to Spontaneous Long-Term Functional Recovery after Stroke in Mice. *J. Neurosci.* **2016**, *36*, 4182–4195. [CrossRef]
109. Rothhammer, V.; Mascanfroni, I.D.; Bunse, L.; Takenaka, M.C.; Kenison, J.E.; Mayo, L.; Chao, C.C.; Patel, B.; Yan, R.; Blain, M.; et al. Type I interferons and microbial metabolites of tryptophan modulate astrocyte activity and central nervous system inflammation via the aryl hydrocarbon receptor. *Nat. Med.* **2016**, *22*, 586–597. [CrossRef]
110. Rothhammer, V.; Borucki, D.M.; Tjon, E.C.; Takenaka, M.C.; Chao, C.C.; Ardura-Fabregat, A.; de Lima, K.A.; Gutierrez-Vazquez, C.; Hewson, P.; Staszewski, O.; et al. Microglial control of astrocytes in response to microbial metabolites. *Nature* **2018**, *557*, 724–728. [CrossRef]
111. Kielian, T. Toll-like receptors in central nervous system glial inflammation and homeostasis. *J. Neurosci. Res.* **2006**, *83*, 711–730. [CrossRef]
112. Krauthausen, M.; Saxe, S.; Zimmermann, J.; Emrich, M.; Heneka, M.T.; Muller, M. CXCR3 modulates glial accumulation and activation in cuprizone-induced demyelination of the central nervous system. *J. Neuroinflammation* **2014**, *11*, 109. [CrossRef]
113. Goldberg, S.H.; van der Meer, P.; Hesselgesser, J.; Jaffer, S.; Kolson, D.L.; Albright, A.V.; Gonzalez-Scarano, F.; Lavi, E. CXCR3 expression in human central nervous system diseases. *Neuropathol. Appl. Neurobiol.* **2001**, *27*, 127–138. [CrossRef]
114. Bsibsi, M.; Ravid, R.; Gveric, D.; van Noort, J.M. Broad expression of Toll-like receptors in the human central nervous system. *J. Neuropathol. Exp. Neurol.* **2002**, *61*, 1013–1021. [CrossRef]
115. Dzamko, N.; Gysbers, A.; Perera, G.; Bahar, A.; Shankar, A.; Gao, J.; Fu, Y.; Halliday, G.M. Toll-like receptor 2 is increased in neurons in Parkinson's disease brain and may contribute to alpha-synuclein pathology. *Acta Neuropathol.* **2017**, *133*, 303–319. [CrossRef] [PubMed]
116. Mestre, H.; Du, T.; Sweeney, A.M.; Liu, G.; Samson, A.J.; Peng, W.; Mortensen, K.N.; Stæger, F.F.; Bork, P.A.R.; Bashford, L.; et al. Cerebrospinal fluid influx drives acute ischemic tissue swelling. *Science* **2020**, *367*, eaax7171. [CrossRef] [PubMed]
117. Lepko, T.; Pusch, M.; Müller, T.; Schulte, D.; Ehses, J.; Kiebler, M.; Hasler, J.; Huttner, H.B.; Vandenbroucke, R.E.; Vandendriessche, C.; et al. Choroid plexus-derived miR-204 regulates the number of quiescent neural stem cells in the adult brain. *EMBO J.* **2019**, *38*, e100481. [CrossRef] [PubMed]
118. Sirko, S.; Behrendt, G.; Johansson, P.A.; Tripathi, P.; Costa, M.; Bek, S.; Heinrich, C.; Tiedt, S.; Colak, D.; Dichgans, M.; et al. Reactive glia in the injured brain acquire stem cell properties in response to sonic hedgehog. [corrected]. *Cell Stem Cell* **2013**, *12*, 426–439. [CrossRef] [PubMed]

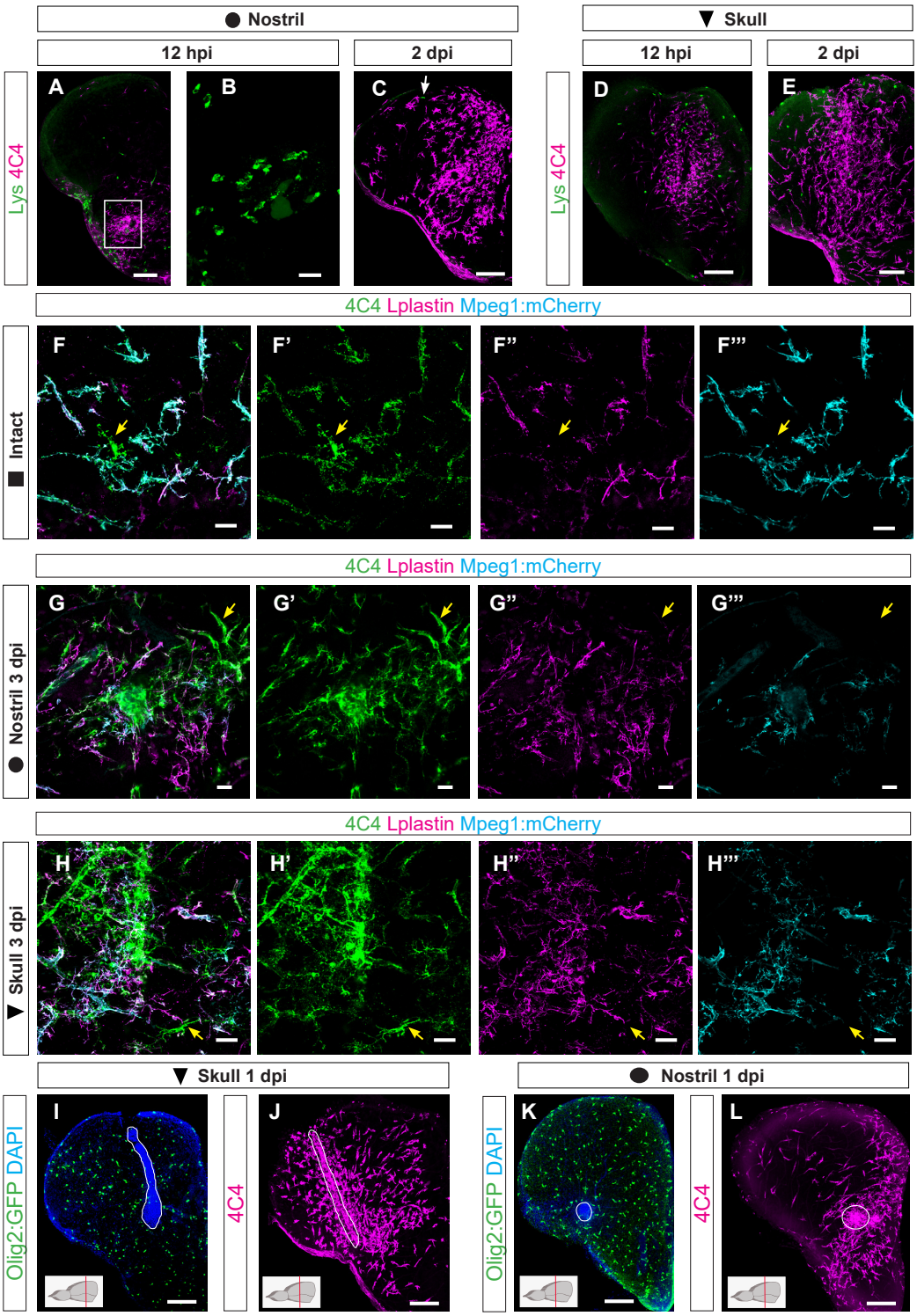

Supplementary Figure S1

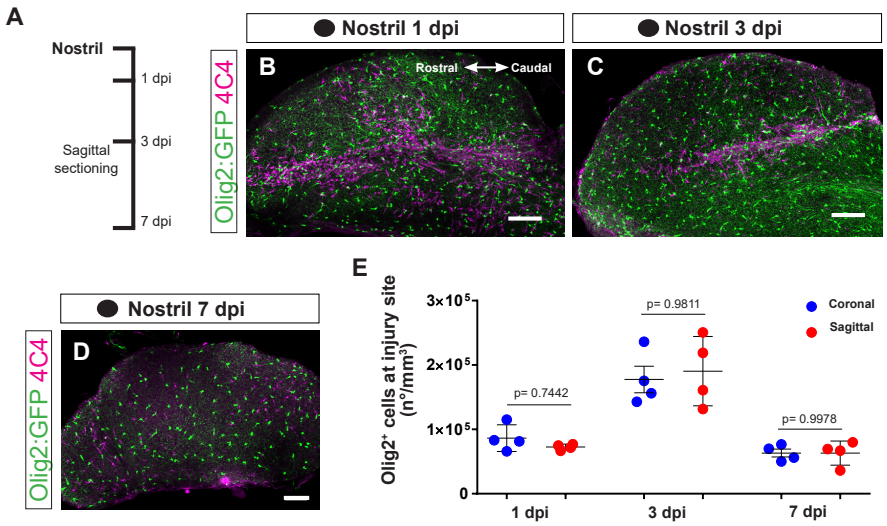

Sanchez-Gonzalez et al., 2021 Supplementary Figure S2

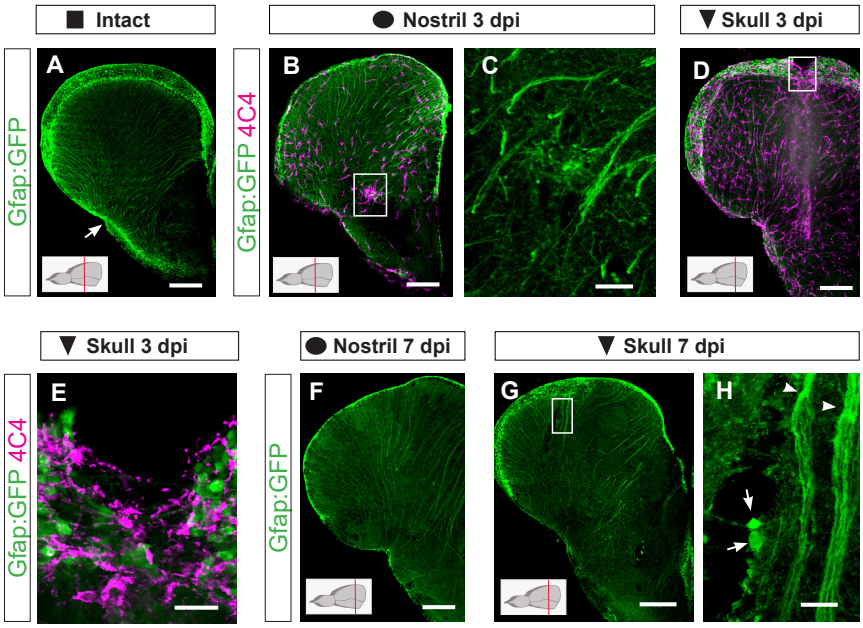

Sanchez-Gonzalez et al., 2021 Supplementary Figure S3

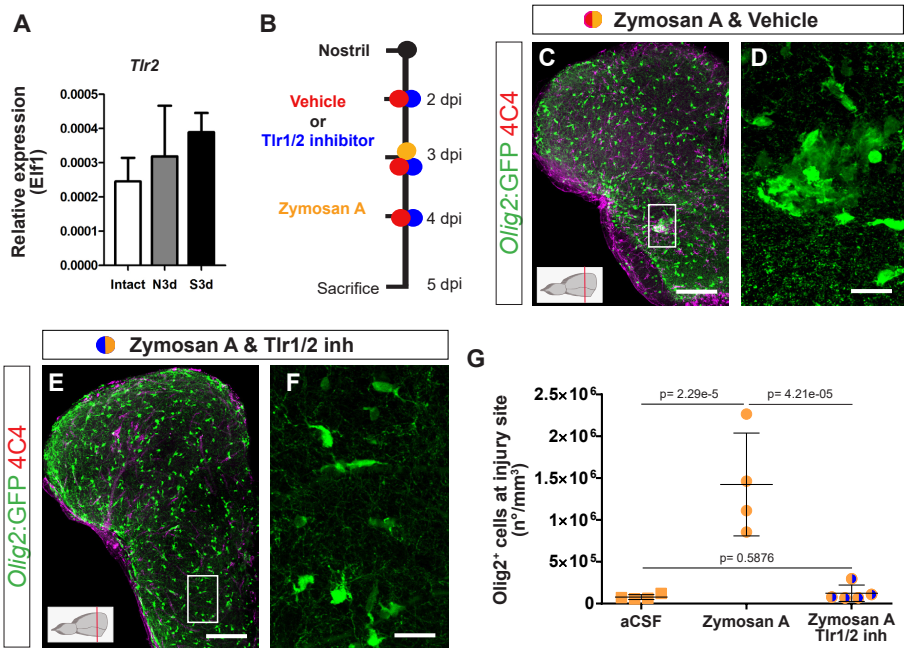

Sanchez-Gonzalez et al., 2021 Supplementary Figure S4

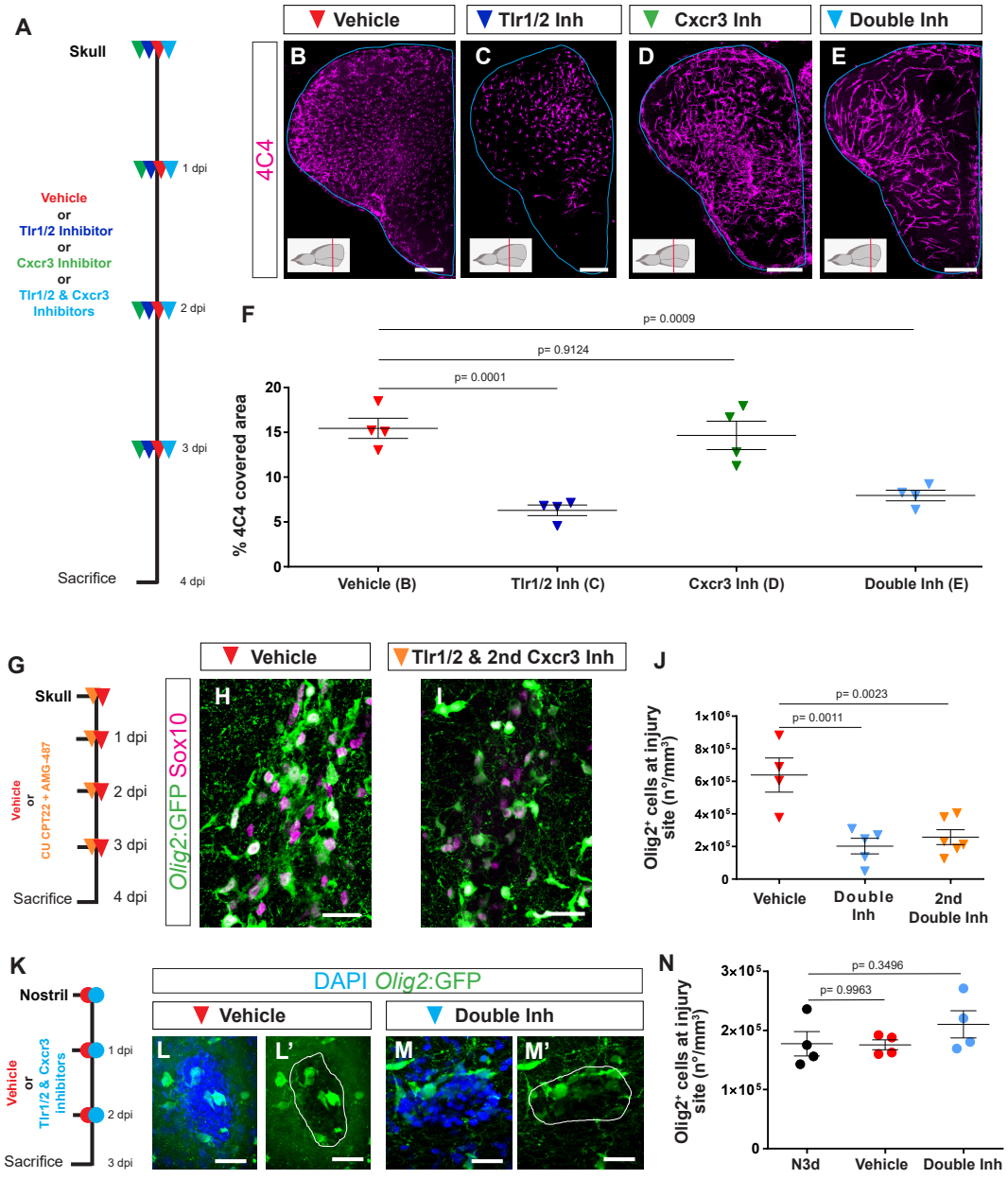

Sanchez-Gonzalez et al., 2021 Supplementary Figure S5

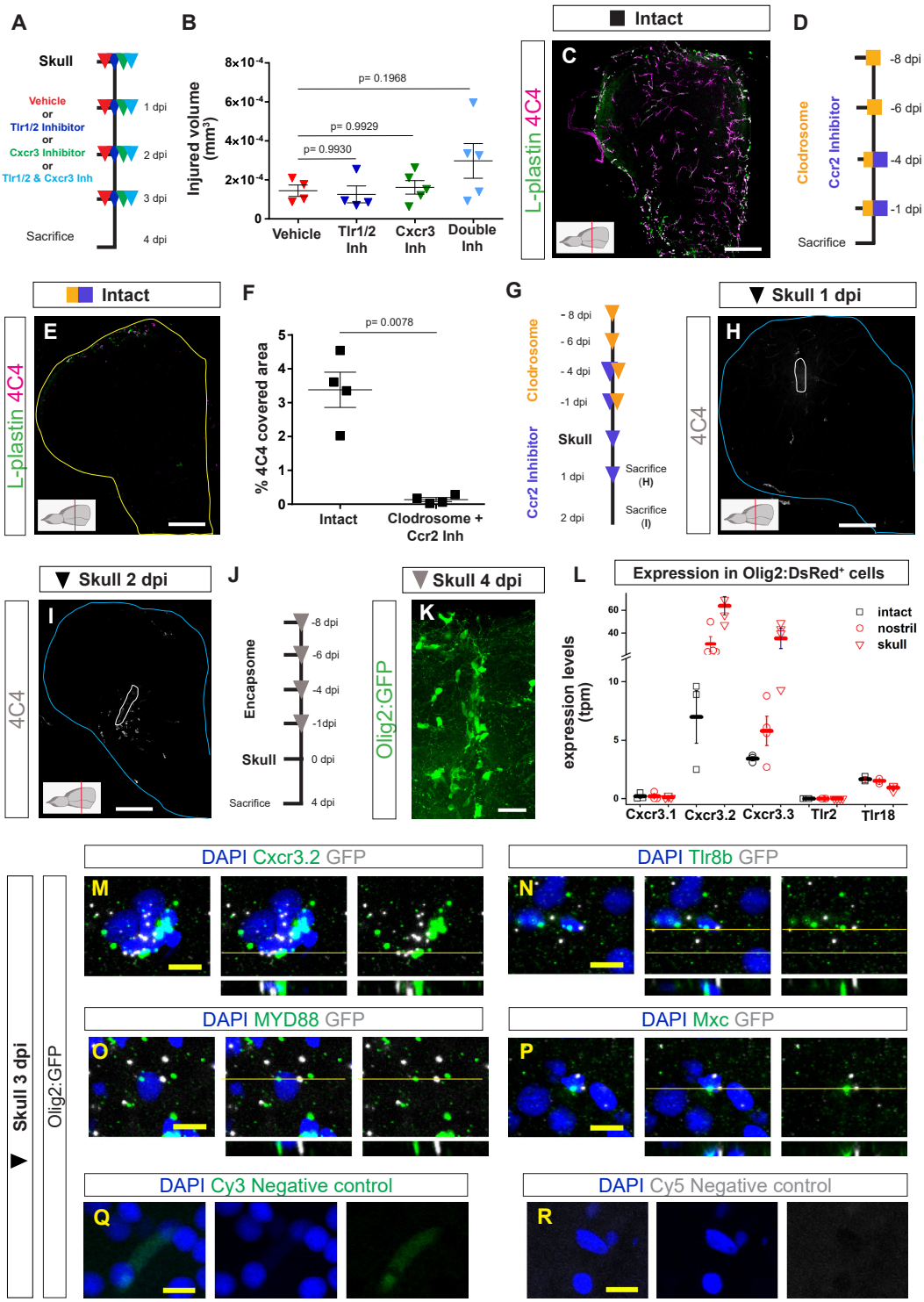

Sanchez-Gonzalez et al., 2021 Supplementary Figure S6

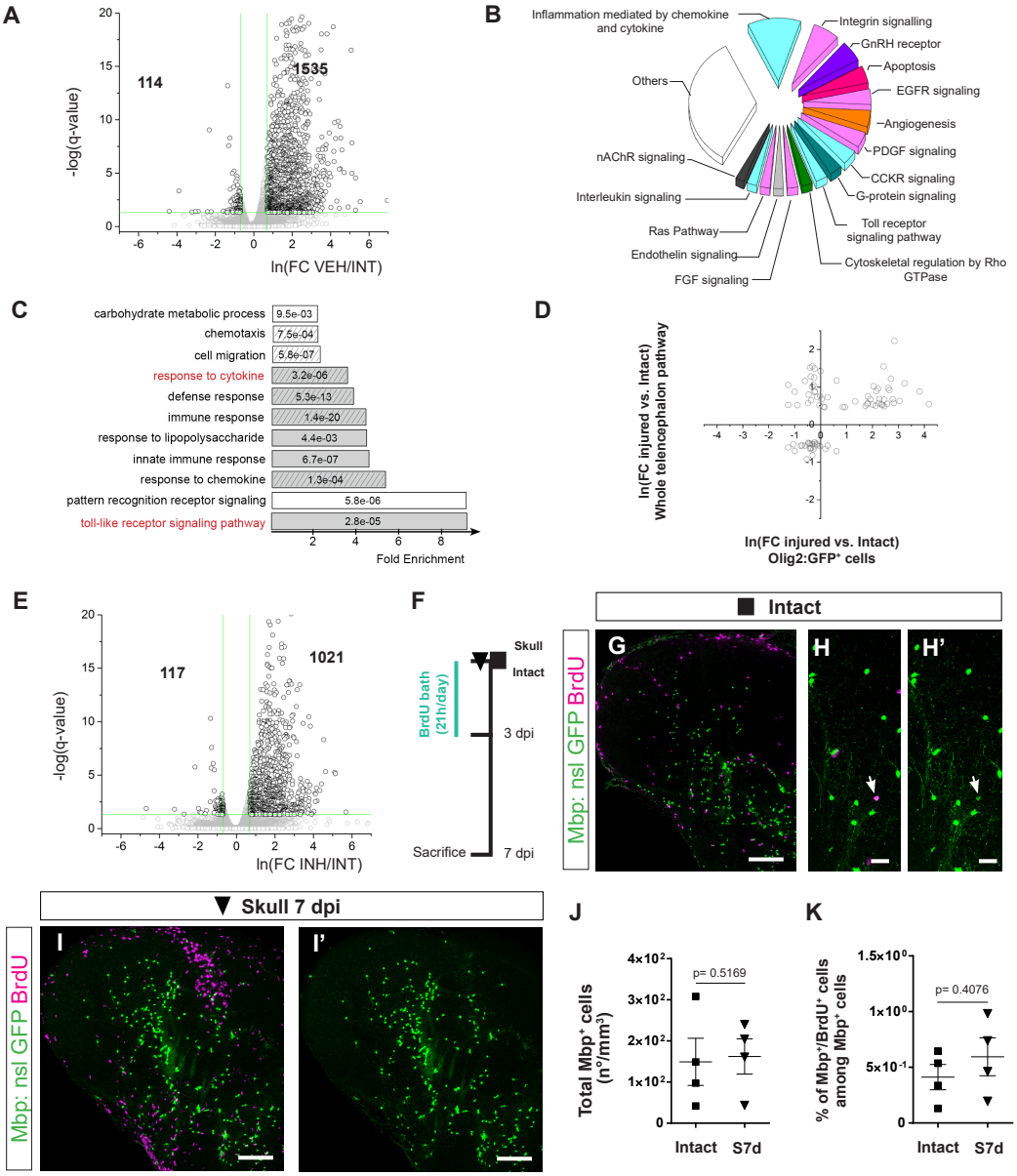

Sanchez-Gonzalez et al., 2021 Supplementary Figure S7

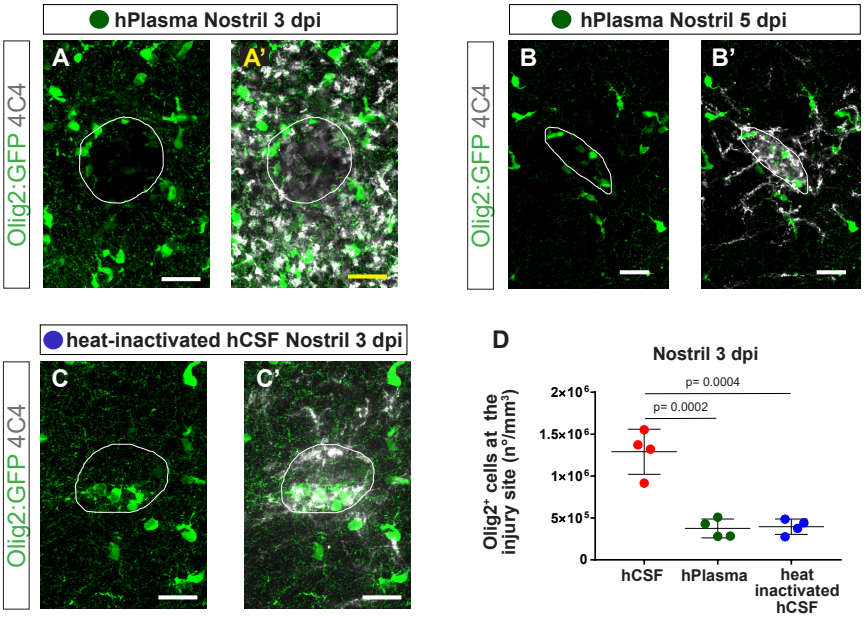

Sanchez-Gonzalez et al., 2021 Supplementary Figure S8

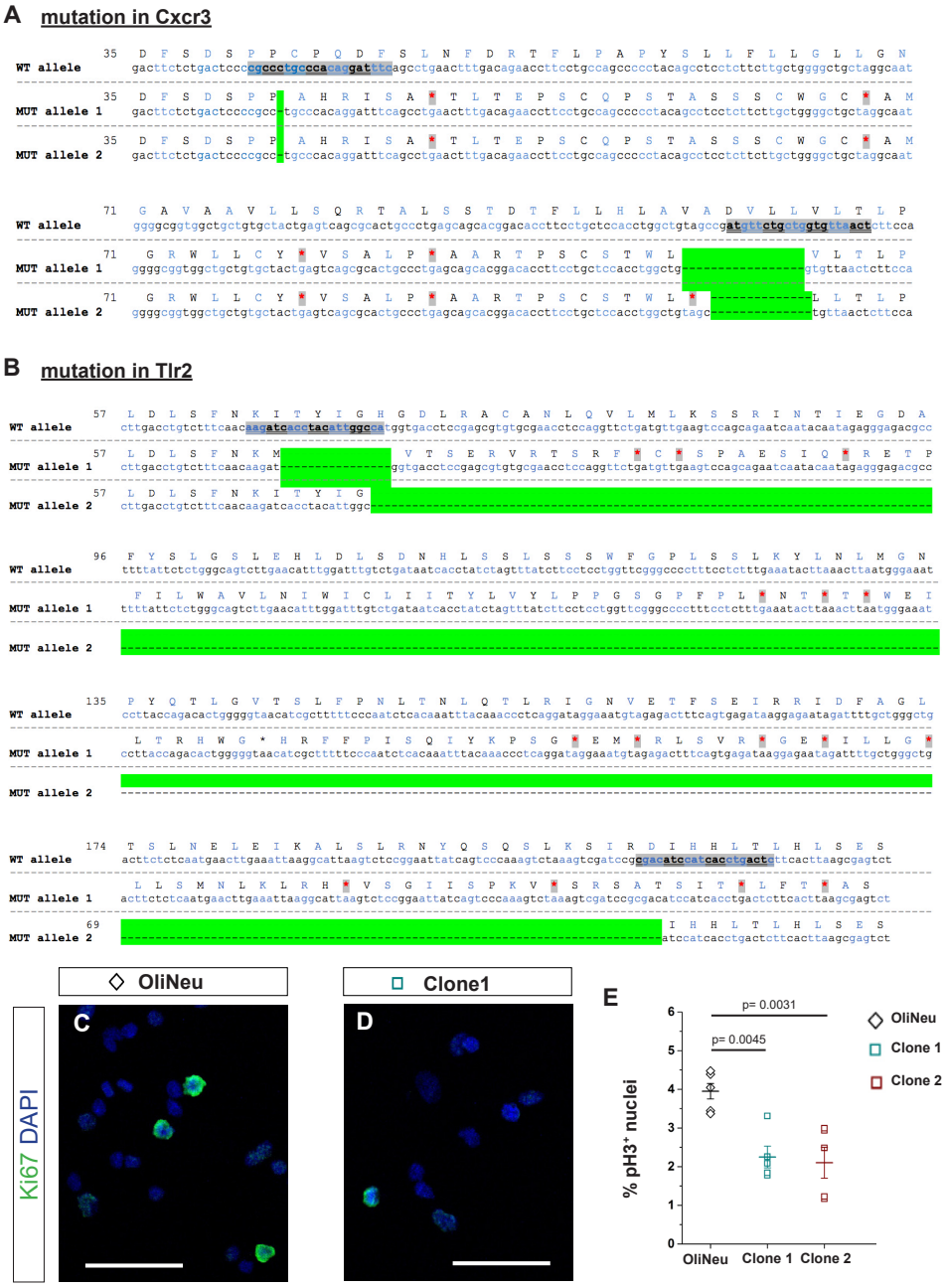

Sanchez-Gonzalez et al., 2021 Supplementary Figure S9

Aim of study II

This study aimed to transcriptomically profile reactive glial cells in the injured murine cerebral cortex and revealed a commonly shared inflammatory signature of reactive glia in response to injury. Moreover, the study involved the innate immunity-associated signaling pathways TLR1/2 and CXCR3 in controlling glial reactivity in the injured murine cerebral cortex.

Shared inflammatory glial cell signature after brain injury, revealed by spatial, temporal and cell-type-specific profiling of the murine cerebral cortex

Christina Koupourtidou*, Veronika Schwarz*, Hananeh Aliee, Simon Frerich, Judith Fischer-Sternjak, Riccardo Bocchi, Tatiana Simon-Ebert, Martin Dichgans, Magdalena Götz, Fabian Theis, Jovica Ninkovic

* These authors contributed equally to the manuscript

For this study, I performed all animal experiments and downstream analyses to investigate the impact of TLR1/2 and CXCR3 signaling on glial reactivity. Furthermore, I was involved in all animal experiments related to the transcriptomic studies of this manuscript and I assisted in the generation of the scRNA-seq and stRNA-seq data sets. Moreover, I was involved in the writing and editing process of this manuscript.

In the course of assembling this dissertation, a working draft of the manuscript has been incorporated. Subsequent to the submission of this dissertation, the manuscript has been accepted for publication in Nature Communications (https://doi.org/10.1038/s41467-024-46625-w). It has also been uploaded to the preprint platform BioRxiv (https://doi.org/10.1101/2023.02.24.529840).

Please note that due to the considerable number of pages, the extended tables are not included in the PDF version of this dissertation, but are available as separate Excel files via the following link:

https://www.dropbox.com/scl/fo/mw9vcz13ga0moozpnvqw5/AJJnOB8D4rK4M8irVEumYJE?rlkey=gnatb2bc4uaojoth91cxcki5w&st=39l795gc&dl=0

Shared inflammatory glial cell signature after brain injury, revealed by spatial, temporal and cell-type-specific profiling of the murine cerebral cortex

Christina Koupourtidou[1,2*], Veronika Schwarz[1,2*], Hananeh Aliee[3], Simon Frerich[2,4], Judith Fischer-Sternjak[5,6], Riccardo Bocchi[5,6,7], Tatiana Simon-Ebert[5,6], Martin Dichgans[4,8,9], Magdalena Götz[5,6,8], Fabian Theis[3,10], Jovica Ninkovic[1,6,8#]

[1]Department of Cell Biology and Anatomy, Biomedical Center (BMC), Ludwig-Maximilians-Universität (LMU), Planegg-Martinsried, Germany
[2]Graduate School of Systemic Neurosciences, LMU, Munich, Germany
[3]Institute of Computational Biology, Helmholtz Zentrum München-German Research Center for Environmental Health, Neuherberg, Germany
[4]Institute for Stroke and Dementia Research, University Hospital, LMU, Munich, Germany
[5]Department of Physiological Genomics, BMC, LMU, Planegg-Martinsried, Germany
[6]Institute of Stem Cell Research, Helmholtz Zentrum München-German Research Center for Environmental Health, Neuherberg, Germany
[7]Department of Basic Neurosciences, University of Geneva, Geneva, Switzerland
[8]Munich Cluster for Systems Neurology SYNERGY, LMU, Munich, Germany
[9]German Centre for Neurodegenerative Diseases, Munich, Germany
[10]Department of Mathematics, Technical University of Munich, Munich, Germany
*these authors equally contributed to the manuscript
[#]Correspondence to: ninkovic@helmholtz-muenchen.de

Abstract (Max 150 words)

Traumatic brain injury leads to a highly orchestrated immune- and glial cell response partially responsible for long-lasting disability and the development of secondary neurodegenerative diseases. A holistic understanding of the mechanisms controlling the responses of specific cell types and their crosstalk is required to develop an efficient strategy for better regeneration. Here, we combined spatial and single-cell transcriptomics to chart the transcriptomic signature of the injured murine cerebral cortex, and identified specific states of astrocytes, microglia, and oligodendrocyte precursor cells contributing to this signature. Interestingly, these cellular populations share a large fraction of injury-regulated genes, including inflammatory programs downstream of the innate immune-associated pathways Cxcr3 and Tlr1/2. Systemic manipulation of these pathways decreased the reactivity state of glial cells associated with poor regeneration. The functional relevance of the newly discovered shared signature of glial cells highlights the importance of our resource enabling comprehensive analysis of early events after brain injury.

Introduction

Traumatic brain injury (TBI) defined as acute brain insult due to an external force, such as the direct impact of a penetrating object or acceleration/deceleration force-induced concussions affects people of all ages and is among the major causes of death and disability[1,2]. TBI-induced primary damage leads to neuronal and glial cell death, axonal damage, edema, and disruption of the blood-brain barrier (BBB)[3,4]. The initial insult is followed by progressive secondary damage, which further induces neuronal circuit dysfunction, neuroinflammation, oxidative stress, and protein aggregation. These cellular changes have been associated with prolonged symptom persistence and elevated vulnerability to additional pathologies, including neurodegenerative disorders[4,5].

TBI-induced pathophysiology evolves through a highly orchestrated response of resident glial cells with peripherally derived infiltrating immune cell populations[3]. After central nervous system (CNS) insult, brain-resident microglia are rapidly activated and change their morphology to a hypertrophic, ameboid morphology[6]. Activated microglia proliferate, polarize, extend their processes, and migrate to the injury site[3,7]. Similarly, oligodendrocyte progenitor cells (OPCs), known as NG2 glia, display rapid cellular changes in response to damage, including hypertrophy, proliferation, polarization, and migration towards the injury site[8–11]. Astrocytes also react to injury with changes in their morphology, gene expression and function in a process referred to as “reactive astrogliosis”[8,12,13]. Reactive astrocytes are characterized by upregulation of intermediate filaments, such as glial fibrillary acidic protein (GFAP), nestin, and vimentin[13–15]. In response to stab-wound injury, astrocytes, in contrast to microglia and OPCs, do not migrate to injury sites, and only a small proportion of astrocytes near blood vessels (juxtavascular astrocytes) proliferate[16]. These initial responses facilitate the formation of a glial border between intact and damaged tissue[12,17,18], which is necessary not only to restrict the damage[12,17–19], but also to promote axonal regeneration and circuit restoration[12,19–21]. However, adequate border establishment requires well-orchestrated glial cell reactions in relative distance to the injury site. For example, the distance of astrocytes and OPCs from the injury site has been demonstrated to shape their reactive state[11,16,22]. Furthermore, cross-communication among cell types in several pathological conditions[23–25], including TBI[26,27], has been reported to determine cell reactivity states. For example, in neuroinflammatory conditions, reactive microglia induce astrocyte neurotoxicity[28]. Moreover, proliferating astrocytes regulate monocyte invasion[26], whereas BBB dysfunction alters astrocyte homeostasis and contributes to epileptic episodes[29,30].

Because the scope of most studies has been restricted to single cellular populations or the interaction of two cell types at most, a detailed investigation of cellular cross-talk after TBI remains lacking. To obtain a holistic understanding of the cellular responses after brain injury, simultaneous examination of multiple cell types in the injury milieu is critical. Therefore, to identify interconnected pathways regulating glial border formation in an unbiased manner, we transcriptomically profiled TBI-induced cell reactivity at spatial and single-cell resolution. Our data provide insights into the spatial, temporal, and single-cell responses of multiple cell types, and reveal a novel, previously overlooked, common injury-induced innate immunity-shared glial signature involving the Toll-like receptor 1/2 (Tlr1/2) and chemokine receptor 3 (Cxcr3) signaling pathways.

Results

Brain injury elicits a localized transcriptomic profile in the murine cerebral cortex

TBI induces coordinated cellular reactions leading to glial border formation and isolation of the injury site from adjacent healthy tissue[12]. Importantly, the TBI-induced cellular response is dependent on the distance to the injury site[9,16]. For unbiased identification of regulatory pathways leading to specific spatially defined reactions of glial cells associated with glial border formation, we used spatial transcriptomic (stRNA-seq, i.e., 10x Visium). Stab-wound injuries were induced at the border between the motor and somatosensory cortex in both hemispheres, harming only the gray matter[31]. Because our main focus was on examining the injury-induced changes in the cerebral cortex, we manually resected the mouse brain (Fig. 1a, E.D. Fig. 1a, b). This allowed us to position two parenchymal sections on a single capture area (E.D. Fig. 1a, b). Each section contained the following brain areas: cortex (CTX), white matter (WM), and hippocampal formation (HPF), as identified on the basis of the Allen brain atlas (Fig. 1b).

This approach provided the advantage to investigate the expression of a multitude of genes from all cell types at the injury site and to examine their dynamics as a function of distance from the injury site. The primary impact initiates a cascade of processes, which involve the reactions of glial cells and infiltrating or resident immune cells[22,32]. To capture the response of infiltrating immune cells, which peaks at 3 days post-injury (dpi)[26], and glial cells, which peaks at 2–5 dpi[11,13,26], we performed stRNA-seq at 3 dpi. Injury-induced alterations were determined by comparison of stab-wounded brain sections to corresponding intact sections (Fig. 1c, E.D. Fig. 1a, b).

Notably, we were able to identify clusters corresponding to specific anatomical structures, e.g., cluster II expressing genes characteristic of cortical layer 2/3 neurons; cluster VIII expressing genes representing layer 4 neurons; and cluster I and cluster IV expressing genes identifying layer 5 and layer 6 neurons, respectively[33] (E.D. Fig. 1c, d, Ext. Table 2). Importantly, the global cortical layer patterning was not affected by the injury, because we also observed similar gene expression patterns identifying the same neuronal layers in the injured brain sections (E.D. Fig. 1d). However, beyond clusters characterizing individual anatomical structures, we identified an injury-induced cluster, cluster VI, localized around the injury core (Fig. 1b, c, E.D. Fig. 1b). Interestingly, cluster VI was distributed throughout cortical layers 1–5 and was absent in the intact brain sections (Fig. 1c, E.D. Fig. 1a, b). Cluster VI was characterized by a specific transcriptomic signature with enrichment in genes associated with reactive astrocytes[12,34–36] (*Gfap*, *Lcn2*, *Serpina3n*, *Vim*, *Lgals1*, *Fabp7*, and *Tspo*) and microglia[37] (*Aif1*, *Csf1r*, *Cd68*, and *Tspo*), which have been associated with CNS damage[12] (Fig. 1d, E.D. Fig. 1c, Ext. Table 3).

To obtain insight into the regulated processes within cluster VI, we performed Gene Ontology (GO) enrichment analysis of significantly upregulated genes (pval < 0.05, $\log_2$ fold change > 1) in this cluster compared with all other clusters. The overrepresented biological processes (BP) were associated with immune response and angiogenesis, whereas the molecular function (MF) and cellular components (CC) indicated changes in genes associated with the extracellular matrix (Fig. 1e, Ext. Table 3). Notably, the above-mentioned processes have been reported to drive glial reaction in response to brain injury and to facilitate glial border formation[19]. Furthermore, processes associated with phagocytosis (lysosome, lytic vacuole, phagocytotic

vesicles) were enriched in cluster VI (Fig. 1e, Ext. Table 3), in line with the previously described importance of phagocytotic processes in the context of brain injuries[38]. To confirm the unique injury-induced expression profile and hence the presence of cluster VI, we validated the expression of the cluster VI genes *Serpina3n*, *Lcn2*, and *Cd68* at the RNA and protein levels. Indeed, the selected candidates were specifically expressed around the injury core, as predicted by our stRNA-seq analysis (Fig. 1f, g), and these expression patterns were also observed at the protein level (Fig. 1h). Although these selected genes were enriched in cluster VI, they displayed unique expression patterns within the injury-induced cluster. Specifically, *Serpina3n* was expressed more broadly than *Lcn2*, whereas *Cd68* displayed a defined expression profile around the injury core (Fig. 1f, g).

To comprehensively determine different expression profiles between the injury core and the perilesional area, we conducted spatial gradient analysis using the SPATA2 analysis pipeline[39]. This allowed us to visualize individual genes and gene set expression patterns as a function of the distance from the injury core (Fig. 2a). For this purpose, we segregated the perilesional area around the injury core into 13 concentric circles (Fig. 2a). In addition, we excluded all subcortical clusters from the analysis and correlated the gene expression profiles along the spatial gradient to a variety of pre-defined models (further details in Methods). To reveal the differences between the injured and perilesional areas, we focused on the genes with "descending" (enriched at the injury core) (Fig. 2b) and "ascending" (depleted at injury core) expression profiles (E.D. Fig. 1e). As expected, all top descending genes were highly enriched at the injury core. However, in the perilesional area (as defined by the border of cluster VI; ~0.5 mm distance from the injury core) some of these genes displayed unique descending rates (Fig. 2b). We observed heterogeneous expression patterning, ranging from injury core-confined expression (e.g., *Alox5ap* and *Rplp0*) to wide-ranging expression (e.g., *Fth1* and *Gfap*) reaching far from the cluster VI border (Fig. 2c). Of note, gene sets associated with the immune response and inflammation were particularly enriched at the injury core (Fig. 2c), whereas gene sets associated with neuronal and synaptic activity were enriched only in the perilesional areas (E.D. Fig. 1f). Similarly to the descending genes, the ascending genes exhibited relatively divergent expression profiles in the perilesional areas (E.D. Fig. 1e). However, approximately 50% of all top 25 ascending genes were associated with mitochondrial functions, in contrast to the descending genes. These mitochondrial genes exhibited almost identical expression profiles in the perilesional area (E.D. Fig. 1e), thus supporting prior findings that brain insult disrupts normally well-regulated mitochondrial function in a coordinated manner[40–42].

In summary, with our spatial gene expression analysis, we identified well-defined anatomical structures as well as an injury-specific cluster characterized by angiogenesis and immune system-associated processes, including phagocytosis. Furthermore, by using spatial gradient analysis, we highlighted injury-induced heterogeneous gene expression profiles in the perilesional area.

Multiple cellular states contribute to injury-induced local transcriptome profiles

Although stRNA-seq enables profiling of transcriptomic changes by preserving spatial information, the profile itself is derived from multiple cells, which are captured in each spot (1–10 cell resolution). To assess the cellular composition of the injured

area and to identify which cell populations defined the transcriptomic profile of cluster VI, we performed single-cell transcriptomic (scRNA-seq) analysis of stab wound-injured cortices and corresponding areas in the intact cortex (3 days post injury, 3 dpi), by using a droplet-based approach (i.e., 10x Chromium) (Fig. 3a). After applying quality control filters, we identified a total of 6322 single cells (Fig. 3b) emerging from both conditions (intact: 2676 cells, 3 dpi: 3646 cells, Fig. 3c, E.D. Fig 2a), which, on the basis of their gene expression, were distributed among 30 distinct clusters. Through this approach, we identified neuronal and glial clusters, including astrocytes, microglia, and oligodendrocyte lineage cells, in addition to vascular cells, pericytes, and multiple types of immune cells (Fig. 3b, E.D. Fig. 2a, b, Ext. Table 5). Additionally, we generated gene expression scores based on established marker genes of well-characterized cell populations in the adult mouse brain (Ext. Table 6). Indeed, the gene scores exhibited enrichment in the corresponding cellular populations, thus further validating our cluster annotation (Fig. 3d).

Interestingly, by comparing the cell distributions between the intact and injured conditions, we observed that several clusters of immune and glial cells were highly abundant exclusively in the injured brain (Fig. 3c, E.D. Fig. 2a). The clusters 8_NKT/T cells, 13_Macrophages/Monocytes, 17_DCs, 18_Monocytes, and 22_DCs, for example, appeared primarily after injury and expressed *Ccr2*[6,22] (E.D. Fig. 2c) in addition to their distinct cell identity markers (E.D. Fig. 2b, Ext. Table 5). Microglia clusters that appeared after injury (11_Microglia and 16_Microglia) exhibited high expression of *Aif1* and low expression of the homeostatic microglia markers *Tmem119* and *P2ry12*[43] (E.D. Fig. 2c). Similarly, the astrocytic clusters 12_Astrocytes and 23_Astrocytes were present primarily in the injured condition and were characterized by high expression of classical reactive astrocyte markers such as *Gfap* and *Lcn2*[34,36] (E.D. Fig. 2d). In addition to microglia and astrocytes, the cluster 15_OPCs was present primarily after injury (E.D. Fig. 2a). Cells from cluster 15_OPCs expressed a combination of genes associated with the cell cycle (G2/M phase, E.D. Fig 2f, Ext. Table 7[44,45]) and *Cspg4* (E.D. Fig. 2e); both hallmarks of Nerve/glial antigen 2 glia (NG2 glia), which rapidly proliferate after brain injury[9].

To elucidate which of these cellular clusters contributed to the injury-specific signature of cluster VI, we mapped the single cell expression data onto the spatial gene expression dataset (Fig. 3e, f, E.D. Fig. 3 and 4) by using Tangram[46]. To include the identical anatomical regions regarding the scRNA-seq data acquisition, we restricted the stRNA-seq dataset to the cortical clusters (clusters I, II, IV, VI, VII, VIII, and IX). The probabilistic mapping predicted that several clusters including 11_Microglia, 16_Microglia, 12_Astrocytes, 23_Astrocytes, 13_Macrophages/Monocytes, 18_Monocytes, and 15_OPCs were localized near the injury core (Fig. 3e, E.D. Fig. 3a). In contrast, neuronal clusters 1_Neurons, 2_Neurons, and 24_Neurons, as well as the astrocytic clusters 3_Astrocytes, 5_Astrocytes, 7_Astrocytes, and 9_Astrocytes, displayed decreased representation around the injury site (Fig. 3e, E.D. Fig. 3a). Additionally, we used the H&E images of the stRNA-seq dataset to estimate the number of nuclei within each spot of the capture area, which, in combination with probabilistic mapping, can be used for deconvolution. To some extent, this analysis further associated the above-mentioned clusters with the injury milieu (Fig. 3f, E.D. Fig. 4a, b). Importantly, not all glial cells contributed to the injury environment (E.D. Fig. 3a, 4b). Most astrocytic clusters, with the exception of clusters 12_Astrocytes and 23_Astrocytes, did not show enriched mapping at the injury site (Fig. 3e, E.D. Fig. 3a). Similar behavior was detected for the oligodendrocyte clusters 20_MOL and 27_COPs (E.D. Fig. 3a). Notably, our deconvolution analysis

supported these observations (E.D. Fig. 4b). In summary, the combination of stRNA-seq with corresponding scRNA-seq datasets allowed us to identify an injury-specific transcriptional profile exhibiting enrichment of individual glial subpopulations, and subsequent depletion of distinct astrocytic and neuronal clusters.

Injury induces common transcriptomic changes in glial cells

Because glial cell reactivity exhibits distinct temporal dynamics in response to injury[11,13,26], we decided to add an additional time point (5 dpi) to our scRNA-seq analysis (Fig. 4a). This experimental design enabled investigation of the transcriptional states of glial cells underlying the observed heterogeneity in glial cell responses. In total, we analyzed 33862 cells (intact: 16567, 3 dpi: 3637, 5 dpi: 13658), which were distributed among 35 clusters (Fig. 4b, E.D. Fig. 5a-c, Ext. Table 8). In line with our previous observations (Fig. 3c), a comparison of cell distribution among all three conditions (intact, 3 dpi, and 5 dpi) elucidated several injury-induced clusters, which were formed exclusively by cells originating from brain-injured animals (E.D. Fig. 5b). However, none of these injury-induced clusters were specific to either the 3 or 5 dpi time point (E.D. Fig. 5b).

To unravel how each population transited from a homeostatic to a reactive state, we focused on individual cell populations. Hence, we further subclustered astrocytes, microglia, and oligodendrocytes (Fig. 4c-e, E.D. Fig. 6). We identified distinct clusters in each of the investigated populations, which were composed primarily of cells from intact (blue clusters) and injured (orange/red clusters) samples (Fig. 4c-e, E.D. Fig. 6c, h, m). Additionally, cells originating from the injured samples expressed typical markers of glial reactivity. We identified clusters AG5, AG6, and AG8 as the main populations of reactive astrocytes (Fig. 4c, E.D. Fig. 6a-e), because these cells expressed high levels of *Gfap*, *Vim*, and *Lcn2*[34,36] (E.D. Fig. 6e). Microglial clusters MG4 and MG6 displayed high expression of *Aif1* and low expression of the homeostatic markers *Tmem119* and *P2ry12*[43](Fig. 4d, E.D. Fig. 6f-j). By subclustering cells belonging to the oligodendrocytic lineage, we were able to identify two populations of OPCs (OPCs1 and OPCs2) (Fig. 4e, E.D. Fig. 6k-o). Cluster OPCs2 was composed primarily of cells from injured samples (Fig. 4e). Of note, we were not able to find a unique marker within the OPCs2 cluster for identifying reactive OPCs (E.D. Fig. 6o). Importantly, cells from the injury-responding clusters, as identified by our previous deconvolution analysis (11_Microglia, 12_Astrocytes, and 15_OPCs) (Fig. 3f, E.D. Fig. 4), also mapped predominantly to the glial subclusters evoked by injury (E.D. Fig. 6d, i, n). Together, these results corroborated the reactive state of these glial subclusters (henceforth referred to as reactive clusters).

By subclustering glial cells, we did not discover any cluster unique to either the 3 or 5 dpi time point. This finding suggests a gradual activation of glial cells in response to injury rather than distinct activation states. To shed light on this possibility, we examined the cell distributions of all subclustered glial cells among all time points (intact, 3 dpi, and 5 dpi) (Fig. 4f-h). Interestingly, we observed prominent changes in the distribution of reactive clusters between time points after injury. More specifically, many of the astrocytes at 3 dpi remained present in the homeostatic clusters and were only partially present in the reactive clusters AG6 and AG8, whereas at 5 dpi, most cells were detected in cluster AG5 (Fig. 4f). Microglia, in contrast, displayed a faster transition to reactivity than astrocytes: at 3 dpi, most cells were already localized in the reactive clusters MG4 and MG6. At 5 dpi, however, most of the cells had begun to

transition back to the homeostatic state, and a high proportion of cells were present in cluster MG3 (Fig. 4g). Similarly, OPCs reacted rapidly after injury, because at 3 dpi, most cells resided in the reactive cluster OPCs2, whereas only several cells were present in this cluster at 5 dpi (Fig. 4h). These results are in line with prior findings showing that microglia and OPCs rapidly respond to injury, and their reactivity peak ranges from 2 to 3 dpi, whereas astrocyte reactivity peaks at 5 dpi[11,13,26].

The enriched immune system-associated processes around the injury site, as indicated by spatial transcriptomics, and the identification of specific reactive subtypes of glial cells populating the injury environment, prompted the question of whether the inflammatory gene expression might be a unique signature of one specific cell type or a common feature of reactive glia. Therefore, within each glial population (Fig. 4 c-e), we extracted the differentially expressed genes (DEGs) of each glial subcluster (pval < 0.05, $\log_2$ fold change > 1.6 or < -1.6) and compared them among all subclusters (E.D. Fig. 7a, b, Ext. Table 9). Interestingly, among all clusters, the highest similarity of upregulated genes was observed between the reactive glial clusters MG4, AG5, and OPCs2, with 66 enriched genes in common (E.D. Fig. 7b). This finding suggested that, in response to injury, individual reactive glial clusters might share some cellular programs. Hence, we performed GO term analysis of the 192 commonly upregulated genes from the comparison of clusters MG4, AG5, and OPCs2, independently of other glial subclusters (Fig. 5a). Most of the commonly regulated processes were associated with cell proliferation (Fig. 5b, Ext. Table 10), which has been reported to be a shared hallmark of glial cell reactivity[13,34]. Moreover, we identified processes associated with innate immunity (Fig. 5b, Ext. Table 10) and numerous genes associated with the type I interferon signaling pathway (*Ifitm3*, *Ifit3*, *Bst2*, *Isg15*, *Ifit3b*, *Irf7*, *Ifit1*, *Ifi27l2a*, *Oasl2*, and *Oas1a*) (Fig. 5c) as well as *Cxcl10*, a ligand activating the Cxcr3 pathway[47]. Indeed, by using RNA scope, we confirmed that *Cxcl10*, *Oasl2*, and *Ifi27l2a* were expressed by a subset of microglia, astrocytes, and OPCs (Fig. 5d-g, E.D. Fig. 8a-g). Furthermore, we observed shared expression of Galectin1 (*Lgals1*) by a subset of microglia, astrocytes, and OPCs at the protein level (E.D. Fig. 9a-d). Notably, the expression of these innate immunity-associated genes was clearly restricted to distinct glial subpopulations, because not all glial cells expressed these markers (Fig. 5d-g, E.D. Fig. 8a-g, E.D. Fig. 9a-d). Additionally, the upregulation of the innate immunity-associated genes (Fig. 5c) after injury is a unique feature of glial cells because neurons never expressed these genes, whereas in vascular cells they were present at low levels in the intact brain (E.D. Fig. 9e, f).

We further asked whether the shared inflammatory signature might be a conserved feature of reactive glia in different pathological conditions. We used a publicly available database describing the response of astrocytes to systemic lipopolysaccharide (LPS) injection.[36] Interestingly, a high proportion of the shared inflammatory marker genes (e.g., *Oasl2* and *Ifit1*) were expressed exclusively in the astrocytic cluster 8 (E.D. Fig. 10a). Astrocytes of cluster 8 were classified in the above-mentioned study as reactive astrocytes in a sub-state capable of rapidly responding to inflammation. Notably, not all inflammatory genes were detected in LPS-induced reactive astrocytes, thus indicating that only a portion of the signature was retained (E.D. Fig. 10b). Furthermore, we investigated whether human iPSC-derived reactive astrocytes displayed similar inflammatory responses to those in stab wound-injured mice. Therefore, we mapped the genes characterizing the two inflammatory clusters of iPSC-derived reactive astrocytes from Leng et al.[48] (IRAS 1 and IRAS2) on our integrated single-cell dataset (Fig. 4b, E.D. Fig. 10c).[49] Interestingly, the inflammatory signatures of both iPSC-derived reactive astrocyte clusters (IRAS 1 and IRAS2) were

335 induced primarily in the subclusters of astrocytes that emerged after injury
336 (11_Astrocytes and 16_Astrocytes) (E.D. Fig. 5a, b, E.D. Fig. 10c, d), thus confirming
337 common reactive astrocytic states between murine and human glia. Of note, the
338 inflammatory signature of the human iPSC-derived astrocytes was not observed
339 exclusively in reactive astrocytes but was highly abundant in other cellular populations
340 (E.D. Fig. 10c, d). This finding strongly emphasizes the need for a holistic cellular view
341 of brain pathologies to identify therapeutical targetable pathways. Our findings
342 revealed a common inflammatory signature present in a subset of reactive glial cells
343 in response to TBI. Moreover, this shared inflammatory signature is largely preserved
344 in different pathological conditions and species.

345 Regulation of injury-induced innate immune responses via the Cxcr3 346 and Tlr1/2 pathways

347 On the basis of the shared regulation of the innate immunity pathways after
348 brain injury, including components of the CXC chemokine receptor 3 (Cxcr3) and Toll-
349 like receptor 2 (Tlr2) pathways (E.D. Fig. 9g), and our recent findings that Cxcr3 and
350 Tlr1/2 regulate OPC accumulation at injury site in the zebrafish brain[49], we
351 investigated the injury-induced transcriptional changes after interference with the
352 Cxcr3 and Tlr1/2 pathways. We used the Cxcr3 antagonist NBI-74330[50] and the Tlr1/2
353 pathway inhibitor CU CPT 22[51] to interfere with the above-mentioned pathways, and
354 performed scRNA-seq analysis at 3 dpi and 5 dpi (henceforth referred to as SW INH
355 or 3/5 dpi_INH if distinct time points are indicated) (Fig. 6a). The specificity of these
356 chemical compounds was validated with a murine knock-out OPC cell line[49]. The data
357 were integrated with our previously acquired datasets (Fig. 4b) from intact (INT) and
358 injured animals (henceforth referred to SW CTRL or as 3/5 dpi_CTRL if distinct time
359 points are indicated). In total, we analyzed 53813 cells (INT: 16649 cells, 3 dpi_CTRL:
360 3643 cells, 3 dpi_INH: 4613 cells, 5 dpi_CTRL: 13766 cells, 5 dpi_INH: 15142) were
361 distributed among 36 clusters (Fig. 6b, E.D. Fig. 11a). Notably, with the integration of
362 additional conditions (3 and 5 dpi_INH), and hence a subsequent increase in the total
363 cell number, we did not observe the emergence of new clusters (E.D. Fig. 11a).
364 Furthermore, even after the integration of SW INH datasets, the overall cluster identity
365 was unaffected, as indicated by high similarity scores among the clusters (E.D. Fig.
366 11b). Because microglia, astrocytes, and OPCs displayed common innate immune-
367 associated gene expression after stab wound injury (Fig. 5c-g), we sought to
368 investigate the possible influence of Cxcr3 and Tlr1/2 pathway inhibition on microglia,
369 astrocytes, and OPCs by further subclustering the above-mentioned cell types. In
370 each investigated cell population, we again identified distinct clusters containing
371 primarily cells from injured samples (Fig. 6c-e, E.D. Fig. 11c-e). Of note, these clusters
372 were composed of cells originating from both SW CTRL and SW INH samples. These
373 results suggested that the inhibition of Cxcr3 and Tlr1/2 pathways after stab-wound
374 injury did not induce new transcriptional states. Instead, the inhibitor treatment
375 resulted in partial downregulation of the inflammatory genes (Fig. 5c) shared among
376 the reactive clusters AG7, MG3, and OPCs2 (Fig. 6f, Ext. Table 11).
377 To address transcriptional changes induced by the inhibitor treatment, we
378 performed differential gene expression analysis of each subcluster between SW CTRL
379 and SW INH at each time point (pval < 0.05, $\log_2$ fold change > 0.7 or $\log_2$ fold change
380 < -0.7). Interestingly, most of the inhibitor-induced changes at 3 and 5 dpi were
381 subcluster specific, because only a few DEGs overlapped (E.D. Fig. 12a-d). To reveal
382 the biological processes regulated in each glial subcluster (Fig. 6c-e), we used the

function compareCluster[52] (clusterProfiler R package) and calculated the enriched functional profiles of each cluster. This function summarized the results into a single object and allowed us to compare the enriched biological processes of all glial subclusters at once. Indeed, by comparing the processes associated with all significantly downregulated genes after treatment at 3 dpi, we identified many programs associated with the innate immune response, which were shared among several glial populations, including reactive astrocytes (clusters AG5, AG6, AG7, and AG9), microglia (clusters MG3 and MG6), and OPCs (cluster OPCs2) (Fig. 6g, Ext. Table 12). Interestingly, although still downregulated at 5 dpi, these immune response-associated processes were no longer shared among different glial populations (Fig. 6h, Ext. Table 12). In contrast, biological processes induced by the inhibitor treatment were cluster specific, independently of the analysis time point (E.D. Fig. 12e, f). Together, our scRNA-seq analysis findings indicated that the Cxcr3 and Tlr1/2 signaling pathways regulate similar processes in initial activation (3 dpi) of different glial cells. However, this activation is followed by cell type-specific transcriptional changes at later stages (5 dpi).

Inhibition of the Cxcr3 and Tlr1/2 signaling pathways does not interfere with oligodendrocyte reactivity and proliferation

Interference with the Cxcr3 and Tlr1/2 signaling pathways after brain injury did not result in the emergence of new cell types or states at either 3 or 5 dpi (E.D. Fig. 11a). Nevertheless, the inhibition of the above-mentioned pathways elicited an overall downregulation of various inflammation-associated genes in the reactive glial clusters AG7, MG3, and OPCs2, particularly at 3 dpi (Fig. 6f, Ext. Table 11). Furthermore, inhibition of the Cxcr3 and Tlr1/2 pathways after injury in the zebrafish telencephalon modulated oligodendrocyte proliferation, thereby decreasing oligodendrocytes in the injury vicinity[49]. To investigate the relevance of Cxcr3 and Tlr1/2 signaling in the mammalian context, we first sought to examine the cluster distribution of oligodendroglial lineage cells among all conditions (INT, SW CTRL and SW INH) and time points (3 and 5 dpi) (E.D. Fig. 13a). Surprisingly, we detected no differences in the cluster distribution of the reactive OPC clusters OPCs2 and OPCs3 between SW CTRL and SW INH cells at 3 or 5 dpi (E.D. Fig. 13b). To further corroborate our scRNA-seq findings, we determined the number of OLIG2$^+$ oligodendrocytes in stab wound-injured mice at 3 dpi (E.D. Fig. 13c). In line with the findings from our computational analysis, we detected no differences in the number of OLIG2$^+$ cells near the injury site between the experimental groups (E.D. Fig. 13d-f). Finally, we determined the proliferation ability of OLIG2$^+$ cells between both experimental groups by labeling all cells in S-phase with the DNA base analogue EdU (0.05 mg/g 5-ethinyl-2′-deoxyuridine i.p. injection 1 hr before sacrifice) and observed no changes in the number of proliferating (OLIG2$^+$ and EdU$^+$) oligodendrocytes (E.D. Fig. 13d, e, g).

In summary, the inhibition of Cxcr3 and Tlr1/2 signaling pathways after stab wound injury in the mouse cerebral cortex, in contrast to findings in the zebrafish brain, did not alter oligodendrocyte proliferation or affected the overall number of oligodendrocyte lineage cells near the injury site early after injury, but did alter their inflammatory signatures.

The Cxcr3 and Tlr1/2 signaling pathways regulate microglial activation in response to injury

The expression of inflammatory genes in microglia is tightly associated with their activation[7,53]. Therefore, we assessed whether the downregulation of inflammatory genes induced by Cxcr3 and Tlr1/2 inhibition (Fig. 6f) might alleviate microglial reactivity. Hence, we examined the cell distribution of subclustered microglia among all three conditions (INT, SW CTRL, and SW INH) and time points (3 and 5 dpi) (Fig. 7a, b). As previously depicted in Fig. 4g, cells derived from intact samples were confined to the homeostatic clusters, whereas cells from the injured samples were distributed primarily in the reactive clusters at 3 dpi, and a transition toward the homeostatic clusters was noticeable at 5 dpi. A direct comparison of SW CTRL and SW INH samples indicated differences in the cell distributions, with a higher proportion of cells localized in the homeostatic clusters after Cxcr3 and Tlr1/2 inhibition (Fig. 7b). Although the discrepancy between conditions was already detectable at 3 dpi, the shift was more pronounced at 5 dpi (Fig. 7b). To further elucidate whether the detected shift in microglia distribution after Cxcr3 and Tlr1/2 pathway inhibition was accompanied by changes in overall cell morphology, we assessed microglia cell characteristics with the automated morphological analysis tool described by Heindl et al.[54]. Brain sections from SW CTRL and SW INH animals were labeled with an anti-IBA1 antibody, and areas near the injury site were analyzed (Fig. 7c). Microglia from SW INH brains displayed significantly smaller cell somata, a less round shape, and greater branch length than microglia from SW CTRL brains (Fig. 7d-f, E.D. Fig. 14a). The inhibition of Cxcr3 and Tlr1/2 signaling pathways decreased branch volume without altering the total number of major branches (E.D. Fig. 14a). In addition, although not significantly altered, microglia from SW INH brains appeared to be more ramified than SW CTRL microglia, because more nodes per major branch were detected. (E.D. Fig 14a).

In summary, our scRNA-seq data implied that Cxcr3 and Tlr1/2 pathway inhibition accelerates the transition from a reactive to a homeostatic microglial cell state early after injury. These findings were further supported by pronounced morphological changes in inhibitor-treated microglia, which are characteristic features of less reactive cells.

Altered astrocyte response after Cxcr3 and Tlr1/2 pathway inhibition

To address the effects of Cxcr3 and Tlr1/2 pathway inhibition on astrocytes after brain injury, we subclustered astrocytes (Fig. 8a) and investigated the cell distribution among all conditions and time points (Fig. 8b). Astrocytes originating from intact conditions were evenly distributed among all homeostatic clusters. However, cells from stab-wounded brains were initially localized in both homeostatic and reactive clusters at 3 dpi, whereas at 5 dpi, most cells were distributed among the reactive clusters. Comparison of astrocyte cell distribution of SW CTRL and SW INH samples indicated noticeable differences at 5 dpi. Most cells originating from the SW CTRL condition were distributed among the reactive clusters AG5, AG6, and AG7, whereas cells originating from the SW INH condition were largely confined to the reactive cluster AG5 (Fig. 8b). Interestingly, cluster AG5 exhibited lower expression of reactivity markers, such as *Gfap* and *Lcn2*, than the reactive clusters AG6 and AG7 (E.D. Fig. 14b). In line with the shifted distribution of SW INH cells to cluster AG5, inhibitor-treated astrocytes also displayed lower expression of *Gfap* and *Lcn2* at 5 dpi

(E.D. Fig. 14c). To determine whether astrocyte reactivity was altered overall, we generated astrocyte reactivity scores (based on Hasel et al.[36]) and compared the reactivity gene set scores among intact, stab wound-injured control, and inhibitor-treated samples (E.D. Fig. 14d). Generally, both reactivity scores (Cl4 and Cl8 in E.D. Fig 14d) were relatively lower in stab wound-injured inhibitor-treated samples at both time points (3 and 5 dpi). However, the fraction of astrocytes expressing these distinct gene sets was unchanged. Therefore, our analysis implied that the inhibitor treatment decreased astrocyte reactivity overall but was not sufficient to promote the return of reactive astrocytes to homeostasis. In line with our findings from the scRNA-seq analysis, also by immunohistochemical analysis, we did not observe differences in the total number of reactive astrocytes between stab-wounded control and inhibitor-treated mice at 5 dpi (E.D. Fig. 14e-i). Both experimental groups showed comparable $GFAP^+$ cell accumulation (E.D. Fig. 14f, g, h), and numbers of $NGAL^+$ (*Lcn2*) and $GFAP^+$ positive astrocytes in the injury vicinity (E.D. Fig. 14f, g, i).

Furthermore, beyond the diminished expression of reactive astrocyte markers in cluster AG5, this cluster was also devoid of proliferating cells, because most cycling cells were confined to clusters AG6 and AG7, as indicated by the scRNA-seq proliferation score (E.D. Fig. 14j, Ext. Table 6). Interestingly, on the basis of our scRNA-seq analysis, interference with Cxcr3 and Tlr1/2 signaling after stab wound injury decreased the fraction of proliferating astrocytes at 3 and 5 dpi, in line with the abundance of SW INH cells composing cluster AG5 (Fig. 8b, E.D. Fig. 14k).

To further investigate potential alterations in proliferation after inhibitor treatment, we assessed astrocyte proliferation with immunohistochemistry in combination with the DNA-base analogue EdU (0.05 mg/g i.p. injection 1 hr before sacrifice) at 3 dpi (Fig. 8c). Indeed, inhibition of the Cxcr3 and Tlr1/2 pathways after injury significantly decreased the proportion of proliferating ($GFAP^+$ and EdU^+) astrocytes in the injury vicinity (Fig. 8d-f). However, the total number of EdU^+ cells was not altered (Fig. 8d, e, g). In summary, our scRNA-seq analysis demonstrated decreased astrocyte reactivity and proliferation rates after inhibitor treatment. However, Cxcr3 and Tlr1/2 pathway inhibition, despite being sufficient to decrease astrocyte proliferation *in vivo*, did not completely revert astrocytes to homeostasis.

506 ## Discussion

507 TBIs have complex pathophysiology involving responses of various types of
508 cells[3,4]. However, most studies have focused on the responses of specific cell types,
509 whereas few have evaluated the interplay among these cells[23,26,55]. Therefore, we
510 developed a comprehensive dataset profiling the transcriptional changes across
511 various cell types in spatial and temporal contexts. Our study used the stab wound
512 injury model in mice[26,31], a mild injury model involving breakdown of the BBB and the
513 activation of both glial and immune cells[26]. Our model's reproducibility and observed
514 reactivity indicates its suitability for studying the basic features of TBI pathophysiology.
515 Spatial transcriptomic analysis of the stab-wounded cortex at 3 dpi revealed an
516 injury-specific cluster, cluster VI, around the injury core without detectable changes in
517 the cortex regions distant from the injury. The specificity of the injury defining the
518 cluster VI signature was validated by the expression patterns of selected genes
519 (*Serpina3n*, *Lcn2*, and *Cd68*) with RNAscope and immunohistochemistry, whose
520 results were in line with those from the stRNA-seq analysis. This observation supports
521 the use of stRNA-seq to detect global changes with spatial information. To
522 complement the clustering analysis, we investigated gene expression patterns by
523 conducting spatial gradient analysis. This analysis revealed gene expression changes
524 in pre-defined gradients spanning from the injury core to the periphery, whereby injury-
525 enriched genes followed various types of descending patterns. By analyzing the gene
526 sets following these descending patterns, we observed an over-representation of
527 processes associated with innate immunity. Complementing these results, cluster VI-
528 enriched genes also revealed the regulation of processes associated with the immune
529 system, in addition to angiogenesis and phagocytosis. Clearing dead cells and debris
530 and re-establishing vasculature to ensure sufficient oxygen supply are critical defense
531 mechanisms that occur early after brain damage[32].
532 Many observed local changes represented by the injury-enriched genes were
533 associated with reactive astrocytes and microglia[12,34–37], thus indicating an
534 overrepresentation of these populations in the injury milieu. Interestingly, we did not
535 identify reactive OPC hallmarks despite clear evidence of reactive OPCs at the injury
536 site[8,56]. This result may be partly explained by the unknown signature of reactive
537 OPCs, because only an increase in proliferation and expression of CSPG4 have been
538 used to identify reactive OPCs to date[9]. Moreover, the combination of stRNA-seq with
539 scRNA-seq analysis is becoming an excellent tool to reveal transcriptomic changes in
540 specific cell types in relation to their predicted location. This capability is of great
541 interest for any focal pathology, given that the reactions of astrocytes[16,] OPCs[11,57], and
542 microglia[57,58] have been found to depend on their distance from the pathological site.
543 Integration of scRNA-seq and stRNA-seq datasets indicated the presence of
544 distinct cell types in the injury environment. We detected multiple populations
545 responding to the injury by enriched or decreased representation in the injured milieu,
546 whereas other cell clusters never responded. Microglial clusters displayed a uniform
547 response to injury because all microglia clusters were found to accumulate at the injury
548 site, and cluster 11_Microglia had the highest correlation. The activation of microglia
549 was consistent with our immunohistochemical analysis findings but differed from the
550 specific activation patterns observed in the APP model of neurodegeneration[57]. In the
551 APP model, certain cells display elevated expression of the disease-associated
552 microglia signature concentrated in areas of plaque deposition, as determined by
553 stRNA-seq. Contrary to microglia, astrocytes showed a heterogeneous response, with
554 clusters 12_Astrocytes and 23_Astrocytes responding to injury and accumulating

around the injury site. In contrast, the remaining astrocytic clusters were underrepresented in the injury area with respect to the rest of the cortex. Interestingly, the injury-enriched astrocytic clusters 12_Astrocytes and 23_Astrocytes displayed unique features corresponding to their location and gene signatures. Cluster 12_Astrocytes for example, expressed high levels of *Gfap*, whereas cluster 23_Astrocytes might represent the recently described atypical astrocytes, which, after focal brain injury, rapidly downregulate GFAP and other astrocytic proteins[30]. Generally, OPCs also responded to the injury, however, cluster 15_OPCs was the only cluster showing enrichment at the injury core. Finally, we detected the responses of peripheral infiltrating macrophages and monocytes and found that clusters 13_Macrophages/Monocytes and 18_Monocytes contributed to the injury milieu. With the integration of the two datasets, we were able to identify the cells populating the injury core, thus offering a possibility for further thorough investigations.

The addition of the dataset generated at 5 dpi allowed us to analyze the temporal changes in response to injury. Microglia displayed elevated reactivity at 3 dpi, whereas at 5 dpi, cells shifted toward the homeostatic clusters. OPCs were characterized by a fast transient response at 3 dpi as very few cells resided in the reactive cluster at 5 dpi. In contrast, astrocyte reactivity peaked at 5 dpi, as most cells at this time point were confined to the reactive clusters, whereas at 3 dpi, many astrocytes still resided in the homeostatic clusters. Together, our data suggest that the activation of glial cells is continuous and does not involve the appearance or disappearance of distinct clusters at any specific time point. Therefore, our resource provides an excellent opportunity to investigate the processes driving cellular reactivity in response to injury in detail.

To provide a proof of principle, we comprehensively examined the genes characterizing each subcluster. In this way, we identified subclusters of astrocytes, microglia and OPCs with shared enriched signatures, including proliferation and activation of innate immune processes. Indeed, proliferation is a hallmark of injury-induced reactivity, including microglia[59], astrocytes[34,60], and OPCs[8,61], thus further validating our approach. The shared inflammatory signature identified in this study is largely present in other brain pathologies, such as in LPS-induced reactive astrocytes[36]. However, although a high proportion of shared inflammatory genes were expressed in the reactive astrocyte cluster 8, not all shared inflammatory genes were detected. This finding implies a common expression of core innate immunity-associated genes in different cell types in response to a variety of stimuli (e.g., LPS or TBI). However, each pathological condition further triggers distinct inflammatory-associated processes, which are uniquely coordinated in each pathology. The inflammatory signature present in the reactive clusters MG4, AG5, and OPCs2 included several IFN-I pathway genes. Among these genes, Interferon regulatory factor 7 (*Irf7*), a transcription factor crucial for IFN-I activity[62], and *Cxcl10*, a well-characterized ligand of the Cxcr3 pathway[47], were detected. Previous studies have demonstrated that Irf7 induces type I IFNs through the activation of TLR2, thus resulting in the transcription of several mediators, including *Cxcl10*[63,64]. In addition, the Tlr2/Irf7 signaling axis has been associated with microglia-mediated inflammation after subarachnoid hemorrhage in mice[65]. Furthermore, we have recently demonstrated that Cxcr3 and Tlr1/2 regulate OPC accumulation at injury site in the zebrafish brain in a redundant and synergistic manner[49]. Our data support the novel concept that the same innate immune pathways are responsible for initiating the response in injury-induced reactive glial clusters.

604 Because both pathways were regulated in several reactive populations, we
605 systemically inhibited the above-mentioned pathways after brain injury by treating the
606 animals simultaneously with a specific antagonist for Cxcr3[50] (NBI-74330) and a Tlr1/2
607 pathway inhibitor (CU CPT 22)[51]. We then performed scRNA-seq analysis at 3 and 5
608 dpi and integrated the datasets with our control analysis. This allowed us to investigate
609 cell type-specific changes emerging after inhibitor treatment. Interestingly, we
610 observed that multiple innate immunity genes, including *Irf7*, were downregulated after
611 inhibition of the Cxcr3 and Tlr1/2 pathways, and clusters AG7, MG3, and OPCs2 were
612 affected the most. These results are in line with our observation that up-regulation of
613 these genes is associated with the emergence of these clusters after injury. However,
614 whether the downregulation of the shared inflammation signature is a direct
615 consequence of the Tlr1/2 and Cxcr3 inhibition in cells themselves, or a consequence
616 of altered cell-cell communication after systemic Tlr1/2 and Cxcr3 inhibition, remains
617 unclear. Additionally, by performing differential gene expression analysis within each
618 subcluster between SW CTRL and SW INH conditions at each time point, we
619 addressed changes induced in each cluster separately. Notably, in response to the
620 inhibitor treatment, innate immune processes were generally downregulated in
621 astrocytes, microglia, and OPCs at 3 dpi, whereas at 5 dpi, the regulation became
622 specific to each cell population. This finding suggests that a shared initial regulation
623 diverges and consequently drives specific reactions in each cell type. In conclusion,
624 we demonstrated that inhibition of the Cxcr3 and Tlr1/2 pathways modulates innate
625 immunity in glial cells on a temporal basis.
626 Next, we examined how the systemic inhibition of the two pathways affected
627 the reactivity of glial cells. Thus, we addressed the numbers of oligodendrocytes
628 (OLIG2$^+$ cells) together with their proliferation. Surprisingly, we did not observe any
629 difference between SW CTRL and SW INH conditions at 3 dpi. This observation
630 contrasts with the findings from our study in zebrafish, in which inhibition of both
631 pathways was found to alleviate reactive gliosis by decreasing the accumulation of
632 oligodendrocytes and their proliferation[49]. This lack of concordance might be due to
633 differences in the injury environment, and additional pathways involved in the
634 accumulation and proliferation of OPCs in the mouse cerebral cortex and may reflect
635 a possible difference between regeneration competent and regeneration incompetent
636 species.
637 In contrast, in examining microglial reactivity via morphological analysis[54], we
638 observed that inhibitor-treated microglia were in a less reactive/activated state than
639 stab wound-injured controls. Specifically, microglia originating from SW INH animals
640 displayed significantly smaller cell somata, a less round shape, and increased branch
641 length, and appeared to be more ramified than microglia of SW CTRL animals. This
642 observation, in combination with the cell distribution in the scRNA-seq analysis,
643 suggests that blocking the Tlr1/2 and Cxcr3 pathways accelerates the microglial
644 transition from a reactive to a homeostatic state.
645 Similarly, astrocytes showed altered reactivity when the Cxcr3 and Tlr1/2
646 signaling pathways were inhibited: inhibitor-treated astrocytes displayed a decrease
647 in expression of reactivity markers. Additionally, we observed a decrease in the
648 number of proliferating astrocytes in the injury vicinity at 3 dpi. However, at 5 dpi, we
649 did not observe differences in the overall astrocyte reactivity state between SW CTRL
650 and SW INH, as indicated by our transcriptomic analysis and the follow-up
651 immunohistochemical assessments. These findings suggested a coordinated
652 response of astrocytes, and presumably glial cells in general, whereby different
653 pathways regulate distinct aspects of glial reactivity. Individual signaling pathways

654 might potentially even be involved in highly divergent functions in different glial cells.
655 In such a scenario, the Tlr1/2 and Cxcr3 pathways may largely regulate proliferation
656 in astrocytes, and cellular morphological aspects in microglia, in line with different
657 brain pathologies inducing various glial responses (for example astrocyte
658 proliferation)[60,66,67]. These findings further emphasize the versatility of our datasets
659 and analysis.
660 In conclusion, the present study provides a comprehensive transcriptomic
661 dataset for analyzing early events after TBI with respect to changes in time, space,
662 and cell type. Additionally, this dataset provides an excellent platform to examine the
663 interplay of a variety of cells in response to injury. A better understanding of injury
664 pathophysiology may provide more opportunities for developing new therapeutic
665 strategies.

666 Acknowledgments

667 We are particularly grateful to the entire Neurogenesis and Regeneration group
668 members for their experimental inputs and discussions and Dr. Alessandro Zambusi
669 for critical reading of the manuscript. We acknowledge the support of the following
670 core facilities: the Bioimaging Core Facility and Bioinformatic Core Facility at the
671 BioMedical Center of LMU Munich, the Laboratory for Functional Genome Analysis
672 (LAFUGA), and the Sequencing Facility at the Helmholtz Zentrum München. This work
673 was supported by the German research foundation (DFG) by the SFB 870; TRR274;
674 SPP 1738 “Emerging roles of non-coding RNAs in nervous system development,
675 plasticity & disease”, SPP1757 “Glial heterogeneity”; SPP2191 “Molecular
676 mechanisms of functional phase separation” (ID 402723784) and the Excellence
677 Strategy within the framework of the Munich Cluster for Systems Neurology (EXC
678 2145/1010 SyNergy – ID 390857198), Fritz Thyssen Stiftung and Ampro Helmholtz
679 Alliance.

680 Author Contributions

681 C.K., V.S. and J.N. conceived the project and experiments. C.K., V.S., J.F.S.,
682 T.S.E. and R.B. performed experiments and analyzed data. C.K., H.A. and S.F.
683 performed the bioinformatic analyses C.K., V.S. and J.N. wrote the manuscript with
684 input from all authors. J.N., M.G., M.D. and F.J.T. supervised research and acquired
685 funding.

686 Declaration of interests

687 The authors declare no conflict of interest.
688

Figure Legends

Figure 1. Spatially resolved transcriptomic changes induced by stab wound injury.

(**a**) Experimental scheme to conduct spatial transcriptomics in intact and stab wound-injured mouse cerebral cortices (3 dpi). Brains were manually resected, and selected areas highlighted in blue or red dashed boxes were positioned on 10x Visium capture areas. (**b**) Brain sections of both conditions contain cortical, hippocampal, and white matter regions. The dashed red lines indicate the injury cores. (**c**) Clustering of gene expression data on spatial coordinates based on highly variable genes and subsequent dimensionality reduction. (**d**) Dot plot illustrating the expression of the 50 most enriched genes in the injury-induced cluster VI. (**e**) Dot plots depicting GO terms of over-represented cluster VI significantly enriched genes (pval < 0.05, $\log_2$ fold change > 1). (**f**) Gene expression of cluster VI-enriched genes *Serpina3n*, *Lcn2*, and *Cd68* in spatial context. (**g,h**) Images depicting expression of *Serpina3n*, *Lcn2*, and *Cd68* at the RNA (**g**) and protein level (**h**) in stab wound-injured cerebral cortices (3 dpi). All images are full z-projections of confocal z-stacks. Scale bars: **g,h**: 150 µm. Abbreviations: CTX = cerebral cortex, WM = white matter, HPF = hippocampal formation, LV = lateral ventricle, CP = choroid plexus, V3 = third ventricle, TH = thalamus, fi = fimbria, dpi = days post injury, BP = biological processes, MF = molecular functions, CC = cellular components, GO = gene ontology.

Figure 2. Stab wound injury elicits distinct gene expression patterning along a spatial gradient.

(**a**) Paradigm for spatial transcriptomic gradient analysis on stab wound-injured mouse cerebral cortices (3 dpi) by using the SPATA2 pipeline. Spatial gradient analysis was conducted only in cortical areas; from the injury core (dark red spots) toward the periphery (light pink) within 13 concentric circle bins. All other areas (gray spots) were neglected. (**b**) Ridge plot depicting the expression of the 30 most descending genes along the gradient, depicted as mean expression of injury 1 and 2. (**c**) Ridge plot displaying the top 30 most descending gene sets along the gradient, depicted as mean expression from injury 1 and 2. Abbreviations: BP = biological processes, MF = molecular functions, CC = cellular components, GO = gene ontology, REACT = reactome.

Figure 3. Combination of spatial and single cell transcriptomics identifies cellular populations contributing to distinct transcriptional responses at the injury site.

(**a**) Experimental scheme to conduct single-cell RNA-sequencing of intact and stab wound-injured cerebral cortices (3 dpi) with the 10x Genomics platform. Red masked areas on brain schemes indicate biopsy areas used for the analysis. (**b**) UMAP plot illustrating 6322 single cells distributed among 30 distinct clusters. Clusters are color-coded and annotated according to their transcriptional identities. (**c**) UMAP plot depicting the distribution of cells isolated from intact (green) and injured (red) cerebral cortices. (**d**) Dot plot indicating strong correlation of post hoc cluster annotation with established cell type-specific gene sets (Ext. Table 6). (**e**, **f**) 3 dpi scRNA-seq cluster

localization along the spatial gradient (Fig. 2), based on probabilistic mapping with Tangram (**e**) and single cell deconvolution (**f**) in a spatial context. Abbreviations: UMAP = uniform manifold approximation and projection, dpi = days post injury, OPCs = oligodendrocyte progenitor cells, COPs = committed oligodendrocyte progenitors, MOL = mature oligodendrocytes, VECV = vascular endothelial cells (venous), VSMCs = vascular smooth muscle cells, VLMCs = vascular and leptomeningeal cells, DAM = disease-associated microglia, BAM = border-associated macrophages, NKT cells = natural killer T cells, DC/DCs = dendritic cells.

Figure 4. Stab wound injury induces defined transcriptional changes in glial subpopulations.

(**a**) Experimental scheme for single-cell RNA-sequencing of intact and stab wound-injured cerebral cortices (3 and 5 dpi) with the 10x Chromium platform. Red masked areas on brain schemes indicate biopsy areas used for the analysis. (**b**) UMAP embedding of integrated and batch-corrected single cell transcriptomes of 33862 cells distributed among 35 distinct clusters. Clusters were color-coded and annotated on the basis of their transcriptional identities. (**c-e**) UMAPs depicting subclustering of astrocytes (9 clusters) (**c**), microglia (8 clusters) (**d**), and oligodendrocytes (10 clusters) (**e**). Cells were further assigned to homeostatic (blue) or reactive (red) clusters according to cell origin (E.D. Fig. 6) and distinct marker expression. (**f-h**) UMAPs illustrating cell distributions at all time points (intact, 3 dpi, and 5 dpi) among subclusters of astrocytes (**f**), microglia (**g**), and oligodendrocytes (**h**). Data were downsampled to an equal number of cells between time points for each cell type (**f-h**). Abbreviations: UMAP = uniform manifold approximation and projection, dpi = days post injury, OPCs = oligodendrocyte progenitor cells, COPs = committed oligodendrocyte progenitors, MOL = mature oligodendrocytes, VECV = vascular endothelial cells (venous), VSMCs = vascular smooth muscle cells, VLMCs = vascular and leptomeningeal cells, BAM = border-associated macrophages, NKT cells = natural killer T cells, DC/DCs = dendritic cells.

Figure 5. Stab wound injury induces common transcriptional changes in reactive glial subpopulations.

(**a**) UpSet plot depicting unique (single points) or overlapping (connected points) DEGs (pval < 0.05, $\log_2$ fold change > 1.6) induced in reactive glial subclusters MG4, AG5, and OPCs2, compared with all other clusters of the respective cell type. A total of 192 commonly shared genes between these clusters are highlighted by the red bar. (**b**) GO term network analysis of the 192 commonly shared genes, associating shared DEGs with the biological processes of proliferation (green dashed line) and innate immunity (orange dashed line). (**c**) Chord diagram illustrating innate immunity GO terms from Fig. 5b and the corresponding genes. (**d**) Experimental paradigm for visualizing shared gene expression in astrocytes and microglia (*C57Bl6/J*) as well as OPCs (*NG2-CreER^{T2}xCAG-GFP*). The dashed gray box on the mouse brain scheme refers to an example imaging area. The red line displays injury core. (**e-g**) RNAscope example images of the shared innate immunity-associated gene *Cxcl10* (magenta) counterstained with GFAP (black) (**e**), IBA1 (black) (**f**), and GFP (NG2$^+$ glia) (black) (**g**) antibodies. Micrographs (**e'-g'**) are magnifications of the red boxed areas in the corresponding overview images. Orange arrowheads in micrograph (**g'-g"**) indicate colocalization of *Cxcl10* with GFP$^+$ cells. All images are single z-plane of confocal z-

788 stacks. Scale bars: (**e-g''**): 20 µm. Abbreviations: DEGs = differentially expressed
789 genes, GO = gene ontology, BP = biological processes.
790
791 **Figure 6. The Cxcr3 and Tlr1/2 pathways orchestrate the innate immune**
792 **response shared among reactive glial cells.**
793
794 (**a**) Experimental scheme for single-cell RNA-sequencing of intact, stab wound-injured
795 control (3/5 dpi_CTRL) and stab wound-injured inhibitor-treated (3/5 dpi_INH) cerebral
796 cortices with the 10x Chromium platform. Red masked areas on brain schemes
797 indicate biopsy areas used for the analysis. (**b**) UMAP embedding of integrated and
798 batch-corrected single cell transcriptomes of 53813 cells. Cells were distributed
799 among 36 distinct clusters, color-coded, and annotated according to their
800 transcriptional identities. (**c-e**) UMAPs illustrating subclustering of astrocytes (9
801 clusters) (**c**), microglia (8 clusters) (**d**) and oligodendrocytes (13 clusters) (**e**). Cells
802 were further assigned to homeostatic (blue), or reactive (red) clusters according to cell
803 origin (E.D. Fig. 10). (**f**) Dot plots depict decreased expression of various shared
804 inflammatory genes (Fig. 4c) in the reactive glial clusters AG7, MG3, and OPCs2 after
805 inhibitor treatment. (**g-h**) GO term networks illustrating common and unique
806 downregulated biological processes of glial subclusters in response to Cxcr3 and
807 Tlr1/2 pathway inhibition at 3 dpi (**g**) and 5 dpi (**h**) (Ext. Table 12). Common
808 downregulation of innate immunity-associated GO terms (highlighted by red dashed
809 lines) are observed at 3 but not at 5 dpi. Abbreviations: UMAP = uniform manifold
810 approximation and projection, dpi = days post injury, OPCs = oligodendrocyte
811 progenitor cells, COPs = committed oligodendrocyte progenitors, MOL = mature
812 oligodendrocytes, VECV = vascular endothelial cells (venous), VSMCs = vascular
813 smooth muscle cells, VLMCs = vascular and leptomeningeal cells, BAM = border-
814 associated macrophages, NKT cells = natural killer T cells, DC/DCs = dendritic cells.
815
816 **Figure 7. Cxcr3 and Tlr1/2 pathway inhibition after stab wound injury**
817 **decreases microglial reactivity.**
818
819 (**a,b**) UMAPs illustrating subclusters of microglia (**a**) and cell distributions (**b**) among
820 those subclusters at all time points (intact, 3 dpi, and 5 dpi) and conditions (CTRL and
821 INH). Data are downsampled to an equal number of cells between time points and
822 conditions (**b**). (**c**) Experimental paradigm for assessing microglial morphology
823 characteristics according to Heindl et al.[54]. The gray box on mouse brain scheme
824 highlights the analyzed area. The red line indicates the injury core. (**d,e**)
825 Representative images of Iba1$^+$ microglia (yellow) in CTRL (**d**) and INH-treated (**e**)
826 mice. Dashed white boxes indicate selected microglia used for 3D reconstruction. All
827 images are full z-projections of confocal z-stacks. (**f**) Scatter plot depicting
828 morphological features of analyzed microglial cells. Each data point represents one
829 microglial cell; a total of 450 cells per condition were analyzed. Data are displayed as
830 median ± interquartile range. p-values were determined with Mann-Whitney U-test.
831 Scale bars: **d,e**: 20 µm. Abbreviations: UMAP = uniform manifold approximation and
832 projection, dpi = days post injury, CTRL = stab wound-injured control animals, INH =
833 stab wound-injured inhibitor-treated animals.
834
835 **Figure 8. Proliferation of reactive astrocytes is decreased after Cxcr3 and**
836 **Tlr1/2 pathway inhibition.**
837

838 (**a,b**) UMAPs illustrating subclusters of astrocytes (**a**) and cell distributions (**b**) among
839 those subclusters at all time points (intact, 3 dpi, and 5 dpi) and conditions (CTRL and
840 INH). Data are downsampled to an equal number of cells between time points and
841 conditions (**b**). (**c**) Experimental paradigm for assessing astrocyte proliferation. The
842 dashed gray box on mouse brain scheme indicates the analyzed area. The red line
843 indicates the injury core. (**d,e**) Representative overview images of proliferating $GFAP^+$
844 (green) and EdU^+ (magenta) astrocytes in CTRL (**d**) and INH-treated (**e**) animals.
845 White dashed lines highlight injury cores. Micrographs (**d'-e''**) are magnifications of
846 white boxed areas in (**d**) and (**e**), respectively. White arrowheads in micrographs
847 indicate colocalization of EdU (**d',e'**) with $GFAP^+$ astrocytes (**d'',e''**). All images are
848 full z-projections of confocal z-stacks. (**f,g**) Dot plots depicting percentage of
849 proliferating ($GFAP^+$ and EdU^+) astrocytes (**f**) and total density of proliferating (EdU^+)
850 cells (**g**) in CTRL and INH-treated animals. Data are shown as mean ± standard error
851 of the mean. Each data point represents one animal. p-values were determined with
852 unpaired t-test. Scale bars: **d,e**: 50 µm (overview), **d'-e''**: 20 µm (micrographs).
853 Abbreviations: UMAP = uniform manifold approximation and projection, dpi = days
854 post injury, EdU = 5-ethinyl-2′-deoxyuridine, i.p. = intraperitoneal injection, CTRL =
855 stab wound-injured control animals, INH = stab wound-injured inhibitor-treated
856 animals.

E.D. Figure 1. Spatial transcriptome of intact and gray matter stab wound-injured mice.

(**a-b**) Spatial transcriptomics in intact and stab wound-injured mice (3 dpi). Brains were manually resected and positioned on 10x Visium capture areas. In each capture area, two brain sections of either intact (**a**) or stab wound-injured cortices (**b**) were collected. (**c**) Clustering of gene expression data on spatial coordinates based on highly variable genes and subsequent dimensionality reduction. (**c**) Dot plot depicting the 5 most enriched genes in each of the 16 identified clusters. (**e**) Expression of neuronal layer scores 2/3, 4, 5 and 6 in intact and injured brain sections on spatial coordinates. The white dashed lines highlight cluster VI borders. Neuronal layer gene set scores are listed in Ext. Table 2. (**e**) Heatmap depicting the expression of the 25 most ascending genes along the spatial trajectory (see Fig. 2) depicted as mean expression of injury 1 and 2. (**f**) Heatmap displaying the 30 most enriched ascending gene sets along the spatial trajectory (see Fig. 2) depicted as mean expression from injury 1 and 2. Abbreviations: BP = biological processes, MF = molecular functions, CC = cellular components, GO = gene ontology, REACT = reactome, dpi = days post injury.

E.D. Figure 2. scRNA-seq clustering of intact and brain-injured mice (3 dpi) and cell-type identification.

(**a**) UMAP plots depicting clustering of cells originating from intact (2676 cells) and injured (3646 cells) conditions among 30 defined clusters. Clusters are color-coded and annotated according to their transcriptional identities. Note that clusters 13_Macrophages/Monocytes, 17_DCs, and 23_Astrocytes are absent in the intact condition. (**b**) Dot plot depicting the expression of the 3 most enriched genes in each of the 30 identified clusters (see Ext. Table 5). (**c-e**) UMAPs highlighting example marker genes to identify microglia/macrophages (**c**), astrocytes (**d**) OPCs (**e**) and cycling cells (**f**). G2/M gene set score is listed in Ext. Table 6. Abbreviations: UMAP = uniform manifold approximation and projection, dpi = days post injury, OPCs = oligodendrocyte progenitor cells, COPs = committed oligodendrocyte progenitors, MOL = mature oligodendrocytes, VECV = vascular endothelial cells (venous), VSMCs = vascular smooth muscle cells, VLMCs = vascular and leptomeningeal cells, BAM = border-associated macrophages, NKT cells = natural killer T cells, DCs = dendritic cells.

E.D. Figure 3. Probabilistic mapping of in scRNA-seq identified cellular clusters on Visium dataset.

(**a**) Probabilistic mapping of in Fig. 2b identified scRNA-seq clusters on the spatial transcriptome dataset (3 dpi). Stab wound injury elicits different mode of reaction in the injury vicinity. Plots are grouped into injury enriched clusters (upper panel) and remaining clusters (lower panel). Abbreviations: OPCs = oligodendrocyte progenitor cells, NKT cells = natural killer T cells, DCs = dendritic cells, MOL = mature oligodendrocytes, VSMCs = vascular smooth muscle cells, COPs = committed oligodendrocyte progenitors, BAM = border-associated macrophages, VLMCs = vascular and leptomeningeal cells, VECV = vascular endothelial cells (venous).

E.D. Figure 4. Single-cell deconvolution-based mapping of in scRNA-seq identified cellular clusters on Visium dataset.

(**a,b**) Deconvolution based mapping of in E.D. Fig. 3 identified scRNA-seq clusters on the spatial transcriptome dataset (3 dpi). Plots are grouped into injury enriched clusters (upper panel) and remaining clusters (lower panel) (**b**). Abbreviations: OPCs = oligodendrocyte progenitor cells, NKT cells = natural killer T cells, DCs = dendritic cells, MOL = mature oligodendrocytes, VSMCs = vascular smooth muscle cells, COPs = committed oligodendrocyte progenitors, BAM = border-associated macrophages, VLMCs = vascular and leptomeningeal cells, VECV = vascular endothelial cells (venous).

E.D. Figure 5. Integration of scRNA-seq datasets of intact and brain-injured mice (3 and 5 dpi), cluster distribution and cell type identification.

(**a,b**) UMAP plots depicting clustering (**a**) and cell distribution of intact (16567 cells), 3 dpi (3637 cells), and 5 dpi (13658 cells) cells among 35 defined clusters (**b**). Clusters were color-coded and annotated according to their transcriptional identities. (**c**) Dot plot depicting expression of the 3 most enriched genes in each of the 35 identified clusters (see Ext. Table 8). Abbreviations: UMAP = uniform manifold approximation and projection, dpi = days post injury, VECV = vascular endothelial cells (venous), MOL = mature oligodendrocytes, DAM = disease-associated microglia, OPCs = oligodendrocyte progenitor cells, NKT cells = natural killer T cells, BAM = border-associated macrophages, VSMCs = vascular smooth muscle cells, COPs = committed oligodendrocyte progenitors, VLMCs = vascular and leptomeningeal cells, DC = dendritic cells.

E.D. Figure 6. Stab wound injury elicits unique gene expression in distinct glial subpopulations.

(**a**) UMAP depicting subclustered astrocytes of integrated and batch-corrected intact, 3 dpi, and 5 dpi datasets. (**b**) Dot plot depicting expression of the 5 most enriched genes in each of the 9 identified clusters. (**c**) UMAP displaying cell distribution of intact (green), 3 dpi (red) and 5 dpi (orange) cells among all 9 astrocytic clusters. Note that clusters AG5, AG6, and AG8 are mainly composed of cells originating from injured cortices. (**d**) UMAP displaying localization of injury-enriched cluster 12_Astrocytes (turquoise, E.D. Fig. 4b) on subclustered astrocytes. (**e**) UMAPs highlighting expression of example marker genes *Gfap*, *Vim* and *Lcn2* to identify reactive astrocyte clusters. (**f**) UMAP depicting subclustered microglia of integrated and batch-corrected intact, 3 dpi, and 5 dpi datasets. (**g**) Dot plot depicting expression of the 5 most enriched genes in each of the 8 identified clusters. (**h**) UMAP displaying cell distribution of intact (green), 3 dpi (red), and 5 dpi (orange) cells among all 8 microglial clusters. Note that clusters MG4 and MG6 are mainly composed of cells originating from injured cortices. (**i**) UMAP displaying localization of injury-enriched cluster 11_Microglia (peach, E.D. Fig. 4b) on subclustered microglia. (**j**) UMAPs highlighting expression of example marker genes *Aif1*, *Tmem119* and *P2ry12* to identify reactive microglial clusters. (**k**) UMAP depicting subclustered oligodendrocytes of integrated and batch-corrected intact, 3 dpi, and 5 dpi datasets. (**l**) Dot plot depicting expression of the 5 most enriched genes in each of the 10 identified clusters. (**m**) UMAP displaying cell distribution of intact (green), 3 dpi (red), and 5 dpi (orange) cells among all 10

clusters. Note that cluster OPCs2 is mainly composed of cells originating from both injured conditions. (**n**) UMAP displaying localization of injury-enriched cluster 15_OPCs (pink, E.D. Fig. 4b) on subclustered oligodendrocytes. (**o**) Dot plot depicting expression of the 30 most enriched genes in cluster OPCs2. Note comparable gene expression of clusters OPCs1 and OPCs2 prevent the identification of unique reactive OPC markers. Abbreviations: UMAP = uniform manifold approximation and projection, dpi = days post injury, OPCs = oligodendrocyte progenitor cells, COPs = committed oligodendrocyte progenitors, MFOL = myelin-forming oligodendrocytes, MOL = mature oligodendrocytes.

E.D. Figure 7. Reactive glial subpopulations share injury-induced transcriptomic signature.

(**a,b**) UpSet plots depicting unique and overlapping downregulated (**a**) and upregulated DEGs (**b**) (pval < 0.05, $\log_2$ fold change > 1.6 or $\log_2$ fold change < -1.6) between different glial subclusters of integrated and batch-corrected intact, 3 dpi, and 5 dpi datasets (Fig. 5c-e). Wherever applicable, DEGs are determined by comparing each glial subcluster to all other subclusters within the respective cell type (further details in Methods). The red bars in (**b**) highlight commonly shared genes between reactive astrocytic, microglial, and oligodendroglial subclusters. Abbreviations: DEGs = differentially expressed genes.

E.D. Figure 8. Reactive glial subpopulations display shared gene expression following injury.

(**a**) Experimental paradigm for assessing shared gene expression in astrocytes, microglia (*C57Bl6/J*), and OPCs (*NG2-CreER^{T2}xCAG-GFP*). The dashed gray box on mouse brain scheme indicates the example imaging area. The red line indicates the injury core. (**b-g**) RNAscope example images of shared innate immunity-associated genes *Oasl2* (**b-d**) and *Ifi27l2a* (**e-g**) (magenta) counterstained with GFAP (black) (**b,e**), IBA1 (black) (**c, f**), and GFP (NG2$^+$ glia) (black) (**d,g**) antibodies. Micrographs (**b'-g''**) are magnifications of the red boxed areas in corresponding overview images. The orange arrowheads in micrograph depict double positive cells. All images are single z-plane of confocal z-stacks. Scale bars: (**e-g''**): 20 µm.

E.D. Figure 9. Reactive glial subpopulations display shared marker expression after injury.

(**a**) Experimental paradigm for assessing shared marker expression in astrocytes, OPCs, and microglia. The dashed gray box on mouse brain scheme indicates the analyzed area. The red line illustrates the injury core. (**b-d**) Representative overview images depicting Galectin1 expression in GFAP$^+$ astrocytes (**b**), NG2$^+$ glia (GFP) (**c**), and IBA1$^+$ microglia (**d**). Micrographs (**b'-d''**) are magnifications of white boxed areas in corresponding overview images. The white dashed lines indicate injury cores. The white arrowheads in the micrographs depict colocalization of Galactin1 (**b'-d'**) with GFAP$^+$ (**b''**), GFP$^+$ (**c''**), and IBA1$^+$ (**d''**) cells. All images are full z-projections of confocal z-stacks. (**e**) Heatmap depicting the shared inflammatory signature gene score between conditions and clusters. (**f**) UMAPs depicting localization of the shared inflammatory signature gene scores among all defined cell clusters. (**g**) Dot plot depicting gene expression of components associated with the Tlr1/2 and Cxcr3

signaling pathways. Genes are adapted and complemented based on Sanchez-Gonzalez et al.[49].Scale bars: **b-d**: 50 µm (overview), **b'-d''**: 20 µm (micrographs).

E.D. Figure 10. Common inflammatory gene signature in murine LPS- and human iPSC-induced reactive astrocytes

(**a,b**) UMAPs illustrating selective marker gene expression of shared inflammatory signature (see Fig. 5c) in subclustered astrocytes based on Hasel et al. 2021. Plots depicting presence (**a**) and absence (**b**) of several shared inflammatory genes in reactive astrocyte cluster 8. (**c,d**) UMAPs depicting localization of IRAS1 and IRAS2 gene scores (**c**) among all defined cell clusters (**d**). IRAS1 and IRAS2 gene scores are based on Leng et al.[48]. Abbreviations: UMAP = uniform manifold approximation and projection, CNT = control, LPS = lipopolysaccharide, Exp = expression, SW = stab wound, IRAS = inflammatory reactive astrocytes signature.

E.D. Figure 11. scRNA-seq data integration of intact and stab wound-injured cortices.

(**a**) UMAP plots depicting cell distribution of integrated and batch-corrected intact (green, 16649 cells), 3 dpi CTRL (red, 3637 cells), 3 dpi INH (pink, 4613 cells), 5 dpi CTRL (orange, 13766 cells), and 5 dpi INH (peach, 15146 cells) datasets. (**b**) Heatmap displaying high cluster similarity of integrated intact and injured CTRL conditions (control, y-axis), and integrated intact, injured CTRL, and injured INH conditions (control and inhibitor-treatment, x-axis). (**c**) UMAP displaying cell distribution of intact (green), 3 dpi CTRL (red), 3 dpi INH (pink), 5 dpi CTRL (orange), and 5 dpi INH (peach) cells among the 9 identified astrocytic clusters as depicted in Fig. 5c. Clusters AG5, AG6, AG7 and AG8 are mainly formed by cells originating from injured CTRL and INH animals. (**d**) UMAP displaying cell distribution of intact (green), 3 dpi CTRL (red), 3 dpi INH (pink), 5 dpi CTRL (orange), and 5 dpi INH (peach) cells among the 8 identified microglial clusters as depicted in Fig. 5d. Clusters MG3 and MG6 are mainly formed by cells originating from injured CTRL and INH animals. (**e**) UMAP displaying cell distribution of intact (green), 3 dpi CTRL (red), 3 dpi INH (pink), 5 dpi CTRL (orange), and 5 dpi INH (peach) cells among the 13 identified oligodendroglial clusters as depicted in Fig. 5e. Clusters OPCs1 and OPCs2 are mainly formed by cells originating from injured CTRL and INH animals. Abbreviations: UMAP = uniform manifold approximation and projection, dpi = days post injury, CTRL = stab wound-injured control mice, INH = stab wound-injured inhibitor-treated mice, VECV = vascular endothelial cells (venous), MOL = mature oligodendrocytes, OPCs = oligodendrocyte progenitor cells, NKT cells = natural killer T cells, BAM = border-associated macrophages, VSMCs = vascular smooth muscle cells, COPs = committed oligodendrocyte progenitors, VLMCs = vascular and leptomeningeal cells, DC = dendritic cells.

E.D. Figure 12. The Cxcr3 and Tlr1/2 pathway inhibition after brain injury induces subcluster specific changes.

(**a-d**) UpSet plots depicting unique and overlapping downregulated (**a,c**) and upregulated (**b,d**) DEGs (pval < 0.05, log_2 fold change > 0.7 or log_2 fold change < -0.7) between different glial subclusters in response to the Cxcr3 and Tlr1/2 inhibition at 3 dpi (**a,b**) and 5 dpi (**c,d**). (**e,f**) GO term networks illustrate distinct, subcluster-

specific biological processes enriched in the set of genes upregulated in response to the Cxcr3 and Tlr1/2 pathway inhibition at 3 dpi (**e**) and 5 dpi (**f**) (see Ext. Table 12). Abbreviations: DEGs = differentially expressed genes, dpi = days post injury.

E.D. Figure 13. OPC reactivity after injury is not altered by the Cxcr3 and Tlr1/2 pathway inhibition.

(**a,b**) UMAPs illustrating subclusters of oligodendrocytes (**a**) and cell distributions among these subclusters (**b**) at all time points (intact, 3 dpi, and 5 dpi) and conditions (CTRL and INH). Data are downsampled to an equal number of cells between time points and conditions (**b**). (**c**) Experimental paradigm for assessing number of oligodendrocytes and OPC proliferation in injury vicinity. The dashed gray box on mouse brain scheme indicates the analyzed area. The red line highlights the injury core. (**d,e**) Representative overview images of proliferating OLIG2$^+$ (gray) and EdU$^+$ (magenta) oligodendrocytes in CTRL (**d**), and INH-treated (**e**) animals. The white dashed lines highlight injury cores. Micrographs (**d'-e''**) are magnifications of the white boxed areas in (**d**) and (**e**), respectively. The white arrowheads in micrographs depict colocalization of EdU (**d',e'**) with OLIG2$^+$ (**d'',e''**) cells. All images are full z-projections of confocal z-stacks. (**f,g**) Dot plots depicting number of oligodendrocytes (OLIG2$^+$ cells) (**f**) and proliferating OPCs (OLIG2$^+$ and EdU$^+$) (**g**) in CTRL and INH-treated animals. Data are shown as mean ± standard error of the mean. Each data point represents one animal. p-values were determined with unpaired t-test. Scale bars: **d,e**: 50 µm (overview), **d',e''**: 20 µm (micrographs). Abbreviations: UMAP = uniform manifold approximation and projection, dpi = days post injury, EdU = 5-Ethinyl-2′-deoxyuridine, i.p. = intraperitoneal injection, CTRL = stab wound-injured control animals, INH = stab wound-injured inhibitor-treated animals, OPCs = oligodendrocyte progenitor cells, COPs = committed oligodendrocyte progenitors, MFOL = myelin-forming oligodendrocytes, MOL = mature oligodendrocytes.

E.D. Figure 14. Reaction of microglia and astrocytes to stab wound injury in absence of the Cxcr3 and Tlr1/2 signaling.

(**a**) Scatter plots depicting morphological microglial features. Each data point represents one microglial cell and in total 450 cells per condition were analyzed. Data are displayed as median ± interquartile range. p-values were determined with Mann-Whitney U-test. (**b**) UMAPs highlighting expression of *Gfap* and *Lcn2* among all astrocytic subclusters. (**c**) Dot plots depicting expression levels of *Gfap* and *Lcn2* in astrocytes. (**d**) Dot plot depicting astrocyte reactivity scores between all time points (intact, 3 dpi, and 5 dpi) and conditions (CTRL and INH). Genes defining astrocyte reactivity scores in E.D. Fig. 12d were extracted from cluster_4 and cluster_8 astrocytes of Hasel et al. 2021[36] (Top 20 genes) and are plotted only on the reactive clusters (AG5, AG6, AG7 and AG9) (**e**) Experimental paradigm for assessing astrocyte reactivity in the injury vicinity. The dashed gray box on mouse brain scheme indicates the analyzed area. The red line highlights the injury core. (**f,g**) Representative overview images of GFAP$^+$ astrocytes (green) and NGAL$^+$ cells (magenta) in CTRL (**f**) and INH-treated (**g**) animals. White dashed lines highlight injury cores. Micrographs (**f'-g''**) are magnifications of white boxed areas in (**f**) and (**g**), respectively. The white arrowheads in micrographs depict colocalization of NGAL (**f',g'**) with GFAP$^+$ astrocytes (**f'',g''**). All images are full z-projections of confocal z-stacks. (**h,i**) Dot plots depicting percentage of area covered with GFAP$^+$ signal (**h**) and density of GFAP$^+$

1105 NGAL^{+} double positive astrocytes (**i**) in injury vicinity of CTRL and INH-treated mice.
1106 Data are shown as mean ± standard error of the mean. Each data point represents
1107 one animal. p-values were determined with unpaired t-test. (**j**) UMAPs highlighting
1108 localization of proliferating astrocytes (pink) to subclusters AG6 and AG7. (**k**)
1109 Histogram illustrating percentage of proliferating astrocytes between all time points
1110 (intact, 3 dpi, and 5 dpi) and condition (CTRL and INH). Proliferating astrocytes were
1111 identified in scRNA-seq datasets by S+G2/M score expression (see Ext. Table 6).
1112 Scale bars: **f,g**: 50 µm (overview), **f'-g''**: 20 µm (micrographs). Abbreviations: UMAP
1113 = uniform manifold approximation and projection, dpi = days post injury, INT = intact
1114 mice, CTRL = stab wound-injured control animals, INH = stab wound-injured inhibitor-
1115 treated animals.
1116

1117 # Materials and Methods

1118 ## Animals

1119 All operations were performed on 8-12 weeks old *C57Bl6/J* male mice, housed,
1120 and handled under the German and European guidelines for the use of animals for
1121 research purposes. Experiments were approved by the institutional animal care
1122 committee and the government of Upper Bavaria (ROB-55.2-2532.Vet_02-20-158).
1123 Anesthetized animals received a stab wound lesion in the cerebral cortex as previously
1124 described[31], by inserting a thin knife into the cortical parenchyma using the following
1125 coordinates from Bregma: RC: -1.2; ML: 1-1.2 and from Dura: DV: -0.6 mm. To
1126 produce stab lesions, the knife was moved over 1mm back and forth along the
1127 anteroposterior axis from -1.2 to -2.2 mm. Animals were sacrificed 3 and 5 days after
1128 the injury (dpi).
1129 For the treatment experiments, animals received inhibitors by gavage feeding.
1130 NBI 74330 (100 mg/kg, R&D Systems #4528) and CU CPT 22 (3 mg/kg, R&D Systems
1131 #4884) were dissolved in DMSO and diluted in corn oil. The vehicle solution consisted
1132 of DMSO diluted in corn oil and was administered to all control animals. To analyze
1133 the proliferative capacity of glial cells we injected 5-Ethinyl-2′-deoxyuridine (EdU, 0.05
1134 mg/g, Thermofisher #E10187) intraperitoneally and animals were sacrificed 1hr after
1135 injection.
1136 For the induction of Cre-mediated recombination in *NG2-CreER^{T2}xCAG-GFP*
1137 mice, tamoxifen (40 mg/ml, Sigma #T5648) was administered orally. Animals received
1138 tamoxifen every second day (400 mg/kg) for a total of 3 times. Mice were injured two
1139 weeks after the last tamoxifen administration and sacrificed at 3dpi.
1140

1141 ## Tissue preparation

1142 Mice were deeply anesthetized and transcardially perfused with phosphate-
1143 buffered saline (PBS) followed by 4% paraformaldehyde (PFA) (wt/vol) dissolved in
1144 PBS. Brains were postfixed in 4% PFA overnight at 4°C, washed with PBS and
1145 cryoprotected in 30% sucrose at 4ºC. Mouse brains used to assess microglia
1146 morphology were embedded in 3% agarose and cut coronally at 100 µm thickness
1147 using a vibratome (HM 650V, Microm). Otherwise, brains were embedded in frozen
1148 section medium Neg-50 (Epredia #6502), frozen and subsequently sectioned using a
1149 cryostat (Thermo Scientific CryoStar NX50). Coronal sections were collected either at
1150 a thickness of 20µm on slides for RNAscope or 40µm for free-floating
1151 immunohistochemistry.
1152

1153 ## Immunohistochemistry

1154 For immunohistochemistry, sections were blocked and permeabilized with 10%
1155 normal goat serum (NGS, vol/vol, Biozol, S-1000)/donkey serum (NDS, vol/vol, Sigma
1156 Aldrich 566460) and 0.5% Triton X-100 (vol/vol), dissolved in 1xPBS while being
1157 incubated overnight at 4°C with the corresponding primary antibodies. Following
1158 primary antibodies were used: anti-CD68 (rat 1:600, BioRad, MCA1957T), anti-
1159 Galactin1 (rabbit 1:200, Abcam, ab138513), anti-GFP (chick 1:400, Aves Labs, GFP-
1160 1020), anti-GFAP (goat 1:300, Abcam, ab53554), anti-GFAP (mouse 1:500, Sigma,

G3893), anti-Iba1 (rabbit 1:500, Wako, 019-19741), anti-NGAL (rabbit 1:500, Thermofisher, PA5-79590), anti-SerpinA3n (goat 1:500, R&D Systems AF4709-SP). Sections were washed with PBS and incubated with secondary antibodies dissolved in 1xPBS solution containing 0.5% Triton X for two hours at room temperature. Following secondary antibodies were used: donkey anti-chick IgY A488 (1:1000, Dianova 703-545-155), goat anti-mouse IgG1 A546 (1:1000, Thermofisher A-21123), goat anti-rabbit IgG A546 (1:1000, Thermofisher A-11010), goat anti-rabbit IgG A633 (1:1000, Thermofisher A-21070), goat anti-rat IgG A488 (1:1000, Thermofisher A-11006). For nuclear labelling, sections were incubated with DAPI (final concentration of 4 µg/mL, Sigma, D9542) for 10 min at room temperature. EdU incorporation was detected by Click-iT™ EdU Alexa Fluor™ 647 Imaging Kit (Thermo Fisher Scientific #C10340) according to the manufacturer's instructions. Staining procedure for microglia morphology analysis was performed as described in Heindl et al.[54]. Stained sections were mounted on glass slides with Aqua-Poly/Mount (Polysciences #18606).

In situ hybridization

RNA in situ hybridization was performed using RNAscope® Multiplex Fluorescent Reagent Kit (ACD) according to the manufacturer's instructions. Briefly, brain sections were fixed in 4% paraformaldehyde at 4 °C for 15 min, ethanol-dehydrated, treated with H_2O_2 and protease-permeabilized for 20min at 40 °C. Brain sections were then incubated for 2 h at 40 °C using the following probes: *Ifi27l2a*: 88617, *Serpina3n*: 430191-C2, *Lcn2:* 313971-C3, *Cd68:* 316611-C2, *Oasl2:* 534501, *Cxcl10*: 408921-C3. Signal was amplified according to the manufacturer's instructions (Cat.Nr: 320293). Subsequently, sections were processed with immunohistochemistry analysis as described above. The primary antibodies used in combination with RNAscope® were as follows: chick antibody to GFP (1:500, Aves Lab, GFP-1020), goat antibody to GFAP (1:300, Abcam, ab53554), rabbit antibody to Iba1 (1:500, Wako, 019-19741)

Image acquisition, processing, and quantitative analysis

Confocal microscopy was performed at the core facility bioimaging of the Biomedical Center (BMC) with an inverted Leica SP8 microscope using the LASX software (Leica). Overview images were acquired with a 10x/0.30 objective, higher magnification pictures with a 20x/0.75, 40x/1.30 or 63/1.40 objective, respectively. Images utilized for the microglia morphology analysis were acquired with an 40x/1.30 objective with an image matrix of 1024x1024 pixel, a pixel scaling of 0.2 µm x 0.2 µm and a depth of 8-bit. Image processing was performed using the NIH ImageJ software (version 2.1.0/1.53f). To acquire overview images, single images were stitched using the ImageJ plug-in tool pairwise stitching (Preibisch et al. 2009).
For all quantifications a minimum of two sections per animal were analyzed. In each section, an area of 300 µm (150µm on each side of the injury) was selected and either the pixel covered area or the number of positive cells in all individual z-planes of an optical z-stack was quantified. Additionally, to account for variations in section thickness, total cell numbers were normalized to the section depth. Statistical analysis was performed using GraphPad Prism (version 9.3.1).

1207 **Spatial transcriptomics analysis**

1208 Mouse brains from 3dpi or intact *C57Bl6/J* mice were embedded and snap
1209 frozen in an isopentane and liquid nitrogen bath as recommended by 10x Genomics
1210 (Protocol: CG000240). During cryosectioning (Thermo Scientific CryoStar NX50) the
1211 brains were resected to generate a smaller sample (Fig. 1a) and two 10µm thick
1212 coronal sections of the dorsal brain area were collected in one capture area. The tissue
1213 was stained using H&E staining and imaged with the Carl Zeiss Axio Imager.M2
1214 Microscope using 10x objective (Protocol: CG0001600). The libraries were prepared
1215 with Visium Spatial Gene Expression Reagent Kits (CG000239) with 18min
1216 permeabilization time and sequenced on an Illumina HiSeq1500 instrument and a
1217 paired-end flowcell (High output) according to manufacturer protocol, with sequencing
1218 depth of 55231 (Intact) and 75398 (3dpi) mean reads per spot. Sequencing was
1219 performed in the Laboratory for Functional Genome Analysis (LAFUGA).
1220 Data were mapped against the mouse reference genome mm10 (GENCODE
1221 vM23/Ensembl 98; builds versions 1.2.0 and 2020A from 10xGenomics) with Space
1222 Ranger 1.2.2. Both datasets were analyzed, and quality checked following the
1223 Scanpy[68] and Squidpy[69] pipeline, selecting spots with at least 1500 reads and a
1224 maximum 45% mitochondrial fraction. Normalization and log transformation was
1225 performed using the counts per million (CPM) strategy with a target count depth of
1226 10,000 using Scanpy's[68] normalize_total() and log1p functions. Following cell count
1227 normalization and scaling (function scale in Scanpy), experimental groups were
1228 integrated. Highly variable gene (HVGs) selection was performed via the function
1229 highly_variable_genes() using the Cell Ranger flavor with default parametrization,
1230 obtaining 2000 HVGs. Unsupervised clustering of cells was done using the Leiden
1231 algorithm[70] as implemented in Scanpy. This allowed classification of multiple clusters
1232 based on marker genes selected using test_overestim_var() between the normalized
1233 counts of each marker gene in a cluster against all others (function
1234 rank_genes_groups in Scanpy). The layer marker score was performed using the
1235 function score_genes (as implemented in Scanpy) based on established marker
1236 genes (Ext. Table 3) described by Zeisel, A. et al 2018[33]. Gene ontology enrichment
1237 analysis was performed using the function enrichGO() (R package: clusterProfiler[52])
1238 on the marker genes for cluster VI (indicated above) selecting the genes with
1239 pval<0.05 and $log_2fc>1$ and the top 10 functions of the three aspects (MF: Molecular
1240 Function; CC: Cellular Component; BP: Biological Process) were presented on a dot
1241 plot.
1242

1243 **Single-cell analysis**

1244 The lesioned grey matter of the somatosensory cortex of C57BL/6J mice at
1245 3dpi and 5dpi or the corresponding region of the noninjured cortex were isolated using
1246 a biopsy punch (∅ 0.25cm) and the cortical cells were dissociated at a single cell level
1247 using the Papain Dissociation System (Worthington, # LK003153) followed by the
1248 Dead Cell Removal kit (Miltenyi Biotec # 130-090-101), according to manufacturer's
1249 instructions. Incubation with dissociating enzyme was performed for 60 min.
1250 Single-cell suspensions were resuspended in 1xPBS with 0.04% BSA and
1251 processed using the Single-Cell 3' Reagent Kits v2 or v3.1 (Ext. Table 13) from
1252 10xGenomics according to the manufacturer instructions. In brief, this included
1253 generation of single cell gel beads in emulsion (GEMs), post-GEM-RT cleanup, cDNA

amplification and library construction. Illumina sequencing libraries were sequenced on a HiSeq 4000 or NovaSeq6000 system (with an average read depth of 30,000 raw reads per cell) according to the manufacturer's instructions for each version. Sequencing was performed in the genome analysis center of the Helmholtz Center Munich

Transcriptome alignment of single-cell data was done using Cell Ranger v3.0.2 and v6.0.0 against the mouse reference genome mm10 (GENCODE vM23/Ensembl 98; builds versions 1.2.0 and 2020A from 10xGenomics). Quality Control (QC) of mapped cells from all datasets integrated was done using recommendations by Luecken and Theis[71] selecting cells with at least 1000 genes, maximum of 50000 reads and 25% mitochondrial fraction. Doublets were removed using the Scrublet framework[72], clusters expressing multiple lineage genes were identified as mixed population and were removed from the further analysis. Normalization was performed using the scran[68] package (R package) followed by log-transformation using Scanpy's log1p functions[68]. Highly variable gene (HVGs) selection was performed via the function highly_variable_genes using the Cell Ranger flavor with default parametrization, obtaining 2000 HVGs. Following cell count normalization and scaling, (function scale in Scanpy) experimental groups were batch corrected with scVI[73,74]. Unsupervised clustering of cells was done using the Leiden algorithm[70] as implemented in Scanpy. This allowed classification of multiple main clusters based on marker genes selected using test_overestim_var between the normalized counts of each marker gene in a cluster against all others (function rank_genes_groups in Scanpy). The top 50 marker genes were used for the cluster annotation using the online available databases for the mouse brain (http://mousebrain.org) and the immune cells (http://rstats.immgen.org/MyGeneSet_New/index.html). Additionally, we generated gene expression scores using the function score_genes (as implemented in Scanpy) based on established marker genes (Table 2) of the main cell populations in the adult mouse brain to further confirm the cluster annotation. Visualization of cell groups is done using Uniform Manifold Approximation and Projection (UMAP)[75], as implemented in Scanpy. Differential gene expression analysis between treated and control conditions was performed using the tool diffxpy (https://diffxpy.readthedocs.io/en/latest/index.html) using the Wald test. Of note, since some glial subclusters are comprised of only few cells, the differential gene analysis did not reveal differential expressed genes in these subclusters.

All the comparisons of the overlapping genes were performed using the R package UpSetR[76] which provides an efficient way to visualize the intersecting gene set in UpSet plot. For cluster comparison Additionally, the gene ontology analysis was performed using the R package clusterProfile[52], using the functions compareCluster (fun:enrichGO) or enrichGO. The visualisation of the functional enrichment results was done using the following visualization methods from the R package enrichplot[52]: dot plot; enrichment map (function: emaplot) (based on the pairwise similarities of the enriched terms calculated by the pairwise_termsim function); and the Gene-Concept Network plot (function: cnetplot).

Spatial alignment of the scRNA-seq data

For the spatial localization of the scRNA-seq data, we used the Python package Tangram[46], focusing on the 3dpi control condition and using only the cortical cluster of the Visium dataset in order to have the same anatomical region. We selected the

training genes using the tool AutoGeneS[77] and used 439 training genes as the union of the top informative marker genes of each cluster in the scRNA-seq data that were detected in the Visium profiles. To find the spatial alignment for the scRNA-seq we used the Tangram[46] function map_cells_to_space() which gave us the probabilistic mapping score. Additionally, we segmented the H&E image, using the Squidpy[69] function segment which was used for deconvolving the Visium data using the Tangram[46] functions count_cell_annotations() and deconvolve_cell_annotations().

Spatial gradient analysis

Spatial gradients extending from the lesion core towards perilesional regions were defined using SPATA[78] and its successor SPATA2[39] (under development; https://themilolab.github.io/SPATA2/). The Scanpy-processed object described above was used as input. Both lesion cores were manually annotated based on the H&E staining using createImageAnnotations(). Visium spots were binned into concentric circles using the following arguments: n_bins_circle = 13, binwidth = "95μm". Spots from non-cortical clusters (III,V,X,XIII,XIV,XV,XII,XVI) were excluded from the analysis using the argument bcsp_exclude. Genes with >50 total counts were screened for their correlation with pre-defined gradients (*e.g.* linear descending) using imageAnnotationScreening(), for both injuries separately. Spot metadata derived from Scanpy and Tangram, as well as genes that correlated most strongly with selected pre-defined gradients (sorted by p_value_mean) were plotted using plotIasHeatmap_merge() and plotIasRidgeplot_merge(), custom adaptations of original SPATA2 functions, in which values represent the bin-wise mean of both injuries. Descending models included 'linear_descending', 'immediate_descending', 'abrupt_descending', 'late_descending'. Ascending models included 'linear_ascending', 'immediate_ascending', 'abrupt_ascending', 'late_ascending' (see function showModels()). For screening of gene sets, the following sets were downloaded from MsigDB (https://www.gsea-msigdb.org/gsea/msigdb/mouse/collections.jsp): Biocarta, KEGG, Reactome, WikiPathways, GO (MF/CC/BP), Hallmark. Per gene set, the mean expression of all included genes was calculated and screened for correlation with the same pre-defined gradients as described for single genes. A snapshot of the utilized state of SPATA2 including custom functions is available at https://github.com/simonmfr/SPATA2/tree/publicationCK.

Data availability

All sequencing data generated in association with this study are available in the Gene Expression Omnibus as a SuperSeries. Access can be provided upon request.

Details of analysis pipeline libraries are listed in Methods and available at https://github.com/NinkovicLab/Koupourtidou-Schwarz-et-al (private repository). A public repository will be created as soon as the manuscript is published. Notebooks and all files in the repository can be provided upon request.

Reference:

1. Majdan, M. *et al.* Years of life lost due to traumatic brain injury in Europe: A cross-sectional analysis of 16 countries. *PLoS Med* **14**, e1002331 (2017).
2. Blennow, K. *et al.* Traumatic brain injuries. *Nat Rev Dis Primers* **2**, 1–19 (2016).
3. Mira, R. G., Lira, M. & Cerpa, W. Traumatic Brain Injury: Mechanisms of Glial Response. *Front Physiol* **12**, 740939 (2021).
4. Puntambekar, S. S., Saber, M., Lamb, B. T. & Kokiko-Cochran, O. N. Cellular players that shape evolving pathology and neurodegeneration following traumatic brain injury. *Brain Behav Immun* **71**, 9–17 (2018).
5. Maas, A. I., Stocchetti, N. & Bullock, R. Moderate and severe traumatic brain injury in adults. *Lancet Neurol* **7**, 728–741 (2008).
6. Donat, C. K., Scott, G., Gentleman, S. M. & Sastre, M. Microglial Activation in Traumatic Brain Injury. *Front Aging Neurosci* **9**, 00208 (2017).
7. Kettenmann, H., Hanisch, U.-K., Noda, M. & Verkhratsky, A. Physiology of Microglia. *Physiol Rev* **91**, 461–553 (2011).
8. Dimou, L. & Götz, M. Glial Cells as Progenitors and Stem Cells: New Roles in the Healthy and Diseased Brain. *Physiol Rev* **94**, 709–737 (2014).
9. Simon, C., Dimou, L. & Gotz, M. Progenitors in the adult cerebral cortex - cell cycle properties and regulation by physiological stimuli and injury. *Glia* **59(6)**, 869–881 (2011).
10. Hughes, E. G., Kang, S. H., Fukaya, M. & Bergles, D. E. Oligodendrocyte progenitors balance growth with self-repulsion to achieve homeostasis in the adult brain. *Nat Neurosci* **16**, 668–676 (2013).
11. von Streitberg, A. *et al.* NG2-Glia Transiently Overcome Their Homeostatic Network and Contribute to Wound Closure After Brain Injury. *Front Cell Dev Biol* **9**, 662056 (2021).
12. Escartin, C. *et al.* Reactive astrocyte nomenclature, definitions, and future directions. *Nat Neurosci* **24**, 312–325 (2021).
13. Robel, S., Berninger, B. & Götz, M. The stem cell potential of glia: lessons from reactive gliosis. *Nat Rev Neurosci* **12**, 88–104 (2011).
14. Buffo, A. *et al.* Origin and progeny of reactive gliosis: A source of multipotent cells in the injured brain. *Proceedings of the National Academy of Sciences* **105**, 3581–3586 (2008).
15. Sirko, S. *et al.* Focal laser-lesions activate an endogenous population of neural stem/progenitor cells in the adult visual cortex. *Brain* **132**, 2252–2264 (2009).
16. Bardehle, S. *et al.* Live imaging of astrocyte responses to acute injury reveals selective juxtavascular proliferation. *Nat Neurosci* **16**, 580–586 (2013).
17. Brenner, M. Role of GFAP in CNS injuries. *Neurosci Lett* **565**, 7–13 (2014).
18. Pekny, M., Wilhelmsson, U. & Pekna, M. The dual role of astrocyte activation and reactive gliosis. *Neurosci Lett* **565**, 30–38 (2014).
19. Sofroniew, M. v. Molecular dissection of reactive astrogliosis and glial scar formation. *Trends Neurosci* **32**, 638–647 (2009).
20. Anderson, M. A. *et al.* Astrocyte scar formation aids central nervous system axon regeneration. *Nature* **532**, 195–200 (2016).
21. Batiuk, M. Y. *et al.* Astrocyte Reactivity: Subtypes, States, and Functions in CNS Innate Immunity. *Trends Immunol* **41**, 758–770 (2020).
22. Sofroniew, M. v. & Vinters, H. v. Astrocytes: biology and pathology. *Acta Neuropathol* **119**, 7–35 (2010).

1394 23. Liddelow, S. A. *et al.* Neurotoxic reactive astrocytes are induced by activated
1395 microglia. *Nature* **541**, 481–487 (2017).
1396 24. Yun, S. P. *et al.* Block of A1 astrocyte conversion by microglia is neuroprotective
1397 in models of Parkinson's disease. *Nat Med* **24**, 931–938 (2018).
1398 25. Marzan, D. E. *et al.* Activated microglia drive demyelination via CSF1R
1399 signaling. *Glia* **69**, 1583–1604 (2021).
1400 26. Frik, J. *et al.* Cross-talk between monocyte invasion and astrocyte proliferation
1401 regulates scarring in brain injury. *EMBO Rep* **19**, e45294 (2018).
1402 27. George, K. K., Heithoff, B. P., Shandra, O. & Robel, S. Mild Traumatic Brain
1403 Injury/Concussion Initiates an Atypical Astrocyte Response Caused by Blood–
1404 Brain Barrier Dysfunction. *J Neurotrauma* **39**, 211–226 (2022).
1405 28. Guttenplan, K. A. *et al.* Neurotoxic reactive astrocytes induce cell death via
1406 saturated lipids. *Nature* **599**, 102–107 (2021).
1407 29. Munoz-Ballester, C., Mahmutovic, D., Rafiqzad, Y., Korot, A. & Robel, S. Mild
1408 Traumatic Brain Injury-Induced Disruption of the Blood-Brain Barrier Triggers an
1409 Atypical Neuronal Response. *Front Cell Neurosci* **16**, 821885 (2022).
1410 30. Shandra, O. *et al.* Repetitive Diffuse Mild Traumatic Brain Injury Causes an
1411 Atypical Astrocyte Response and Spontaneous Recurrent Seizures. *The*
1412 *Journal of Neuroscience* **39**, 1944–1963 (2019).
1413 31. Buffo, A. *et al.* Expression pattern of the transcription factor Olig2 in response
1414 to brain injuries: implications for neuronal repair. *Proc Natl Acad Sci U S A* **102**,
1415 18183–18188 (2005).
1416 32. Shechter, R. & Schwartz, M. CNS sterile injury: Just another wound healing?
1417 *Trends Mol Med* **19**, 135–143 (2013).
1418 33. Zeisel, A. *et al.* Molecular Architecture of the Mouse Nervous System. *Cell* **174**,
1419 999-1014.e22 (2018).
1420 34. Sirko, S. *et al.* Astrocyte reactivity after brain injury—: The role of galectins 1
1421 and 3. *Glia* **63**, 2340–2361 (2015).
1422 35. Zamanian, J. L. *et al.* Genomic analysis of reactive astrogliosis. *J Neurosci* **32**,
1423 6391–6410 (2012).
1424 36. Hasel, P., Rose, I. V. L., Sadick, J. S., Kim, R. D. & Liddelow, S. A.
1425 Neuroinflammatory astrocyte subtypes in the mouse brain. *Nat Neurosci* **24**,
1426 1475–1487 (2021).
1427 37. Jurga, A. M., Paleczna, M. & Kuter, K. Z. Overview of General and
1428 Discriminating Markers of Differential Microglia Phenotypes. *Front Cell Neurosci*
1429 **14**, 1–18 (2020).
1430 38. Yu, F. *et al.* Phagocytic microglia and macrophages in brain injury and repair.
1431 *CNS Neurosci Ther* **28**, 1279–1293 (2022).
1432 39. Ravi, V. M. *et al.* Spatially resolved multi-omics deciphers bidirectional tumor-
1433 host interdependence in glioblastoma. *Cancer Cell* **40**, 639-655.e13 (2022).
1434 40. Motori, E. *et al.* Inflammation-induced alteration of astrocyte mitochondrial
1435 dynamics requires autophagy for mitochondrial network maintenance. *Cell*
1436 *Metab* **18**, 844–859 (2013).
1437 41. Göbel, J. *et al.* Mitochondria-Endoplasmic Reticulum Contacts in Reactive
1438 Astrocytes Promote Vascular Remodeling. *Cell Metab* **31**, 791-808.e8 (2020).
1439 42. di Pietro, V. *et al.* Fusion or fission: The destiny of mitochondria in traumatic
1440 brain injury of different severities. *Sci Rep* **7**, 1–13 (2017).
1441 43. Ochocka, N. *et al.* Single-cell RNA sequencing reveals functional heterogeneity
1442 of glioma-associated brain macrophages. *Nat Commun* **12**, 1151 (2021).

44. Baranek, T. *et al.* High Dimensional Single-Cell Analysis Reveals iNKT Cell Developmental Trajectories and Effector Fate Decision. *Cell Rep* **32**, 108116 (2020).
45. Tirosh, I. *et al.* Dissecting the multicellular ecosystem of metastatic melanoma by single-cell RNA-seq. *Science (1979)* **352**, 189–196 (2016).
46. Biancalani, T. *et al.* Deep learning and alignment of spatially resolved single-cell transcriptomes with Tangram. *Nat Methods* **18**, 1352–1362 (2021).
47. Colvin, R. A., Campanella, G. S. V., Sun, J. & Luster, A. D. Intracellular domains of CXCR3 that mediate CXCL9, CXCL10, and CXCL11 function. *Journal of Biological Chemistry* **279**, 30219–30227 (2004).
48. Leng, K. *et al.* CRISPRi screens in human iPSC-derived astrocytes elucidate regulators of distinct inflammatory reactive states. *Nat Neurosci* **25**, 1528–1542 (2022).
49. Sanchez-Gonzalez, R. *et al.* Innate Immune Pathways Promote Oligodendrocyte Progenitor Cell Recruitment to the Injury Site in Adult Zebrafish Brain. *Cells* **11**, 520 (2022).
50. Torraca, V. *et al.* The CXCR3-CXCL11 signaling axis mediates macrophage recruitment and dissemination of mycobacterial infection. *Dis Model Mech* **8**, 253–69 (2015).
51. Cheng, K., Wang, X., Zhang, S. & Yin, H. Discovery of Small-Molecule Inhibitors of the TLR1/TLR2 Complex. *Angewandte Chemie International Edition* **51**, 12246–12249 (2012).
52. Wu, T. *et al.* clusterProfiler 4.0: A universal enrichment tool for interpreting omics data. *The Innovation* **2**, 100141 (2021).
53. Villapol, S., Loane, D. J. & Burns, M. P. Sexual dimorphism in the inflammatory response to traumatic brain injury. *Glia* **65**, 1423–1438 (2017).
54. Heindl, S. *et al.* Automated Morphological Analysis of Microglia After Stroke. *Front Cell Neurosci* **12**, 106 (2018).
55. Han, R. T., Kim, R. D., Molofsky, A. v. & Liddelow, S. A. Astrocyte-immune cell interactions in physiology and pathology. *Immunity* vol. 54 Preprint at https://doi.org/10.1016/j.immuni.2021.01.013 (2021).
56. Eugenín-von Bernhardi, J. & Dimou, L. NG2-glia, more than progenitor cells. *Adv Exp Med Biol* (2016) doi:10.1007/978-3-319-40764-7_2.
57. Chen, W. T. *et al.* Spatial Transcriptomics and In Situ Sequencing to Study Alzheimer's Disease. *Cell* **182**, (2020).
58. Mazaheri, F. *et al.* TREM2 deficiency impairs chemotaxis and microglial responses to neuronal injury. *EMBO Rep* **18**, 1186–1198 (2017).
59. Gowing, G., Vallières, L. & Julien, J. P. Mouse model for ablation of proliferating microglia in acute CNS injuries. *Glia* **53**, (2006).
60. Sirko, S. *et al.* Reactive glia in the injured brain acquire stem cell properties in response to sonic hedgehog. [corrected]. *Cell Stem Cell* **12**, 426–439 (2013).
61. Simon, C., Lickert, H., Gotz, M. & Dimou, L. Sox10-iCreERT2 : a mouse line to inducibly trace the neural crest and oligodendrocyte lineage. *Genesis* **50**, 506–515 (2012).
62. Ning, S., Pagano, J. S. & Barber, G. N. IRF7: activation, regulation, modification and function. *Genes Immun* **12**, 399–414 (2011).
63. Dietrich, N., Lienenklaus, S., Weiss, S. & Gekara, N. O. Murine Toll-Like Receptor 2 Activation Induces Type I Interferon Responses from Endolysosomal Compartments. *PLoS One* (2010) doi:10.1371/journal.pone.0010250.

64. Perkins, D. J. & Vogel, S. N. Space and time: New considerations about the relationship between Toll-like receptors (TLRs) and type I interferons (IFNs). *Cytokine* vol. 74 171–174 Preprint at https://doi.org/10.1016/j.cyto.2015.03.001 (2015).
65. Xu, S. *et al.* Transcriptome Analysis of Microglia Reveals That the TLR2/IRF7 Signaling Axis Mediates Neuroinflammation After Subarachnoid Hemorrhage. *Front Aging Neurosci* **13**, 645649 (2021).
66. Lange Canhos, L. *et al.* Repetitive injury and absence of monocytes promote astrocyte self-renewal and neurological recovery. *Glia* **69**, (2021).
67. Heimann, G. *et al.* Changes in the Proliferative Program Limit Astrocyte Homeostasis in the Aged Post-Traumatic Murine Cerebral Cortex. *Cerebral Cortex* **27**, 4213–4228 (2017).
68. Wolf, F. A., Angerer, P. & Theis, F. J. SCANPY: large-scale single-cell gene expression data analysis. *Genome Biol* **19**, 15 (2018).
69. Palla, G. *et al.* Squidpy: a scalable framework for spatial omics analysis. *Nat Methods* **19**, 171–178 (2022).
70. Traag, V. A., Waltman, L. & van Eck, N. J. From Louvain to Leiden: guaranteeing well-connected communities. *Sci Rep* **9**, 5233 (2019).
71. Luecken, M. D. & Theis, F. J. Current best practices in single-cell RNA-seq analysis: a tutorial. *Mol Syst Biol* **15**, e8746 (2019).
72. Wolock, S. L., Lopez, R. & Klein, A. M. Scrublet: Computational Identification of Cell Doublets in Single-Cell Transcriptomic Data. *Cell Syst* **8**, 281-291.e9 (2019).
73. Lopez, R., Regier, J., Cole, M. B., Jordan, M. I. & Yosef, N. Deep generative modeling for single-cell transcriptomics. *Nat Methods* **15**, 1053–1058 (2018).
74. Gayoso, A. *et al.* A Python library for probabilistic analysis of single-cell omics data. *Nat Biotechnol* **40**, 163–166 (2022).
75. McInnes, L., Healy, J., Saul, N. & Großberger, L. UMAP: Uniform Manifold Approximation and Projection. *J Open Source Softw* **3**, 861 (2018).
76. Conway, J. R., Lex, A. & Gehlenborg, N. UpSetR: An R package for the visualization of intersecting sets and their properties. *Bioinformatics* **33**, 2938–2940 (2017).
77. Aliee, H. & Theis, F. J. AutoGeneS: Automatic gene selection using multi-objective optimization for RNA-seq deconvolution. *Cell Syst* **12**, 706-715.e4 (2021).
78. Kueckelhaus, J. *et al.* Inferring spatially transient gene expression pattern from spatial transcriptomic studies. *bioRxiv* 2020.10.20.346544 (2020) doi:10.1101/2020.10.20.346544.

Koupourtidou, Schwarz, et. al. Fig. 1

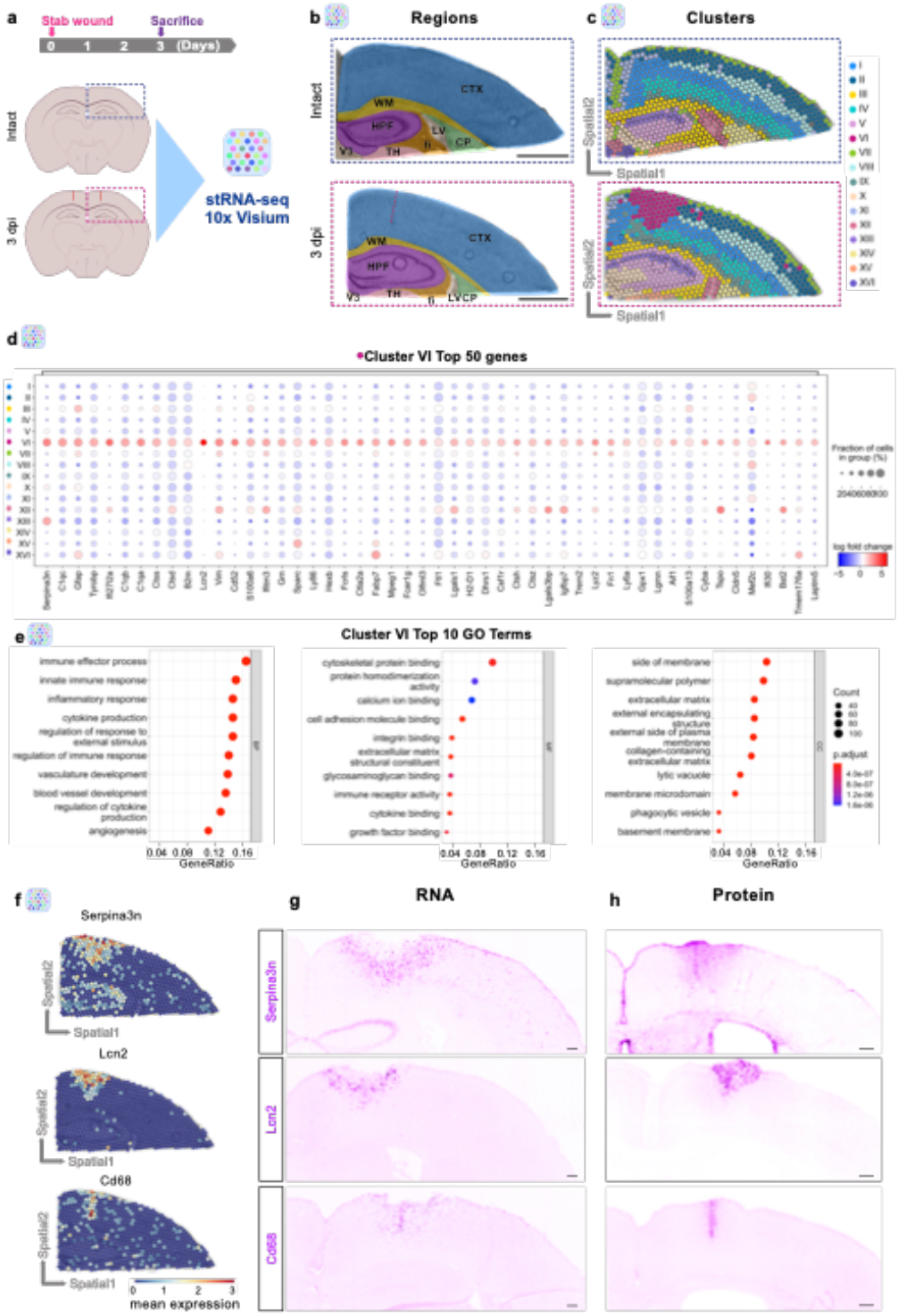

Koupourtidou, Schwarz, et. al. Fig. 2

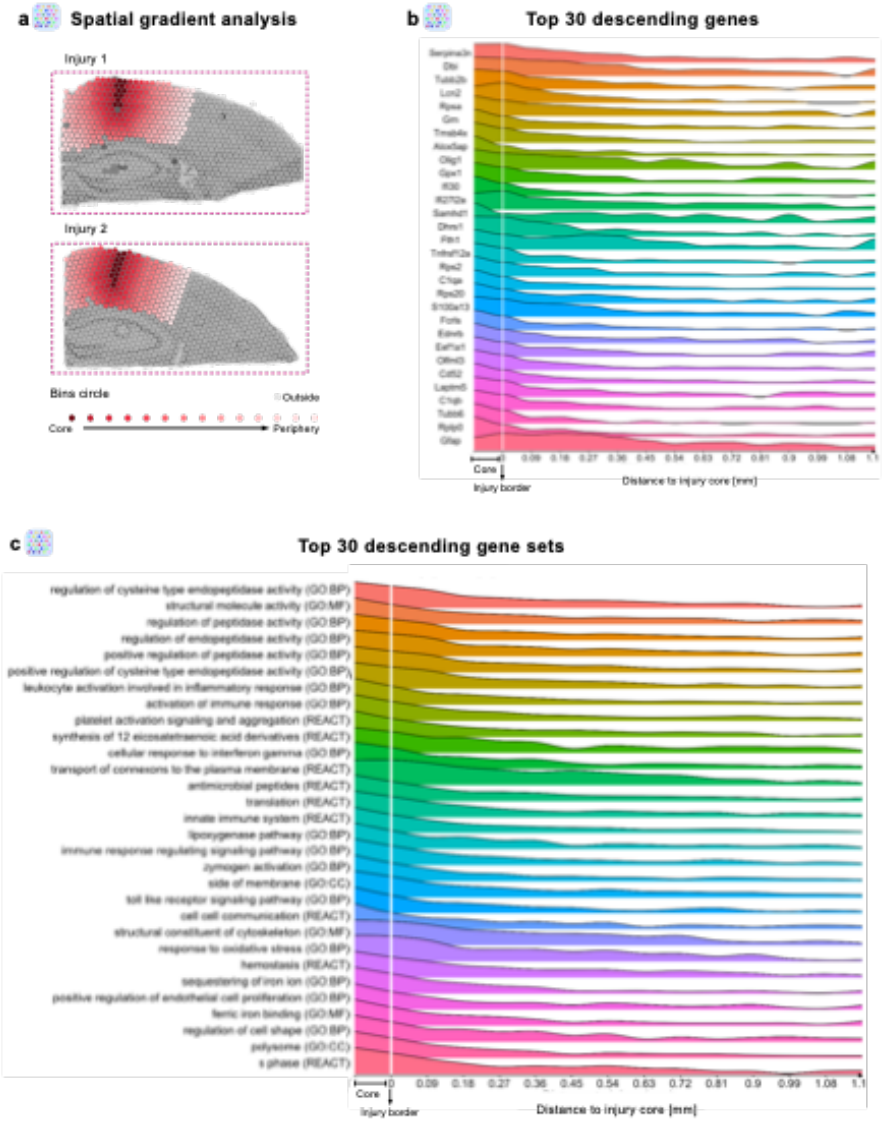

Koupourtidou, Schwarz, et. al. Fig. 3

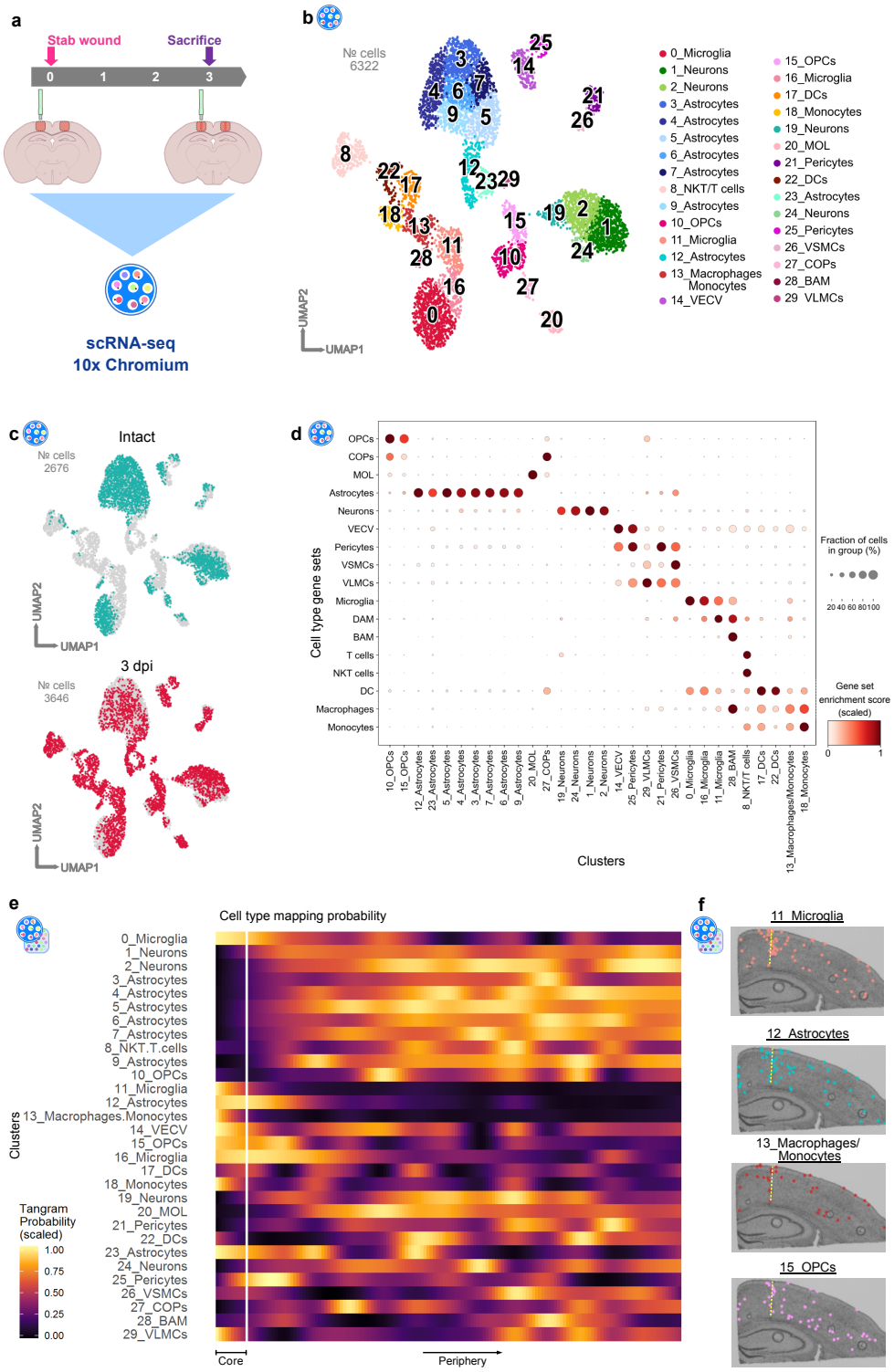

Koupourtidou, Schwarz, et. al. Fig. 4

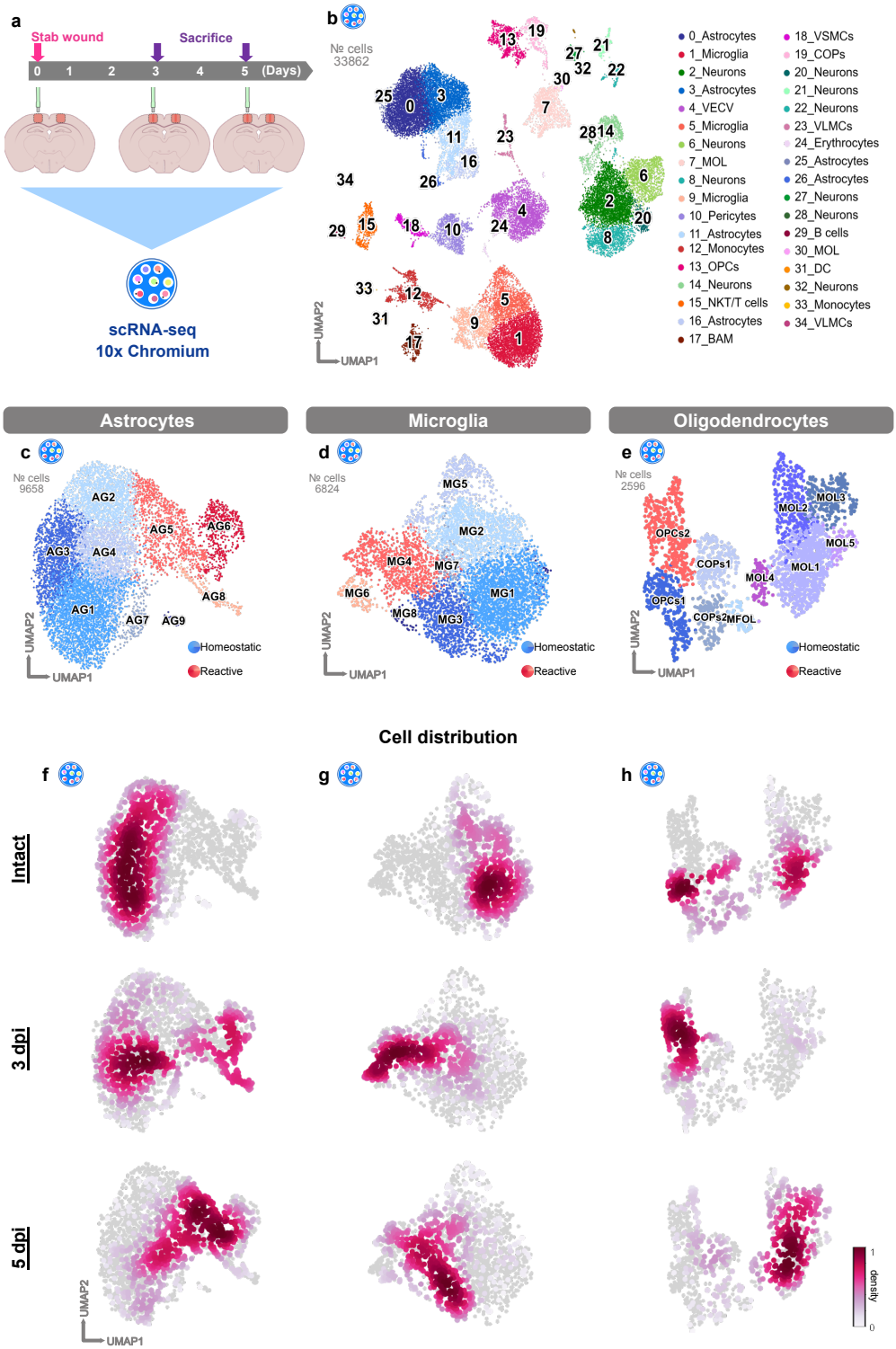

Koupourtidou, Schwarz, et. al. Fig. 5

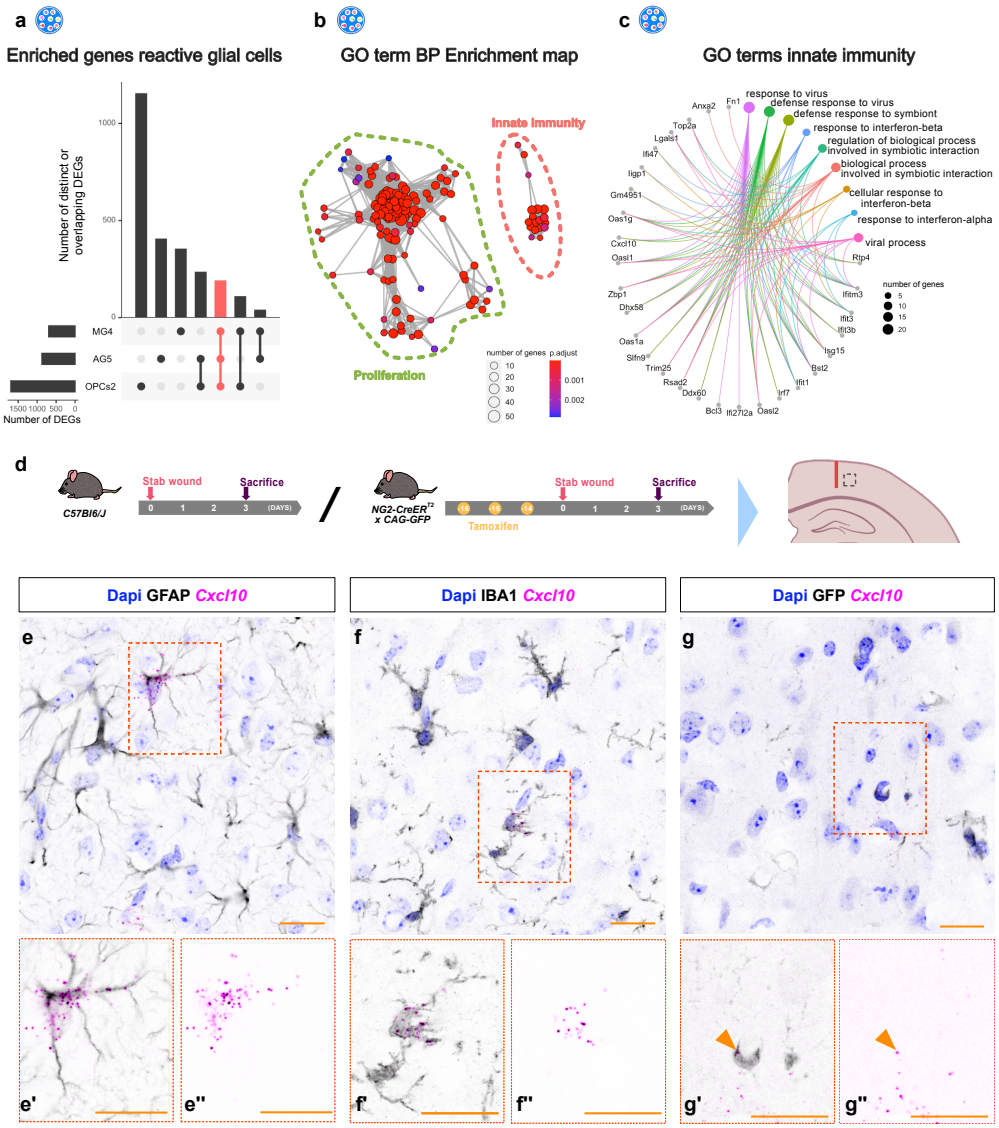

Koupourtidou, Schwarz, et. al. Fig. 6

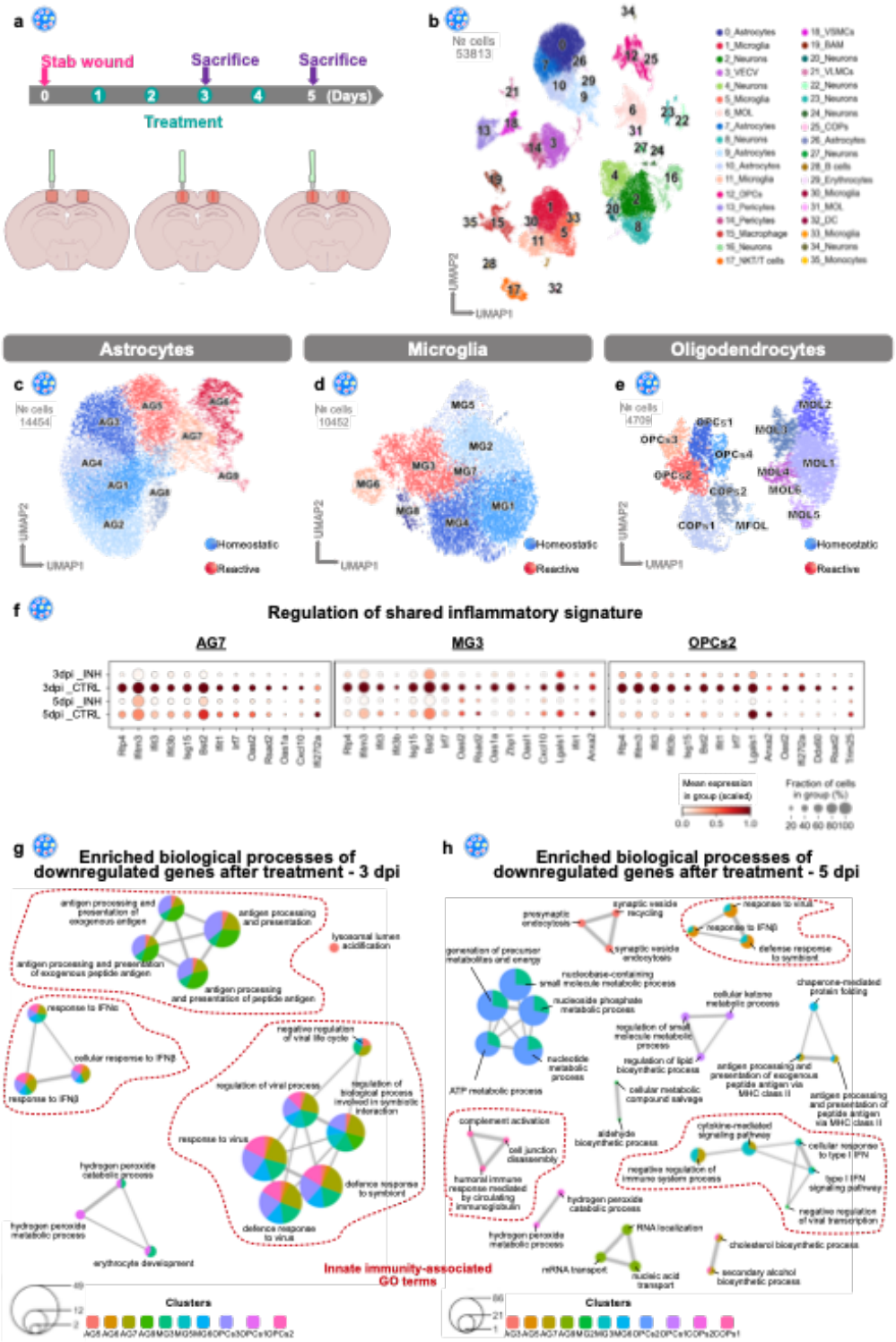

Koupourtidou, Schwarz, et. al. Fig. 7

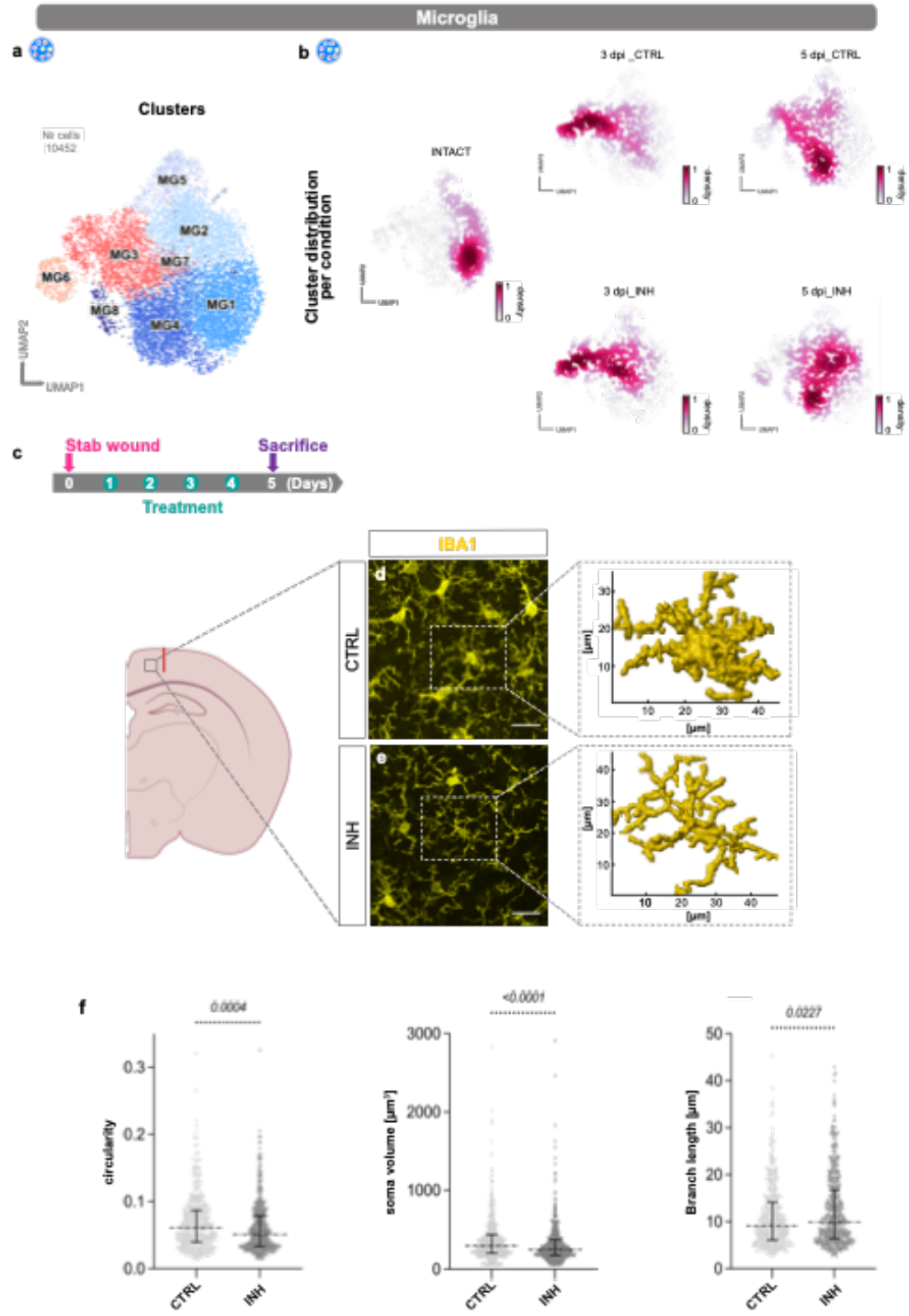

Koupourtidou, Schwarz, et. al. Fig. 8

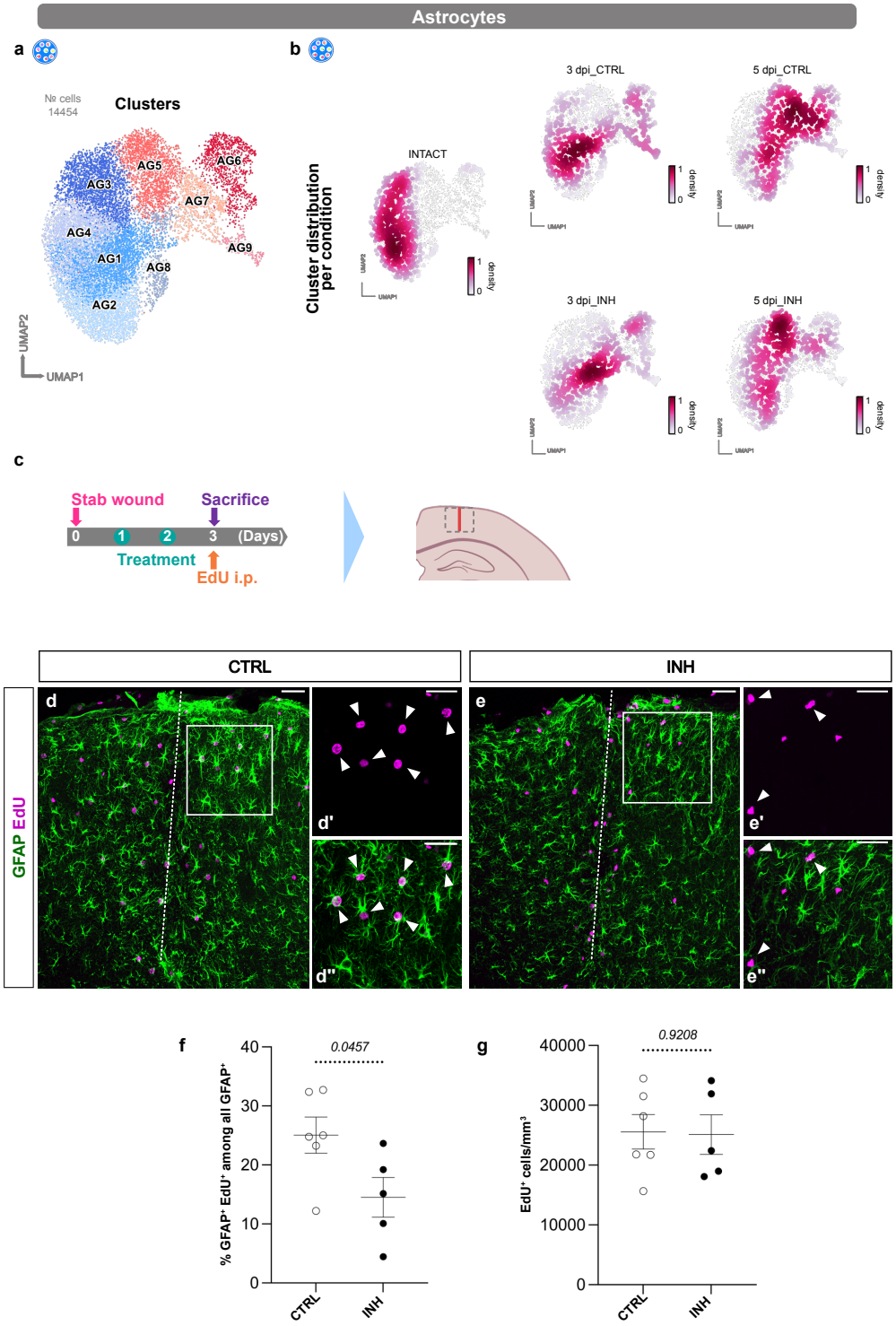

Koupourtidou, Schwarz, et. al. ED_Fig. 1

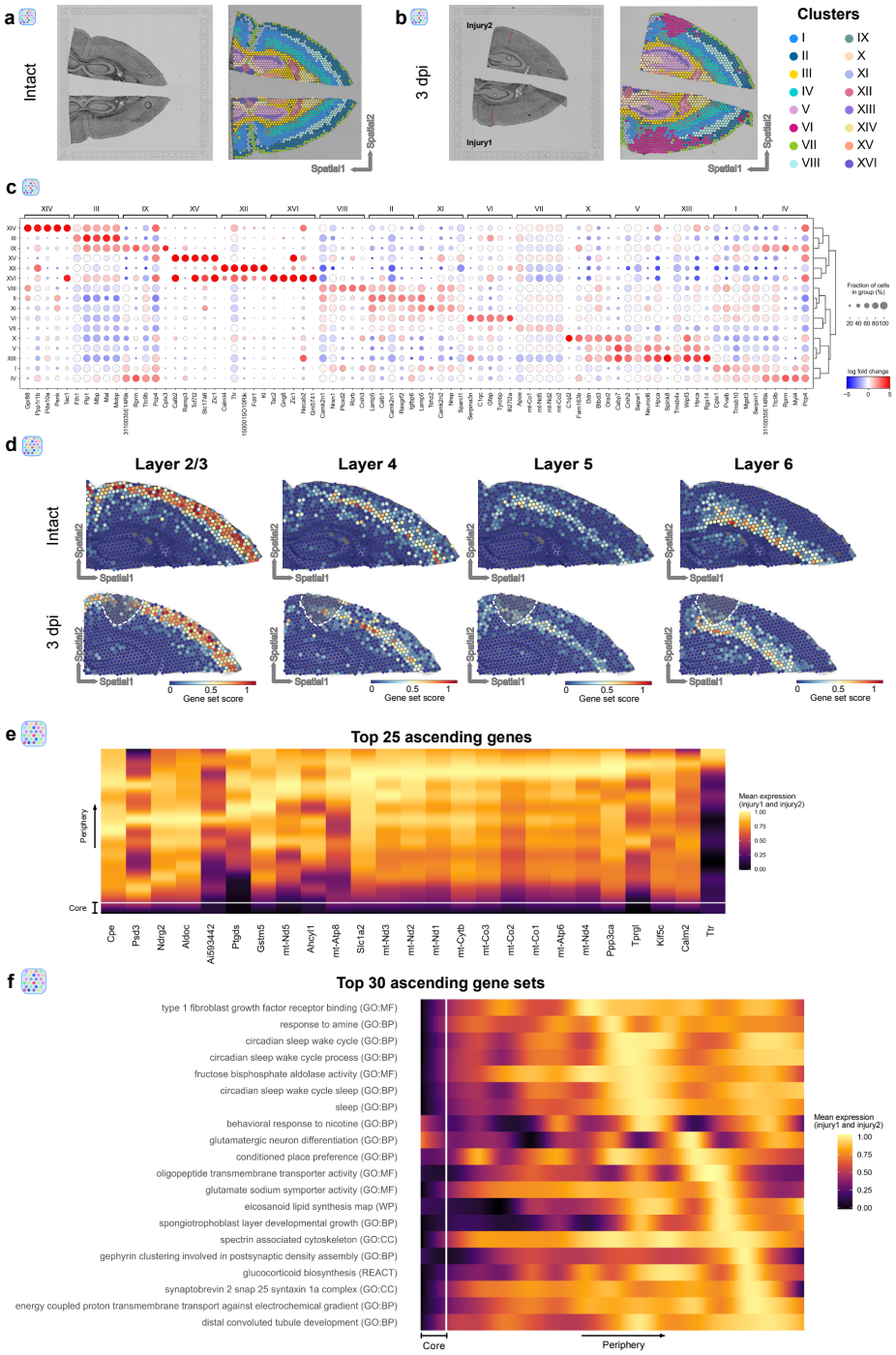

Koupourtidou, Schwarz, et. al. ED_Fig. 2

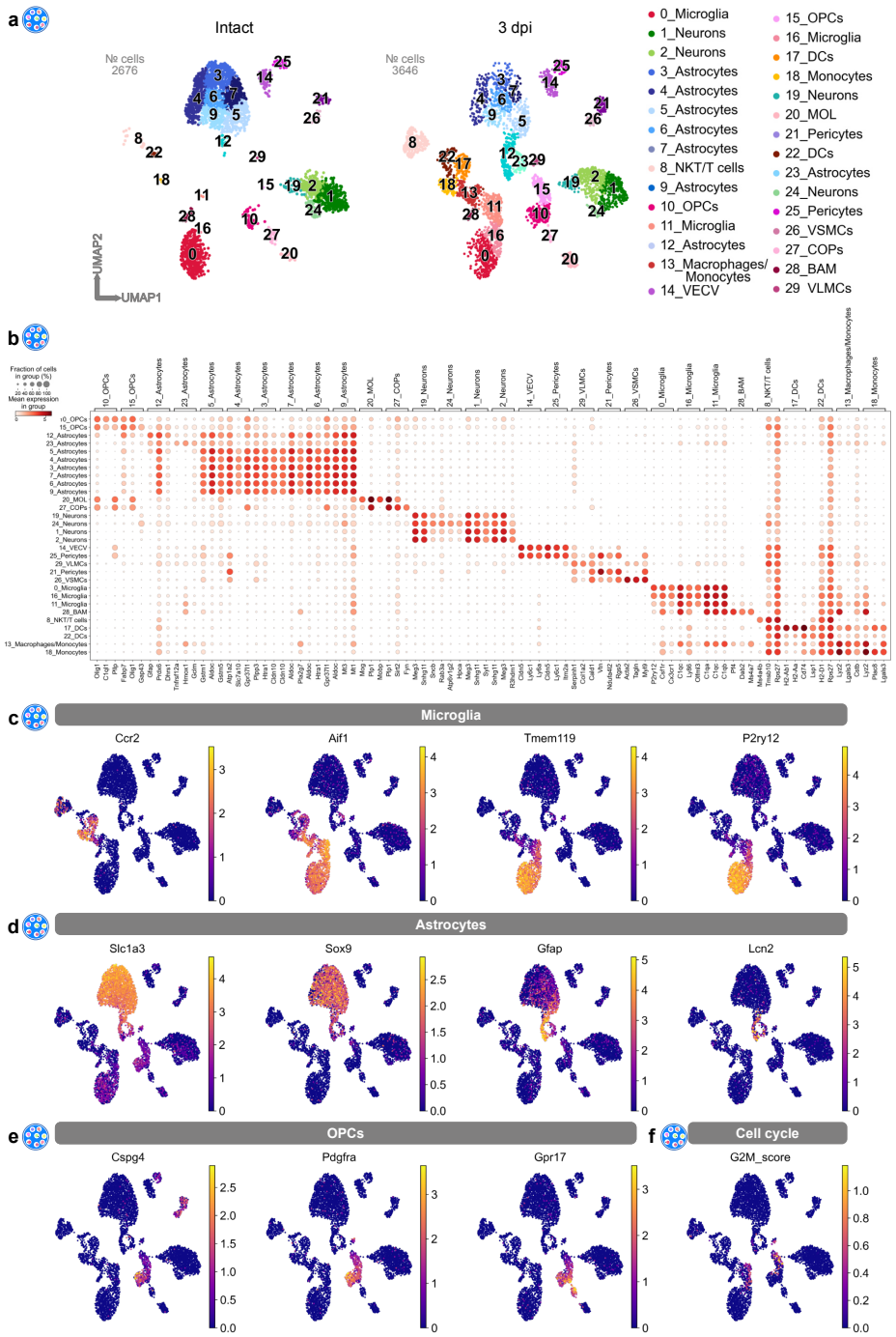

Koupourtidou, Schwarz, et. al. ED_Fig. 3

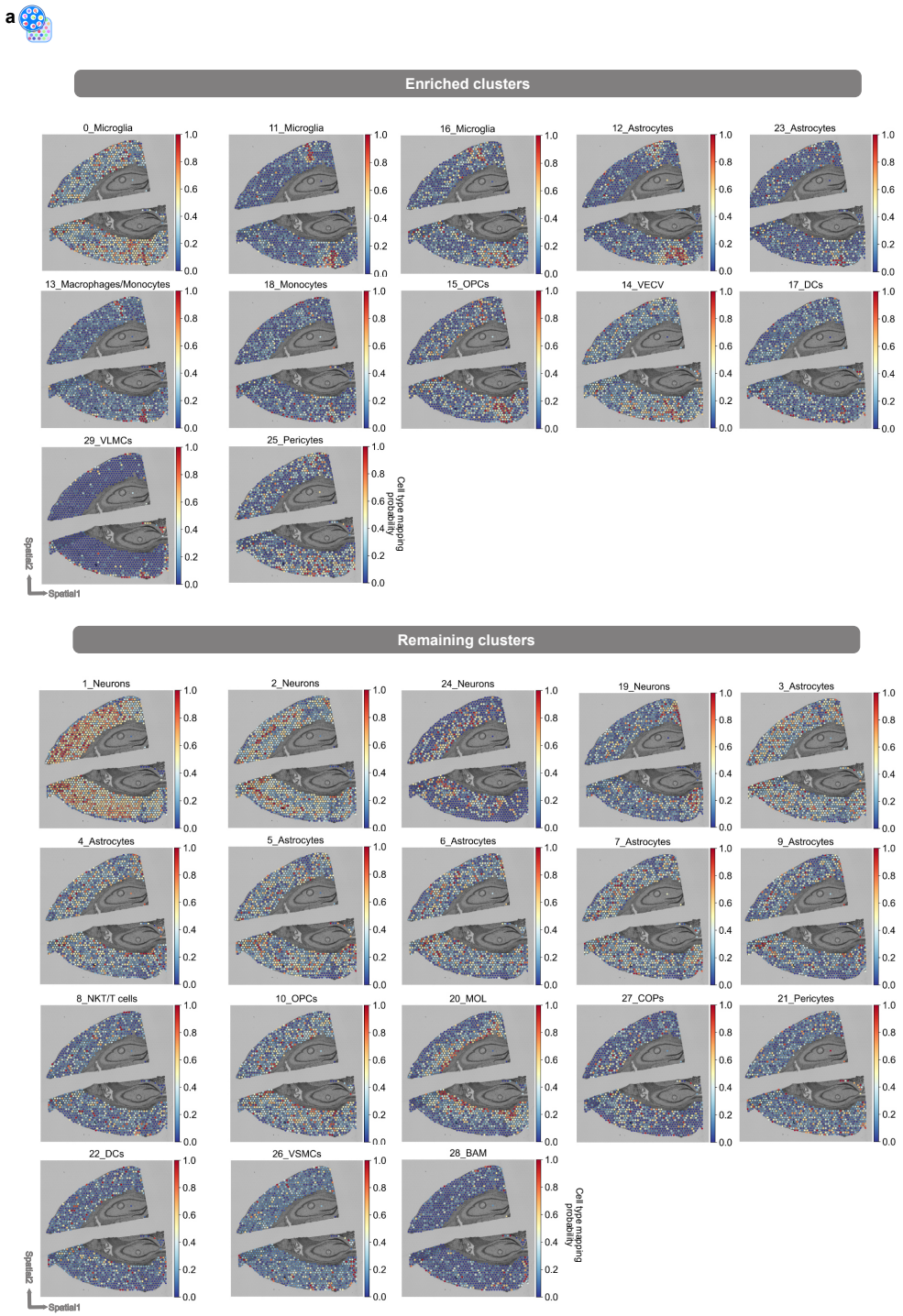

Koupourtidou, Schwarz, et. al. ED_Fig. 4

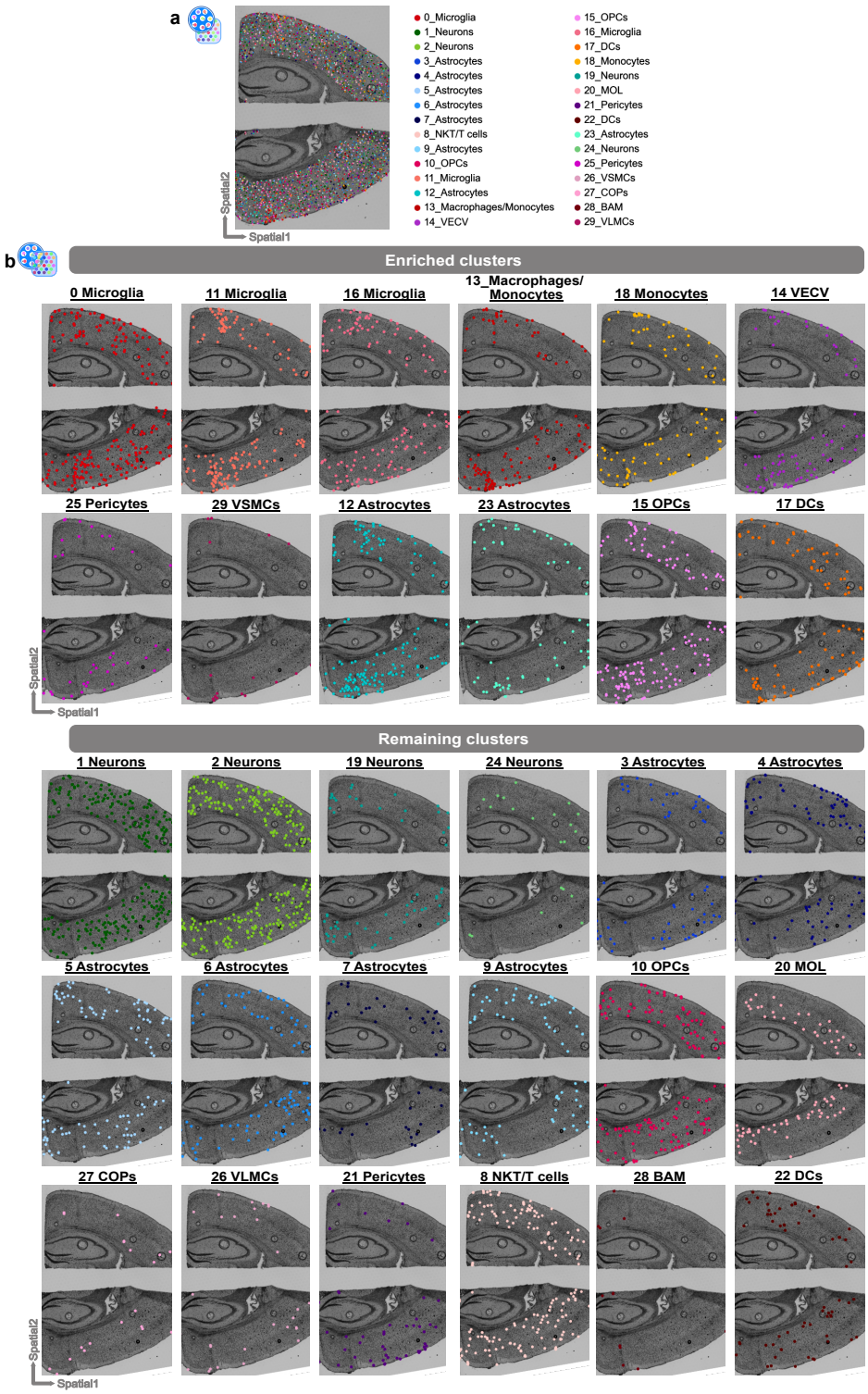

Koupourtidou, Schwarz, et. al. ED_Fig. 5

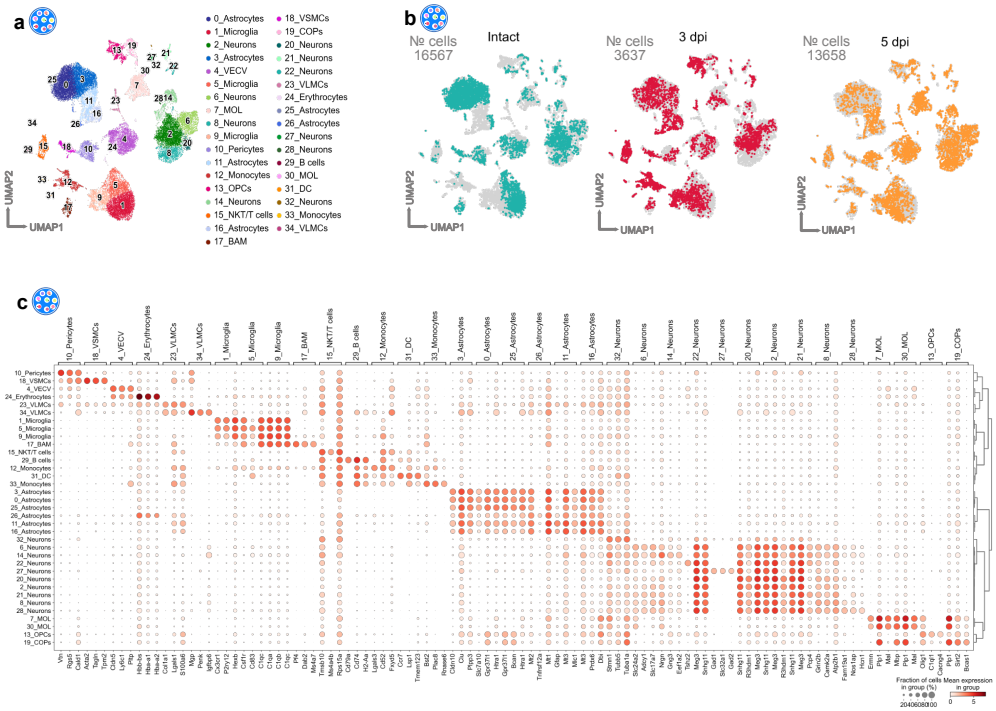

Koupourtidou, Schwarz, et. al. ED_Fig. 6

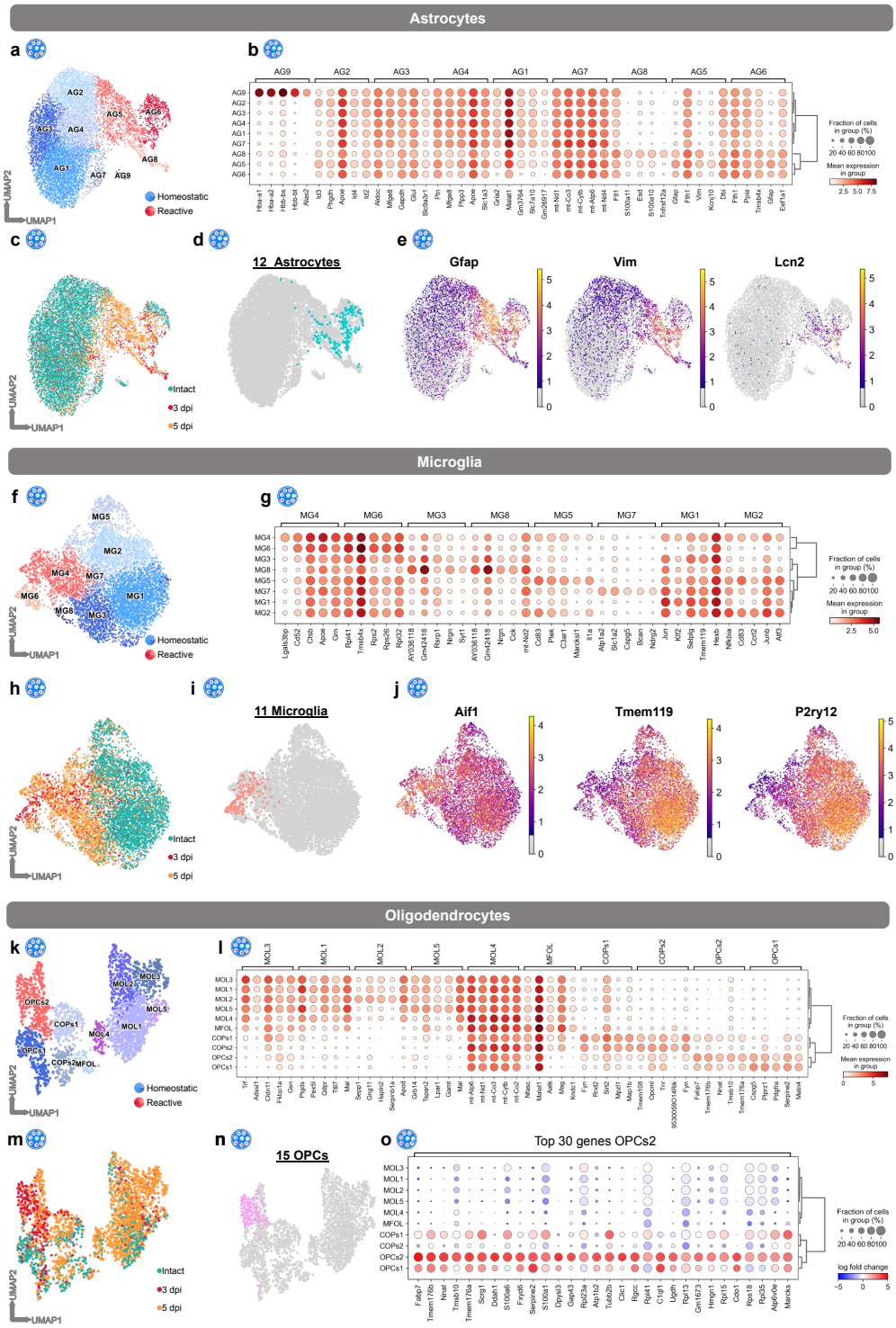

Koupourtidou, Schwarz, et. al. ED_Fig. 7

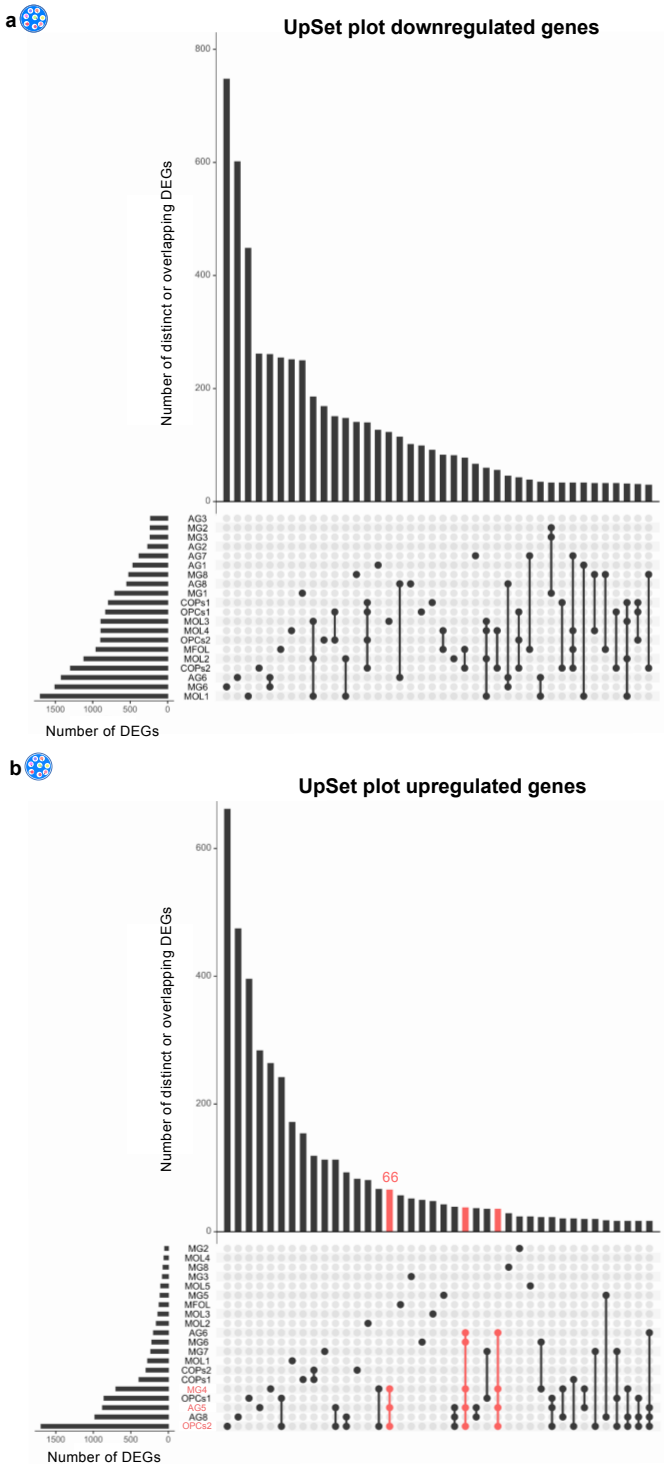

Koupourtidou, Schwarz, et. al. ED_Fig. 8

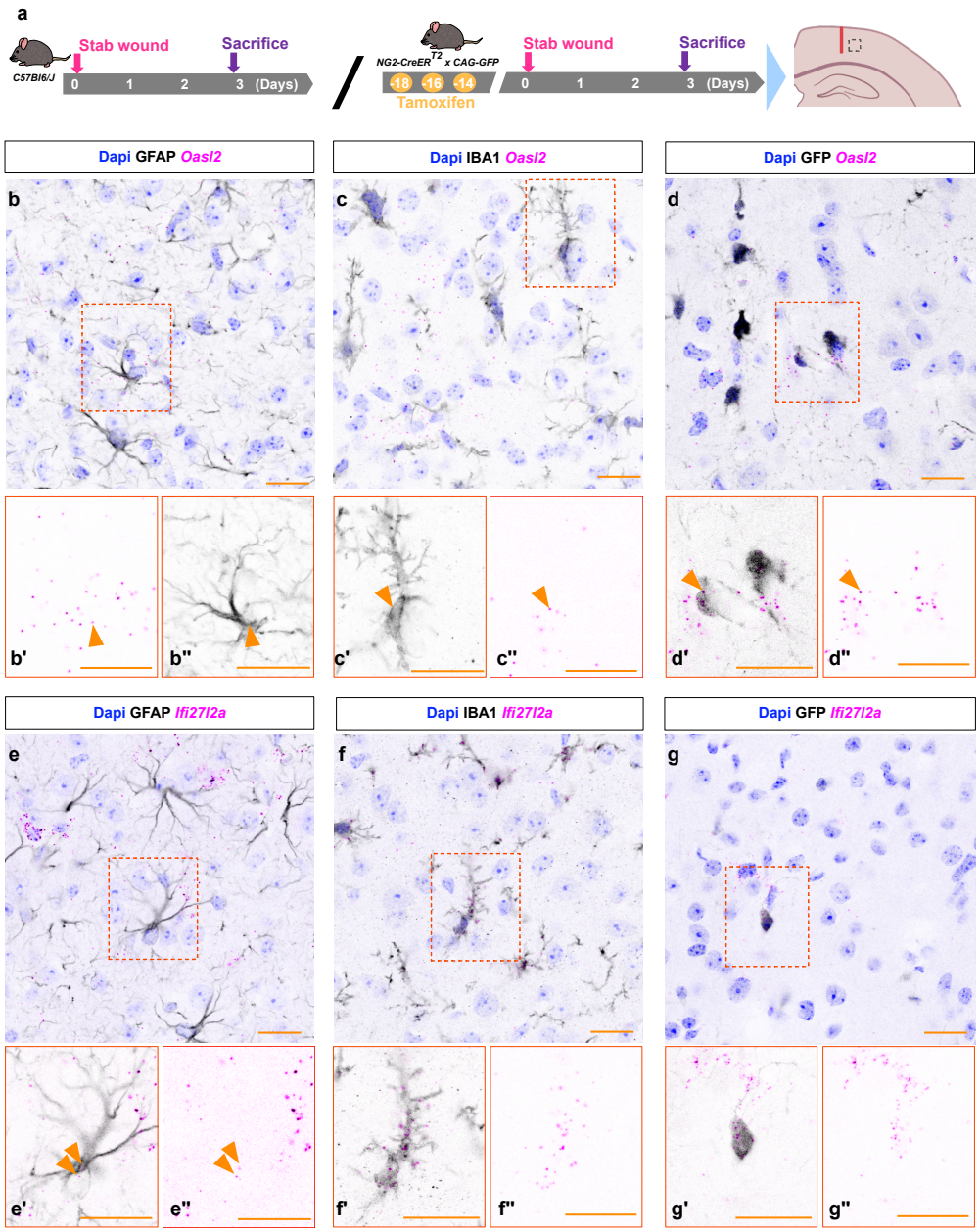

Koupourtidou, Schwarz, et. al. ED_Fig. 9

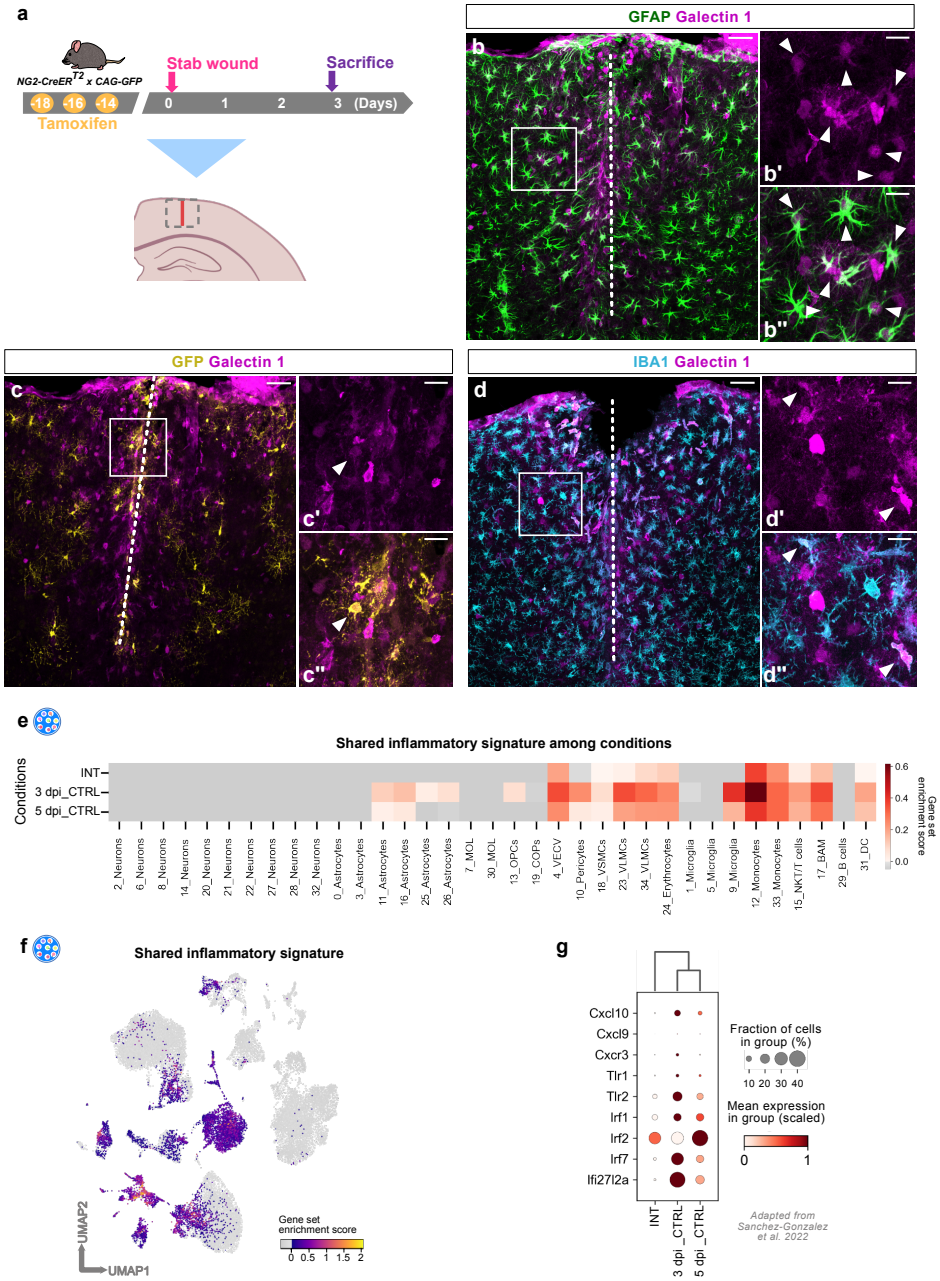

Koupourtidou, Schwarz, et. al. ED_Fig.10

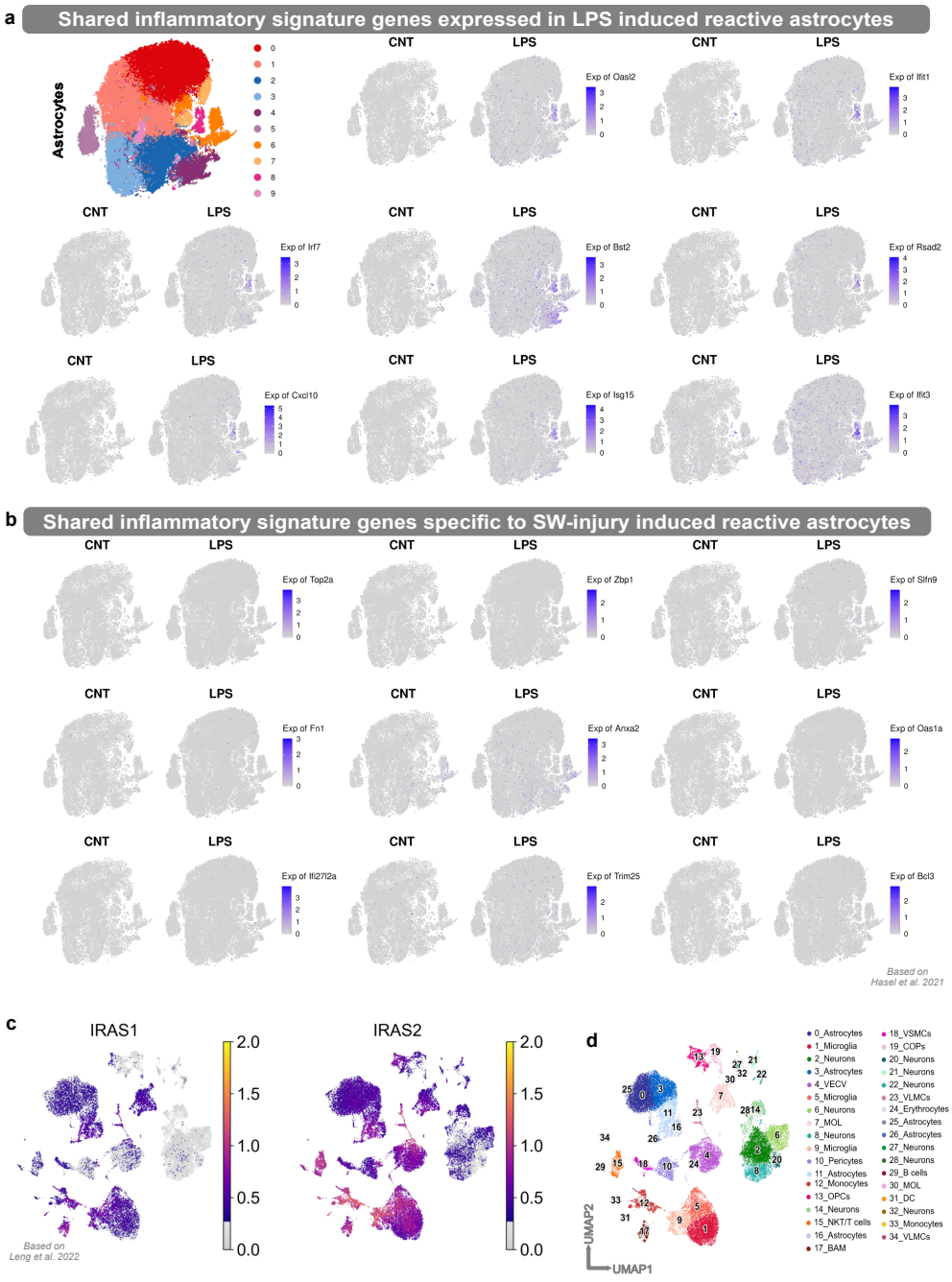

Koupourtidou, Schwarz, et. al. ED_Fig. 11

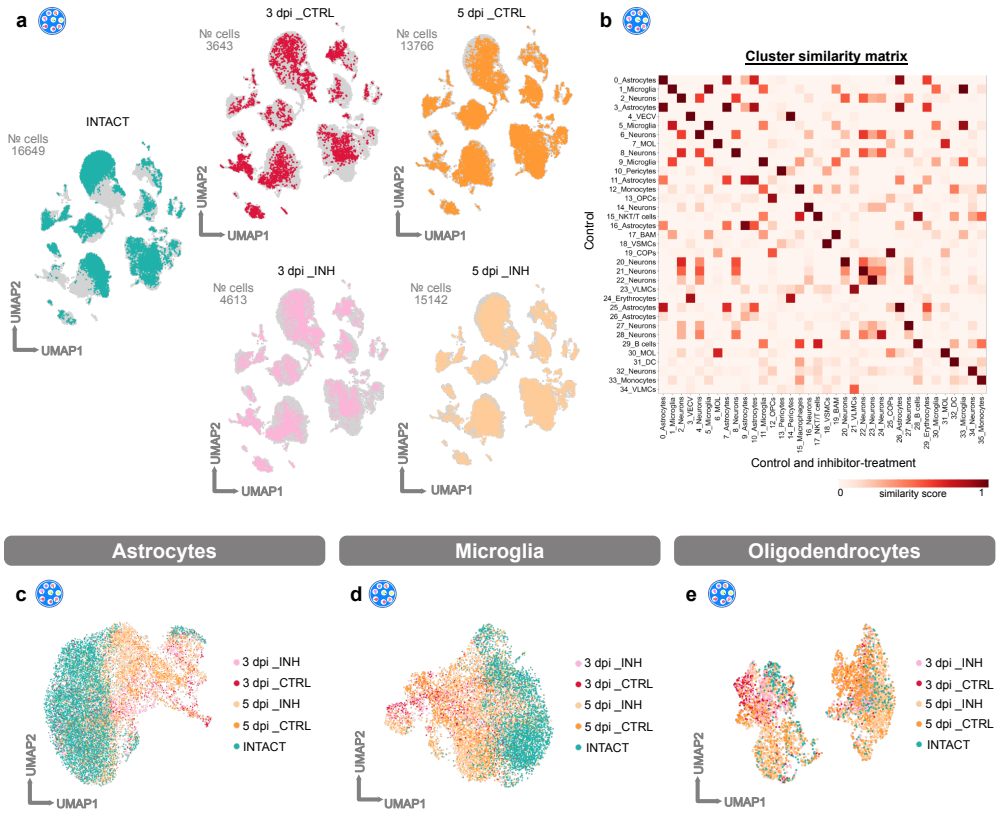

Koupourtidou, Schwarz, et. al. ED_Fig. 12

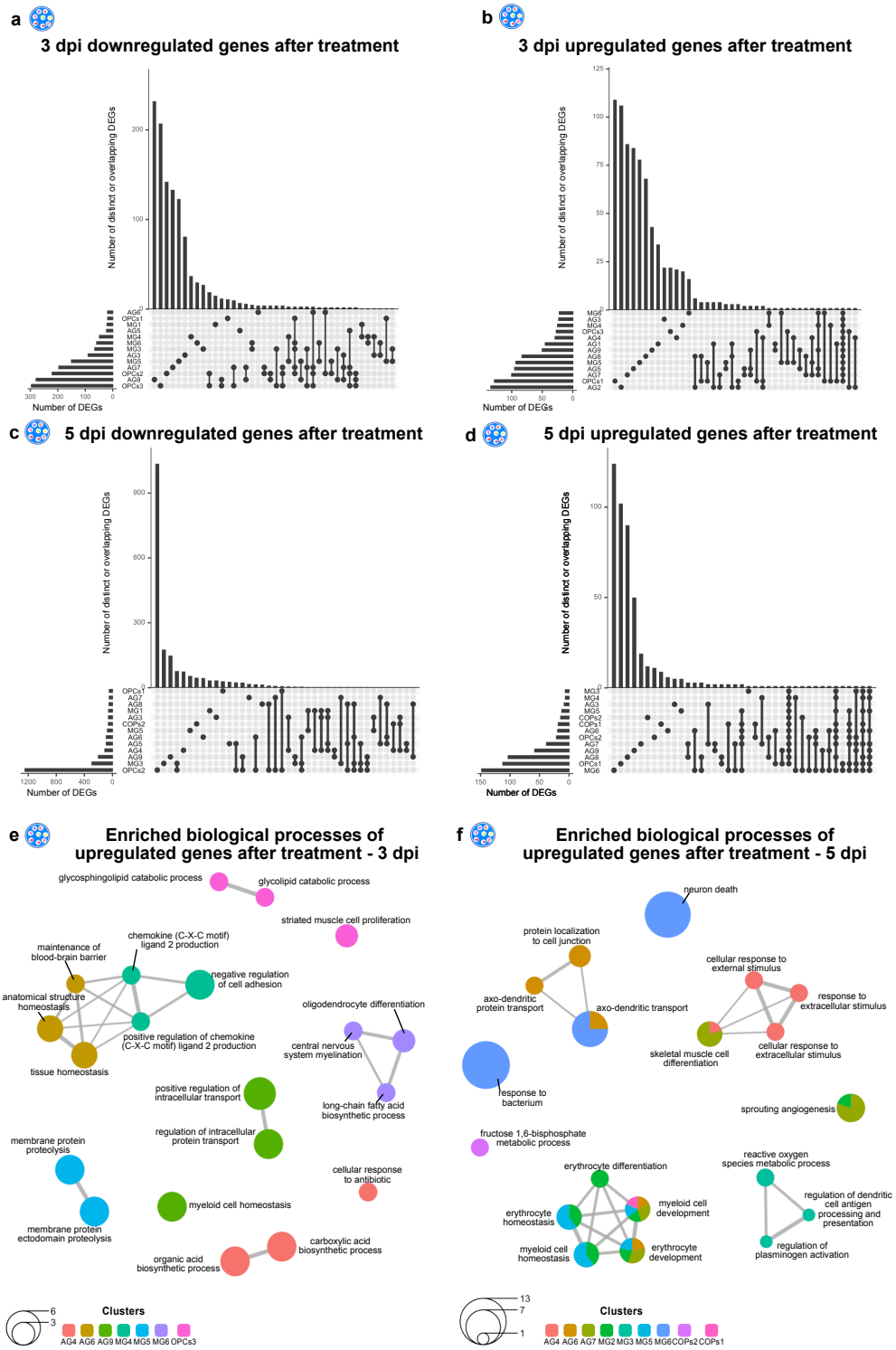

Koupourtidou, Schwarz, et. al. ED_Fig. 13

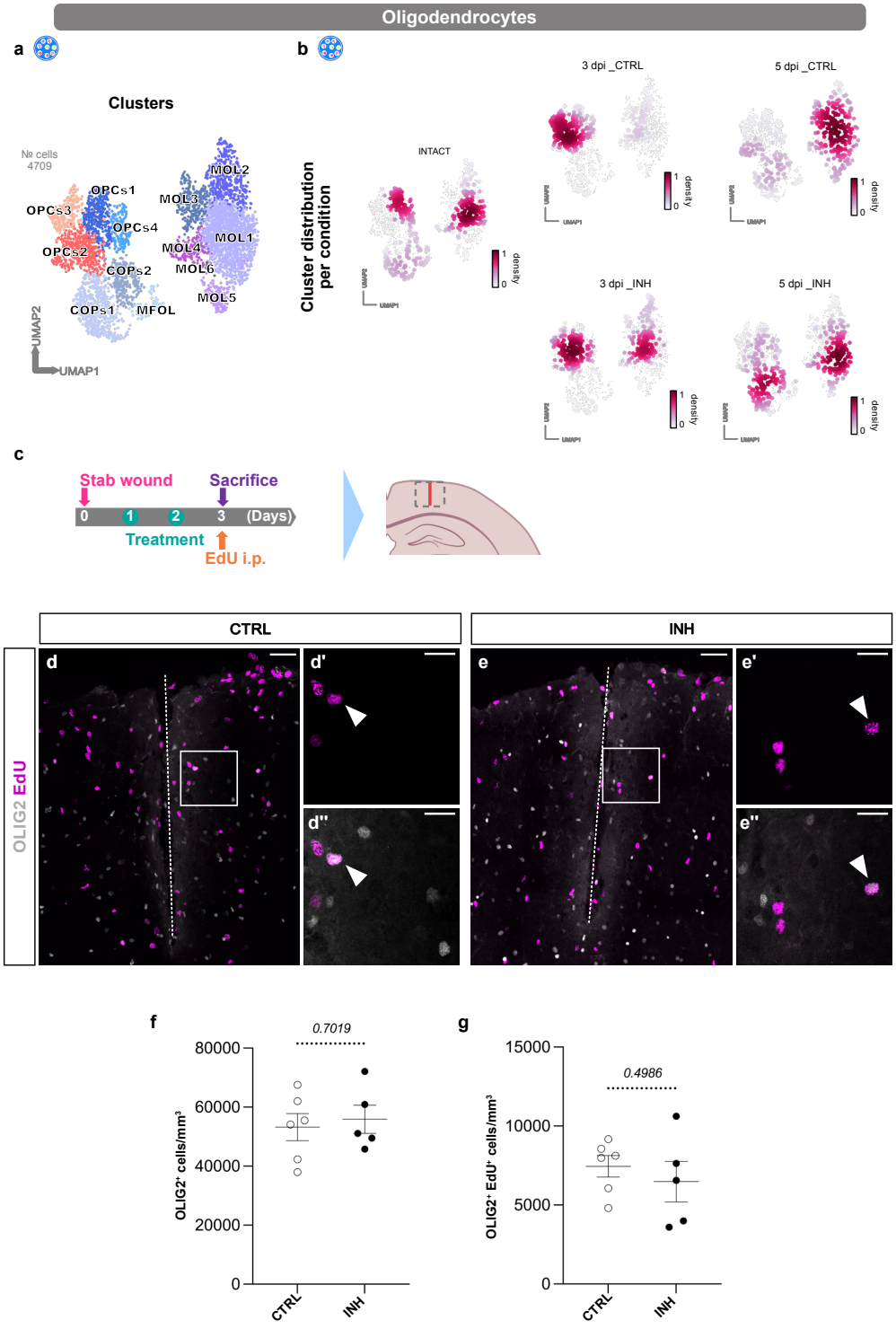

Koupourtidou, Schwarz, et. al. ED_Fig. 14

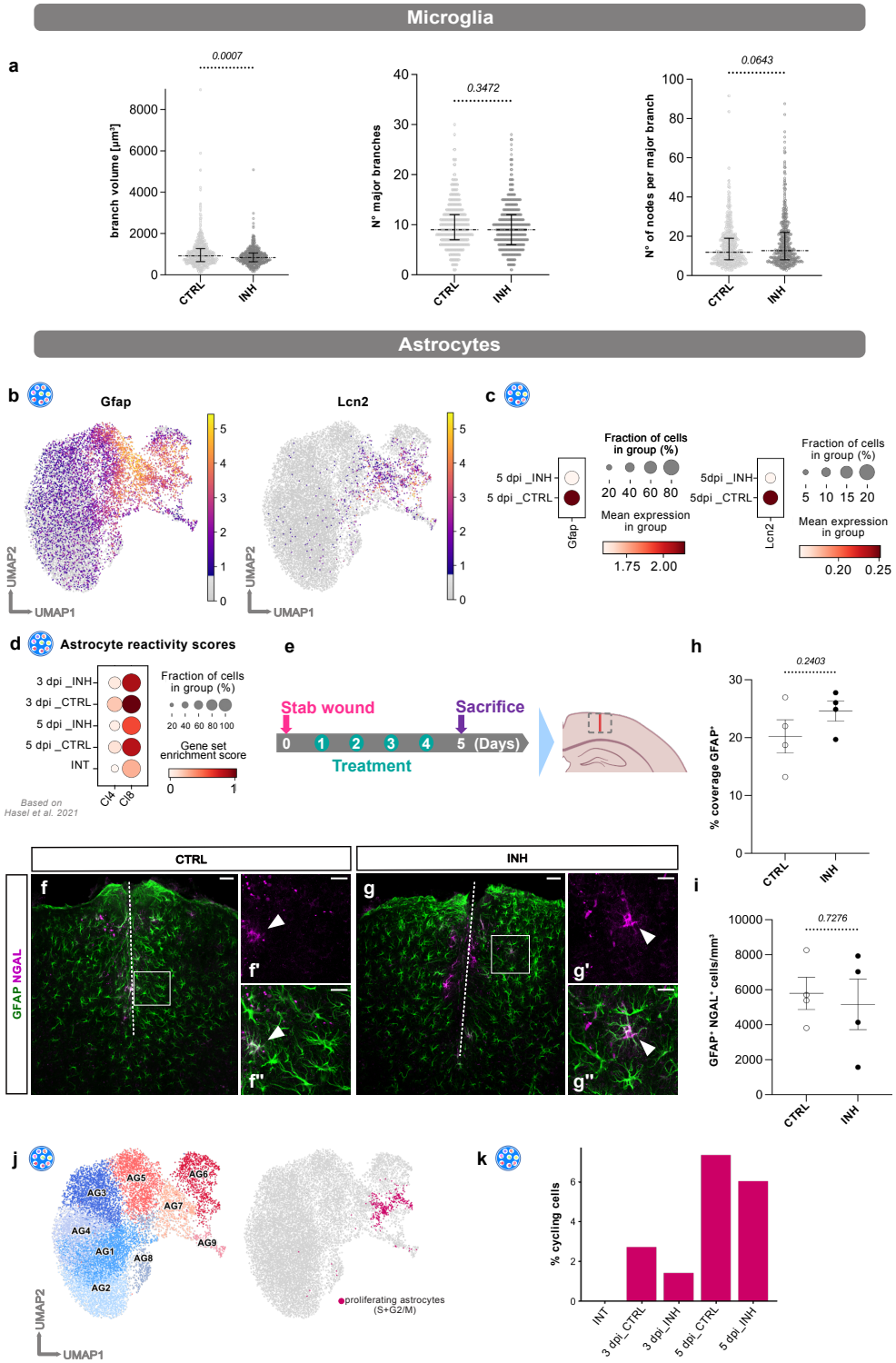

Aim of study III

This study aimed to explore the plasticity of mature oligodendrocytes in response to cortical damage. We uncovered a subset of mature murine oligodendrocytes, termed AO cells, that simultaneously expressed astro- and oligodendroglial genes in response to cortical injuries. Furthermore, AO cells displayed the capacity to differentiate into astrocytes following cortical stab wound injury in adult mice.

In the mouse cortex, oligodendrocytes regain a plastic capacity, transforming into astrocytes after acute injury

Xianshu Bai, Na Zhao, Christina Koupourtidou, Li-Pao Fang, Veronika Schwarz, Laura C. Caudal, Renping Zhao, Johannes Hirrlinger, Wolfgang Walz, Shan Bian, Wenhui Huang, Jovica Ninkovic, Frank Kirchhoff, and Anja Scheller

For this study, I assisted in all animal experiments related to the transcriptomic study and the generation of the scRNA-seq data sets.

This study has been published in Developmental Cell (2023), 58(13):1153-1169.

DOI: https://doi.org/10.1016/j.devcel.2023.04.016

Article

Developmental Cell

In the mouse cortex, oligodendrocytes regain a plastic capacity, transforming into astrocytes after acute injury

Graphical abstract

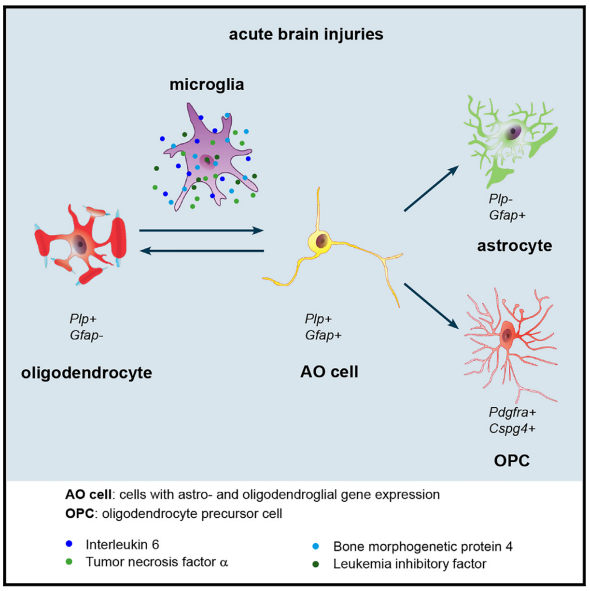

Highlights

- Upon acute brain injuries, oligodendrocytes can activate astroglial genes
- Oligodendrocytes can become astrocytes via the transitional AO cell status
- Microglia-derived IL-6 drives the transition of oligodendrocytes to AO cells

Authors

Xianshu Bai, Na Zhao, Christina Koupourtidou, ..., Jovica Ninkovic, Frank Kirchhoff, Anja Scheller

Correspondence

anja.scheller@uks.eu (A.S.), xianshu.bai@uks.eu (X.B.)

In brief

Bai et al. identify a subset of cells in mice with concomitant activation of astro- and oligo-dendroglial genes (termed AO cells), derived from oligodendrocytes upon acute brain injury. AO cells differentiate into astrocytes, oligodendrocytes, and oligodendrocyte precursors, and microglial-derived interleukin-6 promotes the transition of mature oligodendrocytes to AO cells.

Bai et al., 2023, Developmental Cell *58*, 1153–1169
July 10, 2023
https://doi.org/10.1016/j.devcel.2023.04.016

CellPress

Developmental Cell

CellPress

Article

In the mouse cortex, oligodendrocytes regain a plastic capacity, transforming into astrocytes after acute injury

Xianshu Bai,[1,*] Na Zhao,[1,10] Christina Koupourtidou,[2,3] Li-Pao Fang,[1] Veronika Schwarz,[2,3] Laura C. Caudal,[1] Renping Zhao,[1,11] Johannes Hirrlinger,[4,5] Wolfgang Walz,[1,6] Shan Bian,[7,8] Wenhui Huang,[1] Jovica Ninkovic,[2,3] Frank Kirchhoff,[1,9] and Anja Scheller[1,12,*]

[1]Molecular Physiology, Center for Integrative Physiology and Molecular Medicine, University of Saarland, 66421 Homburg, Germany
[2]Department of Cell Biology and Anatomy, Ludwig-Maximilians-Universität München, 82152 Planegg-Martinsried, Germany
[3]Institute of Stem Cell Research, Helmholtz Zentrum Munich, 85764 Neuherberg-Munich, Germany
[4]Carl-Ludwig-Institute for Physiology, Leipzig University, 04103 Leipzig, Germany
[5]Department of Neurogenetics, Max-Planck-Institute for Multidisciplinary Sciences, 37075 Göttingen, Germany
[6]Department of Psychiatry, University of Saskatchewan, 107 Wiggins Road, Saskatoon, SK S7N 5E5, Canada
[7]Institute for Regenerative Medicine, Shanghai East Hospital, School of Life Sciences and Technology, Tongji University, 200092 Shanghai, China
[8]Frontier Science Center for Stem Cell Research, Tongji University, 200092 Shanghai, China
[9]Experimental Research Center for Normal and Pathological Aging, University of Medicine and Pharmacy of Craiova, 200349 Craiova, Romania
[10]Present address: Institute of Anatomy and Cell Biology, University of Saarland, 66421 Homburg, Germany
[11]Present address: Biophysics, Center for Integrative Physiology and Molecular Medicine, University of Saarland, 66421 Homburg, Germany
[12]Lead contact
*Correspondence: anja.scheller@uks.eu (A.S.), xianshu.bai@uks.eu (X.B.)
https://doi.org/10.1016/j.devcel.2023.04.016

SUMMARY

Acute brain injuries evoke various response cascades directing the formation of the glial scar. Here, we report that acute lesions associated with hemorrhagic injuries trigger a re-programming of oligodendrocytes. Single-cell RNA sequencing highlighted a subpopulation of oligodendrocytes activating astroglial genes after acute brain injuries. By using PLP-DsRed1/GFAP-EGFP and PLP-EGFP$_{mem}$/GFAP-mRFP1 transgenic mice, we visualized this population of oligodendrocytes that we termed AO cells based on their concomitant activity of astro- and oligodendroglial genes. By fate mapping using PLP- and GFAP-split Cre complementation and repeated chronic *in vivo* imaging with two-photon laser-scanning microscopy, we observed the conversion of oligodendrocytes into astrocytes via the AO cell stage. Such conversion was promoted by local injection of IL-6 and was diminished by IL-6 receptor-neutralizing antibody as well as by inhibiting microglial activation with minocycline. In summary, our findings highlight the plastic potential of oligodendrocytes in acute brain trauma due to microglia-derived IL-6.

INTRODUCTION

Oligodendrocytes, the myelin-forming cells of the central nervous system (CNS), are terminally differentiated and originate from their oligodendrocyte precursor cells (OPCs, also termed NG2 glia) under both physiological and pathological conditions.[1,2] Although mammalian oligodendrocytes appear to be particularly sensitive to injuries,[3] their lower vertebrate counterparts display a more plastic behavior.[4] In the goldfish optic tract, oligodendrocytes not only survive nerve lesion but also dedifferentiate into elongated bipolar cells before they start to myelinate again.[5] So far, similar dedifferentiation of mammalian oligodendrocytes has been suggested by *in vitro* studies[6,7] and in an epigenetic analysis of MBP-Cre/*loxP* fate mapping.[8]

In the mammalian adult brain, the plastic behavior within the oligodendrocyte lineage is far better established for OPCs, which have consistently been found to generate astrocytes after brain injuries, whereas under healthy conditions, only embryonic OPCs could generate astroglial cells.[9–12] The contribution of astrocytes formed by OPCs in the injured adult brain appeared variable and strongly dependent on animal models and/or injury paradigms. OPC-derived astrocytes were detected in a variety of insults such as stab wound injury (SWI), spreading depression in gray matter or cryoinjury.[13–16] However, in general, varying numbers of astrocytes were found,[15–17] mostly explainable with time points of inducing the lesion pertaining to the age and time of recombination induction and variable time windows of analysis after injury.

CellPress

Developmental Cell
Article

Here, we examined the plasticity of mature oligodendrocytes (MOLs) in the mouse brain after acute cortical injuries *in vivo*. By analyzing a variety of genetically modified mouse models, we provide strong evidence that in addition to OPCs, MOLs can give rise to astrocytes participating in glial scar formation after acute cortical injuries. Triggered by microglia-derived IL-6, oligodendrocytes undergo a transitional cell stage (termed AO cells), with astro- and oligodendroglial properties.

RESULTS

Acute injury induces the generation of astrocytes from cells of the oligodendrocyte lineage

To investigate the differentiation potential of oligodendrocyte lineage cells (OLCs, i.e., OPCs and oligodendrocytes) to generate astrocytes *in vivo*, we employed Cre/*loxP* fate mapping by taking advantage of NG2-CreER^{T2} knockin mice.[12] Our previous studies have shown that this mouse line faithfully labels OPCs and their progeny oligodendrocytes upon tamoxifen-induced recombination.[12,18] To label OLCs, we injected tamoxifen in 7-week-old NG2-CreER^{T2} × R26-lsl-tdTomato mice starting either 10 or 30 days before a SWI (dbi) and analyzed cellular responses 1 week post-injury (wpi) (Figures 1A and 1B). We detected lesion-induced glial fibrillary acidic protein (GFAP) expression in 25.5% ± 4.4% of the total tdTomato (tdT)$^+$ cells when gene recombination was induced 10 dbi (Figures 1C, 1D, and 1G). Over 70% of the GFAP$^+$tdT$^+$ cells (71.5% ± 6.5%, Figure 1H) were also platelet-derived growth factor receptor alpha (PDGFRα)-positive (Pα^+, an established marker of OPCs) and therefore classified as OPCs (Figures 1E and 1H, GFAP$^+$tdT$^+$ and Pα^+). We regarded the remaining 28.5% ± 6.5% (Figure 1H) of recombined and Pα-negative cells as *bona fide* astrocytes (Figure 1E, GFAP$^+$tdT$^+$ but Pα^-, arrowheads). Their identity could be further substantiated by glutamine synthetase (GS) immunoreactivity and a typical astroglial morphology with fine, highly arborized processes and contacts with blood vessels (Figure 1F). The percentage of astrocytes among all recombined tdT$^+$ cells was strongly increased when analyzed 4 weeks after injury (7.1% ± 1.0% to 19.6% ± 0.8%). Under physiological, non-injury control conditions, no astrocytes were generated from OPCs, as described before.[9,12,19]

When leaving 30 days instead of 10 days between tamoxifen injection and SWI (Figure 1B), the proportion of astrocytes (GFAP$^+$tdT$^+$ and Pα^-) was further increased and twice as large (Figure 1G, 14.1% ± 2.3% vs. 7.1% ± 1.0%) at 1 wpi, whereas that of OPCs remained constant (Figure 1G, 19.6% ± 2.1% vs. 18.4% ± 3.8%). As previous studies suggested, longer time periods between tamoxifen injection and analysis lead to higher quantities of mature recombined oligodendrocytes in NG2-CreER^{T2} or PDGFRα-CreER^{T2} mice.[12,19,20] Hence, the higher number of newly generated astrocytes seems to correlate with the higher percentage of recombined tdT$^+$ oligodendrocytes. Thereby, these data provided the first hint that not only OPCs but also a subpopulation of MOLs might generate astrocytes after SWI. Additionally, in NG2-CreER^{T2} × R26-tdT × hGFAP-EGFP$_C$ triple transgenic mice (Figure S1), we observed numerous Pα^+tdT$^+$ OPCs (51.6% ± 2.5%) as well as a similar number of Pα^-tdT$^+$ cells (48.4% ± 3.0%) with activated hGFAP promoter activity at 1 wpi (EGFP$^+$). The latter cells exhibited roundish cell bodies and few fine processes, different from typical reactive astrocytes. After 4 weeks, we could identify tdT$^+$EGFP$^+$ cells, now immune-positive for GFAP (4 wpi, Figure S1).

Although these data, based on inducible Cre/*loxP* recombination and cell-specific EGFP expression, already suggested that not only OPCs but also oligodendrocytes might generate astrocytes, these experiments did not allow unequivocal discrimination of astrocytes derived from either OPCs or oligodendrocytes.

Astroglial differentiation from oligodendrocytes after acute trauma

To further test the origin of astrocytes directly from oligodendrocytes, we used GFAP-N-terminal (NCre) and proteolipid protein (PLP)-C-terminal (CCre) transgenic mice (split-Cre mice)[21] that permanently label the newly formed cells by Cre complementation (Figures 2A and S2). Under healthy conditions, however, no reporter gene was expressed in any cell, suggesting no simultaneous activation of GFAP and PLP promoters in the same cell. In addition, CCre expression could only be detected in MOLs (>95% of glutathione S-transferase π^+ [GSTπ^+], Figures 2B and 2C), but not in OPCs (Figures 2D and 2E), suggesting exclusive activation of PLP promoter in oligodendrocytes. After cortical injury, we found strong reporter expression indicating efficient split-Cre complementation (Figures 2G and S2), which was absent on the contralateral (cl) side (Figures 2F and S2). Simultaneously, we did not only detect GFAP expression but also observed a typical astroglial morphology in these cells (Figure 2I, GFAP$^+$tdT$^+$CCre$^+$) derived from PLP-CCre-expressing oligodendrocytes (Figure 2H, GSTπ^+). The generation of GFAP$^+$tdT$^+$ cells could also be observed in PLP-CreER^{T2} transgenic mice, but we were not able to detect other cells than astrocytes in GFAP-CreER^{T2} mice (Figure S3). These data provide strong genetic evidence that astrocytes can be generated from oligodendrocytes after SWI.

Quantification of recombined cells in split-Cre mice at the lesion site (LS) (Figures 2J–2L) showed an increase in the total number of recombined cells over time (Figure 2L). However, the ratios between the recombined glial cell types did not change during the time period of analysis (Figure 2M). The astrocytes represented the majority of recombined cells (Figures 2J and 2M). The remaining cells were mainly oligodendrocytes or OPCs (Figures 2J, 2K, and 2M) at equal amounts. These split-Cre data suggest that oligodendrocyte-derived recombined cells can become astrocytes within 4 weeks.

To investigate whether the injury-evoked oligodendrocyte-derived astrocytes further proliferate, we performed a BrdU-assay in split-Cre mice (Figure 2A) with immunostaining employing markers of OPCs, oligodendrocytes, and astrocytes. About 70% of the recombined cells were BrdU$^+$ (71.7% ± 7.8%) and a majority of them were astrocytes (Figures 2N and 2O, GFAP$^+$BrdU$^+$reporter$^+$/BrdU$^+$reporter$^+$, 80.6% ± 2.3%), strongly suggesting that similar to *bona fide* reactive astrocytes, oligodendrocyte-derived astrocytes proliferate in response to injuries. In addition, oligodendrocyte-derived astrocytes showed typical astroglial phenotypes, functionally by gap junctional coupling with adjacent cells, as shown by biocytin-labeling after cell loading during patch-clamp recording,[22] and morphologically by their endfeet contacting blood vessels (asterisk

Developmental Cell
Article

CellPress

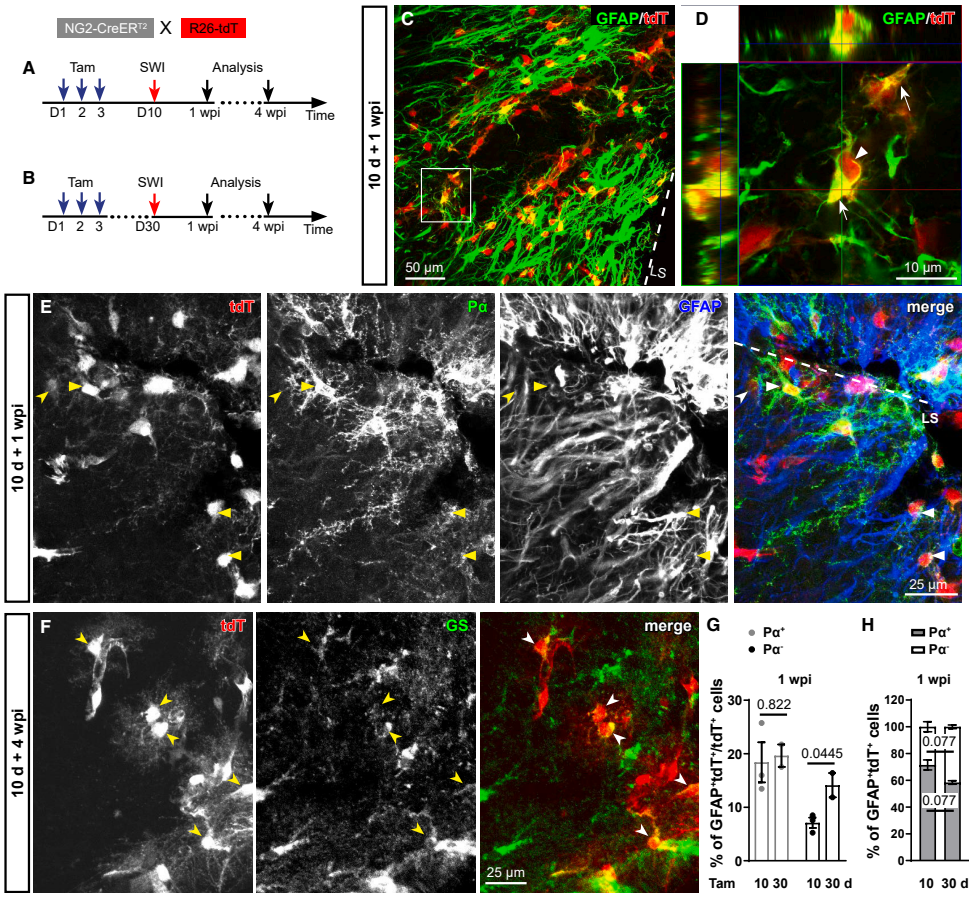

Figure 1. Oligodendrocyte lineage cells give rise to astrocytes after stab wound injury (SWI)

(A and B) Experimental schemes.

(C) Intensive GFAP expression in recombined cells in NG2-CreER^{T2} mice.

(D) Orthogonal projection of a GFAP-expressing recombined cell.

(E) GFAP expression of OPCs (Pα^+tdT$^+$, triangles) and astrocytes (Pα^-tdT$^+$, arrowheads) adjacent to the injury.

(F) 4 weeks after SWI, GS$^+$tdT$^+$ astrocytes (arrowheads) could still be detected adjacent to the lesion.

(G) Increased number of GFAP$^+$ recombined astrocytes 1 wpi after a 30-day period left for gene recombination compared with a 10-day period (n = 3 [10 days] and 2 mice [30 days], unpaired t test).

(H) Quantification of OPCs (Pα^+) and astrocytes (Pα^-) in the total GFAP$^+$tdT$^+$ cells 1 wpi (n = 3 [10 days] and 2 mice [30 days], unpaired t test). Abbreviation: LS, lesion site.

See also Figure S1.

in Figures 2P and 2Q). Therefore, all these data strongly suggest that oligodendrocyte-derived astrocytes are *bona fide* astrocytes.

In split-Cre mice, we detected recombined cells distributed in a cortical layer-dependent gradient with the highest number of newly generated astrocytes in the upper cortical layers and less toward the corpus callosum (Figure S2; Table S1). In contrast, newly generated oligodendrocytes were mainly observed in the deeper cortical layers next to the corpus callosum but less in the upper layers closer to the pia, displaying a similar distribution pattern as recombined oligodendrocytes in non-lesioned NG2-CreER^{T2} mice. These results indicate that

CellPress
Developmental Cell
Article

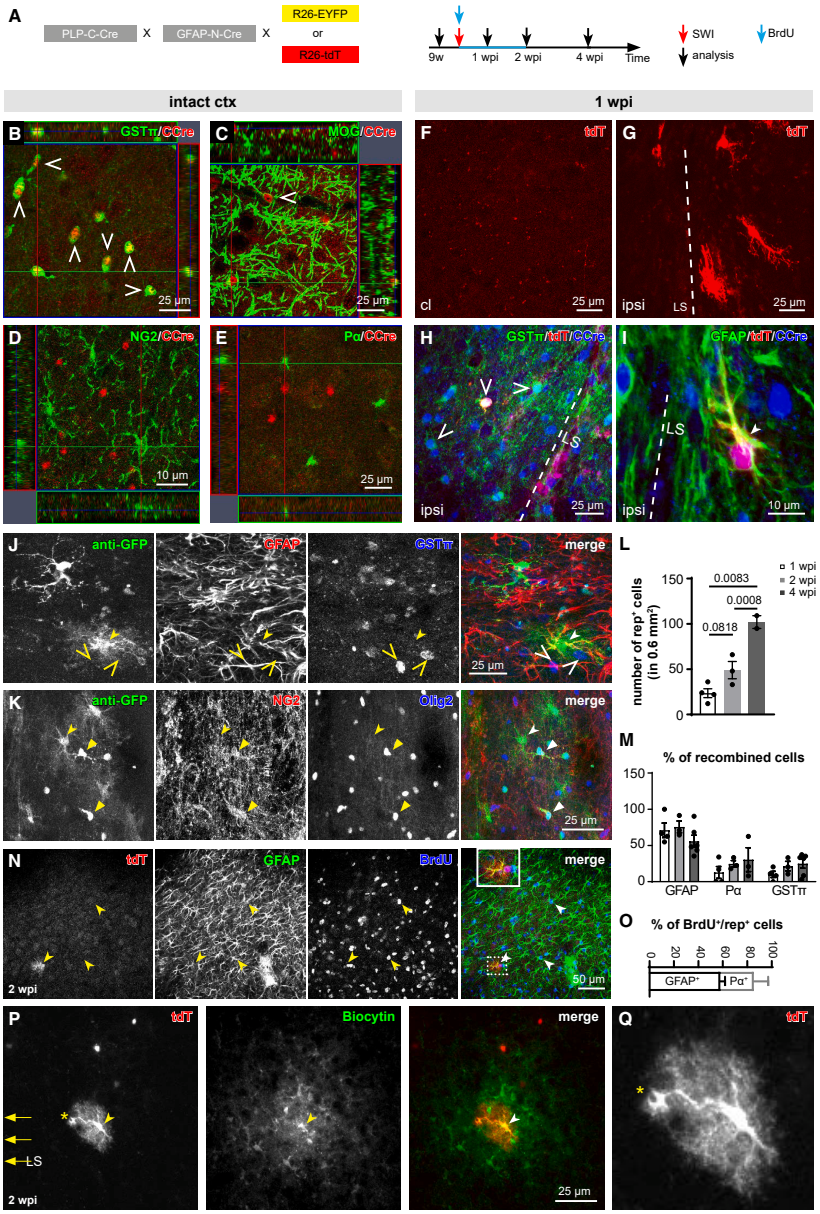

(legend on next page)

Developmental Cell
Article

CellPress

intrinsic properties of local niches appear unaffected by lesion size or transgenic mouse model and that oligodendroglial differentiation is preferred in the area near the corpus callosum (Figure S2; Table S1).

Injured oligodendrocytes generate a plastic cell type distinct from OPCs

Since the split-Cre fate mapping provided genetic evidence only for the endpoint of astrocyte generation from injured oligodendrocytes, we asked whether we could detect a transitional stage where oligodendrocytes activate astroglial genes. To answer this question, we analyzed single-cell RNA sequencing (scRNA-seq) data obtained from wild-type animals at 3 and 5 dpi of SWI[23] (Figures 3A and 3B). The clusters of OPCs and MOLs were clearly separated from each other (Figures 3C and 3D). Besides OPCs, a subset of the MOL indeed expressed astroglial genes (Figure 3E). This population was higher at 5 dpi than at 3 dpi (Figure 3F; Table S2, 31.3% vs. 19.5%). However, we could not detect this population of cells with both MOL and astroglial transcripts to identify them in wild-type mice.

To characterize cells at this transitional stage toward the generation of astrocytes, we took advantage of double fluorescent PLP-DsRed1/hGFAP-EGFP$_A$ mice (Figure 4A). The transitional stage was observed based on the simultaneous expression of DsRed1 and EGFP, indicating coincident activity of PLP and GFAP promoters. These transitional cells (with overlapping astro- and oligodendroglial transcriptomes) were termed AO cells. Indeed, directly adjacent to the LS intensive astro- and oligodendroglial promoter activation could be observed (Figure 4A, at 13 dpi) and numerous AO cells could be identified already at 3 dpi (Figure 4C, asterisks). Such fluorescently labeled cells, however, were never detected in the intact cortex (Figure 4B). AO cells displayed a rather simple morphology (diameter around 10 μm) with few processes (Figure 4D, arrows) and DsRed1 protein aggregates at all observed time points between 3 and 14 dpi. Such aggregates are a characteristic property of many reef coral fluorescent proteins such as DsRed1 indicating a long-term expression.[24] Here, these DsRed1 aggregates imply a start of expression prior to the injury, i.e., in uninjured PLP-DsRed1-positive oligodendrocytes. In a volume of 2.4×10^{-2} mm^3 at the LS, about 50 AO cells were found (21 cells/1×10^{-2} mm^3). Please note, only a minority (23.5%) of all putative AO cells with coincident promoter activity could be recognized by simultaneous expression of EGFP and DsRed1 due to the limited penetrance of the transgenes (only 42.7% of S100B$^+$ astrocytes express the GFAP-EGFP and 55.1% of GSTπ^+ oligodendrocytes express the PLP-DsRed1 transgenes, Figure S4), whereas only few OPCs express DsRed1 either ipsilateral (il) or cl (2.1% and 1.7%, respectively, Figure S4). As expected, AO cells were positive for oligodendrocyte lineage markers (Figure 4E, Sox10, 96% ± 3%; Figure S5, Olig2, 93% ± 2%). We could also observe numerous AO cells expressing the MOL marker myelin regulatory factor (MyRF) and GSTπ (Figures 4F and 4G). However, AO cells did not express the markers of astrocytes (Camsap1 or GFAP, Figures 4H and S5, respectively), stem cells (Figure 4I, Sox2), OPCs (Pα), neurons (NeuN), or microglia (Iba1) (Figure S5). These data indicate that AO cells belong to the oligodendrocyte lineage but are distinct from OPCs as well as from stem cells or astrocytes.

To further confirm the oligodendroglial properties of AO cells, we used a complementary approach by analyzing double transgenic PLP-EGFP$_{mem}$/GFAP-mRFP1 mice (Figure 4J). Hence, here membrane-bound EGFP labels oligodendrocytes, whereas the red mRFP1 is expressed in astrocytes under physiological conditions (Figure 4K). In these PLP-EGFP$_{mem}$ mice, all EGFP-expressing cells are MOLs (Figure S4, 100%, GSTπ^+). From 2 dpi on, similar to PLP-DsRed1/GFAP-EGFP mice, we observed double-labeled AO cells expressing EGFP and mRFP1 (Figures 4L and 4M, asterisk/arrows). Similar to DsRed1 also its mutant form mRFP1 frequently forms aggregates after longer expression periods. This was very apparent in the adjacent astrocytes (Figures 4L). In contrast, a uniform distribution of cytosolic mRFP1 was found in AO cells, thereby indicating a short time of GFAP promoter activity. In PLP-EGFP$_{mem}$/GFAP-mRFP1 mice, we could detect several marker proteins for myelin in AO cells with EGFP expression in the membrane (Figures 4N–4P) but never the OPC marker Pα (Figure 4Q). Despite transgenic human hGFAP promoter activity in AO cells, the protein itself, encoded by the endogenous mouse gene, could never be detected (Figure 4R). Since the GFAP gene is very sensitive to pathological alterations, we asked whether another astroglia-specific gene, the glutamate/aspartate transporter (GLAST), would also be activated in AO cells, as suggested by the scRNA-seq results (Figure 3). For that purpose, we crossbred PLP-EGFP$_{mem}$, mice with the astrocyte-specific knockin mouse GLAST-CreER^{T2} × R26-tdT and induced recombination directly after the SWI (Figure S3). We also observed tdT$^+$ and EGFP$^+$ cells at the LS. Since these cells were also immuno-positive for GFAP, we regarded them as astrocytes generated from AO cells as well.

These results further confirm our notion that AO cells originate from oligodendrocytes, are different from OPCs, can activate

Figure 2. Split-Cre complementation uncovers the potential of mature oligodendrocytes to generate astrocytes after SWI

(A) Scheme of the transgene and experimental schedule of N, O.

(B–E) Split-Cre C-terminal fragment (CCre) was exclusively detectable in mature oligodendrocytes (GSTπ, MOG) in the intact cortex (B and C), but not in OPCs (NG2, Pα; D and E).

(F and G) No recombination was observed in the intact cortex (F) but adjacent to the lesion (G).

(H and I) CCre expression in recombined oligodendrocytes (GSTπ, H) and astrocytes (GFAP, I) at the lesion 1 wpi.

(J and K) Recombined cells could give rise to astrocytes (GFAP$^+$), oligodendrocytes (GSTπ^+), and OPCs (NG2$^+$).

(L and M) Although the number of total recombined cells increased with time (1, 2, and 4 wpi) at the lesion site (0.6 mm^{-2}) (L), the proportion of recombined cell types did not change (M). (L: n = 4 [1 wpi], 3 [2 wpi], and 2 mice [4 wpi], one-way ANOVA Tukey's comparisons test; M: n = 4 [1 wpi], 3 [2 wpi], and 3–6 mice [4 wpi].)

(N and O) BrdU was mainly incorporated by recombined astrocytes (N), indicating their proliferative capacity with few proliferating OPCs (O) (n = 3 mice).

(P) A biocytin-filled individual tdT$^+$ astrocyte revealed coupling within the network of protoplasmic astrocytes in the lesion side.

Abbreviations are as follows: cl, contralateral; il, ipsilateral; LS, lesion site.

See also Figure S2 and Table S1.

CellPress
Developmental Cell
Article

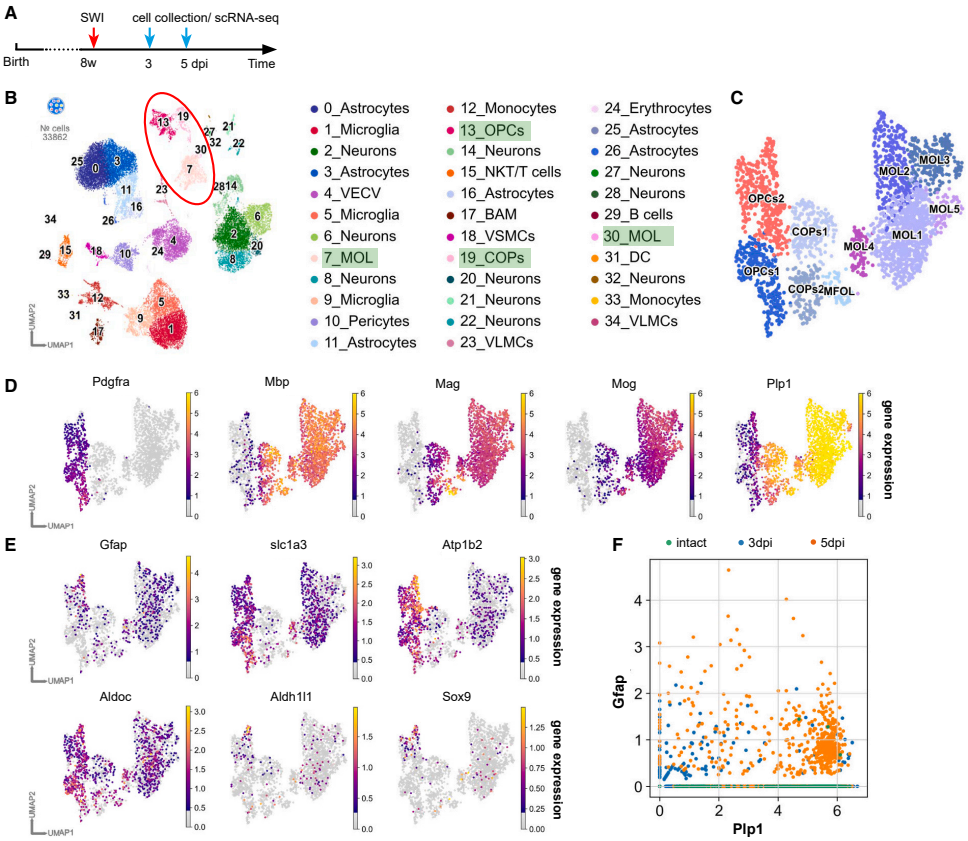

Figure 3. Oligodendrocytes activate astroglial genes after acute brain injuries

(A) Scheme of experiment.[23]

(B) UMAP plot depicting cell clusters including OPCs and MOLs.

(C) UMAP plot illustrating subclustered oligodendrocyte lineage cells.

(D) Differentiation of OPCs an MOLs based on the expression of OL lineage markers.

(E) Expression of astroglial genes in MOLs, including *Gfap*, *slc1a3*, *Atp1b2*, *Aldoc*, *Aldh1l1*, and *Sox9*.

(F) Increase of MOLs expressing *Gfap* and *Plp1* concomitantly at 3 and 5 dpi with no expression in intact tissue.

Abbreviations are as follows: COP, committed oligodendrocyte precursor; MOLs, mature oligodendrocytes; UMAP, uniform manifold approximation and projection.

See also Table S2.

astrocyte-specific genes, and can change their fate to the astroglial lineage.

Whole-cell membrane currents of AO cells are highly variable

To characterize the physiological properties of AO cells, in addition to marker protein expression, we performed whole-cell patch-clamp recordings and tested for the patterns of membrane currents that are characteristic of OPCs, oligodendrocytes, and astrocytes. After SWI of PLP-DsRed1/GFAP-EGFP mice at P20 (Figure 5A), AO cells (Figure 5B) were recorded with a KCl-based intracellular solution and held at −80 mV. Whole-cell membrane currents of AO cells were dominated by K^+ currents, were dominated by the lack of voltage-gated Na^+ currents, and were, thereby, very typical for glia. However, individual AO cells displayed a high variability with respect to the presence of voltage-gated, outwardly rectifying K^+ currents, symmetrical non-rectifying or inwardly rectifying K^+ currents

Developmental Cell
Article

CellPress

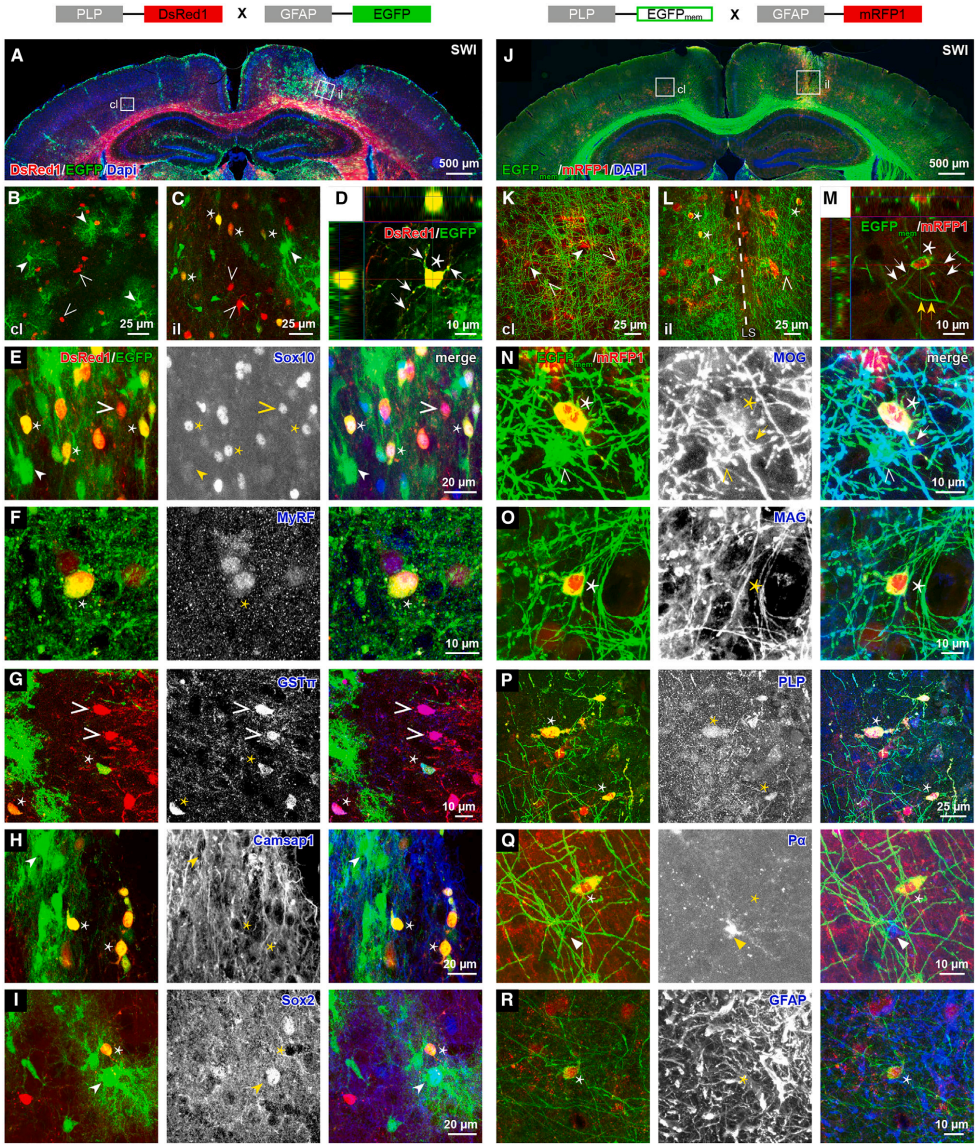

Figure 4. Acute injuries induce a transitional stage of oligodendrocyte lineage cells, AO cells

(A and J) Intensive glial reaction close to the lesion site (SWI) in cortex of PLP-DsRed1/GFAP-EGFP$_A$ (13 dpi) and PLP-EGFP$_{mem}$/GFAP-mRFP1 (7 dpi) mice.
(B–D) Magnified views of contralateral (B) and ipsilateral tissue (C) highlights DsRed$^+$/EGFP$^+$ AO cells (asterisks) (D).
(K–M) Magnified views of contralateral (K) and ipsilateral tissue (L) highlights EGFP$_{mem}^+$mRFP1$^+$ AO cells (asterisks) and thin processes (white arrows) (M). Yellow arrows indicate myelin of adjacent oligodendrocytes.

(legend continued on next page)

CellPress

Developmental Cell
Article

(Figures 5C–5F). Furthermore, we compared whole-cell currents and their membrane properties in identified OPCs (NG2-EYFP), oligodendrocytes (PLP-DsRed1), and astrocytes (GFAP-EGFP) under physiological, non-injury conditions (without SWI, cl) and in their activated state after SWI (il). AO cells typically exhibited a slightly more positive resting membrane potential (−67.8 ± 4.2 mV) than OPCs (Figure 5G, −79.5 ± 1.4 mV [cl] and −81.1 ± 1.6 mV [il]). AO cells had a higher membrane resistance (R_m = 92 ± 10 MΩ) than astrocytes (Figure 5H, R_m = 33 ± 2 MΩ [cl] and R_m = 68 ± 9 MΩ [il]), but not than oligodendrocytes (R_m = 60 ± 5 MΩ [cl] and R_m = 95 ± 8 MΩ [il]) or OPCs (R_m = 63 ± 6 MΩ [cl] and R_m = 91 ± 10 MΩ [il]).

The high variability of electrophysiological properties among individual AO cells did not allow them to be classified as oligodendrocytes, astrocytes, or OPCs but rather suggested a unique class with transitional properties. Indeed, a similar variability we observed at the level of transgene expression. AO cells in the lesioned area displayed a broad and variable range of EGFP and DsRed1 levels (i.e., EGFP/DsRed1 ratio). Cells with high DsRed1 expression were still assigned to the oligodendrocyte lineage, whereas higher EGFP expression indicated a rather astroglial identity (Figures 5I–5L). When AO cells were formed from oligodendrocytes, the transgenic GFAP promoter would be activated, and the PLP promoter activity (the endogenous as well as the transgenic) would decrease; subsequently, transcription would stop. Since the half-life of DsRed1 is 4.6 days,[25] DsRed1 was still detectable in AO cells when the PLP promoter activity had ceased (Figure 5M).

These results indicate that AO cells are cells in transition, thereby explaining their variability of membrane properties and transgene expression levels.

In vivo 2P-LSM visualizes the conversion of oligodendrocytes to astrocytes directly

To directly monitor the change from oligodendrocyte to astrocyte, we performed *in vivo* two-photon laser scanning microscopy (2P-LSM). In PLP-DsRed1/GFAP-EGFP mice, we could detect AO cells already at 3 dpi (Figures 6A–6C, cells 2 and 3) remaining in this stage for the next days. We show exemplarily the tracing of a single oligodendrocyte (Figure 6A, DsRed1$^+$ EGFP$^-$, cell 1, open triangle) with no EGFP-expression 3 dpi with DsRed1 aggregates in its processes (Figure 6B, arrows)[24] turning into an AO cell (DsRed1$^+$EGFP$^+$) 5 dpi (Figure 6B, cell 1). At 6 dpi, cell 1 stopped DsRed1 expression but continued EGFP expression at 6 dpi (Figure 6C, arrowhead). The other two AO cells (cells 2 and 3) showed an increased level of EGFP (Figure 6B, 5 dpi) and a low level of DsRed1, recognizable by a higher EGFP fluorescence compared with DsRed1 at 6 dpi (Figure 6C; Video S1). Repeated observation of AO cells showed their potential to generate astrocytes. However, we could also observe AO cells (one example given in Figure S6, 6 dpi, asterisk) switching off the GFAP-EGFP transgene and turning back into a DsRed1$^+$ cell, i.e., an oligodendrocyte, observed after 4 wpi (Figure S6, open triangle). We did never observe an EGFP-expressing astrocyte that activated the PLP-DsRed1 transgene.

These observations could be confirmed in a second transgenic mouse line, in PLP-EGFP$_{mem}$/GFAP-mRFP1 mice. An oligodendrocyte (Figure 6D, EGFP$^+$mRFP1$^-$, open triangle) started to express mRFP1 at 2 dpi (Figure 6E, asterisk) and expressed both fluorescent proteins still at 30 dpi (Figures 6F–6H, asterisks). However, only mRFP1 expression remained at 50 dpi (Figure 6I, arrowhead; Video S2). We also observed oligodendrocytes becoming AO cells and going back to EGFP$_{mem}^+$ oligodendrocytes (see example in Figure S6). These results were affected by the longer half-life of membrane-bound EGFP in comparison with the cytosolic EGFP, like other membrane-confined proteins.[26] We never found mRFP$^+$ astrocytes that activated the PLP-EGFP$_{mem}$ gene. In addition, we never observed hints for phagocytosis in astrocytes neither in oligodendrocytes nor in the AO cells of both mouse lines. In total, we could follow 38 oligodendrocytes (of 120 in n = 17 mice) to convert via the AO cells into either astrocytes or become oligodendrocytes again (Figure 6J). In contrast to split-Cre mice with 67% of AO cells becoming astrocytes, by *in vivo* 2P-LSM we observed only 1.7% (2 cells) becoming transgene-expressing astrocytes. We explain this small number by the fact that not all astrocytes express the hGFAP-EGFP transgene. In addition, several AO cells could not be followed over a longer period of time due to the loss of cranial window clarity, impaired light transmission, and increased light scattering of the developing glial scar.

The long-term, repeated *in vivo* imaging data from two distinct transgenic mouse lines confirm that transitional AO cells originate from oligodendrocytes and either stay in the oligodendrocyte lineage or convert to astrocytes.

Generation and differentiation of AO cells is influenced by cytokines

To test how common the formation of AO cells is, we performed two other injury models: pial vessel disruption (PVD, representing a small hemorrhagic, arterial vessel stroke), and transient middle cerebral artery occlusion (MCAO, representing a reversible large vessel stroke). We observed AO cells adjacent to LSs of both insults (Figure S7, 1 week after PVD and 3 days after MCAO). Therefore, we concluded that acute cortical injuries in general induce the formation of AO cells. A common feature of the three injury models is the associated disruption of the blood vessel, which could result in the elevation of various cytokines and inflammatory factors at the LS. The endogenous, CNS-based expression of cytokine mRNAs was tested by quantitative real-time PCR (qPCR) at different time points after the injury, with GFAP gene activity as an internal indicator of glial activation (Figure 7A). However, indeed, the endogenous expression of tumor necrosis factor α (TNFα), interleukin-6 (IL-6) (Figure 7A), leukemia inhibitory factor (LIF), bone morphogenetic protein 4 (BMP4),

(E–I) EGFP$^+$/DsRed1$^+$ AO cells expressed the oligodendrocyte lineage marker Sox10 (E), MyRF (F), and GSTπ (G) but neither the astrocyte lineage marker Camsap1 (H) nor the stem cell marker Sox2 (I).
(N–R) EGFP$_{mem}^+$mRFP1$^+$ AO cells expressed the mature oligodendrocyte markers MOG (N), MAG (O), and PLP (P), but neither the OPC marker Pα (Q), nor the astrocyte marker GFAP (R).
See also Figure S5.

Developmental Cell
Article

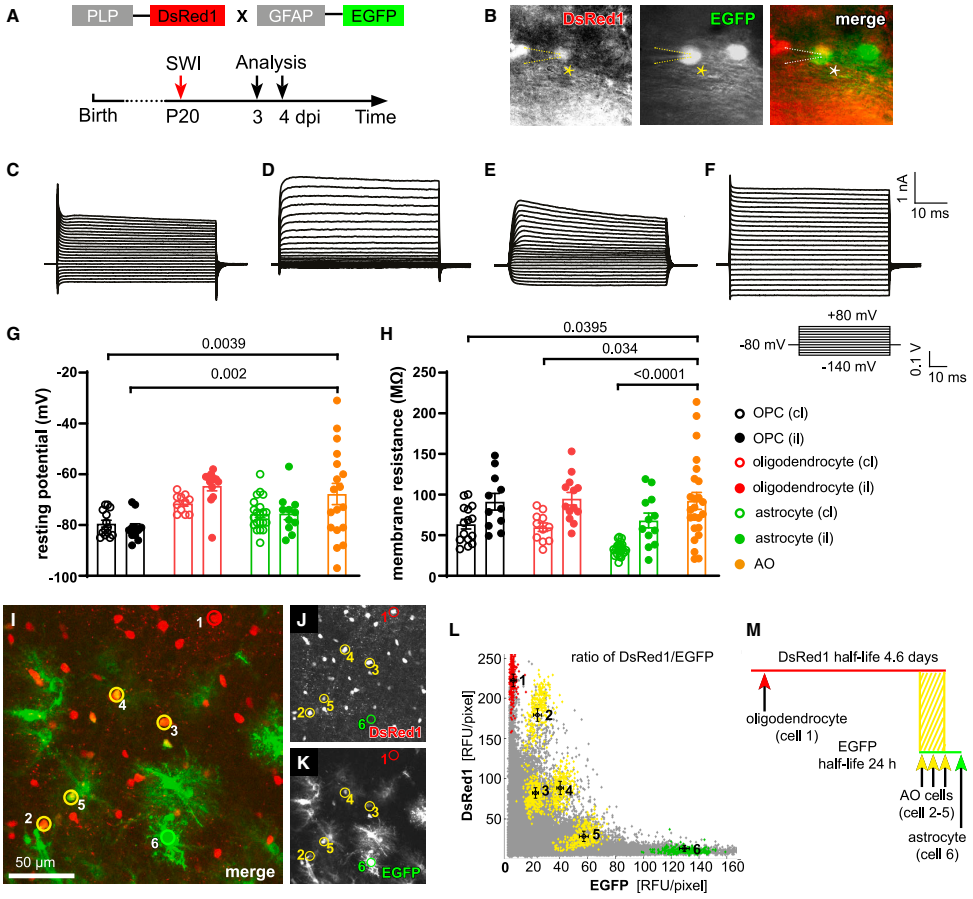

Figure 5. AO cells display variable electrophysiological properties and transgene expression

(A) Time schedule of experiment.

(B) Patched AO cell (EGFP$^+$DsRed1$^+$, asterisk) identified next to astrocyte (EGFP$^+$DsRed1$^-$, arrowhead) and oligodendrocyte (EGFP$^-$DsRed1$^+$, open triangle).

(C–F) AO cells with different membrane properties.

(G) Large variability among AO cells compared with other glial cell types in contralateral and ipsilateral issue (n = 11–21 cells from N = 4–6 mice, Ordinary one-way ANOVA Dunnett's multiple comparisons test).

(H) Broad variability in AO cells with differences to astrocytes of the contralateral side, but not to activated glial cells at the injury side (n = 11–24 cells from N = 4–6 mice, Ordinary one-way ANOVA Dunnett's multiple comparisons test).

(I–L) Quantification of different expression ratios of DsRed1/EGFP in AO cells ranging from orange (DsRed1 > EGFP) and yellow (DsRed1 = EGFP) to green (DsRed1 < EGFP) (cells 2–5) fluorescence. Oligodendrocytes (cell 1) and astrocytes (cell 6) serve as controls.

(M) Temporal overlap of fluorescent protein expression in glial cells as suggested by their half-life. PLP-promoter controlled DsRed1 (with half-life of ~4.6 days) is still present when acute injuries activate EGFP expression in AO cells (half-life ~24 h).[25]

and ciliary neurotrophic factor (CNTF) was upregulated after SWI, however, at different timescales (Figure S7).

BMP4 and IL-6 induce neural stem cells and OPCs to differentiate into astrocytes rather than oligodendrocytes,[27,28] whereas LIF facilitates oligodendrocyte differentiation.[29] To investigate whether these cytokines could regulate the fate commitment of oligodendrocytes *in vivo*, we investigated the number of AO cells in PLP-DsRed1/GFAP-EGFP mice after cortical cytokine injection. AO cell numbers increased after IL-6 injection (Figures 7B and 7C, 1.98- ± 0.04-fold), whereas the intracortical injection of IL-6 neutralizing antibody inhibited AO cell formation at 3 and 7 dpi (Figures 7D and 7E). These results strongly suggested that

CellPress
Developmental Cell
Article

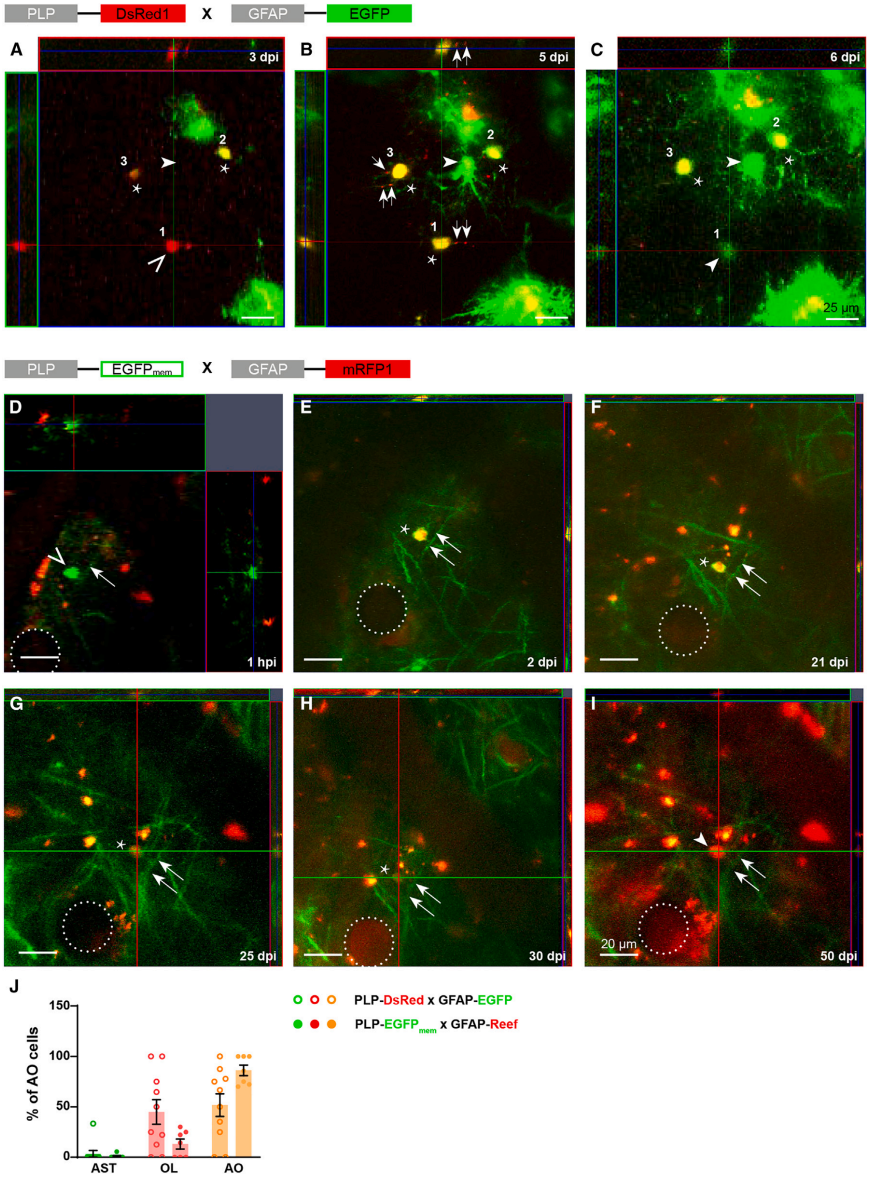

Figure 6. *In vivo* 2P-LSM visualizes formation of AO cells from mature oligodendrocytes and their differentiation fate

(A–C) *In vivo* imaging of AO cells in PLP-DsRed1/GFAP-EGFP mice. Oligodendrocyte (1, open triangle) and AO cells (2, 3, asterisks) detected 3 days after SWI (A). Visualization of oligodendrocyte-derived AO cell (1, asterisk) with two AO cells (2, 3, asterisk) staying at the AO cell stage with varied DsRed1/EGFP ratios (B). Note the appearance of an EGFP-expressing astrocyte (arrowhead in B). AO cells (1, 2, 3) downregulated DsRed1 expression with a single-cell expressing EGFP only (1, arrowhead) 6 dpi (C).

(legend continued on next page)

Developmental Cell
Article

IL-6 facilitates AO cell generation. In contrast, LIF reduced AO cell numbers (Figure 7C, 0.6- ± 0.11-fold) compared with saline (SA). BMP4 did not show any effect on AO cell formation (Figure 7C). Please note that already the saline injection is a mild SWI per se.

Microglia respond immediately to pathological stimuli and release cytokines including TNFα that also regulates IL-6 expression. Minocycline (Mino) inhibits microglial activation and polarization toward the pro-inflammatory phenotype,[30] concomitantly TNFα signaling and IL-6 expression are repressed in microglia.[31,32] To investigate whether microglia-derived IL-6 is the major trigger for AO cell formation, we inhibited microglial early activation by the intraperitoneal injection of Mino after SWI from day 1 for three consecutive days and analyzed AO cell density at 7 dpi (Figures 7F and 7G). Indeed, Mino treatment diminished AO cell formation induced by SWI, thereby substantiating that the release of IL-6 by microglia on acute brain injuries triggers AO cell formation (Figure 7H, 20.1 ± 5.6 vs. 7.4 ± 1.8, n = 9 [SA] and n = 10 [Mino]). A further comparison of cl and il TNFα and IL-6 mRNA levels by qPCR clearly showed that Mino reduces il TNFα and IL-6 (Figure 7I).

In conclusion, our data suggest that a subset of oligodendrocytes, triggered by IL-6 released by pro-inflammatory microglia, become multipotent transitional cells that can generate astrocytes in acute injuries.

DISCUSSION

Oligodendrocytes regain a plastic phenotype after acute brain injuries

Oligodendrocytes are commonly regarded as mature, non-proliferating, and terminally differentiated cells. However, over the last decades, accumulating evidence suggests a more plastic cell fate of oligodendrocytes. Since these data were mainly obtained by studies of lower vertebrates, in human tumor tissue or the peripheral nervous system,[4,33–35] their relevance for the understanding of oligodendrocytes in the adult mammalian CNS remained limited. In goldfish, for example, oligodendrocytes dedifferentiate to bipolar cells with retracted myelinating processes upon retinal axon degeneration,[5] morphologically similar to AO cells. However, also in mammals, injuries can disconnect myelinating processes from oligodendroglial cell bodies. In *ex vivo* preparations of the mouse optic nerve, oxygen-glucose deprivation (mimicking a stroke injury) induced a loss of myelinated oligodendrocyte processes.[36] In the periphery, myelinating Schwann cells dedifferentiate after nerve injuries. They rapidly downregulate myelin proteins (peripheral membrane protein 22, myelin basic protein (MBP), and periaxin) and subsequently express marker proteins for non-myelinating Schwann cells such as GFAP.[33,37] In humans, some oligodendroglioma cells were found to express GFAP.[34,35] Such gliofibrillary (GFAP-expressing) oligodendrocytes were also described as transitional cells exhibiting astroglial and oligodendroglial properties[38–40] with the ability to differentiate into astrocytes. The latest evidence was provided by combining MCAO and MBP-Cre/*loxP* fate mapping. Epigenetic characterization of the *gfap* promoter region in MBP-Cre reporter-labeled oligodendrocytes described a putative mechanism of how to generate a cell with astroglial properties.[8] Additionally, RNA-seq studies have indicated subtypes of oligodendrocytes in the healthy CNS as well as in the spinal cord after injury.[41,42] Here, we combined extended neurogenetic approaches and direct *in vivo* visualization of various stages of an injury-evoked conversion of oligodendrocytes to astrocytes and could highlight the enormous plasticity of this terminally differentiated cells dormant in the mammalian CNS.

AO cells are transitional precursor cells

The morphology of AO cells resembles that of bipolar O-2A progenitor cells displaying round somata and few, fine processes, as described in the 1980s.[43] O-2A cells belong to the oligodendrocyte lineage and give rise to astrocytes and oligodendrocytes *in vitro* dependent on the presence of fetal calf serum or BMPs.[44,45] Similarly, the AO cells described here differentiate into both cell types as well but *in vivo*, and their fate is also modulated by local cues, provided by the complexity of the cortical niche.

Although O-2A cells (subsequently characterized as OPCs) express NG2 and Pα,[46] AO cells in this study were always negative for OPC or stem cell markers. In the GFAP-EGFP mouse lines A (GFEA) and C (GFEC), we identified about 15% and 1% of EGFP$^+$ cells as OPCs by their expression of Pα, respectively (shown in Figure S4E). In the PLP-DsRed1 line, we characterized about 1.8% of DsRed1-expressing cells as OPCs. However, AO cells never expressed Pα but MOL markers GSTπ and MyRF. Therefore, our results suggest that GFAP-EGFP$^+$/PLP-DsRed1$^+$ cells (i.e., AO cells) were derived from oligodendrocytes rather than from OPCs and that these AO cells are distinct from OPCs. Electrophysiological properties of AO cells such as membrane resistance, resting membrane potential, and K^+ current expression were quite variable, thereby further stressing a transitional status. This is also indicated by the variable level of PLP and GFAP promoter activities, i.e., DsRed1/EGFP expression ratios.

The *in vivo* 2P imaging visualizes that AO cells originate from oligodendrocytes. This observation was further substantiated by the analysis of DsRed1 expression. After prolonged promoter activity and, hence, long-term expression, the reef coral fluorescent protein DsRed1 precipitates in the cytosol and forms fluorescent aggregates.[24] Since we found such DsRed1 deposits in processes of newly generated AO cells of PLP-DsRed1/GFAP-EGFP mice after injury, the DsRed1 expression might have commenced in oligodendrocytes before the injury. The related protein mRFP1

(D–I) *In vivo* imaging of AO cells in PLP-EGFP$_{mem}$/GFAP-mRFP1 mice. An oligodendrocyte (open triangle) detected 1 hpi (D), started to express mRFP1 (asterisks) from 2 dpi till 30 dpi (E–G), with variable EGFP/mRFP1 ratios. An AO cell became an astrocyte (mRFP1$^+$/EGFP$^-$) 50 dpi (I). Note that membrane-bound EGFP$_{mem}$ (arrows in D–I) was still detectable 50 dpi in a newly differentiated astrocyte characterized by long-term GFAP promoter activity.
(J) AO cells developed into astrocytes or oligodendrocytes observed *in vivo*. Majority of the AO cells did not change their status at the end of the experiment (PLP-DsRed1 × GFAP-EGFP n = 10 mice, PLP-EGFPmem × GFAP-Reef n = 17 mice).
Abbreviation is as follows: hour post injury (hpi).
See also Figure S6.

CellPress
Developmental Cell
Article

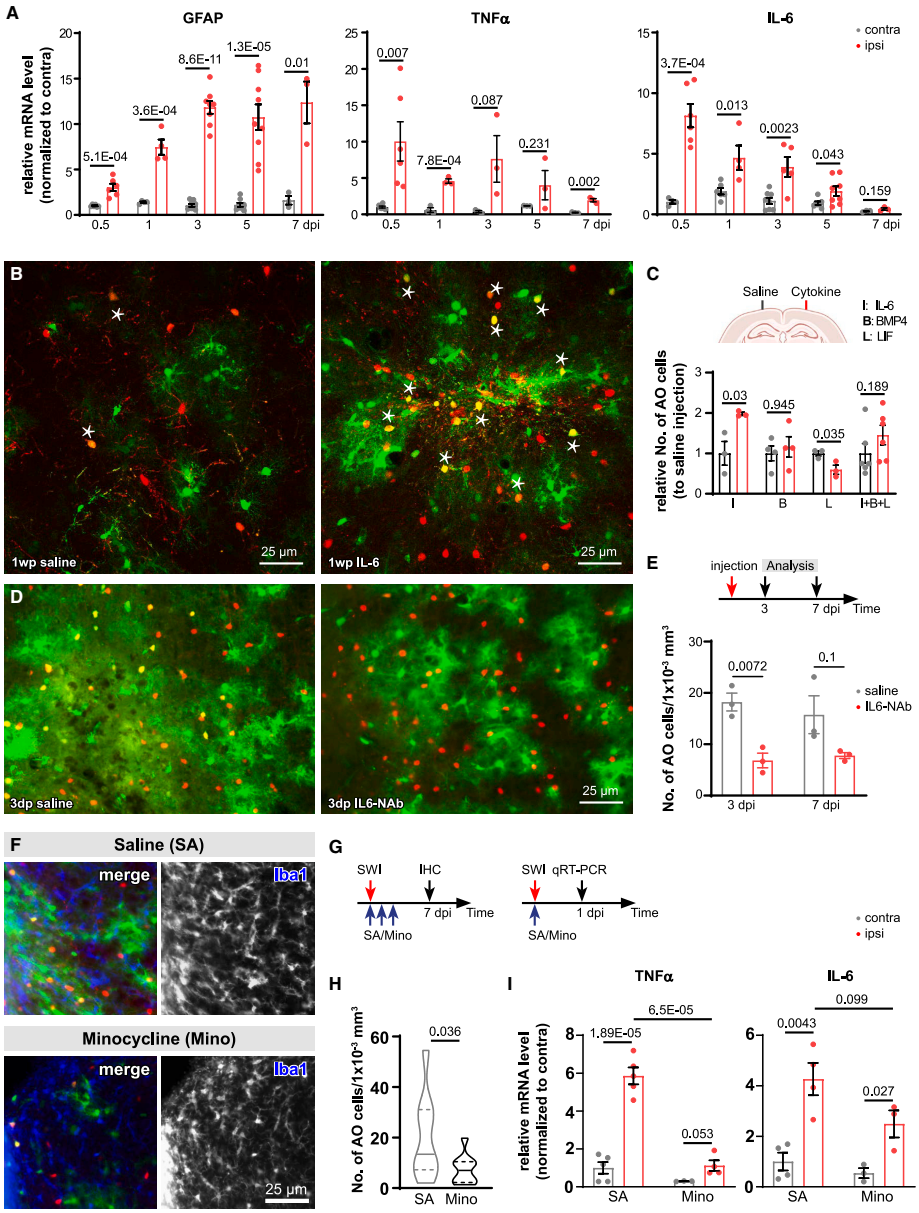

Figure 7. Microglia-derived cytokines modulate AO cell activation after SWI

(A) GFAP and cytokines upregulation after SWI at the lesion site (n = 4–6 mice [0.5 dpi], 3–6 mice [1 dpi], 3–9 mice [3 dpi], 3–9 mice [5 dpi], 3 mice [7 dpi], and multiple t tests).

(legend continued on next page)

Developmental Cell
Article

precipitates as well after prolonged expression. Since in PLP-EGFP$_{mem}$/GFAP-mRFP1, we observed a homogeneous distribution of mRFP1 (like any other soluble protein), this finding implies only a short period of GFAP promoter activity; hence, AO cells, formed from green fluorescent (membrane-bound EGFP) oligodendrocytes, activate the GFAP promoter but express mRFP1 only shortly. Our data demonstrate a continuous transformation of one cell type (oligodendrocyte) to another (astrocyte) with intermediate AO cells. Upon injury, AO cells are an additional transitional stage of glia-restricted precursor cells different from OPCs, representing another cellular component of oligodendroglial heterogeneity.[41]

Further identification of AO cell-specific markers will facilitate the characterization of these cells in the mouse and even in the human brain. So far, the AO cell was recognized mainly by double expressions of DsRed1 and EGFP, which only brings about 20% of the total potential cell population. Human brain organoids are self-organized three-dimensional cultures recapitulating accurately many features of human brains at early developing stages. This powerful tool provides a human cell-based platform to study human brain evolution, development, and disorders. Therefore, using iPSC-derived organoids transfected with PLP-DsRed1 and GFAP-EGFP could become a tool for the further analysis of AO cells as well as studying these cells in the human brain context.

Influence of cytokines on AO cell formation and its subsequent differentiation fate

In the injured CNS, the level of cytokines or growth factors is modulated by different mechanisms. Acute brain traumata (SWI, PVD, or MCAO) are accompanied by the disruptions of blood vessels and a subsequent influx of different peptides or factors from the peripheral blood. However, also, the stimulated activity of endogenous genes can contribute to enhanced the level of various cytokines as described previously[47,48] and shown here. Microglia respond immediately to pathological stimuli and polarize into a pro-inflammatory phenotype, which activates TNFα signaling and IL-6 expression. IL-6 can activate the GFAP promoter[49] as shown by increased AO cell numbers after IL-6 injection. In contrast, LIF[50] keeps cells in the oligodendrocyte lineage,[29,51] in line with our observation that LIF injection inhibits the formation of AO cells. However, *in vitro* experiments suggest an astrogliogenic function for LIF.[8,52] Although the acute injection of LIF inhibits AO cell formation, injury-evoked LIF might be responsible for astrocyte formation of AO cells. The same might be true for BMP4, which has been suggested to induce astroglial differentiation from OPCs or oligodendrocytes.[53,54] Single BMP4 injections did not increase AO cell numbers, in contrast to a combined injection with IL-6 and LIF, which indicates the BMP4 function in inducing astrocyte differentiation, as shown for precursor cells.[52] IL-6, LIF, and BMP4 act in a defined temporal pattern of cytokine activity in post-injury processes. IL-6 induces AO cell formation from oligodendrocytes and LIF and BMP4 might subsequently affect the astrocyte-specific differentiation. This temporal expression pattern of cytokines is tightly coupled to their local distribution within the cortical layers and in distance to the injury site, thereby forming transient differentiation niches.[9,16,55–57]

Abundance of astrocytes derived from oligodendrocytes

Previous studies suggested that cells of the oligodendrocyte lineage, mainly OPCs, could generate astrocytes after brain damage. However, how robust this process is remained controversial, attributable to the variety of animal models (transgenic mice and rats), lesion paradigms, duration of recombination after induction, or other methodologies.[13,15–17,19,58] For example, shorter time intervals left for recombination intervals (like 3–5 days after tamoxifen injection) preferentially results in more labeled OPCs rather than oligodendrocytes.[12] In some recent studies, about 5% and 5.7% GFAP$^+$reporter$^+$ astrocytes (of total recombined cells) could be found after SWI using Olig2-CreER^{T2} or NG2-Cre BAC transgenic mice.[16,17] In NG2-CreER^{T2} × R26-tdT mice, we observed a very reliable CreER^{T2} expression controlled from the endogenous NG2/cspg4 locus.[12] We detected a high percentage of GFAP$^+$tdT$^+$ cells (25.5% of total recombined cells). Of these, about 30% were astrocytes and about 70% were OPCs. We observed even more astrocytes (14.1% vs. 7.1%) when we analyzed mice with a higher percentage of recombined oligodendrocytes, which duplicate between 10 and 30 days post-tamoxifen injection in the cortex of P60 mice.[59] In all the various mouse lines of this study, we detected AO cells differentiation to astrocytes; however, the quantities of AO cell-derived astrocytes differed due to various degrees of transgenic modifications. In NG2-CreER^{T2} mice, all cells of the oligodendrocyte lineage including their putative progeny (AO cells, oligodendrocytes, and OPCs) were labeled, whereas in split-Cre mice (generated by non-homologous recombination), only AO cells and their progeny could be observed. Therefore, the 7.1% (1 wpi) labeled astrocytes from all recombined cells in NG2-CreER^{T2} mice appear small compared with split-Cre mice (68.1%, 1 wpi), but they are calculated from different reference points.

Heterogeneity of astrocytes

During injury-induced proliferation, the number of astrocytes increases by 10%–20%.[60,61] For split-Cre mice, we estimated the percentage of astrocytes derived from AO cells/oligodendrocytes to reach up to 5% (tdT$^+$GFAP$^+$ of the total GFAP$^+$ cells).

(B and C) AO cells formed at 1 week after IL-6 (B), BMP4, LIF, and BMP4/IL-6/LIF injection (C). Quantification of relative AO cell numbers (C) revealed distinct impact of cytokines on oligodendroglial plasticity (n = 3 mice [IL-6], 4 mice [BMP4], 3 mice [LIF], 6 mice [BMP4/IL-6/LIF], and two-sided unpaired t test).
(D and E) Intracortical administration of IL-6 neutralizing antibody (IL-6-Nab, D) inhibited AO cell formation at 3 and 7 dpi (n = 3 mice [3 dpi] and 3 mice [7 dpi], and two-sided unpaired t test, E).
(F–H) Inhibition of microglial activation with minocycline (Mino; F and G) inhibited AO cell formation at 7 dpi (n = 9 [SA] and 10 mice [Mino], and two-sided unpaired t test).
(I) Minocycline inhibited TNF-α and IL-6 mRNA upregulation in the ipsilateral side at 1 dpi (n = 4–5 mice [SA], n = 3–4 mice [Mino], and two-way ANOVA Tukey's multiple comparisons test).
See also Figure S7.

CellPress

Developmental Cell
Article

Obviously, astrocytes originating from oligodendrocytes constitute a significant portion of cells in the glial scar. Given the limited penetrance of the split-Cre transgenes, this number could even be higher.[21] Whether these astrocytes fulfill a specialized function during scar formation or perform more classical astroglial tasks (such as regulating extracellular ion and transmitter homeostasis or enhancing neuronal energy supply) remains to be determined. Recently, two different classes of astrocytes were described within a glial scar. Although A1 astrocytes were triggered by microglial cytokine release and became neurotoxic, A2 astrocytes started to release various growth factors and appeared to be neuroprotective.[62,63] Remembering the early *in vitro* work of Ffrench-Constant and Raff, it is very tempting to speculate that AO cell-derived astrocytes could comprise a major portion of the A2 astrocytes.[64] Local, environmental cues and controlled switching of cell lineages generate additional dimension of heterogeneity.[65] Indeed, astrocytes display unique profiles of gene expression and cell behavior after acute and chronic injuries.[66]

Targeting the plasticity of oligodendrocytes as well as the function of oligodendrocyte-derived astrocytes could become an exciting field to explore novel routes in treating acute brain trauma.

Limitations of the study

Using 2P-LSM, we showed the direct switch of oligodendrocytes into astrocytes. However, due to technical (clarity of cranial window) and ethical (3R regulation for animal experiments) reasons, the number of observed transitions was small compared with the more frequent incidence detected in split-Cre mice. However, with these imaging experiments, we provide additional *in vivo* evidence that oligodendrocytes can become transitional AO cells after acute injuries and give rise to astrocytes and oligodendrocytes. These transitional AO cells are characterized by transgenic protein expression, cell-specific marker expression, and electrophysiological properties. A further characterization of AO cells, i.e., taking advantage of further gene profiling of AO cells and subsequent genetic manipulation, will be an interesting approach to follow-up. The results from split-Cre mice showed that AO cells can also give rise to OPCs. At this point, we cannot rule out that the observed reporter$^+$ oligodendrocytes in split-Cre mice are partially derived from a subset of AO cell-derived OPCs. Nevertheless, our study highlights that not only OPCs but also mature oligodendrocytes act as a distinct and additional source of astrocytes in response to acute brain injuries.

STAR★METHODS

Detailed methods are provided in the online version of this paper and include the following:

- KEY RESOURCES TABLE
- RESOURCE AVAILABILITY
  - Lead contact
  - Materials availability
  - Data and code availability
- EXPERIMENTAL MODELS AND SUBJECT DETAILS
  - Mice
- METHOD DETAILS
  - Animal surgeries
  - Minocycline treatment
  - Intracortical injection of IL-6 antibody
  - *In vivo* two-photon laser-scanning microscopy (2P-LSM)
  - Immunohistochemistry
  - DAB immunostaining
  - DAB.Proliferation analysis
  - Tamoxifen-induced gene recombination
  - Whole-cell patch-clamp analysis
  - Quantitative real-time PCR (qRT-PCR)
  - Microscopic analysis
- QUANTIFICATION AND STATISTICAL ANALYSIS

SUPPLEMENTAL INFORMATION

Supplemental information can be found online at https://doi.org/10.1016/j.devcel.2023.04.016.

ACKNOWLEDGMENTS

We thank Daniel Schauenburg and colleagues for animal husbandry, Frank Rhode for technical and Davide Gobbo for experimental assistance. This work was supported by grants from the Deutsche Forschungsgemeinschaft (SPP 1757 and SFB 894 to F.K.; FOR2289 to F.K. and A.S.; SPP1757 Young Investigator grant to X.B., KI 503/14 to F.K. and W.H., HU 2614/1-1 to W.H.), the BMBF (EraNet-Neuron BrIE to F.K.), the European Commission (FP7-People ITN-237956 and H2020-MSCA-ITN-2016 EU-GliaPhD to F.K.), and University of Saarland (HOMFOR2015 to A.S. and HOMFORexzellenz2017 and NanoBioMed Young Investigator Grant 2021 to X.B.).

AUTHOR CONTRIBUTIONS

X.B., J.H., F.K., and A.S. conceived the project. X.B., C.K., V.S., and A.S. performed surgeries. X.B. and L.-P.F. performed pharmacological intervention. X.B. performed 2P-LSM imaging and data analysis. X.B., L.C.C., and R.Z. performed quantitative real-time PCR and corresponding data analysis. N.Z. performed electrophysiology and corresponding data analysis. X.B., W.H., and A.S. performed immunostaining. C.K. and V.S. performed scRNA-seq and data analysis with J.N.. J.H. and S.B. provided materials. W.W. introduced the PVD model. X.B., N.Z., C.K., V.S., L.C.C., R.Z., and A.S. analyzed data. X.B., F.K., and A.S. wrote the manuscript with comments of other authors.

DECLARATION OF INTERESTS

The authors declare no competing interests.

INCLUSION AND DIVERSITY

We support inclusive, diverse, and equitable conduct of research.

Received: September 23, 2022
Revised: February 16, 2023
Accepted: April 25, 2023
Published: May 22, 2023

REFERENCES

1. Guo, Q., Scheller, A., and Huang, W. (2021). Progenies of NG2 glia: what do we learn from transgenic mouse models? Neural Regen. Res. *16*, 43–48. https://doi.org/10.4103/1673-5374.286950.
2. Nishiyama, A., Boshans, L., Goncalves, C.M., Wegrzyn, J., and Patel, K.D. (2016). Lineage, fate, and fate potential of NG2-glia. Brain Res. *1638*, 116–128. https://doi.org/10.1016/j.brainres.2015.08.013.
3. Fern, R.F., Matute, C., and Stys, P.K. (2014). White matter injury: ischemic and nonischemic. Glia *62*, 1780–1789. https://doi.org/10.1002/glia.22722.

Developmental Cell
Article

4. Jeserich, G., Klempahn, K., and Pfeiffer, M. (2008). Features and functions of oligodendrocytes and myelin proteins of lower vertebrate species. J. Mol. Neurosci. *35*, 117–126. https://doi.org/10.1007/s12031-008-9035-0.

5. Ankerhold, R., and Stuermer, C.A. (1999). Fate of oligodendrocytes during retinal axon degeneration and regeneration in the goldfish visual pathway. J. Neurobiol. *41*, 572–584.

6. Tegla, C.A., Cudrici, C., Rozycka, M., Soloviova, K., Ito, T., Singh, A.K., Khan, A., Azimzadeh, P., Andrian-Albescu, M., Khan, A., et al. (2011). C5b-9-activated, K(v)1.3 channels mediate oligodendrocyte cell cycle activation and dedifferentiation. Exp. Mol. Pathol. *91*, 335–345. https://doi.org/10.1016/j.yexmp.2011.04.006.

7. Rosano, C., Felipe-Cuervo, E., and Wood, P.M. (1999). Regenerative potential of adult O1+ oligodendrocytes. Glia *27*, 189–202.

8. Kohyama, J., Kojima, T., Takatsuka, E., Yamashita, T., Namiki, J., Hsieh, J., Gage, F.H., Namihira, M., Okano, H., Sawamoto, K., and Nakashima, K. (2008). Epigenetic regulation of neural cell differentiation plasticity in the adult mammalian brain. Proc. Natl. Acad. Sci. USA *105*, 18012–18017. https://doi.org/10.1073/pnas.0808417105.

9. Zhu, X., Hill, R.A., Dietrich, D., Komitova, M., Suzuki, R., and Nishiyama, A. (2011). Age-dependent fate and lineage restriction of single NG2 cells. Development *138*, 745–753. https://doi.org/10.1242/dev.047951.

10. Huang, W., Guo, Q., Bai, X., Scheller, A., and Kirchhoff, F. (2019). Early embryonic NG2 glia are exclusively gliogenic and do not generate neurons in the brain. Glia *67*, 1094–1103. https://doi.org/10.1002/glia.23590.

11. Huang, W., Bai, X., Stopper, L., Catalin, B., Cartarozzi, L.P., Scheller, A., and Kirchhoff, F. (2018). During development NG2 glial cells of the spinal cord are restricted to the oligodendrocyte lineage, but generate astrocytes upon acute injury. Neuroscience *385*, 154–165. https://doi.org/10.1016/j.neuroscience.2018.06.015.

12. Huang, W., Zhao, N., Bai, X., Karram, K., Trotter, J., Goebbels, S., Scheller, A., and Kirchhoff, F. (2014). Novel NG2-CreERT2 knock-in mice demonstrate heterogeneous differentiation potential of NG2 glia during development. Glia *62*, 896–913. https://doi.org/10.1002/glia.22648.

13. Alonso, G. (2005). NG2 proteoglycan-expressing cells of the adult rat brain: possible involvement in the formation of glial scar astrocytes following stab wound. Glia *49*, 318–338. https://doi.org/10.1002/glia.20121.

14. Tamura, Y., Eguchi, A., Jin, G., Sami, M.M., and Kataoka, Y. (2012). Cortical spreading depression shifts cell fate determination of progenitor cells in the adult cortex. J. Cereb. Blood Flow Metab. *32*, 1879–1887. https://doi.org/10.1038/jcbfm.2012.98.

15. Tatsumi, K., Takebayashi, H., Manabe, T., Tanaka, K.F., Makinodan, M., Yamauchi, T., Makinodan, E., Matsuyoshi, H., Okuda, H., Ikenaka, K., and Wanaka, A. (2008). Genetic fate mapping of Olig2 progenitors in the injured adult cerebral cortex reveals preferential differentiation into astrocytes. J. Neurosci. Res. *86*, 3494–3502. https://doi.org/10.1002/jnr.21862.

16. Dimou, L., Simon, C., Kirchhoff, F., Takebayashi, H., and Götz, M. (2008). Progeny of Olig2-expressing progenitors in the gray and white matter of the adult mouse cerebral cortex. J. Neurosci. *28*, 10434–10442. https://doi.org/10.1523/JNEUROSCI.2831-08.2008.

17. Komitova, M., Serwanski, D.R., Lu, Q.R., and Nishiyama, A. (2011). NG2 cells are not a major source of reactive astrocytes after neocortical stab wound injury. Glia *59*, 800–809. https://doi.org/10.1002/glia.21152.

18. Huang, W., Bai, X., Meyer, E., and Scheller, A. (2020). Acute brain injuries trigger microglia as an additional source of the proteoglycan NG2. Acta Neuropathol. Commun. *8*, 146. https://doi.org/10.1186/s40478-020-01016-2.

19. Kang, S.H., Fukaya, M., Yang, J.K., Rothstein, J.D., and Bergles, D.E. (2010). NG2+ CNS glial progenitors remain committed to the oligodendrocyte lineage in postnatal life and following neurodegeneration. Neuron *68*, 668–681. https://doi.org/10.1016/j.neuron.2010.09.009.

20. Zhu, X., Bergles, D.E., and Nishiyama, A. (2008). NG2 cells generate both oligodendrocytes and gray matter astrocytes. Development *135*, 145–157. https://doi.org/10.1242/dev.004895.

21. Hirrlinger, J., Scheller, A., Hirrlinger, P.G., Kellert, B., Tang, W., Wehr, M.C., Goebbels, S., Reichenbach, A., Sprengel, R., Rossner, M.J., and Kirchhoff, F. (2009). Split-cre complementation indicates coincident activity of different genes in vivo. PLoS One *4*, e4286. https://doi.org/10.1371/journal.pone.0004286.

22. Houades, V., Koulakoff, A., Ezan, P., Seif, I., and Giaume, C. (2008). Gap junction-mediated astrocytic networks in the mouse barrel cortex. J. Neurosci. *28*, 5207–5217. https://doi.org/10.1523/JNEUROSCI.5100-07.2008.

23. Koupourtidou, C., Schwarz, V., and Ninkovic, J. (2023). Shared inflammatory glial cell signature after brain injury revealed by spatial, temporal and cell-type-specific profiling of the murine cerebral cortex. Preprint at bioRxiv. https://doi.org/10.1101/2023.02.24.529840.

24. Hirrlinger, P.G., Scheller, A., Braun, C., Quintela-Schneider, M., Fuss, B., Hirrlinger, J., and Kirchhoff, F. (2005). Expression of reef coral fluorescent proteins in the central nervous system of transgenic mice. Mol. Cell. Neurosci. *30*, 291–303. https://doi.org/10.1016/j.mcn.2005.08.011.

25. Verkhusha, V.V., Kuznetsova, I.M., Stepanenko, O.V., Zaraisky, A.G., Shavlovsky, M.M., Turoverov, K.K., and Uversky, V.N. (2003). High stability of Discosoma DsRed as compared to Aequorea EGFP. Biochemistry *42*, 7879–7884. https://doi.org/10.1021/bi034555t.

26. Hare, J.F., and Taylor, K. (1991). Mechanisms of plasma membrane protein degradation: recycling proteins are degraded more rapidly than those confined to the cell surface. Proc. Natl. Acad. Sci. USA *88*, 5902–5906.

27. Sabo, J.K., Aumann, T.D., Merlo, D., Kilpatrick, T.J., and Cate, H.S. (2011). Remyelination is altered by bone morphogenic protein signaling in demyelinated lesions. J. Neurosci. *31*, 4504–4510. https://doi.org/10.1523/JNEUROSCI.5859-10.2011.

28. Yanagisawa, M., Nakashima, K., Takizawa, T., Ochiai, W., Arakawa, H., and Taga, T. (2001). Signaling crosstalk underlying synergistic induction of astrocyte differentiation by BMPs and IL-6 family of cytokines. FEBS Lett. *489*, 139–143.

29. Deverman, B.E., and Patterson, P.H. (2012). Exogenous leukemia inhibitory factor stimulates oligodendrocyte progenitor cell proliferation and enhances hippocampal remyelination. J. Neurosci. *32*, 2100–2109. https://doi.org/10.1523/JNEUROSCI.3803-11.2012.

30. Kobayashi, K., Imagama, S., Ohgomori, T., Hirano, K., Uchimura, K., Sakamoto, K., Hirakawa, A., Takeuchi, H., Suzumura, A., Ishiguro, N., and Kadomatsu, K. (2013). Minocycline selectively inhibits M1 polarization of microglia. Cell Death Dis. *4*, e525. https://doi.org/10.1038/cddis.2013.54.

31. Henry, C.J., Huang, Y., Wynne, A., Hanke, M., Himler, J., Bailey, M.T., Sheridan, J.F., and Godbout, J.P. (2008). Minocycline attenuates lipopolysaccharide (LPS)-induced neuroinflammation, sickness behavior, and anhedonia. J. Neuroinflammation *5*, 15. https://doi.org/10.1186/1742-2094-5-15.

32. Lee, S.M., Yune, T.Y., Kim, S.J., Kim, Y.C., Oh, Y.J., Markelonis, G.J., and Oh, T.H. (2004). Minocycline inhibits apoptotic cell death via attenuation of TNF-alpha expression following iNOS/NO induction by lipopolysaccharide in neuron/glia co-cultures. J. Neurochem. *91*, 568–578. https://doi.org/10.1111/j.1471-4159.2004.02780.x.

33. Salzer, J.L. (2008). Switching myelination on and off. J. Cell Biol. *181*, 575–577. https://doi.org/10.1083/jcb.200804136.

34. van der Meulen, J.D., Houthoff, H.J., and Ebels, E.J. (1978). Glial fibrillary acidic protein in human gliomas. Neuropathol. Appl. Neurobiol. *4*, 177–190.

35. Kleihues, P., Louis, D.N., Scheithauer, B.W., Rorke, L.B., Reifenberger, G., Burger, P.C., and Cavenee, W.K. (2002). The WHO classification of tumors of the nervous system. discussion 226–219. J. Neuropathol. Exp. Neurol. *61*, 215–225.

CellPress

Developmental Cell
Article

36. Salter, M.G., and Fern, R. (2005). NMDA receptors are expressed in developing oligodendrocyte processes and mediate injury. Nature *438*, 1167–1171. https://doi.org/10.1038/nature04301.

37. Harrisingh, M.C., Perez-Nadales, E., Parkinson, D.B., Malcolm, D.S., Mudge, A.W., and Lloyd, A.C. (2004). The Ras/Raf/ERK signalling pathway drives Schwann cell dedifferentiation. EMBO J. *23*, 3061–3071. https://doi.org/10.1038/sj.emboj.7600309.

38. Matyja, E., Taraszewska, A., and Zabek, M. (2001). Phenotypic characteristics of GFAP-immunopositive oligodendroglial tumours Part I: immunohistochemical study. Folia Neuropathol. *39*, 19–26.

39. Kros, J.M., Schouten, W.C., Janssen, P.J., and van der Kwast, T.H. (1996). Proliferation of gemistocytic cells and glial fibrillary acidic protein (GFAP)-positive oligodendroglial cells in gliomas: a MIB-1/GFAP double labeling study. Acta Neuropathol. *91*, 99–103.

40. Tena-Suck, M.L., Moreno-Jiménez, S., Alonso, M., Aguirre-Crux, L., and Sánchez, A. (2008). Oligodendrogliomas in relation to astrocytes differentiation. Clinicopathologic and immunohistochemical study. Ann. Diagn. Pathol. *12*, 313–321. https://doi.org/10.1016/j.anndiagpath.2008.02.002.

41. Marques, S., Zeisel, A., Codeluppi, S., van Bruggen, D., Mendanha Falcão, A., Xiao, L., Li, H., Häring, M., Hochgerner, H., Romanov, R.A., et al. (2016). Oligodendrocyte heterogeneity in the mouse juvenile and adult central nervous system. Science *352*, 1326–1329. https://doi.org/10.1126/science.aaf6463.

42. Floriddia, E.M., Lourenço, T., Zhang, S., van Bruggen, D., Hilscher, M.M., Kukanja, P., Gonçalves dos Santos, J.P., Altınkök, M., Yokota, C., Llorens-Bobadilla, E., et al. (2020). Distinct oligodendrocyte populations have spatial preference and different responses to spinal cord injury. Nat. Commun. *11*, 5860. https://doi.org/10.1038/s41467-020-19453-x.

43. Raff, M.C., Miller, R.H., and Noble, M. (1983). A glial progenitor cell that develops in vitro into an astrocyte or an oligodendrocyte depending on culture medium. Nature *303*, 390–396.

44. Hampton, D.W., Asher, R.A., Kondo, T., Steeves, J.D., Ramer, M.S., and Fawcett, J.W. (2007). A potential role for bone morphogenetic protein signalling in glial cell fate determination following adult central nervous system injury in vivo. Eur. J. Neurosci. *26*, 3024–3035. https://doi.org/10.1111/j.1460-9568.2007.05940.x.

45. Agresti, C., Aloisi, F., and Levi, G. (1991). Heterotypic and homotypic cellular interactions influencing the growth and differentiation of bipotential oligodendrocyte-type-2 astrocyte progenitors in culture. Dev. Biol. *144*, 16–29.

46. Nishiyama, A., Lin, X.H., Giese, N., Heldin, C.H., and Stallcup, W.B. (1996). Co-localization of NG2 proteoglycan and PDGF alpha-receptor on O2A progenitor cells in the developing rat brain. J. Neurosci. Res. *43*, 299–314. https://doi.org/10.1002/(SICI)1097-4547(19960201)43:3.

47. Bauer, S. (2009). Cytokine control of adult neural stem cells. Ann. N. Y. Acad. Sci. *1153*, 48–56. https://doi.org/10.1111/j.1749-6632.2009.03986.x.

48. Zhao, C., Fancy, S.P., Magy, L., Urwin, J.E., and Franklin, R.J. (2005). Stem cells, progenitors and myelin repair. J. Anat. *207*, 251–258. https://doi.org/10.1111/j.1469-7580.2005.00456.x.

49. Shu, M., Zhou, Y., Zhu, W., Wu, S., Zheng, X., and Yan, G. (2011). Activation of a pro-survival pathway IL-6/JAK2/STAT3 contributes to glial fibrillary acidic protein induction during the cholera toxin-induced differentiation of C6 malignant glioma cells. Mol. Oncol. *5*, 265–272. https://doi.org/10.1016/j.molonc.2011.03.003.

50. Mondal, D., Pradhan, L., and LaRussa, V.F. (2004). Signal transduction pathways involved in the lineage-differentiation of NSCs: can the knowledge gained from blood be used in the brain? Cancer Investig. *22*, 925–943.

51. Mayer, M., Bhakoo, K., and Noble, M. (1994). Ciliary neurotrophic factor and leukemia inhibitory factor promote the generation, maturation and survival of oligodendrocytes in vitro. Development *120*, 143–153.

52. Bonaguidi, M.A., McGuire, T., Hu, M., Kan, L., Samanta, J., and Kessler, J.A. (2005). LIF and BMP signaling generate separate and discrete types of GFAP-expressing cells. Development *132*, 5503–5514. https://doi.org/10.1242/dev.02166.

53. See, J., Zhang, X., Eraydin, N., Mun, S.B., Mamontov, P., Golden, J.A., and Grinspan, J.B. (2004). Oligodendrocyte maturation is inhibited by bone morphogenetic protein. Mol. Cell. Neurosci. *26*, 481–492. https://doi.org/10.1016/j.mcn.2004.04.004.

54. Cheng, X., Wang, Y., He, Q., Qiu, M., Whittemore, S.R., and Cao, Q. (2007). Bone morphogenetic protein signaling and olig1/2 interact to regulate the differentiation and maturation of adult oligodendrocyte precursor cells. Stem Cells *25*, 3204–3214. https://doi.org/10.1634/stemcells.2007-0284.

55. Rivers, L.E., Young, K.M., Rizzi, M., Jamen, F., Psachoulia, K., Wade, A., Kessaris, N., and Richardson, W.D. (2008). PDGFRA/NG2 glia generate myelinating oligodendrocytes and piriform projection neurons in adult mice. Nat. Neurosci. *11*, 1392–1401. https://doi.org/10.1038/nn.2220.

56. Viganò, F., Möbius, W., Götz, M., and Dimou, L. (2013). Transplantation reveals regional differences in oligodendrocyte differentiation in the adult brain. Nat. Neurosci. *16*, 1370–1372. https://doi.org/10.1038/nn.3503.

57. Jessberger, S., Toni, N., Clemenson, G.D., Ray, J., and Gage, F.H. (2008). Directed differentiation of hippocampal stem/progenitor cells in the adult brain. Nat. Neurosci. *11*, 888–893. https://doi.org/10.1038/nn.2148.

58. Tripathi, R.B., Rivers, L.E., Young, K.M., Jamen, F., and Richardson, W.D. (2010). NG2 glia generate new oligodendrocytes but few astrocytes in a murine experimental autoimmune encephalomyelitis model of demyelinating disease. J. Neurosci. *30*, 16383–16390. https://doi.org/10.1523/JNEUROSCI.3411-10.2010.

59. Young, K.M., Psachoulia, K., Tripathi, R.B., Dunn, S.J., Cossell, L., Attwell, D., Tohyama, K., and Richardson, W.D. (2013). Oligodendrocyte dynamics in the healthy adult CNS: evidence for myelin remodeling. Neuron *77*, 873–885. https://doi.org/10.1016/j.neuron.2013.01.006.

60. Buffo, A., Rite, I., Tripathi, P., Lepier, A., Colak, D., Horn, A.P., Mori, T., and Götz, M. (2008). Origin and progeny of reactive gliosis: A source of multipotent cells in the injured brain. Proc. Natl. Acad. Sci. USA *105*, 3581–3586. https://doi.org/10.1073/pnas.0709002105.

61. Bardehle, S., Krüger, M., Buggenthin, F., Schwausch, J., Ninkovic, J., Clevers, H., Snippert, H.J., Theis, F.J., Meyer-Luehmann, M., Bechmann, I., et al. (2013). Live imaging of astrocyte responses to acute injury reveals selective juxtavascular proliferation. Nat. Neurosci. *16*, 580–586. https://doi.org/10.1038/nn.3371.

62. Liddelow, S.A., Guttenplan, K.A., Clarke, L.E., Bennett, F.C., Bohlen, C.J., Schirmer, L., Bennett, M.L., Münch, A.E., Chung, W.S., Peterson, T.C., et al. (2017). Neurotoxic reactive astrocytes are induced by activated microglia. Nature *541*, 481–487. https://doi.org/10.1038/nature21029.

63. Liddelow, S.A., and Barres, B.A. (2016). Regeneration: not everything is scary about a glial scar. Nature *532*, 182–183. https://doi.org/10.1038/nature17318.

64. Ffrench-Constant, C., and Raff, M.C. (1986). The oligodendrocyte-type-2 astrocyte cell lineage is specialized for myelination. Nature *323*, 335–338. https://doi.org/10.1038/323335a0.

65. Hewett, J.A. (2009). Determinants of regional and local diversity within the astroglial lineage of the normal central nervous system. J. Neurochem. *110*, 1717–1736. https://doi.org/10.1111/j.1471-4159.2009.06288.x.

66. Zamanian, J.L., Xu, L., Foo, L.C., Nouri, N., Zhou, L., Giffard, R.G., and Barres, B.A. (2012). Genomic analysis of reactive astrogliosis. J. Neurosci. *32*, 6391–6410. https://doi.org/10.1523/JNEUROSCI.6221-11.2012.

67. Madisen, L., Zwingman, T.A., Sunkin, S.M., Oh, S.W., Zariwala, H.A., Gu, H., Ng, L.L., Palmiter, R.D., Hawrylycz, M.J., Jones, A.R., et al. (2010). A robust and high-throughput Cre reporting and characterization system for the whole mouse brain. Nat. Neurosci. *13*, 133–140. https://doi.org/10.1038/nn.2467.

68. Srinivas, S., Watanabe, T., Lin, C.S., William, C.M., Tanabe, Y., Jessell, T.M., and Costantini, F. (2001). Cre reporter strains produced by targeted insertion of EYFP and ECFP into the ROSA26 locus. BMC Dev. Biol. *1*, 4.

Developmental Cell
Article

69. Nolte, C., Matyash, M., Pivneva, T., Schipke, C.G., Ohlemeyer, C., Hanisch, U.K., Kirchhoff, F., and Kettenmann, H. (2001). GFAP promoter-controlled EGFP-expressing transgenic mice: a tool to visualize astrocytes and astrogliosis in living brain tissue. Glia *33*, 72–86. https://doi.org/10.1002/1098-1136(20010101)33:1<72::AID-GLIA1007>3.0.CO;2-A.

70. Lalo, U., Pankratov, Y., Kirchhoff, F., North, R.A., and Verkhratsky, A. (2006). NMDA receptors mediate neuron-to-glia signaling in mouse cortical astrocytes. J. Neurosci. *26*, 2673–2683. https://doi.org/10.1523/JNEUROSCI.4689-05.2006.

71. Hirrlinger, P.G., Scheller, A., Braun, C., Hirrlinger, J., and Kirchhoff, F. (2006). Temporal control of gene recombination in astrocytes by transgenic expression of the tamoxifen-inducible DNA recombinase variant CreERT2. Glia *54*, 11–20. https://doi.org/10.1002/glia.20342.

72. Leone, D.P., Genoud, S., Atanasoski, S., Grausenburger, R., Berger, P., Metzger, D., Macklin, W.B., Chambon, P., and Suter, U. (2003). Tamoxifen-inducible glia-specific Cre mice for somatic mutagenesis in oligodendrocytes and Schwann cells. Mol. Cell. Neurosci. *22*, 430–440.

73. Sobottka, B., Ziegler, U., Kaech, A., Becher, B., and Goebels, N. (2011). CNS live imaging reveals a new mechanism of myelination: the liquid croissant model. Glia *59*, 1841–1849. https://doi.org/10.1002/glia.21228.

74. Mori, T., Tanaka, K., Buffo, A., Wurst, W., Kühn, R., and Götz, M. (2006). Inducible gene deletion in astroglia and radial glia–a valuable tool for functional and lineage analysis. Glia *54*, 21–34. https://doi.org/10.1002/glia.20350.

75. Karram, K., Goebbels, S., Schwab, M., Jennissen, K., Seifert, G., Steinhäuser, C., Nave, K.A., and Trotter, J. (2008). NG2-expressing cells in the nervous system revealed by the NG2-EYFP-knockin mouse. Genesis *46*, 743–757. https://doi.org/10.1002/dvg.20440.

76. Besnard, F., Brenner, M., Nakatani, Y., Chao, R., Purohit, H.J., and Freese, E. (1991). Multiple interacting sites regulate astrocyte-specific transcription of the human gene for glial fibrillary acidic protein. J. Biol. Chem. *266*, 18877–18883.

77. Masood, K., Besnard, F., Su, Y., and Brenner, M. (1993). Analysis of a segment of the human glial fibrillary acidic protein gene that directs astrocyte-specific transcription. J. Neurochem. *61*, 160–166.

78. Brenner, M., Kisseberth, W.C., Su, Y., Besnard, F., and Messing, A. (1994). GFAP promoter directs astrocyte-specific expression in transgenic mice. J. Neurosci. *14*, 1030–1037.

79. Wight, P.A., Duchala, C.S., Readhead, C., and Macklin, W.B. (1993). A myelin proteolipid protein-LacZ fusion protein is developmentally regulated and targeted to the myelin membrane in transgenic mice. J. Cell Biol. *123*, 443–454. https://doi.org/10.1083/jcb.123.2.443.

80. Fuss, B., Mallon, B., Phan, T., Ohlemeyer, C., Kirchhoff, F., Nishiyama, A., and Macklin, W.B. (2000). Purification and analysis of in vivo-differentiated oligodendrocytes expressing the green fluorescent protein. Dev. Biol. *218*, 259–274. https://doi.org/10.1006/dbio.1999.9574.

81. Hua, R., and Walz, W. (2006). Minocycline treatment prevents cavitation in rats after a cortical devascularizing lesion. Brain Res. *1090*, 172–181. https://doi.org/10.1016/j.brainres.2006.03.072.

82. Fang, L.P., Liu, Q., Meyer, E., Welle, A., Huang, W., Scheller, A., Kirchhoff, F., and Bai, X. (2023). A subset of OPCs do not express Olig2 during development which can be increased in the adult by brain injuries and complex motor learning. Glia *71*, 415–430. https://doi.org/10.1002/glia.24284.

83. Timper, K., Denson, J.L., Steculorum, S.M., Heilinger, C., Engström-Ruud, L., Wunderlich, C.M., Rose-John, S., Wunderlich, F.T., and Brüning, J.C. (2017). IL-6 improves energy and glucose homeostasis in obesity via enhanced central IL-6 trans-signaling. Cell Rep. *19*, 267–280. https://doi.org/10.1016/j.celrep.2017.03.043.

84. Cupido, A., Catalin, B., Steffens, H., and Kirchhoff, F. (2014). Surgical procedures to study microglial motility in the brain and in the spinal cord by in vivo two-photon laser-scanning microcopy. In Confocal and Multiphoton Laser-Scanning Microscopy of Neuronal Tissue: Applications and Quantitative Image Analysis, L. Bakota and R. Brandt, eds. (Springer), pp. 37–50.

85. Fang, L.P., Zhao, N., Caudal, L.C., Chang, H.F., Zhao, R., Lin, C.H., Hainz, N., Meier, C., Bettler, B., Huang, W., et al. (2022). Impaired bidirectional communication between interneurons and oligodendrocyte precursor cells affects social cognitive behavior. Nat. Commun. *13*, 1394. https://doi.org/10.1038/s41467-022-29020-1.

CellPress

Developmental Cell
Article

STAR★METHODS

KEY RESOURCES TABLE

REAGENT or RESOURCE	SOURCE	IDENTIFIER
Antibodies		
Goat anti-GFP	Rockland	Cat# 600-101-215, RRID: AB_218182
Goat anti-PDGFRα (Pα)	R&D Systems	Cat# AF1062, RRID: AB_2236897
Goat anti-Sox10	R&D Systems	Cat# AF2864, RRID: AB_442208
Goat anti-MOG	Abcam	Cat# ab115597, RRID: AB_10898950
Rabbit anti-GFAP	Dako Cytomation	Cat# Z0334, RRID: AB_10013382
Rabbit anti-Cre	Novagen/Millipore	Cat# 69050-3, RRID: AB_10806983
Rabbit anti-S100B	Abcam	Cat# ab52642, RRID: AB_882426
Rabbit anti-Iba1	Wako	Cat# 019-19741, RRID: AB_839504
Rabbit anti-Sox2	R&D Systems	Cat# MAB2018, RRID: AB_358009
Rabbit anti-DsRed	Clontech	Cat# 632496, RRID: AB_10013483
Rabbit anti-Olig2	Gift from Dr. Charles D. Stiles, Harvard University	N/A
Rabbit anti-MyRF	Oasis Biofarm	Cat# OB-PRB007
Mouse anti-GSTπ	BD Transduction Laboratories	Cat# 610718, RRID: AB_398041
Mouse anti-glutamine synthethase	Transduction Laboratories	Cat# 610518, RRID: AB_397880
Mouse anti-MAG	House made	Clone 513
anti-Camsap1	Dr. Hiroaki Asou, Keio University	N/A
anti-PLP	Dr. Klaus-Armin Nave, Max Planck Institute for Multidisciplinary Sciences	N/A
anti-NeuN	Merck Millipore	Cat# MAB377, RRID: AB_2298772
Rat anti-NG2	Dr. Jacqueline. Trotter, University of Mainz	N/A
Rat anti-BrdU	Abcam	Cat# ab6326, RRID: AB_305426
Goat anti mouse IL-6 neutralizing antibody	R&D systems	Cat# AF-406-NA, RRID: AB_354478
Alexa 488-conjugated donkey anti-mouse	Invitrogen	Cat# A-21202, RRID: AB_141607
Alexa 647-conjugated donkey anti-mouse	Invitrogen	Cat# A-31571, RRID: AB_162542
Alexa 546-conjugated donkey anti-rabbit	Invitrogen	Cat# A10040, RRID: AB_2534016
Alexa488-conjugated anti-goat	Invitrogen	Cat# A-11055, RRID: AB_2534102
Alexa647-conjugated anti-goat	Invitrogen	Cat# A-21447, RRID: AB_2535864
Cy5 Donkey anti-rat	Jackson	Cat# 712-175-153, RRID: AB_2340672
Biotinylated rabbit anti-goat IgG	Invitrogen	Ca# 31732, RRID: AB_228393
VECTASTAIN Elite ABC-Peroxidase Kit	Vector Laboratories	Cat# PK-6100, RRID: AB_2336819
DAB	Dako Agilent	Cat# K5007, RRID: AB_2888627
Chemicals, peptides, and recombinant proteins		
Recombinant mouse IL-6	Biomol	Cat# 348149.10
Recombinant mouse BMP4	Abcam	Cat# ab245810
Recombinant mouse LIF	Neuromics	Cat# PR80000
Atto 647N-Streptavidin	Sigma-Aldrich	Cat# 94149
Minocyclin hydrochloride	Ratiopharm	PZN-04921808
Buprenorphine	Sigma-Aldrich	Cat# 53152-21-9
Biocytin	Sigma-Aldrich	Cat# B4261
Tamoxifen	Sigma-Aldrich	Cat# T5648
5-bromo-2'-deoxyuridine	Sigma-Aldrich	Cat# B5002

(*Continued on next page*)

Developmental Cell
Article

CellPress

Continued

REAGENT or RESOURCE	SOURCE	IDENTIFIER
Deposited data		
Single cell RNA seq dataset	Koupourtidou et al.[23]	https://doi.org/10.1101/2023.02.24.529840; GEO: GSE226211
Experimental models: Organisms/strains		
Mouse: NG2-CreERT2	Huang et al.[12]	Cspg4$^{tm1.1(cre/ERT2)Fki}$, MGI:5566862 (NGCE)
Mouse: Rosa26-lsl-tdTomato	Madisen et al.[67]	Gt(ROSA)26Sor$^{tm14(CAG-tdTomato)Hze}$ (Ai14), MGI:3809524
Mouse: Rosa26-lsl-EYFP	Srinivas et al.[68]	Gt(ROSA)26Sor$^{tm1(EYF)Cos}$, MGI:2449038
Mouse: hGFAP-EGFP line A	Nolte et al.[69]	Tg(GFAP-EGFP)1Hket, MGI:6188855 (GFEA)
Mouse: hGFAP-EGFP line C	Lalo et al.[70]	- / (GFEC)
Mouse: hGFAP-mRFP1	Hirrlinger et al.[24]	- / (GRFT)
Mouse: hGFAP-NCre line T	Hirrlinger et al.[21]	Tg(GFAP-Ncre)Vfki, MGI: 3833398 (GCNT)
Mouse: hGFAP-CreERT2	Hirrlinger et al.[71]	Tg(GFAP-cre/ERT2)^{1Fki}, MGI: 4418665, (GCTF)
Mouse: PLP-CCre line K	Hirrlinger et al.[21]	Tg(Plp1-Ccre)Rfki, MGI: 3833397 (PCCK)
Mouse: PLP-CreERT2	Leone et al.[72]	Tg(Plp1-cre/ERT2)1Ueli, MGI:2663093
Mouse: PLP-mEGFP	Sobottka et al.[73]	N/A
Mouse: PLP-DsRed1 line B	Hirrlinger et al.[24]	- / (PRDB)
Mouse: Glast-CreERT2	Mori et al.[74]	Slc1a3$^{tm1(cre/ERT2)Mgoe}$, MGI:3830051
Mouse: NG2-EYFP	Karram et al.[75]	Cspg4$^{tm1.1Trot}$, MGI:3846720
Oligonucleotides		
BMP4 qRT-PCR forward: GAGCCATTCCGTAGTGCCAT	This study	N/A
BMP4 qRT-PCR reverse: ACGACCATCAGCATTCGGTT	This study	N/A
IL-6 qRT-PCR forward: GAGTGGCTAAGGACCAAGACC	This study	N/A
IL-6 qRT-PCR reverse: AACGCACTAGGTTTGCCGA	This study	N/A
LIF qRT-PCR forward: CCCAGCATCCCAGAACCATT	This study	N/A
LIF qRT-PCR reverse: AGAGCTGGGTTGCTTGAGTC	This study	N/A
TNFα qRT-PCR forward: ACGGCATGGATCTCAAAGAC	This study	N/A
TNFα qRT-PCR reverse: GTGGGTGAGGAGCACGTAGT	This study	N/A
GFAP qRT-PCR forward: TGGAGGAGGAGATCCAGTTC	This study	N/A
GFAP qRT-PCR reverse: AGCTGCTCCCGGAGTTCT	This study	N/A
CNTF qRT-PCR forward: GACCTGACTGCTCTTATGGAATCT	This study	N/A
CNTF qRT-PCR reverse: AGGTTCTCTTGGAGGTCCG	This study	N/A
ATPase qRT-PCR forward: GGATCTGCTGGCCCCATAC	This study	N/A
ATPase qRT-PCR reverse: CTTTCCAACGCCAGCACCT	This study	N/A

(*Continued on next page*)

CellPress

Developmental Cell
Article

Continued

REAGENT or RESOURCE	SOURCE	IDENTIFIER
Software and algorithms		
FIJI	www.fiji.sc	RRID: SCR_002285
GraphPad Prism 9.0	Graphpad	RRID: SCR_002798
Adobe InDesign 2022	Adobe	RRID: SCR_021799
Adobe Illustrator 2022	Adobe	RRID: SCR_010279
Others		
ketamine (Ketabel, 100mg/ml)	bela-pharm	N/A
xylazine (Rumpon®)	Bayer Healthcare	N/A

RESOURCE AVAILABILITY

Lead contact

Further information and requests for resources and reagents should be directed to and will be fulfilled by the lead contact, Anja Scheller (anja.scheller@uks.eu).

Materials availability

All transgenic mice used in this study generated by our colleagues are available on request and are subject to MTA agreement. All mice generated by the Kirchhoff lab are available for research purposes without MTA.

Data and code availability

Single cell RNA sequencing data used in this study are available on GEO under the accession GSE226211. The raw microscopy data that support the findings of this study are available from the lead contact upon reasonable request. Any additional information required to reanalyze the data that support the findings is available from the lead contact upon request. This study did not generate any code.

EXPERIMENTAL MODELS AND SUBJECT DETAILS

Mice

Mouse breeding and animal experiments were performed in the animal facilities of the University of Saarland. In this study, heterozygous male and female mice at the age of 8-14 weeks were used, with the exception of electrophysiological experiments were P20 mice were investigated. Split-Cre DNA recombinase mice for coincidence detection as well as inducible Cre DNA recombinase mice (NG2-CreER^{T2}, GFAP-CreER^{T2}, PLP-CreER^{T2} and Glast-CreER^{T2}) were always used in combination with floxed reporter (homozygous for Rosa26-lsl-EYFP or Rosa26-lsl-tdTomato, Table S3) mice to show successful recombination. In addition, we crossed the NG2-CreER^{T2} mice with green astrocyte specific fluorescent mice GFAP-EGFP$_C$ (later referred to as NG2-CreER^{T2} x GFAP-EGFP). Fluorescent astrocyte mouse line (GFAP-EGFP$_A$) was bred to an oligodendroglial specific mouse with DsRed1 expression under control of the murine PLP promoter, and a GFAP-mRFP1 mouse line to PLP-EGFP$_{mem}$. For the generation of the various transgenic hGFAP mouse lines, a 2.2 kb fragment 59 upstream of the open reading frame of the human GFAP gene (hGFAP promoter) has been used.[76–78] To study physiological properties of astrocytes as well as highlighting AO cells and their progeny, we used this promoter for transgenic expression of fluorescent proteins (EGFP, mRFP1), the tamoxifen-inducible Cre DNA recombinase CreER^{T2} as well as the N-terminal Cre fragment in Split-Cre mice.[24,69–71]

Four different mouse lines were used to express transgenic proteins under control of the plp1 promoter. The PLP-EGFP$_{mem}$ mouse line used the original published promoter to generate the Plp1 specific expression.[79]The DsRed1 and CCre-Split-Cre mice were generated by our lab and a modified plp1 promoter sequence was used.[79,80] Briefly, the ATG start codon of the protein in exon 1 was mutated to allow translation start for the transgenes at the appropriate transgenic ATG while keeping the Plp1 exon/intron sequence for splicing intact.[80] The same promoter was used to generate the PLP-CreER^{T2} mice. Because the PLP transgenic mouse lines were generated by non-homologous recombination extensive analyses were performed by us ensuring the exclusive labeling of mature oligodendrocytes (Figures S3 and S4). A more detailed description of tamoxifen protocols and mouse lines can be found in Table S3.

Mice were kept at the animal facility of the CIPMM in a 12 h light/dark cycle at 20°C with humidity at 55-70% and fed a breeding diet (V1125, Sniff) *ad libitum*.

This study was carried out at the University of Saarland in strict accordance with recommendations of European and German guidelines for the welfare of experimental animals. Animal experiments were approved by Saarland state's "Landesamt für Gesundheit und Verbraucherschutz" in Saarbrücken/Germany (animal license numbers: 71/2010, 72/2010, 65/2013, 36/2016 and 08/2021).

Developmental Cell
Article

METHOD DETAILS

Animal surgeries

Stab wound injury (SWI) was performed in young (postnatal day 20) or adult anesthetized mice (ketamine/xylazine) in 0.9 % NaCl (140 mg/10 mg per 1 kg body weight). The skull was thinned with dental drill laterally 1.5 mm and longitudinally 2 mm from bregma, followed by a 1 mm deep stab wound made with a scalpel.

For pial vessel disruption (PVD) a cortical craniotomy (3 mm diameter, center: approximately located (bregma considered as 0) laterally 1.5 mm and longitudinally 2 mm) was made in anesthetized mice.[81] A medium (class II) vessel was disrupted with sharp forceps (#5, Fine Science Tool, Heidelberg, Germany) without interference of larger (class I) vessels. Bleeding was stopped with ice-cold 0.9 % NaCl solution.

Middle cerebral artery occlusion (MCAO) was performed in adult mice.[82] Mice were anesthetized with inhalation of Isoflurane/Oxygen/N_2O mixture (2%/49%/49%). The left common carotid artery (CCA) and the external carotid artery were ligated with silk sutures and an arteriotomy was performed on the CCA. Then a silicon-coated filament (Doccol Corp, CA) was inserted into the CCA and advanced through the internal carotid artery until it reached the origin of the middle cerebral artery. After 45 min of occlusion, the filament was removed and the wound closed. For energy recovery, 10 % glucose (1 ml/20 g body weight) solution was injected i.p.

Cytokine injection was made in the center of a cortical craniotomy. A glass pipet was filled with 0.3 μl of saline, recombinant mouse BMP4 (500 μg/ml in PBS), recombinant mouse LIF (200 μg/ml in PBS), recombinant mouse IL-6 (100 μg/ml) or a combination of BMP4/LIF, BMP4/IL-6, IL-6/LIF or BMP4/IL-6/LIF. Injection was performed with a programmable syringe pump (540060, TSE systems, Germany). Saline was injected to the contralateral side as internal injection control. Therefore, the relative number of AO cells of each mouse was normalized to the number from saline injections of the same mouse.

After surgeries, the wound was closed and appropriate pain killers were given up to three days.

Minocycline treatment

Minocycline hydrochloride (5 mg/ml) was dissolved in 0.9% NaCl solution by sonication and was administered by intraperitoneal injection (50 mg/kg body weight) once daily for three consecutive days from the first day of SWI.[31] For qRT-PCR, minocycline was injected only one dose right after the SWI and the samples were collected at 1 dpi.

Intracortical injection of IL-6 antibody

Animals were placed on a stereotactic device and anaesthetized with Isoflurane/Oxygen/N_2O mixture (2%/49%/49%). The injection site (lateral=1.5 mm and longitudinal=2 mm from bregma) was drilled and saline or neutralizing IL-6 antibody[83] (2 μg in 200 nl per mouse, dissolved in saline) was injected with a NanoFil syringe (World Precision Instruments). IL-6 antibodies in saline or the same volume of saline were injected into the somatosensory cortex at the position of 1 mm and 0.5 mm from pia, 100 nl each, in 2 minutes.

In vivo two-photon laser-scanning microscopy (2P-LSM)

For 2P-LSM a 3 mm-diameter cortical craniotomy (lateral=1.5 mm and longitudinal=2 mm from bregma) was made.[84] The center was stabbed with a needle (0.46 mm x 2 mm) and rinsed with cortex buffer (in mM: 125 NaCl, 5 KCl, 10 glucose, 10 HEPES, 2 $CaCl_2$, 2 $MgSO_4$ (pH$\sim$ 7.4)) until the bleeding stopped. A 3 mm coverslip was placed on the brain and fixed with dental cement (RelyX®, 3M-ESPE, Neuss, Germany). More than twenty GFAP-EGFP/PLP-DsRed1 and ten PLP-$EGFP_{mem}$/GFAP-mRFP1 mice were investigated up to ten times in between 30 days after the injury at different time intervals. A several AO cells could not be followed due to technical problems such as window blurring upon glial scar formation or bone regrowth. To be as stringent as possible, we disregarded all observations on "AO cells becoming astrocytes" when we could not unequivocally identify the oligodendroglial origin of an AO cell, even when thereby sacrificing the percentage of astrocytes coming from an oligodendrocyte.

Immunohistochemistry

Mice were perfused with PBS followed by 4% PFA. After post-fixation, brain slices in 40 μm thickness were prepared with vibratome.[85] Slices were incubated with blocking solution (5 % horse serum and 0.3 % of Triton in PBS) followed by primary antibody incubation at 4°C overnight. After three times of washing with 1x PBS, slices were incubated with secondary antibodies for two hours at room temperature.

To identify the gap junction of newly generated astrocytes in the lesion site, we loaded the tdT^+ astrocyte with 4 mM biocytin dissolved in KCl based pipette solution. Slices were postfixed with 4 % PFA at 4°C overnight and immunostained with Atto 647N-Streptavidin secondary antibody at the next day.

DAB immunostaining

For DAB staining, after primary antibody incubation, biotinylated secondary anti-goat antibody was incubated, followed by incubation with freshly prepared AB mix of Vector Elite ABC Kits.

DAB.Proliferation analysis

Split-Cre mice received drinking water containing 5-bromo-2'-deoxyuridine (BrdU) (1 mg/ml) for two consecutive weeks following SWI *ad libitum*.

CellPress

Developmental Cell
Article

Tamoxifen-induced gene recombination

To induce reporter expression in CreER^{T2}-mice, tamoxifen dissolved in cornoil or mygliol (10 mg/ml) was intraperitoneally injected (100 mg / kg body weight) t once per day as indicated in the experimental schemes.

Whole-cell patch-clamp analysis

The lesioned brain of young mice (P20, 3 or 4 dpi) was dissected and placed in ice-cooled, carbogen-saturated Ca^{2+}-free preparation solution (in mM: 126 NaCl, 3 KCl, 25 $NaHCO_3$, 1.2 NaH_2PO_4, 3 $MgCl_2$ and 15 Glucose). Acute 300 μm frontal vibratome sections (Leica VT 1200S) were obtained. After at least 1 h recovery in oxygenated aCSF (in mM: 126 NaCl, 3 KCl, 25 $NaHCO_3$, 15 glucose, 1.2 NaH_2PO_4, 2 $CaCl_2$, and 2 $MgCl_2$ at 35°C), they were subsequently transferred to a recording chamber mounted on an upright microscope (Axioscope 2 FSmot, Zeiss, Germany) and continuously perfused with aCSF (126 NaCl, 3 KCl, 25 $NaHCO_3$, 15 glucose, 1.2 NaH_2PO_4, 1 $MgCl_2$ and 2.5 $CaCl_2$, room temperature; 20–23°C) at a flow rate of 2–5 ml/min. AO cells, astrocytes, oligodendrocytes and OPCs were identified by their respective fluorescence using conventional epifluorescence illumination. Images were taken with a QuantEM 512SC camera (Photometrics, Tucson, United States). Whole-cell voltage-clamp recordings were obtained with an EPC10 patch-clamp amplifier (HEKA, Lambrecht/Pfalz, Germany), low pass-filtered at 3 kHz and data acquisition was controlled by Patchmaster (HEKA). Currents were recorded at 20 kHz. Patch electrodes were pulled from borosilicate glass capillaries (OD: 1.5 mm; Hilgenberg GmbH, Germany) using a micropipette puller (Model P-97, Sutter Instruments Co., CA) and had a resistance between 4 and 7 MΩ. Patch pipettes were filled with an intracellular solution (in mM: 120 KCl, 5 $MgCl_2$, 5 EGTA, 10 HEPES and 5 Na_2ATP (pH∼ 7.2)).

Analysis was performed with IGOR Pro Version 6.22 (Wavemetrics, Inc., USA), Microsoft Excel and GraphPad Prism 8.0. Glial cells were voltage-clamped at −80 mV (V_{hold}). Whole-cell membrane currents were evoked by a series of hyper- and depolarizing voltage steps ranging from −140 to 80 mV with an increment of 10 mV.

Quantitative real-time PCR (qRT-PCR)

Mice were perfused with PBS at 0.5, 1, 3, 5 and 7 dpi. Cortical mRNA from ipsi- and contralateral tissue was collected within 0.2 mm thickness and 2 mm width (1 mm from lesion site to each direction). The level of mRNA was detected by qRT-PCR. Primers for qRT-PCR are listed in the STAR Methods.

Microscopic analysis

Three brain slices per mouse and at least three animals per group were examined. Overview images were obtained with the slide scanner AxioScan.Z1 (Zeiss). Confocal images were taken by a laser-scanning microscope (LSM-710, Zeiss), processed with ZEN software (Zeiss) and displayed as single optical sections, orthogonal image stacks or maximum intensity projections. For statistical analysis raw or linearly processed image data were used. Figures presented in this work were modified with image processing tools of ImageJ (Fiji) and Zen 2011 software (Zeiss, Oberkochen, Germany).

In all figures the following symbols were used for the different cell types: triangles indicate OPCs, open triangles oligodendrocytes, arrowheads astrocytes and asterisks AO cells.

QUANTIFICATION AND STATISTICAL ANALYSIS

For cell counting in NG2-CreER^{T2} and NG2-CreER^{T2} x GFAP-EGFP mice, the NG2-positive, vessel-associated pericytes were excluded by their morphology. For region-dependent cell counting, 6-8 z-stacks were taken without overlap along the lesion site (about 0.6 mm^2 area of the 40-μm, frontal brain sections) and three stacks at the contralateral side. The volumes for cell counting are listed in Table S4. We performed double-immunostainings to identify the glial cell types that contribute to the recombined (tdT^+) cell population (Figure S2). Please note that only three detection channels were available for cell characterization (tdT^+ and two for GFAP, Pα or GSTπ). Therefore, we always were left with an unidentified cell population (Figure S2). Since this population increased with time after injury, they probably were astrocytes that had downregulated their GFAP expression, a phenomenon common to non-activated cortical astrocytes.

Three animals of every experimental age group and mouse line were studied in three independent experiments. Cells counted at the lesion site were observed in a region 0-300 μm from the lesion in both directions. Statistical differences were analyzed using the two-tailed unpaired *t*-test for two-group comparison, one-way or two-way ANOVA for comparisons among more than two groups (also indicated in the figure legends accordingly) with Prism Graphpad 9.0. Data are shown as mean ± SEM.

Developmental Cell, Volume *58*

Supplemental information

In the mouse cortex, oligodendrocytes regain a plastic capacity, transforming into astrocytes after acute injury

Xianshu Bai, Na Zhao, Christina Koupourtidou, Li-Pao Fang, Veronika Schwarz, Laura C. Caudal, Renping Zhao, Johannes Hirrlinger, Wolfgang Walz, Shan Bian, Wenhui Huang, Jovica Ninkovic, Frank Kirchhoff, and Anja Scheller

Supplementary information for

In the mouse cortex oligodendrocytes regain a plastic capacity transforming into astrocytes after acute injury

Xianshu Bai[1,11], Na Zhao[1,2], Christina Koupourtidou[3,4], Li-Pao Fang[1], Veronica Schwarz[3,4], Laura C. Caudal[1], Renping Zhao[1,5], Johannes Hirrlinger[6,7], Wolfgang Walz[1,8], Shan Bian[9,10], Wenhui Huang[1], Jovica Ninkovic[3,4], Frank Kirchhoff[1] and Anja Scheller[1,11,12]

[1] Molecular Physiology, Center for Integrative Physiology and Molecular Medicine, University of Saarland, 66421 Homburg, Germany

[2] Current address: Institute of Anatomy and Cell Biology, University of Saarland, 66421 Homburg, Germany

[3] Department of Cell Biology and Anatomy, Ludwig-Maximilians-Universität München, 82152 Planegg-MartinsriedGermany

[4] Institute of Stem Cell Research, Helmholtz Zentrum Munich, 85764 Neuherberg-Munich, Germany

[5] Current address: Biophysics, Center for Integrative Physiology and Molecular Medicine, University of Saarland, 66421 Homburg, Germany

[6] Carl-Ludwig-Institute for Physiology, Leipzig University, 04103 Leipzig, Germany

[7] Department of Neurogenetics, Max-Planck-Institute for Multidisciplinary Sciences, 37075 Göttingen, Germany

[8] Department of Psychiatry, University of Saskatchewan, 107 Wiggins Road, Saskatoon, Canada SK S7N 5E5

[9] Institute for Regenerative Medicine, Shanghai East Hospital, School of Life Sciences and Technology, Tongji University, Shanghai, China.

[10] Frontier Science Center for Stem Cell Research, Tongji University, Shanghai, China.

[11] Corresponding authors

[12] Lead Contact

Xianshu Bai:

Email: xianshu.bai@uks.eu **Phone:** +49 6841 1616442 **ORCID:** 0000-0002-4758-1645

Anja Scheller:

Email: anja.scheller@uks.eu **Phone:** +49 6841 1616443 **ORCID:** 0000-0001-8955-2634

Supplementary Figures and legends

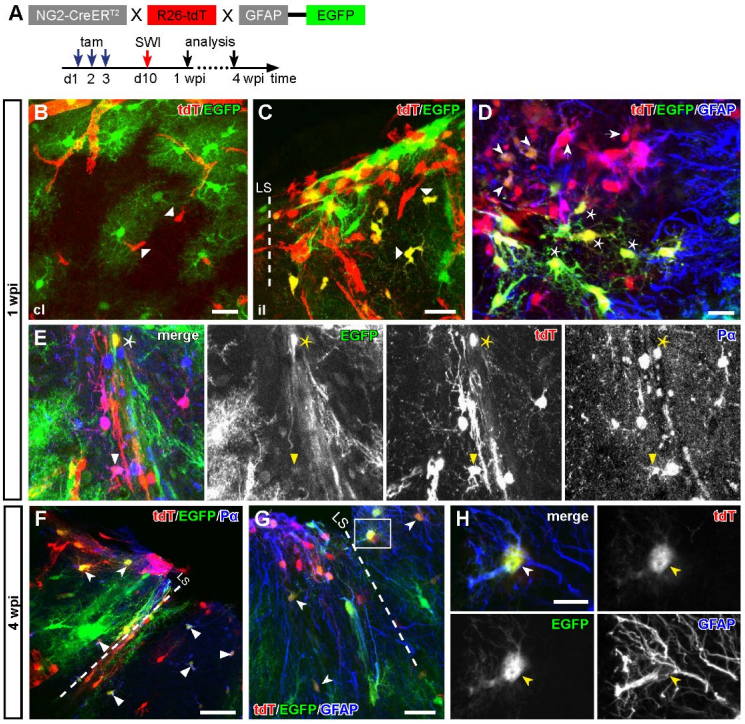

Figure S1. Mature oligodendrocytes can activate the transgenic GFAP promoter, Related to Figure 1.

(A) Protocol of DNA recombination induction and analysis of NG2-CreER^{T2} x hGFAP-EGFP$_{GFEC}$ mice.

(B) No overlay of EGFP and tdT in the contralateral side. Scale bar = 25 µm.

(C) At the lesion site, a high quantity of cells co-expressed tdT and EGFP 1 wpi, some with the morphology of NG2 glia (triangle). Scale bar = 25 µm.

(D) Two subpopulations of tdT$^+$EGFP$^+$ cells could be found: tdT$^+$EGFP$^+$GFAP$^+$ (arrowheads, regarded as astrocytes) and tdT$^+$EGFP$^+$GFAP$^-$ (asterisks, AO cells). Since in the transgenic

GFAP-EGFP$_C$ mice only 38.5 ± 6.3 % of S100B$^+$ astrocytes expressed EGFP in the cortical grey matter, tdT$^+$GFAP$^+$EGFP$^-$ astrocytes were found as well (arrow). Scale bar = 25 µm.

(E) Observation of EGFP$^+$ OPCs (EGFP$^+$tdT$^+$Pα$^+$, triangles, 51.6 ± 2.5 %, 97/194 cells, n = 3) and oligodendroglial cells (EGFP$^+$tdT$^+$Pα$^-$, asterisks, 48.4 ± 3.0 %) with transgenic GFAP promoter activity at the ipsilateral side of NG2-CreER^{T2} x GFAP-EGFP$_c$ mice. Scale bar = 25 µm.

(F) At 4 wpi recombined cells with tdT and EGFP expression can be found either expressing (OPCs, triangles) or lacking Pα (astrocytes, arrowheads). Scale bar = 25 µm.

(G) EGFP$^+$tdT$^+$GFAP$^+$ *bona fide* astrocytes were detectable 4 wpi. Scale bar = 25 µm.

(H) Magnification of GFAP$^+$ recombined astrocyte with EGFP and tdT expression 4 wpi. Scale bar = 10 µm.

Abbreviations: tdT: tdTomato, wpi: week post injury, Triangles: OPCs, arrowheads/arrow: astrocytes, asterisks: AO cells.

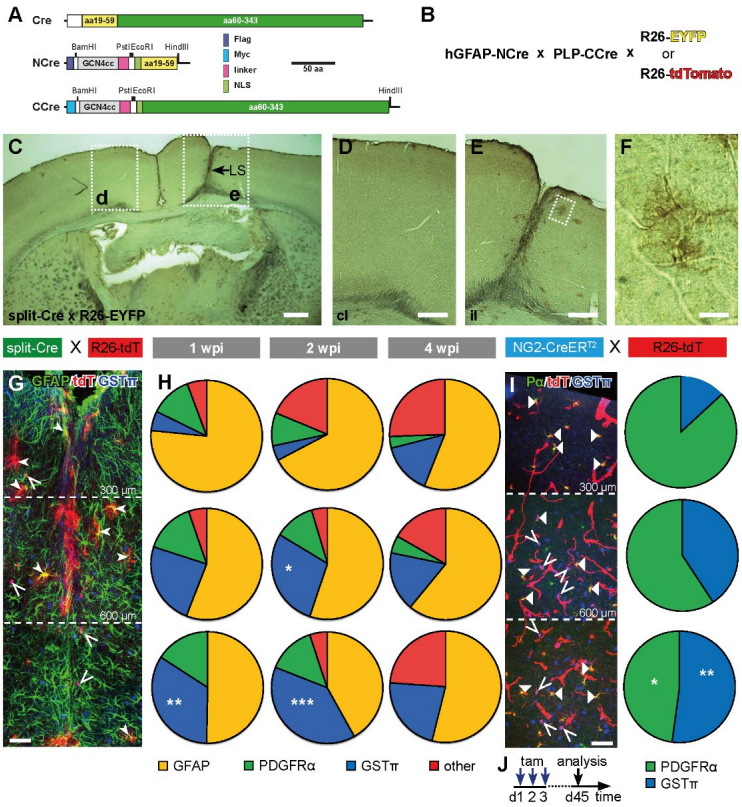

Figure S2. Cortical SWI induces coincident activation of GFAP and PLP promoters, Related to Figure 2.

(A) Split-Cre transgene.

(B) Scheme of split-Cre recombination.

(C-F) DAB staining of GFP in split-Cre x R26-EYFP mouse 1 wpi revealed exclusive recombination in the lesion site (C, E) but not in the contralateral side (C, D). Magnified view showed clear morphology of recombined *bona fide* astrocyte (F). Scale bars in C = 500µm, D, E = 200 µm, F = 40 µm.

(G) Distribution of recombined cells along the lesion site in split-Cre mice. Scale bar = 50 µm.

(H) Quantification of recombined astrocytes ($GFAP^+$, yellow), oligodendrocytes ($GST\pi^+$, blue), OPCs ($P\alpha^+$, green) and other cells (unidentified, red) in layer I-III (0-300 µm), layer IV-V (300-600 µm)and layer VI (>600 µm) of split-Cre mice at 1, 2 and 4 wpi (n = 5-6 mice (1 wpi), 5-6 mice (2 wpi), 2-6 mice (4 wpi), one-way ANOVA tukey's comparisons test, *: $p < 0.05$, **: $p < 0.01$ and ***: $p < 0.001$, compared with same population at the same time point to layer I-III).

(I) Overview and quantification of the distribution of OPCs ($P\alpha^+$) and oligodendrocytes ($GST\pi^+$) in layer I-III, layer IV-V and layer VI of the intact cortex of NG2-$CreER^{T2}$ x R26-tdT mice (n = 3 mice, one-way ANOVA tukey's comparisons test, *: $p < 0.05$ and **: $p < 0.01$, compared with same population at the same time point to layer I-III). Scale bar = 50 µm.

(J) Experimental schedule for the analysis of NG2-$CreER^{T2}$ mice.

Triangles: OPCs, open triangles: oligodendrocytes, arrowheads: astrocytes. Arrowheads: astrocytes, open triangles: oligodendrocytes.

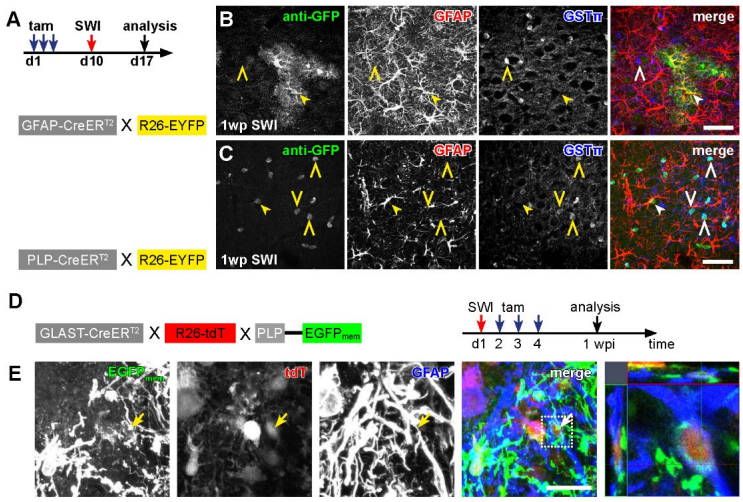

Figure S3. Identification of astrocyte differentiation from oligodendrocyte using glia specific CreERT2 mice, Related to Figure 2.

(A) Experimental schedules for tamoxifen induced recombination before SWI.

(B) In GFAP-CreER^{T2} x R26-EYFP mice recombined cells were GFAP+ astrocytes, but no oligodendrocytes could be observed. Scale bar = 50 µm.

(C) In PLP-CreER^{T2} x R26-EYFP mice recombined astrocytes could be detected when the SWI was performed ten days after tamoxifen injection in addition to GSTπ+ oligodendrocytes. Therefore, the transgenic GFAP promoter was activated in recombined oligodendrocytes (PLP-CreER^{T2}), while recombined astrocytes (GFAP-CreER^{T2}) stay in their lineage. Scale bar = 50 µm.

(D) Crossbreeding of PLP-EGFP$_{mem}$ with the astrocyte-specific Cre-inducible mouse line GLAST-CreER^{T2}. Tamoxifen was administrated at the second day after SWI to label oligodendrocytes with Glast locus activity.

(E) At 1 wpi, $EGFP_{mem}$+/tdT+/GFAP+ cells appeared around the lesion site, indicating that oligodendrocytes do not only activate the GFAP promoter, but also other astrocytic promoters as detected for the GLAST gene. Scale bar = 20 µm.

Abbreviations: SWI: stab wound injury.

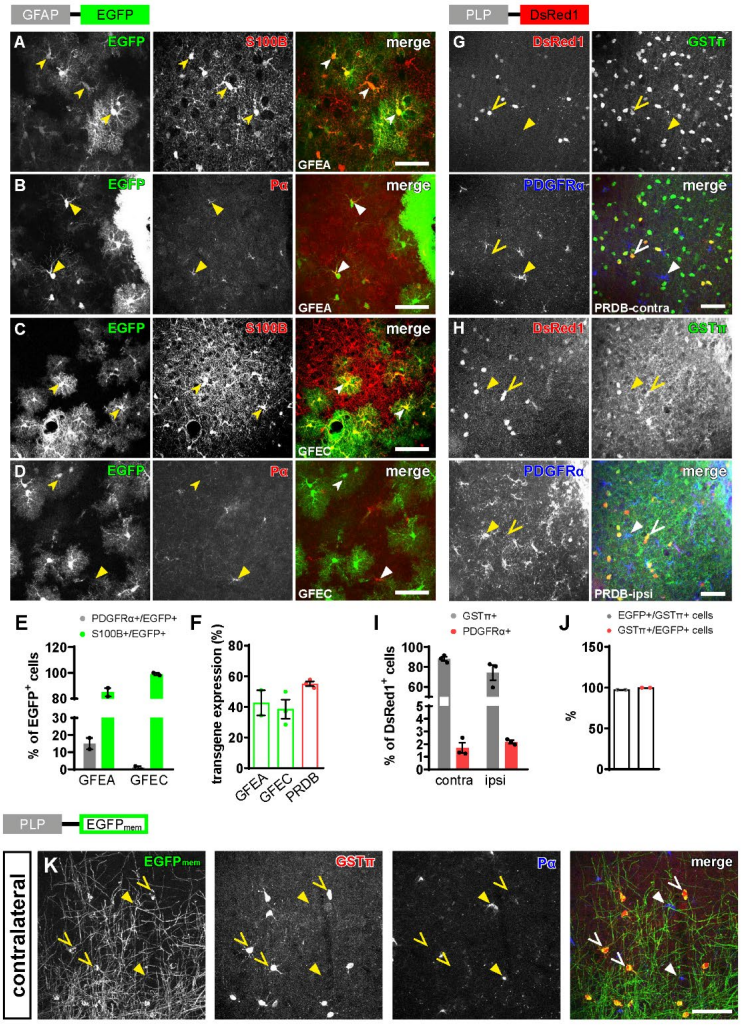

Figure S4. Analysis of transgene expression in hGFAP-EGFP, PLP-DsRed1 and PLP-EGFP$_{mem}$ mice, Related to Figure 4.

(A-E) Quantification of EGFP-expressing astrocytes (EGFP$^+$S100B$^+$) and OPCs (EGFP$^+$Pα$^+$) cells in both transgenic mouse lines with EGFP expression under control of the human GFAP promoter (hGFAP-EGFP$_A$ and hGFAP-EGFP$_C$). Scale bars = 50 µm.

(F) Transgene efficacy in hGFAP-EGFP$_A$, hGFAP-EGFP$_C$ and PLP-DsRed1 mice.

(G-I) Quantification of oligodendrocytes (GSTπ$^+$) and OPCs (Pα$^+$) expressing DsRed1 in contralateral (G) and ipsilateral (H) sides of PLP-DsRed1 mouse cortex. Scale bars = 50 μm.

(J, K) About 98% of mature oligodendrocytes (GSTπ$^+$) expressed EGFP and all EGFP$^+$ cells were mature oligodendrocytes. open triangles: oligodendrocytes, arrowheads: astrocytes, triangles: OPCs. Scale bar = 50 μm.

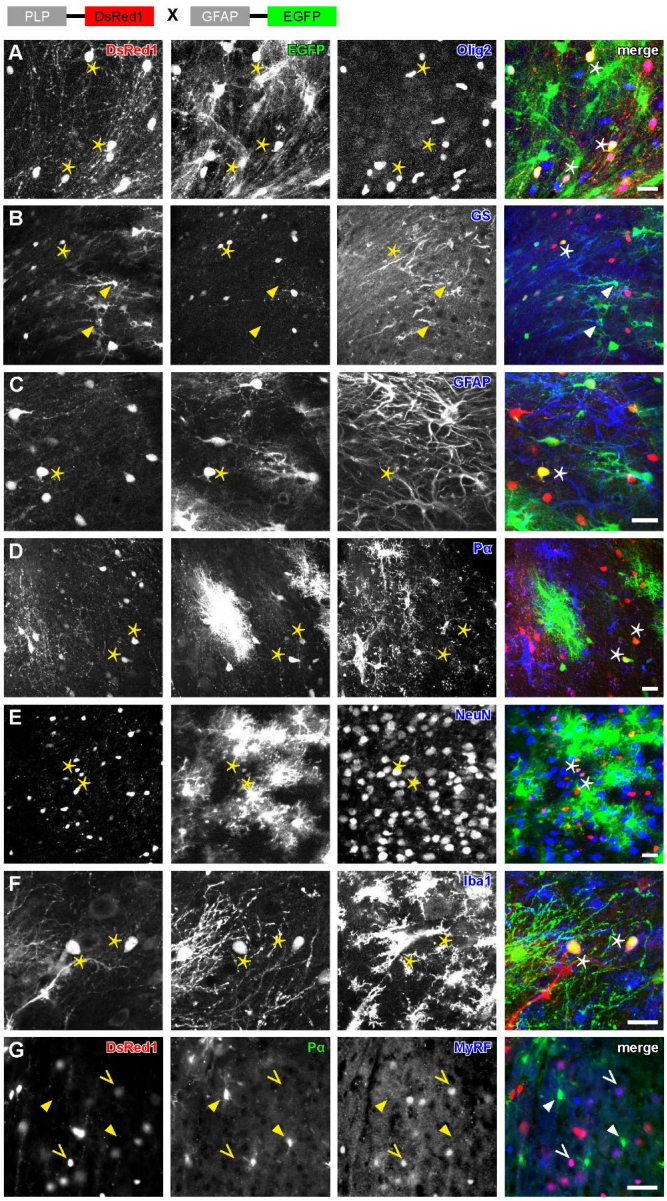

Figure S5. Immunohistochemical analysis of AO cells with cell-specific markers in PLP-DsRed1/GFAP-EGFP mice, Related to Figure 4.

(A) AO cells (asterisks) were positive for the oligodendrocyte lineage marker Olig2. Scale bar = 20 μm.

(B, C) AO cells were negative for astrocyte marker GS (B) or GFAP (C). Scale bars = 20 μm.

(D-F) AO cells (asterisks) were negative for markers of OPC (Pα, D), neurons (NeuN, E) and microglia (Iba1, F). Scale bars = 20 μm.

(G) DsRed1^{+} cells were positive for mature OL marker MyRF but not for Pα. Scale bar = 40 μm.

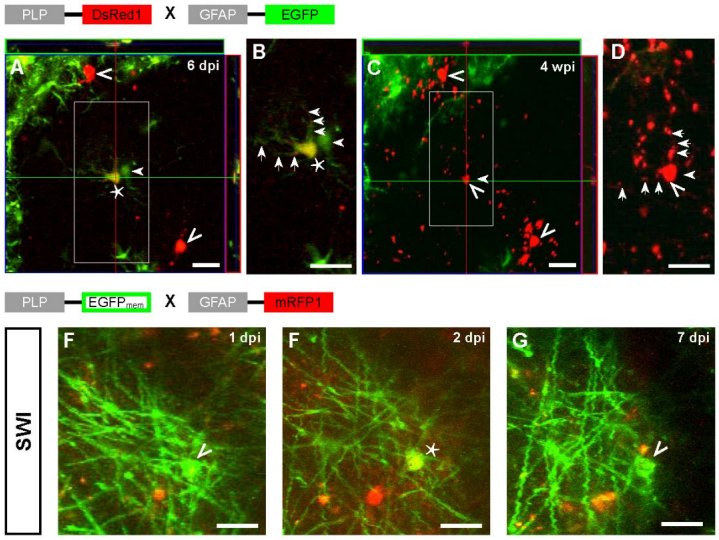

Figure S6. *In vivo* 2PLSM visualizes the differentiation of AO cells into oligodendrocytes, Related to Figure 6.

(A-D) Three weeks of AO cell tracing in PLP-DsRed1/GFAP-EGFP mouse revealed the conversion/differentiation of an AO cell (asterisk) into an oligodendrocyte (open triangles in A, C). Scale bars = 20μm.

(B, D) Magnified views of the AO cell (asterisk) that down-regulated EGFP expression in somata and processes (arrows) and differentiated into an oligodendrocyte (open triangle) four weeks after SWI. Note the disappearance of an EGFP-expressing astrocyte (arrowhead) between 6 dpi (A, B) and 28 dpi (C, D). Scale bars = 20μm.

(E-G) An oligodendrocyte started to express mRFP1 to become an AO cell at 2 dpi (asterisk in E) and lost mRFP1 expression already at 7 dpi (open triangle, G). Scale bars = 20μm.

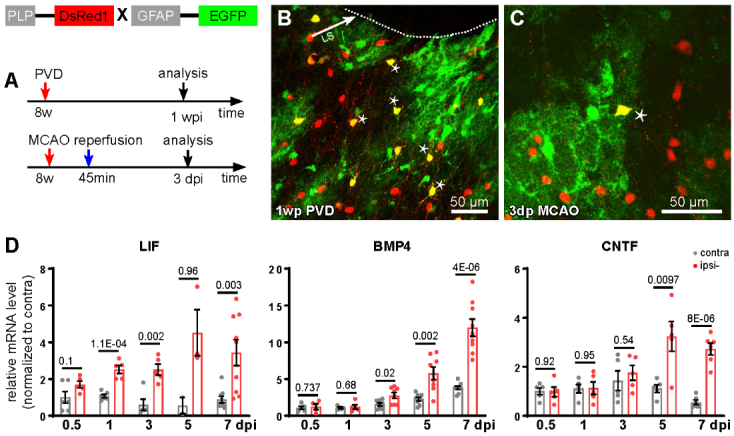

Figure S7. Various cytokines are upregulated after stab wound injury, Related to Figure 7.

(A) Experimental schedules.

(B, C) AO cells (asterisks) appeared adjacent to the lesion (LS) one week after PVD (arrow, B) and in penumbra three days after MCAO (45 min occlusion, C).

(D) LIF, BMP4 and CNTF mRNA was upregulated in the lesion site at different time points after SWI (two-sided unpaired t-test).

Aim of study IV

This study aimed to understand the influence of injury-induced environmental cues on direct neuronal reprogramming and revealed the chromatin-binding protein HMGB2 as a critical mediator for efficient astrocyte-to-neuron fate conversion.

Hmgb2 improves astrocyte to neuron conversion by increasing the chromatin accessibility of genes associated with neuronal maturation in a proneuronal factor-dependent manner

Priya Maddhesiya*, Tjasa Lepko*, Andrea Steiner-Mezzardi, Veronika Schwarz, Juliane Merl-Pham, Finja Berger, Stefanie M. Hauck, Lorenza Ronfani, Marco Bianchi, Giacomo Masserdotti, Magdalena Götz and Jovica Ninkovic

* These authors contributed equally to the manuscript

For this study, I assisted in the RNA-seq library preparation. Furthermore, I participated in paper editing and reviewing.

The manuscript was submitted to Genome Biology and has also been uploaded to the preprint platform BioRxiv, where it can be accessed via the following link:

DOI: https://doi.org/10.1101/2023.08.31.555708

Please note that due to the considerable number of pages, the extended tables are not included in the PDF version of this dissertation, but are available as separate excel files via the following link:

https://www.dropbox.com/scl/fo/l91s2xes9q3sr5161na3h/AEwqf3nTo5pcpOq1tj_6joc?rlkey=li8gdnyw6345sm6zb6msq3xnk&st=1mrwnug5&dl=0

Hmgb2 improves astrocyte to neuron conversion by increasing the chromatin accessibility of genes associated with neuronal maturation in a proneuronal factor-dependent manner

Priya Maddhesiya[1, 2, 3, §], Tjasa Lepko[1, 2, 3, §], Andrea Steiner-Mezzardi[3], Veronika Schwarz[1, 2, 3], Juliane Merl-Pham[4], Finja Berger[1, 2, 3], Stefanie M. Hauck[4], Lorenza Ronfani[5], Marco Bianchi[5], Giacomo Masserdotti[3, 7], Magdalena Götz[3, 7, 8] and Jovica Ninkovic[1, 2, 3, 8, *]

[1] Biomedical Center Munich (BMC), Department of Cell Biology and Anatomy, Medical Faculty, LMU, Munich, Germany

[2] Graduate School of Systemic Neurosciences, LMU, Munich, Germany

[3] Institute of Stem Cell Research, Helmholtz Zentrum Munich, Munich, Germany

[4] Research Unit Protein Science and Metabolomics and Proteomics Core, Helmholtz Centre Munich, German Research Center for Environmental Health, Neuherberg, Germany

[5] School of Medicine, Vita-Salute San Raffaele University, Milan, Italy

[6] Division of Genetics and Cell Biology, IRCCS San Raffaele Hospital, Milan, Italy

[7] Biomedical Center Munich (BMC), Institute of Physiological Genomics, LMU, Munich, Germany

[8] Munich Cluster for Systems Neurology SYNERGY, LMU, Munich, Germany

[§] These authors contributed equally to this work

* Correspondence to jovica.ninkovic@helmholtz-munich.de

Abstract

Background:

Direct conversion of reactive glial cells to neurons is a promising avenue for neuronal replacement therapies after brain injury or neurodegeneration. The overexpression of neurogenic fate determinants in glial cells results in conversion to neurons. For repair purposes, the conversion should ideally be induced in the pathology-induced neuroinflammatory environment. However, very little is known regarding the influence of the injury-induced neuroinflammatory environment and released growth factors on the direct conversion process.

Results:

We established a new *in vitro* culture system of postnatal astrocytes without epidermal growth factor that reflects the direct conversion rate in the injured, neuroinflammatory environment *in vivo*. We demonstrated that the growth factor combination corresponding to the injured environment defines the ability of glia to be directly converted to neurons. Using this culture system, we showed that chromatin structural protein high mobility group box 2 (HMGB2) regulates the direct conversion rate downstream of the growth factor combination. We further demonstrated that Hmgb2 cooperates with neurogenic fate determinants, such as Neurog2, in opening chromatin at the loci of genes regulating neuronal maturation and synapse formation. Consequently, early chromatin rearrangements occur during direct fate conversion and are necessary for full fate conversion.

Conclusions:

Our data demonstrate novel growth factor-controlled regulation of gene expression during direct fate conversion. This regulation is crucial for proper maturation of induced neurons and could be targeted to improve the repair process.

Background

Innovative approaches to stimulate tissue regeneration and functional restoration of the central nervous system are required, because the adult mammalian brain has limited ability to replace lost neurons [1–4]. Direct conversion of glial cells to neurons (induced neurons, iN) is a promising avenue for successful repair [2,5,6]. The overexpression of several neurogenic factors, alone or in combination, induces the conversion of several cell types, including astrocytes, pericytes, oligodendrocyte progenitors and fibroblasts, into post-mitotic neurons with different well-defined neurotransmitter identities [7–24]. These strong inducers of the neurogenic fate are transcription factors (TFs) that specify neuronal fate during development [7]. Many of these TFs have recently been shown to have pioneering factor activity and to bind closed chromatin configurations [5,25,26]. Indeed, recent insights regarding the fundamentals of neuronal fate specification have revealed that changes in chromatin structure might be a key factor in the stable acquisition of neuronal fate [27,28], in line with the pioneering activity of fate determinants inducing fate conversion. Despite their remarkable strength, defined single pioneering TFs (e.g., Neurog2) cannot successfully reprogram some starting cell types or cell states induced by culturing conditions [14]. The inability of Neurog2 to activate gene expression has been associated with epigenetic silencing of target loci [14,29]. Interestingly, forskolin (an agonist of adenylyl cyclase) and dorsomorphin (an inhibitor of BMP signaling) enhance the chromatin accessibility mediated by Neurog2, thus suggesting that additional pathways contribute to Neurog2's trailblazing properties [30,31]. In fact, treating Neurog2-expressing cells with these small molecules results in chromatin opening at a substantial number of sites, including CRE half-sites or HMG box motifs [30]. Thus, small molecules or a combination of other TFs may be necessary to induce successful or efficient reprogramming, depending on the starting populations, although Neurog2 is a pioneer factor that can overcome the lineage barrier. In addition to several factors associated with chromatin, microRNAs and small molecules have been found to improve the conversion efficiency and maturation status of reprogrammed neurons despite being unable to induce conversion on their own [12,15,32,33]. These findings support a model in which multi-level lineage barriers maintain cell identity and must be overcome for cells to acquire neuronal fate adequate for repair purposes. Comprehensive understanding of these barriers is at the core of successful iN generation and the functional restoration of the damaged CNS.

Importantly, most of these barriers have been identified through the use of defined and stable *in vitro* systems. However, for repair purposes, iNs must be generated in the injured environment. The intricacy of the injured milieu is an obstacle to understanding the molecular mechanisms of direct neuronal conversion *in vivo*. Injury triggers the release of several signaling factors with precise temporal resolution that can either resolve or strengthen the lineage barriers [34]. For example, epidermal growth factor (EGF) levels spike within 24 hours after brain injury and remain elevated for 3 days before returning to baseline. In contrast, basic fibroblast growth factor (bFGF) levels begin to rise 4 hours after damage and remain elevated for 14 days [34]. Infusion of bFGF into the brain after traumatic brain injury, for example, greatly enhances cognitive performance in animals by increasing neurogenesis [35]. Additionally, EGF infusion enhances neurogenesis via enlargement of the neurogenic precursor pool in the neurogenic niche after ischemia injury [36]. Moreover, forced Neurog2 expression in glial cells, along with the bFGF2 and EGF growth factors, enhances neuronal reprogramming *in vivo* [37]. Importantly, EGF receptor (EGFR) signaling has been proposed to regulate both global chromatin state and the accessibility of specific loci [38]. Furthermore, interaction of EGFR signaling and chromatin remodelers from the SWI/SNF family is critical for the expansion of beta cells after pancreas injury [39]. Similarly, FGF signaling orchestrates chromatin organization during neuronal differentiation [40]. Together, environmental signals

are likely to be integrated into the lineage barriers defining the propensity of starting glial cells to be converted to postmitotic neurons.

To investigate the embedding of growth factors in lineage barriers relevant to *in vivo* direct neuronal reprogramming after brain injury, we developed an *in vitro* model with altered growth factor composition. We showed that, in this model, neurogenic fate determinants induced astrocyte to neuron conversion with a diminished efficiency comparable to the conversion rate observed *in vivo.* This system allowed us to identify Hmgb2 as a novel regulator in the context of direct astrocyte to neuron conversion. We showed that high levels of Hmgb2 alleviate the lineage barrier and promote efficient establishment of neuronal fate. Our data suggest that Hmgb2-dependent chromatin opening of regulatory elements controls the expression of neuronal maturation genes and enables the establishment of the full neurogenic program, thereby resulting in efficient astrocyte to neuron conversion.

Results

Growth factors shape the lineage barriers to glia to neuron conversion

To investigate the contributions of injury-induced growth factors to lineage barriers to maintaining glial fate in the injured mammalian brain, we established a new *in vitro* model with the growth factor composition adjusted to better reflect the local environment after injury. After brain injury, levels of EGF peak within the first 24 h and return to baseline levels 3 days post injury (dpi). In contrast, FGF levels increase by 4 h after injury and persist until 14 dpi [41]. To mimic the dynamics in the *in vivo* environment, we cultured astrocytes, obtained from postnatal murine cerebral cortex (P5–P7) for 10 days in the presence of only bFGF, then compared the direct conversion rates to neurons in this culture with the conversion efficiency in the widely used culture conditions containing both EGF and bFGF [42,43]. To convert astrocytes into neurons, we transduced cells with an MLV-based retrovirus for expression of the neurogenic TFs reported to reprogram astrocytes (Neurog2, Pou3f2 or Sox11; Fig. 1a) *in vitro* and a fluorescent reporter protein. The expression of the fluorescent reporter protein was used to identify the transduced cells. The identity of the transduced cells was probed 7 days after viral transduction (days *in vitro* (div); Fig. 1a). Only cells expressing doublecortin (DCX) and having at least one process longer than three cell somata diameters were identified as neuronal cells, according to Gascon et al. [44] (Fig. 1b, c). The transduction of astrocytes with control viruses for expression of either GFP or dsRed did not induce glia to neuron conversion in any culturing conditions (Suppl. Fig. 1a-d). In contrast, the transduction of astrocytes isolated from EGF+bFGF culture with several neurogenic fate determinants did induce their conversion, and neurons at different maturation stages (on the basis of the complexity of their processes) were observed after 7 div (Fig. 1b, d). Interestingly, neither Neurog2 nor Pou3f2 induced the direct conversion of astrocytes grown in the presence of only bFGF, whereas the culturing conditions did not significantly alter the conversion by overexpression of Sox 11 (Fig. 1d). Because the culture condition with bFGF contained only half the usual growth factors, we assessed the conversion rate of cultures containing only EGF. Importantly, Neurog2 induced the conversion of astrocytes grown with only EGF at the same rate as astrocytes grown in EGF+bFGF culture medium (Suppl. Fig. 1d-f), in line with the specific role of bFGF in decreasing the conversion rate.

This difference in direct conversion could be explained by the selection of particular cell types during astrocyte expansion with growth factors. Therefore, we assessed the identity of the transduced cells 24 h after transduction by using immunocytochemistry (Suppl. Fig. 2a). Most cells expressed the astrocyte marker S100β in both culture conditions, without any significant differences (Suppl. Fig. 2b, c, f). Similarly, we did not observe any differences in the proportion of GFAP+ cells (Suppl. Fig. 2d-f). In line with reports that astrocytes *in vitro* express the TF Olig2 [45], most cells in both culture conditions expressed Olig2 (Suppl. Fig. 2g-i). Moreover, we observed only a small proportion of DCX+ neuronal progenitors or αSMA+ pericytes in both cultures (Suppl. Fig. 2d-i), thus indicating comparable cellular compositions between cultures, according to the analyzed marker expression. Interestingly, we observed lower proliferation rates of astrocytes grown in bFGF than EGF+bFGF conditions, on the basis of the expression of Ki67 or pH3 (Suppl. Fig. 2j-n). This finding suggested that bFGF-grown astrocytes might further differentiate, epigenetically silence neuronal loci and become less prone to direct conversion, as previously shown for long-term astrocyte cultures [46]. To examine this possibility, we cultured astrocytes for 7 days in bFGF culture conditions, added EGF and grew astrocytes for an additional 7 days with EGF+bFGF (Suppl. Fig 3a). The conversion rate of these astrocytes was compared with that of astrocytes cultured in either EGF+bFGF or bFGF for 14 days (Suppl. Fig. 3b, f). As expected, longer culturing of cells in

either bFGF or EGF+bFGF decreased the direct reprogramming rate (Suppl. Fig. f), as previously described [46]. However, the post-culturing of initially bFGF-grown astrocytes in EGF+bFGF for 7 days improved their reprogrammability, and we observed no differences in the proportions of generated neurons compared with astrocytes continuously cultured in EGF+bFGF (Suppl. Fig. 3b, c, f). Moreover, the conversion rate of EGF+bFGF-grown astrocytes decreased after culturing in bFGF for 7 days, and no differences were observed between this culture and continuously bFGF cultured astrocytes (Suppl. Fig. 3d-f). Together, the cell identity marker analysis and the alterations in the culture composition experiments suggested that growth factor conditions define the astrocytic lineage barriers and consequently the rate of direct conversion to neurons, on the basis of neurogenic factor overexpression.

High mobility group box 2 (Hmgb2) levels are decreased in bFGF astrocyte culture

To identify factors responsible for maintaining the astrocytic lineage barrier, we performed label-free LC-MS/MS-based proteome analysis of astrocytes cultured with either bFGF or EGF+bFGF for 10 days. In total, we detected approximately 1700 proteins, of which 157 showed differences in levels between culture conditions (1.5-fold change, $p<0.05$): 68 significantly enriched in the EGF+bFGF culture and 89 significantly enriched in the bFGF culture (Fig. 1e, Suppl. Table 1). Gene Ontology (GO) analysis revealed an enrichment of cytoskeleton-associated processes in the protein set enriched in the bFGF-grown culture (Fig. 1f; Suppl. Table 1), whereas transport across the mitochondrial membrane, metabolic processes and chromatin-associated processes were enriched in the EFG+bFGF induced proteome (2-fold enrichment, $p<0.05$; Fig. 1g). These data are in line with recent evidence indicating that changes in the mitochondrial proteome during astroglia to neuron conversion determine the extent of the direct conversion [47]. Moreover, because chromatin state has been reported to regulate lineage barriers in reprogramming [44,48–52], we searched for chromatin-associated factors differentially enriched between culture systems. The chromatin architectural protein Hmgb2 was 1,88-fold enriched in EGF+bFGF compared with bFGF cultures (Fig. 1e). This enrichment was confirmed by western blotting (Fig. 1h, j). Interestingly, we also observed that the HMGB2 protein family member HMGB1 was enriched in the EGF+bFGF culture condition, although at a lower level (Fig. 1e). In the adult mouse brain, Hmgb2 is specifically expressed in cells committed to the neurogenic lineage (transit amplifying progenitors, neuroblasts) in both neurogenic niches [53] in addition, traumatic brain injury induces Hmgb2 expression in a subset of reactive astrocytes (Suppl. Fig. 4). These findings suggest that HMGB2 might be an important factor improving direct conversion in the EGF+bFGF culture.

Hmgb2 levels define the rate of direct astrocyte to neuron conversion

To test whether Hmgb2 might have functional relevance in fate conversion, we transduced astrocytes, grown for 10 days in medium containing either EGF+bFGF or bFGF, with Hmgb2-encoding retrovirus (Fig. 2a), and assessed the identity of the transduced cells 7 days later, on the basis of DCX expression and cell morphology (see above; Fig. 1b-d). Overexpression of Hmgb2 did not alter cell identity in either culture condition (Fig. 2b-e). Most cells retained their astrocyte identity and expressed GFAP (Fig. 2e). However, when we co-transduced the bFGF-grown astrocytes with retroviruses for expression of Neurog2-dsRED and Hmgb2-GFP, we observed a 2.5-fold greater conversion rate in the co-transduced cells than cells transduced with Neurog2 only (Fig. 2c, d). Interestingly, the co-overexpression of Neurog2+Hmgb2 did not further improve the conversion of EGF+bFGF-grown astrocytes,

because the conversion rate of Neurog2+Hmgb2 co-transduced astrocytes was comparable to that of Neurog2-transduced astrocytes in this culture condition (Fig. 2b, d).

Improvement in the Neurog2-mediated conversion rate of bFGF-grown astrocytes prompted us to investigate whether this improvement might be factor-specific. Therefore, we assessed the effect of Hmgb2 overexpression on Pou3f2-mediated fate conversion, given that the neurogenic capability of Pou3f2 was also diminished in bFGF-grown astrocytes (Fig. 1d). Similarly to the Neurog2-mediated conversion, the simultaneous overexpression of Hmgb2 and Pou3f2 in EGF+bFGF-grown astrocytes did not result in higher conversion rates, whereas the factor combination significantly increased the conversion rate in bFGF-grown astrocytes (Suppl. Fig. 1g). Together, these data suggested that Hmgb2 does not induce direct conversion on its own but increases the ability of neurogenic factors to overcome the lineage barriers.

To test whether Hmgb2 might be necessary for direct astrocyte to neuron conversion, we isolated astroglia from Hmgb2-deficient mice ($Hmgb2^{MUT/MUT}$) and their siblings ($Hmgb2^{WT/MUT}$ and $Hmgb2^{WT/WT}$), cultured them in the direct conversion permissive conditions (EGF+bFGF) and induced conversion by Neurog2 overexpression (Fig. 3a). Neurog2 overexpression induced direct conversion of $Hmgb2^{WT/WT}$ and $Hmgb2^{WT/MUT}$ astrocytes (Fig. 3b-d), in agreement with our previous findings demonstrating high responsiveness of EGF+bFGF-grown astrocytes (Fig. 1d). However, the conversion rate of Hmgb2-deficient ($Hmgb2^{MUT/MUT}$) astroglia significantly decreased compared to WT siblings (Fig. 3c, d). These findings supported our hypothesis that Hmgb2 levels define the astrocytic lineage barrier.

Prospero homeobox protein 1 (Prox1) overexpression improves direct glia to neuron conversion in FGF only culture

To understand the Hmgb2-dependent lineage barrier in direct glia to neuron conversion, we compared the transcriptional changes induced by Neurog2 overexpression in the bFGF and EGF+bFGF cultured cells 48 h after transduction. Cells transduced with different viruses were purified by FACS, and genes regulated by Neurog2 overexpression were compared (Suppl. Fig. 5). We identified differences in the expression of 443 genes (321 up-regulated and 122 down-regulated genes, fold change > 2, padj < 0.05) induced by Neurog2, as compared with that in control CAG-GFP virally transduced cells in the EGF+bFGF culture condition (Suppl. Fig. 6 a, Suppl. Table 2). In the bFGF culture, Neurog2, as compared with the respective CAG-GFP transduced control, induced 171 genes (137 up-regulated and 34 down-regulated genes, fold change > 2, padj < 0.05) (Suppl. Fig. 6 b, Suppl. Table 2). GO analysis (biological processes, fold enrichment > 2 and $p < 0.05$) of genes (321) upregulated in EGF+bFGF culture revealed enrichment in the terms nervous system development, neuronal differentiation, and migration (Fig. 4a), in line with the ability of Neurog2 to successfully convert astroglia to neurons. Unexpectedly, the significantly enriched biological processes in the set of the 137 up-regulated genes in the bFGF culture were also associated with regulation of neurogenesis, nervous system development and synaptic signaling (Fig. 4b), thereby indicating that Neurog2 overexpression at least partially induced the neuronal fate in astrocytes grown in the bFGF condition. Indeed, we observed that 96 genes were induced by Neurog2 in both bFGF and EGF+bFGF cultures (Fig. 4c), and were enriched in GO biological processes associated with regulation of neurogenesis, nervous system development, neuronal differentiation and migration (Suppl. Fig. 6c). In addition, in the bFGF culture, the 41 genes uniquely induced by Neurog2 (Fig. 4c) were associated with GO biological processes of cardiac muscle tissue development, leukocyte differentiation, response to lithium-ion and neurotransmitter receptor

to the plasma membrane (Suppl. Fig. 6d). These findings suggested that, in contrast to the EGF+bFGF culture, in the bFGF culture, Neurog2 induced other fates along with neuronal processes possibly interfering with the establishment of the neuronal identity [54]. Furthermore, we identified 225 uniquely Neurog2-induced genes in the EGF+bFGF culture (Fig. 4c) associated with the GO biological processes regulation of membrane potential and ephrin receptor pathway (Suppl. Fig. 6d), which regulate neuronal maturation and axonogenesis [55,56]. Moreover, previously reported Neurog2-induced genes necessary for successful conversion, such as *Neurod4*, *Insm1*, *Hes6*, *Slit1*, *Sox11* and *Gang4* [46] were up-regulated in both cultures (Fig. 4d). Nevertheless, genes such as *Dscaml1*, *Prox1*, *Lrp8* and *Shf* were induced in only the EGF+bFGF culture. Importantly, the co-expression of Neurog2 and Hmgb2 in bFGF-grown astrocytes induced the expression of these genes to levels similar to those detected in the Neurog2-transduced EGF+bFGF culture (Fig. 4d). Therefore, the bFGF culture established the lineage barrier by interfering with the induction of a small, specific set of genes relevant for the conversion. To test this hypothesis, we selected one candidate, Prox1, and evaluated whether it might help overcome the bFGF only medium restrictive conditions. We overexpressed Prox1 in the bFGF-cultured cells and observed only a small increase in the conversion rate (Fig. 4e). However, after the co-expression of Neurog2 and Prox1 in bFGF-cultured astrocytes, we observed a significant increase in the proportion of generated neurons similar to the conversion rate induced by Neurog2 in the EGF+bFGF culture and the bFGF-cultured astrocytes co-transduced with Neurog2 and Hmgb2 (Fig. 4e). Moreover, microRNA-mediated knockdown of Prox1 decreased the Neurog2-mediated conversion of EGF+bFGF cultured astrocytes, in line with previous reports [46]. This conversion rate was also comparable to the rate of Neurog2-mediated conversion of bFGF-cultured astrocytes (Fig. 4e).

Hmgb2-dependent expression of a specific set of neuronal maturation genes is necessary for efficient direct glia to neuron conversion

Our data suggested that low Hmgb2 expression levels in the bFGF culture could decrease astrocyte to neuron conversion via several non-mutually exclusive mechanisms: a) failure to activate the full neurogenic program induced in EGF+bFGF culture, b) prevention of the silencing of the conflicting alternative lineages and c) induction of a different neurogenic program from that in the EGF+bFGF culture. To directly test these possibilities, we analyzed the transcriptomic changes induced by the overexpression of Hmgb2 alone or in combination with Neurog2 in both bFGF and EGF+bFGF cultures.

Interestingly, Hmgb2 overexpression induced only several differentially expressed genes (DEGs) in either EGF+bFGF or bFGF cultures with respect to CAG-GFP control viral transduction ((Suppl. Fig. 6e, f; FC >2, padj < 0.05): two DEGs in the bFGF condition and four DEGs in the EGF+bFGF culture condition, Suppl. Table 2). This transcriptomic analysis, together with the lack of change in the conversion rate after Hmgb2 overexpression in both bFGF and EGF+bFGF astrocytes (Fig. 2d), suggested that Hmgb2 did not implement any specific neurogenic program on its own. Notably, the overexpression of Hmgb2 together with Neurog2 in the bFGF culture, as compared with control viral transduction, induced 255 genes (Fig. 3 g). This gene set was significantly enriched in GO biological processes associated with neural development, neuronal migration, axon guidance and synaptic signaling (Fig. 4f), similarly to the GO biological processes induced by Neurog2 alone in the EGF+bFGF condition (Fig. 4a). In addition, we observed downregulation of 164 genes (Suppl. Table 3) enriched in regulation of cell adhesion, actin filament organization, stress fiber assembly, and regulation of protein phosphorylation (Suppl. Fig. 6g), thus suggesting that simultaneous overexpression of Neurog2 and Hmgb2 suppresses gene expression that may block successful conversion of astroglia to neurons, possibly through post-translational modifications [57].

However, the down-regulated genes were not associated with specific glial or alternative fates induced by Neurog2 in the bFGF culture (Suppl. Fig. 6g).

To determine whether the dual overexpression of Neurog2+Hmgb2 might trigger similar transcriptional programs in the bFGF culture and the Neurog2-transduced the EGF+bFGF culture, we compared induced genes among three conditions: reprogramming prone culture (EGF+bFGF transduced with Neurog2 vs control virus), reprogramming resistant culture (bFGF transduced with Neurog2 vs control virus) and revived reprogramming culture (bFGF transduced with Neurog2+Hmgb2 vs control virus). We identified 88 genes that were shared across all three conditions (Fig. 4g) and were enriched in GO biological processes associated with neurogenesis, neuronal differentiation and migration, and trans-synaptic signaling (Suppl. Fig. 6h), in line with our findings that all conditions at least partially induced the neurogenic program. Furthermore, 46 genes (for example, *Prox1*, *Lrp8*, *Shf* and *Dscaml1*) were shared exclusively between the reprogramming prone conditions (bFGF Neurog2+Hmgb2 and EGF+bFGF Neurog2). This gene set was enriched in GO biological processes associated with axonogenesis, positive regulation of neurogenesis, neuron projection guidance, and nervous system development, thus implying that the upregulation of genes induced by the simultaneous overexpression of Neurog2 and Neurog2+Hmgb2 in the bFGF culture are associated with the acquisition of a more mature neuronal phenotype.

Together, our data suggested that the Hmgb2 protein aids in implementing the Neurog2-dependent, neurogenic program in astrocytes by facilitating the induction of a specific set of neurogenic, neuronal maturation-associated genes.

Hmgb2 increases the chromatin accessibility of regions associated with the neurogenic program

We hypothesized that the establishment of the full neurogenic program by high levels of Hmgb2 is associated with Hmgb2-dependent chromatin changes. Therefore, we performed assay for transposase-accessible chromatin with high-throughput sequencing (ATAC-seq) on the cells from the same sorting samples used to generate transcriptomic libraries (Suppl. Fig. 5). We first examined the genome-wide chromatin accessibility profile at transcription start sites (TSSs ± 3.0 Kb) in both bFGF and EGF+bFGF cultures after the overexpression of Hmgb2, Neurog2, Neurog2+Hmgb2 and CAG-GFP control. The accessibility profile of Hmgb2 overexpressing astrocytes was comparable to that of the control regardless of the culture condition (Fig. 5a), in line with the lack of changes in the transcriptome and conversion rate analysis (Fig. 2e; Suppl. Fig. 6e, f). We did not observe any discernible increase in chromatin accessibility with simultaneous overexpression of Neurog2+Hmgb2 compared with Neurog2 in EGF+bFGF culture. However, we observed a substantial increase in chromatin accessibility after simultaneous overexpression of Neurog2+Hmgb2 compared with Neurog2 in the bFGF culture (Fig. 5b). This increase in TSS (±3 kb) accessibility might have been due to at least two mutually non-exclusive mechanisms: a) widespread TSS opening after Hmgb2 overexpression, or b) lineage specific changes. Therefore, we analyzed the TSS accessibility of neuronal cell-type-specific genes [58] (Fig. 5c). Whereas we observed the accessibility of these sites increased after both Neurog2 and Neurog2+Hmgb2 overexpression in the EGF+bFGF culture condition, in the bFGF culture condition, the increase in these sites was detectable only after simultaneous overexpression of Neurog2+Hmgb2 but not Neurog2 alone (Fig. 5c). Interestingly, the TSS opening was comparable between bFGF and EGF+bFGF astrocytes after Neurog2+Hmgb2 overexpression (Fig. 5c), in line with an increased conversion rate. Next, we wondered whether the Hmgb2-dependent increase in accessibility

342 might be confined to neuronal genes or whether it might also occur in genes specific for other
343 cell lineages. Therefore, we analyzed the dependence of the promoter accessibility of genes
344 identifying ES cells [59,60], endothelial cells [61–63], and microglial cells [64,65] on Hmgb2
345 levels in bFGF culture (Fig. 5d). We found no significant differences in accessibility between
346 the Hmgb2, Neurog2 or Neurog2+Hmgb2 treated astrocytes and the controls, thus indicating
347 that the accessibility change after Neurog2+Hmgb2 overexpression was specific for neuronal
348 fate.

349 To identify direct conversion relevant changes in chromatin accessibility dependent on
350 Hmgb2 levels, we determined the significant differentially accessible sites (DASs) after
351 overexpression of Neurog2 and Neurog2+Hmgb2, compared with CAG-GFP-transduced cells,
352 in the bFGF and EGF+bFGF culture conditions. In the bFGF culture, Neurog2 overexpression
353 resulted in 612 DASs (445 more accessible sites (MASs) and 167 less accessible sites (LASs);
354 Fig. 5e, Suppl. Table 4). Combined overexpression of Neurog2+Hmgb2 in the bFGF culture
355 resulted in 1213 DASs (1062 MASs and 151 LASs; Fig. 5e, Suppl. Fig. 7a). However, this
356 increase in accessibility did not change the accessibility profile induced by Neurog2 and
357 Neurog2+Hmgb2 in the bFGF culture, because we observed a similar distribution of MAS in
358 the gene bodies, promoters and intergenic regions (Suppl. Fig. 7b, c). Importantly, the Hmgb2-
359 associated increase in MASs was not observed in EGF+bFGF astrocyte culture (Fig 5e), in
360 agreement with our transcriptome analysis. To reveal the processes influenced by MASs, we
361 analyzed genes associated with these sites (defined as genes within 3 kb upstream and
362 downstream of the MAS) in GO analysis. MASs induced by the simultaneous overexpression
363 of Neurog2+Hmgb2 in the bFGF culture were associated with nervous system development,
364 synaptic membrane adhesion, axon guidance, synapse assembly and chemical synaptic
365 transmission (Fig. 5f, Suppl. Table 5). This finding suggests that Hmgb2 (together with
366 Neurog2) increases the accessibility of genes involved in neuronal maturation. Indeed, the
367 promoters of synapse-associated genes such as *Kif1a* [66,67], *Artn* [68] and *Rasd2* [69] were
368 closed in the bFGF culture after either control viral transduction or Hmgb2 overexpression (Fig.
369 5h), in line with the astrocytic fate of these cells. Moreover, Neurog2+Hmgb2 overexpression
370 opened the synapse-associated promoters to a significantly greater extent than Neurog2 alone
371 (Fig. 5g, h). We then asked whether the chromatin opening state of all or only a subset of
372 Neurog2-induced maturation genes depended on the expression of Hmgb2. Therefore, we
373 compared the MASs induced by Neurog2 in the two conversion prone conditions
374 (overexpression of Neurog2 in EGF+bFGF and overexpression of Neurog2+Hmgb2 in bFGF
375 culture) with MASs induced by Neurog2 in the conversion resistant condition (overexpression
376 of Neurog2 in bFGF culture). We identified 395 MASs commonly induced in both conversion
377 prone conditions (Fig. 6a). These MASs were enriched in processes associated with synapse
378 formation (GO biological processes such as nervous system development, synaptic
379 organization, trans-synaptic signals, potassium transport, and synaptic membrane adhesion;
380 Fig. 6b, Suppl. Table 6). Importantly, the increase in the accessibility of these synapse-
381 associated loci correlated with the increased expression of these genes after Neurog2+Hmgb2
382 overexpression in bFGF culture (Suppl. Fig. 8 a, b). However, we also observed 268 MASs
383 induced by Neurog2 in all three conditions (Fig. 6a) that were enriched in synaptic processes
384 (Fig. 6c, Suppl. Table 6). Therefore, these data suggested that the chromatin containing only a
385 subset of genes associated with neuronal maturation was dependent on Hmgb2. However, the
386 accessibility of these genes appeared to be instrumental for direct conversion.

387 Together, our data supported a model in which Hmgb2 fosters the establishment of the full
388 neurogenic program by increasing the accessibility and consequently the expression of
389 neuronal maturation genes, thus leading to improved neuronal maturation.

Hmgb2-dependent chromatin sites contain both E-boxes and Pou factor binding sites important for neuronal maturation

HMG proteins play a major role in controlling gene expression by increasing chromatin accessibility [70–72]. Therefore, we sought to identify the potential TF binding motifs enriched in the Hmgb2-dependent set of MASs (395 sites in Fig. 6a). To do so, we performed *de novo* motif enrichment analysis using BaMMmotif software. Motifs containing the consensus binding sequence of the Tal-associated TF family (Neurod1, Neurog2, Neurod2, Atoh1 and Msgn1) were enriched in Hmgb2-dependent set of MASs (Fig. 6d, Suppl. Table 7). In addition, we identified the motif that best matched the consensus sequence of the TF family of POU domain factors, such as Pou2f2 (Fig. 6e, Suppl. Table 7). Pou2f2 is a direct Neurog2 target [73] and has been reported to be involved in the implementation of proper neuronal identity [74,75]. This finding suggested that in the bFGF culture, some of the E-box motif sites bound by Neurog2 (Tal related factors) were inaccessible, but with the addition of Hmgb2, these sites became accessible, thereby increasing Neurog2-binding and enhancing reprogramming efficiency. Additionally, we investigated MASs with consensus binding sequences for both Tal-associated factors (Neurog2) and POU domain factors. We identified that 56 of 395 MASs contained binding motifs for both TF families, and were associated with neuronal maturation (GO processes: regulating actin filaments assembly, chemotaxis, and potassium ion transport; Suppl. Fig. 8d and Suppl. Table 7), including the Robo-Slit pathway. Robo-Slit pathway has been reported to regulate not only axonal pathfinding but also neuronal maturation [76]. Moreover, we observed enrichment in genes associated with the negative regulation of proliferation, thus possibly improving the terminal differentiation of converted cells. Interestingly, *de novo* motif analysis of the common 268 Neurog2-induced MASs identified the binding motif of the TF family of Tal-associated factors, but not of the POU domain factors (Fig. 6d). These data suggested that Hmgb2 levels set the lineage barrier by controlling the accessibility of both the direct Neurog2 targets and targets of TFs downstream of Neurog2, such as Pou3f2 or Neurod.

To directly test the importance of Hmgb2 in neuronal maturation, we analyzed the neurite complexity of the converted neurons in the conversion prone cultures (overexpression of Neurog2 in EGF+bFGF and overexpression of Neurog2+Hmgb2 in bFGF culture) and the conversion resistant culture (overexpression of Neurog2 in bFGF culture) in induced neurons with Sholl analysis 7 days after viral transduction (Fig. 7a). Indeed, Neurog2-induced neurons in the bFGF culture showed fewer intersections than the Neurog2-induced neurons in the EGF+bFGF culture (Fig. 7b, c). Lower neurite complexity is indicative of less mature neurons. The complexity of neurites in neurons generated from bFGF astrocytes by the combined overexpression of Neurog2 and Hmgb2 increased compared to overexpression of Neurog2 only. These converted neurons were indistinguishable from those generated by overexpression of Neurog2 in the EGF+bFGF-cultured astrocytes (Fig. 7b, c).

Discussion

The establishment of neuronal identity during direct astrocyte to neuron conversion is achieved in very different environmental context from that of the bona fide neurogenesis occurring during embryonic development or in adult brain neurogenic niches [49,51]. This includes not only the different starting populations [49] but also the unique signaling milieus [77–79]. The growth factors released after injury regulate the conversion process, including neuronal maturation and neural circuit repair. Here, we presented a novel *in vitro* system to study the influence of growth factors on fate conversion. Using this system, we showed that EGF, potentially provided by the injured environment, is necessary for efficient neuronal conversion and proper maturation via the regulation of the chromatin binding protein Hmgb2. In combination with several different neurogenic fate determinants, Hmgb2 is capable of inducing the full neurogenic program, as indicated by Hmgb2 gain and loss of function experiments. Our model predicted that prolonged injury-induced elevation in bFGF levels decreased the reprogrammability of astrocytes to neurons. However, the FGF signal per se did not prevent the induction of a set of processes associated with neurogenesis and neuronal fate in astrocytes during Neurog2-mediated conversion. This finding is in line with reports that the FGF promotes neurogenesis [80–82], although the neuronal subtypes generated in such context differ [82]. Importantly, the chromatin states in direct conversion and during embryonic neurogenesis may differ: the chromatin states during neurogenesis require fewer re-arrangements in embryonic development, because large numbers of neurogenic gene loci in radial glial cells, the neuronal stem cells of the developing CNS, are already in an open configuration [83,84]. Interestingly, genes involved in synapse formation and neuronal maturation are already in an active chromatin state without detectable gene expression in both radial glia and committed neuronal progenitors [83,85], thus implying the existence of an active inhibitory mechanism keeping the progenitor state primed toward neurogenesis and preventing their premature differentiation. Importantly, Hmgb2 opens the loci of these classes of genes during astrocyte to neuron conversion, thus supporting the concept that overexpression of Neurog2+Hmgb2 endows postnatal astrocytes with some stem cell features. This concept is also in line with the expression of Hmgb2 during activation of quiescent neural stem cells in the adult brain [53] and its role in adult neurogenesis [86]. However, we did observe immediate expression of synaptic genes in postnatal astrocytes without the maintenance of these primed neuronal states, thus suggesting that the mechanisms preventing premature differentiation operating in the neuronal stem cells are not established during astrocyte to neuron conversion. This possibility reinforces the concept that direct neuronal conversion does not fully recapitulate the developmental trajectory underlying neuronal differentiation [44,48]. Instead, the overexpression of reprogramming factors induces early re-arrangements of chromatin along with changes in gene expression. However, during late morphological and functional maturation stages of the induced neurons, changes in chromatin are negligible [87]. Moreover, in our *in vitro* system, we did not observe any changes in astrocyte proliferation due to the overexpression of Hmgb2 alone or in combination with different neurogenic TFs, thus further limiting the spectrum of neural stem cell features induced in the postnatal astrocytes. Interestingly, Hmgb2 induces similar chromatin changes in postnatal astrocytes to the HMG group protein A2, a different HMG-box-containing family member in gliogenic radial glial cells. These chromatin changes are sufficient to prolong the neurogenic phase during cortical development and lead to the generation of new postnatal neurons [88]. During this period, progenitors normally generate glial cells, thus potentially implicating similar mechanisms in the Hmga2-mediated extension of neurogenic period and the Hmgb2-mediated direct astrocyte to neuron conversion. Because Hmga2 is associated with Polycomb signaling [89], testing whether the same system would be operational during the Hmgb2-dependent conversion

479 should prove interesting, because Ezh2 maintains the lineage barriers during fibroblast to
480 neuron conversion [90]. Both Hmgb2 and Hmga2 bind AT-rich DNA segments with little to
481 no sequence specificity [91][71]. Nevertheless, we observed highly specific Hmgb2-dependent
482 opening of chromatin containing late neuronal maturation genes, thus prompting questions
483 regarding HMG protein binding specificity. This specificity could be provided by an interacting
484 protein, e.g., neurogenic TF Neurog2, because we observed an enrichment of the typical E-box
485 binding sequence in the promoters when Hmgb2 was overexpressed in astrocytes. However,
486 our findings did not reveal a direct interaction of Hmgb2 with Neurog2 via WB or mass
487 spectrometry, thus making this scenario unlikely. An alternative explanation may be that
488 Hmgb2 stabilizes the regulatory loops (transactivation domains, TADs) involved in the
489 expression of synaptic genes. The regulatory roles of such domains have been demonstrated
490 for neurogenesis downstream of Neurog2 during embryonal cerebral cortex development [92].
491 Moreover, both Hmgb2 and Hmga2 have been implicated in TAD establishment [93,94]. The
492 stabilization of regulatory loops induced by Neurog2 may indeed provide a mechanistic
493 explanation for the Hmgb2-dependent opening of chromatin regions containing the Neurog2
494 binding E-boxes. These data further challenge the common belief that Neurog2 is a pioneer
495 TF. In contrast to the on-target pioneering function of Ascl1 during reprogramming [87,95], in
496 fibroblast to neuron conversion, Neurog2 requires additional factors, such as forskolin and
497 dorsomorphin or Sox4, that are necessary for not only late neuronal maturation but also the
498 induction of early reprogramming changes [73,96]. We demonstrated that, at least in the case
499 of astrocyte to neuron conversion, Neurog2 function is dependent on Hmgb2. Because Hmgb2
500 increases the accessibility of various sites, including the binding motif of the Neurog2 target
501 Pou2f2 [92], our data suggested that Neurog2 must open the chromatin of maturation genes
502 that are transcriptionally regulated by direct Neurog2 targets. Our study provides mechanistic
503 insights into previously described improvements in neuronal reprogramming with the infusion
504 of EGF and FGF [37]. Interestingly, EGF and FGF exhibit different temporal dynamics post-
505 injury, with a very narrow expression window and a presumably diminished activity window
506 of EGF [41]. This window correlates with the expression of Hmgb2, thus suggesting that
507 prolonged expression the either EGF or Hmgb2 after TBI might be important in the success of
508 neuronal replacement therapies. Furthermore, our model may also explain the lower direct
509 conversion rates induced by Neurog2 in some starting cellular populations, such as
510 oligodendrocyte precursor cells [97], in which the promoters might not yet be open. Similarly,
511 such multilevel control is compatible with the ability of Neurog2 to induce different neuronal
512 subtypes or maturation stages in different, permissive starting cells [46,96,98,99], given that
513 maturation loci defining the neuronal subtype could be differentially accessible for Neurog2
514 direct targets.

515 Interestingly, the overexpression of Neurog2 in bFGF-grown astrocytes induced not only a
516 partial neurogenic program but also additional transcriptional programs associated with
517 alternative fates, such as cartilage formation and immune cell differentiation. The induction of
518 alternative fates or a failure to repress the original fate can lead to abortive conversion and
519 concomitant death of reprogrammed cells [100], thereby possibly mechanistically explaining
520 the lower Neurog2-mediated conversion efficiency in the bFGF culture. Because Hmgb2
521 overexpression does not specifically repress the astrocytic fate, yet significantly improves the
522 conversion efficiency, the abortive direct conversion is unlikely to explain the lower efficiency
523 in direct conversion. Interestingly, we did not observe Hmgb2-dependent opening of regions
524 associated with alternative fate genes, thus supporting the idea that alternative fate induction is
525 independent of the Hmgb2-induced changes in chromatin states. Hmgb2-dependent changes in
526 the transcription rate [101], RNA stability or RNA splicing could account for the enrichment
527 of alternative fates observed in mRNA analysis, because Hmgb2 has been proposed to have an

RNA-binding domain [91]. Importantly, we observed changes in chromatin opening for only genes associated with the neurogenic lineage.

Conclusions

Together, our results provide a mechanistic framework for translating environmental signals into a specific program involved in neuronal maturation downstream of the neurogenic fate determinants via chromatin modification. Interestingly, this aspect of neuronal reprogramming is the least understood and stands to be further improved, particularly *in vivo*.

Figure Legends:

Figure 1. Astrocyte growth conditions define the rate of direct astrocyte to neuron conversion

(**a**) Schemes depicting viral vector design and the experimental paradigm used for astrocyte to neuron conversion. (**b-c´´**) Micrographs illustrating the identity of Neurog-Neurog2 transduced cells 7 days after transduction in the EGF+bFGF (b) and bFGF (c) culture conditions. b´, b´´, c´ and c´ are magnifications of boxed areas in b and c, respectively. Yellow arrows indicate successfully converted cells, whereas white arrowheads indicate cells failing to convert. Scale bars: 100 µm in b and c; 50 µm in b´, b´´, c´ and c´´. (**d**) Dot plot depicting the proportion of transduced cells converting to neurons in EGF+bFGF and bFGF cultures 7 days after transduction with different neurogenic fate determinants. Data are shown as median±IQR; each single dot represents an independent biological replicate. Significance was tested with two-tailed Mann-Whitney test. p-values: black font corresponds to the comparison to the control and colored to the comparison between EGF+bFGF and bFGF. (**e**) Volcano plot depicting proteins enriched in astrocytes cultured in bFGF (magenta circles) and EGF+bFGF (green diamonds) culture conditions (fold change >1,5; p value <0,05). (**f**, **g**) Plots depicting the top five enriched GO terms in protein sets enriched in bFGF (f) and EGF+bFGF (g) cultures. (**h**) Western blot depicting levels of Hmgb2 protein in EGF+bFGF and bFGF astrocyte cultures. (**j**) Dot plot showing the relative levels of Hmgb2 (normalized to actin) in EGF+bFGF and bFGF cultures. Data are shown as median±IQR; single dots represent independent biological replicates. Paired-t-test was used for the significance test. Abbreviation: GO, Gene Ontology.

Figure 2. Hmgb2 is sufficient for successful Neurog2-mediated direct astrocyte to neuron conversion.

(**a**) Scheme depicting the experimental paradigm used for astrocyte to neuron conversion. (**b-c´´´**) Micrographs showing the identity of Neurog2- and Hmgb2-expressing virally transduced cells 7 days after transduction in EGF+bFGF (a) and bFGF cultures (b). b´, b´´, b´´´, c´, c´´ and c´´´ are magnifications of the boxed areas in a and b, respectively. Yellow arrows indicate co-transduced cells expressing Neurog2 and Hmgb2, yellow arrowheads indicate cells transduced only with Hmgb2-encoding virus, and blue arrowheads indicate cells transduced with only Neurog2-encoding virus. Scale bars: 100 µm in b and c; 50 µm in b´. b´´, b´´´, c´, c´´ and cb´´´. (**d**) Dot plot depicting the proportion of transduced cells converting to neurons in EGF+bFGF and bFGF cultures 7 days after transduction. Data are shown as median±IQR; single dots represent independent biological replicates. Significance was tested with two-tailed Mann-Whitney test. (**e**) Histogram depicting the identities of cells transduced with the indicated factors 7 days after transduction. Abbreviation: FP, fluorescent protein.

Figure 3. Hmgb2 is necessary for successful Neurog2-mediated direct astrocyte to neuron conversion.

(**a**) Scheme depicting the experimental paradigm used for astrocyte to neuron conversion. (**b, c**) Micrographs showing the identities of Neurog2-expressing virally transduced cells 7 days after transduction in EGF+bFGF culture of astrocytes derived from Hmgb2-deficient animals (c) and their siblings (b). Scale bars: 100 µm. (**d**) Dot plot depicting the proportion of Hmgb2-deficient or control cells converting to neurons 7 days after transduction with Neurog2. Data

are shown as median±IQR; single dots represent independent biological replicates. Significance was tested with two-tailed Mann-Whitney test. Abbreviation: FP, fluorescent protein.

Figure 4. Neurog2 induces incomplete neuronal fate in bFGF culture.

(**a, b**) Plots depicting enriched GO biological process terms in gene sets induced by Neurog2 in EGF+bFGF culture (a) and bFGF culture (b) 48 hours after viral transduction. Orange text represents the GO terms not associated with neuronal fate. Green and magenta text represent GO terms specifically enriched in EGF+bFGF culture and bFGF culture, respectively. (**c**) Venn diagram illustrating the overlap of Neurog2-induced transcripts in EGF+bFGF and bFGF culture 48 h after viral transduction. (**d**) Heat map showing Neurog2- or Neurog2+HMGB2-mediated induction of core neurogenic factors (according to Masserdotti et al., 2013) in EGF+bFGF and bFGF cultures. (**e**) Dot plot depicting the proportion of transduced cells converting to neurons in EGF+bFGF and bFGF cultures 7 days after transduction in Prox1 deficient or Prox-1 overexpressing cells. Data are shown as median±IQR; single dots represent independent biological replicates. Significance was tested with two-tailed Mann-Whitney test. (**f**) Plot showing GO terms enriched in the gene set upregulated in bFGF culture by Neurog2 and Hmgb2 expression 48 h after viral transduction. GO terms in green text are also induced by Neurog2 alone in EGF+bFGF culture (panel a). (**g**) Venn diagram illustrating the overlap of Neurog2-induced transcripts in EGF+bFGF and bFGF culture with Neurog2 and Hmgb2-induced transcripts after overexpression in bFGF culture 48 h after viral transduction. (**h**) Plot depicting enriched GO biological process terms in gene sets induced in the reprogramming prone condition (46 genes set; Fig. 4g). GO terms in green text are also induced by Neurog2 alone in EGF+bFGF culture. Abbreviations: FP, fluorescent protein; GO, Gene Ontology.

Figure 5. Hmgb2 improves the capability of Neurog2 to open promoters of neuronal maturation-associated genes.

(**a,b**) Heat maps depicting opening of promoters by Neurog2 and Hmgb2 or their combination in EGF+bFGF (green, a) and bFGF (magenta, b) culture. Scale: 1 kb (**c**) Heat maps depicting ATAC signals in the promoters of the core neurogenic genes (Fig. 4d) 48 h after Neurog2, Hmgb2 or Neurog2+Hmgb2 overexpression in EGF+bFGF and bFGF cultures. (**d**) IGV tracks showing the ATAC signal in the promoters of genes identifying non-neuronal lineages 48 h after Neurog2, Hmgb2 or Neurog2+Hmgb2 overexpression in bFGF culture. (**e**) Histogram depicting the number of more (MAS) or less (LAS) accessible sites identified by ATAC 48 h after Neurog2, Hmgb2 or Neurog2+Hmgb2 overexpression in EGF+bFGF (green) and bFGF (magenta) cultures. (**f**) Plot depicting enriched GO biological process terms in the promoter set opened by Neurog2+Hmgb2 in bFGF culture 48 hours after viral transduction. (**g**) Heat map showing ATAC signal in the promoters of neuronal maturation related genes (red in panel e) 48 h after Neurog2, Hmgb2 or Neurog2+Hmgb2 overexpression in bFGF culture. (g) IGV tracks showing the ATAC signal in the promoters of representative genes involved in neuronal maturation 48 h after Neurog2, Hmgb2 or Neurog2+Hmgb2 overexpression in FGF culture. Green boxes indicate differentially accessible sites.

Figure 6. Hmgb2-dependent promoters contain an E-box and Pou2f2 factor binding motif.

(**a**) Venn diagram illustrating the overlap in ATAC signals for MASs after Neurog2 overexpression in EGF+bFGF and bFGF cultures, with MASs induced by Neurog2 and Hmgb2 overexpression in bFGF culture 48 h after viral transduction. (**b**, **c**) Plots depicting enriched GO biological process terms in 395 peak set MASs in panel a (b) and 268 peak set MASs in panel a (b). (**d, e**) Transcription factor consensus sequences identified in 268 peak set MASs in panel a (d) and 395 peak set MASs in panel a (e), identified with *de novo* motif analysis. The motif image from the BaMM web server shows the likelihood of each nucleotide at each motif position. The color intensity reflects the probability, with darker colors indicating higher probabilities. Tables show transcription factors binding these motifs. Abbreviations: MAS, more accessible site; TF, transcription factor.

Figure 7. Hmgb2 and Neurog2 overexpression increases complexity of iN.

(**a**) Scheme depicting the experimental paradigm used for Shool analysis. (**b**) Representative thresholded images of neuronal cells used for Sholl analysis. (**c**) Sholl analysis of induced neurons by concurrent overexpression of Neurog2 and Neurog2+Hmgb2 in EGF and EGF+bFGF culture 7 days after viral transduction. Abbreviations: MAS, more accessible site; TF, transcription factor.

645 ***Suppl. Figure Legends:***

646

647 **Suppl. Figure 1. Growth conditions define the direct conversion rate.**

648 (**a**) Scheme depicting the experimental paradigm used for astrocyte to neuron conversion. (**b-**
649 **e**) Micrographs depicting the fate of transduced cells after control viral transduction in
650 EGF+bFGF (b), bFGF (c), EGF (d) culture and Neurog2 overexpression in EGF culture (e) 7
651 days after viral transduction. Scale bars: 50 µm. (**f**, **g**) Dot plots showing direct conversion
652 efficacy of Neurog2 overexpression in EGF culture (f) as well as Pou2f2, and Pou3f2+Hmgb2
653 overexpression in EGF+bFGF and bFGF culture (g). Data are shown as median±IQR; single
654 dots represent independent biological replicates. Significance was tested with two-tailed Mann-
655 Whitney test. Abbreviations: FP, fluorescent protein.

656

657 **Suppl. Figure 2: Characterization of the starting population in EGF+bFGF and bFGF**
658 **culture.**

659 (**a**) Scheme depicting the experimental paradigm used to characterize initially transduced cells.
660 (**b**, **c**, **d**, **e**, **g**, **h**, **j**, **k**, **l**, **m**) Micrographs illustrating identity assessment of control virally
661 transduced cells 24 h after transduction. Yellow arrows indicate identity marker positive
662 transduced, GFP-positive cells. Scale bars: 50 µm. (**f, i, n**) Dot plots showing the proportion of
663 transduced cells with the indicated identity. Data are shown as median±IQR; single dots
664 represent independent biological replicates. Significance was tested with two-tailed Mann-
665 Whitney test.

666

667 **Suppl. Figure 3: The growth factor induced barrier is reversible.**

668 (**a**) Scheme depicting the experimental paradigm used to address the stability of the growth
669 factor induced lineage barrier. (**b-e**) Micrographs illustrating the identity of control virus (b, d)
670 and Neurog2-encoding virus (c, e) transduced cells cultured first in bFGF and then in
671 EGF+bFGF (b, c), and of cells cultured first in EGF+bFGF and then bFGF (d, e). Identity
672 assessment was performed 7 days after viral transduction. Scale bar in b-e: 50 µm. (**f**) Dot plots
673 showing the proportions of transduced cells acquiring neuronal identity 7 days after viral
674 transduction. Data are shown as median±IQR; single dots represent independent biological
675 replicates. Significance was tested with two-tailed Mann-Whitney test.

676

677 **Suppl. Figure 4: Traumatic brain injury induces Hmgb2 expression in gray matter**
678 **reactive astrocytes.**

679 (**a**) Scheme depicting the experimental paradigm. (**b-c´**) Micrographs showing the expression
680 of Hmgb2 in the intact (b) and injured hemisphere (c) 5 days after injury. (c´) Orthogonal
681 projections of the optical Z-stack depicting the expression of Hmgb2 in astrocytes of the injured
682 hemisphere. Scale bars in b and c 100 µm and in c´ 10 µm.

683

684 **Suppl. Figure 5: Isolation of transduced cells for RNAseq and ATACseq.**

(**a**) Scheme depicting the workflow used to isolate transduced cells 48 h after transduction for omic analysis. (**b**) Plots demonstrating the FACS sorting gates and settings used to sort cells transduced with control, Neurog2 and Hmgb2 expressing viruses.

Suppl. Figure 6. Neurog2+Hmgb2 overexpression in bFGF culture induces a transcriptional subset necessary for successful direct conversion.

(**a-b**) Volcano plots of differentially expressed genes (DEGs) induced by Neurog2 in EGF+bFGF culture (a) and bFGF culture (b) 48 hours after viral transduction. (**c**) Plot depicting enriched GO biological processes of 96 shared genes (Fig. 4c) induced by Neurog2 in both EGF+bFGF and bFGF culture 48 hours after viral transduction. (**d**) Plot depicting enriched GO biological processes of uniquely induced genes by Neurog2 in EGF+bFGF culture (225 gene set; in Fig. 4c, green text) and bFGF culture (41 gene set in Fig. 4c, magenta text) 48 hours after viral transduction. (**e**, **f**) Volcano plot of DEGs induced by Hmgb2 in EGF+bFGF culture (f) and bFGF culture (g) 48 hours after viral transduction. (**g**) Plot depicting enriched GO biological processes of genes downregulated by Neurog2+Hmgb2 overexpression in bFGF culture 48 hours after viral transduction. Red text highlights processes associated with cytoskeletal remodeling, and blue depicts processes involved in adhesion. (**h**) Plot depicting enriched GO biological processes of the gene set commonly induced by Neurog2 in EGF+bFGF, bFGF culture and by Neurog2+Hmgb2 in bFGF culture (88 genes in Fig. 4g). Black text highlights processes associated with neurogenesis.

Suppl. Figure 7. Hmgb2 increases the ability of Neurog2 to open chromatin in bFGF culture.

(**a**) Heat map depicting accessibility of MASs induced by Hmgb2 (9 MASs), Neurog2 (445 MASs) and the combination of Neurog2+Hmgb2 (1062 MASs) in bFGF culture 48 h after viral transduction. Scale: 1 kb. (**b-c**) Pie charts of genomic distribution of MASs induced by Neurog2 (b) and the combination of Neurog2+Hmgb2 (c) in bFGF culture 48 h after viral transduction.

Suppl. Figure 8. Additional sites opened by Hmgb2 and Neurog2 overexpression are associated with the establishment of synaptic contacts and/or maturation of neurons.

(**a**) IGV tracks showing the ATAC signals of genes associated with synapse formation/function 48 h after viral transduction in bFGF culture. Boxes indicate signals significantly broadened by co-expression of Neurog2 and Hmgb2. (**b**) Box plots depicting expression of synapse-associated genes (from panel a) after control, Neurog2, Hmgb2 and Neurog2+Hmgb2 overexpression in bFGF culture 48 hours after viral transduction. (**c**) Venn diagram illustrating the overlap of MASs with the Tal-associated factor binding motif (motif 1, E-box) and POU domain factor binding motif (motif 2, POU) induced by Neurog2 in EGF+bFGF culture and induced by Neurog2+Hmgb2 in bFGF culture. (**d**) Plot depicting GO biological processes enriched in genes with promoters containing binding motifs for both Tal-associated factors and POU domain factors (56 promoters in c).

726 ***Suppl. Table Legends:***

727 **Suppl. Table 1. GO analysis of processes enriched in the EGF+bFGF and bFGF only**
728 **proteomes.**

729 **Suppl. Table 2. Full list of differentially regulated genes between different conditions.**

730 **Suppl. Table 3. GO analysis associated with RNA-seq analysis.**

731 **Suppl. Table 4. Full list of MAS and DAS with their genomic location.**

732 **Suppl. Table 5. GO analysis associated with ATAC analysis.**

733 **Suppl. Table 6. GO analysis associated ATAC peaks enriched in different**
734 **reprogramming conditions.**

735 **Suppl. Table 7. Full list of MAS and DAS with Neurog2 and Pou TF binding motifs.**

736

Material and Methods

Experimental animals

Experiments were conducted on both, female and male animals, which were either wild types (C57BL/6J mice) or transgenic Hmgb2-/- animals on a C57BL/6 background [102]. The Hmgb2-/- mice do not show gross phenotypical abnormalities and do not differ to wild-type siblings (Ronfani et al., 2001). For all *in vitro* experiments, animals at postnatal stage P5-P6 were used. Injuries were done in adult 8-10 weeks old animals. Animals were kept under standard conditions with access to water and food ad libitum. All animal experimental procedures were performed in accordance with the German and European Union guidelines and were approved by the Institutional Animal Care and Use Committee (IACUC) and the Government of Upper Bavaria under license number: AZ 55.2-1-54-2532-171-2011 and AZ 55.2-1-54-2532-150-11. All efforts were made to minimize animal suffering and to reduce the number of animals used.

Stab wound injury

Prior to every surgery, mice were deeply anesthetised by intra-peritoneal injection of sleep solution (Medetomidin (0,5mg/kg) / Midazolam (5mg/kg) / Fentanyl (0,05mg/kg)) complemented by local lidocaine application (20 mg/g). After the injection of the anaesthesia, mice were checked for pain reactions by pinching their tail and toes. Stab wound injury was performed in the somatosensory cortex, as previously described [97,103]. The following coordinates relative to Bregma were used: medio-lateral: 1,0 µm; rostro-caudal: -1,2 µm to -2,2 µm; dorso-ventral: -0,6 µm. Anaesthesia was antagonized with an subcutan injection of awake solution (Atipamezol (2,5mg/kg) / Flumazenil (0,5mg/kg) / Buprenorphin (0,1mg/kg)) and the mice were kept on a pre-warmed pad until they were awake and recovered from the surgery.

Perfusion and tissue section preparation

Prior to perfusion, animals were deeply anesthetized with overdoses of cocktail of ketamine (100 mg/kg) / xylazine (10 mg/kg). Subsequently, they were transcardially perfused first with cold PBS, followed by fresh ice-cold 4% PFA in PBS for 20 minutes. The brain was then removed from the skull, post-fixed in the same fixative overnight at 4 °°C, cryoprotected in 30% sucrose and cut at the cryostat at 40 µm tick sections.

Preparation of PDL-coated glass coverslips

Glass coverslips were washed first with acetone and boiled for 30 min in ethanol containing 0,7% (v/v) HCl. After two washing steps with 100% ethanol, coverslips were dried at RT and autoclaved for 2 h at 180 °C. Coverslips were washed with D-PBS and coated with poly-D-lysine (PDL, 0.02 mg/ml) solution for at least 2 h at 37 °C. Following coating, coverslips were washed three times with autoclaved ultrapure water, dried in the laminar flow and stored at 4 °C until needed.

Primary culture of postnatal cortical astroglial cells

Postnatal cortical astroglia were isolated and cultured as described previously [104]. Following decapitation of postnatal (P5-P6) wild-type C57BL/6J mice, the skin and the skull were removed, and the brain was extracted avoiding any tissue damage and placed into the 10 mM HEPES solution for dissection. After separating the two hemispheres, the meninges was removed and white matter of cerebral cortex was dissected using fine forceps and collected in a tube with astrocyte medium (Fetal calf serum-FCS (10% (v/v)); Horse serum-HS (5% (v/v)); glucose (3,5 mM); B27 supplement; Penicillin/Streptomycin (100 I.U/ml Pen and 100 µg/ml Strep) in DMEM/F12+GlutaMAX). The tissue was mechanical dissociated with a 5 ml pipette and placed into uncoated plastic flasks for cell expansion in astrocyte medium supplemented with the two growth factors EGF (10 ng/ml) + bFGF (10 ng/ml each) or with bFGF (10 ng/ml) only as specified for each experiment. After 4-5 days, the medium was exchanged and supplied with the fresh growth factors. After 10 days of culturing, cultured cells were rinsed with DPBS and contaminating oligodendrocyte precursor cells were removed by brusquely shaking the culture flasks several times. Astroglial cells were then detached from the flask by trypsinization and seeded onto poly-D-lysine (PDL)-coated glass coverslips at a density of $8x10^4$ cells per well in a 24-well plate with astrocyte medium for immunohistochemical analysis. For the ATAC-seq and RNA-seq experiments, cells were plated in T75 flasks with a seeding density of $3x10^6$ cells per flask. 2-4 h after seeding, the cells were transduced with different retroviral vectors in a ratio of 1 µl virus per 1 ml medium to prevent virus toxicity. Astrocyte medium was changed 12-18 h after viral transduction to differentiation medium (glucose (3,5 mM); B27 supplement; Penicillin/Streptomycin (100 I.U/ml Pen and 100 µg/ml Strep) in DMEM/F12+GlutaMAX) containing neither EGF nor bFGF up to the immunocytochemical analysis timepoint. The cells were cultured as indicated in each experiment. Cells were fixed in cold 4% PFA for 20 min and rinsed with cold D-PBS before immunocytochemical analysis.

For the ATAC-seq and RNA-seq experiments, the cells were kept in the astrocyte medium and collected 48 h after viral transduction. Astrocytes were detached from the flask by trypsinization, prepared for the FACS and sorted for the following ATAC-seq and RNA-seq experiments according to the fluorophore expression.

The astroglial cultures from the Hmgb2-/- transgenic animals were prepared as described above, however, the cortical tissue from each animal was kept separately and placed into the small T25 flask. In addition, the tips of the tails were used for genotyping as described in [102]. The cultures from Hmgb2-/- transgenic mice were grown only in the double growth factor condition containing EGF+bFGF.

Immunocytochemistry and immunohistochemistry

Immunostaining was performed on cell culture samples or free-floating brain sections. Specimens were treated with blocking buffer (0,5% Triton-X-100; 10% normal goat serum (NGS) in D-PBS) to reduce non-specific binding. The same buffer was used to dilute the primary antibodies. The specimens were incubated with the primary antibody mixture overnight at 4°C (brain tissue) °C or for 2 hours at RT (cell culture samples), followed by 3x 10 min washing steps with PBS. In order to visualize primary antibody binding, samples were exposed to appropriate species and/or subclass specific secondary antibodies conjugated to Alexa Fluor 488, 546 or 647 (Invitrogen) for about 90 min at RT protected from light. Secondary antibodies were diluted 1:1000 in blocking buffer. Nuclei were visualized with DAPI (4',6-diamidino-2-phenylindole) that was added to the mix of secondary antibodies. Following extensive washing steps with PBS, coverslips or sections were mounted with Aqua Poly/Mount (Polysciences) and imaged.

Following primary antibodies were used: Chick-anti-GFP (Aves Lab, GFP-120; 1:1000); Rabbit-anti-RFP (Rockland, 600-401-379; 1:500); Mouse IgG1-anti-GFAP (Sigma-Aldrich, G3893; 1:500); Rabbit-anti-GFAP (DakoCytomation, Z0334; 1:1000); Mouse IgG1κ-anti-S100β (Sigma-Aldrich, S2644; 1:500); Rabbit-anti-OLIG2 (Thermo Fischer, AB9610; 1:500); Mouse IgG2a-anti-αSMA (Sigma-Aldrich, A2547; 1:400); Rabbit-anti-Ki67 (Abcam, 15580; 1:200); Rat-anti-Ki67 (DakoCytomation, M7249; 1:200); Rabbit-anti-PH3 (Ser10) (Thermo Fischer, 06-570; 1:200); Guinea pig-anti-DCX (Thermo Fischer, AB-2253; 1:1000); Mouse IgG2b-anti-β-III-TUBULIN (Sigma-Aldrich, T8660; 1:500); Mouse IgG1-anti-NEUN (Chemicon, MAB 377; 1:250); Rabbit-anti-HMGB2 (Abcam, ab67282; 1:1000); Mouse IgG2aκ-anti-HMGB2 (Sigma-Aldrich, 07173-3E5; 1:500); Mouse IgG2aκ-anti-HMGB2 antibody requires termal (15 min at 95°C) antigen retrieval using the citrate buffer (10 mM; pH 6). Primary antibody binding was revealed using class-specific secondary antibody coupled to Alexa fluorophore (Invitrogen, Germany). All secondary antibodies were used at dilution 1:1000.

Image acquisition and quantifications

Immunostainings were analysed with a fluorescent Microscope Axio Imager M2m (Zeiss) using the ZEN software (Zeiss) with a 20x or 40x objective. Fluorescent-labelled sections were photographed with FV1000 confocal laser-scanning microscope (Olympus), using the FW10-ASW 4.0 software (Olympus). The quantifications of *in vitro* cultured cells were performed using the ZEN software (Zeiss) analysing at least 25 randomly taken pictures per coverslip depending on the number of transduced cells. In total, 100-200 retroviral vector-transduced cells were quantified from randomly chosen fields on a single coverslip. 3 coverslips in each experiment (biological replicate) were analysed. The number of experiments is indicated in corresponding Figure. The number of induced neurons was expressed as a percentage out of all transduced cells.

To analyse the number of apoptotic cells, between 350-550 DAPI labelled cells were counted from 5 randomly selected fields on one coverslip.

In the reprogramming experiments of the astrocytes isolated from Hmgb2+/+, Hmgb2+/- and Hmgb2-/- animals, each of the single animals was considered as a biological replicate and at least 3 coverslips were counted per animal. We analysed in total 6 litters containing wild-type, heterozygous or homozygous littermates.

Western blots using the Fiji software as previously described [105] . All lanes of interest were outlined using the rectangular selection tool and the signal intensity of each band was calculated by determining the area under the peak. The measurements of the corresponding α-ACTIN bands were used to normalize the amount of proteins loaded on the gel.

Sholl Analysis

We analysed only DCX positive cells 7 days after viral transduction. Single cells were isolated and subjected to Sholl analysis using the ImageJ plug-in 'Sholl Analysis'. We used the following parameters: starting radius 5µm; ending radius 500 µm; radius step size 5 µm. The number of crossings per cell were visualized and analysed using Origin.

FACS analysis and sorting

Astrocytes were collected by trypsinization 48 h after retroviral transduction, washed, resuspended in DPBS and analysed using a FACS Aria II instrument (BD Biosciences) in the FACSFlowTM medium. Debris and aggregated cells were gated out by forward-scatter area (FSC-A) and side-scatter area (SSC-A). Forward scatter area (FSC-A) vs. forward scatter width (FSC-W) was used to discriminate doublets from single cells. To set the gates for the sorting, untransduced astrocytes were recorded. Sorted cells were collected in DPBS, counted and divided into two batches: 50000 cells were immediately processed for ATAC-seq and the remaining cells were collected for RNA-seq library preparation.

ATAC-sequencing

Assay for Transposase Accessible Chromatin with high-throughput sequencing (ATAC-seq), a method to detect genome-wide chromatin accessibility, was performed following the published protocol [106,107]. Briefly, right after the FACS sorting, 50000 cells were lysed, the nuclei were extracted and resuspended with the transposase reaction mix (25 µl 2x TD buffer (Illumina); 2,5 µl Transposase (Illumina); 22,5 µl nuclease free water), following by transposition reaction for 30 minutes at 37°C °C. To stop the transposition reaction, samples were purified using a Qiagen MinElute PCR (Qiagen) purification kit according to the manufacturer instructions. Open chromatin fragments were first amplified for 5 cycles and then for additional 7-8 cycles, as determined by RT-qPCR, using the combination of primer Ad1_noMX (5' AATGATACGGCGACCACCGAGATCTACACTCGTCGGCAGCGTCAGATGTG 3') and the Nextera Index Kit (Illumina) primer N701-N706. Libraries were purified using a Qiagen MinElute PCR purification kit (Qiagen) and their quality was assessed using the Bioanalyzer High-Sensitivity DNA kit (Agilent) according to the manufacturer's instructions. The concentration of each library was measured by Qubit using the provided protocol. Libraries were pooled for sequencing and the pool contained 20 ng of each library. Prior to sequencing, pooled libraries were additionally purified with AMPure beads (ratio 1:1) to remove contaminating primer dimers and quantified using Qubit and the Bioanalyzer High-Sensitivity DNA kit (Agilent). 50-bp paired-end deep sequencing was carried out on HiSeq 4000 (Illumina).

ATAC-sequencing analysis:

For the analysis of bulk ATAC-seq data, we followed the Harvard FAS Informatics ATAC-seq guidelines. The quality of raw FASTQ reads were checked using FastQC (Version 0.11.9). The low quality read (< 20bp) and adapter sequences were trimmed by Cutadapt (Version 4.0). The trimmed reads were mapped to the mouse reference genome (mm10) by using Bowtie2 (parameter: --very-sensitive -X 1000 --dovetail). Samtools were then used to convert and sort the sam files into bam files. Peak calling step was performed with Genrich for each sample separately to identify accessible regions. Genrich peak caller has a mode (-j) assigned to ATAC-Seq analysis mode and allows running all of the post-alignment steps via peak-calling with one command. Mitochondrial reads and PCR duplicates were removed by -e chrM and -r argument respectively. To generate count table matrix for differential analysis bam2counts (intePareto R-based package) was used to count reads fall into specific genomic positions by importing all the bam files and merging all the bed files into one (importing GenomicRanges and GenomicAlignments libraries). DESeq2 (version 1.26.0) was used for differential accessibility analysis of the count data. The relatively more open and closed sites are called MAS and LAS respectively (fold change (FC) > 2 and adjusted P-value < 0.05) and the annotation of these sites were performed using R-based packages Chip-seeker (TSS ± 3.0 Kb)

(version 1.28.3). For visualization, the bamcovage deeptools (version 3.5.1) were used to normalize the data by importing the scaling factor from DESeq2 (version 1.36.0). The normalized bigwig files used to visualize the coverage using deeptools and samtools. These bigwig files were loaded into the IGV tool to visualize the peak at the gene level. The Venn diagrams were made using the BioVenn web application tool. The Gorilla tool was used to generate the GO Biological processes, with a cut-off of enrichment > 2 and p-value of < 0.01.

Motif analysis

BaMMmotif (https://bammmotif.soedinglab.org/home/) was used to perform *de novo* motif enrichment analysis by providing MASs fasta sequence [108] as input and all detected accessible sites fasta sequences as background using default parameters. We selected the motifs with an AvRec score above 0.5 as candidates for further analysis. The mouse database HOCOMOCO v11 was used for motif annotation, and the most significant transcription factors matching the motif with e-values below 0.001 were considered as potential binders.

Preparation of libraries for RNA-sequencing

Sorted cells were resuspended in 100 µl extraction buffer of the PicoPureTM RNA isolation kit (Thermo Fischer Scientific) and the RNA was extracted according to the manufacturer's instructions. The Agilent 2100 Bioanalyzer was used to assess RNA quality and concentration. For the RNA-seq library preparation, only high-quality RNA with RIN values >8 were used. cDNA was synthesized from 10 ng of total RNA using SMART-Seq v4 Ultra Low Input RNA Kit (Takara Bio), according to the manufacturer's instructions. The total number of amplification cycles was determined by RT-qPCR side reaction according to manufacturer's instruction. PCR-amplified cDNA was purified by immobilization on AMPure XP beads. Prior to generating the final library for sequencing, the Covaris AFA system was used to perform cDNA shearing in Covaris microtubes (microTUBE AFA Fiber Pre-Slit Snap-Cap 6x16mm), resulting in 200-500 bp long cDNA fragments that were subsequently purified by ethanol precipitation. Prior to library preparation using the MicroPlex Library Preparation kit v2 (Diagenode) according to the user manual, the quality and concentration of the sheared cDNA were assessed using an Agilent 2100 Bioanalyzer. Final libraries were evaluated using an Agilent 2100 Bioanalyzer and the concentration was measured with Qubit Fluorometer (Thermo Fischer Scientific). The uniquely barcoded libraries were multiplexed onto one lane and 100-bp paired-end deep sequencing was carried out at the HiSeq 4000 (Illumina) generating ~20 million reads per sample.

Transcriptome data analysis (Bulk RNA Seq):

The raw paired-end FASTQ files were mapped to the mouse reference genome (mm10) using STAR RNA-seq aligner (version 2.7.2b). Aligned reads in the BAM files were then quantified by HTSeq-count (Version 0.9.1) based on annotation file GENCODE Release M25 (GRCm38.p6). The gene-level count matrix was imported into the R/Bioconductor package DESeq2 (version 1.26.0) for normalization and differential expression with FC > 2, adjusted P-value < 0.05. Venn diagrams were created using the web application BioVenn tool and heatmaps were generated using gplots and RColorBrewer R-based/Bioconductor tools. For GO enrichment analysis of the assigned set of genes we used the GOrilla tool by providing background genes. The enriched GO term (biological processes) possessing enrichment > 2,

962 containing at least 1% of the input genes and p-value specified in the figure legend were
963 visualized using Origin.

964

965 **Protein isolation and Western blot**

966 Postnatal cortical astroglia were isolated and cultured as described above. After 10 days of
967 culturing with growth factors EGF+bFGF or bFGF, cells were detached from the flask by
968 trypsinization, washed and counted. $0{,}5x10^6$ cells were lysed in RIPA buffer containing
969 cOmplete Protease Inhibitor cocktail (Roche). Protein extraction and Western blotting is
970 performed as previously described [109]. The following antibodies were used: Rabbit-anti-
971 HMGB2 (Abcam, ab67282; 1:5000); Mouse-anti-ACTIN (Millipore, MAB1501; 1:10000);
972 HRP-coupled anti-mouse IgG1 (GE Healthcare, NA931; 1:20000) and HRP-coupled anti-
973 rabbit IgG (Jackson ImmunoResearch,111-036-045; 1:20000).

974

975 **Quantitative mass spectrometry**

976 Treated adherent astrocytes were lysed and subjected to tryptic protein digest using a modified
977 FASP protocol [110]. Proteomic measurements were performed on a LTQ Orbitrap XL mass
978 spectrometer (Thermo Scientific) online coupled to an Ultimate 3000 nano-HPLC (Dionex).
979 Peptides were enriched on a nano trap column (100 µm i.d. × 2 cm, packed with Acclaim
980 PepMap100 C18, 5 µm, 100 Å, Dionex) prior to separation on an analytical C18 PepMap
981 column (75 µm i.d. × 25 cm, Acclaim PepMap100 C18, 3 µm, 100Å, Dionex) in a 135 min
982 linear acetonitrile gradient from 3% to 34% ACN. From the high resolution orbitrap MS pre-
983 scan (scan range 300 – 1500 m/z), the ten most intense peptide ions of charge ≥ +2 were
984 selected for fragment analysis in the linear ion trap if they exceeded an intensity of at least 200
985 counts. The normalized collision energy for CID was set to a value of 35. Every ion selected
986 for fragmentation was excluded for 30 s by dynamic exclusion. The individual raw-files were
987 loaded to the Progenesis software (version 4.1, Waters) for label free quantification and
988 analyzed as described [111,112]. MS/MS spectra were exported as Mascot generic file and
989 used for peptide identification with Mascot (version 2.4, Matrix Science Inc., Boston, MA,
990 USA) in the Ensembl Mouse protein database (release 75, 51765 sequences). Search
991 parameters used were as follows: 10 ppm peptide mass tolerance and 0.6 Da fragment mass
992 tolerance, one missed cleavage allowed, carbamidomethylation was set as fixed modification,
993 methionine oxidation and asparagine or glutamine deamidation were allowed as variable
994 modifications. A Mascot-integrated decoy database search was included. Peptide assignments
995 were filtered for an ion score cut-off of 30 and a significance threshold of $p < 0.01$ and were
996 reimported into the Progenesis software. After summing up the abundances of all peptides
997 allocated to each protein, resulting normalized protein abundances were used for calculation of
998 fold-changes and corresponding p-values.

999

1000 **Expression plasmids**

1001 In order to overexpress different neurogenic transcription factors in the astroglial cells, we used
1002 Moloney murine leukemia virus (MMLV)-derived retroviral vectors, expressing neurogenic
1003 fate determinants under the regulatory control of a strong and silencing-resistant pCAG
1004 promoter. All our construct encode a neurogenic factor followed by an internal ribosomal entry
1005 site (IRES) and either GFP or dsRED as reporter proteins, allowing simultaneous reporter
1006 expression. For control experiments, we used a retrovirus encoding for the fluorescent proteins

1007 (GFP or dsRED) behind the IRES driven by the same CAG promoter. We used the following
1008 expression vectors: pCAG-IRES-GFP [43]; pCAG-IRES-dsRED [43]; pCAG-Neurog2-IRES-
1009 dsRED [43]; pCAG-Pou3f2 -IRES-dsRED [113]; pCAG-Sox11-IRES-GFP [46]; pCAG-
1010 Hmgb2-IRES-GFP(this work).

1011

1012 **Cloning pCAG-Hmgb2-IRES-GFP construct**

1013 cDNA for Hmgb2 were synthetized at Genscript, containing BamHI and HindIII in order to
1014 clone them into the pENTR1A entry vector. The cDNAs were then transferred to the retroviral
1015 destination vector pCAG-IRES-dsRED/GFP using the Gateway cloning method (Invitrogen)
1016 according to the manufacturer's instructions. The correct sequence was confirmed using Sanger
1017 sequencing before viral vector production.

1018

1019 **Retroviral vector production**

1020 The VSV-G-pseudotyped retroviruses were prepared using the HEK293-derived retroviral
1021 packaging cell line (293GPG) (Ory et al., 1996) that stably express the gag-pol genes of murine
1022 leukemia virus and vsv-g under the control of a tet/VP16 transactivator as previously described
1023 (Heinrich et al., 2011). The viral particles were stored in TNE (Tris-HCl pH=7,8 (50mM);
1024 NaCl (130mM); EDTA (1mM)) buffer at -80 0C until use.

1025 **Statistical analysis**

1026 Numbers of biological replicates can be seen on the dot plots or in the figure legend in case of
1027 the bar charts. All results are presented as median ± interquartile range (IQR). IQR was
1028 calculated in RStudio [114], using the default method based on type 7 continuous sample
1029 quantile. For the reprogramming experiments, statistical analysis was performed in Origin
1030 using non-parametric Mann-Whitney U test unless differently specified for particular
1031 experiments.

Declarations

Availability of data and materials

Proteome data set is available at PRIDE database (https://www.ebi.ac.uk/pride/). The dataset identifier is PXD044288. During the review process the data could be accessed using the following username: reviewer_pxd044288@ebi.ac.uk and password: C9naS7jL.

The RNAseq and ATACseq datasets are available at Gene Expression Omnibus (GEO). The accession number is pending. The reviewer token will be provided upon request.

Competing interests

All authors declare no competing interest.

Funding

This work was supported by the German research foundation (DFG) through SFB 870 (J.N. and M.G.); TRR274/1 (ID 408885537) (J.N.); SPP 1738 "Emerging roles of non-coding RNAs in nervous system development, plasticity & disease" (J.N.); SPP1757 "Glial heterogeneity" (J.N.); the Fritz Thyssen Foundation (J.N.); SPP2191 "Molecular mechanisms of functional phase separation" (ID 402723784, project number 419139133) (J.N.); SPP1935 "Deciphering the mRNP code: RNA-bound determinants of post-transcriptional gene regulation" (J.N.); ERC Chrono Neurorepair (M.G.) and the Graduate School for Systemic Neurosciences GSN-LMU (V.S., F.B., P.M. and T.L.).

Authors' contributions

P.M., T.L. and J. N. conceived the project and designed experiments. A.S.-M., V.S., F.B., and J.N. performed experiments. J. M.-P. and S.M.H. analyzed proteome. L.R. and M. B. provided Hmgb2 KO animals. P. M. and J.N. wrote the manuscript with input from all authors.

Acknowledgments

We thank all members of the Neurogenesis and Regeneration group for experimental input, discussions and critical reading of the manuscript. We acknowledge the support of the following core facilities: the Bioimaging Core Facility at the BioMedical Center of LMU Munich and the Sequencing Facility at the Helmholtz Zentrum München.

1065 **References:**

1066 1. Barker RA, Götz M, Parmar M. New approaches for brain repair—from rescue to
1067 reprogramming. Nature 2018 557:7705 [Internet]. 2018 [cited 2022 Aug 16];557:329–
1068 34. Available from: https://www.nature.com/articles/s41586-018-0087-1

1069 2. Götz M, Bocchi R. Neuronal replacement: Concepts, achievements, and call for
1070 caution. Curr Opin Neurobiol [Internet]. 2021 [cited 2022 Aug 18];69:185–92. Available
1071 from: https://pubmed.ncbi.nlm.nih.gov/33984604/

1072 3. Torper O, Götz M. Brain repair from intrinsic cell sources: Turning reactive glia into
1073 neurons. Prog Brain Res. 2017.

1074 4. Griesbach GS, Masel BE, Helvie RE, Ashley MJ. The Impact of Traumatic Brain Injury
1075 on Later Life: Effects on Normal Aging and Neurodegenerative Diseases. J
1076 Neurotrauma. 2018;35.

1077 5. Bocchi R, Masserdotti G, Götz M. Direct neuronal reprogramming: Fast forward from
1078 new concepts toward therapeutic approaches. Neuron [Internet]. 2022 [cited 2022 Aug
1079 18];110:366–93. Available from: https://pubmed.ncbi.nlm.nih.gov/34921778/

1080 6. Zhou Y, Shao A, Yao Y, Tu S, Deng Y, Zhang J. Dual roles of astrocytes in plasticity
1081 and reconstruction after traumatic brain injury. Cell Communication and Signaling.
1082 BioMed Central Ltd.; 2020.

1083 7. Amamoto R, Arlotta P. Development-inspired reprogramming of the mammalian
1084 central nervous system. Science (1979) [Internet]. 2014;343:1239882. Available from:
1085 http://www.ncbi.nlm.nih.gov/pubmed/24482482

1086 8. Berninger B, Costa MR, Koch U, Schroeder T, Sutor B, Grothe B, et al. Functional
1087 properties of neurons derived from in vitro reprogrammed postnatal astroglia. J
1088 Neurosci [Internet]. 2007;27:8654–64. Available from:
1089 http://www.ncbi.nlm.nih.gov/entrez/query.fcgi?cmd=Retrieve&db=PubMed&dopt=Cita
1090 tion&list_uids=17687043

1091 9. Buffo A, Vosko MR, Erturk D, Hamann GF, Jucker M, Rowitch D, et al. Expression
1092 pattern of the transcription factor Olig2 in response to brain injuries: implications for
1093 neuronal repair. Proc Natl Acad Sci U S A [Internet]. 2005/12/07. 2005;102:18183–8.
1094 Available from:
1095 http://www.ncbi.nlm.nih.gov/entrez/query.fcgi?cmd=Retrieve&db=PubMed&dopt=Cita
1096 tion&list_uids=16330768

1097 10. Grande A, Sumiyoshi K, López-Juárez A, Howard J, Sakthivel B, Aronow B, et al.
1098 Environmental impact on direct neuronal reprogramming in vivo in the adult brain. Nat
1099 Commun [Internet]. 2013;4. Available from: http://dx.doi.org/10.1038/ncomms3373

1100 11. Heinrich C, Blum R, Gascón S, Masserdotti G, Tripathi P, Sánchez R, et al. Directing
1101 Astroglia from the Cerebral Cortex into Subtype Specific Functional Neurons. McKay

RDG, editor. PLoS Biol [Internet]. 2010/05/27. 2010;8:e1000373. Available from: http://www.ncbi.nlm.nih.gov/entrez/query.fcgi?cmd=Retrieve&db=PubMed&dopt=Citation&list_uids=20502524

12. Herrero-Navarro Á, Puche-Aroca L, Moreno-Juan V, Sempere-Ferràndez A, Espinosa A, Susín R, et al. Astrocytes and neurons share region-specific transcriptional signatures that confer regional identity to neuronal reprogramming. Sci Adv. 2021;7.

13. Liu F, Zhang Y, Chen F, Yuan J, Li S, Han S, et al. Neurog2 directly converts astrocytes into functional neurons in midbrain and spinal cord. Cell Death Dis. 2021;12.

14. Masserdotti G, Gillotin S, Sutor B, Drechsel D, Irmler M, Jørgensen HF, et al. Transcriptional Mechanisms of Proneural Factors and REST in Regulating Neuronal Reprogramming of Astrocytes. Cell Stem Cell [Internet]. 2015;17:74–88. Available from: https://linkinghub.elsevier.com/retrieve/pii/S1934590915002234

15. Mattugini N, Bocchi R, Scheuss V, Russo GL, Torper O, Lao CL, et al. Inducing Different Neuronal Subtypes from Astrocytes in the Injured Mouse Cerebral Cortex. Neuron [Internet]. 2019;103:1086-1095.e5. Available from: https://linkinghub.elsevier.com/retrieve/pii/S0896627319306932

16. Ninkovic J, Steiner-Mezzadri A, Jawerka M, Akinci U, Masserdotti G, Petricca S, et al. The BAF complex interacts with Pax6 in adult neural progenitors to establish a neurogenic cross-regulatory transcriptional network. Cell Stem Cell. 2013;13.

17. Niu W, Zang T, Zou Y, Fang S, Smith DK, Bachoo R, et al. In vivo reprogramming of astrocytes to neuroblasts in the adult brain. Nat Cell Biol [Internet]. 2013;15:1164–75. Available from: http://www.ncbi.nlm.nih.gov/pubmed/24056302

18. Pereira M, Birtele M, Shrigley S, Benitez JA, Hedlund E, Parmar M, et al. Direct Reprogramming of Resident NG2 Glia into Neurons with Properties of Fast-Spiking Parvalbumin-Containing Interneurons. Stem Cell Reports [Internet]. 2017;9:742–51. Available from: https://www.ncbi.nlm.nih.gov/pubmed/28844658

19. Zhang L, Lei Z, Guo Z, Pei Z, Chen Y, Zhang F, et al. Development of Neuroregenerative Gene Therapy to Reverse Glial Scar Tissue Back to Neuron-Enriched Tissue. Front Cell Neurosci. 2020;14.

20. Vierbuchen T, Wernig M. Direct lineage conversions: unnatural but useful? Nat Biotechnol [Internet]. 2011/10/15. 2011;29:892–907. Available from: http://www.ncbi.nlm.nih.gov/entrez/query.fcgi?cmd=Retrieve&db=PubMed&dopt=Citation&list_uids=21997635

21. Lujan E, Chanda S, Ahlenius H, Sudhof TC, Wernig M. Direct conversion of mouse fibroblasts to self-renewing, tripotent neural precursor cells. Proc Natl Acad Sci U S A [Internet]. 2012/02/07. 2012;109:2527–32. Available from: http://www.ncbi.nlm.nih.gov/entrez/query.fcgi?cmd=Retrieve&db=PubMed&dopt=Citation&list_uids=22308465

1140 22. Marro S, Pang ZP, Yang N, Tsai MC, Qu K, Chang HY, et al. Direct lineage
1141 conversion of terminally differentiated hepatocytes to functional neurons. Cell Stem Cell
1142 [Internet]. 2011/10/04. 2011;9:374–82. Available from:
1143 http://www.ncbi.nlm.nih.gov/entrez/query.fcgi?cmd=Retrieve&db=PubMed&dopt=Cita
1144 tion&list_uids=21962918

1145 23. Treutlein B, Lee QY, Camp JG, Mall M, Koh W, Shariati SA, et al. Dissecting direct
1146 reprogramming from fibroblast to neuron using single-cell RNA-seq. Nature [Internet].
1147 2016;534:391–5. Available from: https://www.ncbi.nlm.nih.gov/pubmed/27281220

1148 24. Pfisterer U, Kirkeby A, Torper O, Wood J, Nelander J, Dufour A, et al. Direct
1149 conversion of human fibroblasts to dopaminergic neurons. Proceedings of the National
1150 Academy of Sciences [Internet]. 2011;108:10343–8. Available from:
1151 http://www.ncbi.nlm.nih.gov/pubmed/21646515

1152 25. Wapinski OL, Vierbuchen T, Qu K, Lee QY, Chanda S, Fuentes DR, et al. Hierarchical
1153 mechanisms for direct reprogramming of fibroblasts to neurons. Cell [Internet].
1154 2013;155:621–35. Available from: http://www.ncbi.nlm.nih.gov/pubmed/24243019

1155 26. Wapinski OL, Lee QY, Chen AC, Li R, Corces MR, Ang CE, et al. Rapid Chromatin
1156 Switch in the Direct Reprogramming of Fibroblasts to Neurons. Cell Rep [Internet].
1157 2017;20:3236–47. Available from: https://www.ncbi.nlm.nih.gov/pubmed/28954238

1158 27. Noack F, Vangelisti S, Raffl G, Carido M, Diwakar J, Chong F, et al. Multimodal
1159 profiling of the transcriptional regulatory landscape of the developing mouse cortex
1160 identifies Neurog2 as a key epigenome remodeler. Nat Neurosci. 2022;25.

1161 28. Pataskar A, Jung J, Smialowski P, Noack F, Calegari F, Straub T, et al. NeuroD1
1162 reprograms chromatin and transcription factor landscapes to induce the neuronal
1163 program. Embo J [Internet]. 2016;35:24–45. Available from:
1164 https://www.ncbi.nlm.nih.gov/pubmed/26516211

1165 29. Heinrich C, Bergami M, Gascón S, Lepier A, Dimou L, Sutor B, et al. Sox2-mediated
1166 conversion of NG2 glia into induced neurons in the injured adult cerebral cortex. Stem
1167 Cell Reports [Internet]. 2014;in press:1000–14. Available from:
1168 http://www.ncbi.nlm.nih.gov/pubmed/25458895

1169 30. Liu M-L, Zang T, Zou Y, Chang JC, Gibson JR, Huber KM, et al. Small molecules
1170 enable neurogenin 2 to efficiently convert human fibroblasts into cholinergic neurons.
1171 Nat Commun [Internet]. 2013;4. Available from: http://dx.doi.org/10.1038/ncomms3183

1172 31. Russo GL, Sonsalla G, Natarajan P, Breunig CT, Bulli G, Merl-Pham J, et al. CRISPR-
1173 Mediated Induction of Neuron-Enriched Mitochondrial Proteins Boosts Direct Glia-to-
1174 Neuron Conversion. Cell Stem Cell. 2021;28.

1175 32. Gascón S, Murenu E, Masserdotti G, Ortega F, Russo GL, Petrik D, et al. Identification
1176 and Successful Negotiation of a Metabolic Checkpoint in Direct Neuronal

1177 Reprogramming. Cell Stem Cell [Internet]. 2016;18:396–409. Available from:
1178 https://linkinghub.elsevier.com/retrieve/pii/S1934590915005482

1179 33. Hu X, Qin S, Huang X, Yuan Y, Tan Z, Gu Y, et al. Region-Restrict Astrocytes Exhibit
1180 Heterogeneous Susceptibility to Neuronal Reprogramming. Stem Cell Reports. 2019;12.

1181 34. Addington CP, Roussas A, Dutta D, Stabenfeldt SE. Endogenous Repair Signaling
1182 after Brain Injury and Complementary Bioengineering Approaches to Enhance Neural
1183 Regeneration: Supplementary Issue: Stem Cell Biology. Biomark Insights. 2015.

1184 35. Sun D, Bullock MR, McGinn MJ, Zhou Z, Altememi N, Hagood S, et al. Basic
1185 fibroblast growth factor-enhanced neurogenesis contributes to cognitive recovery in
1186 rats following traumatic brain injury. Exp Neurol. 2009;216.

1187 36. Ninomiya M, Yamashita T, Araki N, Okano H, Sawamoto K. Enhanced neurogenesis
1188 in the ischemic striatum following EGF-induced expansion of transit-amplifying cells in
1189 the subventricular zone. Neurosci Lett. 2006;403.

1190 37. Grande A, Sumiyoshi K, López-Juárez A, Howard J, Sakthivel B, Aronow B, et al.
1191 Environmental impact on direct neuronal reprogramming in vivo in the adult brain. Nat
1192 Commun [Internet]. 2013;4. Available from: http://dx.doi.org/10.1038/ncomms3373

1193 38. Hung LY, Tseng JT, Lee YC, Xia W, Wang YN, Wu ML, et al. Nuclear epidermal
1194 growth factor receptor (EGFR) interacts with signal transducer and activator of
1195 transcription 5 (STAT5) in activating Aurora-A gene expression. Nucleic Acids Res.
1196 2008;36.

1197 39. Choi HS, Choi BY, Cho YY, Mizuno H, Kang BS, Bode AM, et al. Phosphorylation of
1198 histone H3 at serine 10 is indispensable for neoplastic cell transformation. Cancer Res.
1199 2005;65.

1200 40. Patel NS, Rhinn M, Semprich CI, Halley PA, Dollé P, Bickmore WA, et al. FGF
1201 Signalling Regulates Chromatin Organisation during Neural Differentiation via
1202 Mechanisms that Can Be Uncoupled from Transcription. PLoS Genet. 2013;9.

1203 41. Addington CP, Roussas A, Dutta D, Stabenfeldt SE. Endogenous Repair Signaling
1204 after Brain Injury and Complementary Bioengineering Approaches to Enhance Neural
1205 Regeneration: Supplementary Issue: Stem Cell Biology. Biomark Insights. 2015.

1206 42. Heinrich C, Blum R, Gascon S, Masserdotti G, Tripathi P, Sanchez R, et al. Directing
1207 astroglia from the cerebral cortex into subtype specific functional neurons. PLoS Biol
1208 [Internet]. 2010/05/27. 2010;8:e1000373. Available from:
1209 http://www.ncbi.nlm.nih.gov/entrez/query.fcgi?cmd=Retrieve&db=PubMed&dopt=Cita
1210 tion&list_uids=20502524

1211 43. Heinrich C, Gotz M, Berninger B. Reprogramming of postnatal astroglia of the
1212 mouse neocortex into functional, synapse-forming neurons. Methods Mol Biol

1213 [Internet]. 2012;814:485–98. Available from:
1214 http://www.ncbi.nlm.nih.gov/pubmed/22144327

1215 44. Gascon S, Masserdotti G, Russo GL, Gotz M. Direct Neuronal Reprogramming:
1216 Achievements, Hurdles, and New Roads to Success. Cell Stem Cell [Internet].
1217 2017;21:18–34. Available from: http://www.ncbi.nlm.nih.gov/pubmed/28686866

1218 45. Hack MA, Sugimori M, Lundberg C, Nakafuku M, Götz M, Gotz M. Regionalization
1219 and fate specification in neurospheres: the role of Olig2 and Pax6. Mol Cell Neurosci
1220 [Internet]. 2004/04/15. 2004;25:664–78. Available from:
1221 http://www.ncbi.nlm.nih.gov/pubmed/15080895

1222 46. Masserdotti G, Gillotin S, Sutor B, Drechsel D, Irmler M, Jørgensen HF, et al.
1223 Transcriptional Mechanisms of Proneural Factors and REST in Regulating Neuronal
1224 Reprogramming of Astrocytes. Cell Stem Cell. 2015;

1225 47. Russo GL, Sonsalla G, Natarajan P, Breunig CT, Bulli G, Merl-Pham J, et al. CRISPR-
1226 Mediated Induction of Neuron-Enriched Mitochondrial Proteins Boosts Direct Glia-to-
1227 Neuron Conversion. Cell Stem Cell. 2021;28.

1228 48. Masserdotti G, Götz M. A decade of questions about the fluidity of cell identity.
1229 Nature. 2020;578.

1230 49. Bocchi R, Masserdotti G, Götz M. Direct neuronal reprogramming: Fast forward
1231 from new concepts toward therapeutic approaches. Neuron. 2022.

1232 50. Gascón S, Masserdotti G, Russo GL, Götz M. Direct Neuronal Reprogramming:
1233 Achievements, Hurdles, and New Roads to Success. Cell Stem Cell. 2017.

1234 51. Ninkovic J, Götz M. Fate specification in the adult brain - lessons for eliciting
1235 neurogenesis from glial cells. BioEssays. 2013;35.

1236 52. Ninkovic J, Götz M. Understanding direct neuronal reprogramming — from pioneer
1237 factors to 3D chromatin. Curr Opin Genet Dev. 2018;52.

1238 53. Kimura A, Matsuda T, Sakai A, Murao N, Nakashima K. HMGB2 expression is
1239 associated with transition from a quiescent to an activated state of adult neural stem
1240 cells. Developmental Dynamics. 2018;247.

1241 54. Mall M, Kareta MS, Chanda S, Ahlenius H, Perotti N, Zhou B, et al. Myt1l safeguards
1242 neuronal identity by actively repressing many non-neuronal fates. Nature [Internet].
1243 2017;544:245–9. Available from: https://www.ncbi.nlm.nih.gov/pubmed/28379941

1244 55. Hsieh CY, Nakamura PA, Luk SO, Miko IJ, Henkemeyer M, Cramer KS. Ephrin-B
1245 reverse signaling is required for formation of strictly contralateral auditory brainstem
1246 pathways. Journal of Neuroscience. 2010;30.

1247 56. Kania A, Klein R. Mechanisms of ephrin-Eph signalling in development, physiology
1248 and disease. Nat Rev Mol Cell Biol. 2016.

1249 57. Hindley C, Ali F, McDowell G, Cheng K, Jones A, Guillemot F, et al. Post-translational
1250 modification of Ngn2 differentially affects transcription of distinct targets to regulate
1251 the balance between progenitor maintenance and differentiation. Development.
1252 2012;139.

1253 58. Zhang ZH, Jhaveri DJ, Marshall VM, Bauer DC, Edson J, Narayanan RK, et al. A
1254 comparative study of techniques for differential expression analysis on RNA-seq data.
1255 PLoS One. 2014;9.

1256 59. Pan G, Thomson JA. Nanog and transcriptional networks in embryonic stem cell
1257 pluripotency. Cell Res. 2007.

1258 60. Tokuzawa Y, Kaiho E, Maruyama M, Takahashi K, Mitsui K, Maeda M, et al. Fbx15 Is
1259 a Novel Target of Oct3/4 but Is Dispensable for Embryonic Stem Cell Self-Renewal and
1260 Mouse Development. Mol Cell Biol. 2003;23.

1261 61. Petrovic N, Schacke W, Gahagan JR, O'Conor CA, Winnicka B, Conway RE, et al.
1262 CD13/APN regulates endothelial invasion and filopodia formation. Blood. 2007;110.

1263 62. Mina-Osorio P, Winnicka B, O'Conor C, Grant CL, Vogel LK, Rodriguez-Pinto D, et
1264 al. CD13 is a novel mediator of monocytic/endothelial cell adhesion. J Leukoc Biol.
1265 2008;84.

1266 63. Lin G, Finger E, Gutierrez-Ramos JC. Expression of CD34 in endothelial cells,
1267 hematopoietic progenitors and nervous cells in fetal and adult mouse tissues. Eur J
1268 Immunol. 1995;25.

1269 64. Jung S, Aliberti J, Graemmel P, Sunshine MJ, Kreutzberg GW, Sher A, et al. Analysis
1270 of Fractalkine Receptor CX 3 CR1 Function by Targeted Deletion and Green Fluorescent
1271 Protein Reporter Gene Insertion . Mol Cell Biol. 2000;20.

1272 65. Schwab JM, Frei E, Klusman I, Schnell L, Schwab ME, Schluesener HJ. AIF-1
1273 expression defines a proliferating and alert microglial/macrophage phenotype
1274 following spinal cord injury in rats. J Neuroimmunol. 2001;119.

1275 66. Okada Y, Yamazaki H, Sekine-Aizawa Y, Hirokawa N. The neuron-specific kinesin
1276 superfamily protein KIF1A is a uniqye monomeric motor for anterograde axonal
1277 transport of synaptic vesicle precursors. Cell. 1995;81.

1278 67. Niwa S, Tanaka Y, Hirokawa N. KIF1Bβ- and KIF1A-mediated axonal transport of
1279 presynaptic regulator Rab3 occurs in a GTP-dependent manner through DENN/MADD.
1280 Nat Cell Biol. 2008;10.

1281 68. Wang R, Rossomando A, Sah DWY, Ossipov MH, King T, Porreca F. Artemin induced
1282 functional recovery and reinnervation after partial nerve injury. Pain. 2014;155.

1283 69. Errico F, Santini E, Migliarini S, Borgkvist A, Centonze D, Nasti V, et al. The GTP-
1284 binding protein Rhes modulates dopamine signalling in striatal medium spiny neurons.
1285 Molecular and Cellular Neuroscience. 2008;37.

1286 70. Bianchi ME, Agresti A. HMG proteins: Dynamic players in gene regulation and
1287 differentiation. Curr Opin Genet Dev. 2005.

1288 71. Štros M. HMGB proteins: Interactions with DNA and chromatin. Biochim Biophys
1289 Acta Gene Regul Mech. 2010.

1290 72. Thomas JO, Travers AA. HMG1 and 2, and related "architectural" DNA-binding
1291 proteins. Trends Biochem Sci. 2001.

1292 73. Smith DK, Yang J, Liu ML, Zhang CL. Small Molecules Modulate Chromatin
1293 Accessibility to Promote NEUROG2-Mediated Fibroblast-to-Neuron Reprogramming.
1294 Stem Cell Reports. 2016;7.

1295 74. Javed A, Mattar P, Lu S, Kruczek K, Kloc M, Gonzalez-Cordero A, et al. Pou2f1 and
1296 Pou2f2 cooperate to control the timing of cone photoreceptor production in the
1297 developing mouse retina. Development (Cambridge). 2020;147.

1298 75. Harris A, Masgutova G, Collin A, Toch M, Hidalgo-Figueroa M, Jacob B, et al.
1299 Onecut factors and Pou2f2 regulate the distribution of V2 interneurons in the mouse
1300 developing spinal cord. Front Cell Neurosci. 2019;13.

1301 76. Gonda Y, Namba T, Hanashima C. Beyond Axon Guidance: Roles of Slit-Robo
1302 Signaling in Neocortical Formation. Front Cell Dev Biol. 2020.

1303 77. Hevner RF. From Radial Glia to Pyramidal-Projection Neuron: Transcription Factor
1304 Cascades in Cerebral Cortex Development. Mol Neurobiol [Internet]. 2006 [cited 2019
1305 Nov 3];33:033–50. Available from: http://www.ncbi.nlm.nih.gov/pubmed/16388109

1306 78. Sofroniew M V. Astrocyte Reactivity: Subtypes, States, and Functions in CNS Innate
1307 Immunity. Trends Immunol. 2020.

1308 79. Burda JE, Sofroniew M V. Reactive gliosis and the multicellular response to CNS
1309 damage and disease. Neuron [Internet]. 2014;81:229–48. Available from:
1310 http://www.ncbi.nlm.nih.gov/pubmed/24462092

1311 80. Kang W, Hébert JM. FGF signaling is necessary for neurogenesis in young mice and
1312 sufficient to reverse its decline in old mice. Journal of Neuroscience. 2015;35.

1313 81. Goldshmit Y, Tang JKKY, Siegel AL, Nguyen PD, Kaslin J, Currie PD, et al. Different
1314 Fgfs have distinct roles in regulating neurogenesis after spinal cord injury in zebrafish.
1315 Neural Dev. 2018;13.

1316 82. Smith KM, Fagel DM, Stevens HE, Rabenstein RL, Maragnoli ME, Ohkubo Y, et al.
1317 Deficiency in Inhibitory Cortical Interneurons Associates with Hyperactivity in Fibroblast
1318 Growth Factor Receptor 1 Mutant Mice. Biol Psychiatry. 2008;63.

1319 83. Pataskar A, Jung J, Smialowski P, Noack F, Calegari F, Straub T, et al. NeuroD1
1320 reprograms chromatin and transcription factor landscapes to induce the neuronal

program. Embo J [Internet]. 2016;35:24–45. Available from: https://www.ncbi.nlm.nih.gov/pubmed/26516211

84. Noack F, Pataskar A, Schneider M, Buchholz F, Tiwari VK, Calegari F. Assessment and site-specific manipulation of DNA (hydroxy-)methylation during mouse corticogenesis. Life Sci Alliance. 2019;2.

85. Aprea J, Prenninger S, Dori M, Ghosh T, Monasor LS, Wessendorf E, et al. Transcriptome sequencing during mouse brain development identifies long non-coding RNAs functionally involved in neurogenic commitment. EMBO Journal. 2013;32.

86. Abraham AB, Bronstein R, Reddy AS, Maletic-Savatic M, Aguirre A, Tsirka SE. Aberrant Neural Stem Cell Proliferation and Increased Adult Neurogenesis in Mice Lacking Chromatin Protein HMGB2. PLoS One. 2013;8:e84838.

87. Wapinski OL, Lee QY, Chen AC, Li R, Corces MR, Ang CE, et al. Rapid Chromatin Switch in the Direct Reprogramming of Fibroblasts to Neurons. Cell Rep [Internet]. 2017;20:3236–47. Available from: https://www.ncbi.nlm.nih.gov/pubmed/28954238

88. Kishi Y, Fujii Y, Hirabayashi Y, Gotoh Y. HMGA regulates the global chromatin state and neurogenic potential in neocortical precursor cells. Nat Neurosci [Internet]. 2012;15:1127–33. Available from: http://www.ncbi.nlm.nih.gov/pubmed/22797695

89. Zhou X, Zhong S, Peng H, Liu J, Ding W, Sun L, et al. Cellular and molecular properties of neural progenitors in the developing mammalian hypothalamus. Nat Commun. 2020;11.

90. Lee SW, Oh YM, Lu YL, Kim WK, Yoo AS. MicroRNAs Overcome Cell Fate Barrier by Reducing EZH2-Controlled REST Stability during Neuronal Conversion of Human Adult Fibroblasts. Dev Cell. 2018;46.

91. Starkova T, Polyanichko A, Tomilin AN, Chikhirzhina E. Structure and Functions of HMGB2 Protein. Int J Mol Sci. 2023;24:8334.

92. Noack F, Vangelisti S, Raffl G, Carido M, Diwakar J, Chong F, et al. Multimodal profiling of the transcriptional regulatory landscape of the developing mouse cortex identifies Neurog2 as a key epigenome remodeler. Nat Neurosci. 2022;25.

93. Zirkel A, Nikolic M, Sofiadis K, Mallm JP, Brackley CA, Gothe H, et al. HMGB2 Loss upon Senescence Entry Disrupts Genomic Organization and Induces CTCF Clustering across Cell Types. Mol Cell. 2018;70.

94. Divisato G, Chiariello AM, Esposito A, Zoppoli P, Zambelli F, Elia MA, et al. Hmga2 protein loss alters nuclear envelope and 3D chromatin structure. BMC Biol. 2022;20.

95. Wapinski OL, Vierbuchen T, Qu K, Lee QY, Chanda S, Fuentes DR, et al. Hierarchical mechanisms for direct reprogramming of fibroblasts to neurons. Cell [Internet]. 2013;155:621–35. Available from: http://www.ncbi.nlm.nih.gov/pubmed/24243019

1357 96. Liu M-L, Zang T, Zou Y, Chang JC, Gibson JR, Huber KM, et al. Small molecules
1358 enable neurogenin 2 to efficiently convert human fibroblasts into cholinergic neurons.
1359 Nat Commun [Internet]. 2013;4. Available from: http://dx.doi.org/10.1038/ncomms3183

1360 97. Heinrich C, Bergami M, Gascón S, Lepier A, Dimou L, Sutor B, et al. Sox2-mediated
1361 conversion of NG2 glia into induced neurons in the injured adult cerebral cortex. Stem
1362 Cell Reports [Internet]. 2014;in press:1000–14. Available from:
1363 http://www.ncbi.nlm.nih.gov/pubmed/25458895

1364 98. Liu ML, Zang T, Zhang CL. Direct Lineage Reprogramming Reveals Disease-Specific
1365 Phenotypes of Motor Neurons from Human ALS Patients. Cell Rep. 2016;14.

1366 99. Kempf J, Knelles K, Hersbach BA, Petrik D, Riedemann T, Bednarova V, et al.
1367 Heterogeneity of neurons reprogrammed from spinal cord astrocytes by the proneural
1368 factors Ascl1 and Neurogenin2. Cell Rep. 2021;36.

1369 100. Treutlein B, Lee QY, Camp JG, Mall M, Koh W, Shariati SA, et al. Dissecting direct
1370 reprogramming from fibroblast to neuron using single-cell RNA-seq. Nature [Internet].
1371 2016;534:391–5. Available from: https://www.ncbi.nlm.nih.gov/pubmed/27281220

1372 101. Chen K, Zhang J, Liang F, Zhu Q, Cai S, Tong X, et al. HMGB2 orchestrates mitotic
1373 clonal expansion by binding to the promoter of C/EBPβ to facilitate adipogenesis. Cell
1374 Death Dis. 2021;12.

1375 102. Ronfani L, Ferraguti M, Croci L, Ovitt CE, Schöler HR, Consalez GG, et al. Reduced
1376 fertility and spermatogenesis defects in mice lacking chromosomal protein Hmgb2.
1377 Development. 2001;128:1265–73.

1378 103. Buffo A, Rite I, Tripathi P, Lepier A, Colak D, Horn AP, et al. Origin and progeny of
1379 reactive gliosis: A source of multipotent cells in the injured brain. Proc Natl Acad Sci U S
1380 A [Internet]. 2008/02/27. 2008;105:3581–6. Available from:
1381 http://www.ncbi.nlm.nih.gov/entrez/query.fcgi?cmd=Retrieve&db=PubMed&dopt=Cita
1382 tion&list_uids=18299565

1383 104. Blum R, Heinrich C, Sanchez R, Lepier A, Gundelfinger ED, Berninger B, et al.
1384 Neuronal network formation from reprogrammed early postnatal rat cortical glial cells.
1385 Cereb Cortex [Internet]. 2010/06/22. 2011;21:413–24. Available from:
1386 http://www.ncbi.nlm.nih.gov/pubmed/20562320

1387 105. Schindelin J, Arganda-Carreras I, Frise E, Kaynig V, Longair M, Pietzsch T, et al. Fiji:
1388 An open-source platform for biological-image analysis. Nat Methods. 2012.

1389 106. Buenrostro JD, Wu B, Chang HY, Greenleaf WJ. ATAC-seq: A method for assaying
1390 chromatin accessibility genome-wide. Curr Protoc Mol Biol. 2015;2015.

1391 107. Buenrostro JD, Giresi PG, Zaba LC, Chang HY, Greenleaf WJ. Transposition of
1392 native chromatin for fast and sensitive epigenomic profiling of open chromatin, DNA-
1393 binding proteins and nucleosome position. Nat Methods. 2013;10.

108. Quinlan AR, Hall IM. BEDTools: A flexible suite of utilities for comparing genomic features. Bioinformatics. 2010;26.

109. Ninkovic J, Pinto L, Petricca S, Lepier A, Sun J, Rieger MAA, et al. The transcription factor Pax6 regulates survival of dopaminergic olfactory bulb neurons via crystallin alphaA. Neuron [Internet]. 2010/11/26. 2010;68:682–94. Available from: http://www.ncbi.nlm.nih.gov/entrez/query.fcgi?cmd=Retrieve&db=PubMed&dopt=Citation&list_uids=21092858

110. Wiśniewski JR, Zougman A, Nagaraj N, Mann M. Universal sample preparation method for proteome analysis. Nat Methods. 2009;6:359–62.

111. Hauck SM, Dietter J, Kramer RL, Hofmaier F, Zipplies JK, Amann B, et al. Deciphering Membrane-Associated Molecular Processes in Target Tissue of Autoimmune Uveitis by Label-Free Quantitative Mass Spectrometry. Molecular & Cellular Proteomics. 2010;9:2292–305.

112. Merl J, Ueffing M, Hauck SM, von Toerne C. Direct comparison of MS-based label-free and SILAC quantitative proteome profiling strategies in primary retinal Müller cells. Proteomics. 2012;12:1902–11.

113. Ninkovic J, Steiner-Mezzadri A, Jawerka M, Akinci U, Masserdotti G, Petricca S, et al. The BAF Complex Interacts with Pax6 in Adult Neural Progenitors to Establish a Neurogenic Cross-Regulatory Transcriptional Network. Cell Stem Cell [Internet]. 2013;13. Available from: http://www.ncbi.nlm.nih.gov/pubmed/23933087

114. RStudio Team. RStudio: Integrated Development for R. RStudio, Inc., Boston, MA. URL http://www.rstudio.com/. RStudio, Inc. 2015;

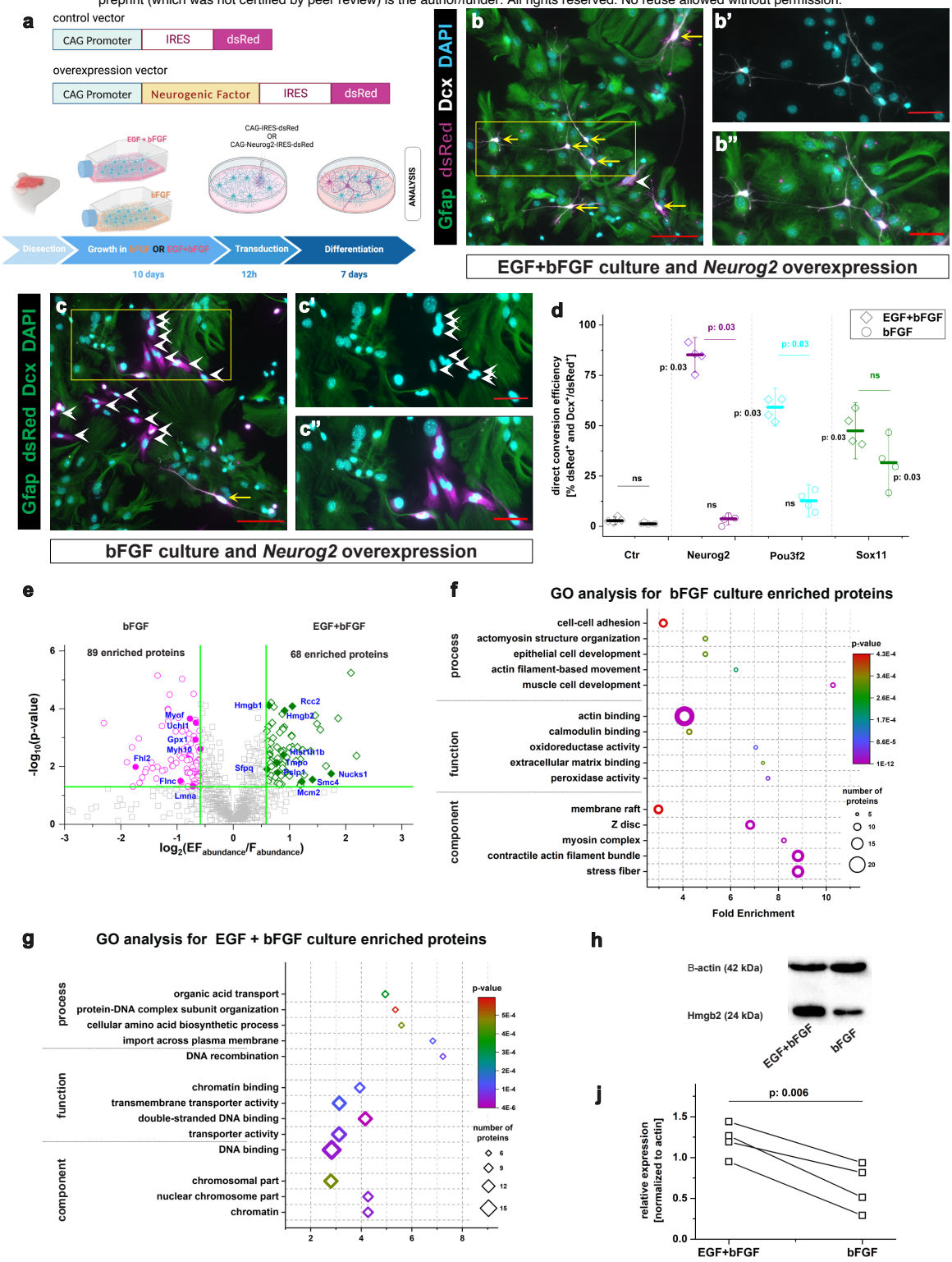

Maddhesiya, Lepko et al, Figure 1

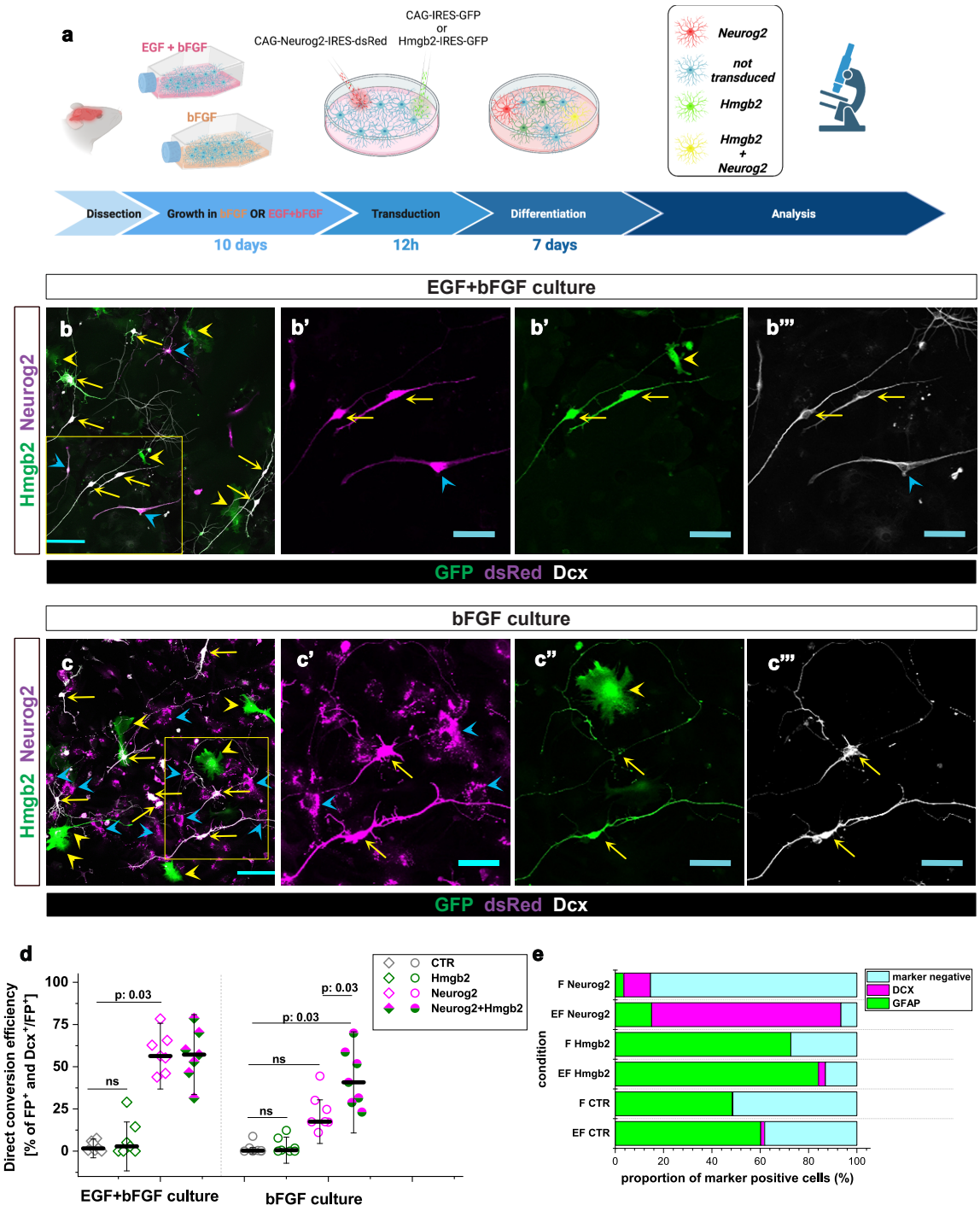

Maddhesiya, Lepko et al Figure 2

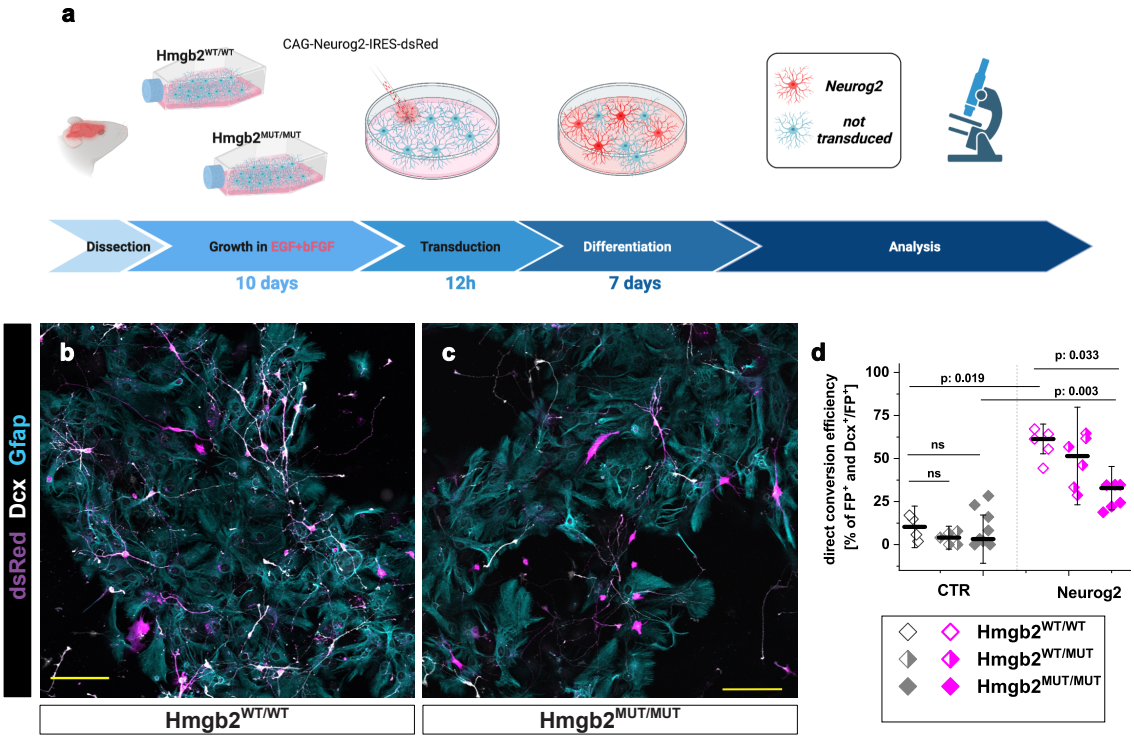

Maddhesiya, Lepko et al Figure 3

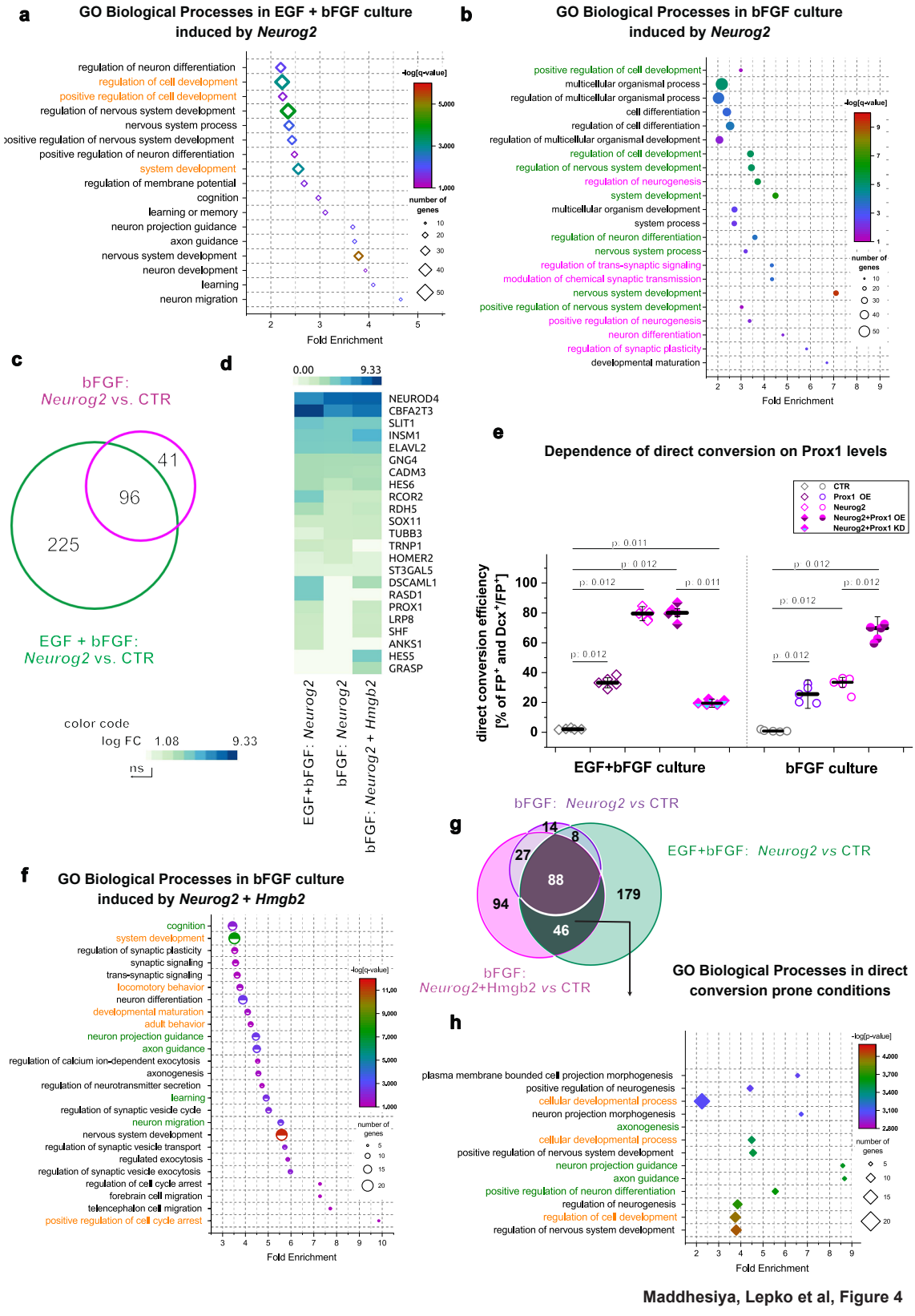

Maddhesiya, Lepko et al, Figure 4

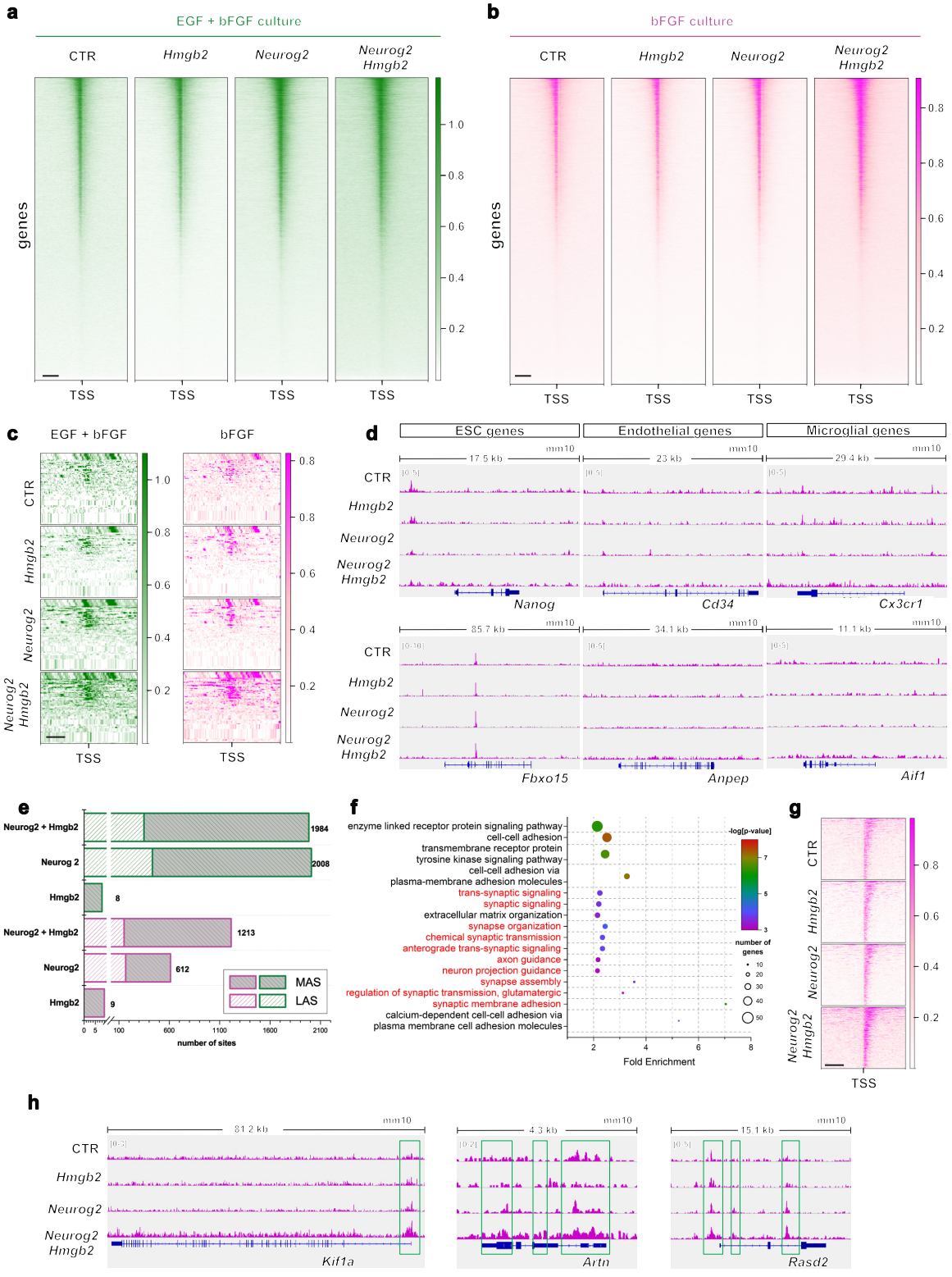

Maddhesiya, Lepko et al, Figure 5

a

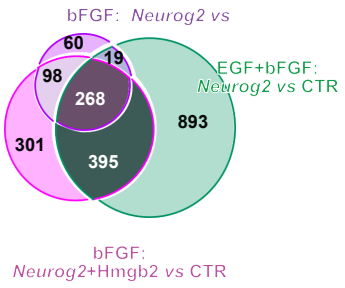

b

GO Biological Processes enriched in direct conversion relevant peaks induced by *Neurog2+Hmgb2* (395 MASs)

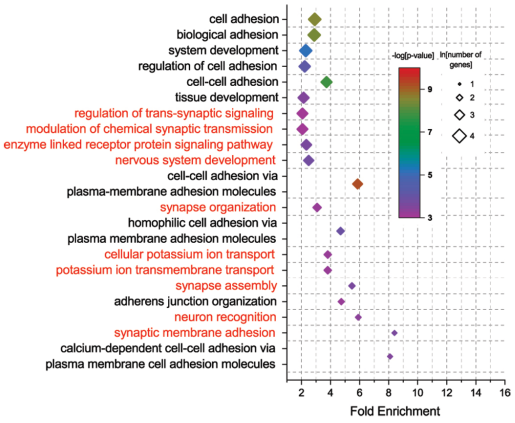

c

GO Biological Processes enriched in shared peaks induced by *Neurog2* (268 MASs)

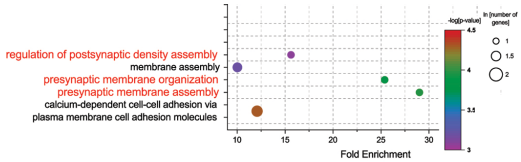

d

TF binding site consensus sequence in shared peaks induced by *Neurog2* (268 MASs)

Motif 1

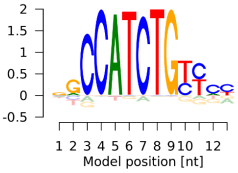

Binding motif for Tal-related TFs

TF	E-value
Neurog2	2.9E-06
Neurod1	3.1E-06
Neurod2	5.4E-06
Atoh1	8.4E-06
Msgn1	3.2E-05

identified in 202 MASs

e

TF binding site consensus sequence in direct conversion relevant peaks induced by *Neurog2+Hmgb2* (395 MASs)

Motif 1

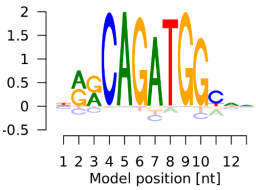

Binding motif for Tal-related TFs

TF	E-value
Neurog2	1.9E-08
Neurod1	4.1E-08
Neurod2	4.2E-08
Atoh1	5.4E-08
Msgn1	1.8E-06

identified in 261 MASs

Motif 2

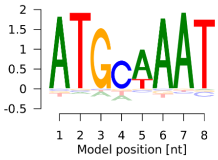

Binding motif for POU TFs

TF	E-value
Pou2f2	7.6E-03

identified in 90 MASs

Maddhesiya, Lepko et al, Figure 6

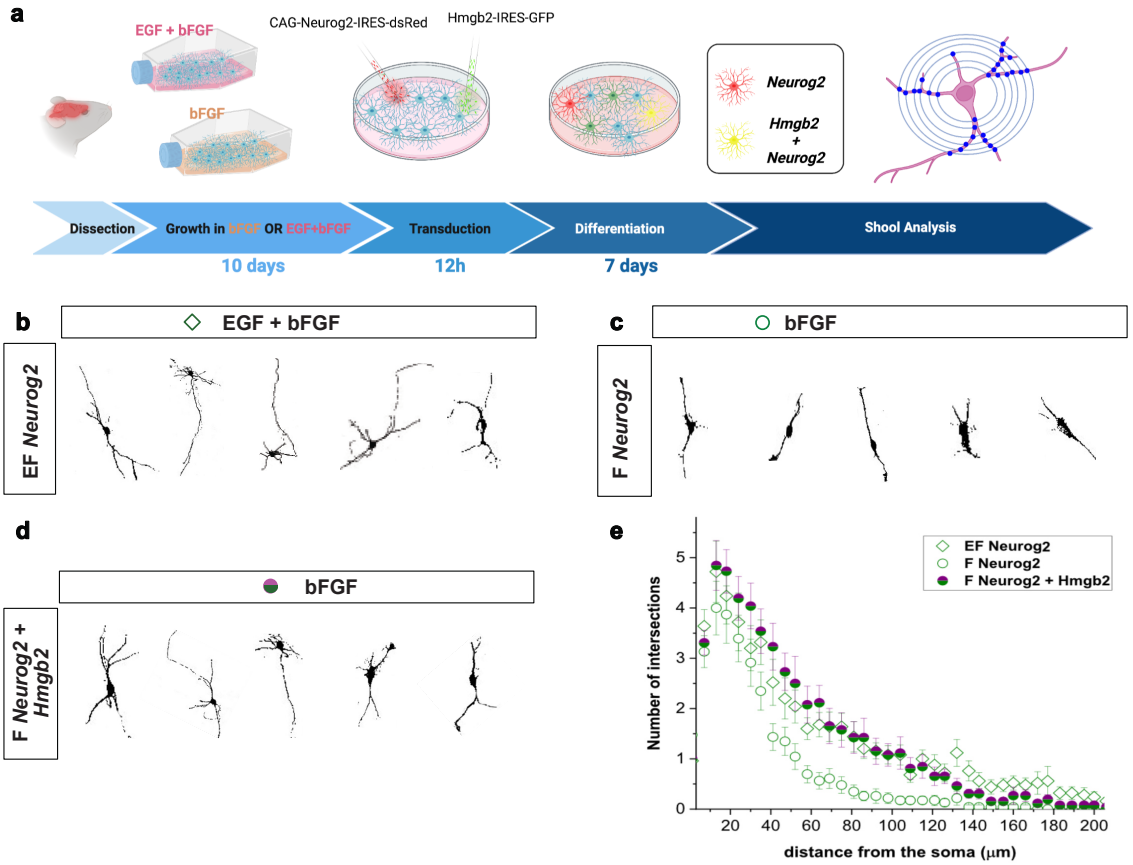

Maddhesiya, Lepko et al, Figure 7

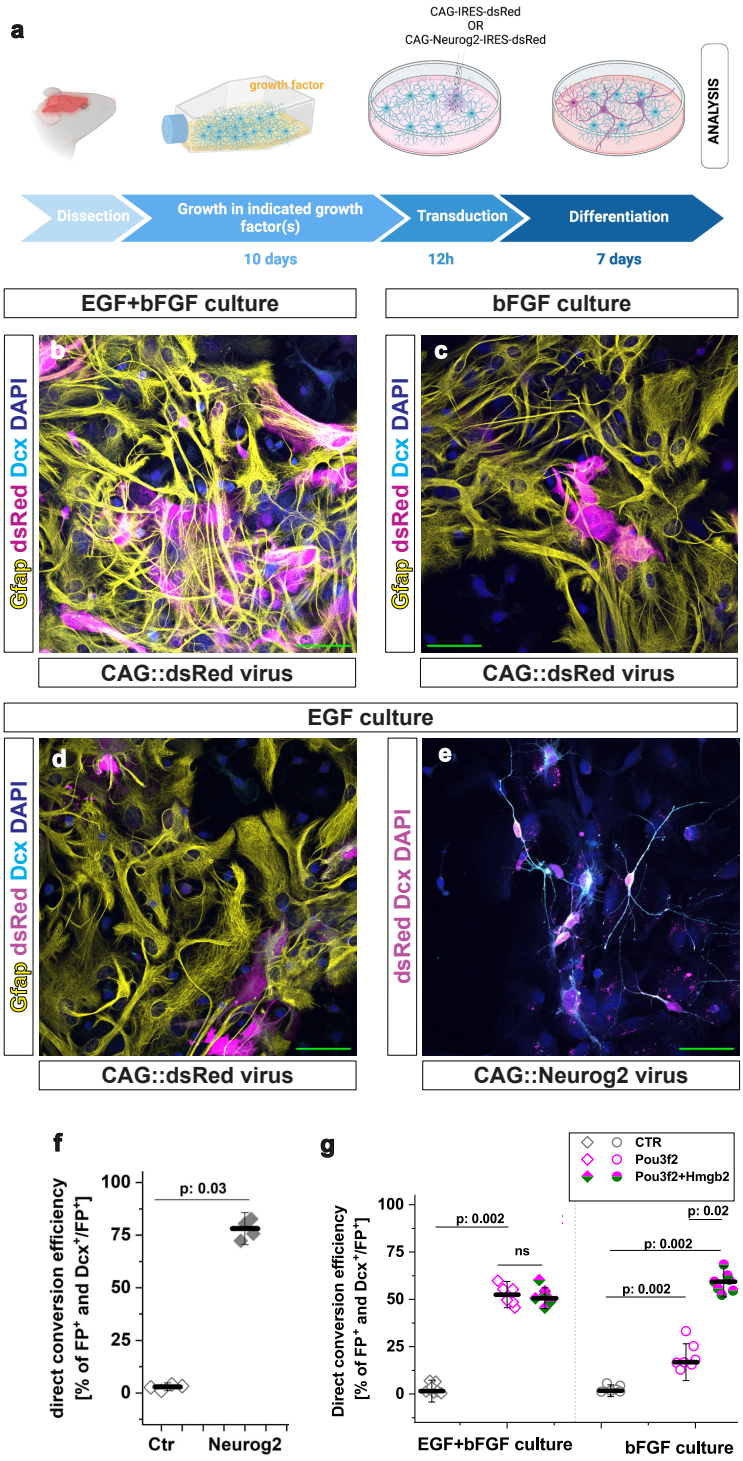

Maddhesiya, Lepko et al, Suppl. Figure 1

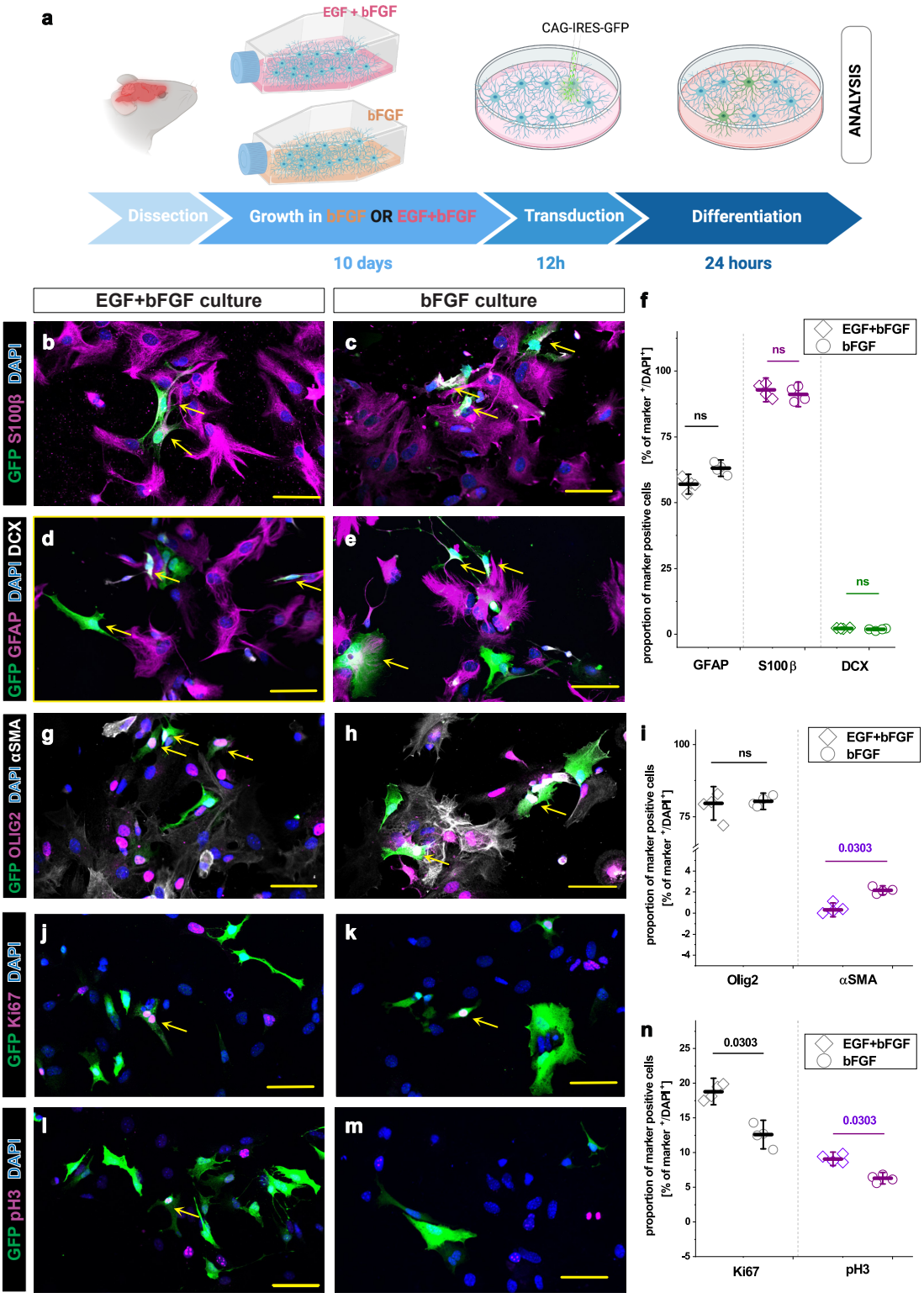

Maddhesiya, Lepko et al, Suppl. Figure 2

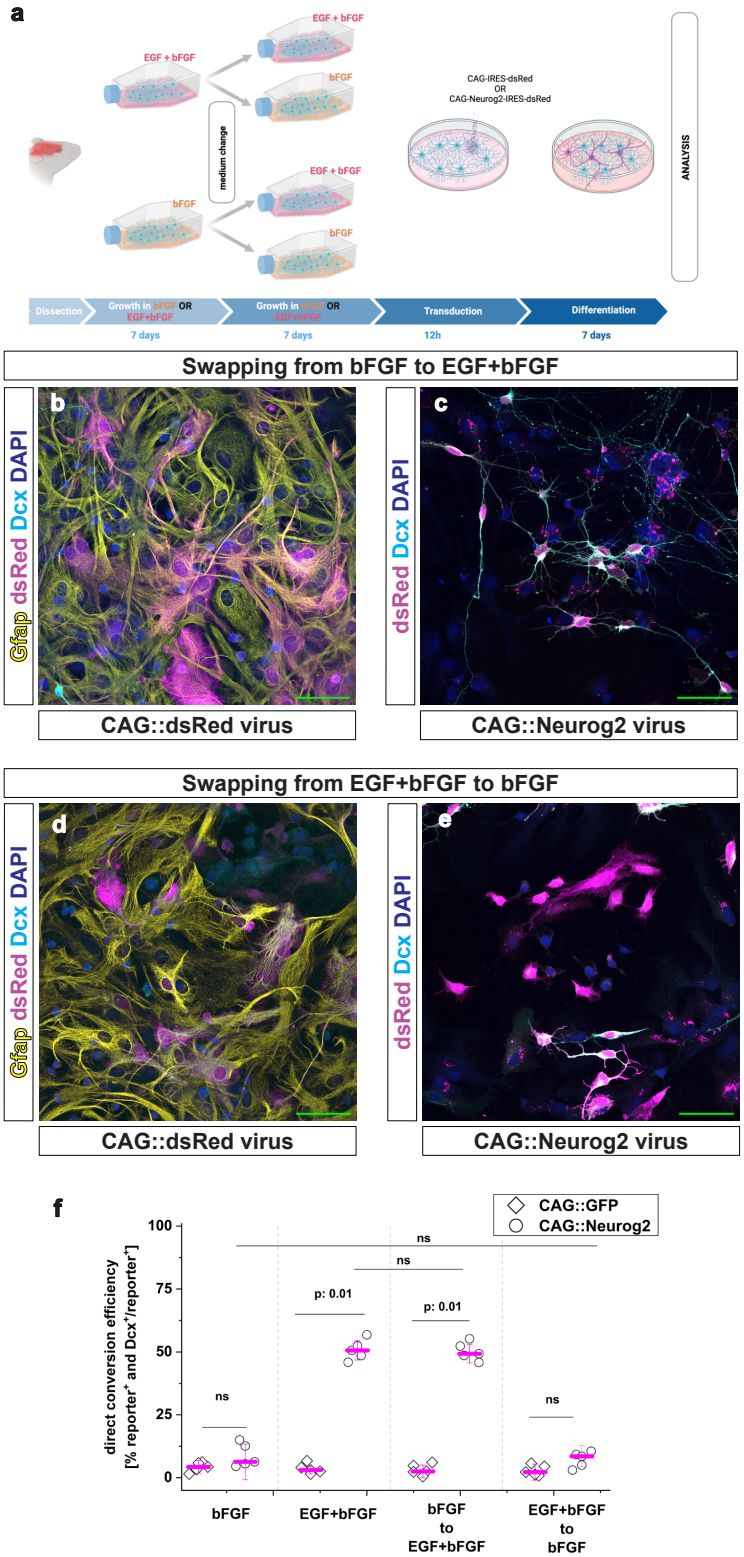

Maddhesiya, Lepko et al, Suppl. Figure 3

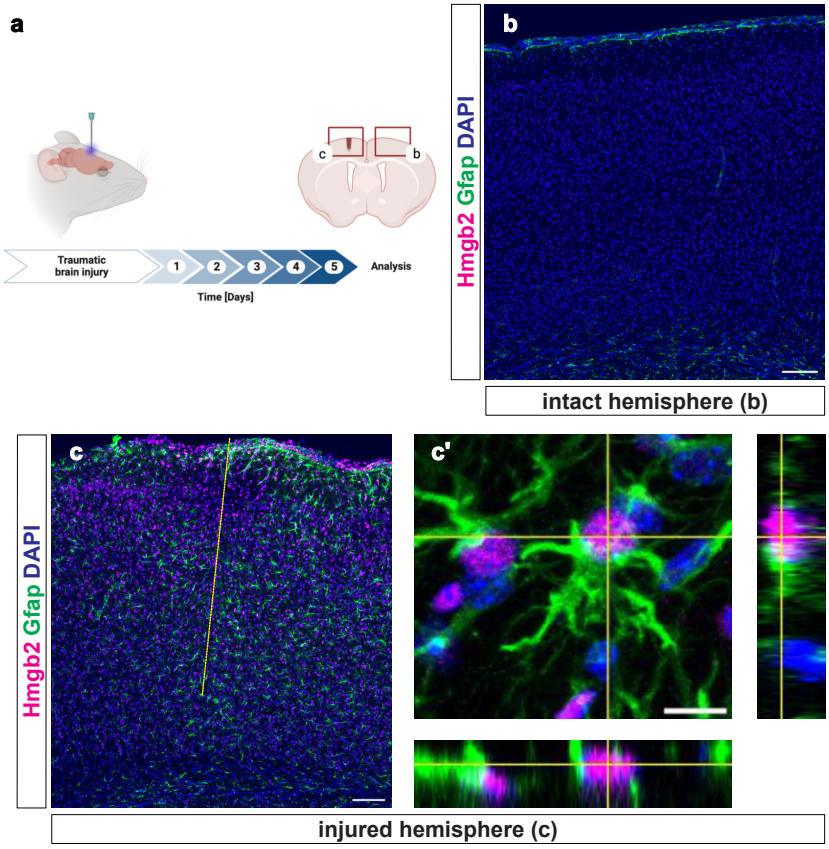

Maddhesiya, Lepko et al, Suppl. Figure 4

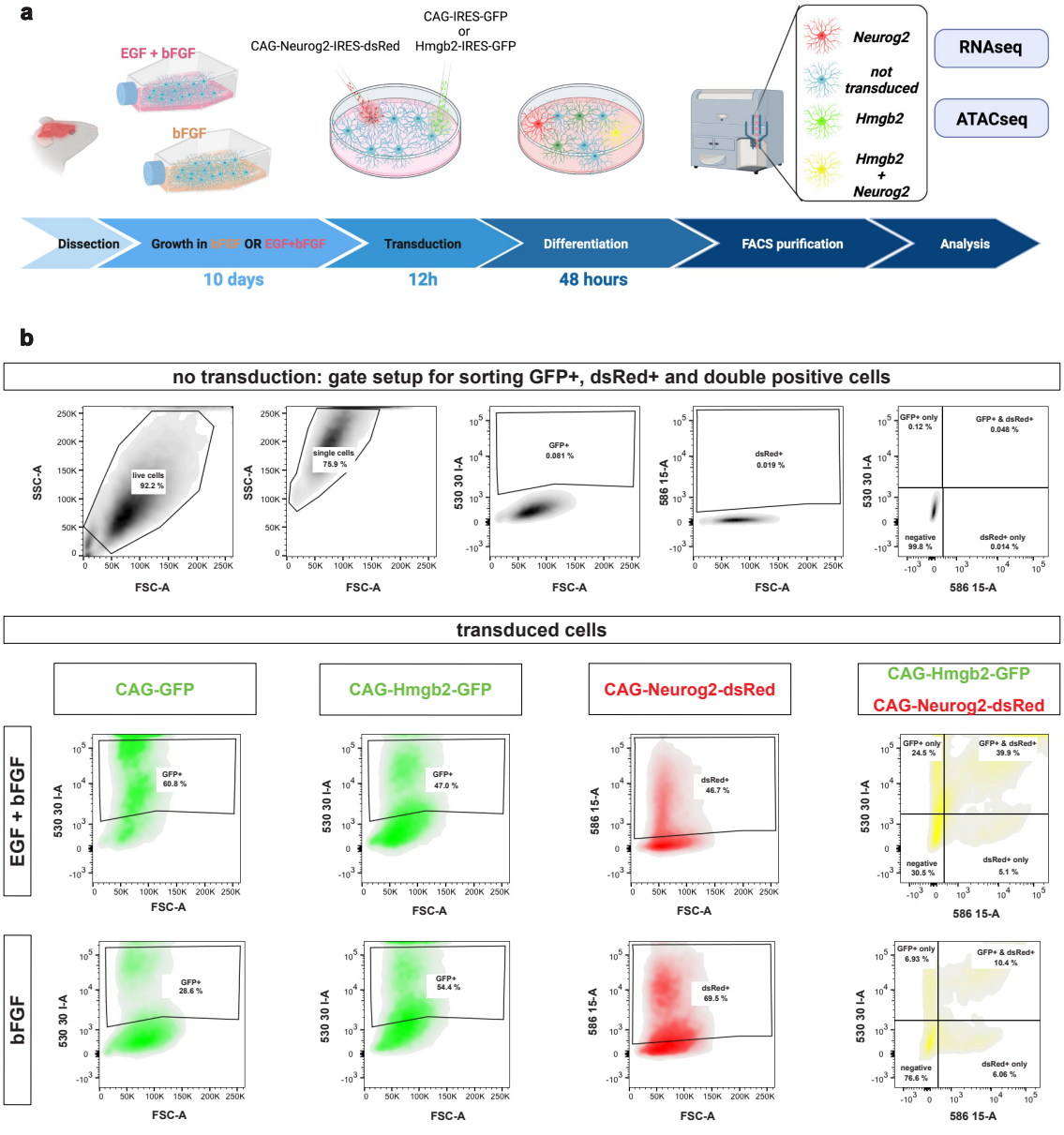

Maddhesiya, Lepko et al, Suppl. Figure 5

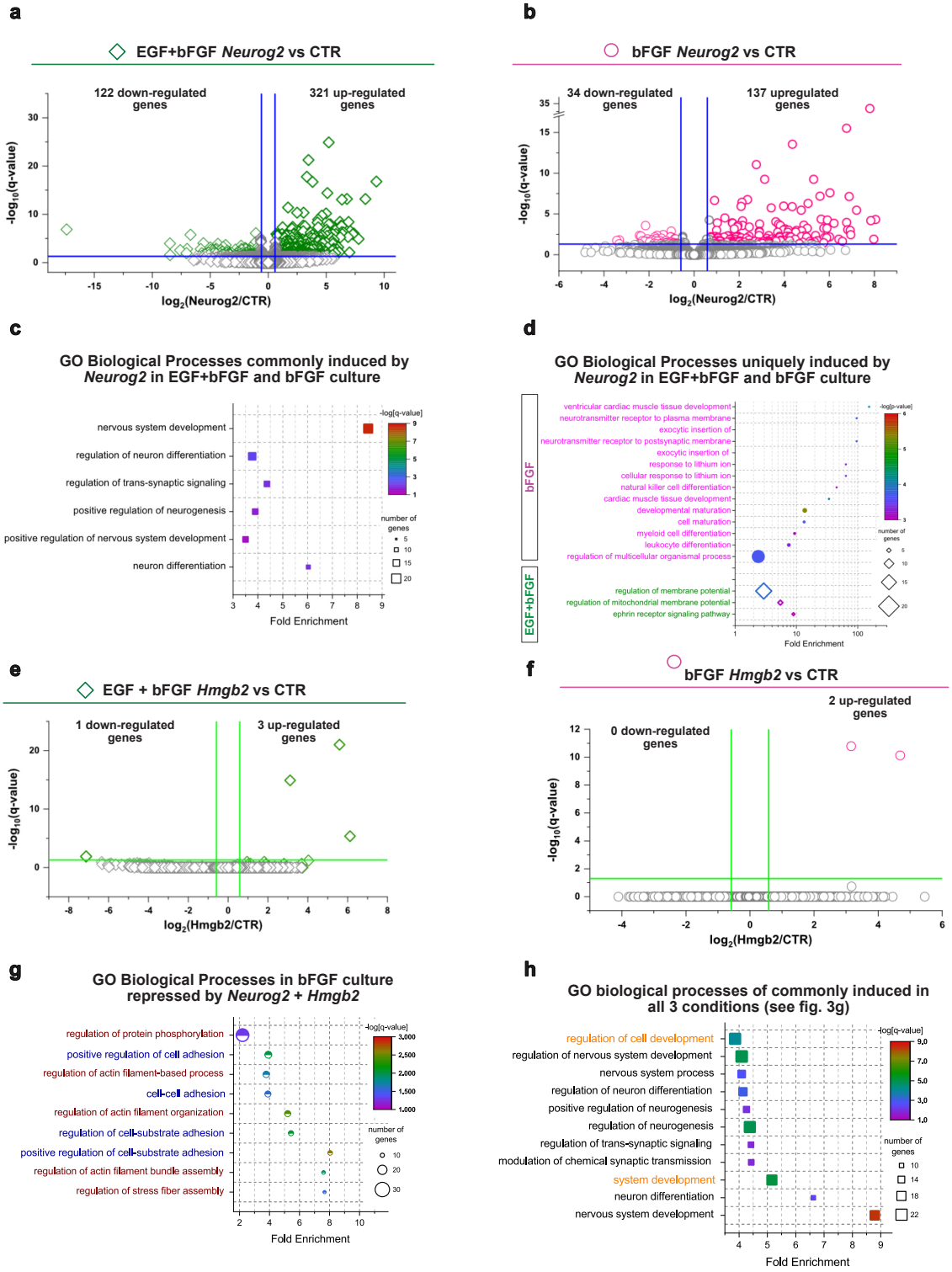

Maddhesiya, Lepko et al, Suppl. Figure 6

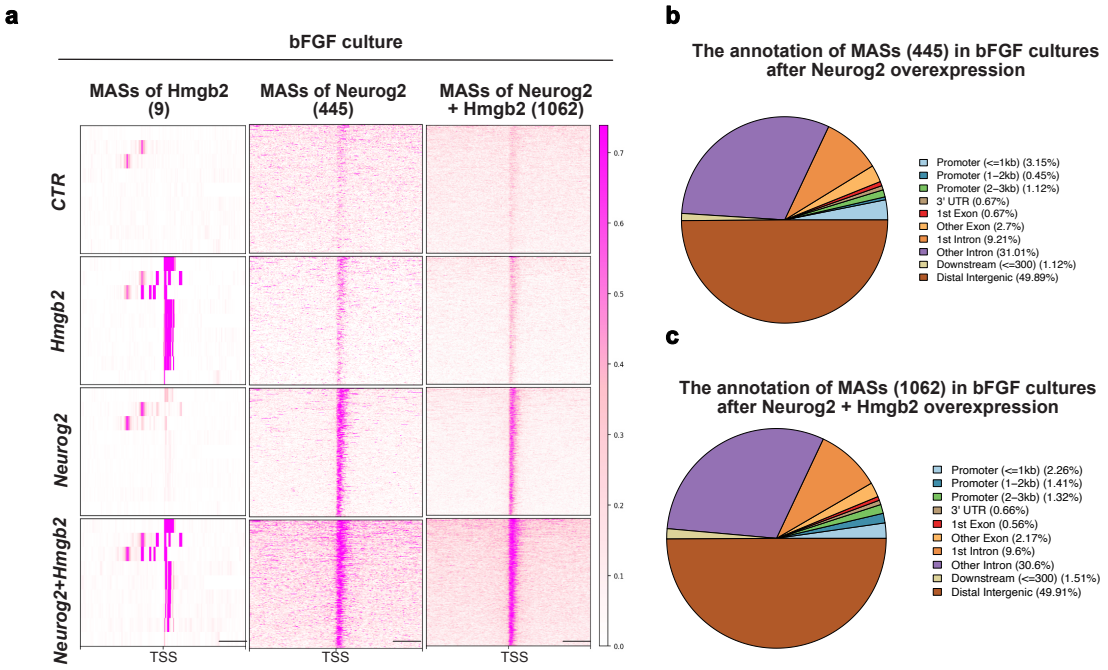

Maddhesiya, Lepko et al, Suppl. Figure 7

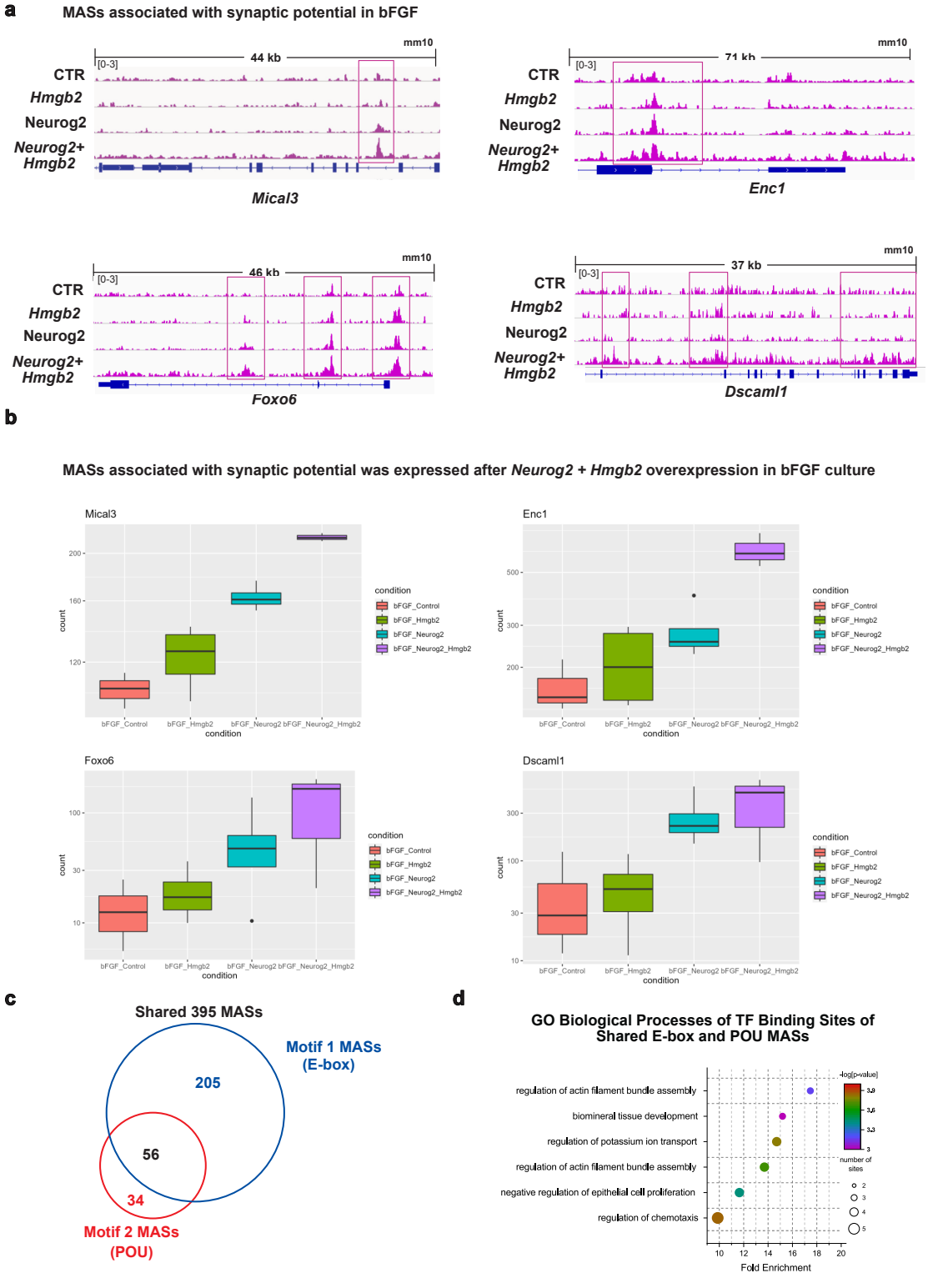

Maddhesiya, Lepko et al, Suppl. Figure 8

DISCUSSION

Worldwide, TBIs account for most death cases among young adults and disabilities across all age groups. Moreover, TBI patients are often confronted with lifelong cognitive, physical, and emotional restrictions and are furthermore at risk for developing neurological diseases later in life (Cruz-Haces et al., 2017; Fan et al., 2022; Maas et al., 2017, 2022). Cellular and functional loss caused by the primary insult cannot be avoided; however, targeting mechanisms of the secondary injury cascade is a promising approach to prevent further cell death and concomitant functional impairment. The extent of the secondary tissue damage is determined by an array of pathological processes, including excessive neuroinflammation, which plays a critical role in orchestrating cellular loss and tissue integrity during the chronic injury phase (Karve et al., 2016). Neuroinflammation is mediated by brain-resident glia and infiltrating peripheral cells, and it has been postulated that neuroinflammatory events following TBI cause more damage than the primary insult itself (Kumar & Loane, 2012; Patterson & Holahan, 2012). Although long-lasting, glia-mediated inflammation promotes continuous tissue- and functional loss, initial glial responses are inevitable for cell debris clearance, the establishment of a protective glial border that restrains the damaged area from the adjacent healthy tissue, and the generation of a permissive environment promoting selective aspects of regeneration such as axonal growth after spinal cord injury (Anderson et al., 2016; Kumar & Loane, 2012). The dual, temporarily regulated function of glial cells, being beneficial during the early post-injury phase and detrimental in the late stages, opens a critical time window for targeted therapeutic intervention (Kumar & Loane, 2012). Therefore, a comprehensive understanding of TBI-induced glial responses is crucial to elucidate the secondary injury mechanisms associated with the long-lasting, detrimental properties of reactive glia.

Divergent glial reaction in the adult zebrafish brain in response to nostril- and skull injury

TBI triggers complex, heterogeneous cellular cascades orchestrated by various cell types (Karve et al., 2016; Mira et al., 2021). Adequate wound healing and tissue restoration requires fine, temporal regulation of neuroinflammatory events following CNS injury. However, in most mammals, neuroinflammation persists long-term, which considerably hampers tissue restoration and promotes neurodegeneration (Kumar & Loane, 2012). Hence, the regeneration-competent zebrafish may serve as a valuable model to uncover mechanisms that drive exacerbated neuroinflammation in mammals. Similar to mammals, injury in the adult zebrafish brain enables peripherally located leukocytes to populate the brain tissue (Kroehne et al., 2011; Kyritsis et al., 2012; Zambusi & Ninkovic, 2020). Moreover, brain-resident microglia change their morphology, proliferate, and accumulate around the injury site within 1 - 2 dpi (Baumgart et al., 2012; März et al., 2011). In addition to microglia, oligodendrocyte lineage cells accumulate around the impact site and increase their proliferation rate (März et al., 2011). Intriguingly, the lesion-induced proliferation and the density increase of oligodendrocyte lineage cells is not a typical cellular response of brain-injured zebrafish but occurs in a context-dependent manner. Harming the adult zebrafish telencephalon in the rostral-caudal direction through the zebrafish nostrils (= nostril injury) triggers immediate inflammatory reactions, including leukocyte infiltration and microglia activation. Stinkingly, oligodendrocyte lineage cells are not increasing their proliferation rate in this injury paradigm. Moreover, the inflammatory response following nostril injury is timely regulated and resolved within 7 dpi (Baumgart et al., 2012; Kyritsis et al., 2012).

On the contrary, if the telencephalon is stab-wounded through the skull in a dorsal-ventral direction (= skull injury), oligodendroglial lineage cells (mainly OLIG2$^+$ OPCs) proliferate and accumulate at the lesion site. Interestingly, oligodendrocyte lineage cell accumulation was robustly detectable from 2 to 14 dpi but was resolved by 35 dpi (März et al., 2011). The OPC regulation following skull injury in the zebrafish is reminiscent of the transient NG2-glia reaction following brain injury in the murine cerebral cortex. Within 2 - 4 days following SWI, NG2-glia appear hypertrophic, increase their proliferation rate, and rapidly migrate toward the impact site. Comparable to zebrafish, NG2-glia morphology, distribution, and cell number in brain-injured mice are normalized by 30 dpi (Buffo et al.,

2005; von Streitberg et al., 2021). The similarities in the response of OPCs between stab wound-injured mice and skull-injured zebrafish might hint toward shared molecular mechanisms between the two species following brain injury. Moreover, these findings suggest that the glial response to brain injury is not an evolutionary fixed trait but a rather regulated process that could potentially be modified to enhance successful regeneration if key regulatory factors are identified.

To reveal cellular mechanisms driving prolonged oligodendrocyte lineage cell reactivity following brain injury, we set out to directly compare the two injury paradigms in the zebrafish brain (nostril vs. skull injury) that display different cellular reaction profiles during the first days after injury (Sanchez-Gonzalez et al., 2022). A remarkable increase in microglia/monocyte densities around the injury site was detectable 1 day following nostril injury. This accumulation, however, was only temporary as the cell density returned to the physiological level and was indistinguishable from the intact brain by 7 dpi, as demonstrated by several studies before (Baumgart et al., 2012; März et al., 2011; Zambusi et al., 2022). Although oligodendroglial lineage cells are not increasing their proliferation rate in response to nostril injury (Baumgart et al., 2012), a transient accumulation around the impact site was observable at 3 dpi, in line with previous observations (Zambusi et al., 2022). Since the number of proliferating oligodendroglial lineage cells is maintained constant throughout the tissue restoration phase (Baumgart et al., 2012), the increase in oligodendroglial cell density around the injury site is potentially a result of migrating cells from nearby, adjacent areas. Moreover, and in line with the microglia/monocyte response, oligodendroglial cell distribution was normalized by 7 dpi. Intriguingly, microglia/monocyte distribution around the impact site was significantly enhanced in skull-injured zebrafish compared to nostril-injured animals at 1 dpi. Besides the difference in microglia/monocyte distribution, in both injury paradigms, oligodendroglial lineage cell density increased significantly at 3 dpi. Although glial reactivity was efficiently resolved in the nostril injury paradigm, skull-injured zebrafish displayed a continuous increase of oligodendroglial cell numbers and enhanced microglia/monocyte distribution around the injury core at 7 dpi. Although previous studies have reported moderate proliferation rates of oligodendroglial cells in response to skull injury (März et al., 2011), the threefold increase of oligodendroglial

cells at 7 dpi cannot solely be explained by the rise in cycling cells but might be rather a result of increased proliferation combined with the migration of nearby cells as it has also been demonstrated in stab wound-injured mice (von Streitberg et al., 2021).

In line with the divergent glial response following brain injury in the adult zebrafish, gene expression profiling of nostril- and skull-injured animals further uncovered distinct gene regulation in response to skull injury. Interestingly, at 1 and 2 dpi, nostril- and skull-injured zebrafish displayed a remarkable overlap in the significantly overrepresented Gene Ontology (GO) terms, suggesting that brain damage triggers a common transcriptional response independent of the injury type. Many of these shared GO terms were associated with immune system activation, proliferation, and angiogenesis. Previous studies have demonstrated that, in the adult zebrafish brain, inflammation is not only essential to remove cellular debris but also to initiate tissue restoration. Inflammatory events trigger increased ependymoglial cell proliferation and are essential for generating new neurons (Kyritsis et al., 2012; Shimizu et al., 2021). Consequently, Kyritsis and colleagues reported decreased ependymoglial cell proliferation and reduced neurogenesis in immunosuppressed brain-injured zebrafish. Moreover, injury-induced inflammation is crucial for CNS restoration and appears to be a common initiator for adequate tissue repair in many organs, including the fin (Kyritsis et al., 2012; Zambusi & Ninkovic, 2020).

Nostril and skull injury induced comparable responses within the first two days after brain injury; however, in line with the deviating glial reaction at 3 dpi, striking transcriptomic differences became first evident at this time point. Skull-injured zebrafish exhibited a high proportion of uniquely regulated genes at 3 dpi, which were never expressed in the nostril injury paradigm throughout the entire tissue restoration phase. These skull injury-induced genes were associated with metabolism and immune system activation. Therefore, it is tempting to speculate that while brain damage in the adult zebrafish triggers pro-regenerative inflammatory processes during the first days to reinstate tissue homeostasis, a subsequent secondary inflammation wave induced during the acute injury phase results in the exacerbating glial response observed after skull injury.

Consistent with the hypothesis that secondary inflammatory events promote prolonged glial reactivity, several genes regulated at 3 dpi in skull-injured zebrafish were implicated with TLR activation and CXCR3 signaling. The TLR family compromises a

remarkable capacity to recognize an array of extrinsic and intrinsic danger molecules, which enables immediate activation of innate immunity cascades to initiate adequate host defense (Mawhinney et al., 2022). Consequently, TLR activation can be considered as one of the first-line defense mechanisms. Among the unique skull injury-induced genes, we also noted several chemokines that signal through a common chemokine receptor, namely CXCR3 (Koper et al., 2018). Chemokines do not initiate immune responses; however, they are essential to redirect peripherally located cells to the injury site, thereby amplifying inflammatory events (Bajetto et al., 2001). The chemokine receptor CXCR3 is mainly activated by CXCL9, 10, and 11. These chemokines are released by various cell types upon tissue damage and stimulation with pro-inflammatory cytokines, including TNFα, IFNβ, and IFNγ (Zhou et al., 2019). CXCR3 is abundantly expressed on activated, regulatory, and memory T-cells and is furthermore present on innate lymphoid cells (Metzemaekers et al., 2020). Under physiological conditions, CXCR3 is not present on naïve, peripherally circulating neutrophils; however, in several inflammatory diseases, such as cystic fibrosis, sepsis, and pneumonia, tissue-infiltrated neutrophils enlarge their chemokine receptor repertoire and express additional receptors, including CXCR3, on their cell surface. Intriguingly, *in vitro*, several inflammation-promoting factors, including TLR agonists, induced the expression of CXCR3 on neutrophils (Hartl et al., 2008; Metzemaekers et al., 2020; Rudd et al., 2019). Considering that CXCR3 expression on tissue-infiltrating neutrophils steadily increased within the first days during influenza infection (Rudd et al., 2019), it is thus tempting to speculate that neutrophils might potentially be implicated with the prolonged glial reactivity prominently seen in skull-injured zebrafish. Neutrophils were detected as early as 12 hours post-injury in nostril- and skull-injured animals; however, even though neutrophil accumulation was quickly resolved in the nostril injury paradigm, neutrophils were still present in the skull-injured animals at 2 dpi. Recent studies have demonstrated that tissue-infiltrated neutrophils are phagocytized by monocyte-derived macrophages (Soehnlein & Lindbom, 2010) or even migrate back to the blood circulation (Powell et al., 2017; Robertson et al., 2014), which is beneficial for resolving inflammation and inducing tissue repair (J. Wang, 2018). However, if neutrophils are not cleared in a timely manner, they can undergo necrosis, release their intracellular, toxic content (Iba et al., 2013), and hence, likely contribute to the prolonged inflammatory environment

observed in skull-injured zebrafish. Furthermore, it is tempting to speculate that neutrophils in skull-injured animals might acquire an altered chemokine receptor profile during the acute wound healing phase, which changes neutrophil function as it has been reported in other inflammatory conditions before (Hartl et al., 2008; Rudd et al., 2019). However, further studies are necessary to determine whether neutrophils are indeed involved in the excessive glial response upon skull injury.

The innate immune pathways TLR1/2 and CXCR3 regulate glial reactivity in brain-injured zebrafish

TLR2 and CXCR3 agonists elicited excessive glial responses in the typically inflammation-resolving nostril injury paradigm. Thus, we pharmacologically inactivated either TLR1/2 or CXCR3 signaling by administering two specific inhibitors (CU CPT 22 for TLR1/2 and NBI 74330 for CXCR3) during the entire wound healing and regeneration phase in an attempt to alleviate glial reactivity in skull-injured animals. Intriguingly, simultaneous inhibition of TLR1/2 and CXCR3 signaling pathways following skull injury resulted in reduced numbers of oligodendroglial cells and decreased accumulation of microglia/monocytes around the injury core at 4 and 7 dpi. However, pharmacological inhibition of CXCR3 signaling alone throughout the first days following injury did not display any alteration in glial cell reactivity, neither in oligodendroglial cell density nor in microglia/monocyte accumulation. On the contrary, exclusive interference with TLR1/2 signaling in response to skull injury efficiently decreased microglia/monocyte accumulation at 4 dpi; however, the oligodendroglial cell density was not changed. Interestingly, in mammals, activated microglia can convert homeostatic astrocytes into a reactive state by secreting IL-1α, TNF, and C1q. Moreover, reactive astrocytes subsequently secreted saturated lipids, which induced neuronal and oligodendroglial cell death (Guttenplan et al., 2021; Liddelow et al., 2017). Consequently, (reactive) microglia have been viewed to initiate widespread glial reactions, negatively impacting neuronal survival and recovery. Even though reactive microglia can alter astrocyte reactivity profiles in mammals, our study in zebrafish revealed that the accumulation of oligodendroglial cells is independent of reactive microglia or brain-invading monocytes. Stab wound injury in microglia/monocyte-depleted animals

resulted in comparable oligodendroglial cell densities at 4 dpi compared to skull-injured wild-type fish. Thus, oligodendroglial cells may have the potential to sense inflammation and respond to injury independently of classical immune cells. In line with our hypothesis, a recent publication by Moyon and colleagues demonstrated that upon chronic demyelination in mice, activated OPCs displayed increased expression of the inflammatory factors IL1-β and CCL2, which dramatically enhanced OPC motility and potentially allowed faster migration to the injury site (Moyon et al., 2015). Consequently, OPCs contain self-regulatory mechanisms by which they can vastly respond and react to a wide array of CNS pathologies.

Altered glial reaction correlates with improved tissue regeneration in brain-injured zebrafish

Skull-injured animals treated with TLR1/2 and CXCR3 pathway inhibitors displayed an altered glial response following injury; thus, we questioned if this effect would influence brain tissue regeneration. We first assessed the injury volume between skull-injured control and TLR1/2 and CXCR3 inhibitor-treated animals at 7 dpi and observed a drastic reduction in the injury size in the double inhibitor-treated animals. Furthermore, and complementary to the decrease in injury volume, TLR1/2 and CXCR3 inhibitor-treated animals displayed an increase in the number of newly generated neurons in the brain parenchyma at 7 dpi. Thus, this finding implies that reduced glial reactivity directly correlates with enhanced tissue regeneration. Corresponding to our study in the adult zebrafish, stab wound injury in the aged African turquoise killifish (*Nothobranchius furzeri*) evoked an exacerbated inflammatory environment alongside glial border formation. Furthermore, aged killifish failed to integrate newborn neurons into the injured brain parenchyma (Van houcke et al., 2021), suggesting that the glia- and immune cell-induced neuroinflammatory microenvironment hampers successful brain repair. In zebrafish, the integration of newly generated neurons in pre-existing circuitries is a highly orchestrated process facilitated by fine temporal regulation of molecular pathways, including the aryl-hydrocarbon receptor (AhR) pathway (Di Giaimo et al., 2018). Injury in the adult zebrafish brain triggers immediate inflammatory events, which are essential to initiate wound

healing responses, enabling adequate tissue restoration (Kyritsis et al., 2012). Concomitantly with neuroinflammation, which commonly takes place within the first few days following nostril injury (Baumgart et al., 2012; Kyritsis et al., 2012; Zambusi et al., 2022), AhR signaling is suppressed. Low AhR levels enhance ependymoglial cell proliferation, whereas high AhR levels increase the number of newly generated neurons, which differentiate from corresponding ependymoglial cells (Barbosa et al., 2015; Di Giaimo et al., 2018). Potentiation of AhR signaling in the first days following injury increased the number of newly generated neurons; however, these cells did not survive long-term (Di Giaimo et al., 2018). Thus, similar to mammals (Arvidsson et al., 2002; Saha et al., 2013), glial- and immune cell-induced neuroinflammation in the regeneration-competent teleost fish impairs tissue restoration. The increase of newborn neurons in the absence of excessive glial response following TLR1/2 and CXCR3 inhibition thus raises the question of whether ependymoglial cells themselves can sense alterations in glial reactivity and consequently adjust their AhR levels to enhance neuronal differentiation, thereby increasing the number of newly generated neurons in the brain parenchyma.

Stab wound injury elicits an anatomically restricted and defined transcriptomic profile in the murine cerebral cortex

TLR1/2 and CXCR3 signaling inhibition following SWI in adult zebrafish alters glial reactivity and improves regeneration. Given that both receptors are expressed by mammalian glial cells (Biber et al., 2002; Bowman et al., 2003; Goldberg et al., 2001; Lehnardt et al., 2006; Olson & Miller, 2004; Omari et al., 2005; Tang et al., 2007), it is therefore tempting to speculate that the pathways mentioned above might also mediate glial reactivity in CNS-injured mammals. It is essential to note that zebrafish findings are not always translatable to mammals. For example, previous studies in adult zebrafish have uncovered crucial roles of the zinc finger transcription factor GATA3 and IL4/STAT6 signaling in initiating and regulating neurogenesis (Bhattarai et al., 2016; Kyritsis et al., 2012). However, neither the lentivirus-mediated overexpression of GATA3 in primary human astrocytes (Celikkaya et al., 2019) nor the induced expression of IL4R in astroglia *in vivo* (Mashkaryan et al., 2020) enhanced mammalian neurogenesis. The divergent cellular

CNS composition might explain the lack of translatability between zebrafish and mammals. In mammals, CNS damage triggers immediate astrocyte responses, which, whenever dysregulated, can exacerbate pathology associated with continuous loss of function (Sofroniew, 2020). However, whether zebrafish possess *bona fide* astrocytes is highly debatable. Time-lapse imaging of the zebrafish spinal cord 2 - 9 days post-fertilization uncovered the potential of ependymoglial cells to differentiate into bushy, astrocyte-like appearing cells (J. Chen et al., 2020). Moreover, cells with complex morphology reminiscent of mammalian astrocytes have been detected in the OB of adult zebrafish (Scheib & Byrd-Jacobs, 2020). It is, however, not disclosed yet if these astrocyte-like cells are distributed throughout the entire CNS of the adult zebrafish (Muñoz-Ballester & Robel, 2023) and if they would fully recapitulate the function of mammalian astrocytes, especially in response to CNS insults.

Thus, to obtain a holistic understanding of the cellular processes that are induced in response to stab wound injury in the murine cerebral cortex (Buffo et al., 2005; Frik et al., 2018; Sirko et al., 2013), we transcriptomically profiled the injury milieu using spatial- and single cell transcriptomics. To capture the transcriptome of peripheral-derived- and tissue-resident glial cells, we conducted spatial transcriptomics (stRNA-seq) at 3 dpi. At this time point, the number of infiltrating $CD45^+$ leukocytes peaked, and glial cell responses were also prominently detectable (Buffo et al., 2005; Frik et al., 2018; von Streitberg et al., 2021). By comparing stab wound-injured tissue sections with corresponding non-injured control sections, we identified a unique cluster, which was present only in the injured brain section. Furthermore, the anatomical location of the injury-induced cluster VI directly correlated with the impact site (Mattugini et al., 2018). Cluster VI was restricted to the injury site and the immediately adjacent areas, as more distant regions did not display any changes in cluster distribution compared to control sections. The confined distribution of cluster VI around the impact site correlates with previous reports demonstrating restricted, localized glial responses upon cortical stab wound injury. Live imaging of astrocytes and NG2-glia following stab wound injury *in vivo*, revealed heterogeneous reactions of these cells, which strongly correlated with their distance to the impact site. Glial cells near the injury displayed cellular hypertrophy and process extension toward the injury site. However, glial reactivity markedly decreased with increased distance from the injury site

(Bardehle et al., 2013; von Streitberg et al., 2021). Consistent with the confined and distance-dependent reaction of glial cells in response to SWI in the murine cerebral cortex, GO term analysis of cluster VI-enriched genes revealed an overrepresentation of biological processes related to immune system activation, cytokine production, and angiogenesis. Importantly, brain damage commonly triggers immune cell activation (Bao et al., 2021,) and in addition, neovascularization has been reported to occur as early as 48 hours following diffuse TBI in rats (Morgan et al., 2007). Thus, spatial transcriptomics conducted in stab-wounded and non-injured animals reliably mirrored already reported cellular events with the advantage of correlating these responses to the exact spatial location. However, up to now, spatial transcriptomics does not represent the transcriptome of individual cells; instead, the transcriptome originates from multiple cells per spot within the capture area (Williams et al., 2022). Considering that brain damage increases the infiltration of peripheral-located cells (Frik et al., 2018) and initiates the migration of brain-resident glial cells to the injury site (Davalos et al., 2005; von Streitberg et al., 2021,) it is therefore likely, that the transcriptome of the injury-induced cluster VI is derived from multiple different cell types.

Cortical stab wound injury induces shared inflammatory signature in reactive glia

To disentangle the contribution of each cell type to the inflammatory environment following SWI, we performed single-cell RNA sequencing (scRNA-seq) of intact and stab wound-injured animals at 3 and 5 dpi. Intriguingly, by comparing the cluster distribution between the intact and the stab wound-injured conditions, we identified cell clusters of immune- and glial cells, which contained exclusively cells from both injured conditions (3 and 5 dpi) but not from intact animals. This finding implied that upon brain injury, new cell types, which are usually not present under physiological conditions, invade the parenchyma and/or that local brain cells acquire distinct (reactive) states, which are characterized by defined transcriptomes. Indeed, during the early days following brain damage, immune cells, such as neutrophils and monocytes, which under physiological conditions are mostly restricted to the periphery, extensively populate the injury area (X. Jin et al., 2012). Moreover, sub-clustering of astrocytes, microglia, and oligodendrocyte lineage cells originating from intact and stab wound-injured animals enabled us to uncover

the transcriptional profiles of homeostatic (non-reactive) and injury-responsive (reactive) glia. The classification of reactive and homeostatic clusters was based on two criteria: 1.) cells residing in the reactive clusters should ideally derive from injured animals, and 2.) cells of the reactive clusters should express previously identified glial reactivity markers. Notably, all reactive glial clusters were primarily composed of cells derived from brain-injured animals. In addition, cells within the reactive astrocyte clusters expressed well-described reactivity markers such as *Gfap*, *Vim*, and *Lcn2* (Burda et al., 2016; Zamanian et al., 2012) and similarly, cells located in reactive microglia subclusters expressed high levels of *Aif1* and low levels of the homeostatic genes *Tmem119* and *P2ry12* (Jurga et al., 2020; Kettenmann et al., 2011; Morillas et al., 2021; Van Wageningen et al., 2019; Villapol et al., 2017). While most of the cells residing in subcluster 'OPCs2' were derived from brain-injured animals, we could not detect genes uniquely expressed within this subcluster that could have been used to characterize injury-responsive, reactive OPCs. However, in line with previous reports, our scRNA-seq analysis defined injury-responsive OPCs as highly proliferative cells (Buffo et al., 2005; Dimou & Götz, 2014; Simon et al., 2011; von Streitberg et al., 2021). Moreover, injury-responsive OPCs residing in cluster 'OPCs2' displayed higher expression levels of genes related to proliferation (*Rgcc*) (Zhao et al., 2023) and motility/migration (*Marcks*, *Tmsb10*) (Z. Chen et al., 2021; Xiao et al., 2019) than the cells in subcluster 'OPCs1', which comprised primarily cells from intact, non-injured animals. Intriguingly, the increased expression of motility/migration and proliferation-associated genes in subcluster 'OPCs2' compared to 'OPCs1' mirrors the biology of OPCs in the pathological brain. Under physiological conditions, OPCs are highly dynamic and proliferative; however, in response to brain damage, OPCs increase their proliferation rate by almost 100-fold, retract their processes, and quickly migrate and accumulate at the injury site (Dimou & Götz, 2014; Hughes et al., 2013; Levine, 2016; von Streitberg et al., 2021). Thus, using scRNA-seq, we accurately disclosed the transcriptome of homeostatic and stab wound injury-responsive glia.

Strikingly, by combining spatial with single-cell transcriptomics, we demonstrated that most reactive glial clusters of astrocytes, microglia, and OPCs were prominently enriched at the impact site and, therefore, locally associated with cluster VI. Moreover, the reactive glial cluster of astrocytes ('AG5'), microglia ('MG4'), and OPCs ('OPCs2') commonly

expressed genes, which were related to proliferation and innate immunity. Indeed, the injury-induced proliferative capacity of astrocytes, microglia, and OPCs upon SWI has been described by several studies before (Bardehle et al., 2013; Lange Canhos et al., 2021; C. Simon et al., 2011; von Streitberg et al., 2021) and consequently it is likely that reactive glia might share additional cellular mechanisms in response to cortical brain injury. We identified several genes of type I interferon signaling commonly shared between all reactive glial cells in response to SWI. Interestingly, Todd and colleagues reported overlapping expression of genes related to type I interferon signaling and MHC class I antigen presentation in microglia and astrocytes 7 days following fluid percussion injury (Todd et al., 2021). Since oligodendrocyte lineage cells were not included in this study, it is unknown whether these cells might co-express the same set of genes as microglia and astrocytes in this particular TBI model. In further studies, it would be interesting to assess whether type I interferon signaling is a common hallmark of reactive glia or if only selective injury types commonly initiate the signaling cascade.

TLR1/2 and CXCR3 pathway inhibition following stab wound injury in the murine cerebral cortex alters microglia and astrocyte reactivity

Among the commonly shared genes related to innate immunity, we identified *Cxcl10*, a ligand for the CXCR3 receptor (Koper et al., 2018), and *Irf7*, which has been implicated with TLR2 signaling (Oosenbrug et al., 2020; S. Xu et al., 2021). Thus, TLR2 and CXCR3 signaling appear to mediate glial reactivity in response to brain injury in both teleost fish and mammals. To assess the impact of TLR2 and CXCR3 signaling in regulating glial cell responses following mammalian cortical SWI, we pharmacologically inhibited TLR1/2 and CXCR3 signaling and performed scRNA-seq at 3 and 5 dpi. Interestingly, we did not observe any glial subcluster composed of cells derived exclusively from inhibitor-treated animals. Consequently, inhibition of TLR1/2 and CXCR3 does not induce new transcriptomic states; instead, pharmacological interference with both pathways following SWI partially downregulated inflammatory genes commonly shared among reactive astrocytes, microglia, and OPCs.

In zebrafish, TLR1/2 and CXCR3 inhibition following brain injury primarily affected OPCs; however, based on our scRNA-seq analysis and the immunohistochemical assessment, we did not observe striking differences in the OPC reaction between brain-injured inhibitor-treated animals and corresponding control mice. Intriguingly, pharmacological interference with TLR1/2 and CXCR3 signaling in primary murine OPC cultures revealed reduced proliferation capacity of inhibitor-treated OPCs (Sanchez-Gonzalez et al., 2022). Furthermore, CRISPR-mediated knockout of TLR2 and CXCR3 in the murine OPC cell line OliNeu (Jung et al., 1995) lowered the chemokine-induced proliferation of OPCs *in vitro* (Sanchez-Gonzalez et al., 2022). While TLR2 and CXCR3 signaling mediate murine OPC proliferation *in vitro*, it is unclear why the pharmacological inhibition of both pathways *in vivo* did not alter OPC proliferation.

In contrast to OPCs, TLR1/2 and CXCR3 pathway inhibition altered microglial activation in response to cortical stab wound injury. Microglia are highly dynamic cells that constantly surveil their environment and rapidly respond to CNS tissue damage (Davalos et al., 2005, 2012). Our scRNA-seq analysis captured the extensive reaction of microglia in response to SWI: By 3 dpi, most cells resided in the reactive microglia subclusters; however, by 5 dpi, microglia transitioned back to a non-reactive state and were consequently localized within the homeostatic subclusters. Notably, microglia of inhibitor-treated animals acquired a non-reactive, homeostatic transcriptome much faster than stab-wounded controls, as by 3 and 5 dpi, more cells resided within the homeostatic clusters. The accelerated transcriptomic shift induced by TLR1/2 and CXCR3 inhibition was additionally accompanied by changes in microglia morphology. Microglia of inhibitor-treated animals appeared less compact and displayed smaller cell somata and greater branch length than stab wound-injured controls, thus resembling less activated and potentially more homeostatic microglia. Since changes in microglia morphology are not necessarily linked to altered function (Vidal-Itriago et al., 2022), it would be interesting to assess in further studies if inhibitor-treated microglia display increased protein abundances of homeostatic microglia markers such as P2Y12 (Jurga et al., 2020). Of note, CNS damage triggers blood-derived monocytes to infiltrate the CNS, where they typically display a uniform round shape without apparent process extension (Han et al., 2020). During differentiation into tissue macrophages, monocytes transition from round-shaped to

process-bearing, ramified cells with concomitant alteration in marker expression, including IBA1 (Ajami et al., 2011; Garcia-Bonilla et al., 2016; Jeong et al., 2013; Tanaka et al., 2003). Considering that the automated morphological analysis (Heindl et al., 2018) was based on the morphology of IBA1$^+$ cells, it cannot be excluded that, in addition to brain-resident microglia, peripherally derived myeloid cells might have been included in the analysis.

In addition to microglia and in line with the general down-regulation of the shared-inflammatory signature in reactive glia, systemic inhibition of TLR1/2 and CXCR3 signaling following SWI altered astrocyte reactivity. Consistent with prior studies (Frik et al., 2018; Lange Canhos et al., 2021), our scRNA-seq analysis mirrored the temporal dynamics of astrocytes in response to SWI. Astrocytes gradually transitioned from a homeostatic to a reactive state over 5 days, as by this point, most cells were dispersedly distributed among all reactive astrocyte subclusters. Contrary, at 5 dpi, astrocytes of inhibitor-treated animals were mainly confined to one reactive astrocyte subcluster ('AG5'), which generally displayed lower expression levels of reactive astrocyte genes, including *Gfap* and *Lcn2*. Even though astrocytes of inhibitor-treated animals exhibited reduced expression of *Gfap* and *Lcn2*, the number of cells expressing the aforementioned reactive genes did not differ. In agreement with our scRNA-seq analysis, the total number of reactive astrocytes (GFAP$^+$/NGAL$^+$) in the injury area was comparable between stab-wounded control and inhibitor-treated animals. In addition to the altered reactive gene expression profile, astrocytes of inhibitor-treated animals displayed reduced proliferation capacity compared to stab wound-injured controls at 3 dpi. Generally, proliferation can be seen as a hallmark of reactive astrocytes following focal TBI or stroke (Muñoz-Ballester & Robel, 2023). However, at this point, it is unclear if and how the effect of TLR1/2 and CXCR3 inhibition on astrocytes (and microglia) would elicit behavioral changes. For example, reduced expression of *Lcn2*/NGAL following ischemic stroke has been demonstrated to alleviate neuronal cell loss and limited stroke-induced neurodegeneration (M. Jin et al., 2014; R. Liu et al., 2022). On the contrary, ablation (Myer et al., 2006) or reduced astrocyte proliferation (Frik et al., 2018; Lange Canhos et al., 2021) in response to cortical damage resulted in exacerbated astrocyte reactivity, increased neuronal- and tissue loss, and behavior deficits in experimental mice. Thus, it would be interesting to address whether the initial effect of TLR1/2 and CXCR3 inhibition on glial reactivity during the acute injury phase influences

neuronal survival, glial reactivity, and behavior at later stages. Moreover, since TLR1/2 and CXCR3 inhibitors were administered systemically, it is unsolved whether the inhibition affects astrocytes and microglia directly or indirectly through changes in the periphery and/or other brain-resident cells.

In summary, we revealed a crucial function of the innate immune system-associated pathways TLR1/2 and CXCR3 in regulating diverse aspects of glial reactivity in brain-injured zebrafish and mice. In zebrafish, inhibition of TLR1/2 and CXCR3 alleviated glial reactivity, increased restorative neurogenesis, and improved tissue regeneration. On the contrary, systemic manipulation of TLR1/2 and CXCR3 signaling in response to cortical brain injury in mice decreased astrocyte reactivity and proliferation. Moreover, interference with TLR1/2 and CXCR3 signaling post-injury resulted in pronounced morphological alterations in microglia. However, the long-term effect of TLR1/2 and CXCR3 inhibition on glial reactivity and regeneration remains to be investigated.

The injury-induced environment is critical for cell fate conversion

A comprehensive understanding of glial reactivity during the post-injury phase is of utmost importance for identifying appropriate targets to reduce the detrimental effects of reactive glia and subsequently enhance endogenous tissue repair. Although long-term glial reactivity is often solely seen to restrict neuronal regeneration, the applicability of glial cells for innovative neuronal replacement strategies is commonly overlooked. Overexpression of neurogenic TFs in a multitude of cells, including (reactive) glia, has been shown to effectively convert these cells into post-mitotic neurons *in vitro* (Berninger et al., 2007; Karow et al., 2012; Masserdotti et al., 2015) and *in vivo* (Buffo et al., 2005; Gascón et al., 2016; Grande et al., 2013; Mattugini et al., 2019). Although neuronal reprogramming comprises a novel strategy to replace lost neurons, the translatability to human patients is still in its infancy. Functional repair of neuronal networks can only be successful if the replacing neurons exhibit the same physiological properties as the lost ones. However, achieving identical neuronal subtypes through direct neuronal reprogramming *in vivo* is far from trivial (Bocchi et al., 2022). Considering that a single neurogenic TF can reprogram an identical cell type into distinct neuronal subtypes if subjected to different CNS regions (Niu

et al., 2015; L. L. Wang et al., 2016) affirms cell-intrinsic properties of the starter cell population as crucial factors in determining neuronal subtype specificity. However, the starting populations' cell identity might not be the only factor influencing glial-to-neuron conversion; the surrounding environment strongly impacts this process, too. Large numbers of converted neurons were prominently obtained in the pathological brain, for example, following SWI, stroke, or in an AD mouse model (Grande et al., 2013; Guo et al., 2014; Heinrich et al., 2014; Mattugini et al., 2019). These findings emphasize that the pathology-induced environment is advantageous for adequate neuronal reprogramming. However, very little is known about how these environmental signals would influence the outcome of direct neuronal reprogramming. Hence, a thorough characterization of glial cell-intrinsic properties combined with a deeper mechanistic understanding of how environmental factors influence the direct conversion processes is inevitable to enable direct neuronal reprogramming as an applicable neuronal replacement strategy.

Reactive gliosis is a widespread reaction of macro- and microglial cells in response to a wide range of CNS pathologies (Sirko et al., 2013, 2015). However, glial cell reactivity is not uniform but highly heterogeneous and injury-dependent (Muñoz-Ballester & Robel, 2023). For example, in response to traumatic injuries, a subset of reactive glial cells demonstrate plastic behavior: some reactive astrocytes acquire stem cell potential and form self-renewing, multipotent neurospheres *in vitro* (Buffo et al., 2008; Sirko et al., 2013), whereas a small proportion of NG2-glia differentiates into astrocytes in adult mice (Dimou et al., 2008; Huang et al., 2018). In line with the capacity of OPCs to generate astrocytes following CNS injury, single-cell transcriptomics of intact and stab wound-injured animals (3 + 5 dpi) highlighted a subpopulation of injury-responsive OPCs, which co-expressed typical astrocytic genes including *Slc1a3*, *Aldoc*, and *Atp1b2* (Bai et al., 2023; Ohlig et al., 2021). Interestingly, astroglial gene expression was not restricted to OPCs; also, mature oligodendrocytes upregulated astrocytic genes following SWI. Thus, this finding suggested that mature oligodendrocytes might de-differentiate into astrocytes in response to acute brain injuries. By using a plethora of transgenic mice in combination with *in vivo* live imaging following SWI, we unraveled the plastic nature of mature, differentiated oligodendrocytes to transition into astrocytes via an intermediate state characterized by co-expression of astro- and oligodendroglial genes. Interestingly, oligodendrocyte-derived

astrocytes displayed proliferative capacity, were interconnected with adjacent astrocytes via gap junctions, and contacted blood vessels with their end feet. Consequently, oligodendrocyte-derived astrocytes exhibited several hallmarks of *bona fide* (reactive) astrocytes (Frik et al., 2018; Kubotera et al., 2019; Lange Canhos et al., 2021; Xing et al., 2019). Due to the concomitant expression of astro- and oligodendroglial genes during the oligodendrocyte-to-astrocyte fate conversion, these intermediate-state cells were termed AO cells. Interestingly, AO cells were prominently detectable in the injury surrounding as early as 2 dpi, and *in vivo* live imaging demonstrated the transition of a small number of AO cells into astrocytes. Intriguingly, some AO cells never acquired an astrocytic fate but instead regained their starter cell identity and stayed within the oligodendroglial lineage. Hence, AO cells are highly plastic cells that can acquire different cell fates upon brain injury. It is thus tempting to speculate that AO cells might contribute to the starter cell pool, which is targeted during *in vivo* neuronal reprogramming. Proliferating glia ($GFAP^+$/$S100\beta^+$ astrocytes and $NG2^+$ glia) were successfully reprogrammed into neurons if retrovirally transduced with Neurog2 and Bcl2 3 days following SWI (Gascón et al., 2016). Moreover, AAV-mediated overexpression of Neurog2 and Nurr1 in cortical astrocytes converted a high number of $GFAP^+$ astrocytes into neurons with appropriate cortical layer identity, whereby ~ 20 % of these reprogrammed neurons derived from proliferating astrocytes (Mattugini et al., 2019). Considering that a large proportion (~ 80 %) of oligodendroglia-derived astrocytes were proliferating, it is likely that AO cells might have been represented in the starter cell pool and potentially also been subjected to diverse reprogramming factors. However, if at all, AO cells can not represent the entire starter cell population. Firstly, oligodendrocyte-derived astrocytes comprised a relatively small population (based on the split-Cre experiment, only 5 % of all $GFAP^+$ cells are derived from AO cells), and secondly, AO cells appeared exclusively in response to acute cortical injuries, whereby astrocyte-to-neuron conversion was already observed in non-injured animals (Mattugini et al., 2019).

Even though glia-to-neuron conversion was apparent in the cortex of intact mice (Mattugini et al., 2019), overall higher conversion rates were achieved in the pathological brain (Heinrich et al., 2014; Mattugini et al., 2019). Consequently, the injury-evoked environment ultimately comprises a fate conversion-favorable milieu. Of note, cortical brain damage induced by ischemia, or SWI, was insufficient to spontaneously convert

proliferating glial cells into neurons (Gascón et al., 2016; Grande et al., 2013), suggesting that the starter cells uphold specific lineage barriers to maintain cell identity. However, the forced expression of selective neurogenic TFs in (reactive) glia *in vivo* is effective, albeit to varying degrees, in overcoming the lineage boundaries, thereby enabling the acquisition of new cell fates (Bocchi et al., 2022; Buffo et al., 2008; Grande et al., 2013). Focal injections of the TF Neurog2 following cortical SWI converted proliferating glia into immature DCX^+ cells. However, enhanced conversion rates were obtained whenever Neurog2 was co-transduced with high titers of the growth factors EGF and bFGF (Grande et al., 2013). Thus, environmental factors positively influence the neuronal fate conversion process; however, how EGF and bFGF would impact the cell fate switch has not been fully understood. Therefore, we established a new *in vitro* culture system in which murine postnatal astrocytes were subjected to different growth factor combinations and were retrovirally transduced with several neurogenic TFs, including Neurog2. Forced expression of Neurog2 in bFGF-grown astrocytes yielded lower neuronal conversion rates than cells grown in EGF- or EGF + bFGF-enriched media. Mass-spectrometry revealed that the chromatin-binding protein HMGB2 (Bronstein et al., 2017) was significantly more abundant in the reprogramming-prone (EGF + bFGF) compared to the reprogramming-insusceptible (bFGF) culture. Intriguingly, overexpression of Hmgb2 alone was insufficient to induce the neuronal fate. Contrary, the co-transduction of Hmgb2 and Neurog2 in the reprogramming-insusceptible culture significantly boosted cell conversion rates and reached cell switch rates comparable to those of the reprogramming-prone culture. Upon SWI, a subset of cortical astrocytes strongly upregulates HMGB2; however, since spontaneous injury-evoked cortical cell fate conversions have not been observed (Gascón et al., 2016; Grande et al., 2013), it further implies that HMGB2 alone cannot induce the neuronal fate. Instead, the combined expression of Hmgb2 and Neurog2 in the reprogramming-insusceptible astrocytic cell culture increased the chromatin accessibility of neuronal maturation genes, thus boosting astrocyte conversion rates. Moreover, forced expression of Hmgb2 and Neurog2 in the reprogramming-insusceptible culture condition significantly enhanced the morphological complexity of the converted neurons.

EGF and bFGF levels are temporally regulated upon brain injury: EGF levels peak 24 hrs following injury and remain elevated for three days before returning to baseline. On

the contrary, bFGF levels increase significantly within 4 hrs post-injury and stay elevated until 14 dpi (Addington et al., 2015). Prolonged exposure of astrocytes to bFGF *in vitro* resulted in decreased Neurog2-induced neuronal conversion rates. However, neuronal reprogramming efficiency was significantly enhanced if Neurog2 and Hmgb2 were co-expressed in astrocytes *in vitro*. Thus, it would be interesting if the co-expression of Neurog2 and Hmgb2 or an elevation of EGF levels in response to SWI would yield higher neuronal conversion rates and long-term survival of the converted cells *in vivo*.

Taken together, we uncovered the before-unknown plastic nature of murine, mature oligodendrocytes to de-differentiate into astrocytes via a transitional astroglial/oligodendroglial cell state in response to cortical damage. Even though the physiological function of the oligodendrocyte-derived astrocytes is still unknown, it is tempting to speculate that these cells might contribute to the starter population pool targeted during *in vivo* neuronal reprogramming. Furthermore, we demonstrated how injury-evoked environmental stimuli influence neuronal fate conversion rates *in vitro* with possible implications for the growth factors EGF and bFGF in mediating the neuronal fate conversion success *in vivo*.

SUMMARY AND OUTLOOK

During my Ph.D. studies, I have contributed to transcriptomically profile glial cell responses following cortical brain injury and investigated the role of TLR1/2 and CXCR3 signaling in reactive glia of brain-injured zebrafish and mice. Using single-cell transcriptomics, we revealed an up-to-now overlooked shared inflammatory signature of reactive glia, which implicated the TLR1/2 and CXCR3 signaling pathways in regulating mammalian glial responses upon brain injury. Systemic manipulation of TLR1/2 and CXCR3 signaling in response to cortical brain injury resulted in decreased astrocyte proliferation and altered microglia morphology within the early post-injury phase (Koupourtidou, Schwarz et al., unpublished data). However, at this point, it is unclear if the altered glial response detected during the initial wound-healing phase would impact long-term gliosis and neuronal survival. Given that pharmacological interference with TLR1/2 and CXCR3 signaling following skull injury in the zebrafish brain alleviated glial reactivity and simultaneously increased neuronal recruitment, and thus improved overall tissue restoration (Sanchez-Gonzalez et al., 2022), it is worthwhile to speculate that changes in the early glial response may also impact excessive long-lasting gliosis in mammals.

Interference with TLR1/2 and CXCR3 signaling in zebrafish and mice altered glial responses upon brain injury, albeit to varying degrees: In skull-injured zebrafish, the treatment mainly affected microglia and oligodendrocyte lineage cells, whereas in brain-injured mice, we observed alterations in microglia and astrocytes; however, apparent changes in the oligodendrocyte lineage were not evident *in vivo*. Since the cellular CNS composition of zebrafish and mice is considerably different, with reactive astrocytes present in all mammalian CNS pathologies (Sofroniew, 2020) but not (yet) described in the adult zebrafish telencephalon, a direct comparison of CNS regenerating and non-regenerating animals of the same biological class is desirable. Hence, it would be interesting to acquire the transcriptome of the brain-injured regeneration-competent spiny mouse (*Acomys cahirinus*) and compare it to the corresponding transcriptome of the widely used regeneration-limited house mouse (*Mus Musculus)*. This cross-comparison may uncover critical pathways crucial for successful brain regeneration in rodents, with the potential for translation to humans.

Using single-cell transcriptomics to comprehensively characterize glial cell responses following SWI in the murine cerebral cortex revealed a subpopulation of mature oligodendrocytes co-expressing typical astrocytic marker genes. Chronic *in vivo* live imaging following SWI also visualized the conversion of mature oligodendrocytes into astrocytes via a transitional astroglial/oligodendroglial cell state (Bai et al., 2023). Oligodendrocyte-derived astrocytes constitute a relatively small population, and it remains unclear to what degree this unique population contributes to the injury-evoked, aversive microenvironment. However, considering that increased glia-to-neuron conversion rates were achieved in the pathological brain, it is likely that the injury-induced astrocytic population might contribute to the starter cell pool targeted during *in vivo* neuronal reprogramming. Hence, it would be interesting to induce direct neuronal reprogramming in brain-injured PLP- and GFAP-split Cre animals (Hirrlinger et al., 2009) and follow the fate of the oligodendrocyte-derived astrocytes using *in vivo* live imaging. In addition, we highlighted that the glia-to-neuron fate conversion success is not restricted to the intrinsic properties of the starter cell; environmental factors significantly influence this process, too. Using an *in vitro* culture system of postnatal astrocytes with altered growth factor combinations allowed us to identify the chromatin-binding protein HMGB2 as a novel regulator in mediating astrocyte-to-neuron conversion. High neuronal conversion rates were achieved in the presence of the growth factors EGF and bFGF; however, the conversion efficiency was significantly decreased if astrocytes were reprogrammed in the presence of bFGF only (Maddhesiya, Lepko et al., unpublished data). This discovery bears potential significance for translational studies: Considering that in response to brain injury in rodents, EGF and bFGF levels are temporally regulated (Addington et al., 2015), it will be essential to determine the exact time point(s) for initiating glia-to-neuron conversion *in vivo*. Furthermore, future studies are inevitable to identify further environmental factors that influence the glia-to-neuron fate switch, especially factors present in the pathological brain. A comprehensive understanding of how cell intrinsic and extrinsic environmental factors influence the process of neuronal fate conversion and the survival of the reprogrammed neurons in the pathological brain is vital for establishing direct neuronal reprogramming as a valuable approach for restoring the complex and highly intricate CNS network after neuronal loss.

BIBLIOGRAPHY

Abbott, N. J., Rönnbäck, L., & Hansson, E. (2006). Astrocyte-endothelial interactions at the blood-brain barrier. Nature Reviews Neuroscience, 7(1), 41–53. https://doi.org/10.1038/nrn1824

Abio, A., Bovet, P., Valentin, B., Bärnighausen, T., Shaikh, M. A., Posti, J. P., & Lowery Wilson, M. (2021). Changes in Mortality Related to Traumatic Brain Injuries in the Seychelles from 1989 to 2018. Frontiers in Neurology, 12, 720434. https://doi.org/10.3389/fneur.2021.720434

Acaz-Fonseca, E., Ortiz-Rodriguez, A., Azcoitia, I., Garcia-Segura, L. M., & Arevalo, M. A. (2019). Notch signaling in astrocytes mediates their morphological response to an inflammatory challenge. Cell Death Discovery, 5, 85. https://doi.org/10.1038/s41420-019-0166-6

Adams, K. L., & Gallo, V. (2018). The diversity and disparity of the glial scar. Nature Neuroscience, 21(1), 9–15. https://doi.org/10.1038/s41593-017-0033-9

Addington, C. P., Roussas, A., Dutta, D., & Stabenfeldt, S. E. (2015). Endogenous Repair Signaling after Brain Injury and Complementary Bioengineering Approaches to Enhance Neural Regeneration: Supplementary Issue: Stem Cell Biology. Biomarker Insights, 10(Suppl 1), 43–60. https://doi.org/10.4137/BMI.S20062

Ajami, B., Bennett, J. L., Krieger, C., McNagny, K. M., & Rossi, F. M. V. (2011). Infiltrating monocytes trigger EAE progression, but do not contribute to the resident microglia pool. Nature Neuroscience, 14(9), 1142–1150. https://doi.org/10.1038/nn.2887

Alam, A., Thelin, E. P., Tajsic, T., Khan, D. Z., Khellaf, A., Patani, R., & Helmy, A. (2020). Cellular infiltration in traumatic brain injury. Journal of Neuroinflammation, 17(1), 328. https://doi.org/10.1186/s12974-020-02005-x

Amorini, A. M., Lazzarino, G., Di Pietro, V., Signoretti, S., Lazzarino, G., Belli, A., & Tavazzi, B. (2017). Severity of experimental traumatic brain injury modulates changes in concentrations of cerebral free amino acids. Journal of Cellular and Molecular Medicine, 21(3), 530–542. https://doi.org/10.1111/jcmm.12998

Ampofo, E., Schmitt, B. M., Menger, M. D., & Laschke, M. W. (2017). The regulatory mechanisms of NG2/CSPG4 expression. Cellular & Molecular Biology Letters, 22, 4. https://doi.org/10.1186/s11658-017-0035-3

Anderson, M. A., Burda, J. E., Ren, Y., Ao, Y., O'Shea, T. M., Kawaguchi, R., Coppola, G., Khakh, B. S., Deming, T. J., & Sofroniew, M. V. (2016). Astrocyte scar formation aids central nervous system axon regeneration. Nature, 532, 195–200. https://doi.org/10.1038/nature17623

Andreone, B. J., Larhammar, M., & Lewcock, J. W. (2020). Cell Death and Neurodegeneration. Cold Spring Harbor Perspectives in Biology, 12, a036434. https://doi.org/10.1101/cshperspect.a036434

Andriessen, T. M. J. C., Jacobs, B., & Vos, P. E. (2010). Clinical characteristics and pathophysiological mechanisms of focal and diffuse traumatic brain injury. Journal of Cellular and Molecular Medicine, 14(10), 2381–2392. https://doi.org/10.1111/j.1582-4934.2010.01164.x

Argaw, A. T., Asp, L., Zhang, J., Navrazhina, K., Pham, T., Mariani, J. N., Mahase, S., Dutta, D. J., Seto, J., Kramer, E. G., Ferrara, N., Sofroniew, M. V., & John, G. R. (2012). Astrocyte-derived VEGF-A drives blood-brain barrier disruption in CNS inflammatory disease. Journal of Clinical Investigation, 122(7), 2454–2468. https://doi.org/10.1172/JCI60842

Arvidsson, A., Collin, T., Kirik, D., Kokaia, Z., & Lindvall, O. (2002). Neuronal replacement from endogenous precursors in the adult brain after stroke. Nature Medicine, 8(9), 963–970. https://doi.org/https://doi.org/10.1038/nm747

Babcock, A. A., Wirenfeldt, M., Holm, T., Nielsen, H. H., Dissing-Olesen, L., Toft-Hansen, H., Millward, J. M., Landmann, R., Rivest, S., Finsen, B., & Owens, T. (2006). Toll-like receptor 2 signaling in response to brain injury: An innate bridge to neuroinflammation. Journal of Neuroscience, 26(49), 12826–12837. https://doi.org/10.1523/JNEUROSCI.4937-05.2006

Bachelerie, F., Ben-Baruch, A., Burkhardt, A. M., Combadiere, C., Farber, J. M., Graham, G. J., Horuk, R., Sparre-Ulrich, A. H., Locati, M., Luster, A. D., Mantovani, A., Matsushima, K., Murphy, P. M., Nibbs, R., Nomiyama, H., Power, C. A., Proudfoot, A. E. I., Rosenkilde, M. M., Rot, A., … Zlotnik, A. (2014). International union of pharmacology. LXXXIX. Update on the extended family of chemokine receptors and introducing a new nomenclature for atypical chemokine receptors. Pharmacological Reviews, 66(1), 1–79. https://doi.org/10.1124/pr.113.007724

Bai, X., Zhao, N., Koupourtidou, C., Fang, L.-P., Schwarz, V., Caudal, L. C., Zhao, R., Hirrlinger, J., Walz, W., Bian, S., Huang, W., Ninkovic, J., Kirchhoff, F., & Scheller, A. (2023). In the mouse cortex, oligodendrocytes regain a plastic capacity, transforming into astrocytes after acute injury. Developmental Cell, 13(58), 1153–1169. https://doi.org/10.1016/j.devcel.2023.04.016

Bajetto, A., Bonavia, R., Barbero, S., Florio, T., & Schettini, G. (2001). Chemokines and their receptors in the central nervous system. Frontiers in Neuroendocrinology, 22(3), 147–184. https://doi.org/10.1006/frne.2001.0214

Bao, W., Lin, Y., & Chen, Z. (2021). The peripheral immune system and traumatic brain injury: Insight into the role of t-helper cells. International Journal of Medical Sciences, 18(16), 3644–3651. https://doi.org/10.7150/ijms.46834

Barbosa, J. S. S., Sanchez-Gonzalez, R., Di Giaimo, R., Baumgart, E. V. V, Theis, F. J. J., Götz, M., & Ninkovic, J. (2015). Live imaging of adult neural stem cell behavior in the intact and injured zebrafish brain. Science, 348(6236), 789–793. https://doi.org/10.1126/science.aaa2729

Bardehle, S., Krüger, M., Buggenthin, F., Schwausch, J., Ninkovic, J., Clevers, H., Snippert, H. J., Theis, F. J., Meyer-Luehmann, M., Bechmann, I., Dimou, L., & Götz, M. (2013). Live imaging of astrocyte responses to acute injury reveals selective juxtavascular proliferation. Nature Neuroscience, 16(5), 580–586. https://doi.org/10.1038/nn.3371

Barker, R. A., Götz, M., & Parmar, M. (2018). New approaches for brain repair - from rescue to reprogramming. Nature, 557(7705), 329–334. https://doi.org/10.1038/s41586-018-0087-1

Barres, B. A. (2008). The Mystery and Magic of Glia: A Perspective on Their Roles in Health and Disease. Neuron, 60(3), 430–440. https://doi.org/10.1016/j.neuron.2008.10.013

Bartanusz, V., Jezova, D., Alajajian, B., & Digicaylioglu, M. (2011). The blood-spinal cord barrier: Morphology and clinical implications. Annals of Neurology, 70(2), 194–206. https://doi.org/10.1002/ana.22421

Batiuk, M. Y., Martirosyan, A., Wahis, J., de Vin, F., Marneffe, C., Kusserow, C., Koeppen, J., Viana, J. F., Oliveira, J. F., Voet, T., Ponting, C. P., Belgard, T. G., & Holt, M. G. (2020). Identification of region-specific astrocyte subtypes at single cell resolution. Nature Communications, 11, 1220. https://doi.org/10.1038/s41467-019-14198-8

Baumgart, E. V., Barbosa, J. S., Bally-Cuif, L., Götz, M., & Ninkovic, J. (2012). Stab wound injury of the zebrafish telencephalon: A model for comparative analysis of reactive gliosis. Glia, 60(3), 343–357. https://doi.org/10.1002/glia.22269

Bayraktar, O. A., Bartels, T., Holmqvist, S., Kleshchevnikov, V., Martirosyan, A., Polioudakis, D., Ben Haim, L., Young, A. M. H., Batiuk, M. Y., Prakash, K., Brown, A., Roberts, K., Paredes, M. F., Kawaguchi, R., Stockley, J. H., Sabeur, K., Chang, S. M., Huang, E., Hutchinson, P., … Rowitch, D. H. (2020). Astrocyte layers in the mammalian cerebral cortex revealed by a single-cell in situ transcriptomic map. Nature Neuroscience, 23(4), 500–509. https://doi.org/10.1038/s41593-020-0602-1

Bell, R. D., Winkler, E. A., Singh, I., Sagare, A. P., Deane, R., Wu, Z., Holtzman, D. M., Betsholtz, C., Armulik, A., Sallstrom, J., Berk, B. C., & Zlokovic, B. V. (2012). Apolipoprotein E controls cerebrovascular integrity via cyclophilin A. Nature, 485(7399), 512–516. https://doi.org/10.1038/nature11087

Bellot-Saez, A., Kékesi, O., Morley, J. W., & Buskila, Y. (2017). Astrocytic modulation of neuronal excitability through K+ spatial buffering. Neuroscience and Biobehavioral Reviews, 77, 87–97. https://doi.org/10.1016/j.neubiorev.2017.03.002

Benfey, M., & Aguayo, A. J. (1982). Extensive elongation of axons from rat brain into peripheral nerve grafts. Nature, 296(5853), 150–152. https://doi.org/10.1038/296150a0

Berninger, B., Costa, M. R., Koch, U., Schroeder, T., Sutor, B., Grothe, B., & Götz, M. (2007). Functional properties of neurons derived from in vitro reprogrammed postnatal astroglia. Journal of Neuroscience, 27(32), 8654–8664. https://doi.org/doi: 10.1523/JNEUROSCI.1615-07.2007

Beschorner, R., Dietz, K., Schauer, N., Mittelbronn, M., Schluesener, H. J., Trautmann, K., Meyermann, R., & Simon, P. (2007). Expression of EAAT1 reflects a possible neuroprotective function of reactive astrocytes and activated microglia following human traumatic brain injury. Histology and Histopathology, 22(5), 515–526. https://doi.org/10.14670/HH-22.515

Bhattarai, P., Thomas, A. K., Cosacak, M. I., Papadimitriou, C., Mashkaryan, V., Froc, C., Reinhardt, S., Kurth, T., Dahl, A., Zhang, Y., & Kizil, C. (2016). IL4/STAT6 Signaling Activates Neural Stem Cell Proliferation and Neurogenesis upon Amyloid-β42 Aggregation in Adult Zebrafish Brain. Cell Reports, 17(4), 941–948. https://doi.org/10.1016/j.celrep.2016.09.075

Biber, K., Zuurman, M. W., Dijkstra, I. M., & Boddeke, H. W. G. M. (2002). Chemokines in the brain: neuroimmunology and beyond. Current Opinion in Pharmacology, 2(1), 63–68. https://doi.org/10.1016/s1471-4892(01)00122-9

Blackshaw, S. (2022). Why Has the Ability to Regenerate Following CNS Injury Been Repeatedly Lost Over the Course of Evolution? Frontiers in Neuroscience, 16, 831062. https://doi.org/10.3389/fnins.2022.831062

Bocchi, R., Masserdotti, G., & Götz, M. (2022). Direct neuronal reprogramming: Fast forward from new concepts toward therapeutic approaches. Neuron, 110(3), 366–393. https://doi.org/10.1016/j.neuron.2021.11.023

Bowman, C. C., Rasley, A., Tranguch, S. L., & Marriott, I. (2003). Cultured astrocytes express toll-like receptors for bacterial products. Glia, 43(3), 281–291. https://doi.org/10.1002/glia.10256

Bradbury, E. J., & Burnside, E. R. (2019). Moving beyond the glial scar for spinal cord repair. Nature Communications, 10(1), 3879. https://doi.org/10.1038/s41467-019-11707-7

Bradbury, E. J., Moon, L. D. F., Popat, R. J., King, V. R., Bennett, G. S., Patel, P. N., Fawcett, J. W., & McMahon, S. B. (2002). Chondroitinase ABC promotes functional recovery after spinal cord injury. Nature, 416(6881), 636–640. https://doi.org/10.1038/416636a

Bradl, M., & Lassmann, H. (2010). Oligodendrocytes: Biology and pathology. Acta Neuropathologica, 119(1), 37–53. https://doi.org/10.1007/s00401-009-0601-5

Braun, M., Vaibhav, K., Saad, N. M., Fatima, S., Vender, J. R., Baban, B., Hoda, M. N., & Dhandapani, K. M. (2017). White matter damage after traumatic brain injury: A role for damage associated molecular patterns. Biochimica et Biophysica Acta - Molecular Basis of Disease, 1863(10), 2614–2626. https://doi.org/10.1016/j.bbadis.2017.05.020

Brazinova, A., Rehorcikova, V., Taylor, M. S., Buckova, V., Majdan, M., Psota, M., Peeters, W., Feigin, V., Theadom, A., Holkovic, L., & Synnot, A. (2021). Epidemiology of Traumatic Brain Injury in Europe: A Living Systematic Review. Journal of Neurotrauma, 38(10), 1411–1440. https://doi.org/10.1089/neu.2015.4126

Bronstein, R., Kyle, J., Abraham, A. B., & Tsirka, S. E. (2017). Neurogenic to gliogenic fate transition perturbed by loss of HMGB2. Frontiers in Molecular Neuroscience, 10, 153. https://doi.org/10.3389/fnmol.2017.00153

Brückner, G., Brauer, K., Härtig, W., Wolff, J. R., Rickmann, M. J., Derouiche, A., Delpech, B., Girard, N., Oertel, W. H., & Reichenbach, A. (1993). Perineuronal nets provide a polyanionic, glia-associated form of microenvironment around certain neurons in many parts of the rat brain. Glia, 8(3), 183–200. https://doi.org/10.1002/glia.440080306

Bruttger, J., Karram, K., Wörtge, S., Regen, T., Marini, F., Hoppmann, N., Klein, M., Blank, T., Yona, S., Wolf, Y., Mack, M., Pinteaux, E., Müller, W., Zipp, F., Binder, H., Bopp, T., Prinz, M., Jung, S., & Waisman, A. (2015). Genetic Cell Ablation Reveals Clusters of Local Self-Renewing Microglia in the Mammalian Central Nervous System. Immunity, 43(1), 92–106. https://doi.org/10.1016/j.immuni.2015.06.012

Buffo, A., Rite, I., Tripathi, P., Lepier, A., Colak, D., Horn, A. P., Mori, T., & Götz, M. (2008). Origin and progeny of reactive gliosis: A source of multipotent cells in the injured brain. Proceedings of the National Academy of Sciences of the United States of America, 105(9), 3581–3586. https://doi.org/10.1073/pnas.0709002105

Buffo, A., Vosko, M. R., Ertürk, D., Hamann, G. F., Jucker, M., Rowitch, D., & Götz, M. (2005). Expression pattern of the transcription factor Olig2 in response to brain injuries: Implications for neuronal repair. Proceedings of the National Academy of Sciences of the United States of America, 102(50), 18183–18188. https://doi.org/10.1073/pnas.0506535102

Burda, J. E., Bernstein, A. M., & Sofroniew, M. V. (2016). Astrocyte roles in traumatic brain injury. Experimental Neurology, 275, 305–315. https://doi.org/10.1016/j.expneurol.2015.03.020

Cartier, L., Hartley, O., Dubois-Dauphin, M., & Krause, K. H. (2005). Chemokine receptors in the central nervous system: Role in brain inflammation and neurodegenerative diseases. Brain Research Reviews, 48(1), 16–42. https://doi.org/10.1016/j.brainresrev.2004.07.021

Celikkaya, H., Cosacak, M. I., Papadimitriou, C., Popova, S., Bhattarai, P., Biswas, S. N., Siddiqui, T., Wistorf, S., Nevado-Alcalde, I., Naumann, L., Mashkaryan, V., Brandt, K., Freudenberg, U., Werner, C., & Kizil, C. (2019). GATA3 promotes the neural progenitor state but not neurogenesis in 3D traumatic injury model of primary human cortical astrocytes. Frontiers in Cellular Neuroscience, 13, 23. https://doi.org/10.3389/fncel.2019.00023

Chanda, S., Ang, C. E., Davila, J., Pak, C., Mall, M., Lee, Q. Y., Ahlenius, H., Jung, S. W., Südhof, T. C., & Wernig, M. (2014). Generation of induced neuronal cells by the single reprogramming factor ASCL1. Stem Cell Reports, 3(2), 282–296. https://doi.org/10.1016/j.stemcr.2014.05.020

Chen, C. Y., Shih, Y. C., Hung, Y. F., & Hsueh, Y. P. (2019). Beyond defense: Regulation of neuronal morphogenesis and brain functions via Toll-like receptors. Journal of Biomedical Science, 26(1), 90. https://doi.org/10.1186/s12929-019-0584-z

Chen, J., Poskanzer, K. E., Freeman, M. R., & Monk, K. R. (2020). Live-imaging of astrocyte morphogenesis and function in zebrafish neural circuits. Nature Neuroscience, 23(10), 1297–1306. https://doi.org/10.1038/s41593-020-0703-x

Chen, Y., Qin, C., Huang, J., Tang, X., Liu, C., Huang, K., Xu, J., Guo, G., Tong, A., & Zhou, L. (2020). The role of astrocytes in oxidative stress of central nervous system: A mixed blessing. Cell Proliferation, 53(3), e12781. https://doi.org/10.1111/cpr.12781

Chen, Z., Zhang, W., Selmi, C., Ridgway, W. M., Leung, P. S. C., Zhang, F., & Gershwin, M. E. (2021). The myristoylated alanine-rich C-kinase substrates (MARCKS): A membrane-

anchored mediator of the cell function. Autoimmunity Reviews, 20(11), 102942. https://doi.org/10.1016/j.autrev.2021.102942

Colonna, M., & Butovsky, O. (2017). Microglia function in the central nervous system during health and neurodegeneration. Annual Review of Immunology, 35, 441–468. https://doi.org/10.1146/annurev-immunol-051116-052358

Corps, K. N., Roth, T. L., & McGavern, D. B. (2015). Inflammation and neuroprotection in TBI. JAMA Neurology, 72(3), 355–362. https://doi.org/10.1001/jamaneurol.2014.3558

Crack, P. J., & Bray, P. J. (2007). Toll-like receptors in the brain and their potential roles in neuropathology. Immunology and Cell Biology, 85(6), 476–480. https://doi.org/10.1038/sj.icb.7100103

Cruz-Haces, M., Tang, J., Acosta, G., Fernandez, J., & Shi, R. (2017). Pathological correlations between traumatic brain injury and chronic neurodegenerative diseases. Translational Neurodegeneration, 6, 20. https://doi.org/10.1186/s40035-017-0088-2

Curtin, J. F., Liu, N., Candolfi, M., Xiong, W., Assi, H., Yagiz, K., Edwards, M. R., Michelsen, K. S., Kroeger, K. M., Liu, C., Muhammad, A. K. M. G., Clark, M. C., Arditi, M., Comin-Anduix, B., Ribas, A., Lowenstein, P. R., & Castro, M. G. (2009). HMGB1 mediates endogenous TLR2 activation and brain tumor regression. PLoS Medicine, 6(1), e10. https://doi.org/10.1371/journal.pmed.1000010

Daglas, M., Truong, P. H., Miles, L. Q., Juan, S. M. A., Rao, S. S., & Adlard, P. A. (2023). Deferiprone attenuates neuropathology and improves outcome following traumatic brain injury. British Journal of Pharmacology, 180(2), 214–234. https://doi.org/10.1111/bph.15950

Davalos, D., Grutzendler, J., Yang, G., Kim, J. V., Zuo, Y., Jung, S., Littman, D. R., Dustin, M. L., & Gan, W. B. (2005). ATP mediates rapid microglial response to local brain injury in vivo. Nature Neuroscience, 8(6), 752–758. https://doi.org/10.1038/nn1472

Davalos, D., Kyu Ryu, J., Merlini, M., Baeten, K. M., Le Moan, N., Petersen, M. A., Deerinck, T. J., Smirnoff, D. S., Bedard, C., Hakozaki, H., Gonias Murray, S., Ling, J. B., Lassmann, H., Degen, J. L., Ellisman, M. H., & Akassoglou, K. (2012). Fibrinogen-induced perivascular microglial clustering is required for the development of axonal damage in neuroinflammation. Nature Communications, 3, 1227. https://doi.org/10.1038/ncomms2230

David, S; Aguayo, A. J. (1981). Axonal Elongation into Peripheral Nervous System “Bridges” after Central Nervous System Injury in Adult Rats. Science, 214(4523), 931–933. https://doi.org/10.1126/science.6171034

David, Y., Cacheaux, L. P., Ivens, S., Lapilover, E., Heinemann, U., Kaufer, D., & Friedman, A. (2009). Astrocytic dysfunction in epileptogenesis: Consequence of altered potassium and glutamate homeostasis? Journal of Neuroscience, 29(34), 10588–10599. https://doi.org/10.1523/JNEUROSCI.2323-09.2009

de Silva, M. J., Roberts, I., Perel, P., Edwards, P., Kenward, M. G., Fernandes, J., Shakur, H., & Patel, V. (2009). Patient outcome after traumatic brain injury in high-, middle- and low-

income countries: Analysis of data on 8927 patients in 46 countries. International Journal of Epidemiology, 38(2), 452–458. https://doi.org/10.1093/ije/dyn189

Dean, T., Ghaemmaghami, J., Corso, J., & Gallo, V. (2023). The cortical NG2-glia response to traumatic brain injury. Glia, 71(5), 1164–1175. https://doi.org/10.1002/glia.24342

Di Giaimo, R., Durovic, T., Barquin, P., Kociaj, A., Lepko, T., Aschenbroich, S., Breunig, C. T., Irmler, M., Cernilogar, F. M., Schotta, G., Barbosa, J. S., Trümbach, D., Baumgart, E. V., Neuner, A. M., Beckers, J., Wurst, W., Stricker, S. H., & Ninkovic, J. (2018). The Aryl Hydrocarbon Receptor Pathway Defines the Time Frame for Restorative Neurogenesis. Cell Reports, 25(12), 3241–3251. https://doi.org/10.1016/j.celrep.2018.11.055

Dias, D. O., Kalkitsas, J., Kelahmetoglu, Y., Estrada, C. P., Tatarishvili, J., Holl, D., Jansson, L., Banitalebi, S., Amiry-Moghaddam, M., Ernst, A., Huttner, H. B., Kokaia, Z., Lindvall, O., Brundin, L., Frisén, J., & Göritz, C. (2021). Pericyte-derived fibrotic scarring is conserved across diverse central nervous system lesions. Nature Communications, 12(1), 5501. https://doi.org/10.1038/s41467-021-25585-5

Dimou, L., & Gallo, V. (2015). NG2-glia and their functions in the central nervous system. Glia, 63(8), 1429–1451. https://doi.org/10.1002/glia.22859

Dimou, L., & Götz, M. (2014). Glial cells as progenitors and stem cells: New roles in the healthy and diseased brain. Physiological Reviews, 94(3), 709–737. https://doi.org/10.1152/physrev.00036.2013

Dimou, L., Simon, C., Kirchhoff, F., Takebayashi, H., & Götz, M. (2008). Progeny of Olig2-expressing progenitors in the gray and white matter of the adult mouse cerebral cortex. Journal of Neuroscience, 28(41), 10434–10442. https://doi.org/10.1523/JNEUROSCI.2831-08.2008

Dong, X. X., Wang, Y., & Qin, Z. H. (2009). Molecular mechanisms of excitotoxicity and their relevance to pathogenesis of neurodegenerative diseases. Acta Pharmacologica Sinica, 30(4), 379–387. https://doi.org/10.1038/aps.2009.24

Dou, C. L., & Levine, J. M. (1994). Inhibition of neurite growth by the NG2 chondroitin sulfate proteoglycan. Journal of Neuroscience, 14(12), 7616–7628. https://doi.org/10.1523/jneurosci.14-12-07616.1994

Dugger, B. N., & Dickson, D. W. (2017). Pathology of Neurodegenerative Diseases. Cold Spring Harbor Perspectives in Biology, 9(7), a028035. https://doi.org/10.1101/cshperspect.a028035

Dumurgier, J., & Tzourio, C. (2020). Epidemiology of neurological diseases in older adults. Revue Neurologique, 176(9), 642–648. https://doi.org/10.1016/j.neurol.2020.01.356

Escartin, C., Galea, E., Lakatos, A., O'Callaghan, J. P., Petzold, G. C., Serrano-Pozo, A., Steinhäuser, C., Volterra, A., Carmignoto, G., Agarwal, A., Allen, N. J., Araque, A., Barbeito, L., Barzilai, A., Bergles, D. E., Bonvento, G., Butt, A. M., Chen, W. T., Cohen-Salmon, M., … Verkhratsky, A. (2021). Reactive astrocyte nomenclature, definitions, and future directions. Nature Neuroscience, 24(3), 312–325. https://doi.org/10.1038/s41593-020-00783-4

Faden, A. I., Wu, J., Stoica, B. A., & Loane, D. J. (2016). Progressive inflammation-mediated neurodegeneration after traumatic brain or spinal cord injury. British Journal of Pharmacology, 173(4), 681–691. https://doi.org/10.1111/bph.13179

Falkner, S., Grade, S., Dimou, L., Conzelmann, K. K., Bonhoeffer, T., Götz, M., & Hubener, M. (2016). Transplanted embryonic neurons integrate into adult neocortical circuits. Nature, 539(7628), 248–253. https://doi.org/10.1038/nature20113

Fan, H., Duan, H., Hao, P., Gao, Y., Zhao, W., Hao, F., Li, X., & Yang, Z. (2022). Cellular regeneration treatments for traumatic brain injury. Medicine in Novel Technology and Devices, 16, 100182. https://doi.org/10.1016/j.medntd.2022.100182

Färber, K., Pannasch, U., & Kettenmann, H. (2005). Dopamine and noradrenaline control distinct functions in rodent microglial cells. Molecular and Cellular Neuroscience, 29(1), 128–138. https://doi.org/10.1016/j.mcn.2005.01.003

Fernandes, K. J. L., Fan, D. P., Tsui, B. J., Cassar, S. L., & Tetzlaff, W. (1999). Influence of the axotomy to cell body distance in rat rubrospinal and spinal motoneurons: Differential regulation of GAP-43, tubulins, and neurofilament-M. Journal of Comparative Neurology, 414(4), 495–510. https://doi.org/10.1002/(sici)1096-9861(19991129)414:4<495::aid-cne6>3.0.co;2-s

Frik, J., Merl-Pham, J., Plesnila, N., Mattugini, N., Kjell, J., Kraska, J., Gomez, R. M., Hauck, S. M., Sirko, S., & Götz, M. (2018). Cross-talk between monocyte invasion and astrocyte proliferation regulates scarring in brain injury. EMBO Reports, 19(5), e45294. https://doi.org/10.15252/embr.201745294

Gadani, S. P., Walsh, J. T., Lukens, J. R., & Kipnis, J. (2015). Dealing with Danger in the CNS: The Response of the Immune System to Injury. Neuron, 87(1), 47–62. https://doi.org/10.1016/j.neuron.2015.05.019

Gaillard, A., Prestoz, L., Dumartin, B., Cantereau, A., Morel, F., Roger, M., & Jaber, M. (2007). Reestablishment of damaged adult motor pathways by grafted embryonic cortical neurons. Nature Neuroscience, 10(10), 1294–1299. https://doi.org/10.1038/nn1970

Ganti, L., Stead, T., Daneshvar, Y., Bodhit, A. N., Pulvino, C., Ayala, S. W., & Peters, K. R. (2019). GCS 15: When mild TBI isn't so mild. Neurological Research and Practice, 1, 6. https://doi.org/10.1186/s42466-018-0001-1

Garcia-Bonilla, L., Faraco, G., Moore, J., Murphy, M., Racchumi, G., Srinivasan, J., Brea, D., Iadecola, C., & Anrather, J. (2016). Spatio-temporal profile, phenotypic diversity, and fate of recruited monocytes into the post-ischemic brain. Journal of Neuroinflammation, 13(1), 285. https://doi.org/10.1186/s12974-016-0750-0

Gascón, S., Murenu, E., Masserdotti, G., Ortega, F., Russo, G. L., Petrik, D., Deshpande, A., Heinrich, C., Karow, M., Robertson, S. P., Schroeder, T., Beckers, J., Irmler, M., Berndt, C., Angeli, J. P. F., Conrad, M., Berninger, B., & Götz, M. (2016). Identification and Successful Negotiation of a Metabolic Checkpoint in Direct Neuronal Reprogramming. Cell Stem Cell, 18(3), 396–409. https://doi.org/10.1016/j.stem.2015.12.003

George, N., & Geller, H. M. (2018). Extracellular matrix and traumatic brain injury. Journal of Neuroscience Research, 96(4), 573–588. https://doi.org/10.1002/jnr.24151

Giaume, C., Kirchhoff, F., Matute, C., Reichenbach, A., & Verkhratsky, A. (2007). Glia: The fulcrum of brain diseases. Cell Death and Differentiation, 14(7), 1324–1335. https://doi.org/10.1038/sj.cdd.4402144

Ginsburg, J., & Huff, J. S. (2023). Closed Head Trauma. StatPearls Publisher. https://www.ncbi.nlm.nih.gov/books/NBK557861/

Goldberg, S. H., Van Der Meer, P., Hesselgesser, J., Jaffer, S., Kolson, D. L., Albright, A. V., González-Scarano, F., & Lavi, E. (2001). CXCR3 expression in human central nervous system diseases. Neuropathology and Applied Neurobiology, 27(2), 127–138. https://doi.org/10.1046/j.1365-2990.2001.00312.x

Gonçalves, J. T., Schafer, S. T., & Gage, F. H. (2016). Adult Neurogenesis in the Hippocampus: From Stem Cells to Behavior. Cell, 167(4), 897–914. https://doi.org/10.1016/j.cell.2016.10.021

Götz, M., & Bocchi, R. (2021). Neuronal replacement: Concepts, achievements, and call for caution. Current Opinion in Neurobiology, 69, 185–192. https://doi.org/10.1016/j.conb.2021.03.014

Grade, S., & Götz, M. (2017). Neuronal replacement therapy: previous achievements and challenges ahead. Npj Regenerative Medicine, 2, 29. https://doi.org/10.1038/s41536-017-0033-0

Grande, A., Sumiyoshi, K., López-Juárez, A., Howard, J., Sakthivel, B., Aronow, B., Campbell, K., & Nakafuku, M. (2013). Environmental impact on direct neuronal reprogramming in vivo in the adult brain. Nature Communications, 4, 2373. https://doi.org/10.1038/ncomms3373

Greve, M. W., & Zink, B. J. (2009). Pathophysiology of traumatic brain injury. Mount Sinai Journal of Medicine: A Journal of Translational and Personalized Medicine, 76(2), 97–104. https://doi.org/10.1002/msj.20104

Gundelfinger, E. D., Frischknecht, R., Choquet, D., & Heine, M. (2010). Converting juvenile into adult plasticity: a role for the brain's extracellular matrix. European Journal of Neuroscience, 31(12), 2156–2165. https://doi.org/10.1111/j.1460-9568.2010.07253.x

Guo, Z., Zhang, L., Wu, Z., Chen, Y., Wang, F., & Chen, G. (2014). In vivo direct reprogramming of reactive glial cells into functional neurons after brain injury and in an Alzheimer's disease model. Cell Stem Cell, 14(2), 188–202. https://doi.org/10.1016/j.stem.2013.12.001

Guttenplan, K. A., Weigel, M. K., Prakash, P., Wijewardhane, P. R., Hasel, P., Rufen-Blanchette, U., Münch, A. E., Blum, J. A., Fine, J., Neal, M. C., Bruce, K. D., Gitler, A. D., Chopra, G., Liddelow, S. A., & Barres, B. A. (2021). Neurotoxic reactive astrocytes induce cell death via saturated lipids. Nature, 599(7883), 102–107. https://doi.org/10.1038/s41586-021-03960-y

Gyoneva, S., & Ransohoff, R. M. (2015). Inflammatory reaction after traumatic brain injury: therapeutic potential of targeting cell-cell communication by chemokines. Trends in Pharmacological Sciences, 36(7), 471–480. https://doi.org/10.1016/j.tips.2015.04.003

Han, D., Liu, H., & Gao, Y. (2020). The role of peripheral monocytes and macrophages in ischemic stroke. Neurological Sciences, 41(12), 3589–3607. https://doi.org/10.1007/s10072-020-04777-9

Hanisch, U.-K., & Kettenmann, H. (2007). Microglia: active sensor and versatile effector cells in the normal and pathologic brain. Nature Neuroscience, 10(11), 1387–1394. http://dx.doi.org/10.1038/nn1997

Harris, N. G., Carmichael, S. T., Hovda, D. A., & Sutton, R. L. (2009). Traumatic brain injury results in disparate regions of chondroitin sulfate proteoglycan expression that are temporally limited. Journal of Neuroscience Research, 87(13), 2937–2950. https://doi.org/10.1002/jnr.22115

Hartl, D., Krauss-Etschmann, S., Koller, B., Hordijk, P. L., Kuijpers, T. W., Hoffmann, F., Hector, A., Eber, E., Marcos, V., Bittmann, I., Eickelberg, O., Griese, M., & Roos, D. (2008). Infiltrated neutrophils acquire novel chemokine receptor expression and chemokine responsiveness in chronic inflammatory lung diseases. Journal of Immunology, 181(11), 8053–8067. https://doi.org/10.4049/jimmunol.181.11.8053

Hasel, P., Rose, I. V. L., Sadick, J. S., Kim, R. D., & Liddelow, S. A. (2021). Neuroinflammatory astrocyte subtypes in the mouse brain. Nature Neuroscience, 24(10), 1475–1487. https://doi.org/10.1038/s41593-021-00905-6

Hayashi, Y., Jinnou, H., Sawamoto, K., & Hitoshi, S. (2018). Adult neurogenesis and its role in brain injury and psychiatric diseases. Journal of Neurochemistry, 147(5), 584–594. https://doi.org/10.1111/jnc.14557

Heindl, S., Gesierich, B., Benakis, C., Llovera, G., Duering, M., & Liesz, A. (2018). Automated morphological analysis of microglia after stroke. Frontiers in Cellular Neuroscience, 12, 106. https://doi.org/10.3389/fncel.2018.00106

Heinrich, C., Bergami, M., Gascón, S., Lepier, A., Viganò, F., Dimou, L., Sutor, B., Berninger, B., & Götz, M. (2014). Sox2-mediated conversion of NG2 glia into induced neurons in the injured adult cerebral cortex. Stem Cell Reports, 3(6), 1000–1014. https://doi.org/10.1016/j.stemcr.2014.10.007

Heins, N., Malatesta, P., Cecconi, F., Nakafuku, M., Tucker, K. L., Hack, M. A., Chapouton, P., Barde, Y. A., & Götz, M. (2002). Glial cells generate neurons: the role of the transcription factor Pax6. Nature Neuroscience, 5(4), 308–315. https://doi.org/10.1038/nn828

Henry, R. J., Ritzel, R. M., Barrett, J. P., Doran, S. J., Jiao, Y., Leach, J. B., Szeto, G. L., Wu, J., Stoica, B. A., Faden, A. I., & Loane, D. J. (2020). Microglial depletion with CSF1R inhibitor during chronic phase of experimental traumatic brain injury reduces neurodegeneration and neurological deficits. Journal of Neuroscience, 40(14), 2960–2974. https://doi.org/10.1523/JNEUROSCI.2402-19.2020

Herculano-Houzel, S. (2009). The human brain in numbers: A linearly scaled-up primate brain. Frontiers in Human Neuroscience, 3, 31. https://doi.org/10.3389/neuro.09.031.2009

Herzog, C., Garcia, L. P., Keatinge, M., Greenald, D., Moritz, C., Peri, F., & Herrgen, L. (2019). Rapid clearance of cellular debris by microglia limits secondary neuronal cell death after brain injury in vivo. Development, 146(9), dev174698. https://doi.org/10.1242/dev.174698

Hirrlinger, J., Scheller, A., Hirrlinger, P. G., Kellert, B., Tang, W., Wehr, M. C., Goebbels, S., Reichenbach, A., Sprengel, R., Rossner, M. J., & Kirchhoff, F. (2009). Split-cre complementation indicates coincident activity of different genes in vivo. PLoS ONE, 4(1), e4286. https://doi.org/10.1371/journal.pone.0004286

Hösli, L., Zuend, M., Bredell, G., Zanker, H. S., Porto de Oliveira, C. E., Saab, A. S., & Weber, B. (2022). Direct vascular contact is a hallmark of cerebral astrocytes. Cell Reports, 39(1), 110599. https://doi.org/10.1016/j.celrep.2022.110599

Hossain-Ibrahim, M. K., Rezajooi, K., MacNally, J. K., Mason, M. R. J., Lieberman, A. R., & Anderson, P. N. (2006). Effects of lipopolysaccharide-induced inflammation on expression of growth-associated genes by corticospinal neurons. BMC Neuroscience, 7, 8. https://doi.org/10.1186/1471-2202-7-8

Hou, Y., Dan, X., Babbar, M., Wei, Y., Hasselbalch, S. G., Croteau, D. L., & Bohr, V. A. (2019). Ageing as a risk factor for neurodegenerative disease. Nature Reviews Neurology, 15(10), 565–581. https://doi.org/10.1038/s41582-019-0244-7

Hsieh, C. L., Niemi, E. C., Wang, S. H., Lee, C. C., Bingham, D., Zhang, J., Cozen, M. L., Charo, I., Huang, E. J., Liu, J., & Nakamura, M. C. (2014). CCR2 deficiency impairs macrophage infiltration and improves cognitive function after traumatic brain injury. Journal of Neurotrauma, 31(20), 1677–1688. https://doi.org/10.1089/neu.2013.3252

Huang, C., Sakry, D., Menzel, L., Dangel, L., Sebastiani, A., Krämer, T., Karram, K., Engelhard, K., Trotter, J., & Schäfer, M. K. E. (2016). Lack of NG2 exacerbates neurological outcome and modulates glial responses after traumatic brain injury. Glia, 64(4), 507–523. https://doi.org/10.1002/glia.22944

Huang, W., Bai, X., Stopper, L., Catalin, B., Cartarozzi, L. P., Scheller, A., & Kirchhoff, F. (2018). During Development NG2 Glial Cells of the Spinal Cord are Restricted to the Oligodendrocyte Lineage, but Generate Astrocytes upon Acute Injury. Neuroscience, 385, 154–165. https://doi.org/10.1016/j.neuroscience.2018.06.015

Hughes, E. G., Kang, S. H., Fukaya, M., & Bergles, D. E. (2013). Oligodendrocyte progenitors balance growth with self-repulsion to achieve homeostasis in the adult brain. Nature Neuroscience, 16(6), 668–676. https://doi.org/10.1038/nn.3390

Iba, T., Hashiguchi, N., Nagaoka, I., Tabe, Y., & Murai, M. (2013). Neutrophil cell death in response to infection and its relation to coagulation. Journal of Intensive Care, 1(1), 13. https://doi.org/10.1186/2052-0492-1-13

Imai, R., Tamura, R., Yo, M., Sato, M., Fukumura, M., Takahara, K., Kase, Y., Okano, H., & Toda, M. (2023). Neuroprotective Effects of Genome-Edited Human iPS Cell-Derived Neural Stem/Progenitor Cells on Traumatic Brain Injury. Stem Cells, 41(6), 603–616. https://doi.org/10.1093/stmcls/sxad028

Izzy, S., Liu, Q., Fang, Z., Lule, S., Wu, L., Chung, J. Y., Sarro-Schwartz, A., Brown-Whalen, A., Perner, C., Hickman, S. E., Kaplan, D. L., Patsopoulos, N. A., El Khoury, J., & Whalen, M. J. (2019). Time-Dependent Changes in Microglia Transcriptional Networks Following Traumatic Brain Injury. Frontiers in Cellular Neuroscience, 13, 307. https://doi.org/10.3389/fncel.2019.00307

Jäkel, S., & Dimou, L. (2017). Glial cells and their function in the adult brain: A journey through the history of their ablation. Frontiers in Cellular Neuroscience, 11, 24. https://doi.org/10.3389/fncel.2017.00024

Jayaraj, R. L., Azimullah, S., Beiram, R., Jalal, F. Y., & Rosenberg, G. A. (2019). Neuroinflammation: Friend and foe for ischemic stroke. Journal of Neuroinflammation, 16(1), 142. https://doi.org/10.1186/s12974-019-1516-2

Jeong, H. K., Ji, K. M., Kim, J., Jou, I., & Joe, E. H. (2013). Repair of astrocytes, blood vessels, and myelin in the injured brain: Possible roles of blood monocytes. Molecular Brain, 6, 28. https://doi.org/10.1186/1756-6606-6-28

Jessberger, S. (2016). Neural repair in the adult brain. F1000Research, 5, 169. https://doi.org/10.12688/f1000research.7459.1

Jin, M., Kim, J. H., Jang, E., Lee, Y. M., Soo Han, H., Woo, D. K., Park, D. H., Kook, H., & Suk, K. (2014). Lipocalin-2 deficiency attenuates neuroinflammation and brain injury after transient middle cerebral artery occlusion in mice. Journal of Cerebral Blood Flow and Metabolism, 34(8), 1306–1314. https://doi.org/10.1038/jcbfm.2014.83

Jin, X., Ishii, H., Bai, Z., Itokazu, T., & Yamashita, T. (2012). Temporal changes in cell marker expression and cellular infiltration in a controlled cortical impact model in adult male C57BL/6 mice. PLoS ONE, 7(7), e41892. https://doi.org/10.1371/journal.pone.0041892

Johnson, N. R., Yuan, P., Castillo, E., Lopez, T. P., Yue, W., Bond, A., Rivera, B. M., Sullivan, M. C., Hirouchi, M., Giles, K., Aoyagi, A., & Condello, C. (2023). CSF1R inhibitors induce a sex-specific resilient microglial phenotype and functional rescue in a tauopathy mouse model. Nature Communications, 14(1), 118. https://doi.org/10.1038/s41467-022-35753-w

Jung, M., Krämer, E., Grzenkowski, M., Tang, K., Blakemore, W., Aguzzi, A., Khazaie, K., Chlichlia, K., von Blankenfeld, G., Kettenmann, H., & Trotter, J. (1995). Lines of murine oligodendroglial precursor cells immortalized by an activated neu tyrosine kinase show distinct degrees of interaction with axons in vitro and in vivo. European Journal of Neuroscience, 7(6), 1245–1265. https://doi.org/10.1111/j.1460-9568.1995.tb01115.x

Jurga, A. M., Paleczna, M., & Kuter, K. Z. (2020). Overview of General and Discriminating Markers of Differential Microglia Phenotypes. Frontiers in Cellular Neuroscience, 14, 198. https://doi.org/10.3389/fncel.2020.00198

Kadry, H., Noorani, B., & Cucullo, L. (2020). A blood–brain barrier overview on structure, function, impairment, and biomarkers of integrity. Fluids and Barriers of the CNS, 17(1), 69. https://doi.org/10.1186/s12987-020-00230-3

Kandel, E. R., Schwartz, J. H., & Jessel, T. M. (1991). Principles of Neural Science (E. R. Kandel, J. H. Schwartz, & T. M. Jessel, Eds.; 3rd ed.). Appleton & Lange.

Karow, M., Sánchez, R., Schichor, C., Masserdotti, G., Ortega, F., Heinrich, C., Gascón, S., Khan, M. A., Lie, D. C., Dellavalle, A., Cossu, G., Goldbrunner, R., Götz, M., & Berninger, B. (2012). Reprogramming of pericyte-derived cells of the adult human brain into induced neuronal cells. Cell Stem Cell, 11(4), 471–476. https://doi.org/10.1016/j.stem.2012.07.007

Karve, I. P., Taylor, J. M., & Crack, P. J. (2016). The contribution of astrocytes and microglia to traumatic brain injury. British Journal of Pharmacology, 173(4), 692–702. https://doi.org/10.1111/bph.13125

Kawai, T., & Akira, S. (2007). Signaling to NF-κB by Toll-like receptors. Trends in Molecular Medicine, 13(11), 460–469. https://doi.org/10.1016/j.molmed.2007.09.002

Kawai, T., & Akira, S. (2010). The role of pattern-recognition receptors in innate immunity: Update on toll-like receptors. Nature Immunology, 11(5), 373–384. https://doi.org/10.1038/ni.1863

Kazim, S. F., Shamim, M. S., Tahir, M. Z., Enam, S. A., & Waheed, S. (2011). Management of penetrating brain injury. Journal of Emergencies, Trauma, and Shock, 4(3), 395–402. https://doi.org/10.4103/0974-2700.83871

Kettenmann, H., Hanisch, U. K., Noda, M., & Verkhratsky, A. (2011). Physiology of microglia. Physiological Reviews, 91(2), 461–553. https://doi.org/10.1152/physrev.00011.2010

Kim, Y., Park, J., & Choi, Y. K. (2019). The role of astrocytes in the central nervous system focused on BK channel and heme oxygenase metabolites: A review. Antioxidants, 8(5), 121. https://doi.org/10.3390/antiox8050121

Kjell, J., & Götz, M. (2020). Filling the Gaps – A Call for Comprehensive Analysis of Extracellular Matrix of the Glial Scar in Region- and Injury-Specific Contexts. Frontiers in Cellular Neuroscience, 14, 32. https://doi.org/10.3389/fncel.2020.00032

Knox, E. G., Aburto, M. R., Clarke, G., Cryan, J. F., & O'Driscoll, C. M. (2022). The blood-brain barrier in aging and neurodegeneration. Molecular Psychiatry, 27(6), 2659–2673. https://doi.org/10.1038/s41380-022-01511-z

Koper, O. M., Kaminska, J., Sawicki, K., & Kemona, H. (2018). CXCL9, CXCL10, CXCL11, and their receptor (CXCR3) in neuroinflammation and neurodegeneration. Advances in Clinical and Experimental Medicine, 27(6), 849–856. https://doi.org/10.17219/acem/68846

Koupourtidou, C., Schwarz, V., Aliee, H., Frerich, S., Fischer-Sternjak, J., Bocchi, R., Simon-Ebert, T., Dichgans, M., Götz, M., Theis, F., & Ninkovic, J. (2023). Shared inflammatory glial cell signature after brain injury, revealed by spatial, temporal and cell-type-specific profiling of the murine cerebral cortex. BioRxiv, 2023.02.24.529840. https://doi.org/10.1101/2023.02.24.529840

Kroehne, V., Freudenreich, D., Hans, S., Kaslin, J., & Brand, M. (2011). Regeneration of the adult zebrafish brain from neurogenic radial glia-type progenitors. Development, 138(22), 4831–4841. https://doi.org/10.1242/dev.072587

Kubotera, H., Ikeshima-Kataoka, H., Hatashita, Y., Allegra Mascaro, A. L., Pavone, F. S., & Inoue, T. (2019). Astrocytic endfeet re-cover blood vessels after removal by laser ablation. Scientific Reports, 9(1), 1263. https://doi.org/10.1038/s41598-018-37419-4

Kumar, A., & Loane, D. J. (2012). Neuroinflammation after traumatic brain injury: Opportunities for therapeutic intervention. Brain, Behavior, and Immunity, 26(8), 1191–1201. https://doi.org/10.1016/j.bbi.2012.06.008

Kyritsis, N., Kizil, C., Zocher, S., Kroehne, V., Kaslin, J., Freudenreich, D., Iltzsche, A., & Brand, M. (2012). Acute inflammation initiates the regenerative response in the adult zebrafish brain. Science, 338(6112), 1353–1356. https://doi.org/10.1126/science.1228773

Lamptey, R. N. L., Chaulagain, B., Trivedi, R., Gothwal, A., Layek, B., & Singh, J. (2022). A Review of the Common Neurodegenerative Disorders: Current Therapeutic Approaches and the Potential Role of Nanotherapeutics. International Journal of Molecular Sciences, 23(3), 1851. https://doi.org/10.3390/ijms23031851

Lange Canhos, L., Chen, M., Falk, S., Popper, B., Straub, T., Götz, M., & Sirko, S. (2021). Repetitive injury and absence of monocytes promote astrocyte self-renewal and neurological recovery. Glia, 69(1), 165–181. https://doi.org/10.1002/glia.23893

Lasagni, L., Francalanci, M., Annunziato, F., Lazzeri, E., Giannini, S., Cosmi, L., Sagrinati, C., Mazzinghi, B., Orlando, C., Maggi, E., Marra, F., Romagnani, S., Serio, M., & Romagnani, P. (2003). An alternatively spliced variant of CXCR3 mediates the inhibition of endothelial cell growth induced by IP-10, Mig, and I-TAC, and acts as functional receptor for platelet factor 4. Journal of Experimental Medicine, 197(11), 1537–1549. https://doi.org/10.1084/jem.20021897

Lee, W. Di, Wang, K. C., Tsai, Y. F., Chou, P. C., Tsai, L. K., & Chien, C. L. (2016). Subarachnoid hemorrhage promotes proliferation, differentiation, and migration of neural stem cells via BDNF upregulation. PLoS ONE, 11(11), e0165460. https://doi.org/10.1371/journal.pone.0165460

Lee, S. W., De Rivero Vaccari, J. P., Truettner, J. S., Dietrich, W. D., & Keane, R. W. (2019). The role of microglial inflammasome activation in pyroptotic cell death following penetrating traumatic brain injury. Journal of Neuroinflammation, 16(1), 27. https://doi.org/10.1186/s12974-019-1423-6

Lehnardt, S., Henneke, P., Lien, E., Kasper, D. L., Volpe, J. J., Bechmann, I., Nitsch, R., Weber, J. R., Golenbock, D. T., & Vartanian, T. (2006). A Mechanism for Neurodegeneration Induced by Group B Streptococci through Activation of the TLR2/MyD88 Pathway in Microglia. Journal of Immunology, 177(1), 583–592. https://doi.org/10.4049/jimmunol.177.1.583

Lehnardt, S., Lehmann, S., Kaul, D., Tschimmel, K., Hoffmann, O., Cho, S., Krueger, C., Nitsch, R., Meisel, A., & Weber, J. R. (2007). Toll-like receptor 2 mediates CNS injury in focal cerebral ischemia. Journal of Neuroimmunology, 190(1), 28–33. https://doi.org/10.1016/j.jneuroim.2007.07.023

Lenz, K. M., & Nelson, L. H. (2018). Microglia and beyond: Innate immune cells as regulators of brain development and behavioral function. Frontiers in Immunology, 9, 698. https://doi.org/10.3389/fimmu.2018.00698

Levine, J. (2016). The reactions and role of NG2 glia in spinal cord injury. Brain Research, 1638, 199–208. https://doi.org/10.1016/j.brainres.2015.07.026

Levine, J. M. (1994). Increased expression of the NG2 chondroitin-sulfate proteoglycan after brain injury. Journal of Neuroscience, 14(8), 4716–4730. https://doi.org/10.1523/jneurosci.14-08-04716.1994

Leyh, J., Paeschke, S., Mages, B., Michalski, D., Nowicki, M., Bechmann, I., & Winter, K. (2021). Classification of Microglial Morphological Phenotypes Using Machine Learning. Frontiers in Cellular Neuroscience, 15, 701673. https://doi.org/10.3389/fncel.2021.701673

Li, D., & Wu, M. (2021). Pattern recognition receptors in health and diseases. Signal Transduction and Targeted Therapy, 6(1), 291. https://doi.org/10.1038/s41392-021-00687-0

Li, Q., & Barres, B. A. (2018). Microglia and macrophages in brain homeostasis and disease. Nature Reviews Immunology, 18(4), 225–242. https://doi.org/10.1038/nri.2017.125

Liddelow, S. A., Guttenplan, K. A., Clarke, L. E., Bennett, F. C., Bohlen, C. J., Schirmer, L., Bennett, M. L., Münch, A. E., Chung, W. S., Peterson, T. C., Wilton, D. K., Frouin, A., Napier, B. A., Panicker, N., Kumar, M., Buckwalter, M. S., Rowitch, D. H., Dawson, V. L., Dawson, T. M., … Barres, B. A. (2017). Neurotoxic reactive astrocytes are induced by activated microglia. Nature, 541(7638), 481–487. https://doi.org/10.1038/nature21029

Liu, G. J., Nagarajah, R., Banati, R. B., & Bennett, M. R. (2009). Glutamate induces directed chemotaxis of microglia. European Journal of Neuroscience, 29(6), 1108–1118. https://doi.org/10.1111/j.1460-9568.2009.06659.x

Liu, R., Wang, J., Chen, Y., Collier, J. M., Capuk, O., Jin, S., Sun, M., Mondal, S. K., Whiteside, T. L., Stolz, D. B., Yang, Y., & Begum, G. (2022). NOX activation in reactive astrocytes regulates astrocytic LCN2 expression and neurodegeneration. Cell Death and Disease, 13(4), 371. https://doi.org/10.1038/s41419-022-04831-8

Loane, D. J., & Kumar, A. (2016). Microglia in the TBI brain: The good, the bad, and the dysregulated. Experimental Neurology, 275, 316–327. https://doi.org/10.1016/j.expneurol.2015.08.018

Lust, K., & Tanaka, E. M. (2019). A Comparative Perspective on Brain Regeneration in Amphibians and Teleost Fish. Developmental Neurobiology, 79(5), 424–436. https://doi.org/10.1002/dneu.22665

Maas, A. I. R., Menon, D. K., David Adelson, P. D., Andelic, N., Bell, M. J., Belli, A., Bragge, P., Brazinova, A., Büki, A., Chesnut, R. M., Citerio, G., Coburn, M., Jamie Cooper, D., Tamara Crowder, A., Czeiter, E., Czosnyka, M., Diaz-Arrastia, R., Dreier, J. P., Duhaime, A. C., … Zemek, R. (2017). Traumatic brain injury: Integrated approaches to improve

prevention, clinical care, and research. The Lancet Neurology, 16(12), 987–1048. https://doi.org/10.1016/S1474-4422(17)30371-X

Maas, A. I. R., Menon, D. K., Manley, G. T., Abrams, M., Åkerlund, C., Andelic, N., Aries, M., Bashford, T., Bell, M. J., Bodien, Y. G., Brett, B. L., Büki, A., Chesnut, R. M., Citerio, G., Clark, D., Clasby, B., Cooper, D. J., Czeiter, E., Czosnyka, M., … Zemek, R. (2022). Traumatic brain injury: progress and challenges in prevention, clinical care, and research. The Lancet Neurology, 21(11), 1004–1060. https://doi.org/10.1016/S1474-4422(22)00309-X

Maddhesiya, P., Lepko, T., Steiner-Mezzardi, A., Schwarz, V., Merl-Pham, J., Berger, F., Hauck, S. M. S. M., Ronfani, L., Bianchi, M., Masserdotti, G., Götz, M., & Ninkovic, J. (2023). Hmgb2 improves astrocyte to neuron conversion by increasing the chromatin accessibility of genes associated with neuronal maturation in a proneuronal factor-dependent manner. BioRxiv. https://doi.org/https://doi.org/10.1101/2023.08.31.555708

Mahmoud, S., Gharagozloo, M., Simard, C., & Gris, D. (2019). Astrocytes maintain glutamate homeostasis in the cns by controlling the balance between glutamate uptake and release. Cells, 8(2), 184. https://doi.org/10.3390/cells8020184

Main, B. S., Villapol, S., Sloley, S. S., Barton, D. J., Parsadanian, M., Agbaegbu, C., Stefos, K., McCann, M. S., Washington, P. M., Rodriguez, O. C., & Burns, M. P. (2018). Apolipoprotein E4 impairs spontaneous blood brain barrier repair following traumatic brain injury. Molecular Neurodegeneration, 13(1), 17. https://doi.org/10.1186/s13024-018-0249-5

Majdan, M., Plancikova, D., Maas, A., Polinder, S., Feigin, V., Theadom, A., Rusnak, M., Brazinova, A., & Haagsma, J. (2017). Years of life lost due to traumatic brain injury in Europe: A cross-sectional analysis of 16 countries. PLOS Medicine, 14(7), e1002331. https://doi.org/10.1371/journal.pmed.1002331

März, M., Schmidt, R., Rastegar, S., & Strahle, U. (2011). Regenerative response following stab injury in the adult zebrafish telencephalon. Developmental Dynamics, 240(9), 2221–2231. https://doi.org/10.1002/dvdy.22710

Mashkaryan, V., Siddiqui, T., Popova, S., Cosacak, M. I., Bhattarai, P., Brandt, K., Govindarajan, N., Petzold, A., Reinhardt, S., Dahl, A., Lefort, R., & Kizil, C. (2020). Type 1 Interleukin-4 Signaling Obliterates Mouse Astroglia in vivo but Not in vitro. Frontiers in Cell and Developmental Biology, 8, 114. https://doi.org/10.3389/fcell.2020.00114

Mason, M. R. J., Lieberman, A. R., & Anderson, P. N. (2003). Corticospinal neurons up-regulate a range of growth-associated genes following intracortical, but not spinal, axotomy. European Journal of Neuroscience, 18(4), 789–802. https://doi.org/10.1046/j.1460-9568.2003.02809.x

Masserdotti, G., Gillotin, S., Sutor, B., Drechsel, D., Irmler, M., Jørgensen, H. F., Sass, S., Theis, F. J., Beckers, J., Berninger, B., Guillemot, F., & Götz, M. (2015). Transcriptional Mechanisms of Proneural Factors and REST in Regulating Neuronal Reprogramming of Astrocytes. Cell Stem Cell, 17(1), 74–88. https://doi.org/10.1016/j.stem.2015.05.014

Mathiisen, T. M., Lehre, K. P., Danbolt, N. C., & Ottersen, O. P. (2010). The perivascular astroglial sheath provides a complete covering of the brain microvessels: An electron microscopic 3D reconstruction. Glia, 58(9), 1094–1103. https://doi.org/10.1002/glia.20990

Mattugini, N., Bocchi, R., Scheuss, V., Russo, G. L., Torper, O., Lao, C. L., & Götz, M. (2019). Inducing Different Neuronal Subtypes from Astrocytes in the Injured Mouse Cerebral Cortex. Neuron, 103(6), 1086–1095. https://doi.org/10.1016/j.neuron.2019.08.009

Mattugini, N., Merl-Pham, J., Petrozziello, E., Schindler, L., Bernhagen, J., Hauck, S. M., & Götz, M. (2018). Influence of white matter injury on gray matter reactive gliosis upon stab wound in the adult murine cerebral cortex. Glia, 66(8), 1644–1662. https://doi.org/10.1002/glia.23329

Mawhinney, M., Kulle, A., & Thanabalasuriar, A. (2022). From infection to repair: Understanding the workings of our innate immune cells. WIREs Mechanisms of Disease, 14(5), e1567. https://doi.org/10.1002/wsbm.1567

Mckee, A. C., & Daneshvar, D. H. (2015). The neuropathology of traumatic brain injury. Handbook of Clinical Neurology, 127, 45–66. https://doi.org/10.1016/B978-0-444-52892-6.00004-0

McKeon, R. J., Schreiber, R. C., Rudge, J. S., & Silver, J. (1991). Reduction of neurite outgrowth in a model of glial scarring following CNS injury is correlated with the expression of inhibitory molecules on reactive astrocytes. Journal of Neuroscience, 11(11), 3398–3411. https://doi.org/10.1523/JNEUROSCI.11-11-03398.1991

Metzemaekers, M., Gouwy, M., & Proost, P. (2020). Neutrophil chemoattractant receptors in health and disease: double-edged swords. Cellular and Molecular Immunology, 17(5), 433–450. https://doi.org/10.1038/s41423-020-0412-0

Michelsen, K. A., Acosta-Verdugo, S., Benoit-Marand, M., Espuny-Camacho, I., Gaspard, N., Saha, B., Gaillard, A., & Vanderhaeghen, P. (2015). Area-specific reestablishment of damaged circuits in the adult cerebral cortex by cortical neurons derived from mouse embryonic stem cells. Neuron, 85(5), 982–997. https://doi.org/10.1016/j.neuron.2015.02.001

Michinaga, S., & Koyama, Y. (2019). Dual roles of astrocyte-derived factors in regulation of blood-brain barrier function after brain damage. International Journal of Molecular Sciences, 20(3), 571. https://doi.org/10.3390/ijms20030571

Michinaga, S., & Koyama, Y. (2021). Pathophysiological responses and roles of astrocytes in traumatic brain injury. International Journal of Molecular Sciences, 22(12), 6418. https://doi.org/10.3390/ijms22126418

Ming, G. li, & Song, H. (2011). Adult Neurogenesis in the Mammalian Brain: Significant Answers and Significant Questions. Neuron, 70(4), 687–702. https://doi.org/10.1016/j.neuron.2011.05.001

Mira, R. G., Lira, M., & Cerpa, W. (2021). Traumatic Brain Injury: Mechanisms of Glial Response. Frontiers in Physiology, 12, 740939. https://doi.org/10.3389/fphys.2021.740939

Morgan, R., Kreipke, C. W., Roberts, G., Bagchi, M., & Rafols, J. A. (2007). Neovascularization following traumatic brain injury: Possible evidence for both angiogenesis and vasculogenesis. Neurological Research, 29(4), 375–381. https://doi.org/10.1179/016164107X204693

Morillas, A. G., Besson, V. C., & Lerouet, D. (2021). Microglia and neuroinflammation: What place for P2RY12? International Journal of Molecular Sciences, 22(4), 1636. https://doi.org/10.3390/ijms22041636

Morizawa, Y. M., Hirayama, Y., Ohno, N., Shibata, S., Shigetomi, E., Sui, Y., Nabekura, J., Sato, K., Okajima, F., Takebayashi, H., Okano, H., & Koizumi, S. (2017). Reactive astrocytes function as phagocytes after brain ischemia via ABCA1-mediated pathway. Nature Communications, 8(1), 1598. https://doi.org/10.1038/s41467-017-00037-1

Moyon, S., Dubessy, A. L., Aigrot, M. S., Trotter, M., Huang, J. K., Dauphinot, L., Potier, M. C., Kerninon, C., Parsadaniantz, S. M., Franklin, R. J. M., & Lubetzki, C. (2015). Demyelination causes adult CNS progenitors to revert to an immature state and express immune cues that support their migration. Journal of Neuroscience, 35(1), 4–20. https://doi.org/10.1523/JNEUROSCI.0849-14.2015

Müller, M., Carter, S., Hofer, M. J., & Campbell, I. L. (2010). Review: The chemokine receptor CXCR3 and its ligands CXCL9, CXCL10 and CXCL11 in neuroimmunity - A tale of conflict and conundrum. Neuropathology and Applied Neurobiology, 36(5), 368–387. https://doi.org/10.1111/j.1365-2990.2010.01089.x

Muñoz-Ballester, C., & Robel, S. (2023). Astrocyte-mediated mechanisms contribute to traumatic brain injury pathology. WIREs Mechanisms of Disease, 15(5), e1622. https://doi.org/10.1002/wsbm.1622

Myer, D. J., Gurkoff, G. G., Lee, S. M., Hovda, D. A., & Sofroniew, M. V. (2006). Essential protective roles of reactive astrocytes in traumatic brain injury. Brain, 129, 2761–2772. https://doi.org/10.1093/brain/awl165

Nasser, M., Bejjani, F., Raad, M., Abou-El-Hassan, H., Mantash, S., Nokkari, A., Ramadan, N., Kassem, N., Mondello, S., Hamade, E., Darwish, H., Zibara, K., & Kobeissy, F. (2016). Traumatic Brain Injury and Blood-Brain Barrier Cross-Talk. CNS and Neurological Disorders Drug Targets, 15(9), 1030–1044. https://doi.org/10.2174/1871527315666160815093525

Ng, S. Y., & Lee, A. Y. W. (2019). Traumatic Brain Injuries: Pathophysiology and Potential Therapeutic Targets. Frontiers in Cellular Neuroscience, 13, 528. https://doi.org/10.3389/fncel.2019.00528

Nguyen, H. T., Hurh, S., Nguyen, L. P., Nguyen, T. U., Park, H. K., Seong, J. Y., Lee, C. S., Ham, B. J., & Hwang, J. I. (2023). Functional Analysis of CXCR3 Splicing Variants and Their Ligands Using NanoBiT-Based Molecular Interaction Assays. Molecules and Cells, 46(5), 281–297. https://doi.org/10.14348/molcells.2023.2096

Ngwenya, L. B., & Danzer, S. C. (2019). Impact of traumatic brain injury on neurogenesis. Frontiers in Neuroscience, 12, 1014. https://doi.org/10.3389/fnins.2018.01014

Ninkovic, J., Mori, T., & Götz, M. (2007). Distinct modes of neuron addition in adult mouse neurogenesis. Journal of Neuroscience, 27(40), 10906–10911. https://doi.org/10.1523/JNEUROSCI.2572-07.2007

Niu, W., Zang, T., Smith, D. K., Vue, T. Y., Zou, Y., Bachoo, R., Johnson, J. E., & Zhang, C. L. (2015). SOX2 reprograms resident astrocytes into neural progenitors in the adult brain. Stem Cell Reports, 4(5), 780–794. https://doi.org/10.1016/j.stemcr.2015.03.006

Nogueira-Rodrigues, J., Leite, S. C., Pinto-Costa, R., Sousa, S. C., Luz, L. L., Sintra, M. A., Oliveira, R., Monteiro, A. C., Pinheiro, G. G., Vitorino, M., Silva, J. A., Simão, S., Fernandes, V. E., Provazník, J., Benes, V., Cruz, C. D., Safronov, B. V., Magalhães, A., Reis, C. A., … Sousa, M. M. (2022). Rewired glycosylation activity promotes scarless regeneration and functional recovery in spiny mice after complete spinal cord transection. Developmental Cell, 57(4), 440–450. https://doi.org/10.1016/j.devcel.2021.12.008

Nomiyama, H., Osada, N., & Yoshie, O. (2011). A family tree of vertebrate chemokine receptors for a unified nomenclature. Developmental and Comparative Immunology, 35(7), 705–715. https://doi.org/10.1016/j.dci.2011.01.019

Ohlig, S., Clavreul, S., Thorwirth, M., Simon-Ebert, T., Bocchi, R., Ulbricht, S., Kannayian, N., Rossner, M., Sirko, S., Smialowski, P., Fischer-Sternjak, J., & Götz, M. (2021). Molecular diversity of diencephalic astrocytes reveals adult astrogenesis regulated by Smad4. EMBO Journal, 40(21), e107532. https://doi.org/10.15252/embj.2020107532

Oliveira-Nascimento, L., Massari, P., & Wetzler, L. M. (2012). The role of TLR2 ininfection and immunity. Frontiers in Immunology, 3, 79. https://doi.org/10.3389/fimmu.2012.00079

Olson, J. K., & Miller, S. D. (2004). Microglia Initiate Central Nervous System Innate and Adaptive Immune Responses through Multiple TLRs. Journal of Immunology, 173(6), 3916–3924. https://doi.org/10.4049/jimmunol.173.6.3916

Omari, K. M., John, G. R., Sealfon, S. C., & Raine, C. S. (2005). CXC chemokine receptors on human oligodendrocytes: Implications for multiple sclerosis. Brain, 128, 1003–1015. https://doi.org/10.1093/brain/awh479

Oosenbrug, T., van de Graaff, M. J., Haks, M. C., van Kasteren, S., & Ressing, M. E. (2020). An alternative model for type I interferon induction downstream of human TLR2. Journal of Biological Chemistry, 295(42), 14325–14342. https://doi.org/10.1074/jbc.RA120.015283

Park, K., & Lee, S. J. (2020). Deciphering the star codings: astrocyte manipulation alters mouse behavior. Experimental and Molecular Medicine, 52(7), 1028–1038. https://doi.org/10.1038/s12276-020-0468-z

Parmar, M., & Björklund, A. (2020). From Skin to Brain: A Parkinson's Disease Patient Transplanted with His Own Cells. Cell Stem Cell, 27(1), 8–10. https://doi.org/10.1016/j.stem.2020.06.008

Patterson, Z. R., & Holahan, M. R. (2012). Understanding the neuroinflammatory response following concussion to develop treatment strategies. Frontiers in Cellular Neuroscience, 6, 58. https://doi.org/10.3389/fncel.2012.00058

Ponsford, J., Always, Y., & Gould, K. R. (2018). Epidemiology and natural history of psychiatric disorders after TBI. Journal of Neuropsychiatry and Clinical Neurosciences, 30(4), 262–270. https://doi.org/10.1176/appi.neuropsych.18040093

Powell, D., Tauzin, S., Hind, L. E., Deng, Q., Beebe, D. J., & Huttenlocher, A. (2017). Chemokine Signaling and the Regulation of Bidirectional Leukocyte Migration in Interstitial Tissues. Cell Reports, 19(8), 1572–1585. https://doi.org/10.1016/j.celrep.2017.04.078

Prinz, M., Jung, S., & Priller, J. (2019). Microglia Biology: One Century of Evolving Concepts. Cell, 179(2), 292–311. https://doi.org/10.1016/j.cell.2019.08.053

Puntambekar, S. S., Saber, M., Lamb, B. T., & Kokiko-Cochran, O. N. (2018). Cellular players that shape evolving pathology and neurodegeneration following traumatic brain injury. Brain, Behavior, and Immunity, 71, 9–17. https://doi.org/10.1016/j.bbi.2018.03.033

Purves, D., Augustine, G. J., Fitzpatrick, D., Hall, W. C., LaMantia, A.-S., Mooney, R. D., Platt, M. L., White, Leonard E.Purves, D., Augustine, G. J., Fitzpatrick, D., Hall, W. C., LaMantia, A.-S., Mooney, R. D., Platt, M. L., & White, L. E. (2018). Neuroscience (D. Purves, G. J. Augustine, D. Fitzpatrick, W. C. Hall, A.-S. LaMantia, R. D. Mooney, M. L. Platt, & L. E. White, Eds.; Sixth Edit). Oxford University Press.

Quraishe, S., Forbes, L. H., & Andrews, M. R. (2018). The extracellular environment of the CNS: Influence on plasticity, sprouting, and axonal regeneration after spinal cord injury. Neural Plasticity, 2018, 2952386. https://doi.org/10.1155/2018/2952386

Ramesh, G., Maclean, A. G., & Philipp, M. T. (2013). Cytokines and chemokines at the crossroads of neuroinflammation, neurodegeneration, and neuropathic pain. Mediators of Inflammation, 2013, 480739. https://doi.org/10.1155/2013/480739

Ransohoff, R. M. (2016). A polarizing question: Do M1 and M2 microglia exist. Nature Neuroscience, 19(8), 987–991. https://doi.org/10.1038/nn.4338

Reichelt, A. C., Hare, D. J., Bussey, T. J., & Saksida, L. M. (2019). Perineuronal Nets: Plasticity, Protection, and Therapeutic Potential. Trends in Neurosciences, 42(7), 458–470. https://doi.org/10.1016/j.tins.2019.04.003

Rice, R. A., Pham, J., Lee, R. J., Najafi, A. R., West, B. L., & Green, K. N. (2017). Microglial repopulation resolves inflammation and promotes brain recovery after injury. Glia, 65(6), 931–944. https://doi.org/10.1002/glia.23135

Rice, R. A., Spangenberg, E. E., Yamate-Morgan, H., Lee, R. J., Arora, R. P. S., Hernandez, M. X., Tenner, A. J., West, B. L., & Green, K. N. (2015). Elimination of microglia improves functional outcomes following extensive neuronal loss in the hippocampus. Journal of Neuroscience, 35(27), 9977–9989. https://doi.org/10.1523/JNEUROSCI.0336-15.2015

Robertson, A. L., Holmes, G. R., Bojarczuk, A. N., Burgon, J., Loynes, C. A., Chimen, M., Sawtell, A. K., Hamza, B., Willson, J., Walmsley, S. R., Anderson, S. R., Coles, M. C., Farrow, S. N., Solari, R., Jones, S., Prince, L. R., Irimia, D., Ed Rainger, G., Kadirkamanathan, V., … Renshaw, S. A. (2014). A zebrafish compound screen reveals modulation of neutrophil reverse migration as an anti-inflammatory mechanism.

Science Translational Medicine, 6(225), 225ra29. https://doi.org/10.1126/scitranslmed.3007672

Rostène, W., Kitabgi, P., & Parsadaniantz, S. M. (2007). Chemokines: a new class of neuromodulator? Nature Reviews Neuroscience, 8(11), 895–903. https://doi.org/10.1038/nrn2255

Roth, T. L., Nayak, D., Atanasijevic, T., Koretsky, A. P., Latour, L. L., & McGavern, D. B. (2014). Transcranial amelioration of inflammation and cell death after brain injury. Nature, 505(7482), 223–228. https://doi.org/10.1038/nature12808

Rothstein, J. D., Dykes-Hoberg, M., Pardo, C. A., Bristol, L. A., Jin, L., Kuncl, R. W., Kanai, Y., Hediger, M. A., Wang, Y., Schielke, J. P., & Welty, D. F. (1996). Knockout of glutamate transporters reveals a major role for astroglial transport in excitotoxicity and clearance of glutamate. Neuron, 16(3), 675–686. https://doi.org/10.1016/S0896-6273(00)80086-0

Rudd, J. M., Pulavendran, S., Ashar, H. K., Ritchey, J. W., Snider, T. A., Malayer, J. R., Marie, M., Chow, V. T. K., & Narasaraju, T. (2019). Neutrophils induce a novel chemokine receptors repertoire during influenza pneumonia. Frontiers in Cellular and Infection Microbiology, 9, 108. https://doi.org/10.3389/fcimb.2019.00108

Russo, M. V., & McGavern, D. B. (2016). Inflammatory neuroprotection following traumatic brain injury. Science, 353(6301), 783–785. https://doi.org/10.1126/science.aaf6260

Saha, B., Peron, S., Murray, K., Jaber, M., & Gaillard, A. (2013). Cortical lesion stimulates adult subventricular zone neural progenitor cell proliferation and migration to the site of injury. Stem Cell Research, 11(3), 965–977. https://doi.org/10.1016/j.scr.2013.06.006

Sanchez-Gonzalez, R., Koupourtidou, C., Lepko, T., Zambusi, A., Novoselc, K. T., Durovic, T., Aschenbroich, S., Schwarz, V., Breunig, C. T., Straka, H., Huttner, H. B., Irmler, M., Beckers, J., Wurst, W., Zwergal, A., Schauer, T., Straub, T., Czopka, T., Trümbach, D., … Ninkovic, J. (2022). Innate Immune Pathways Promote Oligodendrocyte Progenitor Cell Recruitment to the Injury Site in Adult Zebrafish Brain. Cells, 11(3), 520. https://doi.org/10.3390/cells11030520

Scheib, J., & Byrd-Jacobs, C. (2020). Zebrafish Astroglial Morphology in the Olfactory Bulb Is Altered With Repetitive Peripheral Damage. Frontiers in Neuroanatomy, 14, 4. https://doi.org/10.3389/fnana.2020.00004

Schiweck, J., Eickholt, B. J., & Murk, K. (2018). Important shapeshifter: Mechanisms allowing astrocytes to respond to the changing nervous system during development, injury and disease. Frontiers in Cellular Neuroscience, 12, 261. https://doi.org/10.3389/fncel.2018.00261

Semple, B. D., Bye, N., Rancan, M., Ziebell, J. M., & Morganti-Kossmann, M. C. (2010). Role of CCL2 (MCP-1) in traumatic brain injury (TBI): Evidence from severe TBI patients and CCL2-/- mice. Journal of Cerebral Blood Flow and Metabolism, 30(4), 769–782. https://doi.org/10.1038/jcbfm.2009.262

Shao, F., Wang, X., Wu, H., Wu, Q., & Zhang, J. (2022). Microglia and Neuroinflammation: Crucial Pathological Mechanisms in Traumatic Brain Injury-Induced Neurodegeneration. Frontiers in Aging Neuroscience, 14, 825086. https://doi.org/10.3389/fnagi.2022.825086

Shimizu, Y., Kiyooka, M., & Ohshima, T. (2021). Transcriptome Analyses Reveal IL6/Stat3 Signaling Involvement in Radial Glia Proliferation After Stab Wound Injury in the Adult Zebrafish Optic Tectum. Frontiers in Cell and Developmental Biology, 9, 668408. https://doi.org/10.3389/fcell.2021.668408

Siebert, J. R., Conta Steencken, A., & Osterhout, D. J. (2014). Chondroitin Sulfate Proteoglycans in the Nervous System: Inhibitors to Repair. BioMed Research International, 2014, 845323. https://doi.org/10.1155/2014/845323

Silver, J., & Miller, J. H. (2004). Regeneration beyond the glial scar. Nature Reviews Neuroscience, 5, 146–156. http://dx.doi.org/10.1038/nrn1326

Simon, C., Götz, M., & Dimou, L. (2011). Progenitors in the adult cerebral cortex: Cell cycle properties and regulation by physiological stimuli and injury. Glia, 59(6), 869–881. https://doi.org/10.1002/glia.21156

Simon, D. W., McGeachy, M. J., Baylr, H., Clark, R. S. B., Loane, D. J., & Kochanek, P. M. (2017). The far-reaching scope of neuroinflammation after traumatic brain injury. Nature Reviews Neurology, 13(9), 572. https://doi.org/10.1038/nrneurol.2017.13

Simons, M., & Nave, K.-A. (2015). Oligodendrocytes: Myelination and Axonal Support. Cold Spring Harbor Perspectives in Biology, 8(1), a020479. https://doi.org/10.1101/cshperspect.a020479

Sirko, S., Behrendt, G., Johansson, P. A., Tripathi, P., Costa, M., Bek, S., Heinrich, C., Tiedt, S., Colak, D., Dichgans, M., Fischer, I. R., Plesnila, N., Staufenbiel, M., Haass, C., Snapyan, M., Saghatelyan, A., Tsai, L. H., Fischer, A., Grobe, K., … Götz, M. (2013). Reactive glia in the injured brain acquire stem cell properties in response to sonic hedgehog glia. Cell Stem Cell, 12(4), 426–439. https://doi.org/10.1016/j.stem.2013.01.019

Sirko, S., Irmler, M., Gascón, S., Bek, S., Schneider, S., Dimou, L., Obermann, J., De Souza Paiva, D., Poirier, F., Beckers, J., Hauck, S. M., Barde, Y. A., & Götz, M. (2015). Astrocyte reactivity after brain injury-: The role of galectins 1 and 3. Glia, 63(12), 2340–2361. https://doi.org/10.1002/glia.22898

Soehnlein, O., & Lindbom, L. (2010). Phagocyte partnership during the onset and resolution of inflammation. Nature Reviews Immunology, 10(6), 427–439. https://doi.org/10.1038/nri2779

Sofroniew, M. V. (2015). Astrocyte barriers to neurotoxic inflammation. Nature Reviews Neuroscience, 16(5), 249–263. https://doi.org/10.1038/nrn3898

Sofroniew, M. V. (2020). Astrocyte Reactivity: Subtypes, States, and Functions in CNS Innate Immunity. Trends in Immunology, 41(9), 758–770. https://doi.org/10.1016/j.it.2020.07.004

Sofroniew, M. V., & Vinters, H. V. (2010). Astrocytes: Biology and pathology. Acta Neuropathologica, 119(1), 7–35. https://doi.org/10.1007/s00401-009-0619-8

Somjen, G. G. (2002). Ion regulation in the brain: Implications for pathophysiology. Neuroscientist, 8(3), 254–267. https://doi.org/10.1177/1073858402008003011

Song, I., & Dityatev, A. (2018). Crosstalk between glia, extracellular matrix and neurons. Brain Research Bulletin, 136, 101–108. https://doi.org/10.1016/j.brainresbull.2017.03.003

Sousa, C., Biber, K., & Michelucci, A. (2017). Cellular and molecular characterization of microglia: A unique immune cell population. Frontiers in Immunology, 8, 198. https://doi.org/10.3389/fimmu.2017.00198

Speicher, A. M., Wiendl, H., Meuth, S. G., & Pawlowski, M. (2019). Generating microglia from human pluripotent stem cells: Novel in vitro models for the study of neurodegeneration. Molecular Neurodegeneration, 14(1), 46. https://doi.org/10.1186/s13024-019-0347-z

Stirling, D. P., Liu, S., Kubes, P., & Yong, V. W. (2009). Depletion of Ly6G/Gr-1 leukocytes after spinal cord injury in mice alters wound healing and worsens neurological outcome. Journal of Neuroscience, 29(3), 753–764. https://doi.org/10.1523/JNEUROSCI.4918-08.2009

Stoker, T. B., Blair, N. F., & Barker, R. A. (2017). Neural grafting for Parkinson's disease: Challenges and prospects. Neural Regeneration Research, 12(3), 389–392. https://doi.org/10.4103/1673-5374.202935

Streeter, K. A., Sunshine, M. D., Brant, J. O., Sandoval, A. G. W., Maden, M., & Fuller, D. D. (2020). Molecular and histologic outcomes following spinal cord injury in spiny mice, Acomys cahirinus. Journal of Comparative Neurology, 528(9), 1535–1547. https://doi.org/10.1002/cne.24836

Stricker, E. M., Zigmond, M. J., Abercrombie, E. D., Berger, T. W., & Grace, A. a. (1990). Compensations after lesions of central dopaminergic neurons: some clinical and basic implications. Trends in Neurosciences, 13(7), 290–296. https://doi.org/10.1016/0166-2236(90)90112-n

Susarla, B. T. S., Villapol, S., Yi, J. H., Geller, H. M., & Symes, A. J. (2014). Temporal patterns of cortical proliferation of glial cell populations after traumatic brain injury in mice. ASN Neuro, 6(3), 159–170. https://doi.org/10.1042/AN20130034

Sweeney, M. D., Sagare, A. P., & Zlokovic, B. V. (2018). Blood-brain barrier breakdown in Alzheimer disease and other neurodegenerative disorders. Nature Reviews Neurology, 14(3), 133–150. https://doi.org/10.1038/nrneurol.2017.188

Tanaka, R., Komine-Kobayashi, M., Mochizuki, H., Yamada, M., Furuya, T., Migita, M., Shimada, T., Mizuno, Y., & Urabe, T. (2003). Migration of enhanced green fluorescent protein expressing bone marrow-derived microglia/macrophage into the mouse brain following permanent focal ischemia. Neuroscience, 117(3), 531–539. https://doi.org/10.1016/S0306-4522(02)00954-5

Tang, S. C., Arumugam, T. V., Xu, X., Cheng, A., Mughal, M. R., Dong, G. J., Lathia, J. D., Siler, D. A., Chigurupati, S., Ouyang, X., Magnus, T., Camandola, S., & Mattson, M. P. (2007). Pivotal role for neuronal Toll-like receptors in ischemic brain injury and functional

deficits. Proceedings of the National Academy of Sciences of the United States of America, 104(34), 13798–13803. https://doi.org/10.1073/pnas.0702553104

Todd, B. P., Chimenti, M. S., Luo, Z., Ferguson, P. J., Bassuk, A. G., & Newell, E. A. (2021). Traumatic brain injury results in unique microglial and astrocyte transcriptomes enriched for type I interferon response. Journal of Neuroinflammation, 18(1), 151. https://doi.org/10.1186/s12974-021-02197-w

Van Houcke, J., Mariën, V., Zandecki, C., Vanhunsel, S., Moons, L., Ayana, R., Seuntjens, E., & Arckens, L. (2021). Aging impairs the essential contributions of non-glial progenitors to neurorepair in the dorsal telencephalon of the Killifish Nothobranchius furzeri. Aging Cell, 20(9), e13464. https://doi.org/10.1111/acel.13464

Van Landeghem, F. K. H., Weiss, T., Oehmichen, M., & Von Deimling, A. (2006). Decreased expression of glutamate transporters in astrocytes after human traumatic brain injury. Journal of Neurotrauma, 23(10), 1518–1528. https://doi.org/10.1089/neu.2006.23.1518

Van Raemdonck, K., Van den Steen, P. E., Liekens, S., Van Damme, J., & Struyf, S. (2015). CXCR3 ligands in disease and therapy. Cytokine and Growth Factor Reviews, 26(3), 311–327. https://doi.org/10.1016/j.cytogfr.2014.11.009

Van Wageningen, T. A., Vlaar, E., Kooij, G., Jongenelen, C. A. M., Geurts, J. J. G., & Van Dam, A. M. (2019). Regulation of microglial TMEM119 and P2RY12 immunoreactivity in multiple sclerosis white and grey matter lesions is dependent on their inflammatory environment. Acta Neuropathologica Communications, 7(1), 206. https://doi.org/10.1186/s40478-019-0850-z

Vasan, L., Park, E., David, L. A., Fleming, T., & Schuurmans, C. (2021). Direct Neuronal Reprogramming: Bridging the Gap Between Basic Science and Clinical Application. Frontiers in Cell and Developmental Biology, 9, 681087. https://doi.org/10.3389/fcell.2021.681087

Verkhratsky, A., & Nedergaard, M. (2018). Physiology of astroglia. Physiological Reviews, 98(1), 239–389. https://doi.org/10.1152/physrev.00042.2016

Vidal-Itriago, A., Radford, R. A. W., Aramideh, J. A., Maurel, C., Scherer, N. M., Don, E. K., Lee, A., Chung, R. S., Graeber, M. B., & Morsch, M. (2022). Microglia morphophysiological diversity and its implications for the CNS. Frontiers in Immunology, 13, 997786. https://doi.org/10.3389/fimmu.2022.997786

Villapol, S., Loane, D. J., & Burns, M. P. (2017). Sexual dimorphism in the inflammatory response to traumatic brain injury. Glia, 65(9), 1423–1438. https://doi.org/10.1002/glia.23171

von Bartheld, C. S., Bahney, J., & Herculano-Houzel, S. (2016). The search for true numbers of neurons and glial cells in the human brain: A review of 150 years of cell counting. Journal of Comparative Neurology, 524(18), 3865–3895. https://doi.org/10.1002/cne.24040

von Streitberg, A., Jäkel, S., Eugenin von Bernhardi, J., Straube, C., Buggenthin, F., Marr, C., & Dimou, L. (2021). NG2-Glia Transiently Overcome Their Homeostatic Network and

Contribute to Wound Closure After Brain Injury. Frontiers in Cell and Developmental Biology, 9, 662056. https://doi.org/10.3389/fcell.2021.662056

Walther, C., & Gruss, P. (1991). Pax-6, a murine paired box gene, is expressed in the developing CNS. Development, 113(4), 1435–1449. https://doi.org/10.1242/dev.113.4.1435

Wang, J. (2018). Neutrophils in tissue injury and repair. Cell and Tissue Research, 371(3), 531–539. https://doi.org/10.1007/s00441-017-2785-7

Wang, J. Q., Gao, M. Y., Gao, R., Zhao, K. H., Zhang, Y., & Li, X. (2023). Oligodendrocyte lineage cells: Advances in development, disease, and heterogeneity. Journal of Neurochemistry, 164(4), 468–480. https://doi.org/10.1111/jnc.15728

Wang, L. L., Su, Z., Tai, W., Zou, Y., Xu, X. M., & Zhang, C. L. (2016). The p53 Pathway Controls SOX2-Mediated Reprogramming in the Adult Mouse Spinal Cord. Cell Reports, 17(3), 891–903. https://doi.org/10.1016/j.celrep.2016.09.038

Wang, W., Li, Y., Ma, F., Sheng, X., Chen, K., Zhuo, R., Wang, C., Zheng, H., Zhang, Y., Bu, G., Chen, X.-F., & Zhong, L. (2023). Microglial repopulation reverses cognitive and synaptic deficits in an Alzheimer's disease model by restoring BDNF signaling. Brain, Behavior, and Immunity, 113, 275–288. https://doi.org/https://doi.org/10.1016/j.bbi.2023.07.011

Weber, J. T. (2012). Altered calcium signaling following traumatic brain injury. Frontiers in Pharmacology, 3, 60. https://doi.org/10.3389/fphar.2012.00060

Weston, R. M., Jones, N. M., Jarrott, B., & Callaway, J. K. (2007). Inflammatory cell infiltration after endothelin-1-induced cerebral ischemia: Histochemical and myeloperoxidase correlation with temporal changes in brain injury. Journal of Cerebral Blood Flow and Metabolism, 27(1), 100–114. https://doi.org/10.1038/sj.jcbfm.9600324

Wilhelmsson, U., Li, L., Pekna, M., Berthold, C. H., Blom, S., Eliasson, C., Renner, O., Bushong, E., Ellisman, M., Morgan, T. E., & Pekny, M. (2004). Absence of glial fibrillary acidic protein and vimentin prevents hypertrophy of astrocytic processes and improves post-traumatic regeneration. Journal of Neuroscience, 24(21), 5016–5021. https://doi.org/10.1523/JNEUROSCI.0820-04.2004

Williams, C. G., Lee, H. J., Asatsuma, T., Vento-Tormo, R., & Haque, A. (2022). An introduction to spatial transcriptomics for biomedical research. Genome Medicine, 14(1), 68. https://doi.org/10.1186/s13073-022-01075-1

Wofford, K. L., Loane, D. J., & Cullen, D. K. (2019). Acute drivers of neuroinflammation in traumatic brain injury. Neural Regeneration Research, 14(9), 1481–1489. https://doi.org/10.4103/1673-5374.255958

Wu, N., Sun, X., Zhou, C., Yan, J., & Cheng, C. (2023). Neuroblasts migration under control of reactive astrocyte-derived BDNF: a promising therapy in late neurogenesis after traumatic brain injury. Stem Cell Research and Therapy, 14(1), 2. https://doi.org/10.1186/s13287-022-03232-0

Wu, Z., Nicoll, M., & Ingham, R. J. (2021). AP-1 family transcription factors: a diverse family of proteins that regulate varied cellular activities in classical hodgkin lymphoma and

ALK+ ALCL. Experimental Hematology and Oncology, 10(1), 4. https://doi.org/10.1186/s40164-020-00197-9

Xiao, R., Shen, S., Yu, Y., Pan, Q., Kuang, R., & Huang, H. (2019). TMSB10 promotes migration and invasion of cancer cells and is a novel prognostic marker for renal cell carcinoma. International Journal of Clinical and Experimental Pathology, 12(1), 305–312.

Xing, L. Y., Yang, T., Cui, S. Sen, & Chen, G. (2019). Connexin hemichannels in astrocytes: Role in CNS disorders. Frontiers in Molecular Neuroscience, 12, 23. https://doi.org/10.3389/fnmol.2019.00023

Xiong, Y., Mahmood, A., & Chopp, M. (2018). Current understanding of neuroinflammation after traumatic brain injury and cell-based therapeutic opportunities. Chinese Journal of Traumatology, 21(3), 137–151. https://doi.org/10.1016/j.cjtee.2018.02.003

Xu, S., Mei, S., Lu, J., Wu, H., Dong, X., Shi, L., Zhou, J., & Zhang, J. (2021). Transcriptome Analysis of Microglia Reveals That the TLR2/IRF7 Signaling Axis Mediates Neuroinflammation After Subarachnoid Hemorrhage. Frontiers in Aging Neuroscience, 13, 645649. https://doi.org/10.3389/fnagi.2021.645649

Xu, X., Yin, D., Ren, H., Gao, W., Li, F., Sun, D., Wu, Y., Zhou, S., Lyu, L., Yang, M., Xiong, J., Han, L., Jiang, R., & Zhang, J. (2018). Selective NLRP3 inflammasome inhibitor reduces neuroinflammation and improves long-term neurological outcomes in a murine model of traumatic brain injury. Neurobiology of Disease, 117, 15–27. https://doi.org/10.1016/j.nbd.2018.05.016

Youle, R. J., & Strasser, A. (2008). The BCL-2 protein family: Opposing activities that mediate cell death. Nature Reviews Molecular Cell Biology, 9(1), 47–59. https://doi.org/10.1038/nrm2308

Yu, G. L., Zhang, Y., & Ning, B. (2021). Reactive Astrocytes in Central Nervous System Injury: Subgroup and Potential Therapy. Frontiers in Cellular Neuroscience, 15, 792764. https://doi.org/10.3389/fncel.2021.792764

Yu, Z. Q., & Zha, J. H. (2012). Genetic ablation of toll-like receptor 2 reduces secondary brain injury caused by cortical contusion in mice. Annals of Clinical and Laboratory Science, 42(1), 26–33.

Zamanian, J. L., Xu, L., Foo, L. C., Nouri, N., Zhou, L., Giffard, R. G., & Barres, B. A. (2012). Genomic analysis of reactive astrogliosis. Journal of Neuroscience, 32(18), 6391–6410. https://doi.org/10.1523/JNEUROSCI.6221-11.2012

Zambusi, A., & Ninkovic, J. (2020). Regeneration of the central nervous system-principles from brain regeneration in adult zebrafish. World Journal of Stem Cells, 12(1), 8–24. https://doi.org/10.4252/wjsc.v12.i1.8

Zambusi, A., Novoselc, K. T., Hutten, S., Kalpazidou, S., Koupourtidou, C., Schieweck, R., Aschenbroich, S., Silva, L., Yazgili, A. S., van Bebber, F., Schmid, B., Möller, G., Tritscher, C., Stigloher, C., Delbridge, C., Sirko, S., Günes, Z. I., Liebscher, S., Schlegel, J., … Ninkovic, J. (2022). TDP-43 condensates and lipid droplets regulate the reactivity of microglia and regeneration after traumatic brain injury. Nature Neuroscience, 25(12), 1608–1625. https://doi.org/10.1038/s41593-022-01199-y

Zhang, X., Wang, D., Zhang, B., Zhu, J., Zhou, Z., & Cui, L. (2020). Regulation of microglia by glutamate and its signal pathway in neurodegenerative diseases. Drug Discovery Today, 25(6), 1074–1085. https://doi.org/10.1016/j.drudis.2020.04.001

Zhao, C., Liu, X., Liu, L., Li, J., Liu, X., Tao, W., Wang, D., & Wei, J. (2023). Smoothened mediates medaka spermatogonia proliferation via Gli1–Rgcc–Cdk1 axis. Biology of Reproduction, 109(5), 772–784. https://doi.org/10.1093/biolre/ioad090

Zheng, R. Z., Lee, K. Y., Qi, Z. X., Wang, Z., Xu, Z. Y., Wu, X. H., & Mao, Y. (2022). Neuroinflammation Following Traumatic Brain Injury: Take It Seriously or Not. Frontiers in Immunology, 13, 855701. https://doi.org/10.3389/fimmu.2022.855701

Zhou, Y., Shao, A., Yao, Y., Tu, S., Deng, Y., & Zhang, J. (2020). Dual roles of astrocytes in plasticity and reconstruction after traumatic brain injury. Cell Communication and Signaling, 18(1), 62. https://doi.org/10.1186/s12964-020-00549-2

Zhou, Y.-Q., Liu, D.-Q., Chen, S.-P., Sun, J., Zhou, X.-R., Xing, C., Ye, D.-W., & Tian, Y.-K. (2019). The Role of CXCR3 in Neurological Diseases. Current Neuropharmacology, 17(2), 142–150. https://doi.org/10.2174/1570159x15666171109161140

Zigmond, M., Bloom, F., Landis, S., Roberts, J., & Squire, L. (1999). Fundamental Neuroscience. Academic Press.

Zlotnik, A., & Yoshie, O. (2012). The chemokine superfamily revisited. Immunity, 36(5), 705–716. https://doi.org/10.1016/j.immuni.2012.05.008

CURRICULUM VITAE

PUBLICATIONS

Bai X, Zhao N, Koupourtidou C, Fang LP, Schwarz V, Caudal LC, Zhao R, Hirrlinger J, Walz W, Bian S, Huang W, Ninkovic J, Kirchhoff F, Scheller A. **In the mouse cortex, oligodendrocytes regain a plastic capacity, transforming into astrocytes after acute injury.** Dev Cell. 2023 Jul 10;58(13):1153-1169.e5. doi: 10.1016/j.devcel.2023.04.016.

Sanchez-Gonzalez R, Koupourtidou C, Lepko T, Zambusi A, Novoselc KT, Durovic T, Aschenbroich S, Schwarz V, Breunig CT, Straka H, Huttner HB, Irmler M, Beckers J, Wurst W, Zwergal A, Schauer T, Straub T, Czopka T, Trümbach D, Götz M, Stricker SH, Ninkovic J. **Innate Immune Pathways Promote Oligodendrocyte Progenitor Cell Recruitment to the Injury Site in Adult Zebrafish Brain.** Cells. 2022 Feb 2;11(3):520. doi: 10.3390/cells11030520.

Dubois CJ*, Cardoit L*, Schwarz V*, Markkanen M, Airaksinen MS, Uvarov P, Simmers J, Thoby-Brisson M. **Role of the K+-Cl- Cotransporter KCC2a Isoform in Mammalian Respiration at Birth.** eNeuro. 2018 Oct 23;5(5):ENEURO.0264-18.2018. doi: 10.1523/ENEURO.0264-18.2018.

* These authors contributed equally to the manuscript

EIDESSTATTLICHE VERSICHERUNG/AFFIDAVIT

DECLARATION OF AUTHOR CONTRIBUTION

Study I: **Innate Immune Pathways Promote Oligodendrocyte Progenitor Cell Recruitment to the Injury Site in Adult Zebrafish Brain.** *Cells* (2022). Rosario Sanchez-Gonzalez, Christina Koupourtidou, Tjasa Lepko, Alessandro Zambusi, Klara Tereza Novoselc, Tamara Durovic, Sven Aschenbroich, Veronika Schwarz, Christopher T. Breunig, Hans Straka, Hagen B. Huttner, Martin Irmler, Johannes Beckers, Wolfgang Wurst, Andreas Zwergal, Tamas Schauer, Tobias Straub, Tim Czopka, Dietrich Trümbach, Magdalena Götz, Stefan H. Stricker and Jovica Ninkovic.

Author contribution in detail:

Conceptualization, R.S.-G., J.N. and M.G.; methodology, R.S.-G., J.N., C.K., T.L., A.Z. (Alessandro Zambusi), K.T.N., T.D., M.I., S.A., V.S., C.T.B. and S.H.S.; software, D.T. and W.W.; formal analysis, T.S. (Tamas Schauer), R.S.-G., T.S. (Tobias Straub), M.I., J.B. and J.N.; resources, H.S., H.B.H., A.Z. (Andreas Zwergal) and T.C.; writing—original draft preparation, R.S.-G. and J.N.; writing—review and editing, all authors. All authors have read and agreed to the published version of the manuscript.

For this study, I was involved in FACS sorting of Olig2:dsRed^{+} cells and the RNAseq library preparation from these FACS-sorted cells. Furthermore, I participated in paper editing and reviewing.

Confirmation of author contributions:

Prof. Dr. Jovica Ninković	Dr. Rosario Sanchez-Gonzalez	Veronika Schwarz
……	……	……

Study II: Shared inflammatory glial cell signature after brain injury, revealed by spatial, temporal and cell-type-specific profiling of the murine cerebral cortex. Christina Koupourtidou*, **Veronika Schwarz***, Hananeh Aliee, Simon Frerich, Judith Fischer-Sternjak, Riccardo Bocchi, Tatiana Simon-Ebert, Martin Dichgans, Magdalena Götz, Fabian Theis, Jovica Ninkovic. *Subsequent to the submission of this dissertation, the manuscript has been accepted for publication in Nature Communications.*

* These authors contributed equally to the manuscript

Author contribution in detail:

C.K., V.S. and J.N. conceived the project and experiments. C.K., V.S., J.F.S., T.S.E. and R.B. performed experiments and analyzed data. C.K., H.A. and S.F. performed the bioinformatic analyses C.K., V.S. and J.N. wrote the manuscript with input from all authors. J.N., M.G., M.D. and F.J.T. supervised research and acquired funding.

For this study, I performed all animal experiments and downstream analyses to investigate the impact of TLR1/2 and CXCR3 signaling on glial reactivity. Furthermore, I was involved in all animal experiments related to the transcriptomic studies of this manuscript and I assisted in the generation of the scRNA-seq and stRNA-seq data sets. Moreover, I was involved in the writing and editing process of this manuscript.

Confirmation of author contributions:

Prof. Dr. Jovica Ninković	Dr. Christina Koupourtidou	Veronika Schwarz
……..	……..	……..

Study III: **In the mouse cortex, oligodendrocytes regain a plastic capacity, transforming into astrocytes after acute injury.** *Developmental Cell* (2023). Xianshu Bai, Na Zhao, Christina Koupourtidou, Li-Pao Fang, Veronika Schwarz, Laura C. Caudal, Renping Zhao, Johannes Hirrlinger, Wolfgang Walz, Shan Bian, Wenhui Huang, Jovica Ninkovic, Frank Kirchhoff, and Anja Scheller.

Author contribution in detail:

X.B., J.H., F.K., and A.S. conceived the project. X.B., C.K., V.S., and A.S. performed surgeries. X.B. and L.-P.F. performed pharmacological intervention. X.B. performed 2P-LSM imaging and data analysis. X.B., L.C.C., and R.Z. performed quantitative real-time PCR and corresponding data analysis. N.Z. performed electrophysiology and corresponding data analysis. X.B., W.H., and A.S. performed immunostaining. C.K. and V.S. performed scRNA-seq and data analysis with J.N.. J.H. and S.B. provided materials. W.W. introduced the PVD model. X.B., N.Z., C.K., V.S., L.C.C., R.Z., and A.S. analyzed data. X.B., F.K., and A.S. wrote the manuscript with comments of other authors.

For this study, I assisted in all animal experiments related to the transcriptomic study and the generation of the scRNA-seq data sets.

Confirmation of author contributions:

Prof. Dr. Jovica Ninković	Dr. Xianshu Bai	Veronika Schwarz
…….	…….	…….

Study IV: **Hmgb2 improves astrocyte to neuron conversion by increasing the chromatin accessibility of genes associated with neuronal maturation in a proneuronal factor-dependent manner.** Priya Maddhesiya*, Tjasa Lepko*, Andrea Steiner-Mezzardi, Veronika Schwarz, Juliane Merl-Pham, Finja Berger, Stefanie M. Hauck, Lorenza Ronfani, Marco Bianchi, Giacomo Masserdotti, Magdalena Götz and Jovica Ninkovic. *This paper has been submitted to Genome Biology.*

* These authors contributed equally to the manuscript

Author contribution in detail:

P.M., T.L. and J. N. conceived the project and designed experiments. A.S.-M., V.S., F.B., and J.N. performed experiments. J. M.-P. and S.M.H. analyzed proteome. L.R. and M. B. provided Hmgb2 KO animals. P. M. and J.N. wrote the manuscript with input from all authors.

For this study, I assisted in the RNAseq library preparation. Furthermore, I participated in paper editing and reviewing.

Confirmation of author contributions:

Prof. Dr. Jovica Ninković	Priya Maddhesiya	Dr. Tjaša Lepko
……..	……..	……..

Veronika Schwarz

……..

ACKNOWLEDGMENTS

First and foremost, I would like to express my deepest gratitude to my supervisor, Jovica, whose expertise, guidance, and enthusiasm have been invaluable throughout the last few years. Thank you for always giving me the feeling that I could talk to as an equal and for always giving me the freedom and support I needed in my research. You were always open to new ideas, and I am incredibly grateful to you for allowing me to realize my own scientific ideas. You've challenged me to grow as a person and scientist and supported me in good and bad times, and I thank you so much for that.

I extend my gratitude to my TAC members, collaborators, and all the people in the Götz department for their valuable input throughout all these years and to the GSN for all the support provided during my Ph.D. Furthermore, I want to express gratefulness to PD Dr. Florence Bareyre and Dr. Mónica M. Sousa for reviewing my dissertation.

Special thanks to my colleague, my partner in crime, and close friend Christina. You have accompanied me on my scientific journey from the beginning, and I could not have wished for a better collaborator. Thanks for all the good times we've spent together, your valuable words, your support, and the encouragement you have given me so selflessly during more difficult times. I'm happy that our paths have crossed, and I'm sincerely grateful for your friendship.

A heartfelt thank you to my dearest friend Finja. I'm deeply thankful to have met you and to call you my friend. Thanks for all the great times and memorable experiences we have shared over the last years in and outside the lab and for always being there for me. I can't wait to raise a glass of Chocosecco to us!

A big thank you to all my current and former colleagues from the Ninković group. I especially want to thank the people I have spent most of my time in the lab: Ale, Sven, Sofia, Klara, Priya, Xenia, Viviane, Anita, and Tamara. I could not have asked for better colleagues. You made even the most stressful periods fun and made the workplace a place to come to with a smile. Thanks also to Rico, Suzan, and Patty for all our discussions and your valuable advice.

I would like to thank my family and all my friends for their unwavering support, encouragement, and understanding throughout this academic endeavor. You have always believed in me, and I am truly thankful for that. Special thanks to my grandma for always listening to me, providing me with lunch packages whenever needed, and lighting countless candles for me these past few years.

My greatest thanks go to my better half, Lars. Thank you for your tireless support, encouraging words, and unconditional love. I couldn't have done any of this without you. I look forward to our new chapter together and can't wait to see what our future holds.

Lastly, I would like to thank my uncle Hans. You have been a true inspiration for me and so many other people. Your passion and joy for science were contagious and clearly infected me. Thanks for all the support you have given me throughout all those years. You will never be forgotten.